Physics of Atomic Nuclei, Vol. 64, No. 2, 2001, pp. 153–168. Translated from Yadernaya Fizika, Vol. 64, No. 2, 2001, pp. 195–210.

NUCLEI
Experiment

Direct Experimental Estimate of Parameters That Determine the Cascade Gamma Decay of Compound States of Heavy Nuclei

E. V. Vasilieva, A. M. Sukhovoj, and V. A. Khitrov

Frank Laboratory of Neutron Physics, Joint Institute for Nuclear Research, Dubna, Moscow oblast, 141980 Russia

Received August 9, 1999; in final form, April 24, 2000

Abstract—A method is proposed for simultaneously determining the interval of the most probable values of the density of levels excited in the radiative capture of slow neutrons and the sum of radiative $E1$ and $M1$ strength functions in the excitation-energy interval extending nearly up to the neutron binding energy. Experimental data on the intensities of two-step photon cascades between the compound state and a given low-lying level of the nucleus being studied are analyzed together with the total radiative widths of neutron resonances. Such an analysis can be performed for nuclei having an arbitrary level density, including deformed ones. The resulting data demonstrate that there are significant deviations from the predictions of commonly accepted level-density models—for example, the Fermi gas model—and specify the range of nuclei and the regions of their excitation energies where a further experimental investigation can furnish new important information about the properties of nuclear matter. © *2001 MAIK "Nauka/Interperiodica".*

1. INTRODUCTION

The total radiative width of neutron resonances, Γ_γ, and the spectra of emitted photons [including the measured intensities $I_{\gamma\gamma}$ of two-step photon cascades that are excited in $(n, 2\gamma)$ reactions and which proceed to given low-lying levels] are determined by the level-density and radiative-strength-function values averaged over the entire region of excitation energies below the neutron binding energy, as well as by the distribution of random deviations from these averaged values. The experimental data on Γ_γ and $I_{\gamma\gamma}$ were obtained to within 10%. However, level densities and radiative strength functions can be extracted from the experimental values of Γ_γ and $I_{\gamma\gamma}$ only by invoking some model concepts; as a consequence, the accuracy of the results obtained in this way is poorly controllable. For example, the level density can be extracted from the spectra of products of nuclear reactions only by using realistic models of the reactions being studied. The situation around radiative strength functions is even less satisfactory. Apart from a direct determination of these quantities from data on $(n, \gamma\alpha)$ reactions in [1] and the estimates obtained in [2, 3] for the radiative strength functions on the basis of the spectra of two-step photon cascades for three even–odd compound nuclei, there are no reliable experimental data on radiative strength functions in the excitation-energy interval $0 < E_{\rm exc} < B_n$, where B_n is the neutron binding energy, although some information about the lifetimes of a number of excited states below B_n is available. Indirectly, the existing model assumptions have been tested many times. This was done, for example, by comparing the calculated and measured results for total radiative widths [4], total intensities of two-step photon cascades [5], and the spectra of emitted gamma rays and cross sections for neutron–nucleus interactions [6].

The main disadvantage of the methods used previously to determine level densities and radiative strength functions is that these methods give no way to accomplish a reasonable variation of the underlying models with the aim of fitting the results of the relevant calculations to experimental data.

Although the measured parameters of any nuclear reaction are determined completely by the relevant level densities and radiative strength functions and by the probability of the emission of all reaction products, the inverse problem cannot be solved unambiguously in general. As a matter of fact, the currently adopted theoretical ideas of processes occurring in nuclei at excitation energies above a few MeV have not yet been developed to such an extent that would make it possible to calculate the parameters of nuclei to the degree of precision as high as that achieved experimentally. By way of example, we indicate that Γ_γ and $I_{\gamma\gamma}$ values calculated according to currently adopted models of level densities and radiative strength functions (these models are usually used to analyze experimental data) may be markedly distinct from the corresponding experimental values. Above all, this is so for nuclei from the region of the $4S$ resonance of the neutron strength function, which present the gravest difficulties for experimental studies.

These discrepancies highlight the inadequacy of simple models currently used to describe level densities and radiative strength functions. An analysis of the possible systematic effects that could be operative in determining $I_{\gamma\gamma}$ revealed no grounds to attribute the observed discrepancies to experimental errors alone [7]. In view of this, it is required to find a direct way to deduce reli-

able experimental information about level densities and about radiative strength functions over as wide an excitation-energy interval as is possible for any nuclei. Experiments that would serve this goal are possible with modern multidetector systems used together with the efficient procedure developed at the Frank Laboratory of Neutron Physics (Joint Institute for Nuclear Physics, Dubna) for extracting information from $\gamma\gamma$ coincidences.

But even at present, comprehensive and reliable information about excitation regions where there are discrepancies with model ideas of level densities and radiative strength functions can be obtained by analyzing accumulated data on the intensities of two-step photon cascades.

2. EXPERIMENTAL DATA

Presently, the distributions of the intensities of two-step photon cascades in 40 nuclei from the region $114 \leq A \leq 200$—^{114}Cd, $^{124, 125}$Te, ^{128}I, $^{135, 137, 138, 139}$Ba, ^{140}La, $^{143, 144, 146}$Nd, ^{150}Sm, $^{156, 158}$Gd, ^{160}Tb, $^{163, 164, 165}$Dy, ^{166}Ho, ^{168}Er, ^{170}Tm, $^{174, 175, 177}$Yb, $^{176, 177}$Lu, $^{178, 179, 180, 181}$Hf, ^{182}Ta, $^{183, 187}$W, $^{188, 190}$Os, ^{192}Ir, ^{196}Pt, ^{198}Au, and ^{200}Hg—have been obtained and analyzed in experiments performed with reactor beams in Dubna, Riga, and Řež.

The form of the energy dependence of the probability of two-step photon cascades terminating at a group of low-lying final states was determined (actually, the result is summed over a 0.5-MeV interval of excitation energies of intermediate levels) for 29 of them (see, for example, [8]).

Usually, the entire sum of the observed intensities saturates 20–50% (about 100% in some nuclei) of the total intensity of primary transitions in neutron-resonance decay. Therefore, an analysis of $I_{\gamma\gamma}$ as a function of the energy of an intermediate level gives a rather clear idea of the general regularities in the development of the process through which a compound state (neutron resonance) deexcites in any nucleus having a large density of states in a given interval ΔE of its excitation energies.

An extrapolation of conclusions drawn from the analysis of $I_{\gamma\gamma}$ to the case where the problem to be solved consists in constructing a complete description of (n, γ) reactions may prove to be incorrect in two cases: (i) if the process of a cascade gamma decay of a compound state (neutron resonance) greatly depends on the structure of its wave function (that such a dependence is in fact exists is suggested by a strong correlation between the ratio of the measured and the calculated cascade intensity, on one hand, and the reduced neutron width of the compound state in an even–odd compound nucleus, on the other hand; see [5]) and (ii) if the radiative strength functions for experimentally unobservable secondary transitions of two-step photon cascades to final levels at $E_f > 1$ MeV differ significantly from analogous quantities for cascades that we have already studied [for example, there are no a priori reasons for ruling out the possibility that the radiative strength function for secondary transitions to high-lying levels (E_f in excess of 1 to 2 MeV) is less or is greater than a similar quantity for a transition that is characterized by the same change in energy, but which terminates at a low-lying state ($E_f < 1$ MeV)—the situation here can be clarified only experimentally].

In any case, the intensity $I_{\gamma\gamma}$ of two-step photon cascades (here, this is the probability of a cascade involving transitions whose energies lie, in an event of compound-nucleus decay, in preset intervals) is determined by the ratios of the widths $\Gamma_{\lambda i}$ and Γ_{if} with respect to the primary and the secondary transition to the total widths $\Gamma_\lambda = \langle\Gamma_{\lambda i}\rangle m_{\lambda i}$ and $\Gamma_i = \langle\Gamma_{if}\rangle m_{if}$ of the compound and the intermediate state of the cascade,

$$I_{\gamma\gamma} = \sum_{J,\pi}(\Gamma_{\lambda i}/\Gamma_\lambda) \times n_{\lambda i} \times (\Gamma_{if}/\Gamma_i); \quad (1)$$

that is, it is determined by the total number m of states that are excited, on average, quite intensively in the decay of the λ and i levels, as well as by the quantity $n_{\lambda i} = \rho\Delta E$, which corresponds to the number of intermediate levels of the cascade in the interval ΔE that are characterized by a preset spin–parity J^π. If we replace the total widths by the products of effective partial widths $\langle\Gamma\rangle$ and the number of levels excited in the decay of the λ and i states, the intensity of the cascades can be represented as

$$I_{\gamma\gamma} = \sum_{J,\pi}(\Gamma_{\lambda i}/\langle\Gamma_{\lambda i}\rangle m_{\lambda i}) \times n_{\lambda i} \times (\Gamma_{if}/\langle\Gamma_{if}\rangle m_{if}). \quad (2)$$

Summation over the entire set of quantum numbers J and π of intermediate and, if necessary, the initial and the final levels of the cascades has been performed here in order to draw a comparison with relevant experimental data.

Expression (2) can be modified by using the relation between the total experimental radiative width and the radiative-strength-function and level-density values determining this width. As a result, we arrive at

$$\begin{aligned}\Gamma_\gamma \cdot I_{\gamma\gamma} &= \sum_{J,\pi}\Gamma_{\lambda i} \times n_{\lambda i} \times (\Gamma_{if}/\Gamma_i) \\ &= \sum_{J,\pi}\Gamma_{\lambda i} \times n_{\lambda i} \times (\Gamma_{if}/\langle\Gamma_{if}\rangle m_{if}).\end{aligned} \quad (3)$$

From (3), we can readily find that the cascade intensity, the calculated and the measured total width of the compound state, and the quantity $B_r = \sum_f \Gamma_{if}/\Gamma_i$ obtained by averaging the probability of emission in specified secondary transitions over a given interval of the energies of intermediate levels i of the cascades are related by the equation

$$\Gamma_\gamma^{\text{calc}} = \Gamma_\gamma^{\text{expt}} \sum_i (I_{\gamma\gamma}^{\text{expt}}/B_r^{\text{calc}})_i. \quad (4)$$

In the representation given by Eq. (3), the product $\Gamma_\gamma \times I_{\gamma\gamma}$ is proportional to the absolute value of the radiative strength function for primary transitions characterized by the energy E_γ,

$$f = \langle \Gamma_{\lambda i} \rangle / (E_\gamma^3 A^{2/3} D_\lambda), \quad (5)$$

where A is the mass of the nucleus and D_λ is the spacing between the decaying states of a given spin and a given parity; concurrently, this product is also proportional to the ratio of the number $n_{\lambda i}$ of intermediate levels excited in the interval ΔE to the total number m_{if} of states excited in the decay of the i level.

For a preset model energy dependence of the density of levels excited by cascade transitions, the use of Eq. (3) ensures the highest possible accuracy in determining the energy dependence of the radiative strength functions for primary transitions, because inevitable discrepancies between the level density (number of levels in a given interval) used and its actual values are compensated to a considerable extent by a positive correlation between the numerator and denominator of the ratio $n_{\lambda i}/m_{if}$, which is determined by specific values of the level density within the chosen model. From expressions (1) and (2), it follows (a) that the cascade intensity is determined exclusively by the form of the dependence of the radiative strength functions for primary and secondary transitions on their energy and not by the absolute values of these radiative strength functions (for example, the intensity in question is absolutely unaffected by the errors in determining the spacing D_λ between the decaying states) and (b) that, in contrast to what occurs in the previously known methods for determining level densities, where the probability of the reaction-product yields is in direct proportion to ρ, a roughly inverse dependence is observed here.

This conclusion is confirmed by the values that are obtained by averaging, over all 40 nuclei, the ratios R of the sums of the experimentally observed cascade intensities to the theoretical result derived according to expression (1) and which are quoted in the table. In our calculations, we used two models of $E1$ radiative strength, that from [9] and that from [10]; the single-particle Weisskopf model for $M1$ transitions; and two models of the level density, that from [11] and that from [12]. The data in the table indicate the direction that should be followed in modifying the model concepts of radiative strength functions and level densities in order to render the theoretical description adequate to the level achieved in experimenting: radiative strength functions for primary transitions should feature an energy dependence that is much more pronounced than that which is predicted in [9, 10] for $E1$ and $M1$ transitions, while the density of the levels that determine the probability of two-step photon cascades to low-lying levels must be much smaller than that predicted by the Fermi gas model.

Here, we would like to highlight the basic condition under which the possible values can be determined for level densities and for radiative strength functions simultaneously. As can be seen from Eqs. (1)–(4), it is above all the density of states excited by cascade transitions that controls the degree of agreement between the calculated intensities and total widths, on one hand, and the corresponding experimental values, on the other hand. (This conclusion immediately follows from the form of the dependence of the coefficient $B_r = \Gamma_{if}/\langle \Gamma_{if} \rangle m_{if}$ on the total number m of levels that are excited in the decay of the i state and on the radiative widths.) It should be noted that the interval of the possible values of the above parameters is effectively reduced precisely by the secondary-transition probability, which directly determines the measured intensities of two-step photon cascades. At $B_r = 1$, it follows from expression (4) that, for any level density specified within one model or another, it is always possible to find strength functions such that they would ensure a faithful reproduction of the experimental values of Γ_γ.

Values obtained by averaging, over 40 nuclei, the ratio R of the experimental intensity of two-step photon cascades to the corresponding intensity computed according to (1) on the basis of various models

Model	[9, 11]	[10, 11]	[9, 12]	[10, 12]
R	2.1(2)	2.6(2)	1.4(1)	1.6(1)

Expressions (1) and (3) were previously used to implement an iterative process of searches for those special features of radiative strength functions and level densities that determine the development of the process through which the cascade gamma decay of compound states in heavy nuclei proceeds. Specifically, these are (i) the most probable density of excited states of both parities that ensures the best fit to the experimental cascade intensities for fixed model assumptions on radiative strength functions and (ii) the most probable values of the sums of $E1$ and $M1$ strength functions for various model assumptions on level densities.

For this purpose, the most probable level-density values yielding the best fit to the dependence of $I_{\gamma\gamma}$ on the excitation energy of the nucleus were determined from Eq. (1) for a set of a few models of radiative strength functions [13]. After that, features that provide the fullest characterization of the level densities were extracted from the dependences obtained for them at the preceding stage, and the region of admissible level-density values was established. A similar procedure was applied to expression (3) as well.

It was found [13] (a) that, over comparatively broad intervals, the resulting level densities agree fairly well with the model from [12] if the generally adopted concepts are used for radiative strength functions and (b) there do not exist radiative strength functions such that they would provide, within the Fermi gas model, a simultaneous fit to $I_{\gamma\gamma}$ and Γ_γ values.

These results comply with those that were obtained within the last step of the analysis as described here: a simultaneous determination of the most probable functional dependences of the level densities and radiative strength functions on the primary-transition energy E_1 (or the excitation energy $E_{\text{exc}} = B_n - E_1$) and an estimation of the region of their probable values.

3. IMPLEMENTATION OF THE ANALYSIS

A nonconventional possibility of simultaneously determining, from experimental data, basic parameters that characterize the process of the cascade gamma decay of a nucleus having a maximum possible level density (above all a deformed nucleus) does indeed exist for the following two reasons:

(a) The results of two independent experiments are simultaneously analyzed in determining two independent quantities, the level density and the radiative strength function.

(b) Because of a tight (albeit not unambiguous) correlation between the level density and the radiative strength function, which determine the intensities of the observed cascade transitions, the cascade-intensity values found for N intervals of excitation energies plus one value of Γ_γ make it possible to estimate (with a comparatively small uncertainty) $2N$ values of the sought parameters. However, the parameters of cascade gamma decay cannot be established without resort to the conditions $\rho > 0$, $\Gamma(E1) > 0$, and $\Gamma(M1) > 0$, which are valid for any interval of excitation energy and any value of the transition energy. As a result, the domain of the sought quantities is found as a solution to the set of $N + 1$ equations and $6N$ inequalities. Naturally, such an analysis implicitly assumes that the sought level density and radiative strength function vary quite smoothly (monotonically) with energy (this assumption, however, does not have far-reaching consequences).

On the basis of relations (1) and (3), it is impossible to determine the sought parameters analytically. For this reason, we have made use of an iterative process of searches for some intermediate level-density and radiative-strength-function values that ensure an ever higher degree of agreement between the experimental values of the cascade intensities and of the total radiative width, on one hand, and their values calculated according to expressions (1) and (3), on the other hand. In order to achieve this, some forms (quite arbitrary in some versions of the calculation and even sometimes absolutely unrealistic) of the dependence of the radiative strength function on the transition energy and of the level density on the excitation energy of the nucleus being considered were specified for a zero-order approximation. For the inputs, we have also used the commonly accepted models of the radiative strength function and the level density [9–12] and their values distorted arbitrarily in various intervals of the photon energy and the excitation energy of the nucleus. Our procedure of searches for pairs of the required values was implemented in the following way: some random functions (identical for different spins and parities of the levels and different for the widths with respect to $E1$ and $M1$ transitions) were added to the logarithms of the input functional dependences of the level density and the radiative strength function. For this, we used the expression

$$f(E) = C\exp((E-U)^2/\sigma^2). \qquad (6)$$

In order to ensure a sufficiently high rate of convergence of the above iterative process, random values of the parameters C, U, and σ appearing in (6) were chosen from the intervals $[-0.2, 0.2]$, $[0, B_n]$, and [0.1 MeV, $0.3B_n$], respectively, by using a random variable uniformly distributed over the interval [0, 1]. If the level-density and radiative-strength-function values distorted in this way provided better agreement between the calculated and measured cascade intensities, they were used as inputs for the next step of the iterative process. Such an iterative process makes it possible to approximate the experimental cascade intensity and the total radiative width as closely as is desirable. However, it was actually terminated as soon as two sets of the random variables ρ and $S = f(E1) + f(M1)$ yielded values of $((I_{\gamma\gamma}^{\text{expt}} - I_{\gamma\gamma}^{\text{expt}})/\delta I_{\gamma\gamma}^{\text{expt}})^2$ that did not exceed 0.5–1.5 per interval. This residual took large values when the experimental cascade intensities showed pronounced fluctuations in the neighboring intervals of the excitation energies of the intermediate levels of the relevant cascades. After that, the iterative process was repeated either with new inputs or with the original ones. A repetition of the process many times in each of the N intervals of the excitation energy resulted in determining the spectrum of random level-density and radiative-strength-function values that reproduce simultaneously the total radiative width and the cascade intensity.

If such a procedure is implemented with the aid of modern computers, one version of the calculation requires, on average, up to a few tens of minutes, the specific value of the machine time being dependent on the choice of the input values of the level density and the radiative strength function and on the accuracy of the fit of the results of the calculations to experimental data. For this reason, we had to restrict ourselves at best to 30 versions for each of the 29 nuclei for which the cascade intensities were determined as functions of the energy of their intermediate level. Usually, the calculation had to be checked thoroughly only at the initial stage of the iterative process if the input parameter values were strongly different from those that are expected within the currently accepted concepts. It is the region in which we can arrive at the point where the mean square of the deviation attains a local minimum, but the values of the level densities and the radiative strength functions at the observed local minima always featured larger deviations from the existing model concepts than the results presented below. It is natural that, at the

points of spurious local minima, the calculated cascade intensities disagreed completely with the relevant experimental values.

The above procedure was implemented for a number of markedly different level-density and radiative-strength-function values, but it always converged to a functional dependence that was common to all these versions and which ensured the best fit of the calculated cascade intensities to their experimental values. Here, we imply that the term "common functional dependence" corresponds to a distribution of random variables that is characterized by a specific mean value and a specific variance (presented below in the figures).

It is natural that, within the proposed method for determining the level density and the radiative strength function, available experimental information about the nucleus under study is exploited to the maximum possible degree. This information includes level densities at the neutron binding energy, together with the excitation energies and quantum numbers of reliably established low-lying levels and modes of their decay below the energy E_{discr} of 1 to 2 MeV for odd and even nuclei. The relevant values were borrowed from available compilations where allowance was fully made for spectroscopic information that we previously obtained by analyzing the parameters of the most intense two-step photon cascades. In addition, we fixed, on the basis of data presented [14], the ratio of the widths with respect to $M1$ and $E1$ transitions for their energies slightly lower than the neutron binding energy B_n.

The most important result deduced from the first stage of our data analysis [13] was that which made it possible to state that the discrepancy between $I_{\gamma\gamma}^{\text{expt}}$ and $I_{\gamma\gamma}^{\text{theor}}$ is due primarily to the discrepancy between the density of levels actually excited in (n, γ) reactions and the concepts formulated in [11] on the subject.

Both in the analysis presented in [13] and in that described below, the form of the relationship between the level density, the radiative strength function, and $I_{\gamma\gamma}$ gives no way to determine the required values from a comparison of experimental data and theoretical results unambiguously and independently. Nonetheless, it is possible to draw quite reliable conclusions on what and in which direction one must modify in the current concepts of photon emission and the number of levels excited as the result of this; moreover, a quantitative measure of the required modification can also be established along these lines.

The above conclusions are based on the results deduced from an analysis of the convergence of the level-density and radiative-strength-function values. These results indicate that the level density and the radiative strength function have well-defined values that depend only slightly on the choice of input approximations for the sought parameters of the process being studied. The main argument in favor of the last statement is illustrated in Fig. 1. Here, we have used absolutely unrealistic inputs for the level density and the radiative strength function—namely, the level density above the region of excited states known precisely from nuclear spectroscopy was set to that at the neutron binding energy, while the strength functions were taken to decrease linearly with increasing transition energy. Nevertheless, the final result of the iterative process fits well in a general pattern that was obtained for quite a wide set of various realistic and unrealistic input values of the level densities and radiative strength functions.

The results displayed in Fig. 1 demonstrate that the procedure used makes it possible to determine the maximum possible level density for all nuclei being considered by varying the inputs for radiative strength functions. The use of an input level density featuring unrealistically large deviations from the expected value at rather realistic inputs for radiative strength functions gives every reason to expect that, by introducing numerous small-amplitude distortions of the input dependence, it will be possible to deduce, for the truly maximum possible level density, an estimate that would enable one to reproduce simultaneously the Γ_γ and $I_{\gamma\gamma}$ values considered here. Naturally, the process is repeated many times [for the random parameters C, U, and σ^2 in expression (6)], and the average over the resulting sample is treated as the most probable value.

3.1. Special Features of the Analysis

That no procedures for reliably and unambiguously determining, from the observed spectra of photons or the spectra of their coincidences, level densities and radiative strength functions over the entire range of the excitation energies of excited levels have been developed so far means, in our opinion, that the problem cannot be solved by traditional methods of data analysis. It is this circumstance that furnished a motivation for devising the present probabilistic approach to assessing these quantities.

In calculating the cascade intensities according to expressions (1)–(3), we will consider only the sum of levels in a given energy interval that are excited by primary $E1$ and $M1$ transitions and the sum $f(E1) + f(M1)$ of strength functions for primary transitions. This approximation is fully justified by the fact that the experimentally estimated contribution of higher multipole orders to the development of the cascade gamma decay of a neutron resonance is significantly smaller than the error in experimentally determining the cascade intensities.

We do not address here the question of whether the concept of the strength function for secondary transitions (of the relevant level density as well) has a physical meaning at low excitation energies of intermediate cascade levels. The existence of a well-defined $I_{\gamma\gamma}$ value that fluctuates only slightly from one interval to another implies that, although the widths with respect to individual secondary transitions are expected to have a

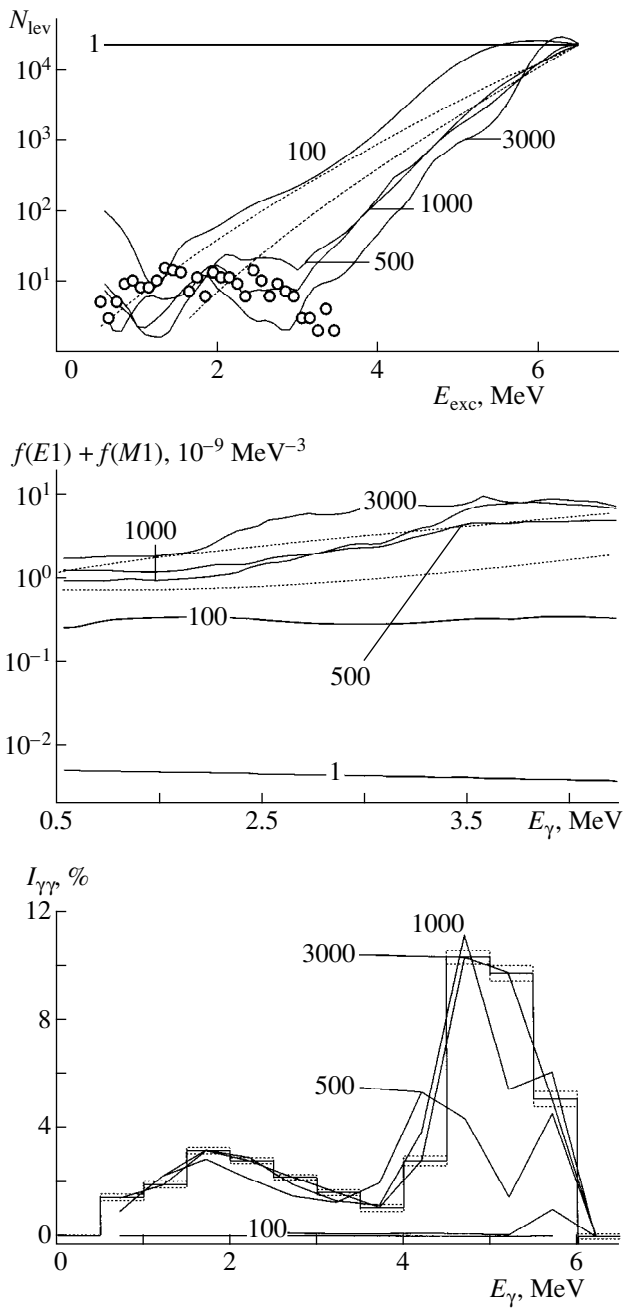

Fig. 1. Examples of intermediate values of the level density and the radiative strength function in the odd–odd nucleus ^{198}Au and corresponding cascade intensity (solid lines). The numbers of iterations are indicated on the curves. The dotted lines represent the predictions of the models from [11, 12] for the level densities and the sum of the predictions from [9, 10] and $f(M1)$ = const for the strength functions. The histogram shows the experimental cascade intensity, together with its statistical uncertainty.

wide scatter, there exist mean values of Γ_{if} and of the number of excited states over the excitation-energy interval ΔE, and it is these mean values that ensure agreement between experimental data and theoretical results calculated according to (3). Wide variations in the values of the radiative strength function for secondary transitions translate into relatively small uncertainties in the value calculated for the coefficient B_r in expressions (1)–(3) owing to a positive correlation between its numerator and denominator. The mean value of B_r over the entire spectrum was determined experimentally and is equal to the sum of all observed cascade intensities that is normalized per event of compound-state decay. As a result, the effect of possible variations in the radiative strength functions for primary and secondary transitions on the sought parameters is weakened.

Yet another question of fundamental importance is that of the relationship between the actual values of the parameters characterizing the process and the most probable estimates as obtained for these parameters by the method proposed here. It was assumed that, if there are no systematic errors much greater than the scatter of random values found for the level densities and for the radiative strength functions, results obtained as averages over the intervals in which the quantities being considered can vary reflect at least the typical features of the parameters that govern the cascade gamma decay of the compound state of a heavy nucleus. This is obviously so if, for the sought parameters, the relevant random values deviate in the two directions from the true value with approximately equal probabilities and if small deviations appear with higher probabilities than large deviations. Of course, the problem in question requires further study, so that the results obtained here cannot be considered to be conclusive.

3.2. Approximations Used in the Present Analysis

Since available experimental data are insufficient for unambiguously determining the complete set of parameters that affect the experimentally measured values of $I_{\gamma\gamma}$ and Γ_γ, there arises the problem of a reasonable choice of assumptions that would make it possible to estimate them as accurately as is possible. As a matter of fact, it is necessary to introduce hypotheses specifying the relation between the densities of opposite-parity levels at various excitation energies of the nucleus being considered and the relation between the forms of the energy dependences of the radiative strength functions of primary and secondary transitions of the same multipole order.

That the densities of levels having opposite parities can be different at low energies is a fact that has been known for a long time. Most frequently, this occurs in near-magic nuclei. The problem was studied theoretically, for example, in [15]. For our analysis, it is important (i) that, in nonmagic nuclei, there are no reasons to expect significant distinctions between the densities of opposite-parity levels even at moderately high energies (for example, above 3 MeV in deformed even–even nuclei) and (ii) that the existing distinctions between the densities of opposite-parity levels decrease with increasing energy.

At this stage of our analysis, it was assumed that $\rho(\pi = +) = \rho(\pi = -)$, but only the sum $\rho(\pi = +) + \rho(\pi = -)$ was contrasted against model concepts. To some extent, this compensated for possible errors associated with the first assumptions. It is worthwhile to note here that procedures for determining the densities of levels characterized by a specific parity have yet to be developed for a major part of the excitation-energy region below the neutron binding energy.

The spin dependence of the level density was not varied in our calculations; in the various versions, it was instead specified in accordance with the parametrization from [11] or from [12]. The eventual results are virtually unaffected by the choice of a specific model. We do not see very strong reasons to expect significant distinctions between the actual and the model spin dependences of the level density: for the majority of nuclei, the ratios of the measured and the calculated intensities of the cascades proceeding to final states having different spins do not suggest any disregarded functional dependence on the spin of the final level of a cascade.

In addition to the inputs listed above, the calculation of the cascade intensities $I_{\gamma\gamma}$ requires specifying the ratios of unknown strength functions for secondary dipole transitions to their values averaged over the spectrum—that is, the quantity B_r given by (4). Presently, the analysis described here can be performed only if some relation between the radiative strength functions for primary and secondary transitions is preset: for a zero approximation, we assume that, if the energy of a primary transition is equal to the energy of a secondary transition, their radiative strength functions are identical.

There is no doubt about the circumstance that, with decreasing excitation energy of the nucleus being studied, the probability of the relevant gamma transition is affected by the structure of the wave functions of the excited states to an ever greater extent; possibly, the degree of correspondence between this probability and the mean probability for the emission of a photon of a given energy by the nucleus at higher energy of its excitation concurrently becomes smaller. This can be verified only by means of experiments measuring, with modern HPGe detectors, the intensities of two-step photon cascades over a maximally broad interval of the energies of their final levels.

It goes without saying that the strength functions for primary and secondary transitions, as well as the relation between the densities of positive- and negative-parity levels, can appear as independent variables in the analysis being discussed. Unfortunately, there then arise the following problems:

(i) In view of an insufficiently high efficiency of the above iterative process, large amounts of machine time are required when the number of relevant parameters is substantially increased.

(ii) The interval of possible values determined for $6N$ parameters from $N + 1$ equations and $6N$ inequalities must become much wider than that in the version that has already been implemented and which involves variations of a smaller number of parameters. As a result, the probability for the emergence of large deviations of values found for the level densities and the radiative strength functions from their true values may increase.

It should be emphasized that the above problems of the method that we propose for determining the level density are inherent in any method for evaluating this quantity on the basis of the spectra of products originating from an arbitrary nuclear reaction. However, our method, in contrast to all others known so far, has the highest (lowest) sensitivity at minimal (maximal) values of the sought quantity and makes it possible to fix precisely the range of spins for which ρ values are determined.

4. MOST PROBABLE FORM OF THE ENERGY DEPENDENCE OF THE DENSITY OF HEAVY-NUCLEUS STATES EXCITED BY CASCADE GAMMA TRANSITIONS

Obviously, level-density and radiative-strength-function values that make it possible to reproduce simultaneously the experimental values of $I_{\gamma\gamma}$ and Γ_γ cannot be negative or indefinitely large. Among the results of our analysis, that which is the most important one and which could not have been expected from the outset is the following: the corridor in which the possible values of the sought quantities vary proved to be so narrow that the values in question could be contrasted against various model concepts. Thus, the objective of the present analysis—searches for models that are capable of providing the best fit to experimental data and a determination of the region where these models fail to reproduce the data—has been attained.

Some of the results that we obtained are presented in Figs. 2–5. An analysis of these results leads, first of all, to some definitive conclusions on the modifications that must be introduced in level-density models so as to reduce the distinctions between the calculated and the measured parameters of the cascade gamma-decay process.

We note that, in some nuclei—predominantly in near-magic and odd–odd ones—the level density found at low excitation energies is sometimes below that which corresponds to the data that we previously obtained for the diagrams of their excited states and decay modes. The emerging pattern can be qualitatively explained by the roughness of the approximation that we adopted in our analysis and which consists in assuming that the $\pi = +$ level densities are equal to their $\pi = -$ counterparts and that the radiative strength functions for cascade transitions are independent of the excitation energy of the decaying state. The possibility

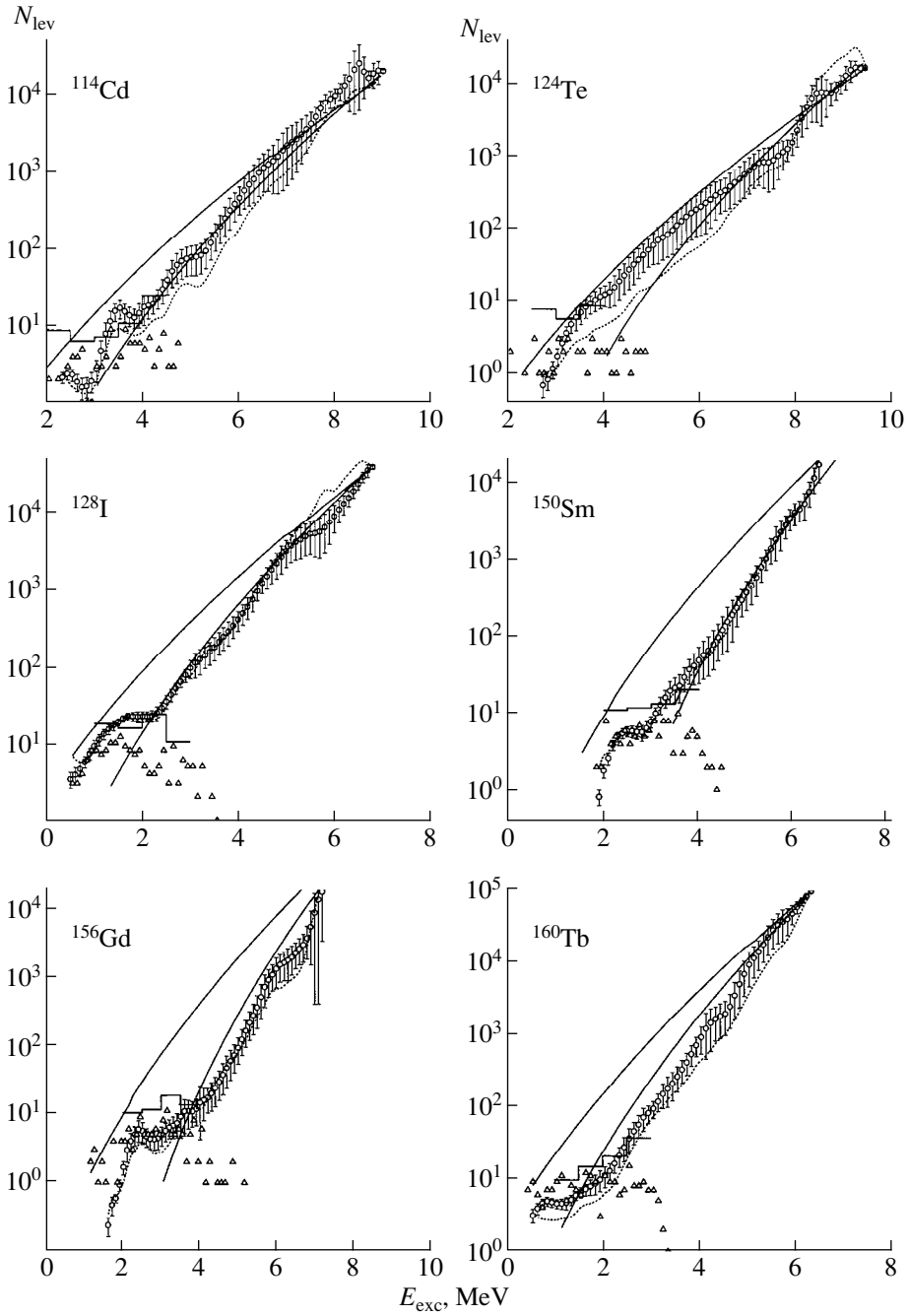

Fig. 2. Number of levels of both parities per 100 keV at various values of the excitation energy E_{exc} for ^{114}Cd, ^{124}Te, ^{128}I, ^{150}Sm, ^{156}Gd, and ^{160}Tb (open circles). The quoted errors correspond to the uncertainties in the analysis performed. The histograms represent data from [18], while the open triangles show the numbers of experimentally revealed intermediate levels excited by sufficiently intense cascades. The dotted curves depict the mean level-density values as obtained under various assumptions on the radiative strength function for $\rho(E_{exc}) = \rho(B_n)$ used as inputs for the iterative process. Also presented for the sake of comparison are the predictions of the models from [11] and [12] (upper and lower solid curves, respectively).

that there are sizable errors in the spectroscopic part of an experiment studying two-step photon cascades cannot be ruled out either. Unfortunately, the sample of accumulated coincidences is statistically insufficient for deducing an unambiguous answer to the above question.

The most probable density of states that are excited in thermal-neutron capture can be characterized as follows. Up to an excitation energy of 1 to 2 MeV (depending on the parity of intranuclear nucleons), available data are compatible with an exponential extrapolation of the Fermi gas model with the parame-

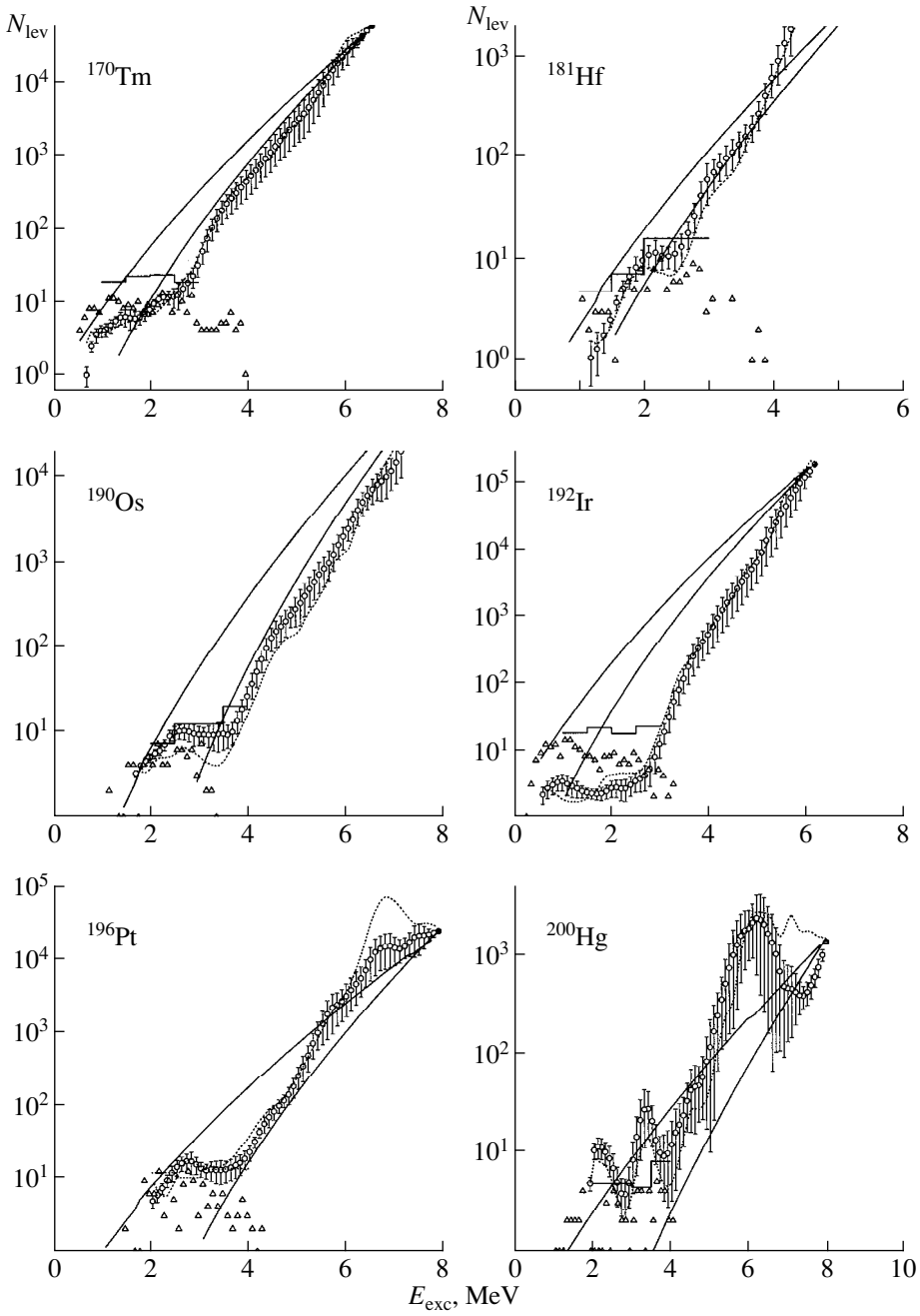

Fig. 3. As in Fig. 2, but for the ^{170}Tm, ^{181}Hf, ^{190}Os, ^{192}Ir, ^{196}Pt, and ^{200}Hg nuclei.

ter values from [11]. From 1 to 2 MeV up to a certain threshold value E_b, the level density changes with nuclear excitation energy much more slowly than what is assumed by any of the existing theoretical concepts on the subject. Above E_b values of about 2 to 3 MeV (3 to 4 MeV) for nuclei odd (even) in N, it is most likely that the level density agrees best of all with the predictions of the generalized model of a superfluid nucleus in its simplest, original, form [12], but with some slight modifications to the model parameters. These modifications, which do not conceal any conceptual content of fundamental importance, were only made to ensure agreement between the level density in the vicinity of the neutron binding energy and the experimentally determined spacing between neutron resonances.

The above shape of the level density found as a function of energy can suggest [16] a qualitative change in the properties of nuclei in the excitation-energy region around the neutron-binding energy. Taking into account previous observations regularly indicating [17] that, in all probability, the spectrum of the intermediate states of the most intense cascades is of a

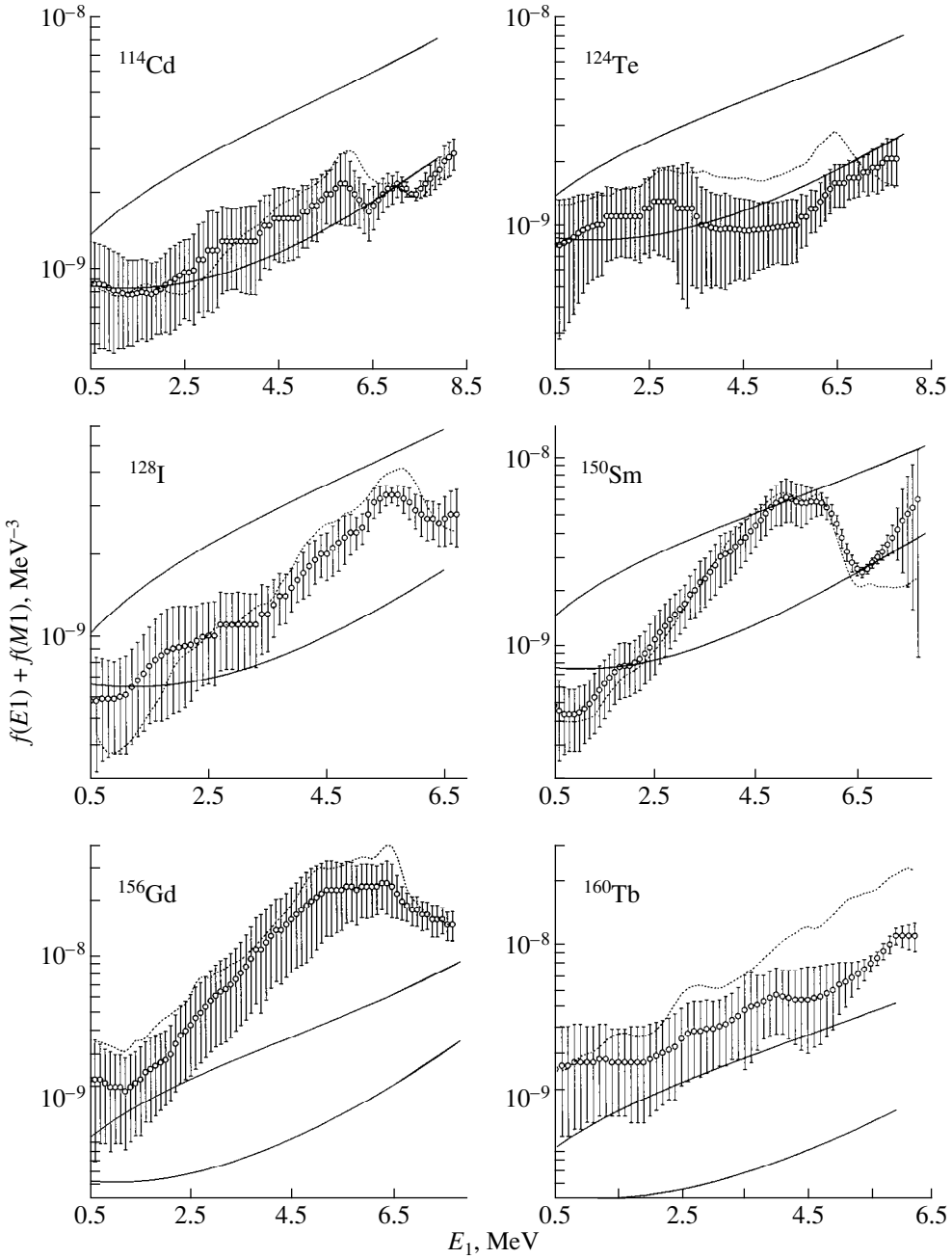

Fig. 4. Sum of the radiative strength functions for $E1$ and $M1$ transitions caused by radiative thermal-neutron capture in the compound nuclei ^{114}Cd, ^{124}Te, ^{128}I, ^{150}Sm, ^{156}Gd, and ^{160}Tb as a function of the energy E_1 of the cascade primary transition (open circles). The quoted errors stem from the uncertainties of our analysis. The dotted curves represent the mean value of $f(E1) + f(M1)$ as obtained with various model values [9, 10] of the input parameters for the iterative process and a fixed input level density $\rho(E_{exc}) = \rho(B_n)$. The solid curves correspond to data based on these model concepts (from [9] for the upper curves and from [10] for the lower curve) and supplemented with the value $f(M1) = \text{const}$ fitted to experimental data.

harmonic character, we can assume that, below the neutron binding energy, vibrational excitations (a small number of high-energy phonons, as can be expected in view of a large spacing between equidistant levels) have a dominant effect on the properties of nuclei. A very fast, exponential (or close to exponential), growth of the level density above the neutron binding energy may be due to dominance of internal excitations at this energy value that involve a fairly large number of quasiparticles.

An independent piece of evidence in favor of the above shape of the level density as a function of energy can be obtained if the number of cascade intermediate levels observed as resolved peaks in the excitation-

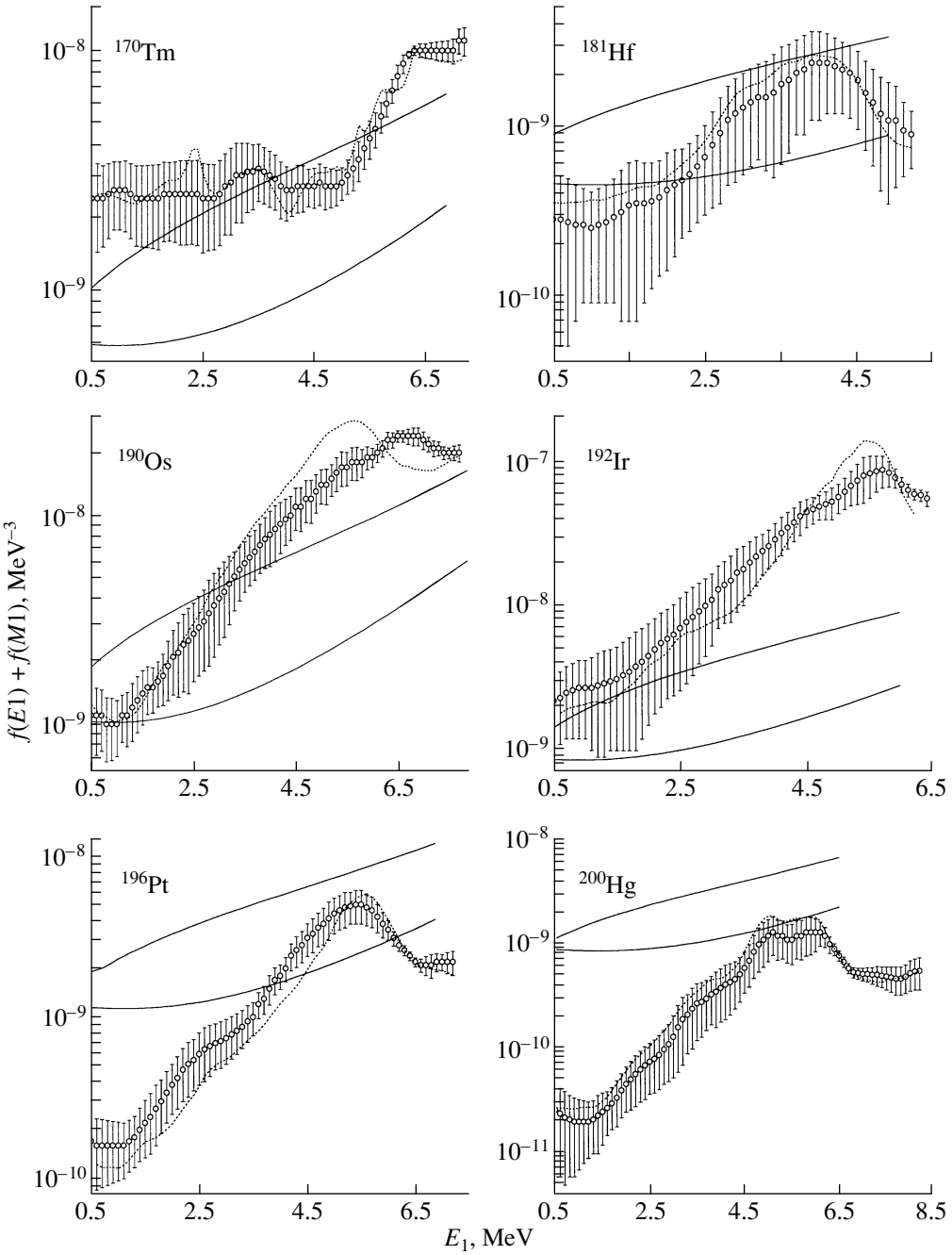

Fig. 5. As in Fig. 4, but for the ^{170}Tm, ^{181}Hf, ^{190}Os, ^{192}Ir, ^{196}Pt, and ^{200}Hg nuclei.

energy region extending to an energy value not lower than 3 to 4 MeV is increased. In practice, this will become feasible upon lowering the sensitivity threshold achieved presently in recording an individual cascade (about 10^{-4} per decay event) by an order of magnitude. This conclusion is suggested by an examination of the results obtained in [18] from a statistical analysis of the deviations of random cascade intensities from the relevant mean value and by an extrapolation of the approximating function to zero value of the experimental sensitivity threshold. For the level density up to excitation energies of 3 to 4 MeV, this analysis gave the first direct estimate contradicting the concepts of the Fermi gas model. This estimate is also displayed in Figs. 2 and 3.

5. MOST PROBABLE VALUES OF THE SUMS OF STRENGTH FUNCTIONS FOR DIPOLE TRANSITIONS

Data on the sum of the strength functions for dipole transitions from a simultaneous determination of the

radiative strength functions and level densities on the basis of expressions (1)–(3) are presented in Figs. 4 and 5. From the resulting sets of random values of $f(E1)$ and $f(M1)$ at a given energy of the primary cascade transition, we determined both their mean value and the probable scatter using conventional relations of mathematical statistics. These results were contrasted against model values obtained in the following way: to the values of $f(E1)$ that were determined in accordance with the models proposed in [9] and [10] (upper and lower solid curves, respectively), we added the value $f(M1)$ = const normalized in such a way that the ratio of the widths with respect to magnetic and electric transitions of energies close to the neutron-binding energy corresponds to the compilation presented in [14]. The aforementioned models were used only to draw a comparison with the level-density and radiative-strength-function values obtained experimentally (although the authors of [10] developed their model for spherical nuclei rather than for deformed ones). This is justified since the objective of the present analysis was to seek the most probable unknown functional dependences of the level densities and radiative strength functions in the form of deviations from known model concepts.

For the sake of comparison, the figures in question present, in addition to experimental values obtained from an iterative process that starts from level-density and radiative-strength-function values admitted by the existing models, analogous quantities as evaluated on the basis of the same iterative process, but with absolutely unrealistic initial values of the level density, $\rho(E_{\text{exc}}) = \rho(B_n)$ = const.

A comparison of the data on the strength functions at such distinct inputs for the iterative process proves that the mean values of the sum $f(E1) + f(M1)$ that were determined from an analysis of the cascade intensities depend only slightly on the choice of inputs; therefore, they can be considered as the most probable values. The accuracy of this conclusion is constrained by the approximations of our analysis that were listed at the beginning of Subsection 3.2.

A comparison of experimental results with the predictions of the models that were proposed in [9, 10] and which are used most frequently to analyze such results leads to the following conclusions:

(i) The sums of $E1$ and $M1$ strength functions do not show a universal dependence on the gamma-transition energy; in all probability, they reflect the general properties of the structure of states between which the cascade transition occurs. This can be seen from a comparison of our results (a) for the pair of Gd isotopes, where the experimental conditions (spin–parities of the levels connected by the cascades in question, Γ_λ, and density of excited levels) are such that, for the isotope pair being considered, the difference of the resulting sums of the strength functions must be less than in any other combination appearing in our comparison, and (b) for even–even and odd–odd nuclei.

(ii) The shape of the sum $f(E1) + f(M1)$ as a function of energy differs from that predicted by the models proposed in [9, 10]. This is valid at least for even–even compound nuclei from the region of the $4S$ maximum of the neutron strength function.

(iii) The sum of the strength functions increases as we go over from near-magic to deformed nuclei and as the photon energy is increased. The values found for the spherical nuclei ^{114}Cd and ^{124}Te are faithfully reproduced by the model from [10] if we assume that the $M1$ strength function is independent of the photon energy. For the ^{128}I, ^{140}La, ^{146}Nd, ^{150}Sm, ^{181}Hf, $^{188, 190}$Os, ^{196}Pt, and ^{200}Hg nuclei, this model as implemented within the same assumption on $M1$ transitions either complies with experimental data or overestimates them for primary transitions of low energies.

(iv) We cannot rule out the possibility that, around the neutron binding energy (at least in some nuclei), the level density noticeably deviates from the nearly monotonic dependences in Figs. 2 and 3. This possibility must be taken into account in order to explain the discrepancies between the resulting absolute values of the sums of the strength functions and the corresponding model predictions for some nuclei having neighboring values of A. In other words, the kink effect clearly seen in the energy dependence of the level density at low energies is much weaker at high energies, if any. A similar type of behavior of the level density as a function of energy was obtained in the theoretical analysis of Ignatyuk [19], although the discrepancy between the predictions of his model and experimental data (see Figs. 2, 3) is quite sizable.

An alternative possibility consists in assuming that strength functions grow significantly owing to the well-known effect of the collective enhancement of the probability of the gamma transition accompanying the decay of states whose wave functions involve sizable vibrational components. Resolving this dilemma requires not only further experimental studies but also a thorough theoretical analysis. If the present interpretation of the results that we obtained is viable at least to some extent, the physical significance of exploring a transition from a superfluid state to a normal one in an exotic system like the nucleus furnishes a sufficient motivation for performing experimental and theoretical studies such as those indicated above.

The relative deviations of the results found here for the strength functions and level densities from their mean values are characterized by a strong negative correlation. In the majority of cases, the correlation coefficient changes from –0.6 to nearly –1, falling, however, down to –0.4 for some nuclei. Since the generated pairs of random values of the parameters that characterize the gamma-decay process always feature some uncorrelated random deviations (the length of the iterative process is severely constrained by the computer poten-

tial), it is natural to conjecture that, in fact, the degree of coupling of the radiative strength functions and the level densities is still stronger—that is, they are not independent variables in Eqs. (1)–(3). It is owing to this circumstance that we are able to determine them simultaneously on the basis of available experimental data and physically motivated constraints on their values.

Effect of Systematic Errors in Determining Cascade Intensities on Level Densities and Radiative Strength Functions

The dependence of the cascade intensity on the energy of intermediate cascade levels was obtained on the basis of data measured with systematic errors. The error in determining the sum of the intensities of all experimentally observed transitions is the most important of these. Its value is virtually equal to the present-day uncertainty in the absolute values of the intensities of the strongest primary high-energy transitions in the spectra of gamma rays from radiative thermal-neutron capture (it is precisely these intensities that are used to normalize $I_{\gamma\gamma}$ values). In order to minimize the effect of this error, we preferred to use predominantly data from the compilation presented on [20] as a reference, since the bulk of these data come from the same facility for almost all elements of the periodic table. If we consider that the total spectra of gamma rays have also been measured for many of the nuclei that we studied (for these gamma rays, it can be deduced on the basis of physical arguments that the sum of the products of the photon energy and the intensity in percent per decay event must be $100B_n$ [21]), it becomes clear that there are no strong reasons to expect a systematic uncertainty in the $I_{\gamma\gamma}$ values that is noticeably greater than the statistical error in our experiment.

The accuracy in determining the most probable values of the level densities and the radiative strength functions is also affected quite sizably by the systematic error with which the experimental spectra are decomposed into components that are dependent on the energies of only primary and only secondary cascade transitions, but the adverse influence of this systematic error is less pronounced than that of the systematic error discussed immediately above. According to [8], insufficient statistics of recorded coincidences would lead to an overestimation (underestimation) of the intensity of cascades where the energy of the primary cascade transition is lower (higher). The corresponding errors can be estimated by using the procedure developed in [18] to analyze the shape of the distribution of random deviations of the cascade intensities from their mean values. As a rule, these errors do not exceed 20% of the resulting value. In practice, it is straightforward to obtain the relevant estimate under the assumption that, for cascades whose primary transitions correspond to emitted-photon energies below $0.5B_n$, the observed intensity must be reduced by, say, 25% if the intensities of the cascades whose primary transitions are of higher energies are increased accordingly. This test was performed for all nuclei. Its basic result is the following: at low excitation energies, the level density can somewhat increase in relation to the data in Figs. 2 and 3, and this can partly explain the discrepancy between the observed number of intermediate cascade levels and the level density determined for ^{192}Ir (see Fig. 3). However, no significant distinction between these results and the data in Figs. 2 and 3 is observed at higher energies—the scatter of the level-density values from different versions of the calculations often exceeds their deviations for different shapes of the dependence of the cascade intensity on the nuclear excitation energy.

In all probability, the scatter of data displayed in Figs. 4 and 5 receives a contribution only from the uncertainties that arise in the strength functions because of ambiguities of the above level-density values and, additionally, because of errors in the experimentally measured parameters of the cascade gamma-decay process.

Since the product $\Gamma_\lambda \times I_{\gamma\gamma}$ and the sought quantity $\Gamma_{\lambda i}$ are related by a linear equation, the experimental relative errors in the total width and in the cascade intensity (they are usually about 10%) lead to errors at the same level in the resulting partial widths. A variation in the energy dependence of $I_{\gamma\gamma}$ at a level of 25%—it was introduced above to estimate the effect that the possible systematic error in determining the energy dependence of $I_{\gamma\gamma}$ can exert on the eventual result—changes, for all nuclei, the sum of the resulting strength functions by a value that usually does not exceed the uncertainties presented in Figs. 4 and 5 for the level densities and the radiative strength functions considered here. In other words, the main contribution to the uncertainty in the level density, as well as to the uncertainty in the sum of the strength functions, comes from the anticorrelation of the level density and the radiative strength functions in the measured functionals of the cascade gamma-decay process and from the paucity of relevant experimental data rather than from statistical uncertainties in the experimental values of the total radiative widths and cascade intensities.

On the basis of the above analysis of the possible methodological errors and on the basis of the results in Figs. 4 and 5 on a determination of the shape of the energy dependence of the radiative strength functions, we can therefore conclude with a high degree of confidence that the models proposed in [9, 10] and combined with the idea that $M1$ transitions are of a single-particle character, $f(M1) = \text{const}$, cannot describe the transition-energy dependences of $f(E1)$ and $f(M1)$ in any nucleus. Moreover, we cannot even rule out the situation where the energy dependences of $f(E1)$ and $f(M1)$ are not identical for neutron resonances characterized by different Γ_n^0 values. That this possibility can

be realized is suggested [5] by the presence of a strong correlation between the intensities of the observed cascades and the reduced neutron width in even–odd compound nuclei. This is precisely the assumption that can also explain qualitatively variations exhibited by the shape of the energy dependence of the radiative strength function in response to changes in the nuclear mass, since the ratio of the reduced neutron width to the spacing between the resonances for a compound state excited by thermal neutrons takes different values for nuclei having different masses. Presently, it is technically feasible to check this hypothesis in studying cascades in individual resonances.

By and large, we can conclude that, at the present stage of experimental investigations into the cascade gamma decay of neutron resonances, the data quoted here for the density of excited states and for radiative strength functions should be considered as those that provide the most probable values of these physical quantities, despite errors in experimental data used to deduce these values and despite a probabilistic character inherent in the above analysis.

6. POSSIBILITIES OF INDEPENDENT EXPERIMENTAL TESTS

The above analysis is disadvantageous in that it cannot yield unambiguous results. Therefore, it is necessary to subject the results of this analysis to an independent test. This does not lead to unsolvable problems. From the data presented in Figs. 2 and 3, it can be seen that, at excitation energies up to half the neutron binding energy in the nuclei being studied, the expected mean spacing between levels excited in the relevant (n, γ) reactions is not less than 2 to 3 keV. If modern detectors and a numerical method for improving the resolution [22] are used, the widths of peaks in the spectra representing the distribution of the intensities of two-step photon cascades exceed these values only slightly; therefore, it is possible to observe directly in experiments almost all excited states of any nucleus up to 3 or 4 MeV, provided that the results presented in Figs. 2 and 3 are correct. For them, one can also determine the intensities of primary transitions (that is, radiative strength functions) as the sum of the intensities of all possible cascades.

The ambiguity in the relationship between the $E1$ and $M1$ radiative strength functions over the entire interval of their values from the actual experimental threshold of 0.52 MeV to the neutron binding energy is an important source of uncertainties in the values that we obtained for the level densities and radiative strength functions. This ambiguity is due to the fact that the cascades singled out for the majority of the nuclei studied here are those that terminate at final levels of the same parity. These are primarily cascades formed by $E1$ and $M1$ transitions. Therefore, there exists a comparatively wide set of their values that makes it possible to reproduce the cascade intensities and the total radiative width simultaneously even if the resulting values deviate from the actual ones. If an attempt is made to describe not only the sum of all observed cascade intensities but also their sums for transitions to final levels of opposite parities individually, the proposed method of analysis is capable in principle of solving this problem as well, at least partly. For the majority of the nuclei that we studied, it would then be required to conduct experiments with high-efficiency detectors and with an anti-Compton shielding. The relevant data would also make it possible to obtain directly the shape of the dependence of the radiative strength functions for secondary transitions on the excitation energy of the final cascade level.

In addition to the aforementioned possibility of obtaining a more precise parity dependence of the level density and a more precise excitation-energy dependence of radiative strength functions in a feasible experiment employing more advanced equipment and extending the number of variables subjected to analysis, there are also possibilities for assessing the reliability of our results on the basis of data obtained previously.

For this, the total population of an individual nuclear state at E_i up to an excitation energy of 3 to 4 MeV can be determined by comparing the intensities of two-step photon cascades with known intensities of individual gamma transitions. This population is equal to the sum of the intensities of all cascades terminating at the above state at E_i; hence, it is determined by the relevant level density and by the $E1$ and $M1$ strength functions. Such a calculation can be performed either on the basis of the models proposed in [9–12] or on the basis of the results obtained in [13] and in the present study. Here, a comparison of the calculated and experimental results provides an additional independent check on the degree to which various concepts of the level densities and of the radiative strength functions correspond to the situation prevalent in actual practice. Unfortunately, reliable data on the decay diagram that are necessary for such analysis appeared only recently and only for ^{168}Er [23].

8. CONCLUSIONS

A model-independent procedure has been proposed for determining, on the basis of experimental data on (n, γ) reactions involving thermal neutrons, the most probable level density and the most probable value of the sum of dipole strength functions for nuclei with an arbitrary level density. Although the results obtained from the analysis performed here cannot be considered to be conclusive, because this analysis relies on some ad hoc assumptions, these results highlight the presence of some serious discrepancies with those that were obtained by extrapolating the existing concepts of the theory of the nucleus to an as-yet-unexplored region of its excitation energy.

At a level of more or less realistic and partly checked hypotheses, the characteristic features of the cascade gamma decay of $A > 100$ nuclei are the following:

(i) Almost over the entire range of excitation energies below the neutron binding energy, the density of excited states is less than that which follows from the generally accepted concepts of the model of a noninteracting Fermi gas. This is so at least for nuclei from the region of the 4*S* maximum of the neutron strength function. In all probability, the level density at excitation energies above $E_b \sim E_{\text{pair}} + 2$ MeV is described best of all by the generalized model of a superfluid nucleus in the earliest version considered in [12]. Yet, we cannot rule out the possibility that the model from [12] systematically overestimates the level density in odd–odd nuclei. This conclusion is valid only in the case where, in a two-step photon cascade, the probability of populating its intermediate level having quantum numbers J^π and occurring in a specified narrow interval of the excitation energy is independent of the structure of the corresponding state *i*. Otherwise, the above conclusion should be associated with some effective density of excited states; that is, one is inclined, in this case, to postulate a selective character of (n, γ) reactions at low energies.

(ii) The properties of a nonmagic deformed nucleus can undergo qualitative changes at excitation energies between about 2 to 4 MeV.

These data are in perfect agreement with the qualitative pattern previously obtained in [24] for the process being studied—namely, the situation is governed by a dominant effect of vibrational excitations on the properties of the nuclei up to excitation energies of about 3 to 4 MeV and by a prevalent effect of quasiparticle excitations at higher excitation energies.

This explanation relies on the fact that the level density is below the predictions of the models disregarding or underestimating the effect of nuclear vibrations on this parameter and an increase in the strength functions for cascade transitions that is correlated in energy with this effect. The latter can be qualitatively explained in the simplest way only by collective effects of the enhancement of the gamma-transition probability that are known from the theory. A competing possibility for explaining the enhancement of the strength function is associated with the fact that, in the region around the neutron binding energy, the mean spacing D_λ between compound states deviates from the averaged dependence toward smaller values. No experimental errors have been found that could explain the results presented here.

Since the present analysis has had to rely on a sample of data on the cascade gamma decays of compound states that was limited by the technical potential of the experimental equipment, the conclusion drawn from this analysis should be considered to be preliminary and, to some extent, hypothetical. Nevertheless, the scale of the observed effects and the possible reasons behind their emergence furnish a sufficient motivation for a further detailed study of the properties of nuclei in the excitation-energy region around half the neutron binding energy, where these properties are expected to undergo sharp changes.

ACKNOWLEDGMENTS

This work was supported by the Russian Foundation for Basic Research (project no. 99-02-17863).

REFERENCES

1. Yu. Andzheevski *et al.*, Soobshch. Ob'edin. Inst. Yad. Issled., Dubna, No. R3-81-433 (1981).
2. S. T. Boneva *et al.*, Z. Phys. A **346**, 35 (1993).
3. V. A. Bondarenko *et al.*, Yad. Fiz. **54**, 901 (1991) [Sov. J. Nucl. Phys. **54**, 545 (1991)].
4. S. M. Zakharova, V. S. Stavinskiĭ, and Yu. N. Shubin, Vopr. At. Nauki Tekh., Ser.: Yad. Konstanty, No. 7, 12 (1971); I. A. Lomachenkov and W. I. Furman, Soobshch. Ob'edin. Inst. Yad. Issled., Dubna, No. R4-85-466 (1985).
5. S. T. Boneva *et al.*, Fiz. Élem. Chastits At. Yadra **22**, 1433 (1991) [Sov. J. Part. Nucl. **22**, 698 (1991)].
6. O. T. Grudzevich, Vopr. At. Nauki Tekh., Ser.: Yad. Konstanty, Nos. 3/4, 94 (1997).
7. S. T. Boneva *et al.*, Fiz. Élem. Chastits At. Yadra **22**, 479 (1991) [Sov. J. Part. Nucl. **22**, 232 (1991)].
8. S. T. Boneva *et al.*, Z. Phys. A **338**, 319 (1991); Nucl. Phys. A **589**, 293 (1995).
9. P. Axel, Phys. Rev. **126**, 671 (1962).
10. S. G. Kadmenskiĭ, V. P. Markushev, and V. I. Furman, Yad. Fiz. **37**, 277 (1983) [Sov. J. Nucl. Phys. **37**, 165 (1983)].
11. W. Dilg *et al.*, Nucl. Phys. A **217**, 269 (1973).
12. A. V. Ignatyuk, in *Proceedings IAEA Consultants Meeting on the Use of Nuclear Theory in Neutron Nuclear Data Evaluation, Trieste, Italy, 1975*, IAEA-190 (Vienna, 1976), Vol. 1, p. 211.
13. V. A. Khitrov and A. M. Sukhovoj, in *Proceedings of VI International Seminar on Interaction of Neutrons with Nuclei, Dubna, 1996*; Preprint No. E3-97-202, OIYaI (Joint Institute for Nuclear Research, Dubna, 1997), p. 207.
14. J. Kopecky, in *Proceedings of the Conference on Neutron Capture Gamma-Ray Spectroscopy and Related Topics, Grenoble, France, 1981* (Bristol, 1981), p. 423.
15. A. I. Vdovin, V. V. Voronov, L. A. Malov, *et al.*, Fiz. Élem. Chastits At. Yadra **7**, 952 (1976) [Sov. J. Part. Nucl. **7**, 380 (1976)].
16. S. T. Boneva *et al.*, in *Proceedings of International Conference on Nuclear Data for Science and Technology, Trieste, Italy, 1997*, Ed. by G. Reffo, A. Ventura, and G. Grandi (Italian Physical Society, Bologna, 1997), p. 799.
17. V. A. Khitrov and A. M. Sukhovoj, in *Proceedings of International Conference on Nuclear Data for Science and Techonolgy, Trieste, Italy, 1997*, Ed. by G. Reffo,

A. Ventura, and G. Grandi (Italian Physical Society, Bologna, 1997), p. 750.

18. A. M. Sukhovoj and V. A. Khitrov, Yad. Fiz. **62**, 24 (1999) [Phys. At. Nucl. **62**, 19 (1999)].
19. A. V. Ignatyuk, *Statistical Properties of Excited Nuclei* (Énergoatomizdat, Moscow, 1983).
20. M. A. Lone, R. A. Leavitt, and D. A. Harrison, Nucl. Data Tables **26**, 511 (1971).
21. L. V. Groshev *et al.*, Nucl. Data Tables **5**, No. 1/2 (1968).
22. A. M. Sukhovoĭ and V. A. Khitrov, Prib. Tekh. Éksp., No. 5, 27 (1984).
23. E. P. Grigoriev *et al.*, Preprint No. E3-99-146, OIYaI (Joint Institute for Nuclear Research, Dubna, 1999).
24. A. M. Sukhovoĭ and V. A. Khitrov, Izv. Akad. Nauk, Ser. Fiz. **61**, 2068 (1997).

Translated by A. Isaakyan

Physics of Atomic Nuclei, Vol. 64, No. 2, 2001, pp. 169–176. Translated from Yadernaya Fizika, Vol. 64, No. 2, 2001, pp. 211–218.

NUCLEI
Experiment

Photofission of Americium Isotopes in the Energy Range 6–12 MeV

A. S. Soldatov

Institute of Physics and Power Engineering, pl. Bondarenko 1, Obninsk, Kaluga oblast, 249020 Russia

Received January 24, 2000; in final form, May 22, 2000

Abstract—By means of the reference method, the cross sections for the fission of the ^{241}Am, ^{242m}Am, and ^{243}Am isotopes were measured at the microtron of the Institute of Physics and Power Engineering (Obninsk). These measurements, which employed the cross section for ^{238}U photofission as a reference, covered the energy range 6–12 MeV scanned with a variable step of 50 to 200 keV. Data on ^{242m}Am photofission in the energy range 6–12 MeV and ^{243}Am photofission in the region between 6 and 7 MeV were obtained for the first time. New results for ^{241}Am reveal that the cross sections for ^{241}Am photofission from previous studies of the present author were exaggerated. The new results for this isotope comply well with data of other authors. It is not confirmed that the fissility of ^{241}Am is less than the fissility of ^{243}Am. The energy dependences of the fissilities of the americium isotopes from photofission data are compared with those that were obtained for these fissilities from data on direct reactions like ^{240}Pu(^{3}He, *df*)^{241}Am. The results of this comparison show that the observed fission thresholds and the plateaulike dependences at energies above 7.5 MeV from the two types of studies comply well. The present data show evidence that, in the energy region around 6 MeV, the photofission cross section has a maximum, which is associated, in all probability, with the low-energy resonance structure in the cross section for dipole photoabsorption. © *2001 MAIK "Nauka/Interperiodica".*

1. INTRODUCTION

In inquiries into the physics of nuclear fission, much attention is being given to systematic experimental investigations of various features of the fission process as functions of the charge and the mass number (Z and A, respectively) of the fissile nucleus. Data on the cross sections $\sigma_f(E)$ for the photon-induced fission process show a considerable scatter in the region of the so-called fission plateau ($E < 12$ MeV). The method used to measure the photofission cross section is among the factors that has a nontrivial effect on this scatter. This is the reason why information obtained in a unified experimental approach is of considerable value in systematic investigations. The present study, which is a part of implementation of a wide program aimed at investigating the energy dependences of the cross sections for actinide photofission by a unified method employing bremsstrahlung radiation from a microtron [1–6], is devoted to measuring these cross sections for three americium isotopes, ^{241}Am, ^{242m}Am, and ^{243}Am.

Previous experiments that studied the photofission of americium isotopes in the energy region $E < 12$ MeV dealt primarily with ^{241}Am [1, 7–9]. No data have been published so far on the ^{242m}Am isomer; as to the ^{243}Am isotope, it has hitherto been studied only in [8], along with ^{241}Am. In just the same way as the results of the present study, all other data on the photofission of americium isotopes were obtained by using bremsstrahlung radiation. Of particular interest is the relationship between the photofission cross sections for the ^{241}Am and ^{243}Am isotopes that was obtained in [8] in the energy region corresponding to the fission plateau: with increasing isotope atomic number, the cross section grows, in contrast to what is known for other nuclei, whose cross sections decrease. This circumstance, together with the fact that the cross sections for ^{241}Am photofission from [1] disagree with those from [8, 9], has been the motivation for performing the experiment reported here.

2. DESCRIPTION OF THE EXPERIMENT

The cross sections for ^{241}Am, ^{242m}Am, and ^{243}Am photofission were measured by using a beam of bremsstrahlung photons from the microtron of the Institute of Physics and Power Engineering (Obninsk). The measurements were performed in the region E_{max} = 6–12.4 MeV of the endpoint of the bremsstrahlung spectrum with a step of 0.05 MeV for $E_{max} < 6.7$ MeV, 0.1 MeV for E_{max} = 6.7–7.7 MeV, and 0.2 MeV for higher energies. For all three isotopes of americium, the data discussed below were obtained in a single experiment. Because of a small thickness of a fissile layer, the exposure time for the ^{242m}Am isomer was increased by a factor of a few units in relation to the exposure times for the other two isotopes. Use was made in the present experiment of a procedure that relies on a relative measurement of photofission cross sections in a bremsstrahlung-photon beam. For a reference isotope, this procedure, which was described in detail elsewhere [1, 2], employs ^{238}U, whose photofission cross section was estimated in [1].

A water-cooled device consisting of a 1-mm-thick tungsten disk and a 12-mm-thick aluminum absorber of electrons served as a braking target. Fissile layers of the oxides of the isotopes being investigated and of ^{238}U

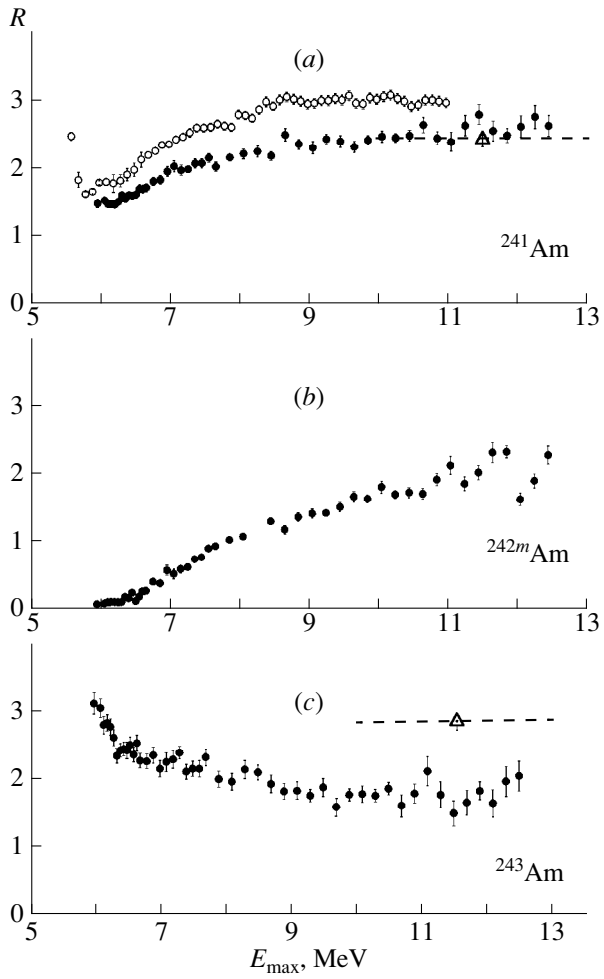

Fig. 1. Ratios of the yields $Y(E_{max})$ from (*a*) ^{241}Am, (*b*) ^{242m}Am, and (*c*) ^{243}Am photofission to the corresponding yields from the photofission of the reference nucleus ^{238}U versus the endpoint energy of the bremsstrahlung spectrum: (closed circles) data of the present study, (open circles) data from [1], and (open triangles and dashed straight lines) data from [8].

were deposited onto aluminum substrates 0.1 mm thick and were arranged in back-to-back geometry. The experiment measured the ratio of the yield of products from the photofission of an isotope being studied, $Y(E_{max})$, to the corresponding yield from the photofission of the reference isotope, $Y_0(E_{max})$,

$$R(E_{max}) = Y(E_{max})/Y_0(E_{max}). \quad (1)$$

For the bremsstrahlung spectrum, the photofission-reaction yield as a function of E_{max} and the photofission cross section $\sigma_f(E)$ as a function of the nuclear excitation energy E are related by the equation

$$Y(E_{max}) = C(E_{max}) \int_0^{E_{max}} \sigma_f(E) N(E, E_{max}) dE, \quad (2)$$

where $N(E, E_{max})$ is the spectrum of bremsstrahlung photons, while $C(E_{max})$ is a factor that depends on the normalization of the spectrum $N(E, E_{max})$, the number of nuclei in the fissile target, and the photon flux incident on it. A similar equation relates the yield from the photofission of the reference nucleus, $Y_0(E_{max})$, and its photofission cross section $\sigma_f^0(E)$.

One holder containing a layer of a fissile isotope being investigated and a layer of the reference substance was used for each isotope. The fissile layers were covered with diaphragms having a hole of diameter 10 mm. Fission fragments were recorded by solid-state tracking detectors from TV mica, which were arranged behind the diaphragms that were rigidly attached to fissile targets and which had a hole diameter of 12 mm. The distance from the fissile layer to the diaphragm was 1.5 mm. The ^{241}Am and ^{243}Am layers were approximately 100 μg/cm^2 thick. The thickness of their ^{238}U counterpart layers was 200 μg/cm^2. In the ^{242m}Am–^{238}U pair, the layer thicknesses were 6 and 4 μg/cm^2, respectively. The holder containing this pair of layers was placed more closely to the braking target than the others, at a distance of 21 mm from its tungsten element—the holders containing ^{243}Am and ^{241}Am were positioned at distances of 42 and 49 mm, respectively.

The fissile substance of the ^{241}Am layer was isotopically pure. The ^{243}Am layer contained 30.3% ^{241}Am, 3.8% ^{244}Cm, and 0.7% ^{242}Cm. The amount of admixtures was determined by means of alpha-spectrometric measurements. On the day of preparation, the fissile substance of the ^{242m}Am layer had the following isotopic composition (in weight ratios): ^{242m}Am : ^{241}Am : ^{243}Am = 1 : 0.162 : 0.006. In contrast to the ^{241}Am and ^{243}Am layers, which were manufactured immediately before the experiment, the ^{242m}Am layer had been prepared 5.75 years earlier. As a result, the isotopic composition of the fissile substance changed to become ^{242m}Am : ^{241}Am : ^{238}Pu : ^{242}Pu : ^{243}Am : ^{242}Cm : ^{237}Np = 0.97 : 0.16 : 0.015 : 0004 : 0.006 : 0.003 : 0.001.

3. EXPERIMENTAL RESULTS AND DISCUSSION

Figure 1 displays the measured values of $R(E_{max})$. The uncertainty $\Delta R(E_{max})$ includes statistical errors in the number of tracks that were recorded by the detectors, errors in viewing the detectors under a microscope, and errors in introducing corrections for the isotopic composition of the fissile substance under study and for the background from spontaneous fission. The results for ^{241}Am are free from the last two components of the error $\Delta R(E_{max})$. For ^{243}Am, the background from spontaneous fission is sizable only at the lowest points on the energy scale, sharply decreasing from 6 to 1% as the energy is increased from E_{max} = 5.95 to 6.1 MeV and further to a negligibly small value. For ^{242m}Am, this background amounted to 80% near the lower boundary of the energy interval under study; with increasing

energy, it decreased down to 10% at E_{max} = 6.6 MeV and still further to a level below 1% of the number of events recorded by the detector of fission fragments.

The aforementioned uncertainty $\Delta R(E_{max})$ does not include a systematic error estimated here at about 15%. This estimate takes into account errors associated with a mechanical realization of the experimental facility used and the error in determining the ratio of the number of nuclei in the target from the fissile isotope being studied and the ^{238}U target. These ratios were measured in a dedicated experiment by exposing, to a beam of 5-MeV monochromatic neutrons, the same combinations of layers as those that were used to measure the ratios of the photofission yields. The statistical accuracy of these measurements was about 3%. The cross sections σ_{nf} for neutron-induced fission were taken to be 1.77, 1.70, and 1.45 b for ^{241}Am [10], ^{242m}Am [11], and ^{243}Am [10], respectively.

The results of the present measurements for the ratios $R(E_{max})$ are shown in Fig. 1*a*, along with the results from [1, 8] for ^{241}Am. Within the measurement errors, the results obtained here are in accord with those from [8], but they are approximately 20% below the dependence $R(E_{max})$ reported in [1]. In order to explain this discrepancy, we recall that, in [1], the ratios of the number of nuclei in the fissile targets under study were measured by using neutrons of energy 14.5 MeV. At this energy value, the scatter of values of the cross section for neutron-induced fission that were obtained by different authors for ^{241}Am is as large as 15%; as can be seen from the data sample quoted in [10], the value chosen in [1] on the basis of the ENDF/B-VI estimate is the largest of all. Moreover, the geometry of the measurements in [1] was different from back-to-back geometry. In view of all this, preference should be given to the present results. In general, the energy dependence $R(E_{max})$ has the same qualitative character within the errors in the two series of measurements.

For the energy dependence of the ratios of the yields from ^{242m}Am and ^{238}U photofission, Fig. 1*b* displays results corrected for the presence of the aforementioned admixtures. Since the admixtures of ^{242}Cm, ^{242}Pu, and ^{237}Np are very small (their concentrations are 0.3, 0.4, and 0.1%, respectively) and since there is not sufficient information about ^{242}Cm photofission, the contribution of the admixtures of these three isotopes was represented, in calculating the relevant corrections, in terms of a 0.8% ^{238}Pu admixture in addition to the actually present 1.5% of ^{238}Pu. This increased the uncertainty in the correction itself by not more than 1.5–2%. Owing to this assumption, it was possible to restrict the inputs used to describe the dependences $R(E_{max})$ measured in the present experiment and in the analogous experiment reported in [6]. Although the total percentage of admixtures in the fissile substances did not exceed 20%, the correction for them was significant because, with decreasing energy, the yield from ^{242m}Am photofission begins to decrease faster from $E_{max} \approx 10$ MeV than the yield from the photofission of the admixtures. In view of this, the error in the results for $R(E_{max})$ is as large as 50% at the lowest point measured here, but it falls down to 5 or even 4% as soon as the energy reaches 7 MeV. Data on ^{242m}Am photofission have been obtained here for the first time.

Figure 1*c* shows the experimental dependences $R(E_{max})$ for ^{243}Am, which were also corrected for the presence of admixtures in the target of fissile ^{243}Am. In taking them into account, it was assumed that the admixture involves only ^{241}Am, but that its amount is 35%. In order to justify this, we recall that the subbarrier reduction of the fissility commences at the same excitation-energy value of 6 MeV for ^{241}Am and for ^{244}Cm and that, at higher energies, the fissility of ^{244}Cm cannot exceed the fissility of ^{241}Am by more than 20% [12–14]. A 0.7% admixture of ^{242}Cm was also included in addition to 30.3% of ^{241}Am. According to my estimates, this increases the uncertainty in the correction by not more than 2 to 2.5%.

Figure 1*c* also shows the ratio $R(E_{max})$ as obtained in [8]. The present data for ^{243}Am deviate considerably from the results presented in [8]. In the energy region covered by the data on $R(E_{max})$ from [8], our dependence goes much lower. On average, the discrepancy is 60%, which is much greater than the uncertainties in the two experiments being discussed.

In the calibration measurements of the experiment reported in [8], the absolute values of the photofission yields and the relative fissilities of ^{241}Am, ^{243}Am, and ^{238}U were determined by the same method as in the present study with the aid of solid-state tracking detectors of fission fragments. Moreover, the results of the calibration measurements in [8] for the ratio of the yields of fragments from ^{241}Am and ^{238}U fission agree with the results of the present experiment within the errors. This gives sufficient ground to believe that the reason behind the discrepancies between the R values for ^{243}Am is not of a methodological character—it may be rooted either in taking into account admixtures or in determining the ratio of the numbers of nuclei in fissile ^{243}Am and ^{238}U targets.

In fissile ^{243}Am substance, the admixtures were indeed significant, but they were dominated by ^{241}Am. It follows that almost all inputs required for introducing corrections for impurities were obtained in the same experiment, so that errors in doing this were minimized. According to estimates, errors stemming from the fact that a 3.8% admixture of ^{244}Cm and a 0.7% admixture of ^{242}Cm were taken into account indirectly could not have a pronounced effects on the results. Although the correction was about 40% in the energy range E_{max} = 10–12 MeV considered here and increased the statistical uncertainty in the corrected values of $R(E_{max})$ from 4% to about 10%, the observed discrepancy can hardly be attributed to this correction.

As was indicated above, the ratio of the number of nuclei in fissile targets from the americium isotopes

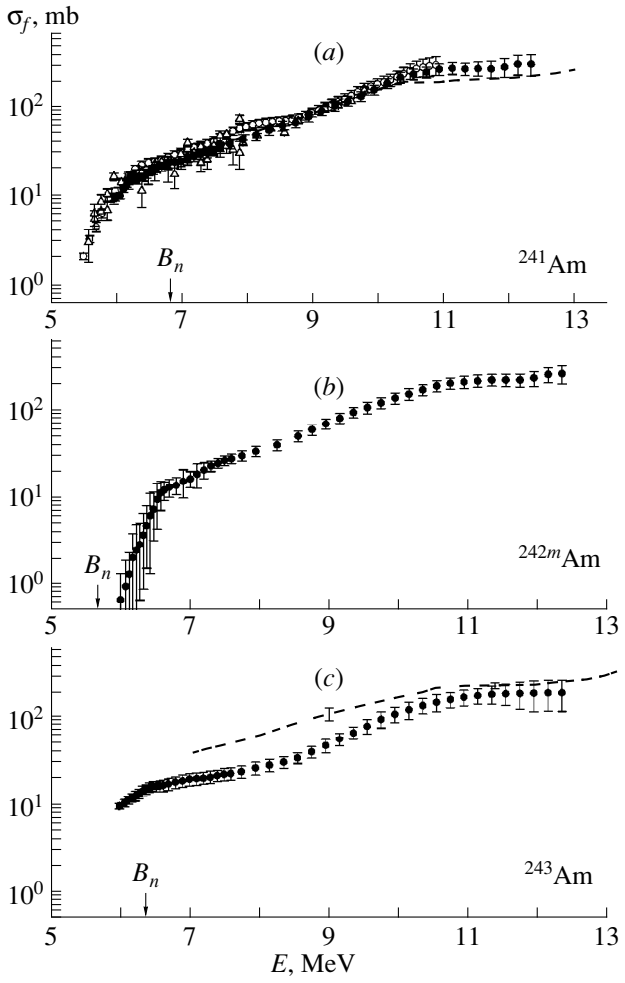

Fig. 2. Cross sections for (*a*) ^{241}Am, (*b*) ^{242m}Am, and (*c*) ^{243}Am photofission as functions of energy: (closed circles) data of the present study, (open circles) data from [1], (open triangles) data from [9], and (dashed curves) data from [8]. The arrows indicate the neutron binding energy B_n.

under study and the number of reference nuclei was determined in a flux of 5-MeV monochromatic neutrons. Both for ^{241}Am and for ^{243}Am, this procedure made use of the cross sections for neutron-induced fission that were obtained from a analysis of available experimental and estimated data presented by the same group of authors [10]. Owing to this, the probability of going beyond a 15% accuracy claimed above for the present determination of the absolute values of the ratios R was reduced to some extent. All the aforesaid gives sufficient grounds to state that the observed deviations from the results obtained in [18] are not associated with the errors in the results of the present experiment.

In order to obtain the integrated dependence $Y(E_{\max})$ for the fissile isotope being studied, the photofission cross section $\sigma_f^0(E)$ for reference nuclei ^{238}U that was estimated in [1] was integrated over the bremsstrahlung spectrum in just the same way as in (2) [15] and the result was multiplied by the ratio $R(E_{\max})$ measured in back-to-back geometry. By applying the iterative method of directional-discrepancy minimization [16], the resulting integrated dependences for the americium isotopes being studied were resolved for the sought photofission cross sections $\sigma_f(E)$. In this procedure, the integral of the photofission cross section was considered as a smooth dependence featuring no errors and having a universal form for the relative measurements of photofission cross sections in the experiments of our group [1–6]. This means that errors in the estimated values of the photofission cross section $\sigma_f^0(E)$ for the reference nucleus were disregarded in our calculations.

The errors in $\sigma_f(E)$ were determined by repeatedly solving Eq. (2) with the left-hand side scattered according to the Poisson law with allowance for the errors $\Delta Y(E_{\max})$ [these errors were calculated from $\Delta R(E_{\max})$ in just the same way as $Y(E_{\max})$ was calculated from $R(E_{\max})$] and by considering the variance of the resulting solutions.

The fission cross sections deduced from the analysis described immediately above are displayed in Fig. 2, where the dark symbols represent the results obtained in the present study.

Figure 2*a* shows the cross sections for ^{241}Am photofission. For this nuclear species, errors in the measurement of $R(E_{\max})$ in the near-threshold energy region are about 3%, which exceeds only slightly the level of errors in preceding experiments of our group that were devoted to measuring fission cross sections by the relative method. For this reason, the cross sections for ^{241}Am photofission were calculated, within the iterative method of directional-discrepancy minimization, by using a standard number of iterative steps [2] that makes it possible to trace the structure of the energy dependence of the cross sections. In particular, the present measurements, which scan the excitation-energy scale in somewhat greater detail than the measurements in [1], revealed a modest peak of width about 200 keV in the region around $E = 6.2$ MeV. It is in connection with the discovery of a similar maximum in the immediate vicinity of the fission threshold and below it in the energy dependence of the fission cross section for the ^{237}Np nucleus [2], which is also odd–even, that the choice of the number of iterations was comprehensively discussed in that study. In addition, Fig. 2*a* displays (triangles) the results from [9], which were also obtained by using bremsstrahlung radiation and which are, by and large, consistent with the present data, with the exception of a few points from [9] that show significant deviations. In the data from [9], there is also a maximum in $\sigma_f(E)$, but it occurs at lower energies (around 6 MeV) than in the present study.

The $\sigma_f(E)$ curve corresponding to the first measurements of our group [1] lies somewhat higher than the energy dependence obtained for this cross section in the present study. The discrepancies between the absolute

values of $\sigma_f(E)$ were discussed above in comparing the data on $R(E_{max})$. The dashed curve represents the cross sections obtained in [8]; within the errors, they agree with the data reported here and the data from [9].

Figure 2*b* displays the cross section for ^{242m}Am photofission as a function of energy. For this nuclear species, the input experimental data as represented by the dependence $R(E_{max})$ are characterized by large statistical uncertainties associated with corrections for the isotopic composition, especially in the low-energy region, where the structure of the fission cross section largely manifests itself. It would hardly be justifiable to apply the above mathematical procedure to a treatment of such data and to discuss the resulting resonances in the photofission cross section. Prior to processing the dependences $Y(E_{max})$ for ^{242m}Am by the method of directional-discrepancy minimization, they were therefore subjected to smoothing, which was performed on the basis of five experimental points in the region of large statistical uncertainties, $E_{max} < 7$ MeV, and on the basis of three experimental points in the region where the reliability of the measurements is higher, $E_{max} > 7$ MeV. The data obtained in the present study furnish information only about the gross behavior of the energy dependence $\sigma_f(E)$. Below the apparent ^{242m}Am fission threshold, which occurs at an energy value around 6.5 MeV, the fission cross sections $\sigma_f(E)$ were found with very large errors. In the region $E > 7$ MeV, the uncertainties in $\sigma_f(E)$ are on the same order of magnitude as the uncertainties in the photofission cross sections for other nuclei that our group studied by the relative method.

In Fig. 2*c*, the cross sections obtained here for ^{243}Am photofission are contrasted against the cross sections from [8]. The discrepancies between the data on the ratios $R(E_{max})$ that were discussed above survive in the results for the cross sections as well. As in the case of ^{242m}Am, large statistical errors and the scatter of points in the data on $R(E_{max})$, which play the role of inputs for calculating the cross sections, required smoothing the dependence $Y(E_{max})$ prior to applying the iterative method of directional-discrepancy minimization. As a result, only the gross behavior of the energy dependence of the photofission cross section and its absolute value were obtained here for ^{243}Am as well. It can clearly be seen from these results that a subbarrier reduction of the cross section commences below the energy value of $E = 6.4$ MeV.

The results obtained in the present study for the photofission of americium isotopes can also compared with experimental data on the fission probability as determined from direct reactions. For this purpose, the photofission cross sections were rescaled into the fissilities by taking the ratios of these cross sections to those for photoabsorption. Since the dipole-photoabsorption process is dominant in the energy region being considered, the fissilities were specified as

$$P_f(E) \approx \sigma_f(E)/\sigma_{c1}(E), \qquad (3)$$

where $\sigma_{c1}(E)$ is the cross section for dipole photoabsorption. Since there are no direct experimental data on the dipole-photoabsorption cross sections for americium isotopes, a superposition of two Lorentzian forms,

$$\sigma_{c1} = \sum_{i=1}^{2} \sigma_i \frac{E^2\Gamma_i^2}{(E^2 - E_i^2)^2 + E^2\Gamma_i^2}, \qquad (4)$$

with the parameters set to $\sigma_1 = 311$ mb, $\Gamma_1 = 2.37$ MeV, $E_1 = 10.77$ MeV, $\sigma_2 = 459$ mb, $\Gamma_2 = 5.13$ MeV, and $E_2 = 13.8$ MeV, which was obtained in [17] for ^{238}U, was used here to approximate the energy dependence $\sigma_{c1}(E)$ in computing $P_f(E)$. In the present relative measurements of the photofission cross sections, the reference cross section for energies above 7 MeV was estimated in [1] on the basis of the same experimental data from [17] on the ^{238}U photofission cross section as those that were used in evaluating the parameters of the Lorentzian forms in [4]. By invoking the same information about the cross section for ^{238}U photofission in multiplying $R(E_{max})$ by the integral of $\sigma_f^0(E)$ over the bremsstrahlung spectrum to evaluate $\sigma_f(E)$ and in dividing this ratio by the dipole-photoabsorption cross section to evaluate the fissilities, we reduced, to some extent, the uncertainties in $P_f(E)$ that are associated with the choice of $\sigma_f^0(E)$ and $\sigma_{c1}(E)$.

The fissilities $P_f(E)$ for ^{241}Am versus energy that were obtained in the present study are shown in Fig. 3*a*, along with the $P_f(E)$ values measured in [17, 18] for the same nucleus ^{241}Am in the relevant direct reaction (^{3}He, *df*). In general, the dependences $P_f(E)$ as obtained in the present study and in [12, 18] are similar: a subbarrier reduction of the fissility with decreasing energy commences at the same point, and the so-called fissility plateau is observed in either case in the energy region from 7 to 11 MeV. Over a major part of the energy interval being studied, the fissility values from the different approaches agree within the experimental errors. Only below 7 GeV does the fissility curve obtained in the present study goes below data deduced from the experiments that explored the above direct reactions. This can be explained by exaggerated values of dipole-photoabsorption cross section $\sigma_{c1}(E)$ that are obtained at low energies from the approximation of the data given in [17]. For the photofission of a number of thorium, uranium, neptunium, and plutonium isotopes, it was shown in the review article of Ostapenko *et al.* [19] that a good description of the dependence $\sigma_{c1}(E)$ by the two Lorentzian forms (4) in the energy region of the giant dipole resonance leads to an overestimation of $\sigma_{c1}(E)$ at low energies.

A resonance-like irregularity at $E = 6.2$ MeV is more spectacular in the dependence $P_f(E)$. In the same energy range, a similar irregularity was observed in [9], but with somewhat larger uncertainties in $P_f(E)$. In

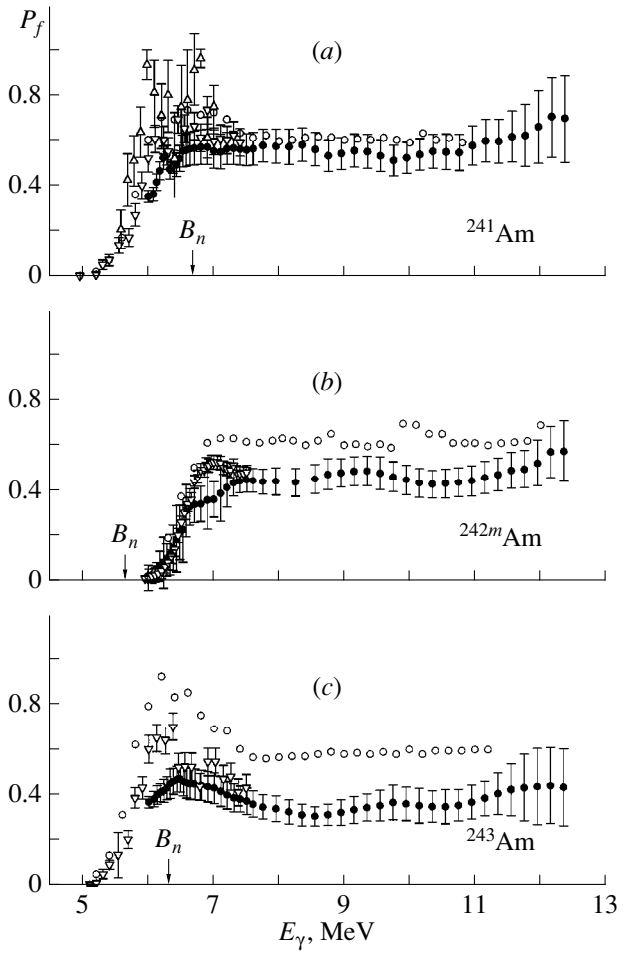

Fig. 3. Fissilities of (*a*) ^{241}Am, (*b*) ^{242m}Am, and (*c*) ^{243}Am as functions of energy according to data on photofission along with those from direct-reaction data: (closed circles) data of the present study, (open circles) data from [18], (open triangles) data from [9], and (open inverted triangles) data from [12]. The arrows indicate the neutron binding energy B_n.

Fig. 3*a*, the triangles represent a segment of the energy dependence of the fissility from [9] in the energy region $E < 7$ MeV. In data from direct reactions, such an irregularity does not stand out against the errors. As to manifestations of a resonance in the fissility of ^{241}Am at energies below the neutron binding energy of B_n = 6.66 MeV, the situation here is similar to that which was observed and discussed in detail for ^{237}Np in [2]. As in [2], a manifestation of the resonance in photofission data and simultaneously its absence from direct-reaction data can hardly be explained in terms of resonances in the fission-barrier penetrability for *Z*-odd nuclei or in terms of the competition between decay widths. In all probability, this is a manifestation of a resonance structure in the dipole-photoabsorption cross section [20].

Figure 3*b* presents a comparison of the fissilities obtained in the present study for the ^{242m}Am isotope with the fissilities of the same nucleus in the relevant direct reactions (*d*, *pf*) [12] and (^{3}He, *tf*) [18]. The subbarrier segments of $P_f(E)$ measured in the three studies agree within the errors, but the energy value from which the fissility begins to decrease is lower by about 300 keV in the photofission data. In the energy region below 7.3 MeV, the fissility is somewhat higher in the direct-reaction data. In just the same way as in the case of ^{241}Am, this seems to be due to the use of the overestimated dipole-photoabsorption cross section from [17] in the present calculation. The fissility plateau is also clearly seen in the dependence $P_f(E)$ for ^{242m}Am. On the plateau, the fissility values disagree with data from [18], but they comply, albeit within a narrow energy interval, with data from [12].

Figure 3*c* displays the fissilities of the ^{243}Am isotope that were obtained in the present experiment and in the experiments that studied the relevant direct reaction (^{3}He, *df*) [12, 18]. In what is concerned with the character of the dependence $P_f(E)$, our data are consistent with those from [12, 18]. Even a modest enhancement of the fissility in the vicinity of the point E = 6.5 MeV can be explained by an overestimation of the dipole-photoabsorption cross section in this energy region [19]. In fact, the fissility maximum at 6.5 MeV occurs very close to the neutron binding energy of B_n = 6.38, and this makes it possible to interpret this maximum as the result of the competition between the fission and the neutron channel of excited-nucleus decay.

In what is concerned with the discrepancies between the fissility values in the plateau region, it should be borne in mind that the dependences $P_f(E)$ obtained from the data on the same direct reaction ^{242}Pu(^{3}He, *df*) ^{243}Am also show variations commensurate with them. Even the large values of the fissility for ^{243}Am in the plateau region do not exceed P_f values obtained in [18] for ^{241}Am. This circumstance is of importance in connection with a comparison of the mean values of the ^{243}Am and ^{241}Am fissilities at 11.5 MeV from [8] (0.61 ± 0.04 and 0.53 ± 0.03, respectively) with those obtained in the present study on the basis of the averaged experimental data for E_{max} from 11 to 12 MeV. The averaged fissilities calculated here for such a comparison with the aid of the relation presented in [8] are 0.38 ± 0.02 and 0.58 ± 0.03 for ^{243}Am and ^{241}Am, respectively. The value for ^{243}Am is much less than that in [8], but the analogous values for ^{241}Am comply within the errors. That the averaged fissility of the ^{243}Am isotope is lower than the fissility of the ^{241}Am isotope, which is also odd–even, but which has fewer neutrons, is quite natural. This is confirmed by the direct-reaction data from [12, 18], which are quoted in the table.

The table lists the averaged values of the fissilities $\bar{P}_f$ of the isotopes investigated in the present experiment. In contrast to those from [8], these results were obtained from the data that are directly associated with the fissilities and which are displayed in Fig. 3. The energy intervals over which averaging has been per-

Averaged values of the fissility P_f in the plateau region, energy intervals ΔE over which averaging has been performed, and apparent fission thresholds E_{app} for the nuclei studied in the present experiment

Fissile nucleus	$\bar{P}_f$, MeV	ΔE, MeV	E_{app}, MeV	Reaction	References
^{241}Am	0.56 ± 0.02	7–12	<6	(γ, *f*)	Present study
	0.53 ± 0.03	10–12	–	(γ, *f*)	[8]
	0.71 ± 0.03	7–10	5.7	(γ, *f*)	[9]
	0.60 ± 0.03	7–7.4	5.8	(^{3}He, *df*)	[12]
	0.61	7.4–10.8	5.7	(^{3}He, *df*)	[18]
^{242m}Am	0.45 ± 0.02	7–12	6.4	(γ, *f*)	Present study
	0.50 ± 0.01	7–7.5	6.5	(^{3}He, *df*)	[12]
	0.62 ± 0.01	7.1–12	6.4	(^{3}He, *df*)	[18]
^{243}Am	0.37 ± 0.02	7–12	<6	(γ, *f*)	Present study
	0.61 ± 0.04	10–12	–	(γ, *f*)	[8]
	0.45 ± 0.03	7.1–7.5	5.7	(^{3}He, *df*)	[12]
	0.58 ± 0.01	7.4–11.2	5.6	(^{3}He, *df*)	[18]

formed are given in a separate column. Also quoted in the table are the apparent fission thresholds taken to mean the energy values that correspond to the fissility equal to half its value in the plateau region. All the numerical values in the table were obtained in the present study by processing graphical data from original investigations. That the $\bar{P}_f$ value for ^{241}Am was much larger in [9] can be explained by the choice of an underestimated photoabsorption cross section in [19] for energies in the range 7–10 MeV.

4. CONCLUSION

In an experiment performed at the microtron of the Institute of Physic and Power Engineering (Obninsk), the cross sections for the photofission of the ^{241}Am, ^{242m}Am, and ^{243}Am isotopes as functions of energy have been determined in the energy range from 6 to 12 MeV. In order to measure the cross sections for the photofission process induced by bremsstrahlung photons, the relative method has been applied with the cross section for ^{238}U photofission as a reference. Data on the cross sections for ^{242m}Am in the energy range from 6 to 12 MeV and for ^{243}Am photofission in the energy range from 6 to 7 MeV have been obtained for the first time. The new results for ^{241}Am have revealed that the cross sections for ^{241}Am photofission were exaggerated in [1]. The results of the present measurements for ^{241}Am comply well with the data of other authors. At an energy value of 6 MeV, the cross sections determined here show evidence for an irregularity that is likely to be associated with the low-energy resonance structure in the dipole-photoabsorption cross section [20] and which is also suggested by earlier data from [9]. A quite unexpected relationship between the ^{241}Am and ^{243}Am fissilities from [8], where the latter was found, in disagreement with model predictions, to be greater than the former, has not been confirmed. A comparison of the americium-isotope fissilities obtained as functions of energy from the present photofission data and from data on direct reactions like ^{240}Pu(^{3}He, *df*)^{241}Am has yielded agreement for the apparent fission thresholds and for the plateaulike dependences at energies above 7.5 MeV.

ACKNOWLEDGMENTS

I am grateful to Yu.B. Ostapenko for enlightening discussions on the results presented in this article and to V.E. Rudnikov for participation in the measurements.

REFERENCES

1. A. S. Soldatov and G. N. Smirenkin, Yad. Fiz. **55**, 3153 (1992) [Sov. J. Nucl. Phys. **55**, 1757 (1992)].
2. A. S. Soldatov *et al.*, Yad. Fiz. **56** (10), 16 (1993) [Phys. At. Nucl. **56**, 1307 (1993)].
3. A. S. Soldatov, V. E. Rudnikov, and G. N. Smirenkin, At. Énerg. **78**, 400 (1995).
4. A. S. Soldatov and G. N. Smirenkin, Yad. Fiz. **58**, 224 (1995) [Phys. At. Nucl. **58**, 182 (1995)].
5. A. S. Soldatov *et al.*, Yad. Fiz. **61**, 1427 (1998) [Phys. At. Nucl. **61**, 1325 (1998)].
6. A. S. Soldatov, A. I. Blokhin, A. V. Ignatyuk, *et al.*, Yad. Fiz. **63**, 34 (2000) [Phys. At. Nucl. **63**, 31 (2000)].
7. L. Katz, A. P. Baerg, and F. Brown, in *Proceedings of 2nd International Conference on Peaceful Uses of Atomic Energy, Geneva, 1958* (UN, Geneva, 1958), Vol. 16, p. 200.
8. I. S. Koretskaya *et al.*, Yad. Fiz. **30**, 910 (1979) [Sov. J. Nucl. Phys. **30**, 472 (1979)].
9. S. J. Watson, D. J. S. Findlay, and M. R. Sene, Nucl. Phys. A **548**, 365 (1992).

10. A. V. Ignatyuk, A. I. Blokhin, V. P. Lunev, *et al.*, Vopr. At. Nauki Tekh., Ser.: Yad. Konstanty, No. 3, 25 (1999).
11. B. I. Fursov *et al.*, in *Proceedings of International Conference on Nuclear Data for Science and Technology, Gatlinburg, Tennessee, 1994*, Vol. 1, p. 269.
12. B. B. Back *et al.*, in *Proceedings of International Symposium on Physics and Chemistry of Fission, Rochester, 1973* (IAEA, Vienna, 1974), Vol. 1, p. 3.
13. B. B. Back *et al.*, in *Proceedings of International Symposium on Physics and Chemistry of Fission, Rochester, 1973* (IAEA, Vienna, 1974), Vol. 1, p. 25.
14. O. I. Osetrov, V. D. Dmitriev, and S. V. Khlebnikov, in *Proceedings of XIII Meeting on Physics of Nuclear Fission, Obninsk, 1995*, p. 258.
15. M. Z. Tarasko *et al.*, At. Énerg. **65**, 290 (1988).
16. M. Z. Tarasko, Preprint No. 1446 FÉI (Institute of Physics and Power Engineering, Obninsk, 1983).
17. J. T. Caldwell *et al.*, Phys. Rev. C **21**, 1215 (1980).
18. A. Gavron *et al.*, Phys. Rev. C **13**, 2374 (1976).
19. Yu. B. Ostapenko *et al.*, Fiz. Élem. Chastits At. Yadra **12**, 1364 (1981) [Sov. J. Part. Nucl. **12**, 545 (1981)].
20. G. A. Bartholomew *et al.*, in *Advances in Nuclear Physics* (Plenum, New York, 1973), Vol. 7.

Translated by A. Isaakyan

Physics of Atomic Nuclei, Vol. 64, No. 2, 2001, pp. 177–178. Translated from Yadernaya Fizika, Vol. 64, No. 2, 2001, pp. 219–220.

NUCLEI
Experiment

Evaluation of the Time of Prompt-Fission-Neutron Emission from ^{252}Cf by Measuring a Two-Particle Correlation Function

Yu. D. Katarzhnov, V. G. Nedopekin, V. I. Rogov, and S. T. Sukhorukov

Institute of Theoretical and Experimental Physics, Bol'shaya Cheremushkinskaya ul. 25, Moscow, 117259 Russia

Received May 26, 2000

Abstract—The time of prompt-fission-neutron emission from ^{252}Cf is evaluated at $\tau_0 \geq (1–2) \times 10^{-19}$ s by measuring a two-neutron correlation function. The final-state interaction of identical neutrons emitted by moving fission fragments is taken into account. © *2001 MAIK "Nauka/Interperiodica".*

The time of prompt-fission-neutron emission is of importance both for studying various neutron-emission mechanisms and for further developing the theory of nuclear fission. According to various theoretical estimates [1–3], this time varies in the interval $(0.5–5) \times 10^{-20}$ s. Present-day facilities are unable to measure directly such short time intervals. By measuring a correlation of two fission neutrons with the aid of nanosecond equipment of resolution about 0.1 ns, one can nevertheless deduce information about the times of prompt-neutron emission—that is, about time intervals that are ten orders of magnitude shorter than the time resolution of the measuring instruments used. Therefore, an experiment aimed at measuring a two-particle correlation function is of great interest not only as a means to evaluate the time of prompt-neutron emission but also as a unique method for measuring such short time intervals, though indirectly.

In [4], we presented the results obtained by measuring the two-neutron correlation function for ^{252}Cf spontaneous fission and evaluated the time of prompt-fission-neutron emission without allowing for the motion of fission fragments in the laboratory frame. Here, we process the extended results of the measurements from [4] more carefully, taking into account the motion of fission fragments, which are known to be the main source of prompt-neutron emission [5]. A more accurate calibration of the energy scale of the facility used is also performed.

A detailed description of our facility and of the procedure of measurements is given elsewhere [4]. Here, we only recall that the correlation function for two neutrons emitted by fragments of the f type (f = l or h for a light or the complementary heavy fragment, respectively) was defined as

$$R_f^{\text{meas}} = N_{12}^f(\mathbf{p}_1, \mathbf{p}_2)N_f/[N_1^f(\mathbf{p}_1)N_2^f(\mathbf{p}_2)] = R^{\text{meas}}(p, q),$$

where N_f is the number of recorded fragments of the f type; $N_1^f(\mathbf{p}_1)$ and $N_2^f(\mathbf{p}_2)$ are the numbers of neutrons that have momenta $\mathbf{p}_1$ and $\mathbf{p}_2$ and which were recorded by detectors 1 and 2, respectively; $N_{12}^f(\mathbf{p}_1, \mathbf{p}_2)$ is the number of coincidences between the recording of a neutron with momentum $\mathbf{p}_1$ by detector 1 and the recording of a neutron with momentum $\mathbf{p}_2$ by detector 2; $p = |\mathbf{p}_1 + \mathbf{p}_2|/2$; and $q = |\mathbf{p}_1 - \mathbf{p}_2|$.

Having analyzed the background, we restricted the kinematical region of neutrons taken for processing to the interval $40 \leq p_1, p_2 \leq 130$ MeV/c. In this region, the background associated with neutron scattering on the surrounding structures was about 13% of the recorded intensity. After introducing corrections for the angular resolution of the system recording fragments [6], we obtained 162 values of the correlation function $R_f^{\text{expt}}(p, q)$ for each type of fragments. By using the χ^2 method, these values were then compared with the theoretical function $R_{nn}(p, q)$ calculated by the formula

$$R_{nn}(p, q) = R_{nn}^{\text{lab}}(p, q)R_{nn}^{\infty},$$

where $R_{nn}^{\text{lab}}(p, q)$ is the normalized correlation function in the laboratory frame—this function also depends on the spatial and time dimensions of the neutron source, r_0 and τ_0, respectively—and R_{nn}^{∞} is an adjustable parameter that takes into account the number of emitted neutrons. The fitted values of this parameter fell within the interval between 0.7 and 0.8. In order to calculate $R_{nn}^{\text{lab}}(p, q)$, we used the formulas obtained in [7] for the two-neutron correlation function in the source rest frame with allowance for the final-state interaction of identical particles and rescaled the results into the laboratory frame. In accordance with the mean masses of light and heavy fragments (106 and 141.9 amu), the spatial parameter r_0 was set to 2.22 and 2.45 fm for light and heavy fragments, respectively. The root-mean-square radius of the neutron-generation region is $R_0 = \sqrt{3}\, r_0$. In taking into account the motion of fission fragments in the laboratory frame, we used the values of

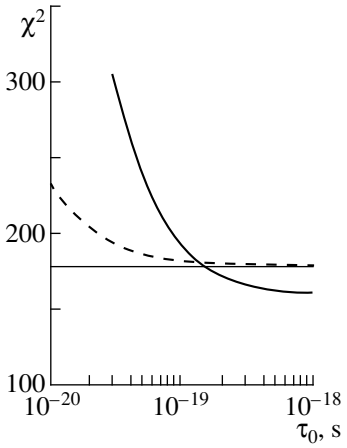

χ^2 as a function of the calculated time of neutron emission by a source for (solid curve) a light fragment and (dashed curve) the complementary heavy fragment. The horizontal line corresponds to $\chi^2 = m + \sqrt{2m}$.

$V_l = 0.0461c$ and $V_h = 0.0345c$ from [8] for the mean velocities of light and heavy fragments, respectively.

The results obtained by comparing experimental data with the calculated values are illustrated in the figure, which shows χ^2 versus the time τ_0 of neutron emission by the source. From this figure, it can be seen that the condition $\chi^2 \le m + \sqrt{2m}$ ($m = 160$ is the number of degrees of freedom) yields $\tau_0 \ge 1.4 \times 10^{-19}$ s for light fragments. The agreement with the theory is inferior for heavy fragments, and we estimate the limit on τ_0 as $\tau_0 \ge (1–2) \times 10^{-19}$ s according to the data on heavy fragments. It is quite natural to fix the parameters r_0 and V_f at the above values, because a variation of these parameters within reasonable limits affects χ^2 only slightly: the resulting changes in χ^2 are much smaller than the statistical error in χ^2.

In summary, we have obtained a more accurate estimate of the time of prompt-neutron emission, $\tau_0 \ge (1–2) \times 10^{-19}$ s, from a refined data treatment with due regard to the motion of fission fragments. It should be noted that, for $\tau_0 \ge 10^{-19}$ s, the contributions to the correlation function in question from the final-state interaction of neutrons (B_i) and from the effect of Fermi statistics (B_0) are negligibly small in the momentum region that we studied. Of greatest interest from the viewpoint of measurement of the two-neutron correlation function is therefore an advancement toward the region of low momentum transfers ($q \longrightarrow 0$), where the contributions B_0 and B_i significantly increase. However, within the experimental approach used, this involves considerable difficulties associated with a heavy background that grows sharply when the neutron-detection threshold is reduced or when the pair detectors are brought closer together because of rescattering on them.

REFERENCES

1. W. A. Friedman and W. G. Lynch, Phys. Rev. C **28**, 16 (1983).
2. D. J. Hinde, D. Hilscher, and H. Rossner, Nucl. Phys. A **502**, 497 (1989).
3. D. Guerreau, Nucl. Phys. News Eur. **1** (6), 13 (1991).
4. Yu. D. Katarzhnov, V. G. Nedopekin, V. I. Rogov, and S. T. Sukhorukov, Yad. Fiz. **62**, 206 (1999) [Phys. At. Nucl. **62**, 170 (1999)].
5. Yu. D. Katarzhnov, V. G. Nedopekin, V. I. Rogov, and S. T. Sukhorukov, At. Énerg. **84**, 529 (1998).
6. M. M. Danilov, Yu. D. Katarzhnov, V. G. Nedopekin, and V. I. Rogov, Yad. Fiz. **46**, 1372 (1987) [Sov. J. Nucl. Phys. **46**, 809 (1987)].
7. R. Lednicky and V. L. Lyuboshits, Yad. Fiz. **35**, 1316 (1982) [Sov. J. Nucl. Phys. **35**, 770 (1982)].
8. H. W. Schmitt, W. E. Kiker, and C. W. Williams, Phys. Rev. B **137**, 837 (1965).

Translated by E. Kozlovskiĭ

Physics of Atomic Nuclei, Vol. 64, No. 2, 2001, pp. 179–185. Translated from Yadernaya Fizika, Vol. 64, No. 2, 2001, pp. 221–228.

NUCLEI
Theory

Dynamical Approach to Calculating Angular Distributions of Fission Fragments

V. A. Drozdov, D. O. Eremenko, S. Yu. Platonov, O. V. Fotina, and O. A. Yuminov

Institute of Nuclear Physics, Moscow State University, Vorob'evy gory, Moscow, 119899 Russia

Received October 12, 1999; in final form, December 21, 1999

Abstract—A dynamical approach is proposed for calculating the angular distributions of fission fragments. The relaxation time for the degree of freedom associated with the projection of the total angular momentum of the nuclear system onto the symmetry axis and the coefficient of damping of the fission mode are the basic parameters of this approach. Experimental data on the anisotropy of the angular distributions of fission fragments and on the multiplicities of prescission neutrons are analyzed within the proposed model for $^{16}O + ^{208}Pb$ (E_{lab} = 110–148 MeV), $^{16}O + ^{232}Th$ (120–160 MeV), $^{16}O + ^{248}Cm$ (110–148 MeV), and $^{16}O + ^{238}U$ (96–148 MeV). The relaxation time and the damping coefficient are estimated at $\tau_K = (5–6) \times 10^{-21}$ s and $\beta = 4 \times 10^{21}$ s^{-1}, respectively. © *2001 MAIK "Nauka/Interperiodica".*

1. INTRODUCTION

The understanding of the role of nuclear dissipation for processes such as deep-inelastic collisions of heavy ions [1], damping of giant multipole resonances [2], and nuclear fission [3] is one of the most spectacular achievements of modern nuclear physics. Nuclear dissipation, which manifests itself as irreversible energy transfer from collective degrees of freedom to internal ones, leads to the emergence of nonconservative forces in the system under study, the amplitude of these forces being characterized by the damping coefficient β. Information about β is usually extracted from an analysis of experimental data on the multiplicities of prescission light particles and of photons, on the mass and energy distributions of fragments originating from the fission of heavy nuclei, on the cross sections for evaporation-residue formation, and on the fission probability [3, 4]. In describing collective nuclear motion, use is usually made of approaches based on the Fokker–Planck equation [5] or on the set of stochastic Langevin equations [3, 6]. Unfortunately, estimates of β that were obtained along these lines show a large scatter from one study to another (sometimes the difference reaches two orders of magnitude [4]). Moreover, the existing theoretical models predict β values in the range from 0.3×10^{21} to 100×10^{21} s^{-1} [4]. Presently, there is no unambiguous information about the energy and the deformation dependence of β either [4, 7]. It therefore seems necessary to extend the range of observables whose analysis can provide information about the damping coefficient. We deem that angular distributions of fragments originating from the fission of heavy nuclei can serve these purposes.

We note that the Halpern–Strutinsky model of transition states [8] is conventionally used to analyze experimental data on angular distributions. It is assumed in this model that, at some transition point on the path to fission, the K distribution (K is the projection of the total angular momentum of the nuclear system onto the fission axis) becomes equilibrium, undergoing no further changes during the subsequent evolution of the fissile system up to the scission point. Traditionally, it is the states at the saddle point of the fission barrier that are considered as such transition states. Recently, there have appeared some pieces of evidence that the time of motion from the saddle to the scission point is comparatively long ($\tau_{ss} \sim 10^{-20}$ s) [3, 4, 9]. For the time of the relaxation of the degree of freedom associated with K, modern estimates are $\tau_K \sim 10^{-20}$ s [9–11]. Since this value is commensurate with τ_{ss}, the effective transition state can occur in between the saddle and the scission point. In addition, Freifelder *et al.* [12] compared the temperature dependence of the experimental values of K_0^2 (variance of the K distribution) with the results of calculations performed within two versions of the transition-state model, which differ in the choice of transition state, that at the saddle point in one version and that at the scission point in the other version. As a result, it appeared that the experimental data lie in between the curves calculated within these two approaches. The last circumstance suggests that the shape of the nuclear system in the effective transition state must be more compact than at the scission point and more stretched than at the saddle point. It should be noted here that, in solving this problem, the authors of [13–15] used the approach based on the assumption that the dinuclear system whose evolution can lead, depending on the value of the impact parameter, to complete fusion, quasifission, or deep-inelastic scattering is formed in a collision of the projectile nucleus with a target nucleus.

In the quasifission process, there occurs intense nucleon exchange between the constituents of the dinuclear system which does not reach, as a rule, deformations that are peculiar to the fission barrier and, the more so, to the ground state. In this case, only the final stage of the fission process—the motion of the fissile system beyond the saddle point to the scission point—does actually proceed. By virtue of this, the anisotropy of the angular distribution for the quasifission process must be more pronounced than that which is predicted by the model assuming the occurrence of a transition state at the saddle point (TSSP model). We note, however, that quasifission is a process characteristic of reactions that proceed on heavy target nuclei and which are induced by $A \geq 20$ projectiles [9, 15]. It follows that, in the case of sufficiently light projectiles, the observed discrepancy between experimental data on the anisotropy of the angular distribution and the TSSP predictions cannot be attributed to the contribution of the quasifission process.

Moreover, the applicability of the TSSP model is questionable at high angular momenta and nuclear temperatures in the region $t \geq B_f(J)$ [9]. It should be noted here that, within the standard statistical approach, the temperature of the nucleus at the saddle point can be calculated with allowance for the possible emission of light particles. In order to calculate the temperature in the case where the effective transition state is beyond the saddle point, we must consider the dynamical aspects of the fission process, taking into account the subsequent emission of light particles at the stage of descent from the saddle to the scission point. We emphasize once again that developing such a model can serve as an effective tool for obtaining new data both on the relaxation time τ_K and on the damping coefficient β.

In the present study, we propose a dynamical model for calculating the angular distributions of fission fragments. Within the proposed approach, data on the angular distributions and multiplicities of prescission neutrons are analyzed for $^{16}O + {}^{208}Pb$ (E_{lab} = 110–148 MeV), $^{16}O + {}^{232}Th$ (120–160 MeV), $^{16}O + {}^{248}Cm$ (110–148 MeV), and $^{16}O + {}^{238}U$ (96–148 MeV) interactions.

2. CALCULATION OF ANGULAR DISTRIBUTIONS OF FISSION FRAGMENTS

In the present study, the evolution of a fissile nucleus is described on the basis of the set of stochastic Langevin equations, which, in the one-dimensional case, can be represented as

$$\frac{dr}{d\tau} = \frac{p}{m},$$
$$\frac{dp}{d\tau} = -\frac{dV(r)}{dr} - \frac{\gamma}{m}p + f(\tau), \quad (1)$$

where r and p are, respectively, the collective coordinate and the corresponding momentum, while m is the inertial parameter. For the collective coordinate, we use the distance between the centers of mass of nascent fission fragments. In Eqs. (1), $f(\tau)$ is a random delta-correlated force,

$$\langle f(\tau)\rangle = 0; \quad \langle f(\tau_1) f(\tau_2)\rangle = 2D\delta(\tau_1 - \tau_2), \quad (2)$$

where D is expressed, through the Einstein relation, in terms of the nuclear temperature and the coefficient of nuclear friction as $D = t\gamma$, being related to the damping coefficient by the equation $\beta = \gamma/m$. For the inertial parameter, we chose the quantity $m = A/4$, which corresponds to fission into two fragments of identical masses. In studies devoted to simulating fission dynamics by using the Fokker–Planck equation [5] or Langevin equations [3], it is often assumed that m is independent of the collective coordinate. Of course, this assumption is made to simplify the calculations. Estimates of the deformation dependence of m that were obtained on the basis of the semiempirical relation from [16] show that variations in the inertial parameter over the segment of the trajectory between the saddle and the scission point do not exceed 10% of $A/4$. Such a small variation in m can lead only to an insignificant increase in τ_{ss}. On the other hand, the time it takes for a fissile system to reach the saddle point is predominantly determined by the relationship between the temperature and the fission-barrier height. In Eqs. (1), the temperature is defined as $t = (E_{int}/a(r))^{1/2}$ with $E_{int} = E^* - p^2/(2m) - V(r, J) - E_{rot}$, where E^* is the total excitation energy, E_{rot} the rotational energy of the system under study, and $a(r)$ is the level-density parameter. We note that the deformation dependence of the level-density parameter plays an important role in analyzing experimental data associated with the fission process and, hence, with the evolution of the shape of the nuclear system [3, 9, 17]. In our study, the level-density parameter was chosen in the form $a(r) = a_1A + a_2A^{2/3}B_S(r)$, where $a_1 = 0.073\ \text{MeV}^{-1}$, $a_2 = 0.095\ \text{MeV}^{-1}$, and $B_S(r)$ is the surface energy of the deformed nucleus. This dependence complies with the result that was presented in [18] and which was obtained for the Woods–Saxon potential. The potential energy $V(r, J)$ [and, accordingly, $B_S(r)$] was calculated within the liquid-drop model with the Myers–Swiatecki parameters by using the procedure proposed in [16], which makes it possible to perform a fast calculation of the potential energy for fissile nuclei over a wide range of A, Z, and J values. Here, we take no account of effects associated with a finite range of nuclear forces because there are no simple and fast methods for calculating relevant corrections either for the level-density parameter or for the potential energy [3].

The initial values of p were generated for each trajectory under the assumption of the normal momentum

distribution at r corresponding to the equilibrium deformation:

$$F(p) = \frac{1}{\sqrt{2\pi mt}}\exp\left\{-\frac{p^2}{2mt}\right\}. \quad (3)$$

Equations (1) were solved with the aid of the Euler difference scheme.

The emission of light particles (protons, neutrons, and alpha particles) was simulated within the approach that is usually used to calculate the multiplicity of light particles for induced fission and which is based on the Langevin equations [3, 19]. The specific implementation was the following. At each time step, the partial decay widths (Γ_n, Γ_p, and Γ_α) with respect to channels involving particle emission were computed within the method of inverse cross sections [20] and a random number η_1 uniformly distributed in the interval (0, 1) was generated. Further, η_1 was compared with the ratio of the time step $\Delta\tau$ in integrating the Langevin equations to the quantity $\tau_{\text{part}} = \hbar/\Gamma$, where $\Gamma = \Gamma_n + \Gamma_p + \Gamma_\alpha$. In the case of $\eta_1 < \Delta\tau/\tau_{\text{part}}$, it was assumed that the emission event had occurred. After that, the type of the emitted particle was sampled. For this purpose, we generated a second random number η_2 uniformly distributed over the interval from zero to unity. This region was broken down into three subintervals according to the value of the ratios Γ_n/Γ, Γ_p/Γ, and Γ_α/Γ, the type of a particle being specified by the subintervals within which the random number η_2 falls. In order to determine the energy of the emitted particle of the i type, we construct the quantity

$$P_i(\varepsilon_k) = \frac{1}{\Gamma_i}\left\{\frac{(2J_i+1)\mu_i}{\pi^2\hbar^2\rho^2(E^*)}\int_0^{\varepsilon_k}\sigma_{\text{inv}}(\varepsilon)\varepsilon\rho_R(\varepsilon)d\varepsilon\right\}, \quad (4)$$

where ρ and ρ_R are the angular-momentum-integrated level densities in the parent and the daughter nucleus, respectively; σ_{inv} is the cross section for the inverse reaction; μ_i is the reduced mass of the emitted particle; and ε_k is the maximum possible energy of the emitted particle (it is determined from the energy-conservation law). The quantity $P_i(\varepsilon_k)$ has the meaning of the probability of the production of an i-type particle whose energy lying in the interval (0, 1) is less than ε_k. Breaking down the interval (0, 1) into a sufficiently large number of equal subintervals and generating a random number η_3 uniformly distributed over the interval (0, 1), we can determine the energy of the emitted particle. The change in the angular momentum of the nucleus upon particle emission was taken into account by assuming that, on average, a neutron, a proton, and an alpha particle carry away angular momenta of $1\hbar$, $1\hbar$, and $2\hbar$, respectively [3]. Upon each emission event, the excitation energy, the potential energy, and the angular momentum of the fissile system were corrected. If the Langevin trajectory approached the scission point, such an event was interpreted as fission. In the case where the value of the collective variable appeared to be less than the corresponding value at the saddle point and where, because of light-particle emission, the internal excitation energy E_{int} simultaneously became less than $\min(B_i, B_f(J))$ [where B_i is the binding energy of the light particle and $B_f(J)$ is the fission barrier], the calculations were ceased, and such an event was treated as the formation of an evaporation residue. But if E_{int} remained greater than $\min(B_i, B_f(J))$ when the temperature decreased (because of light-particle emission) to a value such that $t < 0.1B_f(J)$ and if the deformation of the fissile system appeared to be less than the deformation at the saddle point, we went over to the statistical branch of the calculation. This was also done when the current time value exceeded $\tau = 10^{-18}$ s. At such a large value of τ, all relaxation processes associated with establishing a quasistationary value of the probability current at the saddle point [9, 21] were completed and the results of the calculations were independent of the conditions of the transition to the statistical branch of the calculations. We emphasize that, in the present study, these conditions were chosen to be more stringent than those, for example, in [3]. Upon the transition to the statistical branch of the calculation, the partial widths with respect to light-particle emission were computed in the same way as in the dynamical branch, while the fission width was calculated on the basis of the Bohr–Wheeler relations with allowance for the Kramers corrections [9]. In that case, use was made of a conventional Monte Carlo procedure, and, in just the same way as in the dynamical calculations, the evaporation cascade was terminated as soon as E_{int} became less than $\min(B_i, B_f(J))$. If a fission event occurred at one of the steps of the evaporation cascade, a transition to the dynamical branch of the calculation was again implemented for such events in order to calculate the relevant angular distribution, but the initial conditions in (3) were chosen this time at the saddle point.

In calculating the angular distributions, we fixed the values of the deformation and of the internal excitation energy at each instant when the current time for a specific Langevin trajectory exceeded an integral multiple of τ_K. This was done until our fissile nuclear system reached the scission point. The last value of the collective coordinate fixed in this way was taken as the effective transition point determining the angular distribution. At this point, we calculated the moments of inertia of the nucleus, $\Im_{\text{II}}$ and $\Im_\perp$, in the rigid-body approximation and the quantity $K_0^2 = (t/\hbar^2)(\Im_{\text{II}}^{-1} - \Im_\perp^{-1})^{-1}$. Further the angular distributions were calculated by using the standard Halpern–Strutinsky expressions [8, 22]. Within this approach, the probability of fission-fragment emission at an angle θ with respect to the beam axis at the fixed values of J and M (the latter being the

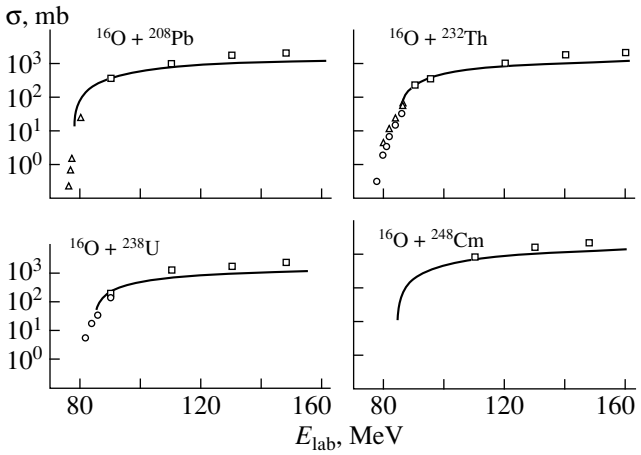

Fig. 1. Calculated cross sections for the complete-fusion versus energy along with experimental data on fission cross sections for various reactions. Open boxes, triangles, and circles represent data from [22], [27], and [28], respectively.

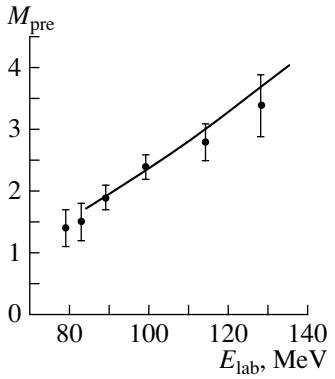

Fig. 2. Multiplicity of prescission neutrons from ^{16}O + ^{208}Pb interaction: (points) experimental data from [29] and (curve) results of the calculation.

projection of the total angular momentum onto the projectile-beam axis) is given by

$$\omega_M^J(\theta) = \sum_{K=-J}^{J} \frac{(2J+1)\left|d_{M,K}^J(\theta)\right|^2 \exp(-K^2/K_0^2)}{\sum_{K=-J}^{J} \exp(-K^2/K_0^2)}, \quad (5)$$

where $d_{M,K}^J(\theta)$ is the Wigner rotation function. As a rule, studies that analyze experimental data on the angular distributions for reactions induced by heavy ions consider the fission of compound systems formed as the result of the interaction of spinless nuclei, associating the observed angular distributions with the first nucleus of the emission cascade—that is, it is assumed that $M = 0$. However, light-particle emission from a hot compound nucleus must lead to a situation where the vector of the total angular momentum does not strictly lie in the plane orthogonal to the beam axis, in which case M can take nonzero values; hence, it is necessary to consider the relevant distributions. As applied to the analysis of angular distributions for reactions induced by heavy ions, this question was investigated in [23, 24], where the authors used, by analogy with K, the Gaussian distribution with respect to M. Under this assumption, the eventual expression for the angular distribution has the form

$$W(\theta) = \sum_{J=0}^{\infty} \frac{(2J+1)T_J \sum_{M=-J}^{J} \omega_M^J(\theta) \exp(-M^2/2M_0^2)}{\sum_{M=-J}^{J} \exp(-M^2/2M_0^2)}, \quad (6)$$

where T_J is the penetrability factor. In the present study, we set $M_0^2 = K_0^2$ [23].

The initial distribution with respect to the angular momentum of the nascent compound nucleus was calculated on the basis of the method proposed in [3]. This approach relies on the use of the partial-wave cross sections calculated for fusion [$\sigma(J)$] within the surface-friction model [25, 26]. In Fig. 1, the calculated cross sections for complete fusion are contrasted against the corresponding experimental data. We note that, for each initial value of the angular momentum, the number of Langevin trajectories was chosen in the present study to be proportional to the partial-wave cross section for fusion.

In the proposed approach to a global analysis of experimental data on the angular distributions and M_{pre}, only β and τ_K were used as adjustable parameters.

3. ANALYSIS OF EXPERIMENTAL DATA ON ANGULAR DISTRIBUTIONS AND PRESCISSION-NEUTRON MULTIPLICITIES

In this section, we present the results obtained from an analysis of experimental data on the anisotropy of the angular distributions and on the prescission-neutron multiplicities for ^{16}O + ^{208}Pb, ^{16}O + ^{232}Th, ^{16}O + ^{248}Cm, and ^{16}O + ^{238}U interactions. For ^{16}O + ^{208}Pb interactions, the experimental data on the angular distribution and on the prescission-neutron multiplicity are shown in Figs. 2 and 3 along with the results of the relevant calculations. It was noted above that, in order to obtain the best fit to the experimental data, we varied the adjustable parameters β and τ_K in calculating the angular distribution and the prescission-neutron multiplicity. Since, within the proposed scheme, the numerical value of τ_K does not affect the calculated multiplicity of prescission light particles, we used only data on M_{pre} in order to derive the coefficient β. From the best fit to the experimental data, we then obtained the value of $\beta = 4 \times 10^{21}$ s^{-1}. By choosing the value of β in this way, we

thereby fixed the mean time of motion of the fissile nuclear system over the potential surface. In order to describe the experimental data on the anisotropy of the angular distributions at the specific β value, we then varied the parameter τ_K. With the aim of demonstrating the sensitivity of the calculated angular distributions to changes in τ_K, curves obtained at various values of this parameter are displayed in Fig. 3. It can be seen that the best fit to the experimental data is achieved at $\tau_K = 5 \times 10^{-21}$ s. It should be noted here that, for our analysis of the angular distributions, we choose experimental values only at those projectile energies that lead to the formation of compound nuclei characterized by excitation-energy values in excess of 50 MeV. This is because, at lower excitation energies, shell effects play an important role [30], in which case it is necessary to take into account the two-humped structure of the fission barrier in calculating the angular distribution (see [31]). For the sake of comparison, the results of the calculations within the standard TSSP model with and without allowance for neutron emission are also shown in this figure. The effect of neutron emission on the anisotropy of the angular distribution was taken into account through a change in the excitation energy of the compound nucleus at the saddle-point configuration according to the procedure described in [32]. In order to break down the prescission-neutron multiplicity into two components—that associated with the emission before the saddle point and that associated with the emission at the stage of descent of the fissile system from the saddle to the scission point—use was made of the neutron multiplicities calculated within the dynamical model described above. In evaluating the anisotropy within the TSSP model, we relied on the simple approximation

$$\frac{W(0^\circ)}{W(90^\circ)} = 1 + \frac{\langle J^2 \rangle}{4K_0^2}. \qquad (7)$$

The use of this relation was motivated by the following arguments. At the $E_{\rm lab}$ values being studied, some section of the initial angular-momentum distribution corresponds to those fission-barrier values at which $B_f(J) \le t$. The application of relations (5) and (6) for the K_0^2 value taken at the saddle point then leads to an unphysical result. In expression (7), K_0^2 is calculated at $\langle J^2 \rangle$ values such that the inequality $B_f(\langle J^2 \rangle) > t$ is satisfied in the energy region under study. From Fig. 3, it can be seen that the experimental data fall in between the results obtained within the two versions of the calculations on the basis of the TSSP model (with and without allowance for the neutron emission). It should be emphasized here that relation (7) was obtained under the assumption of $M = 0$. As was shown in [31], the inclusion of the degree of freedom associated with M reduces the anisotropy of the angular distribution. Depending on the choice of M_0^2, the curve representing

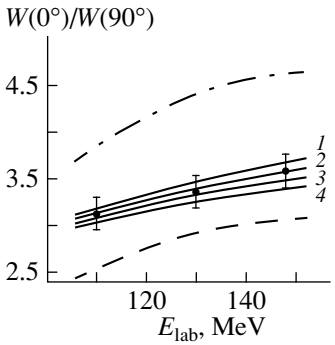

Fig. 3. Angular anisotropy of the fission-fragment yield from $^{16}O + ^{208}Pb$ interactions. The points correspond experimental data from [22]. The solid curves represent the results of the calculations within the proposed approach at $\beta = 4 \times 10^{21}$ s^{-1} [τ_K = (*1*) 4×10^{-21}, (*2*) 5×10^{-21}, (*3*) 6×10^{-21}, and (*4*) 7×10^{-21} s]. The dashed and the dash-dotted curve show the results of the calculations within the TSSP model without and with allowance for neutron emission, respectively.

the results of the calculations allowing for neutron emission may lie much more closely to the experimental data. As can be seen from Figs. 2 and 3, the proposed dynamical approach ensures a consistent description of experimental data on the angular distributions and prescission-neutron multiplicities. Although it cannot be stated that, for the interaction type under consideration, this approach leads to better agreement between the calculated and the experimental values of the angular-distribution anisotropy than the standard TSSP model, we believe that the dynamical calculations better reproduce the slope of the energy dependence of the angular-distribution anisotropy.

The results of the dynamical calculations for the angular-distribution anisotropy and prescission-neutron multiplicity $M_{\rm pre}$ for $^{16}O + ^{232}Th$, $^{16}O + ^{238}U$, and $^{16}O + ^{248}Cm$ interactions are displayed in Figs. 4 and 5, along with relevant experimental data. We emphasize that, for these interactions, the multiplicity of prescission neutrons and the anisotropy of the angular distribution were calculated at the same values of β and τ_K as for $^{16}O + ^{208}Pb$ interactions. This was done because we wanted to check the correctness of the chosen parameters and because there are no experimental data on the prescission-neutron multiplicity $M_{\rm pre}$ for $^{16}O + ^{248}Cm$ and $^{16}O + ^{238}U$ interactions. In such cases, the calculated values of $M_{\rm pre}$ are compared with the predictions of the systematics composed by Kozulin *et al.* [34]. Those authors indicate, however, that, for heavy compound nuclei, there are some discrepancies between the predictions of their systematics and experimental data. This is likely to be the reason why our results deviate somewhat from the results of the calculations performed within the above systematics (see Fig. 4). In addition, the example of $^{16}O + ^{232}Th$ interactions, for which we present both the data of the systematics for

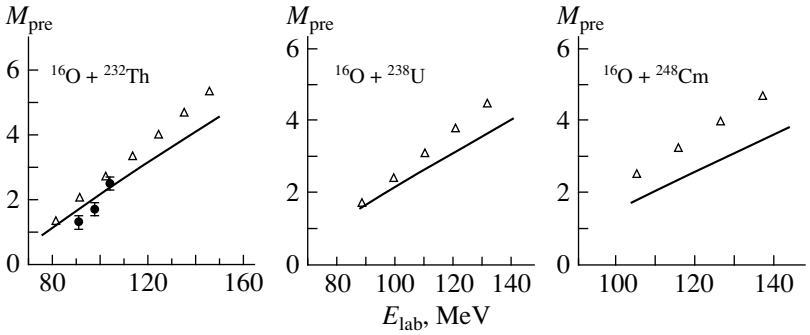

Fig. 4. Multiplicities of the prescission neutrons for various reactions: (closed circles) experimental data for $^{16}O + ^{232}Th$ interactions [33], (open triangles) results of the calculations based on the systematics from [34], and (solid curve) results of the calculations at $\beta = 4 \times 10^{21}$ s^{-1}.

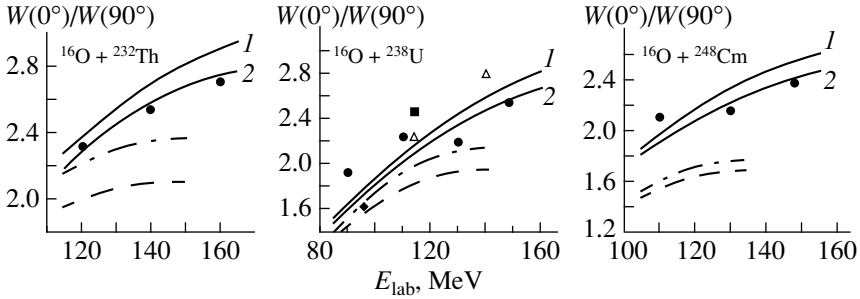

Fig. 5. Angular anisotropy of the fission-fragment yield for various reactions. Points correspond to experimental data from (●) [22], (■) [35], (◆) [13], and (△) [36] (the quoted studies give no information about errors in the measurements of the anisotropy of angular distributions). The solid curves represent the results of the calculations at $\beta = 4 \times 10^{21}$ s^{-1} [τ_K = (*1*) 5×10^{-21} and (*2*) 6×10^{-21} s]. The dashed and the dash-dotted curves show the results of the calculations within the TSSP model without and with allowance for neutron emission, respectively.

M_{pre} and experimental data shows that the M_{pre} values calculated within the proposed dynamical approach are in better agreement with the experimental results.

Figure 5 shows the results of the calculations based on the TSSP model [see Eq. (7)]. We do not display these results for the entire energy interval being considered because, for heavy compound systems and at high projectile energies, we have $B_f(\langle J^2 \rangle) \leq t$, in which case relation (7) becomes meaningless. As can be seen from Fig. 5, the experimental data on the anisotropy of the angular distributions for these interactions (in contrast to those for $^{16}O + ^{208}Pb$ interactions) cannot be described within the TSSP model even upon taking into account the degree of freedom associated with M. For the interactions being discussed, the best fit to the data on the anisotropy of the angular distributions within the proposed approach could be achieved at the value of $\tau_K = 6 \times 10^{-21}$ s, which differs insignificantly from the corresponding value for $^{16}O + ^{208}Pb$ interactions (the results of the calculations with $\tau_K = 5 \times 10^{-21}$ s are also presented in Fig. 5). From the data shown in Figs. 3 and 5, we can therefore conclude that the value of τ_K lies in the range $(5–6) \times 10^{-21}$ s. On the whole, we can highlight good agreement between the experimental and the calculated values of the anisotropy of the angular distributions. This suggests that our choice of τ_K and β values was correct. It is also worth noting that the value obtained for τ_K is close to the estimates ($\tau_K = 8 \times 10^{-21}$ s) obtained in [11] from the analysis of data on the anisotropy of the angular distributions for a number of reactions, but the difference between K_0^2 and the corresponding value at the saddle point was considered in that study only for those events where the temperature of the fissile system was higher than the fission barrier. No attention was given there to the dynamical aspects of the evolution of the compound nuclear system either—in particular, the stochastic nature of the motion of a nucleus over the potential-energy surface toward the scission point was disregarded. The value determined in the present study for the damping coefficient β is smaller than the corresponding results obtained in [3, 7, 37]; nevertheless, it indicates that the regime of the aperiodic damping [3] is typical of collective nuclear motion.

In summary, the data presented here (Figs. 2–5) demonstrate that, in analyzing the angular distributions for reactions induced by heavy ions, it is necessary to take into account the dynamical aspects of nuclear fis-

sion—in particular, the change in K_0^2 during the motion of a fissile nuclear system over the potential-energy surface from the equilibrium to the scission configuration. This conclusion is valid at least in the cases where the nuclear temperature is commensurate with or higher than the fission barrier.

4. CONCLUSION

A dynamical model is proposed for calculating angular distributions of fission fragments. Within this model, the angular distribution is interpreted as a superposition of various contributions caused by the distribution of the effective transition-point position in deformation space. The existence of this distribution in turn is associated with the stochastic nature of the motion of a fissile nuclear system from the equilibrium to the scission configuration. In this case, the time of relaxation of the degree of freedom associated with K (projection of the total angular momentum onto the fission axis) and the damping coefficient play a decisive role in the calculation of the positions of such transition points on the deformation axis. Experimental data on the anisotropy of the angular distributions and on the multiplicities of prescission neutrons for ^{16}O + ^{208}Pb ($E_{\rm lab}$ = 110–148 MeV), ^{16}O + ^{232}Th (120–160 MeV), ^{16}O + ^{248}Cm (110–148 MeV), and ^{16}O + ^{238}U (96–148 MeV) interactions have been analyzed within the proposed approach. It has been shown that the shape of the angular distributions is substantially affected by the dynamical features of the induced-fission process. In addition, a global analysis of data on the anisotropy of the angular distributions and on the prescission-neutron multiplicity $M_{\rm pre}$ makes it possible to obtain new information about the values of the relaxation time τ_K and of the damping coefficient β.

ACKNOWLEDGMENTS

This work was supported in part by the Russian Foundation for Basic Research (project no. 98-02-16911-a) and the State Program Universities of Russia (grant no. 5335).

REFERENCES

1. V. A. Volkov, *Deep-Inelastic-Transfer Reactions* (Énergoizdat, Moscow, 1982).
2. J. R. Nix and A.J. Sierk, in *Proceedings of International School–Seminar on Heavy Ion Physics, Dubna, 1985* (Ob'edin. Inst. Yad. Issled., Dubna, 1987), p. 453.
3. I. I. Gonchar, Fiz. Élem. Chastits At. Yadra **26**, 932 (1995) [Phys. Part. Nucl. **26**, 394 (1995)].
4. D. Hilscher and H. Rossner, Ann. Phys. (Paris) **17**, 471 (1992).
5. E. Strumberger, K. Dietrich, and K. Pomorsky, Nucl. Phys. A **529**, 522 (1991).
6. Y. Abe, C. Gregoire, and N. Delagange, J. Phys. (Paris) **47**, C4-329 (1986).
7. P. Paul and M. Thoennessen, Annu. Rev. Nucl. Sci. **44**, 65 (1994).
8. R. Vandenbosch and J. R. Huizenga, *Nuclear Fission* (Academic, New York, 1973).
9. J. O. Newton, Fiz. Élem. Chastits At. Yadra **21**, 821 (1990) [Sov. J. Part. Nucl. **21**, 349 (1990)].
10. M. A. Butler, S. S. Datta, R. T. de Souza, *et al.*, Phys. Rev. C **34**, 2016 (1986).
11. V. S. Ramamurthy and S. S. Kapoor, Phys. Rev. Lett. **54**, 178 (1985).
12. R. Freifelder, M. Prakash, and J. M. Alexander, Phys. Rep. **133**, 315 (1986).
13. J. Toke, R. Bock, G. X. Dai, *et al.*, Phys. Lett. B **142**, 258 (1984).
14. H. Keller, K. Lützekirchen, J. V. Kratz, *et al.*, Z. Phys. A **326**, 313 (1987).
15. B. B. Back, Phys. Rev. C **31**, 2104 (1985).
16. J. P. Leston, Phys. Rev. C **51**, 580 (1995).
17. J. Töke and J. Swiatecki, Nucl. Phys. A **372**, 141 (1981).
18. A. V. Ignatyuk *et al.*, Yad. Fiz. **21**, 1185 (1975) [Sov. J. Nucl. Phys. **21**, 612 (1975)].
19. K. Pomorski *et al.*, Nucl. Phys. A **605**, 87 (1996).
20. M. Blann, Phys. Rev. C **21**, 1770 (1980).
21. P. Grange, Nucl. Phys. A **428**, 37c (1984).
22. B. B. Back *et al.*, Phys. Rev. C **32**, 195 (1985).
23. B. B. Back and S. Bjornholm, Nucl. Phys. A **302**, 343 (1978).
24. R. Dyer *et al.*, Nucl. Phys. A **322**, 205 (1979).
25. J. Marten and P. Fröbrich, Nucl. Phys. A **545**, 854 (1992).
26. P. Fröbrich, Phys. Rep. **116**, 337 (1984).
27. T. Murakami *et al.*, Phys. Rev. C **34**, 1353 (1986).
28. Z. Liu *et al.*, Phys. Rev. C **54**, 761 (1996).
29. H. Rossner *et al.*, Phys. Rev. C **45**, 719 (1992).
30. V. M. Strutinsky, Nucl. Phys. A **502**, 67c (1989).
31. D. O. Eremenko *et al.*, J. Phys. G **22**, 1077 (1996).
32. P. Fröbrich and H. Rossner, Z. Phys. A **349**, 99 (1994).
33. A. Saxena *et al.*, Phys. Rev. C **49**, 932 (1994).
34. É. M. Kozulin, A. Ya. Rusanov, and G. N. Smirenkin, Yad. Fiz. **56** (2), 37 (1993) [Phys. At. Nucl. **56**, 166 (1993)].
35. S. A. Karamyan *et al.*, Yad. Fiz. **6**, 494 (1967) [Sov. J. Nucl. Phys. **6**, 360 (1967)].
36. A. Gavron *et al.*, Phys. Rev. Lett. **52**, 589 (1984).
37. B. B. Back, in *Proceedings of International School–Seminar on Heavy Ion Physics, Dubna, 1993*, p. 317.

Translated by A. Isaakyan

Physics of Atomic Nuclei, Vol. 64, No. 2, 2001, pp. 186–193. Translated from Yadernaya Fizika, Vol. 64, No. 2, 2001, pp. 229–237.

NUCLEI
Theory

Soft Dipole Mode in the ^{11}Li Nucleus within the Asymptotic-Potential Approximation

G. F. Filippov* and Yu. A. Lashko

Bogolyubov Institute for Theoretical Physics, National Academy of Sciences of Ukraine, Metrologicheskaya ul. 14b, Kiev, 252143 Ukraine

Received November 3, 1999; in final form, March 17, 2000

Abstract—A soft dipole mode in the ^{11}Li nucleus treated within the microscopic three-cluster model is studied in the asymptotic-potential approximation. The model faithfully reproduces the energy and the root-mean-square radius of the ground state and the behavior of the effective photodisintegration cross section at low energies above the threshold for ^{11}Li breakup, suggesting the existence of two resonance states in this region. *© 2001 MAIK "Nauka/Interperiodica".*

1. INTRODUCTION

An intense electric-dipole transition that was experimentally found [1] to occur in the ^{11}Li nucleus from the ground state to the region of the low above-threshold energies is usually attributed to the excitation of a soft dipole mode in this nucleus (see, for example, [2]). The question of the nature of this transition amounts to resolving the dilemma as to whether it is due to the existence of a resonance in the continuous spectrum of ^{11}Li or the properties of this transition are determined exclusively by the proximity of the ^{11}Li ground state to the threshold for the breakup of this nuclear system into ^{9}Li and two neutrons.

The soft dipole mode of the ^{11}Li nucleus has already been discussed in theoretical studies. In [3], the wave functions of the ground state of this nucleus and of the continuum states to which the $E1$ transition proceeds were constructed within the method of three-particle hyperharmonics. The effect of the Pauli exclusion principle was simulated by introducing a repulsive potential in partial waves that involve forbidden states. This made it possible to obtain the intensity of the electric-dipole transition as a function of energy. This function has a maximum near the energy value of 0.6 MeV above the threshold for the three-body breakup of ^{11}Li. The position of the peak agrees with the experimental results reported in [1].

In just the same way as in [3], we will perform the ensuing analysis in a hyperspherical basis, restricting, however, this basis to the hyperharmonics characterized by the minimum possible values of the grand orbital; of the linear combinations of these hyperharmonics, we will further consider only those that are allowed by the Pauli exclusion principle. We also note that in [3], the ^{9}Li cluster was considered as an inert core, whereby the possibility of exchange of the valence neutrons and the p-shell neutrons belonging to the core was excluded. Of the requirements imposed by the Pauli exclusion principle, only that piece was satisfied in [3] which corresponds to the ability of the repulsive potential to suppress the approach of valence neutrons to the heavy cluster. It is obvious that this description is not complete. Within the method proposed here to construct basis functions, the identity of nucleons is rigorously taken into account; as a result, the allowed ^{11}Li states assume the form of superpositions of ^{9}Li states corresponding to the orbital-angular-momentum values of $\mathscr{L}$ = 1, 2, and 3, the coefficients in this superposition being dependent on the vectors of the neutron clusters. As to the grand-orbital content of continuum states to which the $E1$ transition occurs, it is also formed on the basis of the Pauli exclusion principle and differs markedly from that proposed in [4]. We will demonstrate below that the contribution of the K = 1 hyperharmonic increases as the neutron clusters move away from the ^{9}Li core and that the K = 3 contribution decreases, but the latter proceeds in such a way that, even in the asymptotic region, it is 13%.

By considering the ^{11}Li nucleus as a system of three clusters,

$$^{11}\mathrm{Li} \longrightarrow {}^{9}\mathrm{Li} + n + n,$$

we will use a simplified version of the resonating-group method, the asymptotic-potential approximation, whose fundamentals were outlined elsewhere [5] in connection with the problem of the soft dipole mode in the ^{6}He nucleus. This approximation heavily relies on the fact that the ^{11}Li nucleus is very soft in the boundary region, where two valence neutrons (two neutron clusters) reside and where the cluster interaction caused by the three-body character of the system is radically simplified. This interaction takes the form of an asymptotic power-law potential decreasing in inverse proportion to the hyperradius cubed. At the same time, the behavior of the three-cluster system in the region of small-hyper-

* e-mail: gfilippov@gluk.ape.org

radius values is simulated by a smoothed extrapolation of the asymptotic potential.

The ensuing exposition is organized as follows. In Section 2, we discuss the most significant features of the ^{11}Li nucleus that distinguish it from the ^{6}He nucleus. In Section 3, we briefly recall some details of the approximation adopted in the present study. We conclude by presenting the results of our calculations.

2. THREE-CLUSTER MODEL OF ^{11}Li AND HARMONIC-OSCILLATOR BASIS STATES

2.1. Minimal-Approximation Basis for Negative-Parity ^{11}Li States

In the standard version of the resonating-group method, it is assumed that the alpha-particle cluster of the ^{6}He nucleus is in the ground state of the translation-invariant shell model (TISM), but, in constructing a harmonic-oscillator basis for the ^{11}Li nucleus, one has to invoke the multiplet of the ^{9}Li-cluster states that belongs to the (1, 2) irreducible representation of the $SU(3)$ group [6]. The choice of this irreducible representation among the irreducible representations that involve the same number of quanta, but which are of lower symmetry, is dictated by the requirement that the potential-energy operator contain the maximum number of interactions in even nucleon-pair states that are triplet in spin and singlet in isospin or singlet in spin and triplet in isospin. In these states, the potential energy of nucleon pairs has a deep minimum; therefore, the nuclear system favors them rather than other (odd) states. The orbital angular momentum $\mathscr{L}$ in the states of the (1, 2) multiplet can take values of 1, 2, and 3. These states are of negative parity. The exchange nucleon–nucleon interaction removes degeneracy in orbital angular momentum, with the result that the $\mathscr{L} = 1$ state appears to be the lowest one. Two unit orthogonal complex vectors **u** and **w** are taken for the independent variables of the wave function of these ^{9}Li states in Fock–Bargmann space. All wave-function constructions are linear in the components of the vector **u** and bilinear in the components of the vector **w**. Listing the basis functions and determining the Hamiltonian in Fock–Bargmann space, we will use the nucleon mass m, the oscillator length r_0, and $\hbar^2/mr_0^2$ for units of mass, length, and energy.

The wave functions of the neutron clusters depend on two normalized Jacobi vectors **a** and **b** [6]. In the harmonic-oscillator basis, the only wave function that is characterized by the orbital-angular-momentum value of $L = 1$ and by the minimal number of quanta and which is allowed by the Pauli exclusion principle has the form

$$\Phi^{-}_{0,\,L=1} = \frac{1}{18}\mathbf{u}\{11(\mathbf{w}\cdot\mathbf{a})^2 - 9(\mathbf{w}\cdot\mathbf{b})^2\} \qquad (1)$$

and belongs to the (1, 0) irreducible representation of the $SU(3)$ group. The "minus" superscript on the wave function indicates that the state in question is of negative parity. Expression (1) is a composition of three blocks; of these, two describe states of the neutron clusters, while the third block is associated with the ^{9}Li cluster. Since the components of the third block do not fix the orbital angular momentum $\mathscr{L}$ of the cluster ^{9}Li, expression (1) appears to be a superposition of $\mathscr{L} = 1$, 2, 3 states; that is,

$$\Phi^{-}_{0,\,L=1,\,M} = \sum_{\mathscr{L},\,M}^{3}\sum_{l,\,m}^{2} A_{\mathscr{L},\,l} C^{L,\,M}_{\mathscr{L}M;\,lm}\psi_{\mathscr{L},\,M}(\mathbf{u},\mathbf{w})\phi_{l,\,m}(\mathbf{a},\mathbf{b}), \qquad (2)$$

where $C^{L,\,M}_{\mathscr{L}M;\,lm}$ are the relevant Clebsch–Gordan coefficients, $\psi_{\mathscr{L},\,M}(\mathbf{u},\mathbf{w})$ are the basis functions of the core states, $\phi_{l,\,m}(\mathbf{a},\mathbf{b})$ are the basis functions of the states of the two-neutron (two-cluster) system under the assumption that the neutrons occur in the p shell, and $A_{\mathscr{L},\,l}$ are coefficients that determine the contribution to the basis function (1) from the core states that are characterized by the orbital angular momentum $\mathscr{L}$ and the states of the two-neutron system that are characterized by the orbital angular momentum l.

It follows that, within the approximation adopted here, the ^{9}Li core is not completely inert—it can go over to excited states, changing the orbital angular momentum $\mathscr{L}$ and its projection M.

If the spin–orbit interaction is not involved in the formation of the wave functions, the ^{11}Li ground state is doubly degenerate because the spin of the proton occurring in the p shell and belonging to the ^{9}Li cluster is unpaired. As soon as the spin–orbit interaction is switched on, the state characterized by the angular momentum of $J = 3/2$ becomes the lowest, while the $J = 1/2$ state accordingly appears to be excited. In the following, we take no account of the spin–orbit interaction, assuming that basic features of the soft dipole mode can be understood without considering the splitting of the $J = 3/2$ and $J = 1/2$ states.

In constructing the harmonic-oscillator basis and in classifying basis functions, we consistently use the scheme of LS coupling, paying special attention to those basis states in which nucleon–nucleon attractive forces are the strongest. This way is natural if we use the quantum numbers of the irreducible representations of the $SU(3)$ group as was done above for the ^{9}Li cluster. Of course, the number of states in the complete basis for the scheme of jj coupling (it is usually used in the mean-field approach) does not differ from the number of states in the complete basis for the scheme of LS coupling. However, actual microscopic calculations employing the potential energy determined solely by nucleon–nucleon forces have to deal with some part of the complete basis within either scheme. Therefore, the

problem of choosing one of the two schemes reduces to the problem of optimally choosing basis states that are of greatest importance for the problem being studied and which correspond to the deepest nucleon–nucleon potential.

Thus, expression (1) is the transform of the TISM wave function of the ^{11}Li ground state in Fock–Bargmann space. This wave function corresponds to the compact configuration of the oscillator-shell model; therefore, it cannot reproduce the soft boundary region of a nucleus. In order to remedy this drawback of the simplest TISM construction, we will seek the transform of the true function $\Psi^-_{L=1,M}$ in the form of a series of the minimal approximation of the hyperspherical-function method (for a detailed explanation, the reader is referred to [6]); that is,

$$\Psi^-_{L=1,M} = \sum_{\nu=0}^{\infty} C^-_{\nu,L=1}\Phi^-_{\nu,L=1,M}, \tag{3}$$

where

$$\begin{aligned}\Phi^-_{\nu,L=1,M} &= N^-_\nu \mathbf{u}_M\{11(\mathbf{w}\cdot\mathbf{a})^2 - 9(\mathbf{w}\cdot\mathbf{b})^2\}(a^2+b^2)^\nu,\\ N^-_\nu &= \frac{1}{18}\frac{1}{2^\nu}\sqrt{\frac{34}{9\nu+34}}\sqrt{\frac{3!}{(\nu+3)!\nu!}},\end{aligned} \tag{4}$$

are basis states that are allowed by the Pauli exclusion principle; the coefficients $C^-_{\nu,L=1}$ are determined by solving the set of linear algebraic equations of the minimal approximation; and $\mathbf{u}_M$ are the cyclic projections of the vector $\mathbf{u}$.

Each of the states in (4) is a linear superposition of the terms $\Phi^-_{\nu,K,L=1}$ corresponding to the grand-orbital values of $K = 0$ and $K = 2$; that is,

$$\begin{aligned}\Phi^-_{\nu,L=1} &= \sqrt{\frac{25(\nu+4)}{27\nu+102}}\Phi^-_{\nu,K=2,L=1}\\ &+ \sqrt{\frac{2(\nu+1)}{27\nu+102}}\Phi^-_{\nu+1,K=0,L=1},\end{aligned} \tag{5}$$

where

$$\begin{aligned}\Phi^-_{\nu,K=2,L=1} &= \frac{1}{2^\nu}\sqrt{\frac{4!}{(\nu+4)!\nu!}}\frac{\sqrt{102}}{18}\mathbf{u}\{(\mathbf{w}\cdot\mathbf{a})^2\\ &-(\mathbf{w}\cdot\mathbf{b})^2\}(a^2+b^2)^\nu,\\ \Phi^-_{\nu+1,K=0,L=1} &= \frac{1}{2^\nu}\sqrt{\frac{3!}{(\nu+3)!(\nu+1)!}}\frac{\sqrt{51}}{18}\\ &\times\mathbf{u}\{(\mathbf{w}\cdot\mathbf{a})^2+(\mathbf{w}\cdot\mathbf{b})^2\}(a^2+b^2)^\nu.\end{aligned}$$

If $\nu = 0$, the weight of the $K = 2$ state is 0.98, while the weight of the $K = 0$ state is as small as 0.02. But if ν approaches infinity, the former and the latter weight tend to 0.93 and 0.07, respectively.

The wave function of the ^{11}Li ground state is frequently interpreted in terms of the shell model, and its content is discussed by analyzing, in particular, the contribution of the allowed *s* orbitals of the valence neutrons against the contribution of their *p* orbitals (see, for example, [7]). At the same time, it follows from expression (3) that the contribution of the *p* orbitals of the valence neutrons is determined by the square of the coefficient $C^-_{\nu=0,L=1}$. For all other orbitals, including *s* orbitals, the corresponding contribution is determined by the sum

$$\sum_{\nu=1}^{\infty}\{C^-_{\nu,L=1}\}^2.$$

An estimate of this sum will be given in Section 3.

2.2. E1-Transition Operator

In the approximation of the three-cluster model for the ^{11}Li nucleus, the electric-dipole-transition operator $\hat{\mathbf{M}}(E1)$ defined in Fock–Bargmann space is the sum of two terms—the raising operator $\hat{\mathbf{M}}^+(E1)$ (when applied to harmonic-oscillator basis functions, it changes their parity and increases the number of oscillator quanta by unity) and the lowering operator $\hat{\mathbf{M}}^-(E1)$ defined as the Hermitian conjugate to the raising operator—that is,

$$\hat{\mathbf{M}}(E1) = \hat{\mathbf{M}}^+(E1) + \hat{\mathbf{M}}^-(E1), \tag{6}$$

where the first term,

$$\hat{\mathbf{M}}^+(E1) = \sqrt{\frac{3}{4\pi}}\frac{e}{\sqrt{11}}\mathbf{a}, \tag{7}$$

differs from the analogous expression for ^{6}He only by the numerical value of the constant factor. The operator $\mathbf{a}$ acting on the ground-state basis functions (4) generates the positive-parity basis functions characterized by the orbital-angular-momentum values of 0, 1, and 2. These functions are investigated in the next section.

2.3. Basis of the Minimal-Approximation for Positive-Parity ^{11}Li States

Electric-dipole transitions change the parity of states. Therefore, such transitions connect the ^{11}Li ground state characterized by a negative parity and an orbital angular momentum equal of unity to positive-parity states characterized by *L* values of 0, 1, and 2. The minimal approximation of the method of hyperharmonics requires first of all constructing, within the harmonic-oscillator basis, the simplest allowed states of ^{11}Li that are characterized by the orbital-angular-

momentum values of $L = 0$, 1, and 2 and by the number of quanta that exceeds the number of quanta in the basis function (1). Let us list the wave functions of these states. The function whose indices of $SU(3)$ symmetry are (0, 1) has the form

$$\Phi^{(0,1)+}_{0,\,L=1,\,M} = \frac{1}{54}\sqrt{\frac{3}{4}}[\mathbf{u}\otimes\mathbf{a}]^1_M\{11(\mathbf{w}\cdot\mathbf{a})^2 - 9(\mathbf{w}\cdot\mathbf{b})^2\}, \quad (8)$$

where $[\mathbf{u}\otimes\mathbf{a}]^L_M$ is the irreducible tensor product of rank L [8], while $(\mathbf{w}\cdot\mathbf{a})$ and $(\mathbf{w}\cdot\mathbf{b})$ are the scalar products of the vectors involved.

Another pair of functions has the (2, 0) $SU(3)$ symmetry; that is, we have

$$\Phi^{(2,0)+}_{0,\,L=2,\,M} = \frac{1}{54}\sqrt{\frac{13}{10}}[\mathbf{u}\otimes\mathbf{a}]^2_M\{11(\mathbf{w}\cdot\mathbf{a})^2 - 9(\mathbf{w}\cdot\mathbf{b})^2\}, \quad (9)$$

$$\Phi^{(2,0)+}_{0,\,L=0} = \frac{1}{54}\sqrt{\frac{13}{10}}[\mathbf{u}\otimes\mathbf{a}]^0_0\{11(\mathbf{w}\cdot\mathbf{a})^2 - 9(\mathbf{w}\cdot\mathbf{b})^2\}. \quad (10)$$

Each of the basis functions in (8)–(10) is the result obtained by applying the $E1$-transition operator to the function in (1) and by subsequently taking a projection onto a state that is pure in the orbital angular momentum. This does not exhaust the list of positive-parity states characterized by the orbital-angular-momentum values of $L = 1$ and 2. Such allowed functions exist for the (1, 2) and (3, 1) irreducible representations as well. They are orthogonal to the functions in (9) and (10); therefore, they cannot arise as the result of the electric-dipole photodisintegration of ^{11}Li.

The states in (8)–(10) are contained in the three-quantum TISM basis, where they have, however, a different norm. This basis also includes the states that represent the excitations of the ^{9}Li cluster and which are not included in our consideration based on the approximation of the resonating-group method. We note here that the basis of the algebraic version of the resonating-group method consists of part of the TISM basis, but the normalization of the functions included in it is generally different from the normalization of the functions in the TISM basis. In addition, the orthogonality of the states involving equal numbers of quanta is defined differently within the algebraic version of resonating group method.

Let us now introduce three branches of the basis functions of the minimal approximation:

$$\Phi^{+}_{\nu,\,L=1,\,M} = N^+_{\nu,1}[\mathbf{u}\otimes\mathbf{a}]^1_M\{11(\mathbf{w}\cdot\mathbf{a})^2 - 9(\mathbf{w}\cdot\mathbf{b})^2\}(a^2+b^2)^\nu,$$
$$N^+_{\nu,1} = \frac{1}{54}\sqrt{\frac{3}{4}}\sqrt{\frac{117}{77\nu+117}}\frac{1}{2^\nu}\sqrt{\frac{4!}{(\nu+4)!\nu!}}; \quad (11)$$

$$\Phi^{+}_{\nu,\,L=2,\,M} = N^+_{\nu,2}[\mathbf{u}\otimes\mathbf{a}]^2_M\{11(\mathbf{w}\cdot\mathbf{a})^2 - 9(\mathbf{w}\cdot\mathbf{b})^2\}(a^2+b^2)^\nu,$$
$$N^+_{\nu,2} = \frac{1}{54}\sqrt{\frac{13}{10}}\sqrt{\frac{453}{293\nu+453}}\frac{1}{2^\nu}\sqrt{\frac{4!}{(\nu+4)!\nu!}}; \quad (12)$$

$$\Phi^{+}_{\nu,\,L=0} = N^+_{\nu,0}[\mathbf{u}\otimes\mathbf{a}]^0_0\{11(\mathbf{w}\cdot\mathbf{a})^2 - 9(\mathbf{w}\cdot\mathbf{b})^2\}(a^2+b^2)^\nu,$$
$$N^+_{\nu,0} = \frac{1}{54}\sqrt{\frac{13}{10}}\sqrt{\frac{101}{41\nu+101}}\frac{1}{2^\nu}\sqrt{\frac{4!}{(\nu+4)!\nu!}}. \quad (13)$$

The grand-orbital content of these states is

$$\Phi^+_{\nu,\,L=1} = \sqrt{\frac{67(\nu+1)}{77\nu+117}}\Phi^+_{\nu+1,\,K=1,\,L=1} + \sqrt{\frac{10(\nu+5)}{77\nu+117}}\Phi^+_{\nu,\,K=3,\,L=1}, \quad (14)$$

where

$$\Phi^+_{\nu+1,\,K=1,\,L=1} = \frac{1}{2^\nu}\sqrt{\frac{4!}{(\nu+4)!(\nu+1)!}}(a^2+b^2)^\nu \times\frac{1}{54}\sqrt{\frac{3}{8}}([\mathbf{u}\times\mathbf{a}]\{6(\mathbf{w}\cdot\mathbf{a})^2 - 4(\mathbf{w}\cdot\mathbf{b})^2\} + 10[\mathbf{u}\times\mathbf{b}](\mathbf{w}\cdot\mathbf{a})(\mathbf{w}\cdot\mathbf{b})),$$

$$\Phi^+_{\nu,\,K=3,\,L=1} = \frac{1}{2^\nu}\sqrt{\frac{5!}{(\nu+5)!\nu!}}(a^2+b^2)^\nu \times\frac{1}{54}\sqrt{\frac{3}{8}}(5[\mathbf{u}\times\mathbf{a}]\{(\mathbf{w}\cdot\mathbf{a})^2 - (\mathbf{w}\cdot\mathbf{b})^2\} - 10[\mathbf{u}\times\mathbf{b}](\mathbf{w}\cdot\mathbf{a})(\mathbf{w}\cdot\mathbf{b})); \quad (15)$$

$$\Phi^+_{\nu,\,L=0} = \sqrt{\frac{26(\nu+1)}{41\nu+101}}\Phi^+_{\nu+1,\,K=1,\,L=0} + \sqrt{\frac{15(\nu+5)}{41\nu+101}}\Phi^+_{\nu,\,K=3,\,L=0},$$

where

$$\Phi^+_{\nu+1,\,K=1,\,L=0} = \frac{1}{2^\nu}\sqrt{\frac{4!}{(\nu+4)!(\nu+1)!}}(a^2+b^2)^\nu \times\frac{1}{54}\sqrt{\frac{13}{30}}((\mathbf{u}\cdot\mathbf{a})[6(\mathbf{w}\cdot\mathbf{a})^2 - 4(\mathbf{w}\cdot\mathbf{b})^2] + 10(\mathbf{u}\cdot\mathbf{b})(\mathbf{w}\cdot\mathbf{a})(\mathbf{w}\cdot\mathbf{b})),$$

$$\Phi^{+}_{\nu,K=3,L=0} = \frac{1}{2^{\nu}}\sqrt{\frac{5!}{(\nu+5)!\nu!}}(a^2+b^2)^{\nu} \times \frac{1}{54}\sqrt{\frac{13}{30}}(5(\mathbf{u}\cdot\mathbf{a})[(\mathbf{w}\cdot\mathbf{a})^2-(\mathbf{w}\cdot\mathbf{b})^2] - 10[\mathbf{u}\cdot\mathbf{b}](\mathbf{w}\cdot\mathbf{a})(\mathbf{w}\cdot\mathbf{b})); \quad (16)$$

$$\Phi^{+}_{\nu,L=2} = \sqrt{\frac{253(\nu+1)}{293\nu+453}}\Phi^{+}_{\nu+1,K=1,L=1} + \sqrt{\frac{40(\nu+5)}{293\nu+453}}\Phi^{+}_{\nu,K=3,L=1},$$

where

$$\Phi^{+}_{\nu+1,K=1,L=2} = \frac{1}{2^{\nu}}\sqrt{\frac{4!}{(\nu+4)!(\nu+1)!}}(a^2+b^2)^{\nu} \times \frac{1}{54}\sqrt{\frac{13}{10}}([\mathbf{u}\otimes\mathbf{a}]^2_M\{6(\mathbf{w}\cdot\mathbf{a})^2-4(\mathbf{w}\cdot\mathbf{b})^2\} + 10[\mathbf{u}\otimes\mathbf{b}]^2_M(\mathbf{w}\cdot\mathbf{a})(\mathbf{w}\cdot\mathbf{b})),$$

$$\Phi^{+}_{\nu,K=3,L=2} = \frac{1}{2^{\nu}}\sqrt{\frac{5!}{(\nu+5)!\nu!}}(a^2+b^2)^{\nu} \times \frac{1}{54}\sqrt{\frac{13}{10}}(5[\mathbf{u}\otimes\mathbf{a}]^2_M\{(\mathbf{w}\cdot\mathbf{a})^2-(\mathbf{w}\cdot\mathbf{b})^2\} - 10[\mathbf{u}\otimes\mathbf{b}]^2_M(\mathbf{w}\cdot\mathbf{a})(\mathbf{w}\cdot\mathbf{b})).$$

It should be noted that the weight of the $K = 3$ hyperharmonic in the $L = 1, 2$ channels is about 43% at $\nu = 0$ and is about 13% in the limit $\nu \longrightarrow \infty$. In the $L = 0$ channel, the weight of the $K = 3$ hyperharmonic is still higher (about 74%) at $\nu = 0$. For $\nu \longrightarrow \infty$, its contribution is about 37%.

The wave functions $\Psi^{+}_{E,L,M}$ of positive-parity states that belong to the ^{11}Li continuum and which occur at energy E above the threshold for three-body breakup can be represented as the superpositions

$$\Psi^{+}_{E,L,M} = \sum_{\nu=0}^{\infty} C^{+}_{\nu,L}(E)\Phi^{+}_{\nu,L,M}. \quad (17)$$

The coefficients $C^{+}_{\nu,L}(E)$ in these superpositions are determined by solving the set of equations that arise in the algebraic version of the resonating-group model and which are presented in the next section.

3. MODEL HAMILTONIAN AND ITS SPECTRUM

Let us make use of the asymptotic-potential approximation [5], which is quite appropriate for soft three-cluster systems like ^{11}Li. In this approximation, the potential-energy operator of ^{11}Li reduces to the sum of two terms, each depending only on the hyperradius. One of these terms decreases in inverse proportion to the hyperradius cubed, while the other decreases in inverse proportion to the fifth power of the hyperradius. At small values of the hyperradius, it is necessary to regularize these terms. This is achieved by going over to the representation of the harmonic-oscillator basis functions, where, in the limit $\nu \longrightarrow \infty$, the matrix $\langle\nu|\hat{U}^{-}|\tilde{\nu}\rangle$ of the potential-energy operator is diagonal [9] and takes the following regularized form for the odd basis states (4):

$$\langle\nu|\hat{U}^{-}|\tilde{\nu}\rangle = \left(\frac{A}{(4\nu+10)^{3/2}} + \frac{B}{(4\nu+10)^{5/2}}\right)\delta_{\nu,\tilde{\nu}}. \quad (18)$$

Here, A and B are coefficients that are determined from the condition that the matrix (18) of the effective potential and the tridiagonal matrix of the kinetic-energy operator between the basis functions (4),

$$\langle\nu|\hat{T}^{-}|\nu\rangle = \frac{1}{2}(2\nu+5), \quad (19)$$

$$\langle\nu+1|\hat{T}^{-}|\nu\rangle = -\frac{1}{2}\sqrt{\frac{(\nu+1)(\nu+4)(9\nu+43)}{9\nu+34}}, \quad (20)$$

reproduce fairly well the observed ground-state energy of the ^{11}Li nucleus [10] reckoned from the threshold for the three-body breakup (–0.3 MeV) and of its ground-state root-mean-square radius (3.2 fm). From this condition, we obtain $A = -37.19$ and $B = -91.19$. We set the oscillator length r_0 to 1.69 fm in order to reproduce correctly the properties of the ^{9}Li cluster.

The coefficients $C^{-}_{\nu,L=1}$ in the expansion of the wave function of the ^{11}Li ground state in the harmonic-oscillator basis (4) are displayed in Fig. 1. A slow decrease of these coefficients with increasing ν and a small value of the coefficient $C^{-}_{\nu=0,L=1}$ (about 0.5) correlate well with the idea that the ^{11}Li boundary region, which is occupied by the neutron clusters, possesses a high degree of softness; the contribution of the state where the clusters are in the p orbitals amounts to 25%. Hence, the contributions of all the remaining configurations, where the neutron clusters occupy the orbitals of the sd shell and of other shells, amount to 75%. We note that these contributions include the corrections associated with the elimination of the center-of-mass motion (recoil effects).

For the model Hamiltonians describing the aforementioned three positive-parity states to which the $E1$ transition from the ground state proceeds, we leave the matrix elements of the potential energy virtually unchanged, setting

$$\langle\nu|\hat{U}^{+}|\tilde{\nu}\rangle = \left(\frac{A}{(4\nu+12)^{3/2}} + \frac{B}{(4\nu+12)^{5/2}}\right)\delta_{\nu,\tilde{\nu}}. \quad (21)$$

As to the kinetic-energy matrices, they have equal diagonal matrix elements,

$$\langle \nu, L = 0|\hat{T}^+|\nu, L = 0\rangle = \langle \nu, L = 1|\hat{T}^+|\nu, L = 1\rangle = \langle \nu, L = 2|\hat{T}^+|\nu, L = 2\rangle = \frac{1}{2}(2\nu + 6), \quad (22)$$

but their off-diagonal matrix elements are different and are given by

$$\langle \nu + 1, L = 0|\hat{T}^+|\nu, L = 0\rangle = -\frac{1}{2}\sqrt{\frac{(\nu + 1)(\nu + 5)(41\nu + 142)}{41\nu + 101}}, \quad (23)$$

$$\langle \nu + 1, L = 1|\hat{T}^+|\nu, L = 1\rangle = -\frac{1}{2}\sqrt{\frac{(\nu + 1)(\nu + 5)(177\nu + 194)}{177\nu + 117}}, \quad (24)$$

$$\langle \nu + 1, L = 2|\hat{T}^+|\nu, L = 2\rangle = -\frac{1}{2}\sqrt{\frac{(\nu + 1)(\nu + 5)(293\nu + 746)}{293\nu + 453}}. \quad (25)$$

None of the three Hamiltonians listed above features bound states; that is, there are only continuum states. For such continuum states normalized to the delta function of momentum, we have calculated the expansion coefficients that are necessary for evaluating the matrix elements for the $E1$ transition from the ^{11}Li ground state to these states and determined the $3 \longrightarrow 3$ phase shifts δ_{L^+}. The analysis of these phase shifts as functions of energy makes it possible to find out whether the ^{11}Li nuclear system has (or does not have) low-energy resonances above the threshold for three-body breakup.

The behavior of three phase shifts δ_{0^+}, δ_{1^+}, and δ_{2^+} in the energy interval from 0 to 5 MeV is illustrated in Fig. 2. The last two phase shifts are close to each other over the energy-interval under study. First, they increase rather fast and reach a maximum value of about 2.3 rad at $E \sim 1$ MeV. Their derivatives $d\delta_{L^+}/dE$ are maximal at $E_r \sim 0.1$ MeV, where there are therefore two resonances with quantum numbers $L^\pi = 1^+$ and 2^+. The width of either resonance as estimated on the basis of the $d\delta_{L^+}/dE$ value by using the conventional formula is

$$\Gamma = 2dE/d\delta_{L^+} \sim 0.35 \text{ MeV}.$$

These resonances are not narrow—their widths exceed the energy E_r at which they occur by a factor greater than 3.

The phase shift δ_{0^+} increases more slowly than the other two phase shifts with increasing energy, and the shape of its energy dependence shows no traces of the $L^\pi = 0^+$ resonance state. The maximum value of this phase shift does not exceed 1.7 rad.

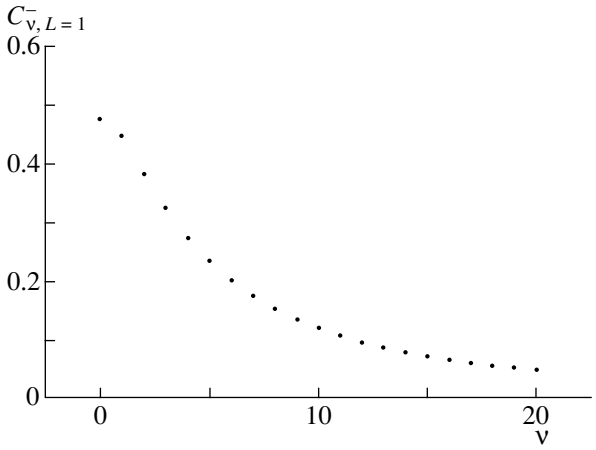

Fig. 1. Coefficients C^-_ν in the expansion of the wave function of the ^{11}Li ground state in the basis functions $\Phi^-_{\nu, L=1, M}$.

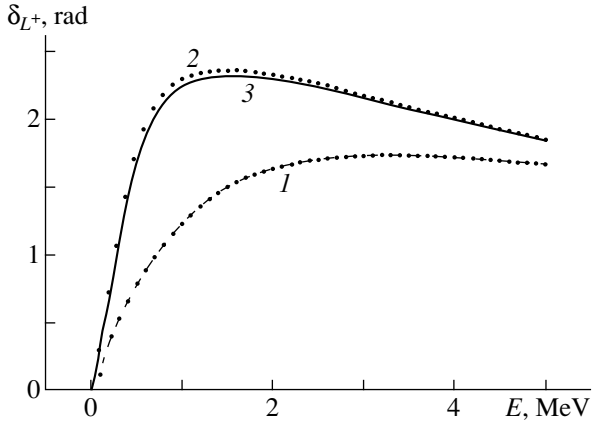

Fig. 2. $3 \longrightarrow 3$ phase shifts δ_{L^+} for even ^{11}Li states as functions of the above-threshold energy: (*1*) δ_{0^+}, (*2*) δ_{1^+}, and (*3*) δ_{2^+}.

4. CROSS SECTION FOR ^{11}Li PHOTODISINTEGRATION

The soft dipole mode in ^{11}Li can be studied theoretically by calculating the intensity of the $E1$ transition from the ground state of the ^{11}Li nucleus to its continuum states. As the result of such a transition, the ^{11}Li nucleus undergoes photodisintegration into three clusters.

At this stage, it is more convenient to use a conventional system of units.

The probability $P(E1)$ of electric-dipole photodisintegration per unit of time is expressed in terms of the reduced probability $B(E1)$ of the $E1$ transition as (see [11])

$$P(E1) = \frac{4\pi^3}{9}\rho_f \omega B(E1), \quad (26)$$

where $\hbar\omega$ is the energy of the photon absorbed by the nucleus and ρ_f is the density of the final states of the ^{11}Li continuum per unit energy interval. In order to calculate this density of states, we introduce two momenta $\mathbf{k}_1$ and $\mathbf{k}_2$ that determine the divergence of the three clusters in the c.m. frame and which are normalized in the same way as the Jacobi vectors **a** and **b**. We denote by $\mathbf{p}_1$ the momentum of the ^{9}Li cluster in the laboratory frame and by $\mathbf{p}_2$ and $\mathbf{p}_3$ the momenta of the neutron clusters. We then have

$$\mathbf{k}_1 = \sqrt{\frac{18}{11}}\left(\mathbf{p}_1 - \frac{\mathbf{p}_2 + \mathbf{p}_3}{2}\right), \quad \mathbf{k}_2 = \frac{1}{\sqrt{2}}(\mathbf{p}_2 - \mathbf{p}_3). \quad (27)$$

Further, we set

$$k^2 = k_1^2 + k_2^2; \quad k_1 = k\cos\gamma, \quad k_2 = k\sin\gamma;$$
$$0 \le \gamma \le \pi/2;$$

therefore, we can write the expression for the density of states as

$$\rho_f = \frac{(4\pi)^2 k^5}{dE/dk}\int_0^{\pi/2} \frac{\sin^2\gamma\cos^2\gamma\, d\gamma}{(2\pi)^6} = \frac{\pi^3 k^4 m}{(2\pi)^6\hbar^2}. \quad (28)$$

The reduced probability $B(E1)$ is given by

$$B(E1) = r_0^2\frac{(2\pi)^6}{(kr_0)^5}\sum_{\mu, M}\left|(\Psi^+_{E, L, M}|\hat{M}_\mu|\Psi^-_{1, M'})\right|^2, \quad (29)$$

where

$$k^2 = \frac{2mE}{\hbar^2}. \quad (30)$$

The factor $(2\pi)^6/(kr_0)^5$ appears upon going over from the functions of the continuous spectrum that are normalized to the delta function $\delta(k - k')$ to the functions normalized to the flux **v**, $\mathbf{v} = \hbar\mathbf{k}/m$.

In order to obtain the cross section for ^{11}Li photodisintegration, the transition probability in (26) must be divided by the speed of light c (the photon-flux density).

For the photodisintegration cross section, this yields

$$\sigma_f(E1) = \frac{4\pi^6}{9\hbar c}\frac{E + \varepsilon}{r_0^3}\sqrt{\frac{m}{2\hbar^2 E}}\sum_{\mu, M}\left|(\Psi^+_{E, L, M}|\hat{M}_\mu|\Psi^-_{1, M'})\right|^2, \quad (31)$$

where $\varepsilon = 0.3$ MeV is the energy required for the three-body decay of the nucleus. The resulting cross section has the dimensions of fm^2.

The explicit expression for the matrix element of the operator $\hat{M}_\mu$ has the form

$$(\Psi^+_{E, L, M}|\hat{M}_\mu|\Psi^-_{1, M'}) = \sum_{\nu=0}^{\infty} C^+_{\nu, L, M}(E)$$
$$\times(\langle\nu, L^+, M|\hat{M}_\mu|\nu, 1^-, M'\rangle C^-_{\nu, 1, M'} \quad (32)$$
$$+ \langle\nu, L^+, M|\hat{M}_\mu|\nu+1, 1^-, M'\rangle C^-_{\nu+1, 1, M'}),$$

where the partial-wave matrix elements are given by

$$\langle\nu, L^+, M|\hat{M}_\mu|\nu, 1^-, M'\rangle = C^{L, M}_{1M'; 1\mu}\frac{1}{\sqrt{11}}\frac{N^-_\nu}{N^+_{\nu, L}},$$

$$\langle\nu, L^+, M|\hat{M}_\mu|\nu+1, 1^-, M'\rangle = C^{L, M}_{1M'; 1\mu}\frac{1}{3\sqrt{11}}\frac{19}{34}\frac{N^+_{\nu, L}}{N^-_{\nu+1}}.$$

Here, the quantity μ takes the values of 1 and –1, which correspond to two possible states of photon polarization.

5. RESULTS OF CALCULATIONS AND CONCLUSION

On the basis of the formulas from the preceding section, we have calculated the effective cross sections σ_{fL^+} for ^{11}Li photodisintegration that correspond to the $E1$ transitions from the ground state to the three continuum states characterized by $L = 0$, 1, and 2. In Fig. 3, these cross sections are shown as functions of energy reckoned from the threshold of the breakup process $^{11}\text{Li} \longrightarrow {}^9\text{Li} + n + n$. The cross sections for the $1^- \longrightarrow 1^+$ and $1^- \longrightarrow 2^+$ transitions have a pronounced peak at an energy of 0.55 MeV above the threshold and decrease with increasing energy rather fast. For the transitions to the $L = 0$ states, the cross sections $\sigma_{fL=0^+}$ change rather slowly, displaying a broad maximum in the vicinity of 1.6 MeV. Its value does not exceed 0.2 mb, which is nearly one order of magnitude smaller than the maximum values of the cross sections $\sigma_{fL=1^+}$ and $\sigma_{fL=2^+}$.

The total photodisintegration cross section

$$\sigma_f(E1) = \sum_L \sigma_{fL^+}$$

in the asymptotic-potential approximation is shown in Fig. 4. The position of the maximum at $E_r = 0.55$ MeV and the half-width $\Gamma = 0.9$ MeV agree well with the experimental values of $E_r = 0.7$ MeV and $\Gamma = 0.8$ MeV presented in [1].

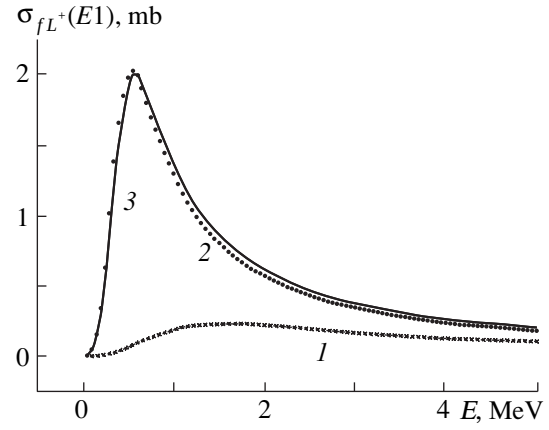

Fig. 3. Effective cross sections $\sigma_{fL^+}(E1)$ for ^{11}Li photodisintegration as functions of the above-threshold energy: (*1*) σ_{f0^+}, (*2*) σ_{f1^+}, and (*3*) σ_{f2^+}.

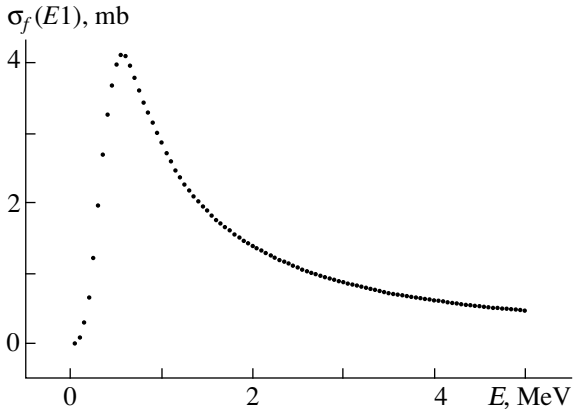

Fig. 4. Total effective cross section $\sigma_f(E1)$ for photodisintegration in the asymptotic-potential approximation as a function of the above-threshold energy.

The maximum value of the total cross section amounts to 4.2 mb, which also complies with experimental data. We note, however, that, in just the same way as in [3], the cross section presented here decreases somewhat more slowly with increasing energy than the experimental cross section.

In summary, the energy and the wave function of the ^{11}Li ground state, as well as the total effective cross section for its electric-dipole photodisintegration, can be correctly reproduced by treating the ^{11}Li nucleus on the basis of the microscopic three-cluster model and by using the approximation of the asymptotic potential in the form of a power-law function of the hyperradius; for this, it is sufficient to retain only basis states associated with the minimal grand-orbital values and allowed by the Pauli exclusion principle. The results of the calculations performed without taking into account the spin–orbit interaction suggest the existence of $L^\pi = 1^+$ and $L^\pi = 2^+$ ($J^\pi = 3/2^+$ and $J^\pi = 5/2^+$ if the spin–orbit interaction is taken into account) resonances of the ^{11}Li nucleus in the low-energy region extending up to 0.5 MeV.

REFERENCES

1. D. Sackett, K. Ieki, A. Galonski, *et al.*, Phys. Rev. C **48**, 118 (1993).
2. Y. Suzuki, K. Ikeda, and H. Sato, Prog. Theor. Phys. **83**, 180 (1990).
3. B. V. Danilin, I. J. Thompson, M. V. Zhukov, *et al.*, Phys. Lett. B **333**, 299 (1994).
4. L. V. Chulkov, B. Jonson, and M. V. Zhukov, Eur. Lett. **24**, 171 (1993).
5. G. F. Filippov, Yu. A. Lashko, and L. P. Shvedov, Yad. Fiz. **62**, 1772 (1999) [Phys. At. Nucl. **62**, 1651 (1999)].
6. G. F. Filippov, Yad. Fiz. **62**, 1237 (1999) [Phys. At. Nucl. **62**, 1164 (1999)].
7. M. V. Zhukov, in *Proceedings of VI International School–Seminar "Heavy Ion Physics," Dubna, Sept. 22–27, 1997* (World Sci., Singapore, 1997), p. 73.
8. D. A. Varshalovich, A. N. Moskalev, and V. K. Khersonskii, *Quantum Theory of Angular Momentum* (Nauka, Leningrad, 1975; World Sci., Singapore, 1988).
9. G. F. Filippov, A. D. Bazavov, K. Kato, and S. V. Korennov, Yad. Fiz. **60**, 635 (1997) [Phys. At. Nucl. **60**, 554 (1997)].
10. T. Kobayashi, Nucl. Phys. A **538**, 343 (1992).
11. A. S. Davydov, *Theory of the Nucleus* (Fizmatgiz, Moscow, 1958).

Translated by A. Isaakyan

Physics of Atomic Nuclei, Vol. 64, No. 2, 2001, pp. 194–202. Translated from Yadernaya Fizika, Vol. 64, No. 2, 2001, pp. 238–246.

NUCLEI
Theory

Role of $U(3(A-1))$ Multiquantum Excited States in Calculating Spectroscopic Quantities for $^{8}_{4}$Be

K. Jankauskas*
University of Klaipeda, ul. Manto 84, LT-5808 Klaipeda, Lithuania
Received October 20, 1999; in final form, April 5, 2000

Abstract—A set of equations for deriving the $SU(3)$-irreducible density matrix for $U(3(A-1))$ multiquantum excited states involved is given. For the $^{8}_{4}$Be nucleus, the binding energies, radii, spectra, electric quadrupole moments, and probabilities $B(E2)$ of electric quadrupole transitions are computed in the multiquantum approximation of the unitary scheme. The values obtained for the above spectroscopic quantities are investigated versus the number of basis functions involved. © *2001 MAIK "Nauka/Interperiodica".*

1. INTRODUCTION

In the unitary scheme, basis functions are specified by the subgroup sequences $U(3(A-1)) \supset SU(3) \times U(A-1)$, $U(A-1) \supset O(A-1) \supset S(A)$, and $SU(3) \supset O^{+}(3)$ [1]. We label them as $\psi([E_1E_2E_3](\omega_1\omega_2\omega_3)\alpha\lambda\kappa\Gamma_0)$, where $[E_1E_2E_3]$ and $(\omega_1\omega_2\omega_3)$ are irreducible representations of the $U(A-1)$ and $O(A-1)$ groups, respectively, while λ denotes the corresponding Young diagram for the permutation group $S(A)$. The symbol $[E_1E_2E_3]$ also specifies irreducible representations $(\lambda\mu) = (E_1 - E_2E_2 - E_3))$ and $[E, 0, 0]$ of the $SU(3)$ and the $U(3(A-1))$ group, respectively, where $E = E_1 + E_2 + E_3$ is the number of oscillator quanta since the basis of the unitary scheme consists of the eigenfunctions of the Hamiltonian of the $3(A-1)$-dimensional harmonic oscillator. The symbols α and κ stand for the multiplicities of the chains $O(A-1) \supset S(A)$ and $SU(3) \supset O^{+}(3)$ occurring in the corresponding multiplet, and Γ_0 denotes all the remaining quantum numbers describing the orbital and spin–isospin wave functions. The wave functions of the $U(3(A-1))$-symmetric ground states involve the minimum number of excitations that still admits, in the reduction associated with the subgroup chain $U(A-1) \supset O(A-1) \supset S(A)$, the emergence of irreducible representations λ of the $S(A)$ group that are allowed by the Pauli exclusion principle. Functions that are labeled by quantum numbers $E > E_{\min}$ represent $U(3(A-1))$ excited states. In [2], the method developed in [3] for taking into account $U(3(A-1))$ multiquantum excited states was employed to calculate the spectroscopic features of the $^{8}_{4}$Be nucleus. These calculations proved to be equivalent to those carried out within the approximate $Sp(2R)$ model proposed in [4, 5]. In order to render a comparison with the results presented in [4, 5] meaningful, the calculations in [2] were performed, in just the same way as in those studies, with a reduced Hamiltonian not including Coulomb interaction.

The present study is devoted to (i) considering the potential of the basis $B1$ (see Section 2) of $E \le E_{\min} + 2$ functions—that is, spectroscopic calculations are performed in the basis extended step by step, whereby the relative weights of the basis functions corresponding to $[E_1E_2E_3]$ and $(\omega_1\omega_2\omega_3)$ representations of different symmetries are revealed—and (ii) performing calculations in the multiquantum approximation of the bases $B2$ and $B3$ involving the functions that are of greatest importance kinematically. The present calculations, relying on the full Hamiltonian and employing various bases and potentials, supplement those reported in [2]. The convergence of these bases is investigated.

The ensuing exposition is organized as follows. The bases used in the calculations are presented in Section 2, together with a compendium of useful formulas and definitions. The matrix elements of physical operators are computed within the density-matrix formalism. The density matrix for $U(3(A-1))$ multiquantum excited states is derived by the method applying the $SU(3)$-irreducible density matrix [3, 6]. An account of this method as applied to the bases $B2$ and $B3$ harnessed in the present study is given in Section 3. Section 4 contains some results of spectroscopic calculations for the $^{8}_{4}$Be nucleus and a relevant discussion.

2. BASES AND USEFUL FORMULAS

According to general principles of supermultiplet theory, $U(3(A-1))$ states associated with the most symmetric Young diagram λ play a key role in describing low-lying levels. Therefore, we consider the bases consisting of the functions labeled by the Young diagram

* e-mail: jonas@ip.ku.lt

$\lambda = [44]$ and the following quantum numbers of the $U(n-1)$ and $O(n-1)$ groups:[1)]

$$E\omega = [4](4),\ [6](4),\ [51](4),\ [42]_\kappa(4),\ [6](6),$$
$$[51](51),\ [42]_\kappa(42)_\alpha \text{ (basis } B1),$$
$$E\omega = [4+2m](4),\ m = 0, 1, \ldots, N \le 12 \text{ (basis } B2),$$
$$E\omega = [4+2m](4),\ m = 0, 1, \ldots, N = 12,\ [6+2m_1](6),$$
$$m_1 = 0, \ldots, N_1 \le 5 \text{ (basis } B3).$$

The quantum numbers $ST = 00$ correspond to the diagram $\lambda = [44]$. The computations were performed for $L = 0$, 2, 4, and 6. For the $[42]_\kappa(42)_\alpha$ states, the repetition multiplicities are $\alpha = 1, 2$ for the chain $O(A-1) \supset S(A)$ and $\kappa = 0, 2$ for the chain $SU(3) \supset O^+(3)$ (at $L = 2$).

For the diagrams $\lambda = [4\ldots4]$, the total Hamiltonian has the form

$$H = V_c + T + V^C, \tag{1}$$

where V_c is the operator of central nucleon–nucleon interaction, T is the kinetic-energy operator, and V^C is the Coulomb energy operator. The central nucleon-nucleon interaction can be represented in the form

$$V_c(r) = W(r) + M(r)p^r + B(r)p^\sigma - H(r)p^\tau, \tag{2}$$

where the operators p^r, p^σ, and p^τ permute, respectively, the orbital, the spin, and the isospin nucleon coordinates. The functions $W(r)$, $M(r)$, $B(r)$, and $H(r)$ are expressed in terms of the commonly used functions $V^{2S+1\,2T+1}(r)$ [7] [$V^{31}(r)$, $V^{13}(r)$, $V^{33}(r)$, and $V^{11}(r)$] as

$$\begin{aligned} W(r) &= \frac{1}{4}(V^{11} + V^{13} + V^{31} + V^{33}),\\ M(r) &= \frac{1}{4}(-V^{11} + V^{13} + V^{31} - V^{33}),\\ B(r) &= \frac{1}{4}(-V^{11} - V^{31} + V^{13} + V^{33}),\\ H(r) &= \frac{1}{4}(V^{11} + V^{13} - V^{31} - V^{33}). \end{aligned} \tag{3}$$

The matrix element of the operator in (2) can be represented in the form

$$\langle\Gamma|V_c|\Gamma'\rangle = \sum_{\nu,\,p} Q_p^{\nu\Gamma\Gamma'} I_p^\nu, \tag{4}$$

where Γ is the set of the quantum numbers specifying a function in the unitary scheme, the Talmi integrals are determined by formula (14.8) from [1], ν labels the type of interaction ($\nu = W, M, B, H$), and Q_p^ν are the components of the two-particle density matrix. In the calculations, we use the various Gaussian potentials [8–10] (the values of the parameters in these potentials are quoted in Table 1)

$$\begin{aligned} V^{2S+1\,2T+1}(r) &= \sum_i V^i_{2S+1\,2T+1}\\ &\times \exp[-(r/\mu^i_{2S+1\,2T+1})^2]. \end{aligned} \tag{5}$$

The expression for the matrix element of the kinetic-energy operator has the form

$$\begin{aligned} \langle\Gamma|T|\Gamma'\rangle &= \left[\left(E + \frac{3(A-1)}{2}\right)\delta(\Gamma\Gamma')\right.\\ &\left. - \frac{1}{A}\sum_p \left(p + \frac{3}{2}\right)Q_p^{W\Gamma\Gamma'}\right]\frac{\hbar^2}{mr_\psi^2}, \end{aligned} \tag{6}$$

where E is the oscillator energy, $Q_p^{W\Gamma\Gamma'}$ is the density matrix for Wigner interaction, and r_ψ is the scale parameter of the radial wave function.

The matrix element of the Coulomb interaction operator is given by

$$\langle\Gamma|V^C|\Gamma'\rangle = \sum Q_p^{C\Gamma\Gamma'} I_p^C, \tag{7}$$

where Q_p^C is the density matrix for the Coulomb interaction, while the interaction integrals (in MeV) have the form

$$I_p^C = \frac{2^p p! \times 1.44 r_\psi}{(2p+1)!!}, \tag{8}$$

where the parameter r_ψ is measured in femtometers. In the case of the diagrams $\lambda = [4\ldots4]$, it is sufficient to know Q^W and Q^M for calculating the matrix element (4), because the remaining quantities are determined from the relations

$$Q_p^B = -Q_p^H = 2(Q_p^W - Q_p^M)/5. \tag{9}$$

The density matrices Q^W and Q^M are given by

$$Q_p^W = \sum_{\bar{E}\bar{\kappa}\bar{L}ll'} Q_{\bar{E}}^{EE'} C^{\bar{E}\varepsilon E}_{\bar{\kappa}\bar{L}l\kappa L} C^{\bar{E}\varepsilon' E'}_{\bar{\kappa}\bar{L}l\kappa L} \langle\varepsilon l\varepsilon' l'|p\rangle, \tag{10}$$

$$Q_p^M = \sum_{\bar{E}\bar{\kappa}\bar{L}ll'} (-1)^\varepsilon Q_{\bar{E}}^{EE'} C^{\bar{E}\varepsilon E}_{\bar{\kappa}\bar{L}l\kappa L} C^{\bar{E}\varepsilon' E'}_{\bar{\kappa}\bar{L}l\kappa L} \langle\varepsilon l\varepsilon' l'|p\rangle. \tag{11}$$

The density matrix Q^C for the Coulomb energy in (7) is readily expressed in terms of Q^W and Q^M. By way of example, we indicate that, for the diagrams $\lambda = [4\ldots4]$, the resulting relation has the form

$$Q_p^C = (7Q_p^W - 2Q_p^M)/30. \tag{12}$$

In Eqs. (10) and (11), $Q_{\bar{E}}$ is the $SU(3)$-irreducible two-particle density matrix; C stands for the Clebsch–Gordan coefficients associated with the chain $SU(3) \supset O^+(3)$; and $\langle\varepsilon l\varepsilon' l'|p\rangle$ are the Brody–Moshinsky coeffi-

[1)] For the sake of brevity, we will use, along with $[E_1E_2E_3]$ and $(\omega_1\omega_2\omega_3)$, the notation E and ω. For the representations of the $U(A-1)$ and $O(A-1)$ groups, we adopt the condensed notation using (ω) instead of $(\omega00)$ and so on.

Table 1

V	V^i_{31}, MeV		V^i_{13}, MeV		V^i_{33}, MeV		V^i_{11}, MeV	
	μ^i_{31}, fm		μ^i_{13}, fm		μ^i_{33}, fm		μ^i_{11}, fm	
	$i = 1$	$i = 2$	$i = 1$	$i = 2$	$i = 1$	$i = 2$	$i = 1$	$i = 2$
V_1	144.86	−83.34	144.86	−83.34	644	0	644	0
	0.82	1.6	0.82	1.6	0.65		0.65	
V_2	144.86	−83.34	144.86	−83.34	16.9	0	16.9	0
	0.82	1.6	0.82	1.6	1.6		1.6	
V_3	389.5	−140.6	389.5	−140.6	1000	–26	1000	–26
	0.7	1.4	0.7	1.4	0.7	1.4	0.7	1.4
V_4	144.86	−83.34	144.86	−83.34	–28.97	16.67	–29	16.66
	0.82	1.6	0.82	1.6	0.82	1.6	0.82	1.6
V_5	–72.5	0	–39.15	0	24.16	0	117.45	0
	1.47		1.62		1.47		1.62	
V_6	69.22	–55.85	69.22	–55.85	20.09	0	20.09	0
	1.141	2.185	1.141	2.185	2.185		2.185	
V_7	118.11	−80.78	118.11	−80.78	24.77	0	24.77	0
	1.172		1.172	2.012	2.012		2.012	

cients [11], which represent a particular case of the coefficients D {see formula (4.1) in [12]}.

The nuclear radii can be determined from the formula for the equivalent density distribution {Eq. (2.3) in [13]}:

$$R = \left(\frac{5}{3}\langle r\rangle^2\right)^{1/2}. \tag{13}$$

Here, $r^2 = \sum_{i=1}^{A-1}\rho_i^2/A$ is the mean-square radius—that is, the mean sum of the squares of the normalized Jacobi coordinates ρ_i. It is convenient to represent its matrix element in the form

$$\langle\Gamma|r^2|\Gamma'\rangle = \frac{2r_\psi^2}{A^2}\sum_p (p+3/2)Q_p^{W\Gamma\Gamma'}. \tag{14}$$

The electric quadrupole moment is defined as the expectation value of the operator $[16\pi/5]^{1/2}O_0^2$ in the $L = L' = M$ state [7]. The operator O_0^2 is defined as

$$O_0^2 = \frac{e}{2}\sum_{i=1}^{A}(1-2t_{0i}^1)Y_{0i}^2(\theta,\varphi)r_i^2, \tag{15}$$

where e is the electron charge, t_{0i}^1 is the isospin projection onto the z axis, Y_{0i}^2 is a spherical harmonic, and r_i^2 is the coordinate of the ith particle. For the diagrams $\lambda = [4\ldots4]$, the matrix element of the operator O_0^2 has the form

$$\langle\Gamma|O_0^2|\Gamma'\rangle = \frac{(A-1)er_\psi^2}{2A}\sum_{\bar E\bar\kappa\bar L ll'}(-1)^{\delta(\varepsilon,\varepsilon')+1+L-\bar L}q_{\bar E}^{EE'}C_{\bar\kappa\bar L l\kappa L}^{\bar E\varepsilon E}C_{\bar\kappa\bar L l'\kappa' L'}^{\bar E\varepsilon' E'}\begin{Bmatrix}\bar L & L' & l'\\ 2 & l & L\end{Bmatrix}$$
$$\times\sqrt{\frac{5(4+|l-l'|)}{64\pi}\,\frac{(2l+1)(2l'+1)(l+l'+2)}{(l+l'+3)(l+l'+1)(l+l'-1)}\,\frac{L(2L-1)(2L+1)}{(L+1)(2L+3)}}I_{\varepsilon l\varepsilon' l'}(r^2), \tag{16}$$

where $q_{\bar E}$ is the $SU(3)$-irreducible single-particle density matrix and C stands for the Clebsch–Gordan coefficients associated with the chain $SU(3)\supset O^+(3)$. The integrals in Eq. (16) are given by

$$I_{\varepsilon l\varepsilon' l'} = \sum_p (p+3/2)\langle\varepsilon l\varepsilon' l'|p\rangle. \tag{17}$$

The probability $B(E2)$ of electric quadrupole transitions is expressed in terms of the matrix element of the operator O_0^2 [7] as

$$B(E2, L\longrightarrow L') = \langle\Gamma' L' M'|O_0^2|\Gamma L M\rangle^2[C_{M0M}^{L'2L}]^{-2}. \tag{18}$$

The matrix elements (16) and (18) do not vanish only for $E' = E, E \pm 2$ states. In the case of symmetric representations of the $SU(3)$ group, there are analytic expressions for the diagonal matrix elements (16) and (18) (see [14]).

3. CALCULATION OF $SU(3)$-IRREDUCIBLE DENSITY MATRIX FOR $U(3(A-1))$ MULTIQUANTUM EXCITED STATES

In dealing with the matrix elements in Section 2, the gravest problems arise in calculating the $SU(3)$-irreducible density matrix. With increasing E, these difficulties go from bad to worse. In this section, the $SU(3)$-irreducible density matrix is computed for the case of the symmetric representations $[\omega + 2m00](\omega 00)$ of the $U(A-1)$ and $O(A-1)$ groups with the bases $B2$ and $B3$. In this case, the computations can be simplified [6]. Both the two-particle and the single-particle density matrix are determined by the set of equations

$$\sum_{\bar{E}} \langle \varepsilon\varepsilon' | p \rangle Q_{\bar{E}}^{EE'} = \tilde{Q}_p^{EE'} \quad (p = 0, 1, \ldots, p_{\max}), \quad (19)$$

where $Q_{\bar{E}}$ is the $SU(3)$-irreducible density matrix and the coefficients are given by

$$\begin{aligned}
&\langle \varepsilon\varepsilon' | p \rangle \\
&= \frac{2p - \varepsilon - k}{p^{1/2}} \Gamma\left(p + \frac{1}{2}\right) [\varepsilon!(\varepsilon + 2k)!]^{1/2} (-1)^{\varepsilon - p} \\
&\times \sum_{s = \max\left(0, \varepsilon - \left[\frac{\varepsilon}{2}\right] - p\right)}^{\min\left(\left[\frac{\varepsilon}{2}\right], \varepsilon + k - p\right)} [s!(\varepsilon + k - s - p)!(\varepsilon - 2s)! \\
&\times (2p + 2s - \varepsilon)!]^{-1}.
\end{aligned} \quad (20)$$

Here, $\varepsilon = E - \bar{E}$; $\varepsilon' = \varepsilon + 2k = E' - \bar{E}$; $p = 0, 1, \ldots, (\varepsilon + \varepsilon')/2$; and the symbol $[\varepsilon/2]$ denotes the integral part of the bracketed number. The nonhomogeneous terms $\tilde{Q}_p^{EE'}$ in the set of Eq. (19) are the components of the density matrix in the canonical basis for the $SU(3)$ group [6]. In the case of $E\omega \equiv [\omega + 2m00](\omega 00)$ states, the quantity $\tilde{Q}_p^{EE'}$ is expressed in terms of the basic density matrix $\tilde{Q}^{0\omega\omega'}$ for the $[\omega 00](\omega 00)$ states (that is, the density matrix corresponding to identical representations E and ω for the same basis) as

$$\tilde{Q}_p^{EE'} = \sum_{\alpha} \tilde{Q}_{p-\alpha}^{0\omega\omega'} D_{p-\alpha,\alpha}^{Nl_K N' l_K'}, \quad (21)$$

where

$$\begin{aligned}
D_{p,\alpha} &= \frac{[\Gamma(N + l_K + 1/2)\Gamma(N + l_{K'} + 1/2)N!N'!]^{1/2}}{\alpha!} \frac{\Gamma((l_K + l_{K'})/2 + 1/2)\Gamma(p + a + 1/2)}{\Gamma((l_K + l_{K'})/2 - p)\Gamma(p + 1/2)} \\
&\times \sum_{mm's} (-1)^{m+m'} \frac{(m + m')!\Gamma((l_K + l_{K'})/2 - p + s)}{s!m!m'(N - m)!(N' - m')!\Gamma(l_K + m + 1/2)\Gamma(l_{K'} + m' + 1/2)}.
\end{aligned} \quad (22)$$

Here, $N = (E - \omega)/2$, $l_K = \omega + (A-2)/2$, $\alpha = m + m' - s$, and summation is actually performed over two indices.

The explicit form of the basic density matrix can easily be derived from the results presented in [1, 6]. By way of example, we indicate that, for the $4 \le A \le 8$ nuclei, the two-particle density matrix for the $U(3(A-1))$ states corresponding to the symmetric representations $[\omega 00](\omega 00)$ at $\omega = E_{\min}$ has the form

$$\tilde{Q}_0^0 = \frac{3}{8}[\omega(\omega + 3) + 16], \quad \tilde{Q}_1^0 = \frac{1}{4}\omega(11 - \omega), \quad \tilde{Q}_2^0 = \frac{3}{8}\omega(\omega - 1). \quad (23)$$

For the same states, the single-particle density matrix is given by

$$\tilde{q}_0^0 = \frac{A(A - 1 - \omega)}{A - 1}, \quad \tilde{q}_1^0 = \frac{A\omega}{A - 1}. \quad (24)$$

For the $U(3(A-1))$ states involving $O(A-1)$ excitations (that is, the $\omega_1 + \omega_2 + \omega_3 = E_{\min} + 2$ states), the basic density matrix can be determined, by invoking fractional-parentage coefficients, with the aid of the method proposed in [6].

4. RESULTS OF THE CALCULATIONS

Presented below are some results that were computed for the ${}^8_4\mathrm{Be}$ nucleus and which make it possible to study the spectroscopic quantities as functions of the quantum numbers associated with the $U(A-1)$ and $O(A-1)$ groups and to clarify the role of $U(3(A-1))$ multiquantum excited states. In these calculations, use was made of the variational values of the parameter r_ψ appearing in the expression for the wave function. The results are presented in Tables 2–7 and in the figure.

Levels that were studied here belong to the $L = 0^+$, 2^+, and 4^+ and 0^+, 2_1^+, 4_1^+, and 6_1^+ rotational bands. No attention has been given here to other levels identified in [15], which correspond, according preliminary calculations, to the Young diagrams [431] (the excitation

Table 2. Changes in the energy (in MeV) and the root-mean-square radius (in fm) in response to the extension of the basis $B1$

L^π	Potential V_4				L^π	Potential V_7			
	1	2	3	4		1	2	3	4
0^+	0(–36.32)	0(–41.18)	0(–44.42)	0(–45.51)	0^+	0(–53.17)	0(–58.44)	0(–61.27)	0(–62.98)
	2.17	2.19	2.21	2.21		2.56	2.60	2.64	2.63
2^+	1.99	2.19	3.0	3.15	2^+	1.36	1.74	2.37	2.42
	2.10	2.17	2.18	2.19		2.56	2.59	2.59	2.60
4^+	6.48	7.65	10.75	9.14	4^+	4.32	6.00	8.75	7.07
	2.10	2.14	2.16	2.15		2.49	2.68	2.56	2.55
0_1^+	21.03	26.45	27.64	26.63	0_1^+	16.96	23.68	24.63	25.17
	2.56	2.57	2.62	2.59		2.91	2.90	2.97	2.95
2_1^+	22.16	28.45	31.50	30.56	2_1^+	17.40	24.39	27.14	27.49
	2.56	2.52	2.48	2.58		2.88	2.86	2.87	2.91
4_1^+	24.62	31.35	33.85	33.95	4_1^+	18.48	25.65	28.17	29.07
	2.53	2.47	2.52	2.54		2.84	2.77	2.82	2.84

Table 3. Binding energy and spacings between the energy levels (in MeV) according to calculations with the basis $B1$

L^π \ Potential	V_1	V_2	V_3	V_6
		$E_{\min}$ approximation		
0^+	0 (–35.75)	0 (–34.93)	0 (–35.52)	0 (–53.96)
2^+	2.10	2.03	2.09	1.49
4^+	6.92	6.67	6.82	4.83
		$E_{\min}$ + 2 approximation		
0^+	0 (–45.59)	0 (–44.41)	0 (–45.86)	0 (–64.12)
2^+	3.25	3.19	3.23	2.57
4^+	9.98	9.74	9.97	8.10
0_1^+	27.12	26.52	27.86	25.62
2_1^+	31.04	30.45	31.56	28.04
4_1^+	34.32	33.84	34.28	30.08

energy range between 16 and 20 MeV) and [422] (the excitation-energy range between 20 and 26 MeV).

As was mentioned in the Introduction, the computations were performed in two steps. The calculations in the $E_{\min}$ + 2 approximation at the first step made it possible to clarify the role of basis states corresponding to different representations $[E_1E_2E_3]$ and $(\omega_1\omega_2\omega_3)$ and the potential of the basis $B1$ (Tables 2–4). At the second step, the computations were performed in the multiquantum approximation by using the bases $B2$ and $B3$ (see figure and Tables 5–7).

4.1. $E_{\min}$ + 2 Approximation

Tables 2 and 3 quote the theoretical values of the binding energy (in parentheses), the spacings between the levels under study, and the root-mean-square radii.

Table 2 demonstrates how the results change as we extend the basis $B1$ step by step. There, we display the values calculated with the potentials V_4 [8] and V_7 [9]. The results obtained in the $E_{\min}$ approximation ([4](4) function) are shown in the first column. The results deduced by employing the basis of two functions {[4](4), [6](4)} are given in the second column. The results in the third column were derived in the basis

Table 4. Coefficients $b(E\omega) \times 10^2$ in the expansion of the wave function $\psi(L)$ for the potential V_4 in the basis $B1$

$E_\kappa\omega_\alpha$ \ L^π	0^+	2^+	4^+	0_1^+	2_1^+	4_1^+
[4](4)	91	91	91	5	–5	–9
[6](4)	22	30	30	90	94	94
[51](4)	–	–8	12	–	15	24
$[42]_0(4)$	30	22	–18	21	–27	–21
$[42]_2(4)$	–	11	–	–	–3	–
[6](6)	12	14	–15	36	13	–5
[51](51)	–	0	0	–	0	1
$[42]_0(42)_1$	3	0	–	3	0	–
$[42]_2(42)_1$	–	0	3	–	2	1
$[42]_0(42)_2$	7	0	–	6	0	–
$[42]_2(42)_2$	–	0	8	–	1	5

Table 5. Changes in the energy (in MeV) and the root-mean-square radius (in fm) in response to the extension of the bases $B2$ and $B3$ for the potential V_4

L^π \ NN_1	0(1*)	2	4	8	12	12 0	12 5	Experimental values [15]
0^+	0 (–36.32)	0 (–44.32)	0 (–47.17)	0 (–48.26)	0 (–48.32)	0 (–48.94)	0 (–50.02)	0 (–56.6)
	2.17	2.21	2.27	2.32	2.34	2.32	2.35	
2^+	2.00	2.50	2.94	3.11	3.12	3.08	3.18	3.04
	2.16	2.21	2.27	2.32	2.33	2.32	2.35	
4^+	6.47	8.76	10.05	10.52	10.54	10.52	10.84	11.4
	2.13	2.18	2.27	2.32	2.33	2.30	2.35	
0_1^+	27.22*	26.04	21.92	18.20	17.35	17.47	16.18	20.2
	2.57	2.55	2.58	2.72	2.79	2.79	2.84	
2_1^+	28.59	27.28	23.31	19.85	19.06	19.23	18.16	22.2
	2.54	2.52	2.58	2.72	2.80	2.81	2.84	
4_1^+	31.35	29.75	26.41	23.65	22.96	23.29	22.60	25.4
	2.48	2.49	2.55	2.67	2.78	2.79	2.82	
6^+	33.00	31.23	29.26	27.56	27.21	27.71	26.95	
	2.58	2.54	2.62	2.74	2.78	2.81	2.84	

* The energies $\varepsilon(L_1)$ are reckoned from the $L = 0$ level (the energy $\varepsilon(0) = -41.18$ MeV was obtained at $N = 1$).

involving all $\omega = (4)$ functions associated with the corresponding value of L (for labeling of the functions involved, see Table 4). The results presented in the fourth column correspond to the full basis $B1$—that is, all functions of the $E_{min} + 2$ approximation that are associated with the diagram $\lambda = [44]$ are used.

The results for the other potentials in the E_{min} and $E_{min} + 2$ approximations are quoted in Table 3. The results for the potentials V_1, V_2, and V_3 are close to the results for V_4, while the results for the potential V_6 are close to the results for V_7.

The structure of the wave function in the $E_{min} + 2$ approximation is shown in Table 4. The states associated with minimum $\omega = (4)$ and, among them, the states corresponding to the most symmetric diagrams $[E_1E_2E_3]$ are of greatest importance kinematically and are therefore dominant. The contribution of the $\omega_1 + \omega_2 + \omega_3 = E_{min} + 2$ states is much less.

For the nearly realistic potentials presented in Table 1, the binding energy (its experimental value is $\omega_{bind} = 56.60$ MeV [15]) and the spacings between the levels in the first band can be calculated in the $E_{min} + 2$ approxi-

Table 6. Changes in the electric quadrupole moments $Q(L)$ (in e fm^2) and the probabilities of electric quadrupole transitions, $B(E2, L \longrightarrow L-2)$ (in e^2 fm^4), in response to the extension of the bases $B2$ and $B3$ for the potential V_4

L^π \ NN_1	0 (1*)	2	4	8	12	12 0	12 5
0^+	0	0	0	0	0	0	0
2^+	–4.02	–5.75	–6.85	–7.65	–7.77	–7.52	–7.96
4^+	–4.87	–6.77	–8.18	–9.16	–9.31	–8.94	–9.68
0_1^+	0	0	0	0	0	0	0
2_1^+	–5.86	–6.94	–8.91	–11.57	–12.81	–12.81	–12.97
4_1^+	–7.06	–8.57	–11.03	–13.93	–15.69	–15.85	–15.99
6^+	–9.64	–10.88	–13.51	–16.46	–17.90	–17.79	–18.33
$2^+ \longrightarrow 0^+$	3.69	8.14	11.57	14.50	14.94	14.03	15.62
$4^+ \longrightarrow 2^+$	3.18	9.48	14.54	18.60	19.20	17.73	20.53
$2_1^+ \longrightarrow 0_1^+$	7.99	11.43	19.25	32.72	40.00	39.87	45.14
$4_1^+ \longrightarrow 2_1^+$	6.83	12.55	24.26	42.32	53.52	54.11	58.70
$6^+ \longrightarrow 4_1^+$	7.81	16.83	30.52	45.32	55.39	56.30	59.45
$6^+ \longrightarrow 4^+$	0.75	3.70	10.57	17.07	17.55	16.67	20.62

* For the levels of the second band, $N = 1$.

Table 7. Coefficients $b(E\omega) \times 10^2$ in the expansion of the wave function $\psi(L)$ for the potential V_4 in the basis $B3$

L^π	0^+	2^+	4^+	0_1^+	2_1^+	4_1^+	6^+
				m			
0	56	–59	65	50	–51	55	0
1	–53	52	–9	–2	5	1	41
2	41	–40	38	–19	21	–25	–46
3	–30	29	–26	32	–34	35	42
4	20	20	18	–35	36	–35	–36
5	–14	13	–12	32	32	31	29
6	9	–9	8	–27	27	25	–22
7	–6	6	–5	22	–21	20	17
8	4	–4	3	–18	17	–16	–13
9	–3	3	–3	15	–14	13	10
10	3	–2	2	–14	12	–11	–8
11	–3	3	–2	13	–12	10	7
12	2	–2	2	–11	10	–8	–5
				m_1			
0	12	–13	13	4	–4	–4	–8
1	–10	10	–9	9	–9	10	13
2	10	–9	8	–15	15	–13	–14
3	–7	7	–6	19	–18	16	13
4	6	–5	5	–21	20	–16	–12
5	–3	3	–3	12	–11	9	6

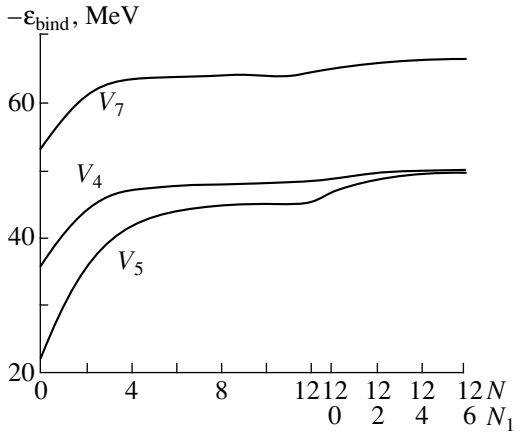

Binding energy ε_{bind} as a function of the number $N + 1 + N_1 + 1$ of the included basis functions.

mation. For example, the result for the binding energy is $\varepsilon_{bind} = 56.90$ MeV in the basis of the [4](4) and [6](6) functions for V_6 and $\varepsilon_{bind} = 56.56$ MeV in the basis of the [4](4), [6](6), $[42](42)_1$, and $[42](42)_2$ functions for V_7. In order to compute the energy levels in the second band, the quadrupole moments $Q(L)$, and the transition probabilities $B(E2, L \longrightarrow L-2)$, it is obviously necessary to supplement the basis with $E > E_{min} + 2$ functions. This is not unexpected because collective effects play an important role in the formation of rotational bands.

4.2. Multiquantum Approximations

An analysis of the results obtained in the $E_{min} + 2$ approximation reveals that the functions corresponding to the most symmetric diagrams E and the minimum value $\omega = (4)$ must be taken into account above all in the basis of $U(3(A-1))$ multiquantum excited states characterized by $E > E_{min} + 2$. To put it differently, it is necessary to include the $[4 + 2m](4)$ multiquantum excited states and, whenever possible, the $[4 + 2m2](4)$ and $[5 + 2m1](4)$ states with $m = 1, 2, \ldots$. Of the $\omega = E_{min} + 2$ [that is, $\omega = (6)$] functions, attention should be given only to the most symmetric $[6 + 2m](6)$ function.

The computations with the reduced Hamiltonian (without Coulomb interaction) in the basis $B2$ consisting of the $[4 + 2m](4)$ functions, $m = 0, 1, \ldots, 10$, were performed in [2], where it was indicated that the method used in these computations is equivalent to the $Sp(2, R)$ approximation [4] and to the method of generalized hyperspherical functions [5]. Here, we present some results of the computations with the full Hamiltonian (1) in the basis $B2$ and in the basis $B3$, which is obtained by supplementing the basis $B2$ with the $[6 + 2m](6)$ functions, $m = 1, 2, \ldots, 6$. The results are given in Tables 5–7 and in the figure.

For the potential V_4, Tables 5 and 6 illustrate the dependence of the energies ε of the levels, the root-mean-square radii $\langle r \rangle^{1/2}$, the quadrupole moments $Q(L)$, and the transition probabilities $B(E2, L \longrightarrow L-2)$ on the number $N + 1$ ($N + 1 + N_1 + 1$) of the functions taken into account in the basis $B2$ ($B3$). In just the same way as in the case of the $E_{min} + 2$ approximation, the results for the potentials V_1, V_2, and V_3 are close to the results for V_4, whereas the results for V_6 are similar to the results for V_7. The results for V_5 differ from the results for the other potentials to a greater extent. The analogous dependences for the binding energy ε_{bind} on N and N_1 are displayed in the figure for the potentials V_4, V_5, and V_7. The coefficients $b(m)$ in the expansions of the wave function $\psi(L)$ in the basis $B3$ are given in Table 7.

5. CONCLUSIONS

(i) From a comparison of the results presented here with those from [2], it follows that the inclusion of the Coulomb interaction has virtually no effect on the structure of the wave functions, the spacings between the energy levels, the values of the quadrupole moments, and the probabilities $B(E2)$.

(ii) For all the potentials used, the extension of the basis leads to the following changes in the energy spectrum: the 0^+, 2^+, and 4^+ and 0_1^+, 2_1^+, 4_1^+, and 6 bands expand and come close together (the spacing between the bands decreases). Owing to this, reasonably good agreement with experimental data can be obtained at some values of N. For example, the theoretical values of the spacings between the energy levels $\varepsilon(L)$ at $N = 5$ and 6 agree well with experimental data for both bands (see Table 5).

(iii) Over the first band, the values of Q and $B(E2)$ are independent of the number of basis functions for $N \geq 7$. This is not so for the second band, where almost all functions from the basis $B2$ must be taken into account.

(iv) The effect of the $[6 + 2m_1](6)$ functions, $m_1 = 0, 1, 2, \ldots$, from the basis $B3$ is substantial only for the binding energies (for the potential V_4, the inclusion of these functions increases the binding energy by 1.7 MeV) and the probabilities $B(E2)$ for the second band.

(v) From a comparison of the binding-energy values in the first and the second column of Table 2, it can be seen that the inclusion of the [6](4) state increases the binding energy ε_{bind} by 4.9 MeV. An extra increase of 9.0 MeV in the binding energy results from taking into account the multiquantum excited states $[4 + 2m](4)$, $m = 2, \ldots, 12$, and $[6 + 2m_1](6)$, $m_1 = 0, 1, 2, \ldots$. The inclusion of the [42](4) state (see the second and the third column in Table 2) additionally increases ε_{bind} by more than 3.2 MeV. It can therefore be expected that, in the case of the potentials V_1–V_4, the binding-energy values complying with experimental data would result from the use of the basis $B3$ supplemented with the $[4 + 2m2](4)$ functions, $m = 0, 1, 2, \ldots$.

Thus, we can hope that the basis $B3$ supplemented with the $[5 + 2m1](4)$ and $[4 + 2m2](4)$ functions, $m = 0, 1, 2, \ldots$, will prove to be sufficient for obtaining satisfactory theoretical values of the aforementioned quantities for the ${}^{8}_{4}\mathrm{Be}$ nucleus.

REFERENCES

1. V. V. Vanagas, *Algebraic Methods in the Theory of the Nucleus* (Mintis, Vilnius, 1970).
2. K. I. Yankauskas, V. A. Vasilyauskas, and A. K. Petrauskas, Yad. Fiz. **59**, 1757 (1996) [Phys. At. Nucl. **59**, 1698 (1996)].
3. A. K. Petrauskas, K. Ĭ. Yankauskas, and V. M. Bondarenko, Yad. Fiz. **55**, 3082 (1992) [Sov. J. Nucl. Phys. **55**, 1723 (1992)].
4. V. Svichulis, Candidate's Dissertation in Mathematics and Physics (Vilnius. Gos. Univ., Vilnius, 1992).
5. G. F. Filippov, V. I. Ovcharenko, and Yu. F. Smirnov, *Microscopic Theory of Collective Nuclear Excitations* (Naukova Dumka, Kiev, 1981).
6. K. Ĭ. Yankauskas and A. K. Petrauskas, *Density Matrix for U(3(n – 1)) Excited States of Nuclei and Its Applications* (Univ. of Klaipeda, Klaipeda, 1997).
7. A. Bohr and B. R. Mottelson, *Nuclear Structure*, Vol. 1: Single-Particle Motion (Benjamin, New York, 1975; Mir, Moscow, 1971).
8. A. V. Volkov, Nucl. Phys. **74**, 33 (1965).
9. A. I. Baz', Yu. T. Grin', V. F. Demin, and M. V. Zhukov, Fiz. Élem. Chastits At. Yadra **3**, 275 (1972) [Sov. J. Part. Nucl. **3**, 137 (1972)].
10. D. Gogny, P. Pires, and R. Tourreil, Phys. Lett. B **32**, 591 (1970).
11. M. Moshinsky, *The Harmonic Oscillator in Modern Physics: From Atoms to Quarks* (Gordon and Breach, New York, 1969; Mir, Moscow, 1972).
12. K. Ĭ. Yankauskas and A. K. Petrauskas, Litov. Fiz. Sb. **38**, 331 (1998).
13. L. R. B. Elton, *Nuclear Sizes* (Oxford Univ. Press, London, 1961; Inostrannaya Literatura, Moscow, 1962).
14. K. I. Yankauskas and A. K. Petrauskas, Yad. Fiz. **62**, 1535 (1999) [K. Yankauskas and A. Petrauskas, Phys. At. Nucl. **62**, 1449 (1999)].
15. F. Ajzenberg-Selove, Nucl. Phys. A **227**, 1 (1974).

Translated by R. Rogalyov

Physics of Atomic Nuclei, Vol. 64, No. 2, 2001, pp. 203–227. Translated from Yadernaya Fizika, Vol. 64, No. 2, 2001, pp. 247–272.

NUCLEI
Theory

Brueckner *G* Matrix for a Planar Slab of Nuclear Matter

M. Baldo[1)], U. Lombardo[1), 2)], É. E. Saperstein, and M. V. Zverev

Russian Research Centre Kurchatov Institute, pl. Kurchatova 1, Moscow, 123182 Russia

Received May 26, 2000

Abstract—The equation for the Brueckner *G* matrix is investigated for planar-slab geometry. A method for calculating the *G* matrix for a planar slab of nuclear matter is developed for a separable form of *NN* interaction. Actually, the separable version of the Paris *NN* potential is used. The singlet $^1S_0$ and the triplet $^3S_1$–$^3D_1$ channel are considered. The present analysis relies on the mixed momentum–coordinate representation, where use is made of the momentum representation in the slab plane and of the coordinate representation in the orthogonal direction. The full two-particle Hilbert space is broken down into the model subspace, where the two-particle propagator is considered exactly, and the complementary subspace, where the local-potential approximation is used, which was proposed previously for calculating the effective pairing potential. Specific calculations are performed for the case where the model subspace is constructed on the basis of negative-energy single-particle states. The *G* matrix is parametrically dependent on the total two-particle energy E and the total momentum $P_\perp$ in the slab plane. Since the *G* matrix is assumed to be further used to calculate the Landau–Migdal amplitude, the total two-particle energy is fixed at the value $E = 2\mu$, where μ is the chemical potential of the system under investigation. The calculations are performed predominantly for $P_\perp = 0$. The role of nonzero values of $P_\perp$ is assessed. The resulting *G* matrix is found to depend greatly on μ in the surface region. © *2001 MAIK "Nauka/Interperiodica".*

1. INTRODUCTION

The present article reports on a continuation of a series of studies devoted to extending Brueckner theory for infinite nuclear matter to nonuniform nuclear systems without invoking the local-density approximation. A method for numerically solving the Bethe–Goldstone equation in semi-infinite nuclear matter was developed in [1–3] for the problem of singlet ^1S pairing. For a separable representation of free nucleon–nucleon interaction, this equation could be solved without recourse to any form of local approximation. The pairing problem was formulated on the basis of the effective pairing interaction in the model subspace where the equation for the pairing gap Δ was obtained. The model subspace was taken there in a form that is conventional for nuclear physics and which includes all negative-energy single-particle states.

The effective pairing interaction $\mathcal{V}_{\text{eff}}$ satisfies an equation that is similar in form to the Bethe–Goldstone equation for the *G* matrix, which is a basic element of the Brueckner theory of nuclear matter. In the pairing problem, there is a simplifying circumstance associated with the fact that pairing in an infinite system occurs at zero total momentum of the two nucleons involved ($\mathbf{P} = 0$). Accordingly, the total orthogonal momentum $\mathbf{P}_\perp$ must vanish in a semi-infinite system. Specific calculations for $^1S_0$-channel pairing in semi-infinite nuclear matter placed in the one-dimensional Woods–Saxon potential well $V(x)$ were performed for the separable 3×3 version [4, 5] of the Paris potential [6]. This potential was tested in the calculations within Brueckner theory in infinite nuclear matter [7, 8].

In this case, the effective interaction $\mathcal{V}_{\text{eff}}$ is found by solving a set of one-dimensional integral equations for six independent components $\Lambda_{ij}(X, X')$, where X and X' are the c.m. coordinates of two nucleons prior to and after the interaction event. We note that the matrix Λ_{ij} $(i, j = 1, 3)$ is symmetric, so that only six coefficients are independent. The kernels of these equations represent the convolutions of the two-particle propagator B_{ij} with the form factors g_i and g_j for the nucleon–nucleon potential (for the sake of brevity, we will often refer to these convolutions as merely propagators). In [2, 3], we proposed, in addition to the precise method for calculating the propagators, quite an accurate approach, the local-potential approximation. This method consists in the following: at a fixed half-sum $X_0 = (X + X')/2$ of the c.m. coordinates of interacting nucleons, the exact expression for $B_{ij}(X_0, t)$ $(t = X - X')$ in the system under investigation is replaced by the approximate expression $B_{ij}^{\text{LPA}}(X_0, t)$ equal to the corresponding expression for infinite nuclear matter placed in the potential well $V_0 = V(X_0)$. Within nuclear matter, the local-potential approximation and the standard local-density approximation have nearly identical accuracies. In the surface region, however, where the local-density approximation is inapplicable, the local-potential approximation provides a satisfactory accuracy in calculating the effective pairing interaction [2, 3].

[1)] Istituto Nazionale di Fisica Nucleare, Sezione di Catania, 57 Corso Italia, I-95129 Catania, Italy.
[2)] Università di Catania, Dipartimento di Fisica, 57 Corso Italia, I-95129 Catania, Italy.

In order to calculate the Brueckner G matrix, we construct here a similar scheme where a precise calculation of the two-particle propagators will be combined with the local-potential approximation. In the Brueckner method, the G matrix specifies the Landau–Migdal amplitude

$$F(\mathbf{r}_1, \mathbf{r}_2, \mathbf{r}_3, \mathbf{r}_4) = \sqrt{Z(\mathbf{r}_1)Z(\mathbf{r}_2)Z(\mathbf{r}_3)Z(\mathbf{r}_4)}G(\mathbf{r}_1, \mathbf{r}_2, \mathbf{r}_3, \mathbf{r}_4; E = 2\mu), \quad (1)$$

where $Z(\mathbf{r})$ is the renormalization factor of the single-particle Green's function $\mathcal{G}$, E is the total energy of two nucleons, and μ is the chemical potential of the system. This amplitude, which is the basic ingredient of the theory of finite Fermi systems [9], plays the role of effective quasiparticle interaction in the theory.

Instead of semi-infinite nuclear matter, we consider a planar nuclear-matter slab placed in the one-dimensional Woods–Saxon potential well $V(x)$ symmetric with respect to the origin—that is, a system that is the closest to finite nuclei. As in semi-infinite systems, the momentum in the plane orthogonal to the x axis is then conserved. Hence, it is convenient to go over in relation (1) to the momentum representation in this plane. In relation to the pairing problem, there arises, however, a significant complication—now, there is no reason to assume that $\mathbf{P}_\perp = 0$. By using Eq. (1) within the nuclear-matter slab to calculate the harmonics of the Landau expansion of the amplitude F [9], we can easily see that the result does indeed involve an integral with respect to $P_\perp$ from zero to the doubled Fermi momentum, k_F. This renders relevant numerical calculations much more cumbersome.

In [10, 11], relation (1) was used to compute the surface values of the zeroth harmonics of the invariant Landau–Migdal amplitudes. Near the nuclear surface, the local values of the nucleon momenta are small; therefore, we can approximately set $P_\perp = 0$. Moreover, the G matrix goes over, at large distances from the nucleus, to the T matrix for free nucleon–nucleon scattering, the calculation of the latter being much simpler. It is this approximation that made it possible to reproduce faithfully in [10, 11] the empirical values of the surface amplitudes. In order to obtain a more detailed description of the coordinate dependence of the Landau–Migdal amplitudes over the entire surface region, it is necessary, however, to calculate the G matrix. With an eye to a subsequent application of the G matrix to precisely this problem, we also restrict here our consideration to small $P_\perp$ values, although the computational scheme remains valid in general for arbitrary $P_\perp$ values. We investigate two channels, the $^1S_0$ singlet channel and the $^3S_1$ triplet channel coupled to the $^3D_1$ one. In the triplet channel, we use the 4×4 PEST4 separable potential, which provides the best description of nucleon–nucleon scattering among all versions of the separable representation of the Paris potential that were discussed in [4].

The Bethe–Goldstone equation for the G matrix differs only slightly in form from the equation for the effective pairing interaction. In solving it, we can use the same prescription for introducing the model subspace and the effective interaction acting in it as in the pairing problem [2, 3]. The procedure is quite conventional: in the full two-particle Hilbert space $\mathcal{S}$, we single out the model subspace $\mathcal{S}_0$ where we calculate precisely the two-particle propagator and express the G matrix in terms of this propagator and the effective interaction. The effective interaction is determined by the Bethe–Goldstone equation in the complementary subspace $\mathcal{S}'$, where the local-potential approximation is used to calculate the two-particle propagator. The model subspace is taken here to be identical to that in the pairing problem; that is, it is constructed in terms of negative-energy single-particle states. For the $^1S_0$ channel at $P_\perp = 0$, the effective interaction for the problem under study therefore coincides with the effective pairing interaction. For the triplet channel, the computational scheme is somewhat more complicated. For example, ten equations arise here instead of a set of six equations for the multipole components of the G matrix. The calculation of the propagators B_{ij} seems more complicated as well, but, at a fixed value of $P_\perp$, the two computational schemes are very similar. As will be seen from the ensuing analysis, the proposed method can be applied, without significant changes, to channels of higher multipole order, for which there is a separable representation of the *NN* potential in [4].

The present article is organized as follows. In Section 2, the general Bethe–Goldstone equation for the G matrix in the $^1S_0$ singlet channel is reduced for planar-slab geometry to a form convenient for numerical calculations. In doing this, we use the separable representation [4] of the *NN* potential and the technique of the mixed coordinate–momentum representation [2, 3]. Owing to the mirror symmetry of the system under study, the equation for the G matrix breaks down into two equations—one for its even components and the other for the odd components, each being defined only at positive x values. It much more straightforward to obtain a numerical solution to the problem in this case than in the case of semi-infinite geometry, where there is no such symmetry. In Section 3, the same is done for the $^3S_1$–$^3D_1$ channel. In Sections 4–8, we comprehensively study a solution to the equation for the G matrix at zero value of the total orthogonal momentum $P_\perp$ of two nucleons. All calculations are performed for the case where the chemical potential of the system is set to the value of $\mu = -8$ MeV, which is typical of stable nuclei. For the two-particle propagators, various forms encountered in solving our problem are considered in Sections 4 and 5. In Sections 6–9, we investigate the G matrix. In Section 9, we analyze the chemical-potential dependence of the G matrix. In Section 10, we estimate the role of nonzero $P_\perp$ values. Section 11 is devoted to discussing basic results. For the Paris potential, Appendix 1 gives formulas for the coordinate representation

of the form factors of the separable representation used in this study. In Appendix 2, we give an account of the method for calculating the free *T* matrix for the triplet channel in the coordinate representation.

2. EQUATION FOR THE *G* MATRIX IN PLANAR-SLAB GEOMETRY: $^1S_0$ SINGLET CHANNEL

In considering nonuniform systems, it is better to proceed from the general equation for the Brueckner *G* matrix in the coordinate representation. It can be written as

$$G(\mathbf{r}_1, \mathbf{r}_2, \mathbf{r}_3, \mathbf{r}_4; E) = \mathcal{V}(\mathbf{r}_1, \mathbf{r}_2)\delta(\mathbf{r}_1 - \mathbf{r}_3)\delta(\mathbf{r}_2 - \mathbf{r}_4) + \int \mathcal{V}(\mathbf{r}_1, \mathbf{r}_2)A(\mathbf{r}_1, \mathbf{r}_2, \mathbf{r}_5, \mathbf{r}_6; E) \times G(\mathbf{r}_5, \mathbf{r}_6, \mathbf{r}_3, \mathbf{r}_4; E)d\mathbf{r}_5 d\mathbf{r}_6, \quad (2)$$

where $\mathcal{V}$ is the potential of nucleon–nucleon interaction and *A* is the two-particle propagator. Within Brueckner theory, this propagator is determined as an integral that involves the product of two single-particle Green's functions as the integrand and which takes into account only the contribution of particle poles ($\mathcal{G}^p$). We note that the so-called *T* matrix (an analog of the Brueckner *G* matrix in conventional many-body theory [12, 13]) is determined by an equation of the type in (2) with the propagator *A* that involves both the two-particle ($\mathcal{G}^p\mathcal{G}^p$) and the two-hole ($\mathcal{G}^h\mathcal{G}^h$) contribution. Thus, the expression for the two-particle propagator in Brueckner theory has the form

$$A(\mathbf{r}_1, \mathbf{r}_2, \mathbf{r}_3, \mathbf{r}_4; E) = \int \frac{d\varepsilon}{2\pi i}\mathcal{G}^p\left(\mathbf{r}_1, \mathbf{r}_2; \frac{E}{2} + \varepsilon\right)\mathcal{G}^p\left(\mathbf{r}_3, \mathbf{r}_4; \frac{E}{2} - \varepsilon\right). \quad (3)$$

In the representation of the single-particle eigenfunctions $\phi_\lambda(\mathbf{r})$ diagonalizing the single-particle Green's function, the propagator *A* is given by

$$A(\mathbf{r}_1, \mathbf{r}_2, \mathbf{r}_3, \mathbf{r}_4; E) = \sum_{\lambda\lambda'} A_{\lambda\lambda'}(E)\phi_\lambda(\mathbf{r}_1)\phi^*_\lambda(\mathbf{r}_3)\phi_{\lambda'}(\mathbf{r}_2)\phi^*_{\lambda'}(\mathbf{r}_4), \quad (4)$$

where

$$A_{\lambda\lambda'}(E) = \int \frac{d\varepsilon}{2\pi i}\mathcal{G}^p_\lambda\left(\frac{E}{2} + \varepsilon\right)\mathcal{G}^p_{\lambda'}\left(\frac{E}{2} - \varepsilon\right) = \frac{(1 - n_\lambda)(1 - n_{\lambda'})}{E - \varepsilon_\lambda - \varepsilon_{\lambda'}}. \quad (5)$$

Here, n_λ and $n_{\lambda'}$ are the single-particle occupation numbers, which are equal to unity (zero) for filled (unfilled) states, while ε_λ and $\varepsilon_{\lambda'}$ are the corresponding single-particle energies.

Equation (2), together with the propagator specified by Eqs. (3)–(5), differs from the analogous equation for the effective pairing interaction [2, 3] only by the form of the projection operator in the numerator on the right-hand side of (5).

In accordance with the above partition of the Hilbert space $\mathcal{S}$ into two parts, the sum in (4) over $\lambda\lambda'$ also breaks down into two terms,

$$A = A_0 + A', \quad (6)$$

where A_0 contains only states that belong to the model subspace $\mathcal{S}_0$, while A' involves all the remaining states.

The standard renormalization procedure leads to an equation for the *G* matrix in the model subspace,

$$G = \mathcal{V}_{\text{eff}} + \mathcal{V}_{\text{eff}}A_0G, \quad (7)$$

where the effective-interaction potential $\mathcal{V}_{\text{eff}}$ is determined by a similar equation in the complementary subspace $\mathcal{S}'$; that is,

$$\mathcal{V}_{\text{eff}} = \mathcal{V} + \mathcal{V}A'\mathcal{V}_{\text{eff}}. \quad (8)$$

We analyze a planar nuclear-matter slab of thickness $2L$ placed in the one-dimensional Woods–Saxon potential well $V(x)$ symmetric with respect to the point $x = 0$,

$$V(x) = \frac{V_0}{1 + \exp((x - L)/d) + \exp(-(x + L)/d)}. \quad (9)$$

For the depth and diffuseness potential parameters (V_0 and d, respectively) and for the slab half-width (L), we choose the values of $V_0 = 50$ MeV, $d = 0.65$ fm, and $L = 8$ fm, which are close to values characteristic of heavy nuclei. As in the case of semi-infinite nuclear matter, the system is nonuniform only in one direction (x axis); in the orthogonal plane [(yz) plane, also referred to as the **s** plane)], the momentum is conserved. In order to solve Eq. (2) [or Eqs. (7) and (8), which are equivalent to it], we can therefore use the technique of a mixed representation [1], where use is made of the coordinate representation in the x direction and of the momentum representation in the orthogonal plane, so that, in expansion (4), the eigenfunctions are represented as

$$\phi_\lambda(\mathbf{r}) = y_n(x)\exp(i\mathbf{k}_\perp \cdot \mathbf{s}), \quad (10)$$

where $y_n(x)$ are the eigensolutions to the one-dimensional Schrödinger equation with the potential (9). The eigenenergies corresponding to the functions in (10) are $\varepsilon_\lambda = \varepsilon_n + k^2_\perp/2m$. For the sake of simplicity, it is assumed here that the effective single-particle mass m^* is equal to the vacuum nucleon mass m. It is straightforward to extend the scheme to the general case of $m^* \neq m$. We note that the potential (9) is symmetric with respect to the point $x = 0$; therefore, the eigenstates y_n of the discrete spectrum have a specific parity—we denote by y^+_n and y^-_n the even and the odd eigenfunc-

tions, respectively. For the continuous spectrum, it is convenient to use definite-parity states as well, which are real, as can easily be seen.

In just the same way as in [2, 3], we will use a separable representation for a realistic nucleon–nucleon potential—specifically, a separable version [4, 5] of the Paris potential [6]. Its appropriateness for calculations within the Brueckner method was demonstrated in [7, 8] for infinite nuclear matter and in [2, 3] for semi-infinite nuclear matter.

Let us first consider the simpler case of the $^1S_0$ singlet channel, where the potential from [4, 5] has the separable 3×3 form,

$$\mathcal{V}(\mathbf{k}, \mathbf{k}') = \sum_{ij} \lambda_{ij} g_i(k^2) g_j(k'^2). \tag{11}$$

Here, $\mathbf{k}$ ($\mathbf{k}'$) is the relative momentum of the incoming (outgoing) nucleons. Following [2, 3], we change a normalization of the form factors in (11) in relation to that used in the original version from [4, 5] in such a way as to ensure fulfillment of the condition $g_i(0) = 1$. The explicit expressions for the renormalized form factors (11) are given in [2, 3].

In the mixed coordinate–momentum representation, the G matrix for the channel being considered can be sought in the form

$$G(k_\perp^2, k_\perp'^2, \mathbf{P}_\perp; x_1, x_2, x_3, x_4; E) = \sum_{ij} G_{ij}(X, X'; E, \mathbf{P}_\perp) g_i(k_\perp^2, x) g_j(k_\perp'^2, x'), \tag{12}$$

where $\mathbf{P}_\perp$ is the total momentum in the **s** plane; $\mathbf{k}_\perp$ ($\mathbf{k}'_\perp$) is the relative momentum prior to (after) the scattering event in the **s** plane; and we have introduced the following notation for coordinates in the x direction: $X = (x_1 + x_2)/2$, $x = x_1 - x_2$, $X' = (x_3 + x_4)/2$, and $x' = x_3 - x_4$. In the mixed representation, the form factors $g_i(k_\perp^2, x)$ are determined by the inverse Fourier transformation of the quantity $g_i(k_\perp^2 + k_x^2)$ with respect to the variable k_x:

$$g_i(k_\perp^2, x) = \int_{-\infty}^{\infty} g_i(k_\perp^2 + k_x^2) e^{-ik_x x} \frac{dk_x}{2\pi}. \tag{13}$$

Their explicit forms are presented in Appendix 1.

An expansion similar to that in (12) is valid for the effective interaction as well:

$$\mathcal{V}_{\text{eff}}(k_\perp^2, k_\perp'^2, \mathbf{P}_\perp; x_1, x_2, x_3, x_4; E) = \sum_{ij} \Lambda_{ij}(X, X'; E, \mathbf{P}_\perp) g_i(k_\perp^2, x) g_j(k_\perp'^2, x'). \tag{14}$$

By substituting the potential (11) and the G-matrix expansion (12) into the original Eq. (2), we find that the coefficients G_{ij} satisfy the set of integral equations

$$G_{ij}(X_{12}, X_{34}; E, \mathbf{P}_\perp) = \lambda_{ij}\delta(X_{12} - X_{34}) + \sum_{lm} \lambda_{il} \int dX_{56} B_{lm}(X_{12}, X_{56}; E, \mathbf{P}_\perp) \times G_{mj}(X_{56}, X_{34}; E, \mathbf{P}_\perp), \tag{15}$$

where the convolutions B_{lm} of the two-particle propagator and the form factors are given by

$$B_{lm}(X_{12}, X_{34}; E, \mathbf{P}_\perp) = \sum_{nn'} \int \frac{d\mathbf{k}_\perp}{(2\pi)^2} \frac{(1 - n_\lambda)(1 - n_{\lambda'})}{E - P_\perp^2/4m - \varepsilon_n - \varepsilon_{n'} - k_\perp^2/m} \times g^l_{nn'}(k_\perp^2, X_{12}) g^m_{n'n}(k_\perp^2, X_{34}). \tag{16}$$

Here, we have introduced the condensed notation $\lambda = (n, \mathbf{P}_\perp/2 + \mathbf{k}_\perp)$ and $\lambda' = (n', \mathbf{P}_\perp/2 - \mathbf{k}_\perp)$ and set

$$g^l_{n,n'}(k_\perp^2, X_{12}) = \int dx_{12} g_l(k_\perp^2, x_{12}) y_n(X_{12} + x_{12}/2) y_{n'}(X_{12} - x_{12}/2). \tag{17}$$

We note that symbolic summation over nn' in (16) includes both actual summation over the discrete spectrum and integration for the continuous spectrum with the standard substitution $\sum_n \longrightarrow \int dp/2\pi$. We also considered that the functions $y_n(x)$ are real-valued.

By performing similar transformations for the renormalized Eq. (7) and by using a more compact notation, we arrive at the set of equations

$$G_{ij}(X, X'; E, \mathbf{P}_\perp) = \Lambda_{ij}(X, X'; E, \mathbf{P}_\perp) + \sum_{lm} \int dX_1 dX_2 \Lambda_{il}(X, X_1; E, \mathbf{P}_\perp) \times B^0_{lm}(X_1, X_2; E, \mathbf{P}_\perp) G_{mj}(X_2, X'; E, \mathbf{P}_\perp), \tag{18}$$

where B^0_{lm} are two-particle propagators in the model subspace that are determined by the sums of the type in (16) with the constraint $(\lambda, \lambda') \in \mathcal{S}_0$.

Finally, Eq. (8) for the effective interaction can be recast into the form

$$\Lambda_{ij}(X, X'; E, \mathbf{P}_\perp) = \lambda_{ij}\delta(X - X') + \sum_{lm} \lambda_{il} \int dX_1 B'_{lm}(X, X_1; E, \mathbf{P}_\perp) \Lambda_{mj}(X_1, X'; E, \mathbf{P}_\perp), \tag{19}$$

where the two-particle propagators B'_{lm} in the complementary subspace are determined by the same sums (16), but with the constraint $(\lambda, \lambda') \in \mathcal{S}'$.

In the following, we will find, as a rule, the G matrix on the basis of the set of Eqs. (18) and (19). In doing this, we calculate the propagators B^0_{lm} precisely and use the local-potential approximation in evaluating the propagators B'_{lm}. The propagators in (16) and their analogs for the model and the complementary subspace involve, in relation to the corresponding propagators of the pairing problem [2, 3], one serious complication associated with the appearance of the dependence in the integrand on the angle ϕ between the momenta $\mathbf{P}_\perp$ and $\mathbf{k}_\perp$. It arises from the dependence of the occupations numbers n_λ and $n_{\lambda'}$ in the numerator of expression (16) on this angle. For example, the condition $n_\lambda = 0$ does indeed correspond to the inequality $\varepsilon_\lambda > \mu$; that is, $\varepsilon_n + (\mathbf{P}_\perp/2 + \mathbf{k}_\perp)^2/2m > \mu$, which explicitly depends on the angle ϕ.

As in the pairing problem, the integral in (16) with respect to momenta converges slowly because of the strong repulsive core in the nucleon–nucleon interaction. This problem is especially serious for the Paris potential. In just the same way as in [2, 3], this problem is solved by renormalizing Eq. (19) with the aid of the analogous equation describing the off-shell T matrix for free nucleon–nucleon scattering at $E = 2\mu$. In a symbolic form, the equation for the T matrix can be written as

$$T(E) = \mathcal{V} + \mathcal{V}A^{\mathrm{fr}}(E)T(E), \tag{20}$$

where $A^{\mathrm{fr}}(E)$ is the propagator for two free nucleons whose total energy is E.

By using the coordinate representation in the x direction and the momentum representation in the orthogonal plane, we expand the T matrix in a form similar to that in (12). Here, the expansion coefficients $T_{ij}(t; E, \mathbf{P}_\perp)$ depend only on the difference $t = X - X'$ and obey the equation

$$T_{ij}(t; E, \mathbf{P}_\perp) = \lambda_{ij}\delta(t) + \sum_{lm}\lambda_{il}\int dt' B^{\mathrm{fr}}_{lm}(t-t'; E, \mathbf{P}_\perp)T_{mj}(t'; E, \mathbf{P}_\perp). \tag{21}$$

The renormalized equation for the effective interaction can be written in the compact form

$$\Lambda_{ij} = T_{ij} + \sum_{lm} T_{il}(B'_{lm} - B^{\mathrm{fr}}_{lm})\Lambda_{mj}. \tag{22}$$

As in the case of $\mathbf{P}_\perp = 0$, the difference kernel of this equation possesses much better convergence properties than that in the original Eq. (19). The scheme for computing the free T matrix in the coordinate representation for $\mathbf{P}_\perp \neq 0$ is presented in Appendix 2.

All the above equations for the G matrix are valid for any system that is nonuniform only in one direction. For a planar slab, they can be simplified by using parity conservation under the inversion $x \longrightarrow -x$. As was noted above, the potential (9) does indeed conserve the parity, and the set of the corresponding eigenfunctions y_n can be broken down into the subset of even functions y_n^+ and the subset of odd functions y_n^-. Therefore, the two-particle propagator (4) can be represented as the sum

$$A = A^s + A^a \tag{23}$$

of the symmetric (even) and antisymmetric (odd) components. The symmetric propagator A^s stems from those terms in the sum in (4) where both states (λ, λ') have the same parity, while the antisymmetric propagator A^a arises from the states of inverse parity. Because the nucleon–nucleon potential $\mathcal{V}$ in Eq. (2) for the G matrix conserves the parity, the propagators of inverse parity are not coupled.

Let us isolate the Born term from the G matrix. The remainder is the correlation component of the G matrix; that is,

$$\delta G = G - \mathcal{V}. \tag{24}$$

The equation for δG can be derived from (2). The result has the form

$$\delta G = \mathcal{V}A\mathcal{V} + \mathcal{V}A\delta G. \tag{25}$$

It is obvious that the correlation part of the G matrix is the sum of a symmetric and an antisymmetric component,

$$\delta G = \delta G^s + \delta G^a. \tag{26}$$

The equations for these components are separated:

$$\delta G^s = \mathcal{V}A^s\mathcal{V} + \mathcal{V}A^s\delta G^s, \tag{27}$$

$$\delta G^a = \mathcal{V}A^a\mathcal{V} + \mathcal{V}A^a\delta G^a. \tag{28}$$

It can easily be verified that the convolutions in (16) involving the symmetric (antisymmetric) propagator A^s are the even (odd) functions of coordinates X and X'; that is,

$$B^s_{lm}(X, X') = B^s_{lm}(X, -X') = B^s_{lm}(-X, X'), \tag{29}$$

$$B^a_{lm}(X, X') = -B^a_{lm}(X, -X') = -B^a_{lm}(-X, X'). \tag{30}$$

On this basis, Eqs. (15)–(22), where integrations are performed over all values of the c.m. coordinates, can be reduced to those where integrals are taken only over positive values of X. For this purpose, we introduce the symmetrized components of the G matrix and of the interaction blocks associated with it (nucleon–nucleon potential, T matrix, and effective interaction):

$$G^{+,-}_{ij}(X, X') = G_{ij}(X, X') \pm G_{ij}(X, -X'), \tag{31}$$

$$\mathcal{V}^{+,-}_{ij}(X, X') = \lambda_{ij}(\delta(X - X') \pm \delta(X + X')), \tag{32}$$

$$T^{+,-}_{ij}(X, X') = T_{ij}(X - X') \pm T_{ij}(X + X'), \tag{33}$$

$$\Lambda_{ij}^{+,-}(X, X') = \Lambda_{ij}(X, X') \pm \Lambda_{ij}(X, -X'). \quad (34)$$

As can be seen, the correlation components $G^{+,-}$ are twice as large as the above quantities $\delta G^{s,a}$. In order to simplify the form of the final equations, this coefficient of 2 must be introduced in the definition of the propagators of specific parity. For example, the propagators in the model subspace become

$$B_{lm}^{0+,0-}(X, X') = 2B_{lm}^{0s,0a}(X, X'). \quad (35)$$

Let us explicitly present the symmetrized equations in the half-space of positive X values for the case of positive parity. For example, Eq. (18) for G^+ reduces to the form

$$G_{ij}^{+}(X, X'; E, \mathbf{P}_\perp) = \Lambda_{ij}^{+}(X, X'; E, \mathbf{P}_\perp) + \sum_{lm}\int_0^\infty dX_1 \int_0^\infty dX_2 \Lambda_{il}^{+}(X, X_1; E, \mathbf{P}_\perp) \times B_{lm}^{0+}(X_1, X_2; E, \mathbf{P}_\perp) G_{mj}^{+}(X_2, X'; E, \mathbf{P}_\perp). \quad (36)$$

The even component of the effective interaction is determined from the renormalized Eq. (22), which takes the form

$$\Lambda_{ij}^{+}(X, X'; E, \mathbf{P}_\perp) = T_{ij}^{+}(X, X'; E, \mathbf{P}_\perp) + \sum_{lm}\int_0^\infty dX_1 \int_0^\infty dX_2 T_{il}^{+}(X, X_1; E, \mathbf{P}_\perp)(B_{lm}^{'+}(X_1, X_2; E, \mathbf{P}_\perp) - B_{lm}^{\mathrm{fr}+}(X_1, X_2; E, \mathbf{P}_\perp))\Lambda_{mj}^{+}(X_2, X'; E, \mathbf{P}_\perp), \quad (37)$$

where the symmetrized propagators in the complementary subspace and in free space are determined by analogy with Eqs. (31)–(34) as

$$B_{lm}^{'+}(X, X') = B_{lm}'(X, X') + B_{lm}'(X, -X'), \quad (38)$$

$$B_{lm}^{\mathrm{fr}+}(X, X') = B_{lm}^{\mathrm{fr}}(|X - X'|) + B_{lm}^{\mathrm{fr}}(|X + X'|). \quad (39)$$

Finally, the symmetric part of the free T matrix can be found by solving the equation

$$T_{ij}^{+}(X, X'; E, \mathbf{P}_\perp) = \lambda_{ij}(\delta(X - X') + \delta(X + X')) + \sum_{lm}\lambda_{il}\int_0^\infty dX_1 B_{lm}^{\mathrm{fr}+}(X, X_1; E, \mathbf{P}_\perp) T_{mj}^{+}(X_1, X'; E, \mathbf{P}_\perp). \quad (40)$$

All of Eqs. (36)–(40) were formulated for $X \geq 0$; therefore, the second nonhomogeneous term in (40), which involves a delta function, does not vanish at the single point $X = 0$.

The equations for the case of negative parity are obtained from the equations for the case of positive parity by substituting a minus sign for a plus in the superscripts and by reversing sign between the two delta functions on the right-hand side of Eq. (40).

It is obvious that the even G^+ matrix acts on the two-particle states of positive parity (that is, on the basis states of the types $|+, +\rangle$ and $|-, -\rangle$) and that the odd G^- matrix acts on the negative-parity states ($|+, -\rangle$, $|-, +\rangle$). We recall that it is the total G matrix

$$G = \frac{1}{2}(G^+ + G^-) \quad (41)$$

that appears in expression (1) for the Landau–Migdal amplitude.

3. EQUATION FOR THE G MATRIX IN THE $^3S_1$–$^3D_1$ TRIPLET CHANNEL

Let us now go over to the $^3S_1$ triplet scattering channel coupled to the $^3D_1$ channel. In this case, the separable expansion (11) is generalized as [4, 5]

$$\mathcal{V}_{S=1}(\mathbf{k}, \mathbf{k}') = \sum_{ij}\lambda_{ij}\hat{g}_i(k^2)\hat{g}_j^{+}(k'^2), \quad (42)$$

where the column $\hat{g}_i$ has two components,

$$\hat{g}_i(k^2) = \begin{pmatrix} g_i^{L=0}(k^2) \\ g_i^{L=2}(k^2) \end{pmatrix}. \quad (43)$$

It was shown in [5] that, in the multipole representation of the Paris potential, the best description of nucleon–nucleon scattering in the channel being considered is achieved in the 4×4 version (PEST4 potential). As in [10, 11], we will use precisely this potential in the calculations. The normalization of the form factors is naturally similar to that in the singlet channel, but renormalization of the two components ($L = 0$ and $L = 2$) is performed simultaneously since the same coefficients λ_{ij} appear in expansion (42) for these components. In the limit $k \longrightarrow 0$, we have $g_i^{L=0}(k^2 = 0) = 1$ and $g_i^{L=2}(k^2 = 0) = 0$. The renormalized expressions for the form factors (43) are presented in Appendix 1.

It can easily be shown that the general Eq. (12) and Eqs. (18) and (19) following from it are valid for the triplet channel as well. The main formal modification is that in the definition of the convolutions in (16), which now become

$$B_{lm}^{S=1}(X_{12}, X_{34}; E, \mathbf{P}_\perp) = \sum_{nn'}\int \frac{d\mathbf{k}_\perp}{(2\pi)^2} \frac{(1 - n_\lambda)(1 - n_{\lambda'})}{E - P_\perp^2/4m - \varepsilon_n - \varepsilon_{n'} - k_\perp^2/m} \times (g_{nn'}^{(0)l}(k_\perp^2, X_{12}) g_{n'n}^{(0)m}(k_\perp^2, X_{34}) + g_{nn'}^{(2)l}(k_\perp^2, X_{12}) g_{n'n}^{(2)m}(k_\perp^2, X_{34})). \quad (44)$$

It should be borne in mind that, in the case of the triplet channel, all multipole expansions like those in (12) and (14) are 2×2 matrices. For the sake of clarity,

we indicate that the explicit form of the components of the relevant matrix for G is

$$G^{LL'}(k_\perp^2, k_\perp'^2, \mathbf{P}_\perp; x_1, x_2, x_3, x_4; E) = \sum_{ij} G_{ij}(X, X'; \mathbf{P}_\perp, E) g_i^{(L)}(k_\perp^2, x) g_j^{(L')}(k_\perp'^2, x'), \quad (45)$$

where L and L' are equal to 0 or 2. We note that, although the form factors $g_i^{(2)}(k^2)$ vanish at $k = 0$, they are commensurate with the form factors $g_i^{(0)}(k^2)$ at $k = k_F$ ($k_F \sim 1.4$ fm^{-1} is the Fermi momentum) (see Fig. 1). It is obvious that all of Eqs. (36)–(40) for the symmetrized G matrix are valid for the triplet channel.

4. TWO-PARTICLE PROPAGATORS B'_{lm} IN COMPLEMENTARY SUBSPACE AT $P_\perp = 0$

In solving Eq. (15) for the G matrix or Eqs. (18) and (19) following from it, the calculation of the propagators in (16) or their analogs for the model and the complementary subspace is a point that presents the most serious mathematical difficulties. Here, we investigate Eq. (19) for the effective interaction in the simplest case of $P_\perp = 0$. In calculating the propagators B'_{lm} in the complementary subspace, it is reasonable to use expression (16) where summation over λ and λ' is restricted to states belonging to this subspace $\mathcal{S}'$. As was noted above, we will use the same model subspace $\mathcal{S}_0$ as in [2, 3], which includes all negative-energy states ($\varepsilon_\lambda, \varepsilon_{\lambda'} < 0$). The complementary subspace $\mathcal{S}'$ then contains not only positive-energy λ and λ' states but also pairs of states such that one of the energies is positive, while the other is negative. It can easily be shown that, at $P_\perp = 0$, the above singlet-channel propagators coincide with the analogous propagators that arise in calculating the effective pairing interaction and which were comprehensively investigated in [2, 3]. Therefore, we restrict our analysis here to the triplet channel.

Instead of a direct calculation of the integrals in (44) [this is the analog of expression (16) in the triplet channel] for a planar slab, we will use the local-potential approximation for this purpose. As was noted in the Introduction, this approximation was tested in [2, 3] for the singlet channel. Here, we admit that it is valid for the triplet channel as well. The accuracy of the local-potential approximation for the triplet channel will be estimated below. It is the formulation of the computational procedure that is now of importance for us because, as follows from the qualitative analysis from [2, 3], the accuracy of the local-potential approximation can be improved by supplementing the model subspace of negative-energy states with some positive-energy states. Within the local-potential approximation, the computational procedure for the triplet channel is generally similar to that for the singlet channel. At a fixed value of the chemical potential μ, it is necessary to calculate first the basis array of the propagators $B_{lm}^{\text{inf}}([V_n], t; E = 2\mu)$ for infinite nuclear matter placed in the potential V_n for a given set of V_n values. In fact, the potential-well depth was varied from zero to 58 MeV with a step of $\delta V = 2$ MeV; that is, we employed the values of $V_n = \delta V \times (n - 1)$, $n = 1, \ldots, 30$. Obviously, the propagators depend only on the difference $t = |X - X'|$ of the coordinates. They were calculated on a fixed mesh specified by $t_k = h(k - 1)$. The free propagators $B_{lm}^{\text{fr}}(t)$ automatically coincide with propagators $B_{lm}^{\text{inf}}([V_{n=1}], t; E = 2\mu)$. Further, we fixed the mesh of the values X_k with a step h in the interval $(0, L + a)$. The parameter a must be taken to be sufficiently large in order to suppress boundary effects (in the present calculations, we set $a = 10$ fm). On this mesh, we constructed the matrix $B_{lm}^{\text{LPA}}(X_i, X_k)$ for the planar slab

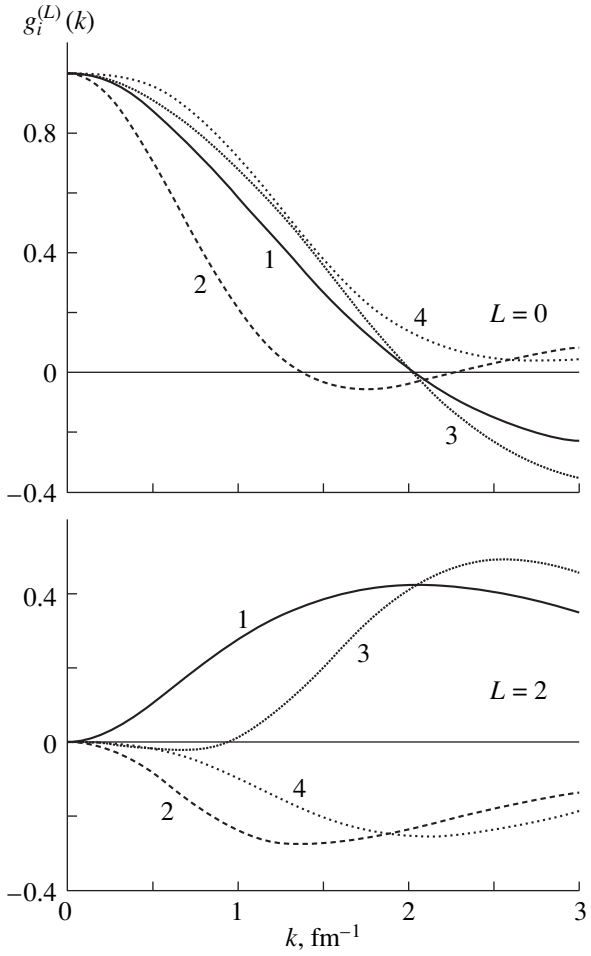

Fig. 1. Form factors $g_i^{(L)}(k)$. Figures on the curves indicate the values of the subscript i.

Table 1. Renormalized constants λ_{ij} (MeV fm^3) and strengths of some terms in the separable form of the Paris nucleon–nucleon potential [5] (3×3 representation for the $^1S_0$ channel and 4×4 representation for the $^3S_1$–$^3D_1$ channel)

i \ j	1	2	3	4
		$S = 0$		
1	-3.65919×10^3	2.16929×10^3	-2.36114×10^1	
2	2.16929×10^3	-1.48465×10^3	5.76074×10^1	
3	-2.36114×10^1	5.76074×10^1	1.71791×10^1	
		$S = 1$		
1	-1.61771×10^3	-1.29611×10^3	8.92091×10^2	4.27077×10^1
2	-1.29611×10^3	7.84747×10^2	1.39388×10^3	-7.86034×10^2
3	8.92091×10^2	1.39388×10^3	-7.45037×10^2	-5.72277×10^2
4	4.27077×10^1	-7.86034×10^2	-5.72277×10^2	1.86482×10^3

under investigation. For this, the potential-well depth $V(X_0 = (X_i + X_k)/2)$ was calculated from (9) at fixed values of X_i and X_k, and the required propagator in the local-potential approximation was found for each $t = |X_i - X_k|$ by means of a linear interpolation between the two adjacent values $B^{\text{inf}}_{lm}([V_n], t; E)$ and $B^{\text{inf}}_{lm}([V_{n+1}], t; E)$ that were chosen in such a way as to ensure fulfillment of the condition $V_n < V(X_0) < V_{n+1}$.

As was noted above, the form factors $g_i(k)$ in the separable expansions (11) and (42) are normalized in such a way that the conditions $g_i(k) \longrightarrow 1$ are satisfied for $k \longrightarrow 0$. This definition of form factors is more convenient than the normalization for the free case [4, 5] since, when we use a normalization to unity, the constants λ_{ij} appearing in the above expansions and having the meaning of the intensity of the corresponding components of the nucleon–nucleon potential carry direct information about the strength of these terms. For both channels, the values of the constants λ_{ij} are quoted in Table 1. As can be seen, the resulting patterns are different in the different channels. The singlet channel ($S = 0$) is dominated by the $ij = 11$, 12, and 22 components, the intensities of all terms carrying the index of 3 being two orders of magnitude smaller. Of course, their contribution cannot be disregarded in calculating the effective interaction $\mathcal{V}_{\text{eff}}$ since, at very high momenta (up to $k = 60$ fm^{-1}), which are present in the integrals for B'_{lm}, the form factor $g_3(k)$, which increases with k, considerably exceeds the form factors $g_1(k)$ and $g_2(k)$, which decrease with increasing k. As a result, the contributions of the large and small components become commensurate for $k \geq 10$ fm^{-1}. At momenta $k \sim k_{\text{F}}$, however, which are important for the calculation of the Landau–Migdal amplitude, the small components of the singlet potential can be disregarded, at least in a qualitative analysis. On the contrary, no terms in the triplet channel ($S = 1$) have intensities that stand out in magnitude; therefore, we must analyze all components. By way of example, we present the results of the calculations for three typical components of the propagator B_{lm}, $lm = 11$, 33, and 23. The behavior of the remaining terms generally reproduces the behavior in one of these three cases. The calculations in this section, as well as the majority of other similar calculations, were performed at the chemical-potential value of $\mu = -8$ MeV peculiar to the beta-stable nuclei.

Figure 2 shows the propagator in a medium, $B^{\text{inf}}_{lm}([V_0], t)$, and the free propagator $B^{\text{fr}}_{lm}(t)$, which coincide with the basis propagators $B^{\text{inf}}_{lm}([V_n], t; E = 2\mu)$ at $n = 26$ and $n = 1$, respectively. As can be seen, the diagonal components have a sharp maximum at $t = 0$ and decrease very fast with increasing t. The t dependence of the off-diagonal component B_{23} is somewhat weaker. In addition, we can see that, at small t values, the propagator in a medium and the free propagator nearly coincide. This circumstance explains why it is reasonable to perform a renormalization of Eq. (19) in terms of the free T matrix (20). Indeed, the kernel of the renormalized Eq. (22) is a much smoother function of the coordinates than the kernel of Eq. (19). In this respect, the situation is qualitatively similar to that in the singlet channel.

We now proceed to analyze the propagators $B^{\text{LPA}}_{lm}(X_1, X_2)$. It was noted above that, in planar-slab geometry, it is more convenient to employ the symmetric propagators $B^{s}_{lm}(X_1, X_2)$ and their antisymmetric counterparts $B^{a}_{lm}(X_1, X_2)$. The properties of the propagators can be analyzed in terms of the variables X_0 and t, which were introduced above; however, it is more straightforward to use the asymmetric coordinates $X = X_1$ and $t = X_2 - X_1$. That the propagators $B^{\text{inf}}_{lm}(X, t)$ decrease fast with increasing t results in that the sym-

metric and antisymmetric propagators $B_{lm}^{\mathrm{LPA}(s,a)}(X, t)$ virtually coincide everywhere, with the exception of the region of extremely small values of X. This can be seen from Fig. 3 by comparing the profile functions $B_{lm}^{\mathrm{LPA}(s,a)}(X)$ and $B_{lm}^{\mathrm{LPA}(s,a)}(X')$ at $X' = 2$ fm for $X <$ 1.5 fm. Even at such small values of X and X', the distinction between two functions is very small. At large X' values, the profiles of the symmetric and antisymmetric propagators in the local-potential approximation are graphically indistinguishable. Below, in this section, we therefore analyze only the symmetric propagators. The profile functions for the propagators $B_{lm}^{\mathrm{LPA}(s)}(X, X')$ in the local-potential approximation are compared in Fig. 4 with those for the free propagators $B_{lm}^{\mathrm{fr}(s)}(X, X' = X + t)$. As might have been expected, the distinction between the propagators in the local-potential approximation and the free propagators is insignificant within the slab ($X' = 2$ fm). On the slab surface ($X' = 8$ fm), this distinction is still smaller, on the whole, but there arises here a specific boundary effect—the propagators in the local-potential approximation are somewhat asymmetric with respect to the point $t = 0$, while the free propagators are symmetric by definition.

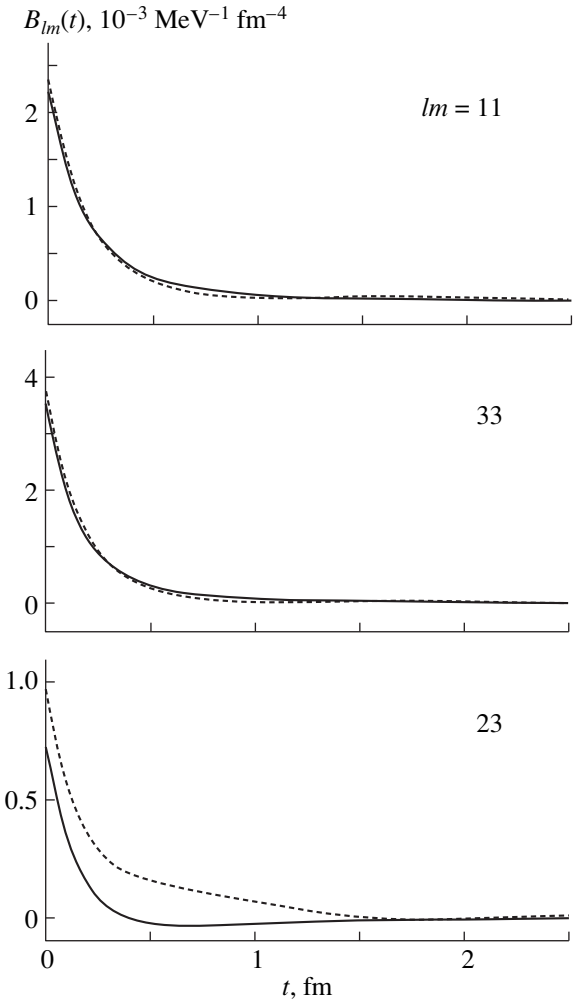

Fig. 2. Components of (solid curves) the propagator in a medium, B_{lm}^{inf} [$V = 50$ MeV], and (dashed curves) the free propagator, B_{lm}^{fr}, for $S = 1$ as functions of the relative coordinate $t = X - X'$ at $\mu = -8$ MeV. The sign of the $lm = 11$, 33 components was reversed.

As in the case of the singlet channel [2, 3], it is convenient to characterize the properties of the two-particle propagators on average by the zeroth moments. By way of example, we indicate that, for the triplet channel, these zeroth moments of the symmetric propagators in the local-potential approximation are defined as

$$\bar{B}_{lm}^{\mathrm{LPA}(s),\,S=1}(X) = \int dt B_{lm}^{\mathrm{LPA}(s),\,S=1}(X, t). \qquad (46)$$

We note that, for functions that decrease fast with increasing t, like the propagators in the local-potential approximation, the definition in (46) and the analogous expression for the zeroth moment in terms of the variables X_0 and t lead to nearly coincident results. Only in a narrow region at the slab surface do there arise distinctions at a level of a few percent.

For the lm values chosen above, the zeroth moments of the propagators in the local-potential approximation are depicted in Fig. 5. As might have been expected, they are virtually independent of X within the slab and change somewhat in the surface region. At large X, $\bar{B}_{lm}^{\mathrm{LPA}}(X)$ asymptotically approach the zeroth moments of the corresponding components of the free propagator,

$$\bar{B}_{lm}^{\mathrm{fr}(s),\,S=1} = \int dt B_{lm}^{\mathrm{fr}(s),\,S=1}(t), \qquad (47)$$

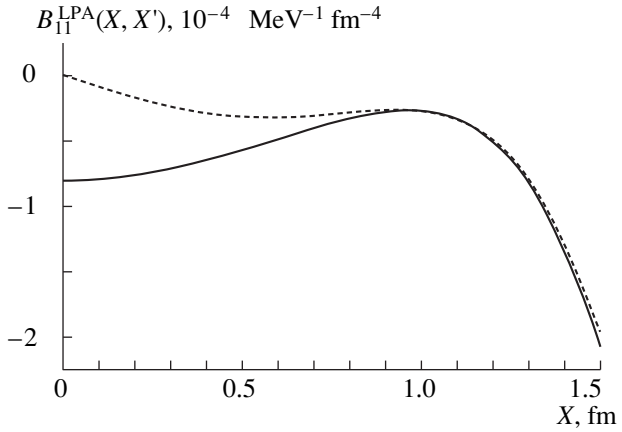

Fig. 3. Profile functions (solid curve) $B_{11}^{\mathrm{LPA}(s)}(X, X')$ and (dashed curve) $B_{11}^{\mathrm{LPA}(a)}(X, X')$ for the propagator in the local-potential approximation for $S = 1$ at $X' = 2$ fm and small X values.

which are of course independent of X. It can be seen that, for the $lm = 11$ and 33 components, the zeroth moments of the propagator in the local-potential approximation within the slab and those of the free propagator nearly coincide; for the $lm = 23$ component, the distinction between these zeroth moments is sizable.

5. TWO-PARTICLE PROPAGATORS B^0_{lm} AT $P_\perp = 0$ IN THE MODEL SUBSPACE

It will be seen below that, at fixed lm values, the symmetric and the antisymmetric propagators in the model subspace differ markedly. This is a typically quantum effect associated with the different structures of single-particle states appearing in the opposite-parity propagators and occurring near the Fermi surface. It is the contribution of precisely these states that stands out owing to the small denominator on the right-hand side of (16). Such a large effect can partly be an artifact of a not very appropriate choice of the model subspace that comprises a very narrow (in the momentum representation) layer of states whose energies lie between $\mu = -8$ MeV and $\mu = 0$. In order to investigate qualitatively the effect that can arise from the extension of the model subspace, we have performed a series of calculations with a few μ values equal to –8, –16, and –24 MeV.

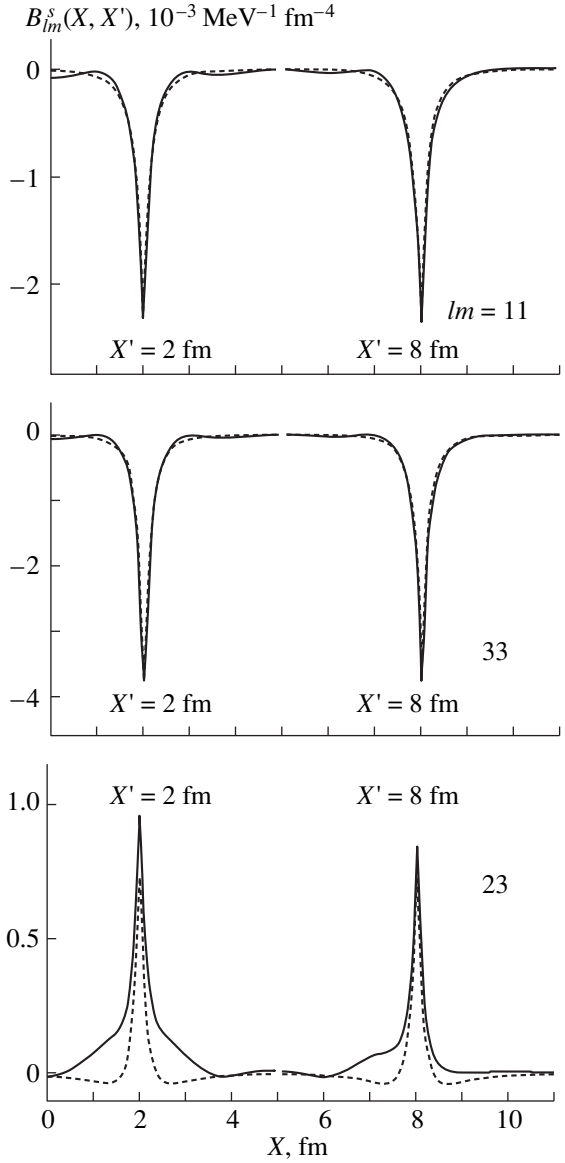

Fig. 4. Profile functions for (solid curve) the propagators $B^{\mathrm{LPA}(s)}_{lm}(X, X')$ in the local-potential approximation and (dashed curve) the free propagators $B^{\mathrm{fr}(s)}_{lm}(X, X')$ for $S = 1$ at $X' = 2$ fm and $X' = 8$ fm.

Let us first consider the $S = 0$ singlet channel. For the example of $lm = 11$, the profile functions of the symmetric and antisymmetric propagators $B^{0s,\,0a}_{11}(X, X' = X_0)$ in the model subspace are compared within the slab ($X_0 = 2$ fm) in Fig. 6 and at the slab surface ($X_0 = 8$ fm) in Fig. 7. As can be seen, the two types of propagators in the model subspace differ markedly both within the slab and on its surface. As the model space is extended, the absolute values of either type of propagator increases, while the relative distinction between B^{0s}_{11} and B^{0a}_{11} decreases. This is so for other lm values as well.

Similar conclusions can be drawn by comparing, at various values of μ, the zeroth moments of the propagators in the model subspace that are calculated by formula (46) with the substitution of the propagators $B^{0s,\,S=0}_{lm}$ and $B^{0a,\,S=0}_{lm}$ for $B^{\mathrm{LPA}(s),\,S=1}_{lm}$. It is the point where a significant distinction between the propagators in the local-potential approximation and the propagators in the model subspace manifest themselves. The former are fast decreasing functions of the variable t, so

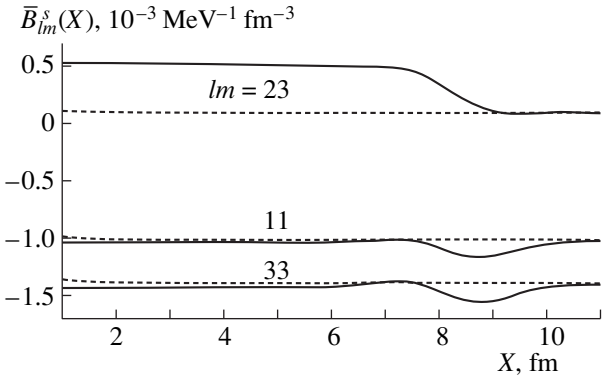

Fig. 5. Zeroth moments of the components of (solid curve) the propagators in the local potential approximation, $\bar{B}^{\mathrm{LPA}(s)}_{lm}(X)$, and (dashed curve) the free propagators, $\bar{B}^{\mathrm{fr}(s)}_{lm}(X)$, for $S = 1$.

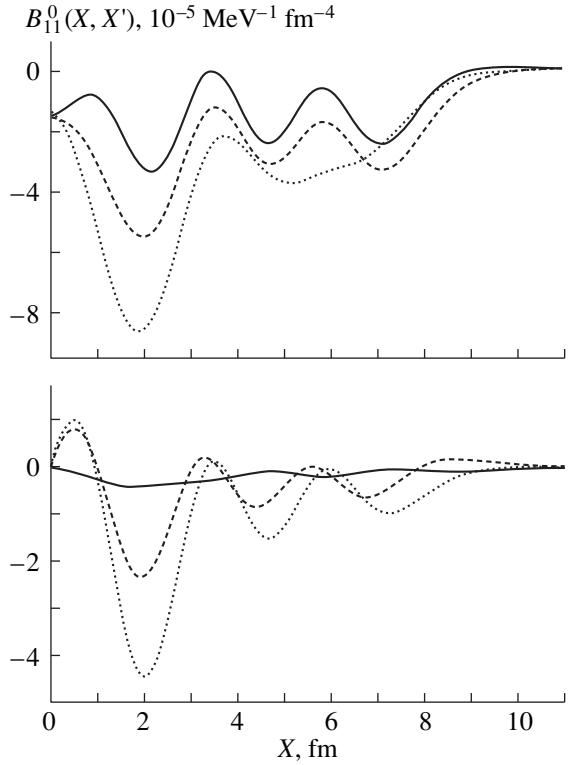

Fig. 6. Profile functions for (upper panel) the symmetric and (lower panel) the antisymmetric propagators $B^0_{11}(X, X')$ in the singlet channel at $X' = 2$ fm for the chemical-potential values of μ = (solid curve) –8, (dashed curve) –16, and (dotted curve) –24 MeV.

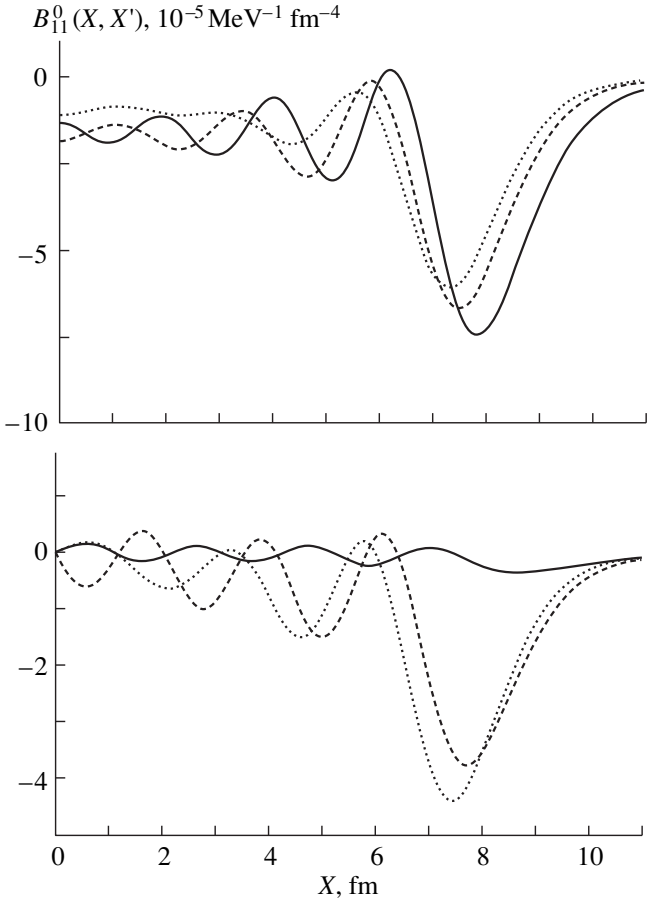

Fig. 7. As in Fig. 6, but for $X' = 8$ fm.

that, if a cutoff $|t| < t_c$ is introduced in the integral in (46), the result proves to be virtually independent of t_c for $t_c \geq 3$ fm. On the contrary, the propagators B^0_{lm} involve large long-range components, with the result that, as a rule, analogous integrals strongly depend on t_c. In our opinion, it is more informative to consider, instead of the integral between infinite limits in (46), the zeroth moment cut off as

$$\langle B_{lm}\rangle^{0s,\,0a}_{S=0}(X) = \int_{-t_c}^{t_c} dt B^{(0s,\,0a),\,S=0}_{lm}(X, X-t). \quad (48)$$

On average, the integral in (48) better reproduces the behavior of the propagator under study in the vicinity of a given point X, since it does not include the contribution that comes from far tails and which carries no significant information. For the large components at $S = 0$, the zeroth moments calculated according to (48) are displayed in Fig. 8.

The results of a similar analysis for the $lm = 11$ component of the two-particle propagator in the triplet channel are shown in Figs. 9 and 10. For the same $lm = 11$, 23, 33 components as in the preceding section, which were chosen here by way of example, the cutoff zeroth moments are displayed in Fig. 11. Here, the distinction between the symmetric and the antisymmetric propagators is still more pronounced; as to the effect originating from the extension of the model subspace, it is more spectacular: the relative distinction decreases with increasing μ. The latter can be considered as direct evidence that the accuracy of the local-potential approximation is improved when the model subspace is extended. This is because the extended subspace includes states that are far from the Fermi surface and which can therefore be taken accurately into account in the local-potential approximation. However, we have seen above that, in the local-potential approximation, the symmetric and the antisymmetric propagators nearly coincide; for this reason, the inclusion of the corresponding contribution in the propagators of opposite symmetries reduces the relative difference between them.

6. ANALYSIS OF THE *G* MATRIX IN THE SINGLET AND IN THE TRIPLET CHANNEL AT $P_\perp = 0$

From an analysis of Eq. (15), we can deduce that its solution $G_{ij}(X, X')$ involves a singular term, a delta

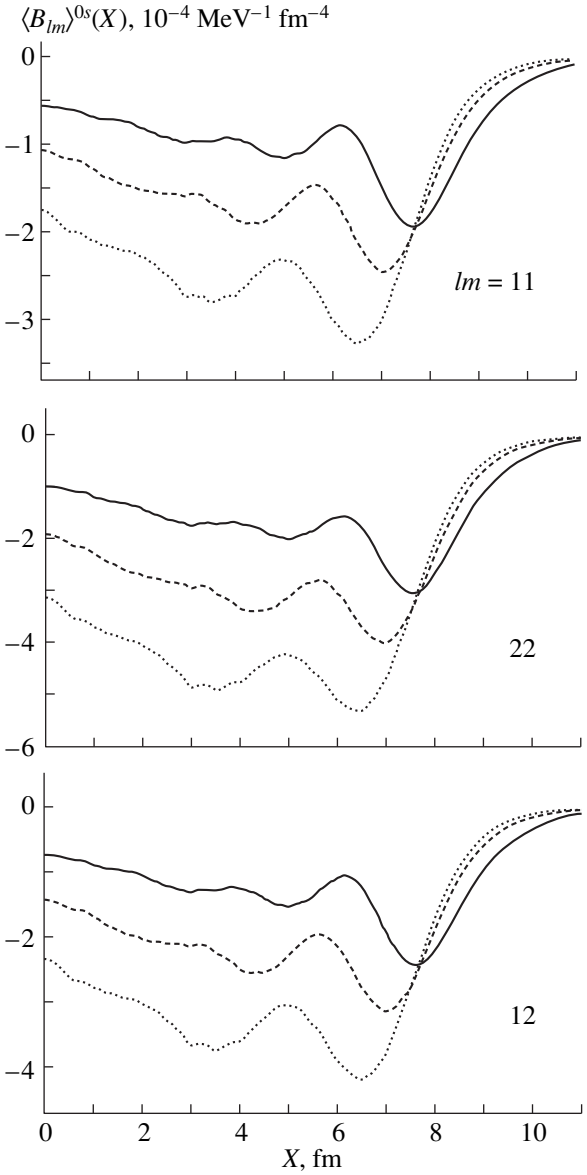

Fig. 8. Cutoff zeroth moments $\langle B_{lm}\rangle^{0s}(X)$ of the components of the propagator in the singlet channel for the chemical-potential values of μ = (solid curve) –8, (dashed curve) –16, and (dotted curve) –24 MeV.

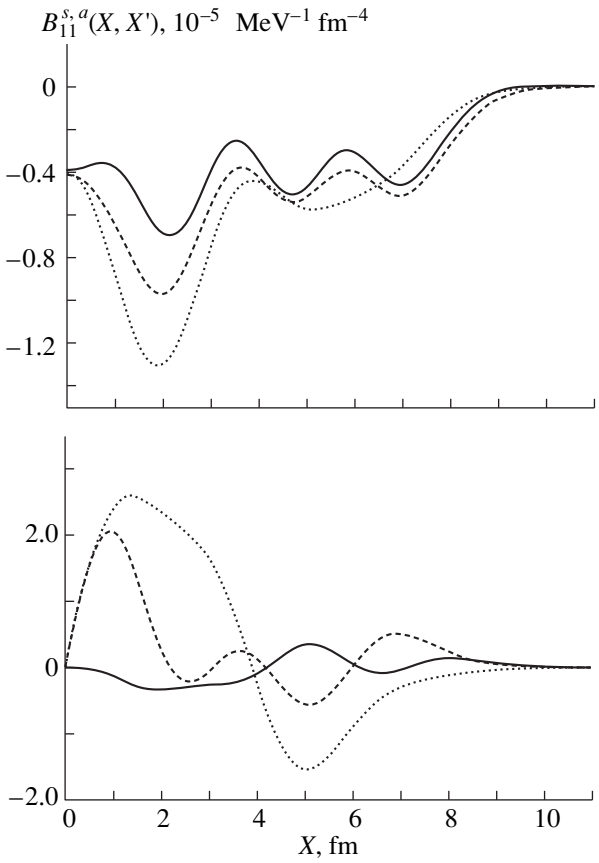

Fig. 9. As in Fig. 6, but for the $S = 1$ triplet channel.

function with the coefficient λ_{ij} equal to that in the nonhomogeneous term on the right-hand side. The correlation part of the G matrix as determined in (24) does not involve singularities; therefore, it is more convenient for a graphic presentation of the results. For this reason, we now proceed to analyze the correlation components of the G matrix,

$$\delta G_{ij}^{+,-}(X, X') = G_{ij}^{+,-}(X, X') - \lambda_{ij}(\delta(X - X') \pm \delta(X + X')) \quad (49)$$

and of the effective interaction,

$$\delta \Lambda_{ij}^{+,-}(X, X') = \Lambda_{ij}^{+,-}(X, X') - \lambda_{ij}(\delta(X - X') \pm \delta(X + X')). \quad (50)$$

Since we consider the G matrix at zero value of $P_\perp$ and a fixed energy $E = 2\mu$, these variables are suppressed in the arguments of G_{ij} and Λ_{ij}.

The definitions in (49) and (50) are valid both for the singlet and for the triplet channel. We begin by analyzing the singlet channel. Figure 12 displays the profile functions $\delta G_{ij}(X, X' = X_0)$ and $\delta \Lambda_{ij}(X, X' = X_0)$ of the correlation parts of the G matrix and of the effective interaction for one of the dominant components, $ij = 11$, in this channel. As usual, the cases of positive and negative parity are investigated separately. In just the same way as in the analysis of the propagators above, we chose the values of $X_0 = 2$ fm (within the slab) and $X_0 = 8$ fm (at the slab surface); for the reasons of space, two curves corresponding to the profile functions for the two X_0 values are placed near each other. In order that the two curves not overlap, they were cut off at $|X - X'| < 4$ fm. It can be seen that, even upon isolating the delta-function Born terms, the G matrix and the effective interaction remain very sharp (deltalike) functions of the difference of the coordinates, and these functions are very similar to each other. The same is true for others ij values. Further, we analyze this question quantitatively.

Let us now address the case of the triplet channel (Fig. 13). We again restrict our consideration to the sin-

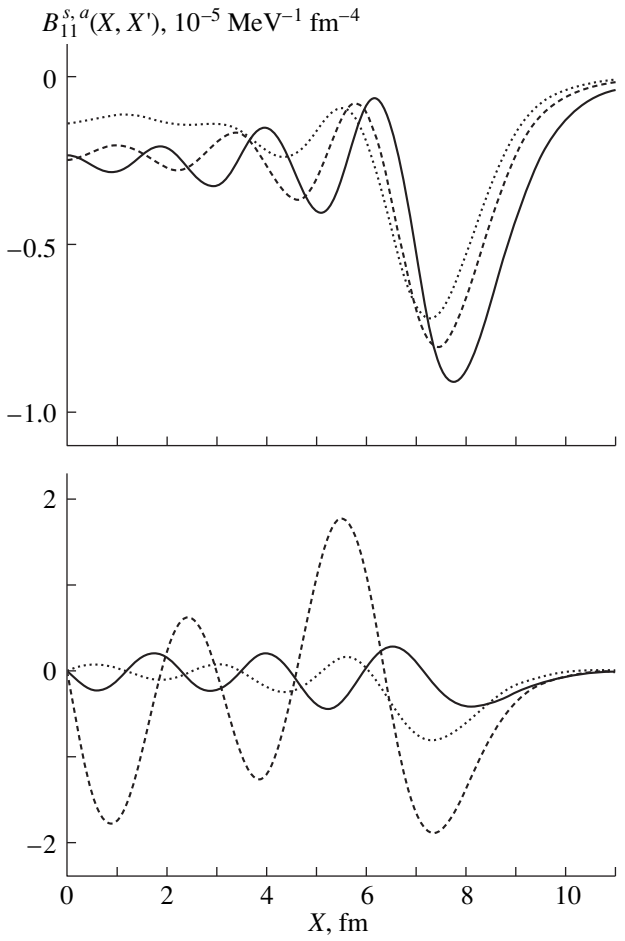

Fig. 10. As in Fig. 6, but for the $S = 1$ triplet channel and $X' = 8$ fm.

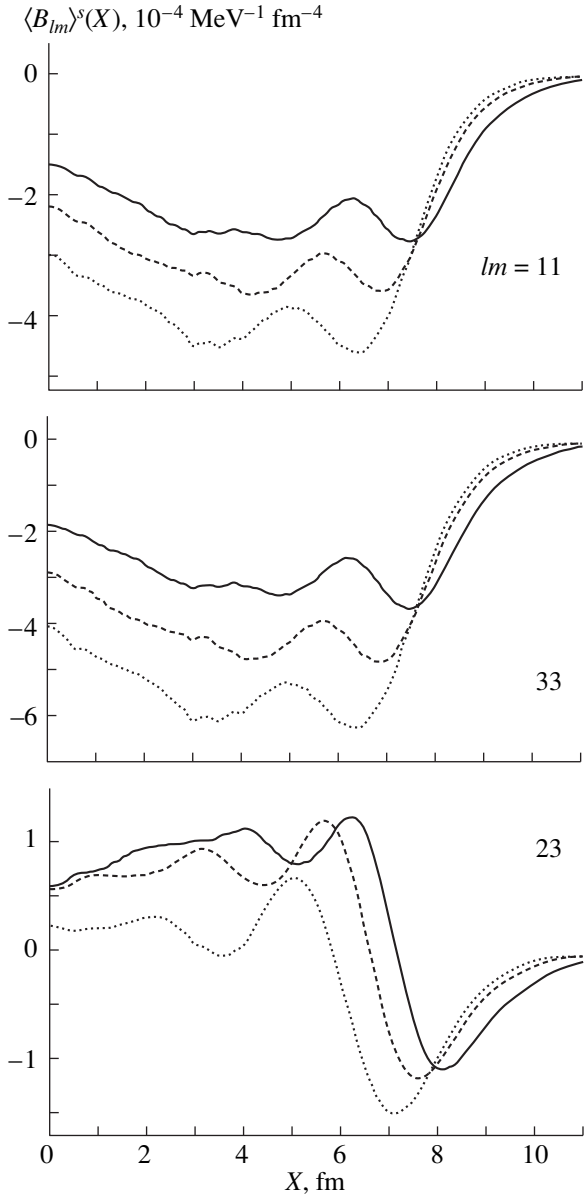

Fig. 11. As in Fig. 8, but for the $S = 1$ triplet channel.

gle component $ij = 11$. A comparison with the singlet channel shows that, although the general patterns are similar in the two cases, there are sizable distinctions. Apart from a distinct local maximum at $X = X'$, the G matrix has a pronounced long-range tail. The tail of the effective interaction is much smaller, but it also exceeds the long-range terms in the singlet channel. The analysis of the G matrix for other ij values (we do not present the corresponding graphs) shows that the situation in the triplet channel is much more diverse than in the singlet channel, the relevant details being greatly dependent on ij values. Only in the case of $ij = 23$ is the pattern virtually identical to that in the singlet channel.

By and large, the distinction between the G matrix and the effective interaction is more pronounced in the triplet channel than in the singlet one. The reason can be understood if we recall the resonance character of the nucleon–nucleon interaction at low energies. Since we investigate the G matrix at a rather low energy, $E = 2\mu = -16$ MeV, the proximity to the virtual level ($\varepsilon_0 = 0.067$ MeV) in the singlet channel or to the real level ($\varepsilon_1 = -2.23$ MeV) in the triplet channel is of importance. To be more specific, the free T matrix—the nonhomogeneous term in Eq. (22)—has a pole at the above energies. It was shown in [14, 15], however, that, in the singlet case, the effective interaction virtually coincides with the free T matrix taken at the negative energy of $E = 2\mu$. This occurs because two contributions of opposite signs to the difference kernel of Eq. (22) compensate each other to a considerable extent. We will see below that the difference of the effective interaction and the T matrix is greater in the triplet channel than in the singlet one, but it is not large either, as a rule. As follows from Eq. (18), the distinction between the G matrix and the effective interaction is associated with the contribution of the propagator B_{lm}^0 in the model subspace. We have seen above that these propagators

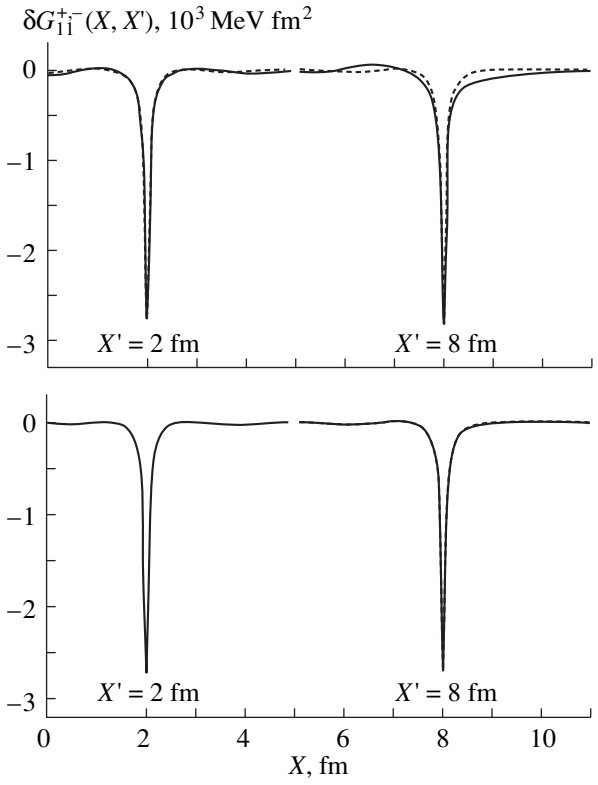

Fig. 12. Profile functions for the (upper panel) even and (low panel) odd components of (solid curves) $\delta G_{11}(X, X')$ and (dashed curves) $\delta\Lambda_{11}(X, X')$ in the singlet channel at $X' = 2$ fm and $X' = 8$ fm.

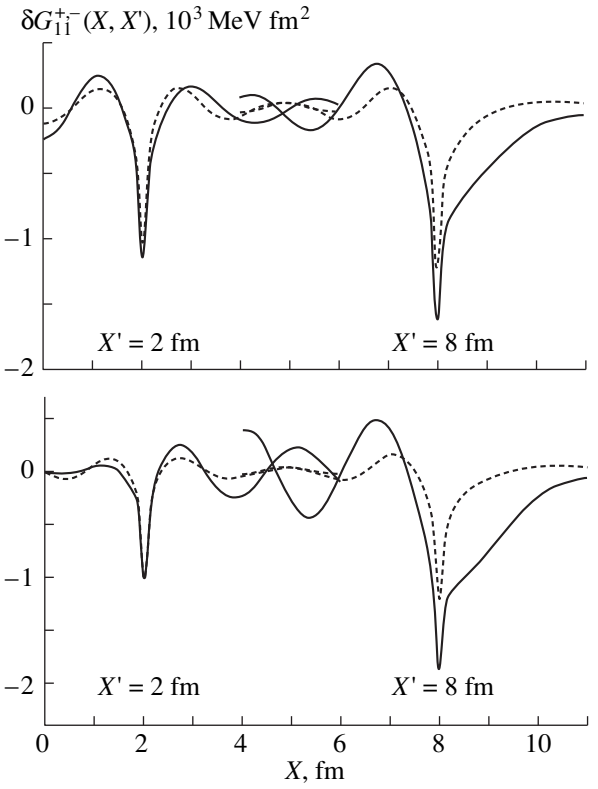

Fig. 13. As in Fig. 12, but for the $S = 1$ triplet channel.

are considerably less in absolute value (by one order of magnitude) than the corresponding propagators B'_{lm} in the complementary subspace. If we return to the original Eq. (15), it may seem that we should not expect a considerable contribution from the term B^0_{lm}—that is, a considerable difference of $G_{ij}(X, X')$ and $\Lambda_{ij}(X, X')$. As always occurs near the pole of a solution, however, even a small change in the kernel of the integral equation can lead to a sizable effect.

7. AVERAGED CHARACTERISTICS OF THE G MATRIX AT $P_\perp = 0$ IN THE SINGLET CHANNEL

Let us first consider the even G^+ matrix. We have already seen that, in the singlet channel, all large components of the G matrix (we recall that these are the ij = 11, 12, and 22 components) are sharp delta like functions of the difference $t = X' - X$ of the coordinates. Hence, each of them can be approximately replaced by the delta function of the corresponding difference coordinate t with the factor $\langle G_{ij}\rangle$ that depends on the average c.m. coordinate X_0 and which is determined by the zeroth moment of $G_{ij}(X, X')$. As in Sections 4 and 5, it is more convenient to use the nonsymmetrized definition of the zeroth moment cut off as

$$\langle G_{ij}\rangle^+_{S=0}(X) = \int_{-t_c}^{t_c} dt G_{ij}^{+,S=0}(X, X+t). \qquad (51)$$

These moments are depicted in Figs. 14–16, along with the corresponding zeroth moments of the effective interaction $\mathcal{V}_{\text{eff}}$,

$$\langle \Lambda_{ij}\rangle^+_{S=0}(X) = \int_{-t_c}^{t_c} dt \Lambda_{ij}^{+,S=0}(X, X+t), \qquad (52)$$

and of the free T matrix,

$$\langle T_{ij}\rangle^+_{S=0} = \int_{-t_c}^{t_c} dt T_{ij}^{+,S=0}(t). \qquad (53)$$

It is obvious that the zeroth moments of the T matrix do not depend on X. We note that the cutoff in the integral for the effective interaction and that in the integral for the T matrix do not have a pronounced impact on the results and are introduced only for the sake of consistency.

It was indicated in Section 5 that this definition of the zeroth moment gives no way to take into account the long-range tails of the G matrix. Although these tails are small, their integrated contribution is often not

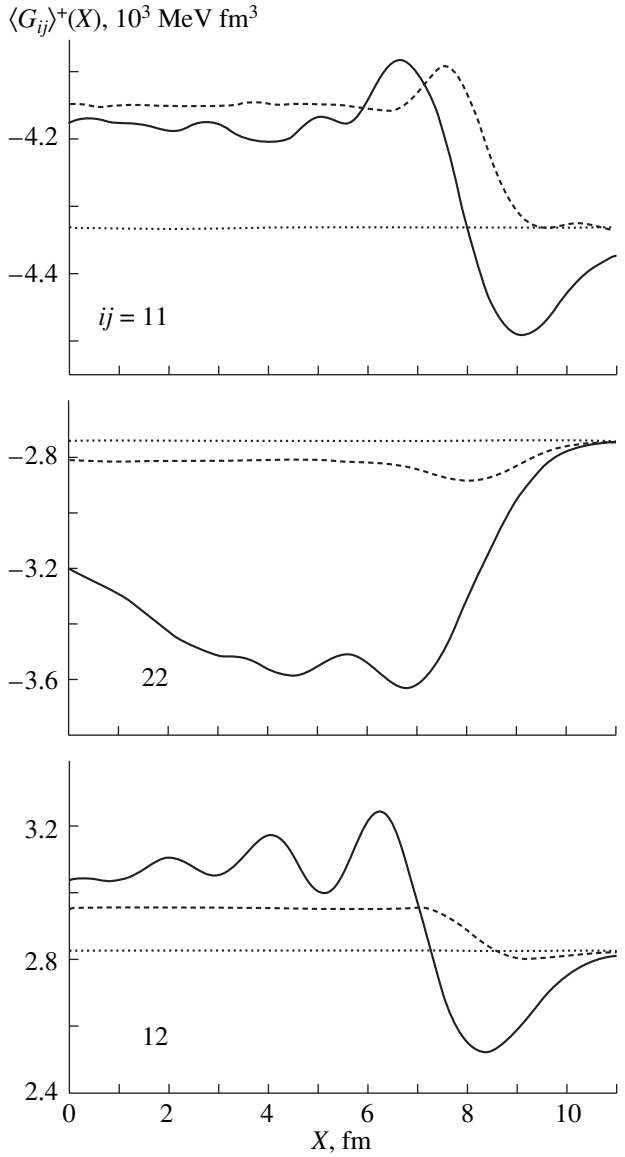

Fig. 14. Zeroth moments of the even components of (solid curve) the *G* matrix, $\langle G_{ij}\rangle^+(X)$; (dashed curve) the effective interaction, $\langle \Lambda_{ij}\rangle^+(X)$; and (dotted curve) the *T* matrix, $\langle T_{ij}\rangle^+(X)$, in the $S = 0$ singlet channel.

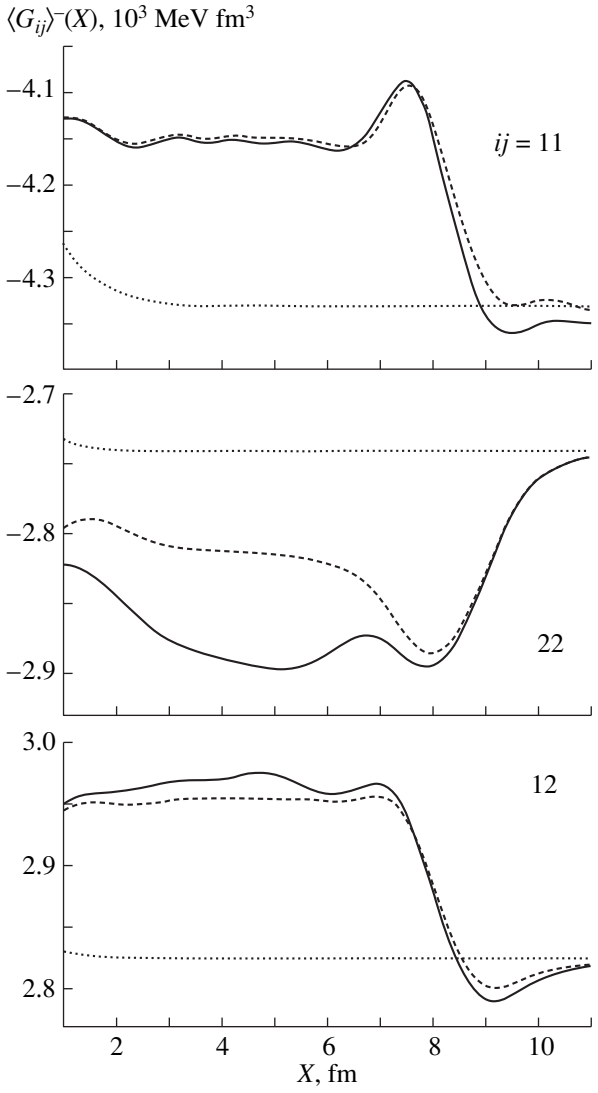

Fig. 15. As in Fig. 14, but for the odd components.

small in relation to the central maximum. That the result of integration in (51) shows a nonnegligible dependence on the cutoff parameter t_c for some *ij* components [there is virtually no such dependence in (52) and (53)] is a signal of this. We will make use of the same value of $t_c = 3$ fm as before. The cutoff zeroth moment characterizes precisely a local maximum of the *G* matrix, not absorbing the long-range terms G_{ij}. The proposed localization method is obviously inadequate for taking into account these long-range terms. At the same time, the above definition of the zeroth moment correctly characterizes, on average, the strength of interaction in the vicinity of the point being considered.

The zeroth moments of the main components of the *G* matrix in the singlet channel are plotted in Fig. 14, along with the zeroth moments of the effective interaction and of the free *T* matrix. It was shown in [14, 15] that, in the singlet channel, the large components of the effective pairing interaction are very close to those of the free *T* matrix. From Fig. 14, it can be seen that this is true for the relevant even combination $\langle \Lambda_{ij}\rangle^+_{S=0}(X)$ and $\langle T_{ij}\rangle^+_{S=0}(X)$ as well. By way of example, we indicate that, for the $ij = 11$ component, the distinction, which seems sizable at first glance, is in fact as small as 5%. As to the quantity $\langle G_{ij}\rangle^+(X)$, only for the $ij = 11$ component does it differ insignificantly from the zeroth moment of the effective interaction and, hence, from the zeroth moment of the *T* matrix. For the remaining two large components, the distinction amounts to 20–25%.

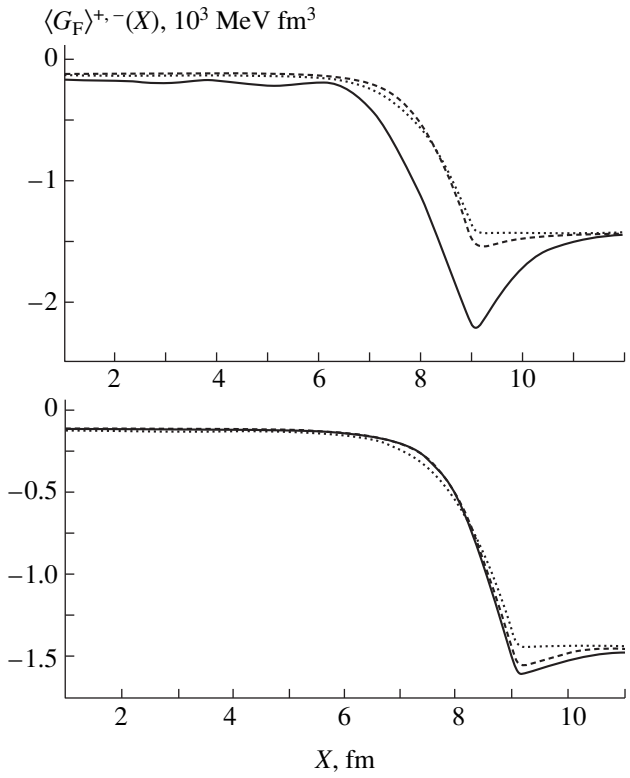

Fig. 16. Quantities obtained by averaging (upper panel) the even and (low panel) the odd components of (solid curve) the G matrix $[\langle G_F\rangle^{+,-}(X)]$, (dashed curve) the effective interaction $[\langle \mathcal{V}_F^{\text{eff}}\rangle^{+,-}(X)]$, and (dotted curve) the T matrix $[\langle T_F\rangle^{+,-}(X)]$ in the $S = 0$ singlet channel over the Fermi surface.

The analogous mean values for the odd G^- matrix, which are given by the same relations (51)–(53), where the plus signs in the superscripts are replaced by minus signs, are plotted in Fig. 15. As can be seen from a comparison with the corresponding curves in Fig. 14, the odd effective interaction shows virtually no distinctions from the even one (the same is true for the corresponding T matrix) everywhere, with the exception of small values of X. This is a direct corollary of the smallness of the effective radius of the relevant quantities. At the same time, the distinctions between the corresponding $ij = 12$ and $ij = 22$ components of the $G^{+,-}$ matrices are quite pronounced. These distinctions are associated with long-range terms in the G matrix, which are partly present even in the calculation of the cutoff zeroth moment and which are associated with the contribution of individual single-particle states belonging to the model subspace. Since different combinations of these states are involved in the expressions for the positive- and the negative-parity propagators, the relevant results are different. It is worth noting that, for a negative parity, the distinction between the G matrix and the effective interaction is modest.

It is not the individual components $\langle G_{ik}\rangle$ but their combination averaged at the Fermi surface that is of prime importance for computing the Landau–Migdal amplitude. For the even G matrix in the singlet channel, this combination is given by

$$\langle G_F\rangle^{+}_{S=0}(X) = \sum_{ij}\langle G_{ij}\rangle^{+}_{S=0}(X)g_i(k_F^2(X))g_j(k_F^2(X)), \quad (54)$$

where we have defined the local Fermi momentum as $k_F(X) = \sqrt{2m(\mu - V(X))}$ for $\mu - V(X) > 0$ and as $k_F(X) = 0$ in the opposite case. This quantity is depicted in the upper panel of Fig. 16, along with the corresponding localized form of the effective interaction,

$$\langle \mathcal{V}_F^{\text{eff}}\rangle^{+}_{S=0}(X) = \sum_{ij}\langle \Lambda_{ij}\rangle^{+}_{S=0}(X)g_i(k_F^2(X))g_j(k_F^2(X)), \quad (55)$$

and the corresponding localized form of the T matrix,

$$\langle T_F\rangle^{+}_{S=0}(X) = \sum_{ij}\langle T_{ij}\rangle^{+}_{S=0}g_i(k_F^2(X))g_j(k_F^2(X)). \quad (56)$$

For the odd G matrix, similar quantities averaged near the Fermi surface are found from Eqs. (54)–(56), where a plus sign in the superscripts is replaced by a minus sign. The relevant results are displayed in the lower panel of Fig. 16.

It can be seen that, for zero spin S, each of the quantities obtained by averaging, at the Fermi surface, the effective interaction and the T matrix for the symmetric case virtually coincide with its antisymmetric counterpart. Moreover, these quantities are very close to each other in the case where the symmetry in question is realized. The last circumstance complies with the results presented in [14, 15], where we analyzed the possibility of approximating the effective pairing interaction in the singlet channel by the free T matrix. The averaged symmetric G matrix has the same form as the effective interaction, but the former is almost twice as great as the latter in absolute value. Within the slab, there are small-amplitude oscillations, which reflect the oscillations of the individual components $\langle G_{ij}\rangle(X)$. The distinctions between the G matrix and the effective interaction is considerably smaller in the case of negative parity. For either sign of parity, the absolute value of the G matrix averaged at the Fermi surface has a sizable surface maximum, which is more pronounced in the case of positive parity.

8. AVERAGED FEATURES OF THE G MATRIX AT $P_\perp = 0$ IN THE TRIPLET CHANNEL

The cutoff zeroth moments of the individual components of the G matrix in the triplet channel are defined

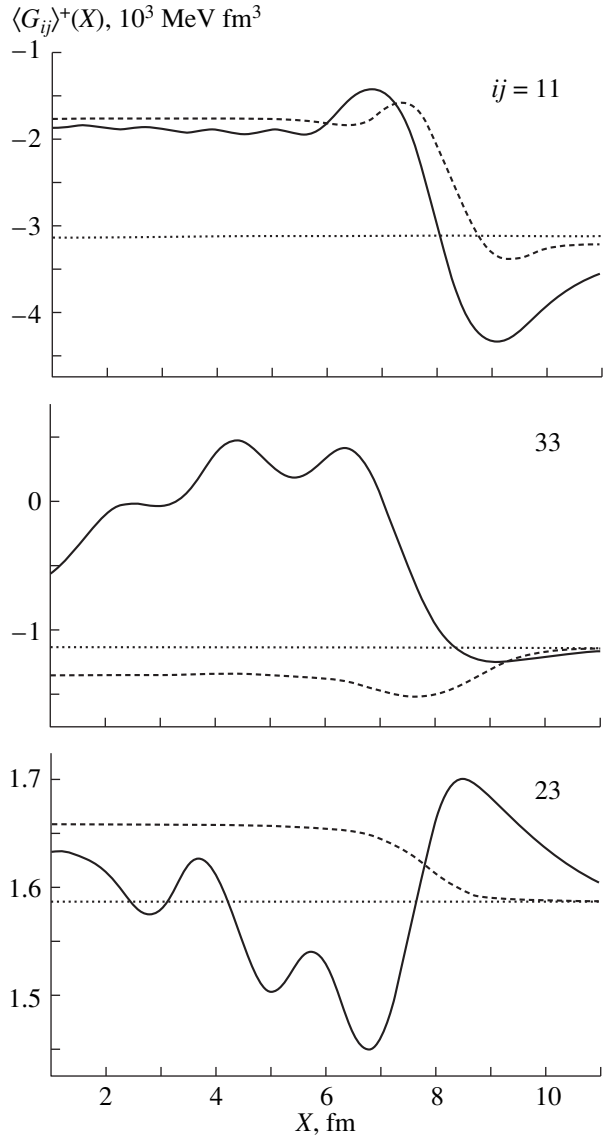

Fig. 17. As in Fig. 14, but for the $S = 1$ triplet channel.

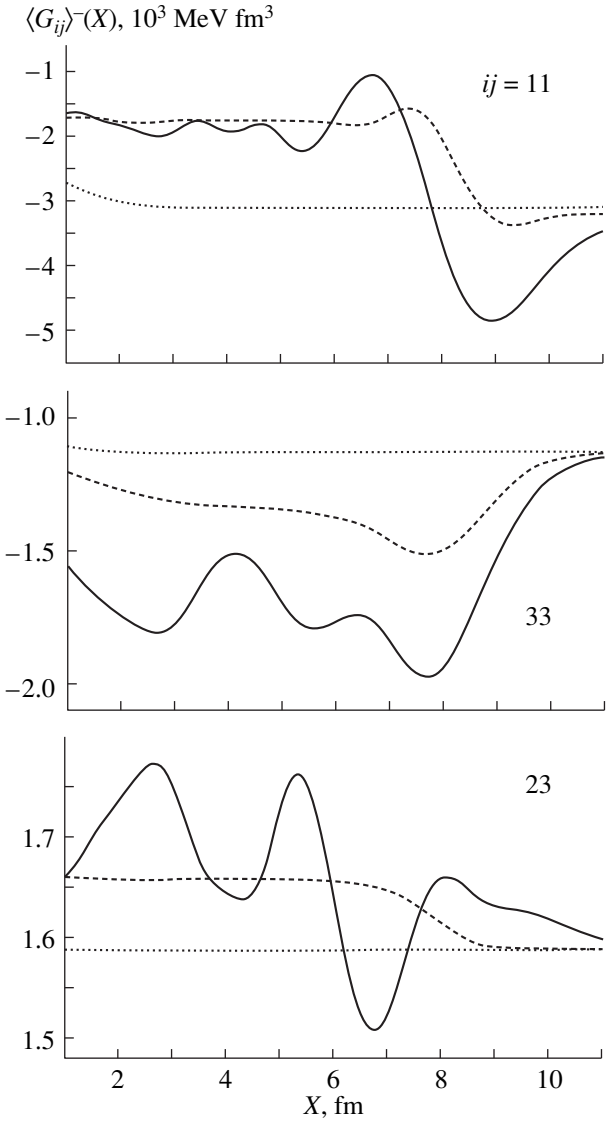

Fig. 18. As in Fig. 14, but for the $S = 1$ triplet channel and for the odd components.

in just the same way as in the singlet channel—that is, they are defined by expression (51) with the substitution of $S = 1$ for $S = 0$ in the case of a positive parity and with the additional substitution of a minus sign in the superscripts for a plus sign in the case of a negative parity. From Table 1, it can be seen that, in the triplet channel—in contrast to what was obtained for the singlet channel—there are no components that stand out in absolute value (maybe, with the exception of the comparatively small $ij = 14$ component). For the case of a positive parity, Fig. 17 displays the zeroth moments of the three components G_{ij}^{+} chosen earlier for analysis. For a negative parity, the corresponding results are shown in Fig. 18. In just the same way as for the singlet channel, we draw a comparison with the zeroth moments of the effective interaction and the free T matrix. Since the total G matrix (41) appears in the Landau–Migdal amplitude, it is this quantity that must be considered as the main result of the present calculation. For this reason, we display the zeroth moments of all ten components of this matrix (Fig. 19). An analysis of the data in the figures being discussed shows that it is difficult here to trace some general regularities (similar, for example, to small distinctions between the effective interaction and the T matrix as observed in the singlet channel): although the difference of $\langle\Lambda_{ij}\rangle(X)$ and $\langle T_{ij}\rangle$ is small for the majority of the ij pairs (it does not exceed 5% for $ij = 23$), there are cases ($ij = 24, 33$) where the difference may be as large as 20 or even 30%. The zeroth moment of the G matrix as a function of X is sometimes ($ij = 11, 24, 44$) reproduced, on average, by the corresponding zeroth moment of the effective

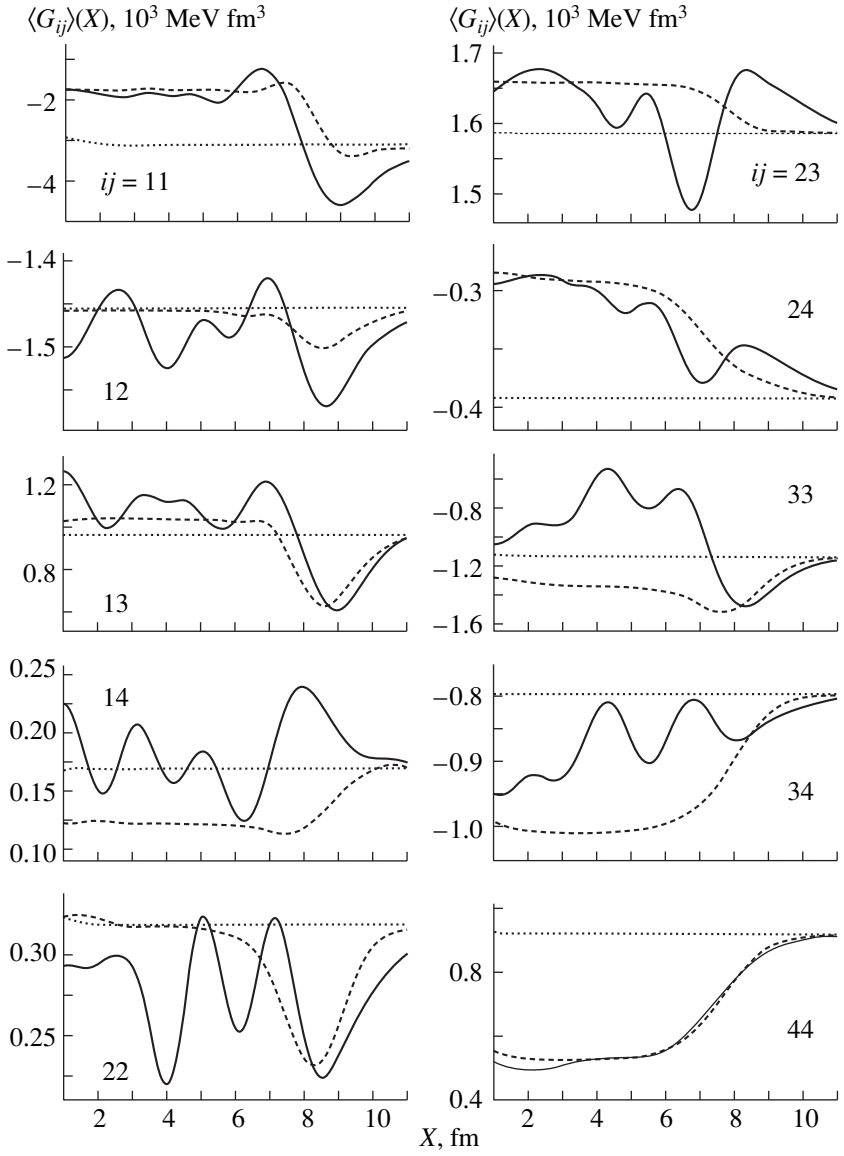

Fig. 19. Zeroth moments of all components of (solid curve) the total G matrix $[\langle G_{ij}\rangle(X)]$, (dashed curve) the effective interaction $[\langle \Lambda_{ij}\rangle(X)]$, and (dotted curve) the T matrix $[\langle T_{ij}\rangle(X)]$ in the $S = 1$ triplet channel.

interaction, but, as a rule, the zeroth moment of the G matrix oscillates about this mean value.

A comparison of the data in Figs. 17 and 18 reveals that the distinctions between the positive- and negative-parity components for the same pair of ij values are still more pronounced than in the singlet channel. In accordance with a qualitative analysis presented in Section 5 and devoted to the effect of the dimension of the model subspace on the two-particle propagators in this subspace, it can be assumed that such a pronounced distinction in the case of the triplet channel is in part an artifact of a not quite adequate choice of the model subspace, which includes an insufficient number of single-particle states. This may be the reason for the poor accuracy of the local-potential approximation in the complementary subspace. This situation is expected to be remedied by extending the model subspace. The problem of optimally choosing a model subspace will be considered elsewhere.

For the triplet channel, we now proceed to analyze the G matrix averaged at the Fermi surface. In contrast to the case of the singlet channel, it appears to be a 2×2 matrix in the space of values of the two-body orbital angular momentum L. Specifically, we have

$$\langle G_{\mathrm{F}}\rangle^{LL'}_{S=1}(X) = \sum_{ij}\langle G_{ij}\rangle_{S=1}(X)g_i^{(L)}(k_{\mathrm{F}}^2(X))g_j^{(L')}(k_{\mathrm{F}}^2(X)), \quad (57)$$

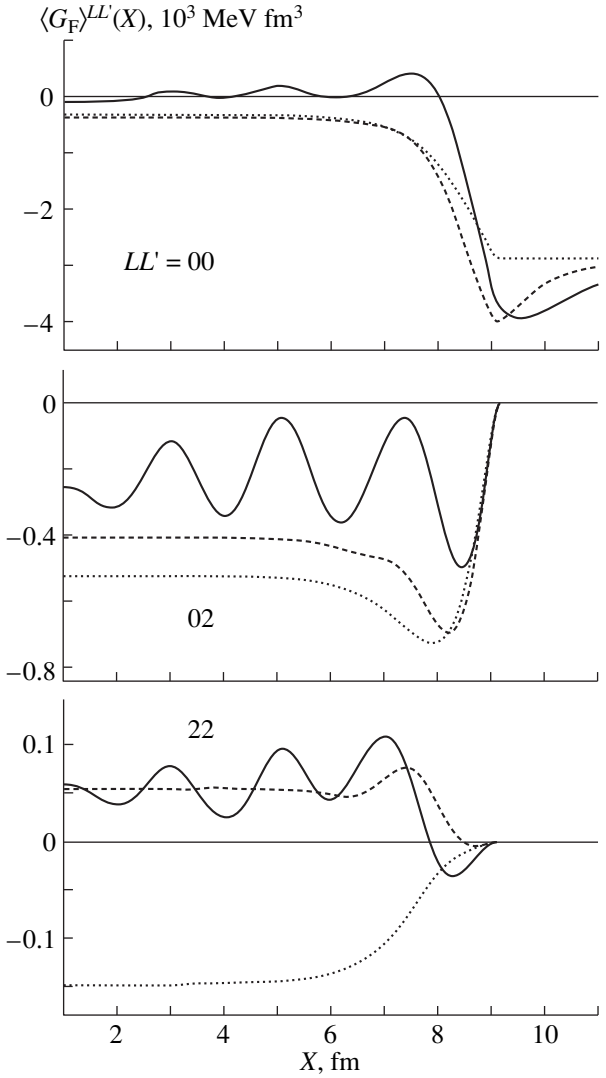

Fig. 20. Quantities obtained by averaging (solid curve) the even G matrix $[\langle G_F\rangle^{LL'}_{S=1}(X)]$, (dashed curve) the effective interaction $[\langle \mathcal{V}^{\text{eff}}_F\rangle^{LL'}_{S=1}(X)]$, and (dotted curve) the T matrix $[\langle T_F\rangle^{LL'}_{S=1}(X)]$ in the triplet channel over the Fermi surface.

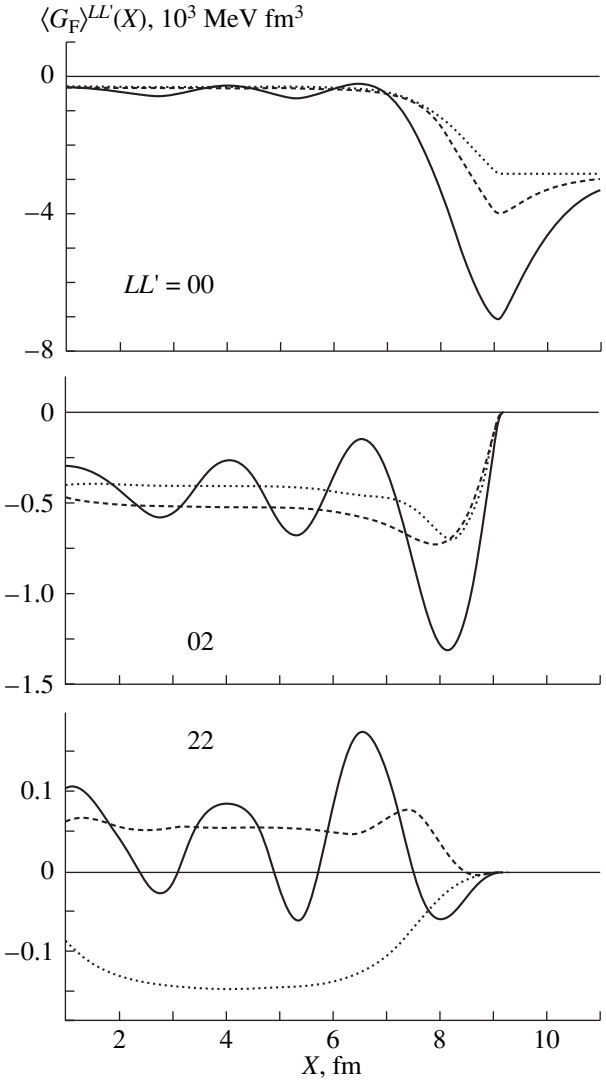

Fig. 21. As in Fig. 20, but for the odd G matrix.

where L, L' = 0, 2. In order to avoid encumbering the presentation, we have suppressed the parity superscripts of plus and minus on the G matrix. The corresponding averaged values for the even and the odd G matrix are displayed in Figs. 20 and 21, respectively. Once again, we can see a strong parity dependence of the averaged G matrix. This dependence seems to be slightly exaggerated in the present calculation, in just the same way as for the individual components $\langle G_{ij}\rangle$. The averaged values that carry the index $L = 2$ are considerably less than the dominant term $\langle G_F\rangle^{00}_{S=1}(X)$. These distinctions are especially pronounced at the slab boundary because of the vanishing of the form factor $g_i^{(2)}(k_F^2(X))$ in the classically forbidden region. It can be seen from Figs. 20 and 21 that, even in the internal region, the D-wave contribution is modest. In just the same way as in the case of the singlet channel, the dominant term of the averaged G matrix features a pronounced surface maximum, which is again sharper for a positive parity.

9. DEPENDENCE OF THE *G* MATRIX ON THE CHEMICAL POTENTIAL OF THE SYSTEM

Thus far, all our calculations of the G matrix have been performed for the fixed chemical-potential value of $\mu = -8$ MeV, which is close to the binding energy (per nucleon) of medium-mass and heavy stable nuclei. In this section, the result is investigated as a function of μ. Previously, a significant μ dependence was found for

the effective pairing interaction [3, 11]. This quantity is equal to the half-sum of the averaged effective interaction (55) in the singlet channel for a positive parity and the analogous quantity $\langle \mathcal{V}_{\rm F}^{\rm eff} \rangle^{-}_{S=0}(X)$ for a negative parity. There are two reasons behind this effect. First, it is a resonance-type dependence on the energy $E = 2\mu$ in the T matrix, which appears to be a nonhomogeneous term in Eq. (22) for the effective interaction. Second, it is quite a sharp dependence on the form-factor momentum in the sum appearing in Eq. (55). These two factors remain operative for the averaged G matrix as well:

$$\langle G_{\rm F} \rangle_{S=0}(X) = \frac{1}{2}(\langle G_{\rm F} \rangle^{+}_{S=0}(X) + \langle G_{\rm F} \rangle^{-}_{S=0}(X)). \quad (58)$$

This quantity at $\mu = -8$ and -4 MeV is displayed in Fig. 22, along with the corresponding effective interaction and the T matrix averaged at the Fermi surface. It can be seen that, in the singlet channel, the μ dependence of the averaged G matrix is more pronounced than that of the effective interaction.

Disregarding the small components involving L, $L' = 2$, we define the analogous quantity in the triplet channel as

$$\langle G_{\rm F} \rangle_{S=1}(X) = \frac{1}{2}(\langle G_{\rm F} \rangle^{+}_{S=1,00}(X) + \langle G_{\rm F} \rangle^{-}_{S=1,00}(X)). \quad (59)$$

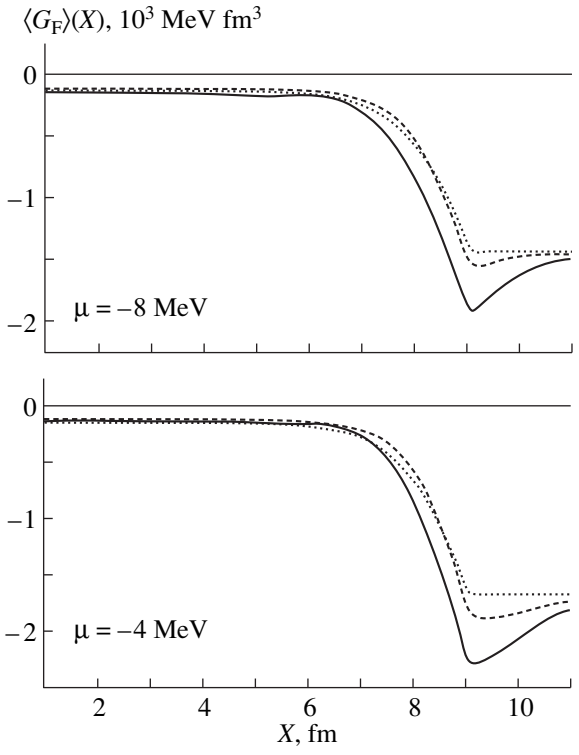

Fig. 22. Quantities obtained by averaging the (solid curve) total G matrix $[\langle G_{\rm F} \rangle_{S=0}(X)]$, (dashed curve) effective interaction $[\langle \mathcal{V}_{\rm F}^{\rm eff} \rangle_{S=0}(X)]$, and (dotted curve) T matrix $[\langle T_{\rm F} \rangle_{S=0}(X)]$ in the singlet channel over the Fermi surface.

In Fig. 23, this truncated averaged G matrix for the triplet channel is plotted for the same two values of μ (along with the effective interaction and the free T matrix, as before). There, the μ dependence of the averaged G matrix is even more dramatic than in the singlet channel: in the surface region, it changes sign in the present case. It is not clear from the outset whether this sign reversal is an artifact that arises from the use of the local-potential approximation in calculating the effective interaction at $\mu = -4$ MeV. Indeed, we have already indicated that the applicability of this approximation to the case of the triplet channel is questionable even at $\mu = -8$ MeV, but the accuracy of the local-potential approximation only becomes poorer with decreasing absolute value of $|\mu|$. However, the statement as it is that the μ dependence is more pronounced for the triplet channel than for the singlet channel is qualitatively understandable and is correct in all probability. The reason for this is associated with the proximity of the pole of the free T matrix on the energy scale. In the triplet case, the relevant pole is closer to the energy $E = 2\mu$ being considered.

10. ESTIMATING THE ROLE OF NONZERO $P_\perp$ VALUES

So far, we have investigated only the simplest case of $P_\perp = 0$. It was not solely because of the simplicity of this case that we restricted our consideration to it—another point in favor of this choice was that only

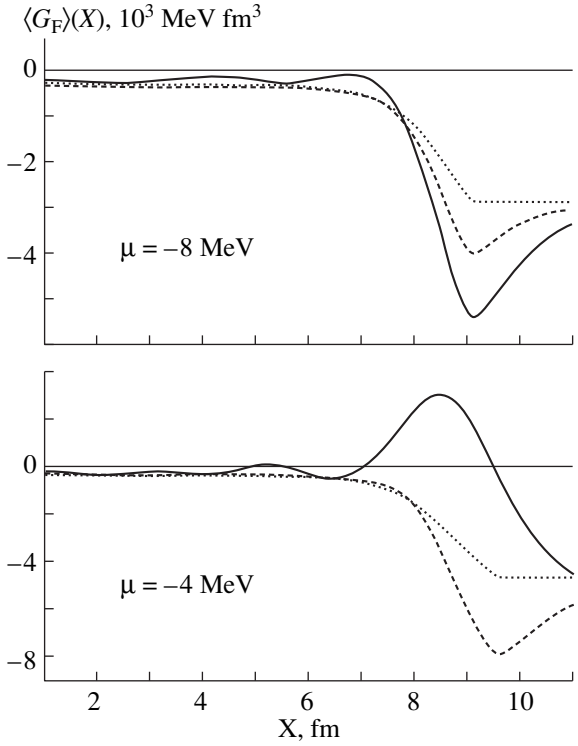

Fig. 23. As in Fig. 22, but for the triplet channel.

extremely low momenta survive in the asymptotic region off the slab. Needless to say, this is not so within the slab and in the surface region, so that computing the Landau–Migdal amplitude over the entire region of X requires knowledge of the G matrix at nonzero values of $P_\perp$. With an eye to a further extension of the theory in question to actual spherical nuclei, the orthogonal momentum in the planar geometry being considered must be associated with the angular momentum in spherical geometry. For points at the surface of a nucleus of radius R, the relation that establishes this correspondence at a fixed value of the total two-body orbital angular momentum $\mathscr{L}$ then has the form

$$P_\perp^2 = \frac{\mathscr{L}(\mathscr{L}+1)}{R^2}. \qquad (60)$$

In heavy nuclei around ^{208}Pb, maximum values $l_{\max}$ of the one-body orbital angular momentum are 6 to 7. Accordingly, we have $\mathscr{L}_{\max} = 12$–14. In calculating the zeroth harmonic of the Landau–Migdal amplitude on the basis of expression (1), summation is performed over all $\mathscr{L}$ from 0 to $\mathscr{L}_{\max}$. In order to assess the role of nonzero $P_\perp$ values, we set $\mathscr{L} = 6$ and $R = 8$ fm in Eq. (60). This yields $P_\perp^2 = 0.656$ fm^{-2}. For a rough estimate of the effect, we also simplify integration in (16) by replacing the relevant integral with respect to the angle between $P_\perp$ and $k_\perp$ by 2π. The emergence of the additional term $P_\perp^2/4m$ in the denominator on the right-hand side of (16) is then the only change in relation to the case of $P_\perp = 0$. The results of the relevant calculations for the averaged G matrix and the averaged effective interaction are displayed in Fig. 24 for both channels being considered. As can be seen, allowances made for nonzero values of $P_\perp$ level out to a considerable extent the surface maxima in the absolute value of the G matrix in both channels and reduce strongly the difference between the effective interaction and the G matrix. In order to explain the above qualitatively, it is sufficient to notice that the addition of a comparatively large quantity to the denominator on the right-hand side of (16) renders the role of the density of states near the Fermi surface less pronounced, thereby suppressing the contribution of the propagator B^0 in the model subspace. But it is this propagator that is responsible both for the distinctions between the G matrix and the effective interaction and for a sharp variation of the G matrix near the surface.

The correct inclusion of nonvanishing $P_\perp$ values is a very cumbersome numerical problem, which will be considered in separate publication.

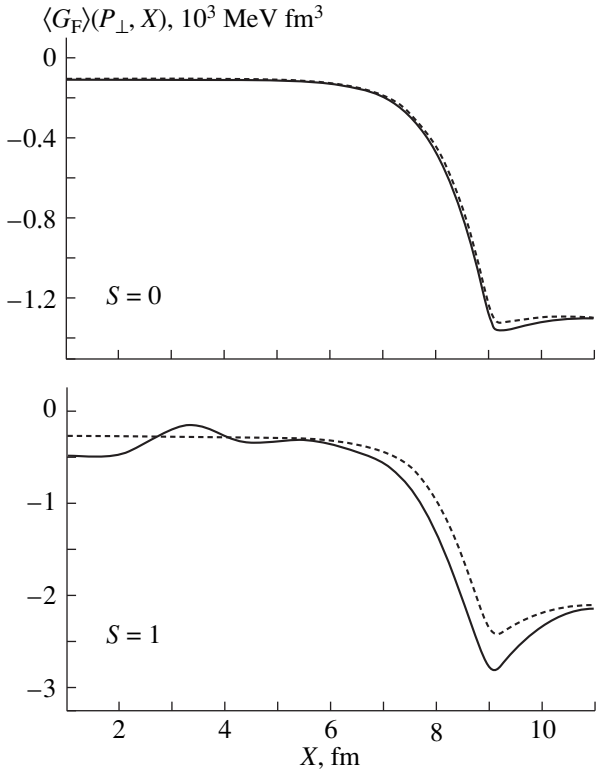

Fig. 24. Quantities obtained by averaging the (solid curve) total G matrix [$\langle G_F\rangle_{S=0}(P_\perp, X)$] and (dashed curve) effective interaction [$\langle \mathscr{V}_F^{\text{eff}}\rangle_{S=0}(P_\perp, X)$] in (upper panel) the singlet and (lower panel) the triplet channel at $P_\perp^2 = 0.656$ fm^{-2} over the Fermi surface.

11. CONCLUSION

For a separable nucleon–nucleon interaction, we have developed a method for numerically calculating the Brueckner G matrix for a planar slab of nuclear matter occurring in a preset one-dimensional potential well. We have relied on the technique that is based on the mixed coordinate–momentum representation and which was previously proposed in [2, 3] for investigating the problem of pairing in semi-infinite nuclear matter. We have considered two channels, the $^1S_0$ singlet and the $^3S_1$–$^3D_1$ triplet channel, that are dominant at low energies. Specific calculations have been performed for a separable version [4, 5] of the Paris nucleon–nucleon potential (3×3 potential in the singlet and 4×4 potential in the triplet channel). The Bethe–Goldstone equation for the G matrix then reduces to a set of one-dimensional integral equations in the coordinate space (six equations in the singlet and ten equations in the triplet channel) whose kernels are given by the convolutions of the two-particle propagators with the form factors of the separable expansion of the nucleon–nucleon potential. The propagators in turn are determined by multidimensional integrals in momentum space (and by sums over discrete eigenstates in the slab potential). The calculation of these propagators presents the most serious mathematical difficulty in the problem under investigation. Instead of precisely calculating these propagators, we have invoked the local-

potential approximation, which was developed in [2, 3] in calculating the effective pairing interaction in the singlet channel. For this purpose, the full two-particle Hilbert space has been broken down into a comparatively small model subspace, where the two-particle propagator has been treated precisely, and a complementary subspace, where the local-potential approximation has been employed to calculate the propagator. The model subspace has been taken in the same form as in the pairing problem—it includes all negative-energy single-particle states. When the model subspace is defined in this way, the effective interaction for the singlet channel in the problem under investigation coincides with the effective pairing interaction calculated in [2, 3], where we demonstrated a rather high accuracy of the local-potential approximation. At the same time, the accuracy of the local-potential approximation in the triplet channel is not known a priori. Pursuing the main goal of developing the computational method in general, we have not investigated this question here in detail. There is indirect evidence that the accuracy of the local-potential approximation is noticeably poorer in the triplet channel than in the singlet channel. However, it has been shown that the accuracy of the local-potential approximation improves when the model subspace is extended. This brings about a problem of paramount importance for the implementation of the proposed method in practice, that of optimizing the choice of model subspace. On one hand, it must be sufficiently large in order to ensure a high precision of the local-potential approximation; on the other hand, it must not be overly large in order that a precise calculation of the propagator in the model subspace not consume very long machine time. A search for optimal (from this point of view) partition of the full Hilbert space will be discussed elsewhere.

The G matrix has been calculated at a fixed total energy of two nucleons that has been set to the doubled chemical potential μ of the system. In addition, the total orthogonal momentum has been fixed at $P_\perp = 0$. The calculations have been performed predominantly for $\mu = -8$ MeV, a value characteristic of stable heavy nuclei. In both channels, the G matrix averaged at the Fermi surface corresponds to a strong attraction in the surface region. The strength of this attraction has a pronounced maximum at the slab surface, especially in the triplet case. In order to find this amplitude in the surface region correctly, it is necessary to take consistently into account the contribution of nonzero $P_\perp$ values. We have roughly estimated their role. It has been shown that the inclusion of these contributions smears the effects obtained at $P_\perp = 0$ somewhat, but it does not eliminate them completely. A calculation of the G matrix with allowance for the contribution from nonzero $P_\perp$ values will be performed in a separate study.

Finally, we have analyzed the dependence of our results on the chemical potential μ. A comparison of the calculations performed at $\mu = -8$ MeV and $\mu = -4$ MeV has revealed a pronounced μ dependence of the G matrix, especially in the surface region. This effect can result in an appreciable μ dependence of the surface values of the invariant Landau–Migdal amplitudes. This is important for a microscopic description of the features of nuclei near the nucleon drip line.

ACKNOWLEDGMENTS

This work was supported in part by the Russian Ministry for Higher Education (grant no. 97-0-6.1-7) and by the Russian Foundation for Basic Research (project nos. 00-02-17319 and 00-15-96590).

APPENDIX 1

Form Factors g_i in the Coordinate Representation

For the case of $^1S_0$ singlet scattering, the form factors $g_i(k^2)$ in Eq. (11) are given by (in the notation similar to that from [2, 3])

$$g_i(k^2) = \sum_{n=1}^{4} \frac{C_{in} k^{2(n-1)}}{(k^2 + \beta_{in}^2)^n}. \tag{A.1}$$

It was noted above that, in our calculations, we have used the potential introduced in [4] and modified in [5]. The coefficients λ_{il} in Eq. (11) and C_{in} in Eq. (A.1) are redefined in such a way as to ensure fulfillment of the equality $g_i(k^2 = 0) = 1$. The renormalized coefficients are related to the corresponding values from [5] (they are labeled with a tilde) as follows:

$$C_{in} = f_i \tilde{C}_{in}, \tag{A.2}$$

$$\lambda_{il} = 2\pi^2 f_i f_l \tilde{\lambda}_{il}, \tag{A.3}$$

$$f_i = \frac{\beta_{i1}^2}{\tilde{C}_{i1}}. \tag{A.4}$$

These formulas were used to calculate the coefficients appearing in (11) and (A.1). The results are presented in [2, 3]. The values of the parameters β_{in} are identical to those in [5].

The Fourier transformation (13) of the form factors (A.1) can be found analytically. The result has the form

$$g_i(k_\perp^2, x) = \sum_{n=1}^{4} C_{in} f_{in}(k_\perp^2, x), \tag{A.5}$$

where

$$f_{i1}(k_\perp^2, x) = \exp(-s_{i1}x)/(2s_{i1}),$$

$$f_{i2}(k_\perp^2, x) = \frac{\exp(-s_{i2}x)}{2s_{i2}}\left[1 - \frac{\beta_{i2}^2}{2s_{i2}^2}(1 + s_{i2}x)\right],$$

$$f_{i3}(k_\perp^2, x) = \frac{\exp(-s_{i3}x)}{2s_{i3}}$$

$$\times\left[1-\frac{\beta_{i3}^2}{s_{i3}^2}(1+s_{i3}x)+\frac{\beta_{i3}^4}{8s_{i3}^4}[3+3s_{i3}x+(s_{i3}x)^2]\right], \quad \text{(A.6)}$$

$$f_{i4}(k_\perp^2, x) = \frac{\exp(-s_{i4}x)}{2s_{i4}}$$

$$\times\left[1-\frac{3\beta_{i4}^2}{2s_{i4}^2}(1+s_{i4}x)+\frac{3\beta_{i4}^4}{8s_{i4}^4}[3+3s_{i4}x+(s_{i4}x)^2]\right.$$

$$\left.-\frac{\beta_{i4}^6}{48s_{i4}^6}[15+15s_{i4}x+6(s_{i4}x)^2+(s_{i4}x)^3]\right],$$

$$s_{in} = \sqrt{\beta_{in}^2+k_\perp^2}.$$

We note that there is a misprint in the expressions that are presented in [2, 3] for the form factors and which are analogous to (A.5) [at the same time, all the calculations were performed correctly in accordance with (A.5)].

It has been indicated above that, for the case of the $^3S_1$ triplet channel coupled to the $^3D_1$ channel, formula (11) is replaced by the matrix expression (42), where the column $\hat{g}_i$ involves two component, $g_i^{L=0}(k^2)$ and $g_i^{L=2}(k^2)$. At the same time, it has been shown in [5] that, in the case of the multipole representation of the Paris potential, the best description of nucleon–nucleon scattering in the channel under consideration is achieved with the 4×4 version (PEST4 potential). In our calculations, we have used precisely this potential. Naturally, the form factors were normalized in a way similar to that adopted to the singlet channel. Obviously, the two components ($L=0$ and $L=2$) must be renormalized simultaneously since the same coefficients λ_{ij} appear in expansion (42) for these components. The form factors $g_i^{L=0}$ have the same form as in the singlet case; that is, they are determined by formulas (A.2)–(A.6). The corresponding renormalized coefficients are presented in [10].

For the $^3D_1$ channel, expression (A.2) for the renormalized form factor is replaced by (see [4])

$$g_i^{L=2}(k^2) = \sum_{n=1}^{4}\frac{C_{in}\beta_{in}^2k^{2n}}{(k^2+\beta_{in}^2)^{(n+1)}}. \quad \text{(A.7)}$$

The relation between the renormalized coefficients $C_{in}^{L=2}$ and the original coefficients from [4, 5] differ somewhat from those in the case of $L=0$, and relation (A.3) is replaced by

$$C_{in}^{L=2} = \frac{f_i^{L=0}}{\beta_{in,\,L=2}^2}\tilde{C}_{in}^{L=2}, \quad \text{(A.8)}$$

where the factor f_i is equal to the corresponding value for $L=0$.

The Fourier transformation of the form factors (A.7) yields

$$f_{i1}^{L=2}(k_\perp^2, x) = \frac{\exp(-s_{i1}x)}{2s_{i1}}\left[1-\frac{\beta_{i1}^2}{2s_{i1}^2}(1+s_{i1}x)\right],$$

$$f_{i2}^{L=2}(k_\perp^2, x) = \frac{\exp(-s_{i2}x)}{2s_{i2}}$$

$$\times\left[1-\frac{\beta_{i2}^2}{s_{i2}^2}(1+s_{i2}x)+\frac{\beta_{i2}^4}{8s_{i2}^4}[3+3s_{i2}x+(s_{i2}x)^2]\right],$$

$$f_{i3}^{L=2}(k_\perp^2, x) = \frac{\exp(-s_{i3}x)}{2s_{i3}}$$

$$\times\left[1-\frac{3\beta_{i3}^2}{2s_{i3}^2}(1+s_{i3}x)+\frac{3\beta_{i3}^4}{8s_{i3}^4}[3+3s_{i3}x+(s_{i3}x)^2]\right.$$

$$\left.-\frac{\beta_{i3}^6}{48s_{i3}^6}[15+15s_{i3}x+6(s_{i3}x)^2+(s_{i3}x)^3]\right], \quad \text{(A.9)}$$

$$f_{i4}^{L=2}(k_\perp^2, x) = \frac{\exp(-s_{i4}x)}{2s_{i4}}$$

$$\times\left[1-2\frac{\beta_{i4}^2}{s_{i4}^2}(1+s_{i4}x)+\frac{3\beta_{i4}^4}{4s_{i4}^4}[3+3s_{i4}x+(s_{i4}x)^2]\right.$$

$$-\frac{\beta_{i4}^6}{12s_{i4}^6}[15+15s_{i4}x+6(s_{i4}x)^2+(s_{i4}x)^3]$$

$$+\frac{\beta_{i4}^8}{384s_{i4}^8}[105+105s_{i4}x+45(s_{i4}x)^2$$

$$\left.+5(s_{i4}x)^3+(s_{i4}x)^4]\right].$$

APPENDIX 2

Coordinate Representation of the T Matrix for Free Nucleon–Nucleon Scattering in the Triplet Channel

In [2, 3], the coordinate representation for the free T matrix in the singlet channel was derived on the basis of the inverse Fourier transformation of the off-mass-shell T matrix that was preliminarily found in the momentum representation. A convenient method for calculating the inverse Fourier integral in the complex plane of the total momentum P_x was developed in [11, 14]. Here, we use the same method for the triplet channel.

In the momentum representation, the free T matrix at the negative energy $E = 2\mu$ is found by solving the set of algebraic equations

$$T_{ij}^{S=1}(P_x, P_\perp; E) = \lambda_{ij} + \sum_{lm} \lambda_{il} B_{lm}^{\mathrm{fr},\,S=1}(P_x, P_\perp; E) T_{mj}^{S=1}(P_x, P_\perp; E), \quad \text{(A.10)}$$

where

$$B_{lm}^{\mathrm{fr},\,S=1}(P_x, P_\perp; E) = \int \frac{d^3k}{(2\pi)^3} \frac{g_l^{L=0}(k^2) g_m^{L=0}(k^2) + g_l^{L=2}(k^2) g_m^{L=2}(k^2)}{E - P_\perp^2/4m - P_x^2/4m - k^2/m}. \quad \text{(A.11)}$$

As can be seen, the scattering matrix at a nonzero value of $P_\perp$ is obtained from the T matrix at $P_\perp = 0$ by the simple substitution $E \longrightarrow \tilde{E} = E - P_\perp^2/4m$. The scattering matrix $T_{ij}(t)$ (we omit here the index $S = 1$ for the sake of brevity) in the coordinate representation is expressed in terms of $T_{ij}(P_x)$ by means of the inverse Fourier transformation

$$T_{ij}(t; \tilde{E}) = \int_{-\infty}^{\infty} \frac{dP_x}{2\pi} T_{ij}(P_x; \tilde{E}) \exp(-iP_x t). \quad \text{(A.12)}$$

For the sake of definiteness, we set, for the time being, $P_\perp = 0$ and $\tilde{E} = E$. The analytic properties of the $T_{ij}(P_x)$ matrix in the singlet channel were studied in [11, 14], and it was shown there that the integral in (A.12) can be transformed into an integral along the contour C embracing the upper half of the imaginary axis (see Fig. 25). It can easily be shown that, in the triplet channel, we can either use the same contour or modify it slightly. Indeed, the analytic properties of the $T_{ij}(P_x)$ matrix are determined primarily by the propagator in (A.11). For the singlet case, it was shown in [11, 14] that the only singularities of $B_{ij}(P_x; E)$ at negative energy $E = 2\mu$ are two cuts on the imaginary axis P_x that are symmetric with respect to the origin and which issue from the points $P_x = \pm i\gamma_0$, where $\gamma_0^2 = -8m\mu$. The only circumstance that was used in proving this statement is the fact that the form factors g_i in the integral in (A.11) are rational functions of k^2. This is valid for the triplet channel as well [see (A.1) for $L = 0$ and (A.7) for $L = 2$]; therefore, the singularities of $B_{ij}^{\mathrm{fr}}(P_x; E)$ occur on the same cuts in Fig. 25 for the triplet case as well. As can be seen from (A.10), all singularities of the propagator B^{fr} are also present in the free T matrix. The T matrix can have, however, its own singularities, poles corresponding to a virtual (in the singlet channel) or a real (in the triplet channel) level. It was indicated in [11, 14] that, in the case of a virtual level at $E = 2\mu < 0$, the poles of the T matrix that are inherent in it lie on the cuts. In the triplet case, there is a real level at the deuteron binding energy ε_d. If the energy $E = 2\mu$ is less than the deuteron binding energy, the two poles of $T_{ij}(P_x)$ are on the imaginary axis between the origin and the points $P_x = \pm i\gamma_0$. Their position is determined by the relation $P_x = \pm i\gamma_d$, where $\gamma_d^2 = -4m(2\mu - \varepsilon_d)$. In order to calculate the T matrix in the triplet channel, we can then use the same contour C as in the singlet case. But if $E = 2\mu > \varepsilon_d$, the poles of $T_{ij}(P_x)$ being considered go over from the imaginary axis to the real axis, again occupying symmetric positions $P_x = \pm\gamma_d$ with respect to the origin. For calculating the T matrix, the contour C must then be slightly deformed in order that it circumvent these poles. The minimal $|\mu|$ value used in our calculations was 4 MeV; therefore, we could consider only the nondeformed contour C. Actually, we used the contour in Fig. 25 with the same parameter values as in [14]—that is, $a = 2$ fm^{-1} and $b = 130$ fm^{-1}. In this case, the contour goes rather far away from the cuts, and it is straightforward to calculate the integral in (A.12) numerically, the result being nearly exact for all t values of our prime interest.

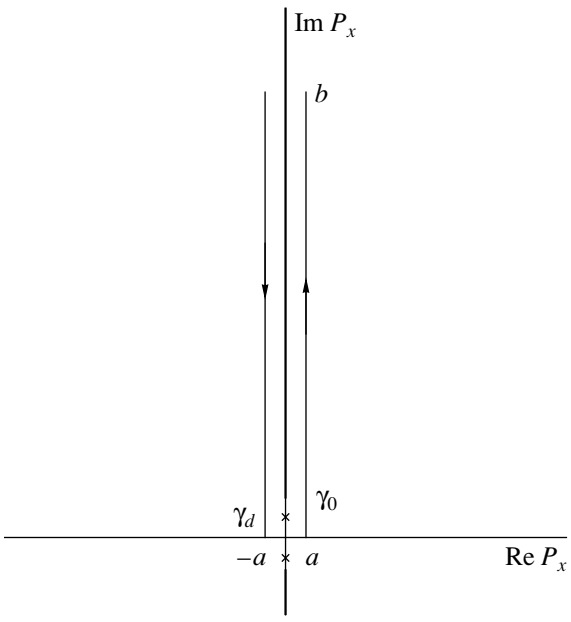

Fig. 25. Contour of integration in the complex plane of P_x for the inverse Fourier transformation (A.12).

It is easy to trace modifications that arise at $P_\perp \neq 0$. The contour C does not change form, but we now have $\gamma_0^2 = -8m\mu + P_\perp^2$. The other singular points in Fig. 25 are shifted in the same way.

The results of the calculations are quoted in Table 2.

Table 2. Components T_{ij} of the free T matrix (MeV fm^3) in the triplet channel at $P_x = 0$ and $E = 2\mu$ [presented in the second column are the renormalized constants λ_{ij} (MeV fm^3) in the separable form (42) of the original Paris nucleon–nucleon potential]

ij	λ_{ij}	$\|\mu\| = 8$ MeV	$\|\mu\| = 4$ MeV
11	-1.6177×10^3	-3.1102×10^3	-5.1280×10^3
12	-1.2961×10^3	-1.4071×10^3	-1.4052×10^3
13	8.9209×10^2	9.2470×10^2	9.3429×10^2
14	4.2708×10^1	1.5917×10^2	1.5567×10^2
22	7.8475×10^2	3.7717×10^2	3.5374×10^2
23	1.3939×10^3	1.5447×10^3	1.5452×10^3
24	-7.8603×10^2	-4.1024×10^2	-4.0296×10^2
33	-7.4504×10^2	-1.0999×10^3	-1.1445×10^3
34	-5.7228×10^2	-7.8394×10^2	-7.8533×10^2
44	1.8648×10^3	9.6492×10^2	9.4510×10^2

REFERENCES

1. M. Baldo, U. Lombardo, E. E. Saperstein, and M. V. Zverev, Yad. Fiz. **58**, 1572 (1995) [Phys. At. Nucl. **58**, 1483 (1995)].
2. M. Baldo, U. Lombardo, E. E. Saperstein, and M. V. Zverev, Yad. Fiz. **60**, 1206 (1997) [Phys. At. Nucl. **60**, 1081 (1997)].
3. M. Baldo, U. Lombardo, E. E. Saperstein, and M. V. Zverev, Nucl. Phys. A **628**, 503 (1998).
4. J. Haidenbauer and W. Plessas, Phys. Rev. C **30**, 1822 (1984).
5. J. Haidenbauer and W. Plessas, Phys. Rev. C **32**, 1424 (1985).
6. M. Lacombe, B. Loiseaux, *et al.*, Phys. Rev. C **21**, 861 (1980).
7. M. Baldo, J. Cugnon, A. Lejeune, and U. Lombardo, Nucl. Phys. A **515**, 409 (1990).
8. M. Baldo, I. Bombaci, G. Giansiracusa, and U. Lombardo, Nucl. Phys. A **545**, 741 (1992).
9. A. B. Migdal, *Theory of Finite Fermi Systems and Applications to Atomic Nuclei* (Nauka, Moscow, 1983, 2nd ed.; Interscience, New York, 1967).
10. M. Baldo, U. Lombardo, E. E. Saperstein, and M. V. Zverev, Yad. Fiz. **60**, 2170 (1997) [Phys. At. Nucl. **60**, 1988 (1997)].
11. M. Baldo, U. Lombardo, E. E. Saperstein, and M. V. Zverev, Phys. Lett. B **421**, 8 (1998).
12. P. Ring and P. Schuck, *The Nuclear Many-Body Problem* (Springer-Verlag, Berlin, 1980).
13. A. A. Abrikosov, L. P. Gor'kov, and I. E. Dzyaloshinskii, *Methods of Quantum Field Theory in Statistical Physics* (Fizmatgiz, Moscow, 1962; Prentice-Hall, Englewood Cliffs, 1963).
14. M. Baldo, U. Lombardo, E. E. Saperstein, and M. V. Zverev, Phys. Lett. (in press).
15. M. Baldo, U. Lombardo, E. E. Saperstein, and M. V. Zverev, Yad. Fiz. **63**, 1454 (2000) [Phys. At. Nucl. **63**, 1377 (2000)].

Translated by A. Isaakyan

Physics of Atomic Nuclei, Vol. 64, No. 2, 2001, pp. 228–232. Translated from Yadernaya Fizika, Vol. 64, No. 2, 2001, pp. 273–277.

NUCLEI
Theory

Microscopic Description of Low-Energy Neutron Scattering on a Deuteron

A. M. Gorbatov, P. V. Komarov*, P. Yu. Nikishov, A. V. Germanov, and D. V. Nechaev**

Tver State University, per. Sadovyĭ 35, Tver, 170002 Russia

Received November 4, 1999; in final form, March 27, 2000

Abstract—Low-energy neutron–deuteron scattering is calculated within the collective adiabatic approach by using a few versions of realistic *NN* interaction. The resulting integrated cross sections for the process are in good agreement with experimental data. © *2001 MAIK "Nauka/Interperiodica".*

1. FORMULATION OF THE PROBLEM

Recent efforts to construct a microscopic description of few-nucleon systems owe their success to the adiabatic character of the motion of such systems in hyperradial space. This property, which was confirmed by numerous calculations [1–4], was used as a basis in developing a collective adiabatic approach, a new method for treating nucleon systems. Within this approach, whose fundamentals were described in detail elsewhere [3–5], it was possible to reproduce faithfully the experimental cross sections for the fusion reaction $d + t \longrightarrow n + \alpha$ [6–8], for the elastic-scattering process $n + \alpha \longrightarrow n + \alpha$ [7, 8], for all binary processes in the four-nucleon system [9, 10], and for some other similar reactions. However, studies devoted to specific applications of the collective adiabatic approach undeservedly ignored three-nucleon processes, which were comprehensively explored, both theoretically and experimentally (for an overview, see, for example, [11]). The present study aims at partly filling this gap. Specifically, we consider the example of low-energy elastic neutron–deuteron scattering ($n + d \longrightarrow n + d$).

We recall that the first step in applying the collective adiabatic approach consists in constructing the relevant functions for all significant channels. The *i*th-channel function $U_i(\rho, \Omega) \equiv U_i$ is an eigenfunction of the operator

$$\hat{Q} = \frac{1}{\rho^2}\left\{-\Delta_{3A-3} + \frac{1}{4}(3A-6)(3A-4)\right\} + \hat{V} \quad (1)$$

(where Δ_{3A-3} is the operator of multidimensional angles, $\hat{V}$ is the operator of *NN* interactions, and *A* is the number of nucleons); that is, it satisfies the equation

$$(\hat{Q} - I_i(\rho))U_i(\rho, \Omega_\rho) = 0. \quad (2)$$

In the asymptotic limit $\rho \longrightarrow \infty$, the eigenvalue $I_i(\rho) \equiv I_i$, referred to as a collective potential, tends to the energy threshold for the *i*th channel.

In the case being considered, there exists only one binary channel, $n + d$, and many democratic channels of $n + n + p$ breakup. Hereafter, we restrict our consideration to low energies, in which case all democratic channels are closed. Only channels characterized by low values of the grand orbital $K = 2s$, $s = 1, 2, 3, \ldots$ can be virtually manifested.

Solutions to Eq. (2) are sought here in the form of a superposition of the cluster function $U^{\mathrm{cl}}_{nd}(\rho, \Omega_\rho) \equiv U^{\mathrm{cl}}_{nd}$ [12, 13] of the $n + d$ channel and all hyperspherical functions $U^{(\nu)}_s(\Omega_\rho) \equiv U^{(\nu)}_s$ [12–14], including the main harmonic $U_0(\Omega_\rho) \equiv U_0$:

$$U_i(\rho, \Omega_\rho) = c(\rho)U^{\mathrm{cl}}_{nd}(\rho, \Omega_\rho) + a_0(\rho)U_0(\Omega_\rho) + \sum_{s=1}^{s_{\max}}\sum_{\nu=1}^{3} a^{(\nu)}_s(\rho)U^{(\nu)}_s(\Omega). \quad (3)$$

The function U^{cl}_{nd} was included in expansion (3) in order to improve convergence in *s* with increasing ρ. The hyperradial coefficients $c(\rho)$, $a_0(\rho)$, and $a^{(\nu)}_s(\rho)$ are determined minimizing the functional

$$\Phi(U) = \frac{\langle U|\hat{Q}|U\rangle}{\langle U|U\rangle} \quad (4)$$

on the class of functions specified by Eq. (3). The wave function of the internal motion of the entire system is expanded in terms of the functions U_i found in the way outlined above:

$$\Psi = \sum_i R_i(\rho)U_i(\rho, \Omega_\rho). \quad (5)$$

After that, the hyperradial coefficients $R_i(\rho)$ appearing in (5) are determined from the known set of hyperradial

* e-mail: pavel.komarov@tversu.ru
** e-mail: pavel.nikishov@tversu.ru

equations [3]

$$\sum_j \left\langle U_i \left| -\frac{\partial^2}{\partial\rho^2} + I_j - E \right| U_j \right\rangle_\Omega R_j(\rho) = 0. \quad (6)$$

By using conventional methods, the required observables are extracted from the asymptotic behavior of $R_i(\rho)$ for $\rho \longrightarrow \infty$ (see [5]).

The basis of potential harmonics for the three-nucleon system virtually coincides with the complete system. Therefore, we include only these harmonics in expansion (3). Specific calculations will be performed with two known versions of realistic *NN* interactions, GPT [15] and SSC_B [16], as well as with the Tver central potential [9]. The first two reproduce fairly well binding energies and radii of light nuclei [17], while the third makes it possible to describe precisely low-energy *NN* scattering and the properties of the extremely light nuclear systems *d*, *t*, and ^{3}He [9].

2. CLUSTER FUNCTION FOR THE BINARY CHANNEL

Since potential harmonics were constructed previously (see, for example, [12, 13]), we consider the first term in expansion (3), $U_{nd}^{\rm cl}$. By definition, this function describes the free motion of the fragments *n* and *d* in their relative angular space. The harmonic that enters into $U_{nd}^{\rm cl}$ with the highest weight is known as a basic harmonic and is denoted by $U_K^{\rm b}$. Following the general rule adopted in the collective adiabatic approach, we normalize $U_{nd}^{\rm cl}$ by the canonical condition

$$\langle U_K^{\rm b} | U_{nd}^{\rm cl} \rangle = 1. \quad (7)$$

Since we consider low-energy scattering, we take into account only zero value of the relative orbital angular momentum, $L = 0$. In this case, the total angular momentum *J* can assume two values, $J = 1/2$ (doublet scattering) and $J = 3/2$ (quartet scattering). In view of the above, $U_{nd}^{\rm cl}$ can be represented as

$$U_{nd}^{\rm cl} = \frac{\hat{A}\rho_{\rm out}^{\mu}(1/2, 1; J)}{\langle U_K^{\rm b} | \hat{A}\rho_{\rm out}^{\mu}(1/2, 1; J)\rangle}, \quad (8)$$

where $(j_n, j_d; J)$ denote the result of composition of the angular momenta of the fragments (neutron j_n and deuteron j_d) into the total angular momentum *J*:

$$J = J_z = 1/2,$$
$$(1/2, 1; 1/2) = \left\{ -\frac{1}{\sqrt{3}}\alpha_{1/2} g_0^{(d)}(\rho_d) + \sqrt{\frac{2}{3}}\alpha_{-1/2} g_1^{(d)}(\rho_d) \right\} \beta_{-1/2}; \quad (9)$$

$$J = J_z = 3/2,$$
$$(1/2, 1; 3/2) = \alpha_{1/2} g_1^{(d)}(\rho_d)\beta_{-1/2}. \quad (10)$$

Here, α_μ and β_μ are, respectively, the spin and the isospin function of the neutron; $g_{J_z}^{(d)}(x)$ is the deuteron wave function characterized by a definite value of the angular-momentum projection onto the *z* axis; and $\rho_d = \rho_{ij}/\sqrt{2}$ is the deuteron hyperradius. A composition of the variable ρ_d with the hyperradius of relative motion, $\rho_{\rm out}$, yields the hyperradius of the full system:

$$\rho^2 = \rho_{\rm out}^2 + \rho_d^2. \quad (11)$$

The operator $\hat{A}$ ensures the antisymmetrization of particles in (8) that belong to the different fragments. The exponent $\mu \equiv \mu_{nd}$ is the polar decrement of the $n + d$ channel (see general formulas in [4]). It was shown to be independent of the quantum numbers of fragment relative motion. For the chosen potentials, all μ_{nd} values are close to 0.42. The basic harmonic in the doublet state has the exponent $K = K_{\rm min} = 0$ and obviously coincides with the triton main harmonic U_0. In the notation adopted in [5, 12], it has the form

$$U_0(\Omega_\rho) = \sqrt{\frac{1}{6\pi^3}} \begin{Vmatrix} + & + \\ + & - \\ - & - \end{Vmatrix}. \quad (12)$$

In the case of quartet scattering, the exponent of the basic harmonic $U_K^{\rm b}$ increases to the value of $K = K_{\rm min} = 2$, the harmonic itself being given by

$$U_2(\Omega_\rho) = \frac{2}{\pi^{3/2}\rho^2} \begin{Vmatrix} & + & + \\ & + & - \\ \rho^2 & + & - \end{Vmatrix}. \quad (13)$$

3. BASIC COMPUTATIONAL FORMULAS

Let us consider the matrix of the operator $\hat{Q}$ from Eq. (4) in the basis of the functions appearing in expansion (3). The matrix elements $\langle U_s^{(\nu)} | \hat{Q} | U_{s'}^{(\nu')} \rangle$ were constructed in [13]. If the Pauli exclusion principle is taken exactly into account, the remaining elements $\langle U_s^{(\nu)} | \hat{Q} | U_{nd}^{\rm cl} \rangle$ and $\langle U_{nd}^{\rm cl} | \hat{Q} | U_{nd}^{cl} \rangle$ can be calculated only numerically. We will use the method of random walks on a hypersphere in terms of cluster variables [18]. First, we perform averaging in spin–isospin space and represent the remaining configuration integrals in a form appropriate for the use of this method.

The result of applying the operator $\hat{Q}$ to a cluster function always has the form of the sum of three char-

Table 1. Binding energies and mass radii of the extremely light nuclei T and ^{3}He

Version of the *NN* potential	E_T, MeV	R_T, fm	$E_{^3\mathrm{He}}$, MeV	$R_{^3\mathrm{He}}$, fm
GPT	–8.1	1.77	–7.35	1.8
SSC_B	–8.63	1.7	–7.91	1.73
TCP	–8.48	1.67	–7.72	1.7
Experiment	–8.48	1.56	–7.72	1.7

acteristic terms that are described in detail elsewhere [6, 7, 13]:

$$\hat{Q}U_{nd}^{\mathrm{cl}} = EU_{nd}^{\mathrm{cl}} + \tilde{U}_{nd}^{\mathrm{cl}} + \hat{V}U_{nd}^{\mathrm{cl}}. \tag{14}$$

Here, $\tilde{U}_{nd}^{\mathrm{cl}}$ arises owing to the presence of the operator Δ_{3A-3} in $\hat{Q}$. As a result, the required overlap integrals become

$$\begin{aligned}\langle U_{nd}^{\mathrm{cl}}|\hat{Q}|U_{nd}^{\mathrm{cl}}\rangle &= E_{nd}\langle U_{nd}^{\mathrm{cl}}|U_{nd}^{\mathrm{cl}}\rangle \\ &+ \langle U_{nd}^{\mathrm{cl}}|\tilde{U}_{nd}^{\mathrm{cl}}\rangle + \langle U_{nd}^{\mathrm{cl}}|\hat{V}|U_{nd}^{\mathrm{cl}}\rangle, \\ \langle U_s^{(\nu)}|\hat{Q}|U_{nd}^{\mathrm{cl}}\rangle &= E_{nd}\langle U_s^{(\nu)}|U_{nd}^{\mathrm{cl}}\rangle \\ &+ \langle U_s^{(\nu)}|\tilde{U}_{nd}^{\mathrm{cl}}\rangle + \langle U_s^{(\nu)}|\hat{V}|U_{nd}^{\mathrm{cl}}\rangle.\end{aligned} \tag{15}$$

The overlap integrals $\langle U_{nd}^{\mathrm{cl}}|\tilde{U}_{nd}^{\mathrm{cl}}\rangle$ and $\langle U_s^{(\nu)}|\tilde{U}_{nd}^{\mathrm{cl}}\rangle$ can easily be obtained from, respectively, $\langle U_{nd}^{\mathrm{cl}}|U_{nd}^{\mathrm{cl}}\rangle$ and $\langle U_s^{(\nu)}|U_{nd}^{\mathrm{cl}}\rangle$ by means of the transformation described in [13]. The most complicated expression emerges for the matrix element involving the *NN* interaction $\hat{V}$. By way of example, we indicate that the expression for computing the overlap integral $\langle U_s^{(\nu)}|\hat{Q}|U_{nd}^{\mathrm{cl}}\rangle$ at $\nu = 3$ (tensor harmonic) has the form

$$\langle U_s^{(3)}|\hat{V}|U_{nd}^{\mathrm{cl}}\rangle = \frac{\pi}{128}\frac{\rho^3}{B_{nd}(\rho)}\frac{1}{\sqrt{\langle U_s^{(3)}|U_s^{(3)}\rangle}}\frac{\int I_{t,s}d\Omega_\rho}{\int d\Omega_\rho}, \tag{16}$$

where

$$B_{nd}(\rho) = \int_0^\rho \left(1 - \frac{x^2}{\rho^2}\right)^{(1+\mu)/2} x\varphi_0^{(d)}(x)dx, \tag{17}$$

Table 2. Doublet (a_2) and quartet (a_4) scattering lengths

Version of the *NN* potential	a_2, fm	a_4, fm
GPT [15]	2.5 ± 0.2	6.6 ± 0.2
SSC_B [16]	2.0 ± 0.2	6.3 ± 0.2
TCP [17]	2.1 ± 0.2	6.6 ± 0.2
Experiment [21]	0.65 ± 0.04	6.35 ± 0.02

$$\begin{aligned}I_{t,s} &= 8h_1^{(0)}\{4(12)_s^t\nu_t^{33} - (23)_s^t(3\nu_t^{31} + \nu_t^{13}) \\ &\times (3(\mathbf{n}_{12}\cdot\mathbf{n}_{23})^2 - 1) - (13)_s^t(-3\nu_t^{33} + \nu_t^{31}) \\ &\times (3(\mathbf{n}_{12}\cdot\mathbf{n}_{13})^2 - 1)\} + 4\sqrt{8}h_1^{(2)}\{[(12)_s^t(3\nu_c^{31} - 2\nu_t^{31}) \\ &+ (23)_s^t(3\nu_t^{33} + \nu_t^{31})](3(\mathbf{n}_{12}\cdot\mathbf{n}_{23})^2 - 1) \\ &- \left[(23)_s^t(3\nu_c^{33} + \nu_c^{31}) - \frac{1}{2}(13)_s^t(-3\nu_c^{33} + \nu_c^{31})\right] \\ &\times (3(\mathbf{n}_{13}\cdot\mathbf{n}_{23})^2 - 1) + (13)_s^t(-3\nu_t^{33} + \nu_t^{31}) \\ &\times (2 - 3((\mathbf{n}_{13}\cdot\mathbf{n}_{12})^2 + (\mathbf{n}_{13}\cdot\mathbf{n}_{23})^2 + (\mathbf{n}_{12}\cdot\mathbf{n}_{23})^2) \\ &+ 9(\mathbf{n}_{13}\cdot\mathbf{n}_{12})(\mathbf{n}_{12}\cdot\mathbf{n}_{23})(\mathbf{n}_{23}\cdot\mathbf{n}_{12}))\},\end{aligned} \tag{18}$$

$$h_1^{(L)} = \left(\frac{\rho_{\mathrm{out},1}}{\rho}\right)^\mu \rho_{23}^{-1}\varphi_L^{(d)}(\rho_{23}). \tag{19}$$

Here, $\varphi_L^{(d)}(x)$ are the radial components of the deuteron wave function, $\nu_x^{\mu\tau} \equiv \nu_x^{\mu\tau}(\rho_{12})$ stands for the central ($x = c$) or the tensor ($x = t$) radial components of the *NN* interaction, $\mathbf{n}_{ij} = \boldsymbol{\rho}_{ij}/\rho_{ij}$, and

$$(ij)_s^t = 2(1+s)\frac{\rho_{ij}^2}{\rho^2}P_{s-1}^{\left(\frac{5}{2},\frac{1}{2}\right)}\left(1 - \frac{\rho_{ij}^2}{\rho^2}\right). \tag{20}$$

We note that, in the worst case, about 0.2×10^6 random walks on a hypersphere are required to achieve a theoretical error not exceeding the experimental uncertainty. The can easily be implement with modern computers.

4. NUMERICAL RESULTS AND DISCUSSION

Using the above algorithm specified by Eqs. (1)–(20), we have first calculated the binding energies E and the mass radii R of the triton and ^{3}He with the chosen potentials. As can be seen from Table 1, all three potentials reproduce well the energy difference ($E_T - E_{^3\mathrm{He}}$), while the TCP potential also reproduces the absolute values of these energies individually.

We note that the bound states of extremely light nuclei can be successfully described by expanding the relevant wave function in terms of a basis that includes

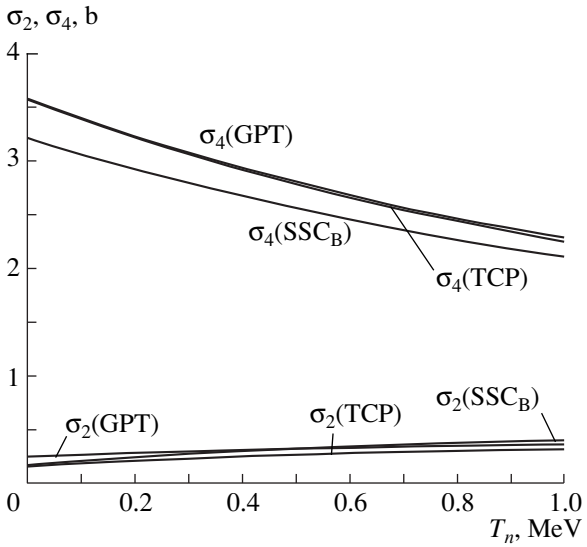

Fig. 1. Cross sections σ_2 and σ_4 for the elastic-scattering process $n + d \longrightarrow n + d$ versus the incident-neutron energy T_n (versions of the potential are indicated in parentheses).

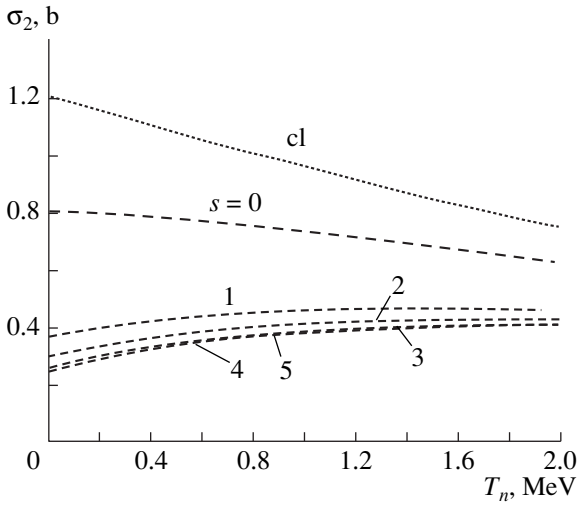

Fig. 2. Role of the potential harmonics in the formation of the cross section σ_2 for the GPT potential: the curve carrying the label "cl" corresponds to the cluster approximation, while the remaining curves represent the contributions of harmonics corresponding to the same excitation index s ($s = (K - K_{min})/2$).

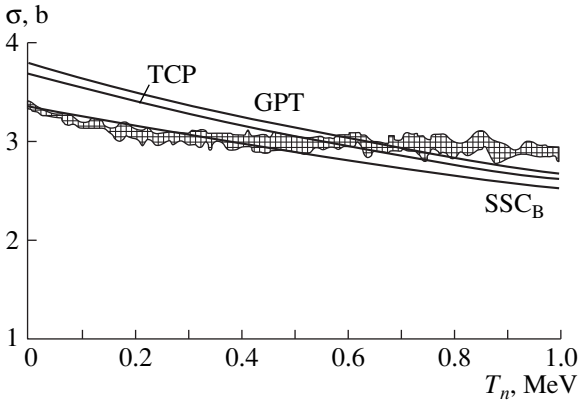

Fig. 3. As in Fig. 1, but for the total cross section $\sigma = \sigma_2 + \sigma_4$. The shaded area shows the scatter of experimental values from [21–23].

only potential harmonics (a complete convergence is achieved by taking into account all $s = s_{max} \leq 15$ potential harmonics). The presence of the cluster function in expansion (3) for the case of $A = 3$ and $L = 0$ substantially improves the convergence in the index s ($s_{max} \leq 5$). This does not affect the values of the observables, because U_{nd}^{cl} involves only the main harmonic and the potential ones.

Figure 1 displays basic features of the continuous spectrum—cross sections for doublet and quartet scattering (σ_2 and σ_4, respectively). Their dependence on the incident-neutron energy T_n shows virtually no qualitative variations in going over from one version of *NN* potential used to another. As in the case of the discrete spectrum, it is incorrect to calculate σ_2 by retaining only the cluster function in (3). The role of the potential harmonics is demonstrated in Fig. 2. The contribution of the potential harmonics to the cross section σ_4 is small for obvious reasons: in the region where the potential of fragment–fragment interaction is operative, the wave function is suppressed by the Pauli exclusion principle.

The calculated values of the doublet and the quartet scattering length (a_2 and a_4, respectively) are quoted in Table 2. The agreement of our results with those from [19], where the values of $a_2 = 2.8 \pm 0.3$ fm and $E_T = 8.3 \pm 0.2$ MeV were obtained for the GPT potential, gives sufficient ground to assume that the experimental data on a_2 require refinement. Figure 3 displays the total cross section. It is clear that the curves calculated for all potentials are within the experimental error.

In conclusion, we emphasize that the expansion in (3) is not complete, because it does not include nonpotential harmonics. From experience gained previously, it is known, however, that they are immaterial. In order to construct a numerically precise channel function, an integral approach where expansion (3) would be used as an input function at the first step of an iteration procedure was proposed in [20].

REFERENCES

1. A. M. Gorbatov *et al.*, Yad. Fiz. **50**, 1551 (1989) [Sov. J. Nucl. Phys. **50**, 962 (1989)].
2. A. M. Gorbatov *et al.*, Yad. Fiz. **49**, 144 (1989) [Sov. J. Nucl. Phys. **49**, 90 (1989)].
3. A. M. Gorbatov, Yad. Fiz. **55**, 44 (1992) [Sov. J. Nucl. Phys. **55**, 26 (1992)].

4. A. M. Gorbatov, Yad. Fiz. **55**, 1791 (1992) [Sov. J. Nucl. Phys. **55**, 991 (1992)].
5. A. M. Gorbatov, Yad. Fiz. **56** (8), 107 (1993) [Phys. At. Nucl. **56**, 1054 (1993)].
6. A. M. Gorbatov, Yad. Fiz. **57**, 651 (1994) [Phys. At. Nucl. **57**, 613 (1994)].
7. A. M. Gorbatov, Yad. Fiz. **59**, 1761 (1996) [Phys. At. Nucl. **59**, 1702 (1996)].
8. A. M. Gorbatov and A. Yu. Khazov, Yad. Fiz. **60**, 844 (1997) [Phys. At. Nucl. **60**, 751 (1997)].
9. A. M. Gorbatov *et al.*, Yad. Fiz. **63**, 501 (2000) [Phys. At. Nucl. **63**, 431 (2000)].
10. A. M. Gorbatov *et al.*, in *Theory of Strongly Interacting Quantum Systems* (Tver. Gos. Univ., Tver, 1999), p. 60.
11. D. R. Tilley, H. R. Weller, and H. H. Hasan, Nucl. Phys. A **474**, 1 (1987).
12. A. M. Gorbatov *et al.*, Izv. Akad. Nauk, Ser. Fiz. **62**, 1046 (1998).
13. A. M. Gorbatov *et al.*, in *Theory of Strongly Interacting Quantum Systems* (Tver. Gos. Univ., Tver, 1999), p. 97.
14. A. M. Gorbatov *et al.*, Yad. Fiz. **40**, 882 (1984) [Sov. J. Nucl. Phys. **40**, 561 (1984)].
15. D. Gogny, P. Piers, and R. de Tourreil, Phys. Lett. B **32**, 591 (1970).
16. R. de Tourreil and D. W. L. Sprung, Nucl. Phys. A **201**, 193 (1973).
17. A. M. Gorbatov *et al.*, Izv. Akad. Nauk, Ser. Fiz. **60** (11), 118 (1996).
18. A. M. Gorbatov and A. Yu. Khazov, Yad. Fiz. **60**, 2161 (1997) [Phys. At. Nucl. **60**, 1979 (1997)].
19. M. A. Hennel, J. Phys. G **3**, 1069 (1977).
20. A. M. Gorbatov *et al.*, Izv. Akad. Nauk, Ser. Fiz. **63**, 1018 (1999).
21. P. Stoler, N. N. Kaushal, and F. Green, Phys. Rev. C **8**, 1539 (1973).
22. P. Stoler, N. N. Kaushal, and F. Green, Phys. Rev. Lett. **29**, 1745 (1972).
23. T. W. Phillips and B. L. Berman, Phys. Rev. C **22**, 384 (1980).

Translated by M. Kobrinsky

Physics of Atomic Nuclei, Vol. 64, No. 2, 2001, pp. 233–242. Translated from Yadernaya Fizika, Vol. 64, No. 2, 2001, pp. 278–288.

NUCLEI
Theory

P-Matrix Approach and Parameters of Low-Energy Scattering in the Presence of a Coulomb Potential

V. A. Babenko and N. M. Petrov*

Bogolyubov Institute for Theoretical Physics, National Academy of Sciences of Ukraine, Metrologicheskaya ul. 14b, Kiev, 252143 Ukraine

Received September 22, 1999; in final form, April 12, 2000

Abstract—The scattering of two charged strongly interacting particles is described on the basis of the *P*-matrix approach. In the *P* matrix, it is proposed to isolate explicitly the background term corresponding to purely Coulomb interaction, whereby it becomes possible to improve convergence of the expansions used and to obtain a correct asymptotic behavior of observables at high energies. The expressions for the purely Coulomb background *P* matrix, its poles and residues, and purely Coulomb eigenfunctions in the *P*-matrix approach are obtained. The nuclear–Coulomb parameters of the low-energy scattering of two charged hadrons are investigated on the basis of this approach combined with the method for isolating the background *P* matrix. Simple explicit expressions for the nuclear–Coulomb scattering length and effective range in terms of the residual *P* matrix are derived. For models of short-range strong interaction, these expressions give a general form of nuclear–Coulomb parameters for low-energy scattering. Specific applications of the general expressions derived in this study are exemplified by considering, on the basis of these expressions, some exactly solvable models of strong interaction, including the hard-core model, and, for these models, the nuclear–Coulomb parameters for low-energy scattering at arbitrary values of the orbital angular momentum are found explicitly for the first time. In particular, the nuclear–Coulomb scattering length and effective range are obtained explicitly for the boundary-condition model, the model of a hard-core delta-shell potential, the Margenau model, and the model of square-well hard-core potential. © *2001 MAIK "Nauka/Interperiodica".*

1. INTRODUCTION

The *P*-matrix approach to describing hadron–hadron interaction was first proposed by Jaffe and Low [1] and was then developed in a number of studies [2–4]. This approach is a modification of the well-known Wigner–Eisenbud $\mathcal{R}$-matrix theory [5, 6]. Within *P*-matrix approach, the scattering amplitude is expressed in terms of the logarithmic derivative of the wave function at the surface of the strong-interaction region—that is, in terms of the *P* matrix—so that it is assumed that the configuration space of the system is broken down into two regions, the external region, where the interaction of particles can be described in terms of a two-particle potential, and the internal region, where strong interaction is dominant. For the *P* matrix, a so-called dispersion relation that appears to be its pole expansion and which establishes its energy dependence can be derived on the basis of quite general assumptions. Observables can then be described in terms of a finite number of parameters.

In [3, 4, 7], a method was proposed for explicitly isolating a free background part in the *P* matrix. This method is advantageous in that it simplifies the implementation of the *P*-matrix approach in specific applications and extends the region of its applicability. The free *P* matrix, which corresponds to the absence of interaction, was isolated as the background part in the aforementioned studies. This is natural in dealing with the scattering of neutral particles. Here, we propose a generalization of the isolation method to the case involving charged particles, so that there is long-range Coulomb interaction in the system along with strong interaction. It is well known that, in this case, scattering theory requires a nontrivial modification. We show that the idea of explicitly isolating a background part in the *P* matrix as put forth in [3, 4, 7] can be implemented for charged particles as well and that, for the background *P* matrix, it is advisable in this case to take the purely Coulomb *P* matrix—that is, the logarithmic derivative of the regular Coulomb function at the surface of the interaction region. It turns out that the isolation of the background Coulomb part offers the same advantages as in the absence of Coulomb interaction.

As an application of the *P*-matrix approach combined with the method for isolating the background Coulomb *P* matrix, we consider the scattering length and the effective range for low-energy nuclear–Coulomb scattering. These parameters are important physical quantities characterizing the scattering of charged hadrons and light nuclei at low energies. We obtain simple explicit expressions for the nuclear–Coulomb parameters of low-energy scattering in terms of the parameters of the residual *P* matrix; these expressions make it possible to analyze and evaluate the nuclear–Coulomb scattering length and effective range and to

* e-mail: pet@gluk.apc.org

find them directly for short-range strong-interaction potentials. As a matter of fact, the expressions that we obtain here determine a general form of the nuclear–Coulomb parameters of low-energy scattering for models of short-range strong interaction. In [8], expressions for the nuclear–Coulomb parameters of low-energy scattering in terms of the P-matrix parameters were obtained without resort to the isolation method. Those expressions are more cumbersome and less convenient in applications than the present ones. Basically, the results presented in [8] therefore cease to be of value and significance.

Much attention has been given to the nuclear–Coulomb parameters of low-energy scattering (see, for example, [9–12]) since these physical quantities play an important role in theoretical and experimental investigations. In some studies (see for example, [13–17]), these parameters were determined explicitly for some specific cases of separable nuclear potentials (in particular, for the Yamaguchi potential). Here, we find a general form of the nuclear–Coulomb scattering parameters for a rather broad class of local strong-interaction models—namely, for models of short-range interaction. General expressions obtained for the low-energy parameters make it possible for the first time to determine these quantities explicitly for a number of exactly solvable hard-core strong-interaction models. We emphasize that it is the use of the simple expressions obtained by the isolation method that made it possible to simplify significantly the relevant consideration. It should also be noted that the investigation presented here was performed for an arbitrary value of the orbital angular momentum l.

2. DISPERSION RELATION FOR THE P MATRIX AND NUCLEAR–COULOMB OBSERVABLES

For the elastic scattering of two charged strongly interacting particles, the radial wave function $\psi_{lk}(r)$ of relative motion in a state characterized by a specific value of the orbital angular momentum l is regular at the origin and satisfies the radial Schrödinger equation

$$\left[\frac{d^2}{dr^2} + E - \frac{l(l+1)}{r^2} - V(r)\right]\psi_{lk}(r) = 0 \qquad (1)$$

with the potential

$$V(r) = V_s(r) + V_c(r), \qquad (2)$$

where $V_s(r)$ is a short-range strong potential (by assumption, it has a finite range R) and $V_{\text{Coul}}(r) = 2\xi k/r$ is a convenient Coulomb potential. For the sake of convenience, we further use the Coulomb parameter

$$\xi \equiv \frac{\mu e_1 e_2}{\hbar^2 k} = \frac{1}{a_B k}, \qquad (3)$$

where a_B is the Bohr radius,

$$a_B \equiv \frac{\hbar^2}{\mu e_1 e_2}, \qquad (4)$$

e_1 and e_2 being the charges of the particles involved in the scattering process. We everywhere use the system of units where the reduced Planck constant and the doubled reduced mass of the two particles are both equal to unity ($\hbar = 2\mu = 1$), so that the energy of the relative motion, E, is expressed in terms of the wave number k as $E = k^2$.

At infinity, the radial wave function satisfies the scattering boundary condition

$$\psi_{lk}(r) \underset{r\to\infty}{\longrightarrow} \bar{\psi}_{lk}(r) \equiv e^{i\delta_l(k)}[\cos\nu_l(k)F_l(\xi, kr) + \sin\nu_l(k)G_l(\xi, kr)], \qquad (5)$$

where $\bar{\psi}_{lk}(r)$ is the asymptotic wave function for the continuous spectrum, while $F_l(\xi, kr)$ and $G_l(\xi, kr)$ are, respectively, the regular and the irregular wave functions [18], whose asymptotic behavior at infinity is given by

$$F_l(\xi, kr) \underset{r\to\infty}{\longrightarrow} \sin\left(kr - \xi\ln 2kr - \frac{l\pi}{2} + \sigma_l(k)\right), \qquad (6)$$

$$G_l(\xi, kr) \underset{r\to\infty}{\longrightarrow} \cos\left(kr - \xi\ln 2kr - \frac{l\pi}{2} + \sigma_l(k)\right). \qquad (7)$$

Here, $\sigma_l(k) \equiv \arg\Gamma(l + 1 + i\xi)$ is the purely Coulomb phase shift, and the total phase shift $\delta_l(k)$ has the form

$$\delta_l(k) = \sigma_l(k) + \nu_l(k), \qquad (8)$$

where $\nu_l(k)$ is the nuclear–Coulomb phase shift.

The P matrix $P_l(E)$ is defined in terms of the logarithmic derivative of the radial wave function at the surface of the strong-interaction region ($r = R$),

$$P_l(E) \equiv \frac{R\psi'_{lk}(R)}{\psi_{lk}(R)}. \qquad (9)$$

In the internal region $r \le R$, we introduce a complete set of orthonormalized eigenfunctions $u_{ln}(r)$ that satisfy the Schrödinger equation (1) and the homogeneous boundary conditions

$$u_{ln}(0) = 0, \quad u_{ln}(R) = 0 \qquad (10)$$

at the ends of the interval [0, R]. Nontrivial solutions that obey the conditions in (10) exist only at some energy eigenvalues E_{ln} that are determined by solving the Sturm–Liouville problem specified by Eqs. (1) and (10). The orthonormalization conditions have the form

$$\int_0^R u_{lm}u_{ln}dr = \delta_{mn}. \qquad (11)$$

By expanding the wave function in the internal region in a series in eigenfunctions $u_{ln}(r)$, we find that,

for the *P* matrix, there is the dispersion relation [1, 3, 4]

$$P_l(E) = P_l(0) + \sum_{n=1}^{\infty} \frac{E}{E_{ln}} \frac{\gamma_{ln}^2}{E - E_{ln}}, \quad (12)$$

where

$$\gamma_{ln} \equiv \sqrt{R} u'_{ln}(R). \quad (13)$$

Relation (12) involves a constant $P_l(0)$, the *P* matrix at zero energy, and it is the isolation of this constant that ensures convergence of the remaining series. The dispersion relation (12), which represents a pole expansion of the *P* matrix, establishes the general form of its energy dependence. This dependence is completely determined by the states of the compound system which are characterized by the energy eigenvalues E_{ln} and the residues γ_{ln}^2. These quantities in turn are controlled by the physical properties of the system in the internal region and are independent of energy *E*.

Let us now establish the relation between the *S* matrix and the *P* matrix. For this, we note that the wave function in the outer region, $\bar{\psi}_{lk}(r)$, can be represented in the general form

$$\bar{\psi}_{lk}(r) = \frac{i}{2}[H_l^{(-)}(\xi, kr) - S_l(k) H_l^{(+)}(\xi, kr)], \quad r > R, \quad (14)$$

where $H_l^{(+)}(\xi, kr)$ and $H_l^{(-)}(\xi, kr)$ are the Coulomb Jost solutions given by

$$H_l^{(\pm)}(\xi, kr) = e^{\mp i\sigma_l(k)}[G_l(\xi, kr) \pm iF_l(\xi, kr)], \quad (15)$$

which represent the diverging and the converging waves distorted by the Coulomb potential. Accordingly, their asymptotic behavior is given by

$$H_l^{(\pm)}(\xi, kr) \xrightarrow[r\to\infty]{} e^{\pm i\left(kr - \xi \ln 2kr - \frac{l\pi}{2}\right)}. \quad (16)$$

By using the matching conditions at the point $r = R$ and definition (9), we find that the *S* matrix can be recast into the form

$$S_l(k) = S_l^{(h)}(k) \frac{P_l^{(-)}(k) - P_l(k)}{P_l^{(+)}(k) - P_l(k)}, \quad (17)$$

where

$$S_l^{(h)}(k) \equiv \frac{H_l^{(-)}(\xi, kR)}{H_l^{(+)}(\xi, kR)} \quad (18)$$

is the *S* matrix corresponding to the scattering on a hard core of radius *R* in the presence of the Coulomb potential and $P_l^{(\pm)}(k)$ are the logarithmic derivatives of the diverging and converging Coulomb waves at the boundary surface,

$$P_l^{(\pm)}(k) \equiv \frac{kRH_l^{(\pm)'}(\xi, kR)}{H_l^{(\pm)}(\xi, kR)}. \quad (19)$$

Hereafter, a prime denotes differentiation with respect to the variable $\rho = kR$. The real and the imaginary part of the function $P_l^{(+)}(k)$ are usually denoted by $\Delta_l(k)$ and $s_l(k)$, respectively; since the relation $P_l^{(+)}(k) = P_l^{*(-)}(k)$ obviously holds, we can write

$$P_l^{(\pm)}(k) = \Delta_l(k) \pm is_l(k), \quad (20)$$

where the functions $s_l(k)$ and $\Delta_l(k)$ are expressed in terms of the Coulomb functions [19] as

$$s_l(k) = \frac{kR}{F_l^2(\xi, kR) + G_l^2(\xi, kR)}, \quad (21)$$

$$\Delta_l(k) = s_l(k)[F_l(\xi, kR)F'_l(\xi, kR) + G_l(\xi, kR)G'_l(\xi, kR)]. \quad (22)$$

With the aid of Eqs. (17) and (20), it can easily be found that the nuclear–Coulomb phase shift can be represented as

$$\nu_l(k) = \zeta_l(k) + \arctan\frac{s_l(k)}{P_l(k) - \Delta_l(k)}, \quad (23)$$

where the phase shift $\zeta_l(k)$ for scattering on a hard core of radius *R* in the presence of the Coulomb interaction is given by

$$\zeta_l(k) \equiv -\arctan\frac{F_l(\xi, kR)}{G_l(\xi, kR)}. \quad (24)$$

Expressions (17) and (23) for the observables reveal a significant drawback of the *P*-matrix approach based on the dispersion formula (12) as an approximation of the *P* matrix: if only a finite number of terms are retained, the observables in question will have an incorrect asymptotic behavior at high energies. By way of example, we indicate that, with increasing energy, the phase shift (23) will then behave as the phase shift $\zeta_l(k)$ for scattering on a hard core; that is, it will tend to infinity,

$$\nu_l(k) \xrightarrow[k\to\infty]{} -kR + O(1). \quad (25)$$

But in fact, the phase shift must vanish at high energies, at least for regular potentials.

3. PURELY COULOMB *P* MATRIX

An incorrect asymptotic behavior of observables at high energies can be avoided by isolating the background part in the *P* matrix. In the presence of Coulomb interaction, we define the background *P* matrix as the

purely Coulomb P matrix—that is, in terms of the logarithmic derivative of the regular Coulomb function,

$$P_l^{(c)}(E) \equiv \frac{kRF_l'(\xi, kR)}{F_l(\xi, kR)}. \quad (26)$$

We recall that the regular Coulomb function $F_l(\xi, \rho)$ is expressed in terms of the confluent hypergeometric function $\Phi(a, b; z)$ as [18]

$$F_l(\xi, \rho) = C_l(\xi)e^{-i\rho}\rho^{l+1}\Phi(l+1-i\xi, 2l+2; 2i\rho), \quad (27)$$

where

$$C_l(\xi) \equiv \frac{2^l}{(2l+1)!}e^{-\pi\xi/2}|\Gamma(l+1+i\xi)| \quad (28)$$

is the Coulomb penetrability factor that is a rather complicated function of energy and which is introduced in order to ensure the required asymptotic behavior of the function $F_l(\xi, \rho)$ at infinity [see Eq. (6)]. If, however, we consider only the internal region $0 \le r \le R$, it is more convenient to introduce a solution that does not involve the factor $C_l(\xi)$ and which possesses simpler properties near the origin. We define such a solution $\phi_l(\xi, \rho)$ through the relation

$$F_l(\xi, \rho) = (2l+1)!!C_l(\xi)\phi_l(\xi, \rho), \quad (29)$$

where the factor $(2l+1)!!$ was introduced in order that, upon switching the Coulomb interaction off, the function $\phi_l(\xi, \rho)$ reduce to the spherical Riccati–Bessel function:

$$\phi_l(0, \rho) = j_l(\rho). \quad (30)$$

The expression for the function $\phi_l(\xi, \rho)$ in terms of a confluent hypergeometric function can easily be found with the aid of Eqs. (27) and (29). The Coulomb P matrix as expressed in terms of the solution $\phi_l(\xi, \rho)$ has the form

$$P_l^{(c)}(E) = \frac{kR\phi_l'(\xi, kR)}{\phi_l(\xi, kR)}, \quad (31)$$

which is analogous to (26).

The positions $E_{ln}^{(c)} \equiv k_{ln}^{(c)^2}$ of the poles of the Coulomb P matrix—they depend on the Bohr radius a_B and on the interaction range R ($E_{ln}^{(c)} = E_{ln}^{(c)}(a_B, R)$)—are defined by the roots of the denominator of the expression on the right-hand side of (31),

$$\phi_l\left(\frac{1}{a_B k_{ln}}, k_{ln}R\right) = 0. \quad (32)$$

The Coulomb eigenfunctions $u_{ln}^{(c)}(r)$, which obey the Schrödinger equation (1) with the purely Coulomb potential and the boundary condition (10), are given by

$$u_{ln}^{(c)}(r) = \frac{\gamma_{ln}^{(c)}}{\sqrt{R}k_{ln}^{(c)}}\frac{\phi_l(\xi_{ln}, k_{ln}r)}{\phi_l'(\xi_{ln}, k_{ln}R)}, \quad (33)$$

where $\xi_{ln} \equiv 1/a_B k_{ln}$ and where the parameters $\gamma_{ln}^{(c)}$, which are determined from the normalization condition for the eigenfunctions, can be found if we use the Green's theorem,

$$u_{lk_1}(R)u_{lk_2}'(R) - u_{lk_1}'(R)u_{lk_2}(R) = (k_1^2 - k_2^2)\int_0^R u_{lk_1}u_{lk_2}dr, \quad (34)$$

for two solutions to Eq. (1) that correspond to two different energy values, k_1^2 and k_2^2. By substituting (33) into (34), going over to the limit $k_1 \longrightarrow k_2 = k_{ln}$, and taking into account Eqs. (11) and (13), we find that the expression for the Coulomb residues $\gamma_{ln}^{(c)^2}$ can be recast into the form

$$\gamma_{ln}^{(c)^2} = \frac{2E_{ln}^{(c)}}{1 - \theta_l(\xi_{ln}, k_{ln}R)/a_B R E_{ln}^{(c)}\phi_l'(\xi_{ln}, k_{ln}R)}, \quad (35)$$

where the function $\theta_l(\xi, \rho)$, which is the derivative of the function $\phi_l(\xi, \rho)$ with respect to the parameter ξ,

$$\theta_l(\xi, \rho) \equiv \frac{\partial\phi_l(\xi, \rho)}{\partial\xi}, \quad (36)$$

can be directly expressed in terms of a confluent hypergeometric function.

Thus, we have completely determined the parameters of the Coulomb P matrix (its poles and residues) and found the Coulomb eigenfunctions. The dispersion relation for the Coulomb P matrix has the form (12); that is,

$$P_l^{(c)}(E) = P_l^{(c)}(0) + \sum_{n=1}^{\infty}\frac{E}{E_{ln}^{(c)}}\frac{\gamma_{ln}^{(c)^2}}{E - E_{ln}}, \quad (37)$$

where the P matrix at zero energy, $P_l^{(c)}(0)$, is given by expression

$$P_l^{(c)}(0) = \frac{zI_{2l}(z)}{I_{2l+1}(z)} - l, \quad (38)$$

which can be directly derived from (31) for $k \longrightarrow 0$ by using the expansion of the regular Coulomb function and its derivatives in terms of Bessel functions [18, 20, 21]. In expression (38), $I_\nu(z)$ are modified Bessel functions and the dimensionless parameter z is given by

$$z \equiv 2\sqrt{2R/a_B}. \quad (39)$$

So far, we have considered the case of Coulomb repulsion ($a_B > 0$). In the case of Coulomb attraction ($a_B <$

0), $P_l^{(c)}(0)$ has the form

$$P_l^{(c)}(0) = \frac{\zeta J_{2l}(\zeta)}{J_{2l+1}(\zeta)} - l, \tag{40}$$

where $J_\nu(\zeta)$ are Bessel functions and $\zeta \equiv 2\sqrt{2R/|a_B|}$.

4. ISOLATING THE PURELY COULOMB BACKGROUND *P* MATRIX

In nuclear–Coulomb *P* matrix (9), we now isolate explicitly the purely Coulomb background *P* matrix (26), following a way that is similar to that used to isolate explicitly the free background *P* matrix in the absence of Coulomb interaction [3, 4, 7]. We represent this transformation in the form

$$P_l(E) = P_l^{(c)}(E) + \hat{P}_l(E). \tag{41}$$

With the aid of Eqs. (12) and (37), it can be shown that, for the residual nuclear–Coulomb *P* matrix $\hat{P}_l(E)$, we have the expansion

$$\hat{P}_l(E) = \hat{P}_l(0) + \sum_{n=1}^{\infty}\left[\frac{E}{E_{ln}}\frac{\gamma_{ln}^2}{E-E_{ln}} - \frac{E}{E_{ln}^{(c)}}\frac{\gamma_{ln}^{(c)^2}}{E-E_{ln}^{(c)}}\right]. \tag{42}$$

By comparing the expansions in (12) and in (42) for the functions $P_l(E)$ and $\hat{P}_l(E)$, respectively, we conclude that the isolation of the purely Coulomb background part in the nuclear–Coulomb *P* matrix according to (41) amounts to a partial summation of the series in (12), where one isolates the part that corresponds to the Coulomb interaction and which is known explicitly. This naturally improves convergence of the original series, thereby making it possible to obtain a more accurate representation of observables as functions of energy. It can be shown that the expansion in (42) converges at the same rate as a series whose general term is proportional to $1/n^4$, while the expansion in (12) converges as $1/n^2$—that is, much more slowly.

By making transformation (41) in Eq. (17) and using the relation

$$P_l^{(c)}(k) - P_l^{(\pm)}(k) = \frac{kRe^{\mp i\sigma_l}}{F_l(\xi, kR)H_l^{(\pm)}(\xi, kR)} \equiv \frac{1}{c_l^{(\pm)}(k)}, \tag{43}$$

which can easily be verified for logarithmic derivatives, we can straightforwardly express the nuclear–Coulomb *S* matrix $S_l^{(cs)}(E) = e^{2i\nu_l(k)}$ in terms of the residual *P* matrix $\hat{P}_l(E)$ as

$$S_l^{(cs)}(E) = \frac{1 + c_l^{(-)}(k)\hat{P}_l(E)}{1 + c_l^{(+)}(k)\hat{P}_l(E)}, \tag{44}$$

where the functions $c_l^{(\pm)}(k)$ are determined according to (43) and obviously satisfy the relation $c_l^{(+)}(k) = c_l^{*(-)}(k)$. With the aid of (44), we can easily represent the nuclear–Coulomb phase shift as

$$\nu_l(k) = -\arctan\frac{F_l^2(\xi, kR)\hat{P}_l(E)}{kR + F_l(\xi, kR)G_l(\xi, kR)\hat{P}_l(E)}. \tag{45}$$

From Eqs. (44) and (45), it is obvious that, if only a finite number of terms are retained in the pole expansion (42) for $\hat{P}_l(E)$, the *S* matrix and the phase shift will have a correct asymptotic behavior at high energies:

$$S_l(k) \xrightarrow[k\to\infty]{} 1, \quad \nu_l(k) \xrightarrow[k\to\infty]{} 0. \tag{46}$$

Thus, an isolation of the purely Coulomb background term in the *P* matrix leads to a correct asymptotic behavior of the observables in question at high energies if the residual *P* matrix is approximated by a finite number of pole terms. We can see that the transformation in (41) has a transparent mathematical and physical substantiation and that its application provides the same advantages as in the absence of Coulomb interaction.

5. EXPRESSIONS FOR THE NUCLEAR–COULOMB PARAMETERS OF LOW-ENERGY SCATTERING IN TERMS OF THE PARAMETERS OF THE RESIDUAL *P* MATRIX

A great number of studies (see, for example, [22–27]) have been devoted to the problem of generalizing and modifying effective-range theory in the presence of long-range Coulomb interaction. As a result, the Coulomb-modified effective-range function $K_{csl}(E)$ was introduced, and the nuclear–Coulomb scattering length and effective range were determined for the case of *S*-wave scattering, as well as for scattering in a state characterized by an arbitrary value of the orbital angular momentum *l*. In [22, 25], it was shown that, in the case of an arbitrary orbital angular momentum, the effective-range expansion in the presence of Coulomb interaction has the form

$$K_l(E) \equiv (2l+1)!!^2 C_l^2(\xi)k^{2l+1}\left[\cot\nu_l(k) + \frac{2\xi}{C_0^2(\xi)}h(\xi)\right] = -\frac{1}{a_l} + \frac{1}{2}r_l k^2 + \ldots, \tag{47}$$

where the function $h(\xi)$ is expressed in terms of the digamma function $\psi(z) \equiv \Gamma'(z)/\Gamma(z)$ as

$$h(\xi) \equiv \mathrm{Re}\,\psi(1 + i\xi) - \ln|\xi|. \quad (48)$$

In the complex plane of energy E, the nuclear–Coulomb effective-range function $K_l(E)$ is analytic in some domain near the origin [26]; hence, it can be expanded in the Maclaurin series (47) in powers of E in the vicinity of the point $E = 0$. Thus, a special role of the function $K_l(E)$ is associated with its analyticity near $E = 0$. The nuclear–Coulomb scattering length a_l and effective range r_l are determined in this case in terms in the coefficients in the expansion (47) of the function $K_l(E)$. We note that, in a large number of studies, the nuclear–Coulomb quantities, such as a_l, r_l, and K_l, are equipped with the additional indices c and s, which label parameters and functions associated with, respectively, Coulomb and short-range interactions. This was done in order to distinguish these quantities from their counterparts in the absence of Coulomb interaction, which are labeled only with the index s. Since we do not consider here the case where there is no Coulomb field, the indices c and s are suppressed on all nuclear–Coulomb quantities.

For a further analysis, it is reasonable to introduce the dimensionless inverse scattering length γ_l and the dimensionless effective range ρ_l as

$$\gamma_l \equiv \frac{l!^2 a_B^{2l+1}}{4a_l}, \quad (49)$$

$$\rho_l \equiv 3l!^2 a_B^{2l-1} r_l. \quad (50)$$

In the particular case of scattering on a hard core of radius R [$\psi_{lk}(R) = 0$, $P_l(E) = \infty$], the parameters γ_l and ρ_l can easily be found in the explicit form [8]

$$\gamma_l^h = \frac{K_\nu(z)}{I_\nu(z)}, \quad (51)$$

$$\rho_l^h = 1 - \mu_l \gamma_l^h + \frac{2(\lambda_l - \beta)}{I_\nu^2(z)}, \quad (52)$$

where the superscript h denotes, as previously, a hard core and $I_\nu(z)$ and $K_\nu(z)$ are modified Bessel functions. The constants ν, λ_l, and μ_l are given by

$$\nu \equiv 2l + 1, \quad (53)$$

$$\lambda_l \equiv l(l+1), \quad (54)$$

$$\mu_l \equiv 4\nu\lambda_l, \quad (55)$$

while the dimensionless parameter β is defined as

$$\beta \equiv \frac{R}{a_B}. \quad (56)$$

As before, the parameter z has the form (39). In order to render the expressions presented below less cumbersome, it is convenient to isolate explicitly, in the low-energy parameters γ_l and ρ_l, the parts that correspond to scattering on a hard core. Accordingly, we set

$$\gamma_l = \gamma_l^h + \hat{\gamma}_l, \quad (57)$$

$$\rho_l = \rho_l^h + \hat{\rho}_l, \quad (58)$$

defining, in this way, the residual low-energy nuclear–Coulomb scattering parameters $\hat{\gamma}_l$ and $\hat{\rho}_l$.

Let us further express the nuclear–Coulomb scattering length and effective range in terms of the residual P matrix. By substituting (45) into (47), we find that the nuclear–Coulomb effective-range function as expressed in terms of the residual P matrix is given by

$$K_l(E) = (2l+1)!!^2 C_l^2(\xi) k^{2l+1}\left[\frac{2\xi}{C_0^2(\xi)}h(\xi) - \frac{G_l(\xi,\rho)}{F_l(\xi,\rho)} - \frac{\rho}{F_l^2(\xi,\rho)\hat{P}_l(E)}\right], \quad (59)$$

where, as before, we use the notation $\rho = kR$. Let us expand the right-hand side of Eq. (59) in a Maclaurin series in powers of energy $E = k^2$. It is obvious that, as long as we are interested neither in the shape parameter nor in higher expansion coefficients, it is sufficient to retain only the terms that are linear in E. We further make use of the known relation for the Coulomb penetrability factor [18],

$$\frac{C_l^2(\xi)}{C_0^2(\xi)} = \frac{2^{2l}}{(2l+1)!^2}(1^2+\xi^2)(2^2+\xi^2)\ldots(l^2+\xi^2), \quad (60)$$

and of the asymptotic expression for the function $h(\xi)$ at low energies [18],

$$h(\xi) \underset{\xi\to\infty}{\simeq} \frac{1}{12\xi^2} + \frac{1}{120\xi^4} + \ldots. \quad (61)$$

The expansions of the Coulomb wave functions in power series in energy E were previously studied by many authors [20, 21, 28, 29]. To terms that are linear in energy, these expansions for the case of Coulomb repulsion can written as

$$F_l(\xi,\rho) = \frac{(2l+1)!C_l(\xi)}{(2\xi)^{l+1}}\frac{z}{2}\left\{I_\nu(z) - \frac{z^3}{96\xi^2}\left[I_{\nu+1}(z) + \frac{2l}{z}I_{\nu+2}(z)\right] + \ldots\right\}, \quad (62)$$

$$G_l(\xi,\rho) \simeq \frac{(2l+1)!C_l(\xi)}{(2\xi)^l C_0^2(\xi)}z\left\{K_\nu(z) + \frac{z^3}{96\xi^2}\left[K_{\nu+1}(z) - \frac{2l}{z}K_{\nu+2}(z)\right] + \ldots\right\}. \quad (63)$$

The dispersion relation for the residual P matrix (42) can be recast into the form

$$\hat{P}_l(E) = \sum_{n=1}^{\infty}\left[\frac{\gamma_{ln}^2}{E-E_{ln}} - \frac{\gamma_{ln}^{(c)^2}}{E-E_{ln}^{(c)}}\right]. \quad (64)$$

This expansion contains no additional parameters and is completely determined by the quantities E_{ln} and γ_{ln}^2. It can be shown that the expansion in (64) converges at the same rate as a series whose general term is proportional to $1/n^2$. The analyticity of the residual P matrix in a vicinity of the point $E = 0$ immediately follows from (64) if all energy eigenvalues differ from zero. The expansion of the residual P matrix in a power series in energy E can be written in the form

$$\hat{P}_l(E) = \hat{P}_l + \hat{Q}_l\rho^2 + \ldots, \quad (65)$$

where

$$\hat{P}_l \equiv \hat{P}_l(0), \quad (66)$$

$$\hat{Q}_l \equiv \frac{1}{R^2}\hat{P}_l'(0) \quad (67)$$

are dimensionless expansion coefficients. We can easily express the quantities $\hat{P}_l$ and $\hat{Q}_l$ in terms of the P-matrix parameters as

$$\hat{P}_l = \sum_{n=1}^{\infty}\left[\frac{\gamma_{ln}^{(c)^2}}{E_{ln}^{(c)}} - \frac{\gamma_{ln}^2}{E_{ln}}\right], \quad (68)$$

$$\hat{Q}_l = \frac{1}{R^2}\sum_{n=1}^{\infty}\left[\frac{\gamma_{ln}^{(c)^2}}{E_{ln}^{(c)^2}} - \frac{\gamma_{ln}^2}{E_{ln}^2}\right]. \quad (69)$$

We also note that, on the basis of Eq. (41), the quantities $\hat{P}_l$ and $\hat{Q}_l$ can be determined from the relations

$$P_l = P_l^{(c)} + \hat{P}_l, \quad (70)$$

$$Q_l = Q_l^{(c)} + \hat{Q}_l, \quad (71)$$

where

$$P_l \equiv P_l(0), \quad (72)$$

$$Q_l \equiv \frac{1}{R^2}P_l'(0) \quad (73)$$

are parameters in the expansion of the P matrix,

$$P_l(E) = P_l + Q_l\rho^2 + \ldots. \quad (74)$$

The parameters $P_l^{(c)}$ and $Q_l^{(c)}$ in the expansion of the purely Coulomb background P matrix can be found explicitly from Eqs. (26) and (62). The results are

$$P_l^{(c)} = l + 1 + \frac{z}{2}\frac{I_{\nu+1}(z)}{I_\nu(z)}, \quad (75)$$

$$2\beta(3Q_l^{(c)} + 1) = l\nu + \left(lz - \frac{\mu_l}{z}\right)\frac{I_{\nu+1}(z)}{I_\nu(z)} + 2(\beta - \lambda_l)\frac{I_{\nu+1}^2(z)}{I_\nu^2(z)}. \quad (76)$$

Substituting now expressions (60)–(63) and (65) into Eq. (59) and taking into account Eq. (47), we arrive at explicit expressions for the inverse scattering length $\hat{\gamma}_l$ and the effective range $\hat{\rho}_l$, also referred to as the dimensionless nuclear–Coulomb residual parameters. The results are given by

$$\hat{\gamma}_l = \frac{1}{2I_\nu^2\hat{P}_l}, \quad (77)$$

$$\frac{\hat{\rho}_l}{z^2\hat{\gamma}_l} = 3\beta\frac{\hat{Q}_l}{\hat{P}_l} + 4\frac{\lambda_l - \beta}{z}\frac{I_{\nu+1}}{I_\nu} - l, \quad (78)$$

where $I_\nu \equiv I_\nu(z)$. In the particular case of interaction in the S state ($l = 0$), the last formulas are somewhat simplified to become

$$\hat{\gamma} = \frac{1}{2I_1^2\hat{P}}, \quad (79)$$

$$\frac{\hat{\rho}}{z^2\hat{\gamma}} = 3\beta\frac{\hat{Q}}{\hat{P}} - \frac{z}{2}\frac{I_2}{I_1}. \quad (80)$$

In the case of Coulomb attraction ($a_B < 0$), all the above formulas are valid upon the substitution of conventional Bessel functions for modified ones:

$$I_\nu(z) \longrightarrow \frac{1}{i^\nu}J_\nu(\zeta), \quad K_\nu(z) \longrightarrow \frac{\pi}{2i^\nu}Y_\nu(\zeta), \quad \zeta = 2\sqrt{2R/|a_B|}. \quad (81)$$

Formulas (77) and (78) yield explicit expressions for the nuclear–Coulomb parameters of low-energy scattering in terms of the residual P matrix. These expressions make it possible to obtain directly a general form of the nuclear–Coulomb scattering length and effective range for models of short-range strong interaction.

6. NUCLEAR–COULOMB PARAMETERS OF LOW-ENERGY SCATTERING FOR EXACTLY SOLVABLE HARD-CORE MODELS

For specific applications of the above general expressions, we will consider some exactly solvable models of hard-core short-range strong interaction. For these, we will find explicitly the nuclear–Coulomb

parameters of low-energy scattering for arbitrary values of the orbital angular momentum.

6.1. Boundary-Condition Model

In the boundary-condition model, the interaction in the internal domain is determined by a single energy-independent parameter, the value of the logarithmic derivative of the wave function at the boundary surface—that is, the constant P_l. It is obvious that the parameter Q_l vanishes in this case. Thus, we have

$$P_l(E) = P_l, \tag{82}$$

$$Q_l = 0, \tag{83}$$

whence it follows that

$$\hat{P}_l = P_l - P_l^{(c)}, \tag{84}$$

$$\hat{Q}_l = -Q_l^{(c)}. \tag{85}$$

The nuclear–Coulomb parameters of low-energy scattering can then be written as

$$\hat{\gamma}_l = \frac{1}{2I_\nu^2(P_l - P_l^{(c)})}, \tag{86}$$

$$\frac{\hat{\rho}_l}{z^2\hat{\gamma}_l} = 3\beta\frac{Q_l^{(c)}}{(P_l^{(c)} - P_l)} + 4\frac{\lambda_l - \beta}{z}\frac{I_{\nu+1}}{I_\nu} - l, \tag{87}$$

where the quantities $P_l^{(c)}$ and $Q_l^{(c)}$ are given by Eqs. (75) and (76).

6.2. Hard-Core Delta-Shell Potential

Let us consider the case where the strong interaction is described by the delta-shell potential concentrated on the sphere of radius R and supplemented with a hard core of radius R_c less than R,

$$V_s(r) = \begin{cases} +\infty, & r < R_c \\ -\dfrac{\lambda}{R}\delta(r - R), & r > R_c. \end{cases} \tag{88}$$

Here, λ is the dimensionless interaction constant. In this case, the wave function in the internal region ($r < R$) is a linear combination of the Coulomb wave functions,

$$\psi_{lk}(r) = A_l(k)[G_l(\xi, kR_c)F_l(\xi, kr) - F_l(\xi, kR_c)G_l(\xi, kr)], \quad R_c < r < R, \tag{89}$$

and satisfies the zero boundary condition at $r = R_c$: $\psi_{lk}(R_c) = 0$. At the boundary surface ($r = R$), the wave function is continuous, but its derivative undergoes a discontinuity,

$$\psi'_{lk}(R + 0) - \psi'_{lk}(R - 0) = -\frac{\lambda}{R}\psi_{lk}(R). \tag{90}$$

By using formulas (89) and (90), we find that, in the case of a hard-core delta-shell potential, the P matrix can be represented as

$$P_l(E) = \rho\frac{G_l(\xi, x)F'_l(\xi, \rho) - F_l(\xi, x)G'_l(\xi, \rho)}{G_l(\xi, x)F_l(\xi, \rho) - F_l(\xi, x)G_l(\xi, \rho)} - \lambda, \tag{91}$$

where $x \equiv kR_c$. With the aid of the definition of the background Coulomb P matrix (26) and the representation in (41), we obtain the residual P matrix for the potential (88) in the form

$$\hat{P}_l(E) = \frac{\rho F_l(\xi, x)/F_l(\xi, \rho)}{G_l(\xi, x)F_l(\xi, \rho) - F_l(\xi, x)G_l(\xi, \rho)} - \lambda. \tag{92}$$

By means of the expansion of the Coulomb functions (62) and (63), we derive the parameters of the residual P matrix, $\hat{P}_l$ and $\hat{Q}_l$, according to (65). The results are

$$\hat{P}_l = \frac{1}{2}\frac{I_\nu(y)/I_\nu(z)}{K_\nu(y)I_\nu(z) - I_\nu(y)K_\nu(z)} - \lambda, \tag{93}$$

$$24\beta^2\hat{Q}_l = (lz^2 - \mu_l)(\lambda + \hat{P}_l) + (\lambda_l - \beta)\frac{(\lambda_l - \alpha)/(\lambda_l - \beta) - 2z[K_\nu(y)I_{\nu+1}(z) + I_\nu(y)K_{\nu+1}(z)]I_\nu(y)/I_\nu(z) + I_\nu^2(y)/I_\nu^2(z)}{[K_\nu(y)I_\nu(z) - I_\nu(y)K_\nu(z)]^2}, \tag{94}$$

where $\alpha \equiv R_c/a_B$ and $y \equiv 2\sqrt{2\alpha}$. By substituting (93) and (94) into (77) and (78), we now find that the nuclear–Coulomb scattering length and effective range for the hard-core delta-shell potential can be represented as

$$\hat{\gamma}_l = \frac{\gamma_l^h(y) - \gamma_l^h(z)}{1 - 2\lambda I_\nu^2(z)[\gamma_l^h(y) - \gamma_l^h(z)]}, \tag{95}$$

$$\frac{\hat{\rho}_l}{\hat{\gamma}_l^2} = \frac{\rho_l^h(y) - \rho_l^h(z)}{[\gamma_l^h(y) - \gamma_l^h(z)]^2} + 2\lambda z I_\nu(z)[lzI_\nu(z) + 4(\beta - \lambda_l)I_{\nu+1}(z)], \tag{96}$$

where $\gamma_l^h(y)$ and $\rho_l^h(y)$ are the low-energy nuclear–Coulomb parameters for a hard core of radius R_c [Eqs. (51) and (52) with substitutions $z \longrightarrow y$ and

$\beta \longrightarrow \alpha$], while $\gamma_l^h(z) \equiv \gamma_l^h$ and $\rho_l^h(z) \equiv \rho_l^h$ are the parameters for the hard core of radius R [Eqs. (51), (52)]. In the limiting case of a delta potential without a core ($R_c \longrightarrow 0, y \longrightarrow 0$, and $\gamma_l^h(y) \longrightarrow \infty$), expressions (95) and (96) reduce to the known expressions for the low-energy nuclear–Coulomb parameters for scattering on a delta function [16, 17]

$$\hat{\gamma}_l = -\frac{1}{2\lambda I_\nu^2(z)}, \tag{97}$$

$$\frac{\hat{\rho}_l}{\hat{\gamma}_l^2} = 2\lambda z I_\nu(z)[lzI_\nu(z) + 4(\beta - \lambda_l)I_{\nu+1}(z)]. \tag{98}$$

6.3. Margenau Model

In the Margenau model [30], strong interaction is simulated by a hard-core square-well potential; Coulomb interaction is assumed to be absent in the internal region. The latter is justified by the fact that, in the internal region, the Coulomb interaction is much weaker than strong interaction. Thus, the total interaction in this model is described by the potential

$$V(r) = \begin{cases} +\infty, & r < R_c \\ -V_0, & R_c < r < R \\ 2\xi k/r, & r > R. \end{cases} \tag{99}$$

In this case, the wave function in the internal region has the form

$$\psi_{lk}(r) = A_l(k)[n_l(KR_c)j_l(Kr) - j_l(KR_c)n_l(Kr)], \quad R_c < r < R, \tag{100}$$

where $K \equiv \sqrt{V_0 + E}$ and j_l and n_l are the spherical Riccati–Bessel functions. The P matrix can then be written as

$$P_l(E) = \rho\frac{j_l(x)n_l'(\rho) - n_l(x)j_l'(\rho)}{j_l(x)n_l(\rho) - n_l(x)j_l(\rho)}, \tag{101}$$

where $x \equiv KR_c$ and $\rho \equiv KR$. From the above, we can easily determine the P-matrix parameters P_l and Q_l. The results are

$$P_l = \rho_0\frac{j_l(x_0)n_l'(\rho_0) - n_l(x_0)j_l'(\rho_0)}{j_l(x_0)n_l(\rho_0) - n_l(x_0)j_l(\rho_0)}, \tag{102}$$

$$2Q_l + 1 = \frac{\lambda_l + P_l - P_l^2}{\rho_0^2} + \frac{b}{[j_l(x_0)n_l(\rho_0) - n_l(x_0)j_l(\rho_0)]^2}, \tag{103}$$

where $b \equiv R_c/R$, $x_0 \equiv K_0R_c$, $\rho_0 \equiv K_0R$, and $K_0 \equiv \sqrt{V_0}$. By using Eqs. (70) and (71) and taking into account Eqs. (75) and (76), we can find the parameters of the residual P matrix—$\hat{P}_l$ and $\hat{Q}_l$; the nuclear–Coulomb parameters of low-energy scattering are given by

$$\frac{1}{I_\nu^2\hat{\gamma}_l} = -2\rho_0\frac{j_l(x_0)n_{l+1}(\rho_0) - n_l(x_0)j_{l+1}(\rho_0)}{j_l(x_0)n_l(\rho_0) - n_l(x_0)j_l(\rho_0)} - z\frac{I_{\nu+1}}{I_\nu}, \tag{104}$$

$$\frac{\hat{\rho}_l}{z^2I_\nu^2\hat{\gamma}_l^2} = -\beta - l\nu + \frac{\mu_l}{z}\frac{I_{\nu+1}}{I_\nu} + 2(\beta - \lambda_l)\frac{I_{\nu+1}^2}{I_\nu^2} + 3\beta\frac{b - [j_l(x_0)n_{l+1}(\rho_0) - n_l(x_0)j_{l+1}(\rho_0)]^2}{[j_l(x_0)n_l(\rho_0) - n_l(x_0)j_l(\rho_0)]^2} + \left[3\nu\xi_0 + 2l\rho_0 + (\beta - \lambda_l)\frac{z}{\xi_0}\frac{I_{\nu+1}}{I_\nu}\right] \times \frac{j_l(x_0)n_{l+1}(\rho_0) - n_l(x_0)j_{l+1}(\rho_0)}{j_l(x_0)n_l(\rho_0) - n_l(x_0)j_l(\rho_0)}, \tag{105}$$

where $\xi_0 \equiv \dfrac{1}{a_BK_0}$.

6.4. Hard-Core Square-Well Potential

For the case of a strong-interaction potential in the form of a square well with a hard core,

$$V_s(r) = \begin{cases} +\infty, & r < R_c \\ -V_0\theta(R - r), & r > R_c, \end{cases} \tag{106}$$

we confine ourselves to determining the nuclear–Coulomb scattering length. For the simpler case of a square-well potential without a core, the nuclear–Coulomb scattering length and the nuclear–Coulomb range were found in [8]. In this case, the wave function in the internal domain has the form

$$\psi_{lk}(r) = A_l(k)[G_l(\Xi, KR_c)F_l(\Xi, Kr) - F_l(\Xi, KR_c)G_l(\Xi, Kr)], \quad R_c < r < R, \tag{107}$$

where $\Xi \equiv \dfrac{1}{a_BK}$, and the P matrix is given by

$$P_l(E) = \rho\frac{F_l(\Xi, x)G_l'(\Xi, \rho) - G_l(\Xi, x)F_l'(\Xi, \rho)}{F_l(\Xi, x)G_l(\Xi, \rho) - G_l(\Xi, x)F_l(\Xi, \rho)}, \tag{108}$$

where, as in the preceding subsection, $x \equiv KR_c$ and $\rho \equiv KR$. In accordance with (70) and (75), the parameter $\hat{P}_l$ of the residual P matrix then assumes the form

$$\hat{P}_l = \rho_0 \frac{F_l(\xi_0, x_0)G_l'(\xi_0, \rho_0) - G_l(\xi_0, x_0)F_l'(\xi_0, \rho_0)}{F_l(\xi_0, x_0)G_l(\xi_0, \rho_0) - G_l(\xi_0, x_0)F_l(\xi_0, \rho_0)} - \frac{z}{2}\frac{I_{\nu+1}(z)}{I_\nu(z)} - (l+1), \quad (109)$$

while the nuclear–Coulomb scattering length is given by

$$\frac{1}{I_\nu^2 \hat{\gamma}_l} = 2\rho_0 \frac{F_l(\xi_0, x_0)G_l'(\xi_0, \rho_0) - G_l(\xi_0, x_0)F_l'(\xi_0, \rho_0)}{F_l(\xi_0, x_0)G_l(\xi_0, \rho_0) - G_l(\xi_0, x_0)F_l(\xi_0, \rho_0)} - z\frac{I_{\nu+1}}{I_\nu} - (\nu+1). \quad (110)$$

7. CONCLUSION

In summary, an explicit isolation of the purely Coulomb background part in the *P* matrix leads to a correct asymptotic behavior of physical observables at high energies when the residual *P* matrix is approximated by a finite number of pole terms. Concurrently, the isolation of the background *P* matrix makes it possible to improve convergence of the remaining expansions. The transformation in (41) has a transparent mathematical and physical substantiation, and its application provides the same advantages as in the absence of Coulomb interaction. In addition, the explicit isolation of the purely Coulomb background part in the *P* matrix makes it possible to obtain the simple general expressions (77) and (78) for the nuclear–Coulomb parameters of low-energy scattering in terms of the residual *P* matrix. With the aid of these expressions, we can directly calculate the nuclear–Coulomb scattering length and effective range for short-range strong-interaction potentials. If the Schrödinger equation for these potentials admits of an exact solution in the presence of Coulomb interaction, the nuclear–Coulomb parameters can be found explicitly. In general, the nuclear–Coulomb parameters for low-energy scattering can be obtained for arbitrary short-range strong-interaction potentials at any value of the orbital angular momentum *l*. On the basis of the expressions derived in the present study, we have found explicitly the nuclear–Coulomb scattering length and effective range for the boundary-condition model, for the model of a hard-core delta-shell potential, for the Margenau model, and for the hard-square-well potential at arbitrary values of the orbital angular momentum.

ACKNOWLEDGMENTS

The work of V.A. Babenko was supported by a scholarship from the National Academy of Sciences of Ukraine for young scientists.

REFERENCES

1. R. L. Jaffe and F. E. Low, Phys. Rev. D **19**, 2105 (1979).
2. B. L. G. Bakker and P. J. Mulders, Adv. Nucl. Phys. **17**, 1 (1986).
3. V. A. Babenko and N. M. Petrov, Ukr. Fiz. Zh. **32**, 971 (1987).
4. V. A. Babenko, N. M. Petrov, and A. G. Sitenko, Can. J. Phys. **70**, 252 (1992).
5. E. P. Wigner and L. Eisenbud, Phys. Rev. **72**, 29 (1947).
6. A. Lane and R. Thomas, *R-Matrix Theory of Nuclear Reactions* (Los Alamos, 1958; Inostrannaya Literatura, Moscow, 1960).
7. V. A. Babenko and N. M. Petrov, Yad. Fiz. **45**, 1619 (1987) [Sov. J. Nucl. Phys. **45**, 1004 (1987)].
8. V. A. Babenko and N. M. Petrov, Yad. Fiz. **59**, 2154 (1996) [Phys. At. Nucl. **59**, 2074 (1996)].
9. L. D. Landau and Ya. A. Smorodinskiĭ, Zh. Éksp. Teor. Fiz. **14**, 269 (1944).
10. G. F. Chew and M. L. Goldberger, Phys. Rev. **75**, 1637 (1949).
11. J. Schwinger, Phys. Rev. **78**, 135 (1950).
12. V. D. Mur, A. E. Kudryavtsev, and V. S. Popov, Yad. Fiz. **37**, 1417 (1983) [Sov. J. Nucl. Phys. **37**, 844 (1983)].
13. H. van Haeringen, Nucl. Phys. A **253**, 355 (1975).
14. H. van Haeringen, J. Math. Phys. **18**, 927 (1977).
15. H. van Haeringen and L. P. Kok, Phys. Lett. A **82**, 317 (1981).
16. L. P. Kok, J. W. de Maag, H. H. Brouwer, and H. van Haeringen, Phys. Rev. C **26**, 2381 (1982).
17. J. W. de Maag, L. P. Kok, and H. van Haeringen, J. Math. Phys. **25**, 684 (1984).
18. *Handbook of Mathematical Functions*, Ed. by M. Abramowitz and I. A. Stegun (Dover, New York, 1965; Nauka, Moscow, 1973).
19. A. G. Sitenko, *Theory of Nuclear Reactions* (World Sci., Singapore, 1990).
20. J. G. Beckerley, Phys. Rev. **67**, 11 (1945).
21. J. Humblet, Ann. Phys. (N.Y.) **155**, 461 (1984).
22. H. A. Bethe, Phys. Rev. **76**, 38 (1949).
23. J. D. Jackson and J. M. Blatt, Rev. Mod. Phys. **22**, 77 (1950).
24. T. L. Trueman, Nucl. Phys. **26**, 57 (1961).
25. E. Lambert, Helv. Phys. Acta **42**, 667 (1969).
26. B. Tromborg and J. Hamilton, Nucl. Phys. B **76**, 483 (1974).
27. A. M. Badalyan, L. P. Kok, M. I. Polikarpov, and Yu. A. Simonov, Phys. Rep. **82**, 31 (1982).
28. F. L. Yost, J. A. Wheeler, and G. Breit, Phys. Rev. **49**, 174 (1936).
29. F. S. Ham, Q. Appl. Math. **15**, 31 (1957).
30. H. Margenau, Phys. Rev. **59**, 37 (1941).

Translated by A. Isaakyan

Physics of Atomic Nuclei, Vol. 64, No. 2, 2001, pp. 243–252. Translated from Yadernaya Fizika, Vol. 64, No. 2, 2001, pp. 289–298.

NUCLEI
Theory

Interference Effect in the Photoproduction of Electron–Positron Pairs on a Nucleus in the Field of Two Light Waves

S. P. Roshchupkin*

Sumy State University, Sumy, 244007 Ukraine, and Applied Physics Institute, National Academy of Sciences of Ukraine, Sumy, 244024 Ukraine

Received September 23, 1999; in final form, May 5, 2000

Abstract—In the general relativistic case, the nonresonance photoproduction of electron–positron pairs on a nucleus in the field of two circularly polarized light waves propagating in one direction is theoretically investigated. It is shown that there are two essentially different kinematical regions: the noninterference region, where the Bunkin–Fedorov quantum parameters play the role of multiphoton parameters, and the interference region, where interference effects are important and where quantum interference parameters are treated as multiphoton parameters. The interference effect is found in the photoproduction of an electron–positron pair on a nucleus in the field of two light waves. This effect occurs in the interference region and is due to the production of an electron–positron pair in the plane spanned by the light wave vector and the incident-photon momentum and to stimulated correlated emission and absorption of photons of the two waves. The cross sections for pair photoproduction on a nucleus in the above kinematical regions are determined for moderately strong fields. It is shown that, in the interference region, the partial cross sections for the case where there is a correlated emission (absorption) of the same number of photons of the two waves can significantly exceed the corresponding cross sections in any other geometry. © *2001 MAIK "Nauka/Interperiodica".*

1. INTRODUCTION

The production of an electron–positron pair by a nucleus in the field of a plane electromagnetic wave has been studied for quite a long time. In such investigations, much attention has been given to resonances associated with the approach of the Green's function for the intermediate electron (positron) in the plane-wave field to the mass shell (see, for example, [1–4]).

Nonresonance spontaneous bremsstrahlung in electron scattering by a nucleus in the field of two light waves propagating in the same direction was investigated in [5] for linearly polarized waves and in [6] for the general case of elliptically polarized waves. These investigations revealed a spontaneous interference bremsstrahlung effect occurring in electron scattering and spontaneous-photon emission at specific angles in the plane spanned by the initial-electron momentum and light wave vector and consisting in the correlated emission and absorption of equal numbers of photons of the two waves.

In the present study, we consider the nonresonance photoproduction of electron–positron pairs on a nucleus in the field of two circularly polarized electromagnetic waves propagating in the same direction. We emphasize that resonances associated with the approach of the Green's function of the intermediate electron (positron) in the two-wave field to the mass shell are not investigated here (this will be the subject of a subsequent publication). We study in detail pair photoproduction in the noninterference and in the interference region; in the latter, we predict an interference effect that occurs not only in pair production in the plane spanned by the initial-electron momentum and light wave vector but also in the stimulated correlated emission and absorption (owing to the interference of waves) of photons of the two waves. It is shown that the partial cross section for pair photoproduction on a nucleus in the interference region can significantly exceed the corresponding cross section in any other geometry. Here, we use the system of units where $\hbar = c = 1$.

2. AMPLITUDE FOR THE PHOTOPRODUCTION OF AN ELECTRON–POSITRON PAIR

Let us choose the 4-potential of an external field as the sum of the potentials of two circularly polarized electromagnetic wave propagating along the z axis; that is,

$$A = A_1(\varphi_1) + A_2(\varphi_2), \tag{1}$$

where

$$A_j(\varphi_j) = \frac{F_j}{\omega_j}(e_{jx}\cos\varphi_j + \delta_j e_{jy}\sin\varphi_j). \tag{2}$$

Here, $\delta_1 = +1$ and $\delta_2 = \pm 1$; $e_{jx} = (0, \mathbf{e}_{jx})$ and $e_{jy} = (0, \mathbf{e}_{jy})$ are the polarization 4-vectors of the waves; F_j and ω_j are, respectively, the field strength and the frequency of the first ($j = 1$) and the second ($j = 2$) wave; and the argument φ_j is given by

$$\varphi_j = \omega_j(t - z), \quad j = 1, 2. \tag{3}$$

* e-mail: roshsp@ssu.sumy.ua

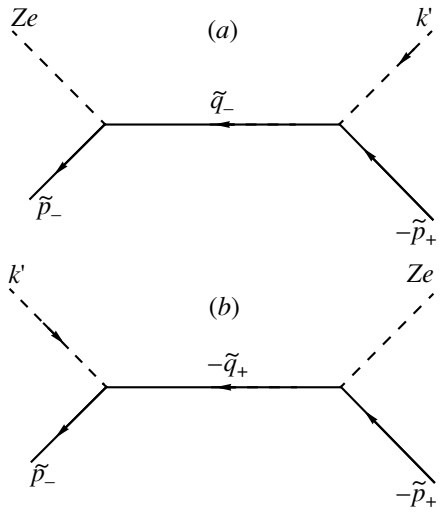

Fig. 1. Diagrams representing the amplitudes for the photoproduction of electron–positron pairs on a nucleus in the field of two light waves. Solid incoming and outgoing lines correspond to the electron and positron wave functions in the field of two waves (Volkow functions), dashed lines correspond to the incident photon (k') and the pseudophoton of the nucleus, and the internal lines represent (*a*) the electron and (*b*) the positron Green's function in the field of two waves.

The pair-photoproduction amplitude is derived in the standard way [4–6]:

$$S = \sum_{l=-\infty}^{\infty} \sum_{s=-\infty}^{\infty} S_{ls}. \tag{4}$$

Here, the partial-wave amplitude corresponding to the emission ($l > 0$, $s > 0$) or the absorption ($l < 0$, $s < 0$) of $|l|$ photons of the first wave and $|s|$ photons of the second wave has the form

$$S_{ls} = -i\frac{8\pi^{5/2}Ze^3}{\sqrt{2\omega'\tilde{E}_+\tilde{E}_-}}\exp(i\phi)[\bar{u}_-H_{ls}u_+]\frac{\delta(q_0)}{\mathbf{q}^2}, \tag{5}$$

where

$$\begin{aligned} H_{ls} = \sum_{l'=-\infty}^{\infty}\sum_{s'=-\infty}^{\infty}\Bigg[& M_{l-l',s-s'}(\tilde{p}_-,\tilde{q}_-)\frac{\hat{\tilde{q}}_- + m_*}{\tilde{q}_-^2 - m_*^2} \\ & \times K_{l's'}(\tilde{q}_-,-\tilde{p}_+) + K_{l's'}(\tilde{p}_-,-\tilde{q}_+) \\ & \times \frac{-\hat{\tilde{q}}_+ + m_*}{\tilde{q}_+^2 - m_*^2}M_{l-l',s-s'}(-\tilde{q}_+,-\tilde{p}_+)\Bigg]. \end{aligned} \tag{6}$$

Here, Ze is the charge of the nucleus involved; ϕ is a phase that is independent of the summation indices; $u_+ \equiv u(-p_+)$ and $\bar{u}_- \equiv \bar{u}(p_-)$ are Dirac bispinors; caret-labeled expressions ($\hat{\tilde{q}}_\pm = \tilde{\gamma}^\mu\tilde{q}_{\pm\mu}$) denote the scalar product of the Dirac matrices $\tilde{\gamma}^\mu$ ($\mu = 0, 1, 2, 3$) and the corresponding 4-vector; $q = (q_0, \mathbf{q})$ is the 4-momentum transfer; and $\tilde{q}_-$ and $\tilde{q}_+$ are the 4-momenta of, respectively, the intermediate electron in the amplitude represented by the diagram in Fig. 1*a* and the intermediate positron in the amplitude represented by the diagram in Fig. 1*b*,

$$q = \tilde{p}_- + \tilde{p}_+ - k' + lk_1 + sk_2, \tag{7}$$

$$\begin{aligned} \tilde{q}_- &= k' - \tilde{p}_+ - l'k_1 - s'k_2, \\ \tilde{q}_+ &= k' - \tilde{p}_- - l'k_1 - s'k_2. \end{aligned} \tag{8}$$

In formulas(5)–(8) we have used the following notation: $k_1 = \omega_1 n = \omega_1(1, \mathbf{n})$ and $k_2 = \omega_2 n = \omega_2(1, \mathbf{n})$ are the photon 4-momenta in the first and the second wave, respectively; $k' = \omega' n' = \omega'(1, \mathbf{n}')$ is the incident-photon 4-momentum; $\tilde{p}_\pm = (\tilde{E}_\pm, \tilde{\mathbf{p}}_\pm)$ are the positron and electron 4-quasimomenta; and m_* is the effective electron (positron) mass in the wave field (1). We have

$$\begin{aligned} \tilde{p}_\pm &= p_\pm + \frac{m^2}{2(k_1p_\pm)}[\eta_1^2 + \eta_2^2]k_1, \\ m_* &= m\sqrt{1 + \eta_1^2 + \eta_2^2}, \end{aligned} \tag{9}$$

where $p_\pm = (E_\pm, \mathbf{p}_\pm)$ are the positron and electron 4-momenta and

$$\eta_j = eF_j/(m\omega_j), \quad j = 1, 2, \tag{10}$$

is a classical relativistically invariant parameter that characterizes the intensity of the first and the second wave.

In expression (6), the operators $M_{l-l',s-s'}$, which determine the amplitude for electron (positron) scattering by a nucleus in the field of two waves [7, 8], and the operators $K_{l's'}$, which determine the amplitude for the photoproduction of an electron–positron pair in the field of two waves [provided that the intermediate electron (positron) is treated as a real one] are given by

$$\begin{aligned} M_{rr'}(\tilde{p}_2,\tilde{p}_1) &= \tilde{\gamma}_0 I_{rr'} + \frac{\omega_1 m^2}{2(k_1\tilde{p}_1)(k_1\tilde{p}_2)}B_{rr'}\hat{k}_1 \\ &+ \frac{m}{4(k_1\tilde{p}_1)}\tilde{\gamma}_0\hat{k}_1\hat{D}_{rr'} + \frac{m}{4(k_1\tilde{p}_2)}\hat{D}_{rr'}\hat{k}_1\tilde{\gamma}_0, \end{aligned} \tag{11}$$

$$\begin{aligned} K_{l's'}(\tilde{p}_2,\tilde{p}_1) &= \hat{\varepsilon}^* I_{l's'} + \frac{\omega_1 m^2}{2(k_1\tilde{p}_1)(k_1\tilde{p}_2)}B_{l's'}\hat{k}_1 \\ &+ \frac{m}{4(k_1\tilde{p}_1)}\hat{\varepsilon}^*\hat{k}_1\hat{D}_{l's'} + \frac{m}{4(k_1\tilde{p}_2)}\hat{D}_{l's'}\hat{k}_1\hat{\varepsilon}^*. \end{aligned} \tag{12}$$

Here, $\hat{\varepsilon}^* = \tilde{\gamma}^\mu\varepsilon_\mu^*$, where ε_μ^* is the incident-photon polarization 4-vector. It should be noted that, in Eq. (11), $r = l - l'$ and $r' = s - s'$; we also have there $\tilde{p}_1 = \tilde{q}_-$ and $\tilde{p}_2 = \tilde{p}_-$ for the amplitude represented by the diagram in Fig. 1*a* and $\tilde{p}_1 = -\tilde{p}_+$ and $\tilde{p}_2 = -\tilde{q}_+$ for the

amplitude represented by the diagram in Fig. 1*b*. In Eq. (12), $\tilde{p}_1 = -\tilde{p}_+$ and $\tilde{p}_2 = \tilde{q}_-$ for the amplitude represented by the diagram in Fig. 1*a* and $\tilde{p}_1 = -\tilde{q}_+$ and $\tilde{p}_2 = \tilde{p}_-$ for the amplitude represented by the diagram in Fig. 1*b*. The functions $B_{rr'}$ and the 4-vector $D_{rr'}$ [7, 8] are then given by

$$B_{rr'} = (\eta_1^2 + \eta_2^2)I_{rr'} + \eta_1\eta_2[I_{r-1,r'+\delta_2} + I_{r+1,r'-\delta_2}], \quad (13)$$

$$\begin{aligned} D_{rr'} &= \eta_1(e_1^* I_{r+1,r'} + e_1 I_{r-1,r'}) \\ &+ \eta_2(e_2^* I_{r,r'+1} + e_2 I_{r,r'-1}), \\ e_j &= e_{jx} + i\delta_j e_{jy}, \quad j = 1, 2, \end{aligned} \quad (14)$$

where an asterisk denotes complex conjugation and where the functions $I_{rr'}$ can be represented as an expansion in a series in Bessel functions of integral orders [7]:

$$\begin{aligned} I_{rr'} &\equiv I_{rr'}(\chi_1, \gamma_1; \chi_2, \gamma_2; \alpha_{12}) \\ &= \exp[-i(\chi_1 r + \delta_2\chi_2 r')]\sum_{j=-\infty}^{\infty}\exp[i(\chi_1 - \delta_2\chi_2)j] \\ &\times J_j(\alpha_{12})J_{r-j}(\gamma_1)J_{r'+\delta_2 j}(\gamma_2). \end{aligned} \quad (15)$$

The arguments of the functions $I_{rr'}$ are given by

$$\begin{aligned} \gamma_j &\equiv \gamma_j(\tilde{p}_2, \tilde{p}_1) = \eta_j m\sqrt{-g_j^2} = \eta_j m|\mathbf{g}_j''|, \\ g_j &\equiv g_j(\tilde{p}_2, \tilde{p}_1) = \frac{\tilde{p}_2}{(k_j\tilde{p}_2)} - \frac{\tilde{p}_1}{(k_j\tilde{p}_1)}; \end{aligned} \quad (16)$$

$$\begin{aligned} \alpha_{12} &\equiv \alpha_{12}(\tilde{p}_2, \tilde{p}_1) = \eta_1\eta_2\frac{m^2}{\Omega_{12}}\left(\frac{1}{n\tilde{p}_1} - \frac{1}{n\tilde{p}_2}\right), \\ \Omega_{12} &= \omega_1 - \delta_2\omega_2; \quad \chi_j = \angle(\mathbf{e}_{jx}, \mathbf{g}_j''), \end{aligned} \quad (17)$$

where $|\mathbf{g}_j''| = |\mathbf{g}_j|\sin\vartheta_j$ (ϑ_j is the angle between the vectors $\mathbf{g}_j$ and $\mathbf{k}_1$) is the absolute value of the $\mathbf{g}_j$ component parallel to the polarization plane. It should be recalled that γ_j (16) is the well-known Bunkin–Fedorov quantum parameter used to specify the case where multiphoton effects come into play [9–11, 7] and that α_{12} (17) is the quantum interference parameter, which governs interference effects in the scattering of an electron (positron) on a nucleus and in the photoproduction of an electron–positron pair in the field of two waves. It should be emphasized that $|\Omega_{12}|$ (17) are combined frequencies that are equal to the difference or the sum of the wave frequencies for identical or opposite wave polarizations ($\delta_2 = +1$ or -1, respectively). If the quantum interference parameter α_{12} exceeds unity, the processes of the correlated emission and absorption of photons of the two waves become operative. But if $\alpha_{12} \ll 1$, the effect of interference processes can be disregarded ($j = 0$), in which case the functions $I_{rr'}$ (15) factorize into the product of Bessel functions determining the independent emission and absorption of photons of the first and the second wave [7].

For electron (positron) velocities satisfying the condition $\nu_\pm \gg Z/137$, expressions (4)–(6) for the amplitude of the photoproduction of an electron–positron pair on a nucleus are valid at arbitrary intensities and frequencies of the two waves. It can easily be shown that, if one of the waves is switched off (for example, at $F_2 = 0$), these expressions reduce to the form describing the amplitude for the photoproduction of an electron–positron pair on a nucleus in the field of one wave [1–4]; if both wave are switched off ($F_1 = F_2 = 0$), we obtain the conventional amplitude for the photoproduction of an electron–positron pair on a nucleus in the absence of external fields [12].

At equal frequencies of the waves ($\omega_1 = \omega_2$), expressions (4)–(6) reduce to the form describing the amplitude for the photoproduction of an electron–positron pair on a nucleus in the field of one wave [5, 6]. In the following, we therefore assume that the frequencies of the waves are not close:

$$|\Delta\omega|/\omega_1 \gtrsim 1. \quad (18)$$

We also assume that they satisfy the condition

$$\omega_j \ll \omega', \quad j = 1, 2. \quad (19)$$

Since the Bunkin–Fedorov parameters γ_j (16) greatly depend on the kinematics of electron scattering and of the emission of a spontaneous photon, we will single out, in just the same way as in [5–7], two kinematical regions: the noninterference region, where it is the quantum Bunkin–Fedorov parameters that specify the condition under which multiphoton effects come into play, and the interference region, where the influence of these parameters, in view of a special type of kinematics, vanishes (all eight parameters γ_j are equal to zero in this region), so that multiphoton processes are determined by the quantum interference parameters α_{12} (17).

3. PHOTOPRODUCTION OF AN ELECTRON–POSITRON PAIR ON A NUCLEUS IN THE NONINTERFERENCE REGION

Here, we will investigate the photoproduction of an electron–positron pair on a nucleus in the noninterference region, where the Bunkin–Fedorov quantum parameters γ_j (16) are not small, appearing to be basic parameters that specify the conditions under which multiphoton effects become operative ($\vartheta_j \sim 1$; hence, the vectors $\mathbf{g}_j$ have a nonzero component parallel to the wave-polarization plane). It should be noted that this region is rather broad. Only the production of an electron–positron pair at specific angles in the plane spanned by the incident-photon momentum and the wave vector of the light wave is excluded in it (see Section 4).

In the noninterference region, the quantum parameters (16) and (17) can be estimated as

$$\gamma_j \sim \gamma_j' = \eta_j \frac{m}{\omega_j}, \quad \alpha_{12} \sim \gamma_1 \xi_2 \sim \gamma_2 \xi_1, \quad j = 1, 2, \quad (20)$$

where

$$\xi_j = \eta_j m/\omega' \quad (21)$$

is a quantum parameter, which is numerically equal to the ratio of the work of the field over the wavelength of the first or the second wave to the incident-photon energy and which determines the integrated features of the process in the noninterference region. Let us now consider the photoproduction of an electron–positron pair on a nucleus in the region of moderately strong fields such that $\xi_j \ll 1$; for the wave intensities, this means fulfillment of the condition

$$\eta_j \ll \omega'/m, \quad (22)$$

in which case we have $\alpha_{12} \ll \gamma_j$, so that multiphoton processes are determined primarily by the relevant Bunkin–Fedorov quantum parameters ($l' \lesssim \gamma_1$, $s' \lesssim \gamma_2$). Considering that $l'\omega_1/\omega' \lesssim \xi_1 \ll 1$ and $s'\omega_2/\omega' \lesssim \xi_2 \ll 1$, we find that, in the region of moderately strong fields satisfying the condition in (22), the amplitude of the photoproduction of an electron–positron pair as given by Eqs. (5)–(12) is simplified significantly. For example, the expressions for the 4-momenta in (7) and (8) and for the amplitudes in (11) and (12) become

$$q = p_- + p_+ - k', \quad \tilde{q}_- = k' - p_+, \quad \tilde{q}_+ = k' - p_-; \quad (23)$$

$$M_{l-l', s-s'} = \tilde{\gamma}_0 I_{l-l', s-s'}, \quad K_{l's'} = \hat{\varepsilon}^* I_{l's'}. \quad (24)$$

From (23), it follows that, in the region of moderately strong fields, there arise no resonances associated with the approach of the Green's function for an intermediate electron or an intermediate positron in the wave field to the mass shell ($\tilde{q}_-^2 \neq m^2$, $\tilde{q}_+^2 \neq m^2$)—that is, the condition in (22) determines the nonresonance region as well. Since the arguments of the functions $I_{l's'}$ and $I_{l-l', s-s'}$ in (24) are independent of the summation indices, the amplitude in Eq. (6) with allowance for relations (24) can easily be summed over all values of the integral indices l' and s'. As a result, the quantity obtained by averaging the noninterference differential cross section evaluated for the production of an electron–positron pair by an unpolarized photon on a nucleus in the field of two moderately strong light waves over the polarizations of the particles constituting the pair assumes the form

$$d\sigma_{ls} = \left|I_{ls}(\chi_1, \gamma_1; \chi_2, \gamma_2; \alpha_{12})\right|^2 d\sigma_*, \quad (25)$$

where $d\sigma_*$ is the differential cross section for the photoproduction of an electron–positron pair on a nucleus in a process where the electron and the positron of given energies are emitted in a specified direction (in the absence of an external field) [12] and where it is necessary to set $\tilde{p}_1 = -p_+$ and $\tilde{p}_2 = p_-$ in the arguments of the functions I_{ls}; that is,

$$\gamma_j = \eta_j m |\mathbf{g}_j| \sin\vartheta_j, \quad \mathbf{g}_j = \frac{1}{\omega_j}\left(\frac{\mathbf{p}_-}{\kappa_-} - \frac{\mathbf{p}_+}{\kappa_+}\right), \quad (26)$$

$$j = 1, 2;$$

$$\alpha_{12} = -\eta_1\eta_2 \frac{m^2}{\Omega_{12}}\left(\frac{1}{\kappa_+} + \frac{1}{\kappa_-}\right), \quad (27)$$

$$\kappa_\pm = E_\pm - |\mathbf{p}_\pm| \cos\theta_\pm, \quad \theta_\pm = \angle(\mathbf{k}_1, \mathbf{p}_\pm).$$

In the case of ultrarelativistic electron and positron energies, expression (25) for the partial-wave cross section is valid at not overly small angles between the wave vector $\mathbf{k}_1$ and the 3-momenta of the electron, the positron, and the incident photon ($\theta_\pm^2 \gg \eta_{1,2} m/E_\pm$, $\theta'^2 \gg \eta_{1,2} m/\omega'$). From (25), it can be seen that, in the region of moderately strong fields satisfying the condition in (22), the cross section for the photoproduction of an electron–positron pair on a nucleus factorizes into the probability of the emission (absorption) of $|l|$ photons of the first wave and $|s|$ photons of the second wave and the cross section for the photoproduction of an electron–positron pair on a nucleus in the absence of an external field, the processes of the emission and absorption of photons of the first and the second wave being generally correlated owing to a nonzero value of the quantum interference parameter α_{12} (27).

Under the condition $\alpha_{12} \ll 1$ (in which case $\gamma_{1,2} \ll \xi_{2,1}^{-1} \gg 1$), the functions I_{ls} (15) in expression (25) can be represented as the product of independent Bessel functions, and the partial-wave cross section takes the form

$$d\sigma_{ls} = J_l^2(\gamma_1) J_s^2(\gamma_2) d\sigma_*. \quad (28)$$

This means that, in this case, the emission (absorption) of photons of the first and the second wave and the photoproduction of an electron–positron pair on a nucleus proceed independently. Since the electron and the positron energy are independent of the number of absorbed or emitted photons of the two waves in the region of moderately strong fields satisfying the condition in (22), the partial-wave cross sections (25) and (28) can easily be summed over all possible absorption and emission processes. As a result, we arrive at a result that might have been expected from the outset: the total cross section coincides with the cross section for the photoproduction of an electron–positron pair on a nucleus in the absence of an external field. In other words, all essentially quantum contributions cancel out completely upon summation; that is,

$$d\sigma = \sum_{l=-\infty}^{\infty} \sum_{s=-\infty}^{\infty} d\sigma_{ls} = d\sigma_*. \quad (29)$$

To conclude this section, we note that, from the energy-conservation law [as represented by the zeroth component of the first relation in Eq. (23)], it follows that, near the reaction threshold ($\omega' \longrightarrow 2m$) and owing to the use of the Born approximation, the above expressions are valid if

$$\frac{Z}{137} \ll \sqrt{\frac{\omega' - 2m}{\omega'}} \ll 1, \tag{30}$$

which is a conventional condition in the absence of external fields.

4. PHOTOPRODUCTION OF AN ELECTRON–POSITRON PAIR ON A NUCLEUS IN THE INTERFERENCE REGION

For the general case of arbitrary intensities, it can be shown that, in the interference region, the amplitudes corresponding to the diagrams in Figs. 1*a* and 1*b* must satisfy the relativistically invariant relations

$$\begin{aligned} g_j^2(\tilde{p}_-, \tilde{q}_-) &= g_j^2(\tilde{q}_-, -\tilde{p}_+) = 0, \\ g_j^2(\tilde{p}_-, -\tilde{q}_+) &= g_j^2(-\tilde{q}_+, -\tilde{p}_+) = 0; \end{aligned} \tag{31}$$

that is, the corresponding vectors $\mathbf{g}_j$ are aligned with the direction of wave propagation. Therefore, these vectors have no component parallel to the polarization plane [$\vartheta_j \ll (\gamma_j')^{-1} \lesssim 1$; see Eqs. (16), (20)]. By virtue of (31), the Bunkin–Fedorov quantum parameters γ_j (16) and the phases χ_j (17) vanish. In the interference region specified by (31), the functions $I_{rr'}$ (15), which determine the pair-photoproduction amplitude given by Eqs. (5) and (6), are therefore simplified significantly, reducing to a Bessel function of integral order:

$$\begin{aligned} I_{rr'}(0, 0; 0, 0; \alpha_{12}) &= J_{r_{12}}(\alpha_{12}), \\ r_{12} &= \frac{1}{2}(r - \delta_2 r'). \end{aligned} \tag{32}$$

From (32), it follows that, in the interference region, the numbers of photons emitted and absorbed by electron and positron from the two waves correlate in such a way that the half-sum ($\delta_2 = -1$) or the half-difference ($\delta_2 = +1$) of these numbers (r and r') appears to be an integer (r_{12}).

Taking into account the change in the notation for the indices in (32), we further rewrite the amplitude for pair production on a nucleus [see Eqs. (4)–(6)]. As a result, the sum (difference) of the integral indices l', s' and l, s can be either even,

$$\begin{cases} l' - \delta_2 s' = 2s_{12}, \\ l' + \delta_2 s' = 0, \end{cases} \quad \begin{cases} l - \delta_2 s = 2l_{12}, \\ l + \delta_2 s = 0, \end{cases} \tag{33}$$

or odd

$$\begin{cases} l' - \delta_2 s' = 2s_{12} - 1, \\ l' + \delta_2 s' = -\delta_2, \end{cases} \quad \begin{cases} l - \delta_2 s = 2l_{12} - 1, \\ l + \delta_2 s = -\delta_2. \end{cases} \tag{34}$$

For the case specified by Eq. (33), we obtain the correlated emission (absorption) of equal numbers of photons in the two waves, and the 4-momenta in (7) and (8) assume the form

$$\begin{aligned} q \longrightarrow q_{(0)} &= \tilde{p}_- + \tilde{p}_+ - k' + l_{12}K_{12}, \\ \tilde{q}_- \longrightarrow \tilde{q}_{-(0)} &= k' - \tilde{p}_+ - s_{12}K_{12}, \\ \tilde{q}_+ \longrightarrow \tilde{q}_{+(0)} &= k' - \tilde{p}_- - s_{12}K_{12}, \end{aligned} \tag{35}$$

where

$$K_{12} = (\Omega_{12}, \mathbf{K}_{12}) = k_1 - \delta_2 k_2. \tag{36}$$

For the case specified by Eq. (34), we instead have

$$\begin{aligned} q \longrightarrow q_{(1)} &= \tilde{p}_- + \tilde{p}_+ - k' + l_{12}K_{12} \\ &\quad - \frac{1}{2}(1 + \delta_2)k_1 - \frac{1}{2}(1 - \delta_2)k_2, \\ \tilde{q}_- \longrightarrow \tilde{q}_{-(1)} &= k' - \tilde{p}_+ - s_{12}K_{12} \\ &\quad + \frac{1}{2}(1 + \delta_2)k_1 + \frac{1}{2}(1 - \delta_2)k_2, \\ \tilde{q}_+ \longrightarrow \tilde{q}_{+(1)} &= k' - \tilde{p}_- - s_{12}K_{12} \\ &\quad + \frac{1}{2}(1 + \delta_2)k_1 + \frac{1}{2}(1 - \delta_2)k_2. \end{aligned} \tag{37}$$

From expressions (35) and (37), it can be seen that, in the interference region, the emission (absorption) of photons from the product electron–positron pair is correlated in such a way that the numbers of emitted (absorbed) photons in the two waves are equal in the first case ($s = -\delta_2 l$, $s' = -\delta_2 l'$) and differ by unity in the second case ($s = -\delta_2 l - 1$, $s' = -\delta_2 l' - 1$), processes where the numbers of the emitted (absorbed) photons in the two waves do not satisfy this condition being suppressed. In the interference region, the amplitude for pair photoproduction on a nucleus eventually assumes the form

$$S = \sum_{l_{12} = -\infty}^{\infty} [S_{l_{12}}^{(0)} + S_{l_{12}}^{(1)}], \tag{38}$$

where $S_{l_{12}}^{(0)}$ and $S_{l_{12}}^{(1)}$ are the partial amplitudes for the correlated emission (absorption) of photons whose numbers in the two waves are equal and differ by unity, respectively. These amplitudes are given by expression (5), where we must make the substitutions $q \longrightarrow q_{(0)}$ and $H_{ls} \longrightarrow H_{l_{12}}^{(0)}$ for the former and $q \longrightarrow q_{(1)}$ and

$H_{ls} \longrightarrow H^{(1)}_{l_{12}}$ for the latter. We also have

$$H^{(0)}_{l_{12}} = \sum_{s_{12}=-\infty}^{\infty} [T^{(0,0)}_{l_{12}-\delta_2 s_{12}} + T^{(1,1)}_{l_{12}-\delta_2 s_{12}+1}],$$
$$H^{(1)}_{l_{12}} = \sum_{s_{12}=-\infty}^{\infty} [T^{(1,0)}_{l_{12}-\delta_2 s_{12}} + T^{(0,1)}_{l_{12}-\delta_2 s_{12}}], \quad (39)$$

$$T^{(a,b)}_{l_{12}-\delta_2 s_{12}} = M^{(a)}_{l_{12}-\delta_2 s_{12}}(\tilde{p}_-, \tilde{q}_{-(b)}) \frac{\hat{\tilde{q}}_{-(b)} + m_*}{\tilde{q}^2_{-(b)} - m^2_*} K^{(b)}_{s_{12}}(\tilde{q}_{-(b)}, -\tilde{p}_+) \quad (40)$$
$$+ K^{(b)}_{s_{12}}(\tilde{p}_-, -\tilde{q}_{+(b)}) \frac{-\hat{\tilde{q}}_{+(b)} + m_*}{\tilde{q}^2_{+(b)} - m^2_*} M^{(a)}_{l_{12}-\delta_2 s_{12}}(-\tilde{q}_{+(b)}, -\tilde{p}_+).$$

Here, $a, b = 0, 1$, and we have used the notation

$$K^{(0)}_{s_{12}}(\tilde{p}_2, \tilde{p}_1) = \hat{\varepsilon}^* J_{s_{12}}(\alpha_{12}) + \frac{\omega_1 m^2}{8(k_1\tilde{p}_1)(k_1\tilde{p}_2)} B^{(0)}_{s_{12}} \hat{k}_1, \quad (41)$$

$$K^{(1)}_{s_{12}}(\tilde{p}_2, \tilde{p}_1) = \frac{m}{4(k_1\tilde{p}_1)} \hat{\varepsilon}^* \hat{k}_1 \hat{D}^{(1)}_{s_{12}} + \frac{m}{4(k_1\tilde{p}_2)} \hat{D}^{(1)}_{s_{12}} \hat{k}_1 \hat{\varepsilon}^*, \quad (42)$$

$$M^{(0)}_{l_{12}-\delta_2 s_{12}}(\tilde{p}_2, \tilde{p}_1) = \tilde{\gamma}_0 J_{l_{12}-\delta_2 s_{12}}(\alpha_{12}) + \frac{\omega_1 m^2}{8(k_1\tilde{p}_1)(k_1\tilde{p}_2)} B^{(0)}_{l_{12}-\delta_2 s_{12}} \hat{k}_1, \quad (43)$$

$$M^{(1)}_{l_{12}-\delta_2 s_{12}}(\tilde{p}_2, \tilde{p}_1) = \frac{m}{4(k_1\tilde{p}_1)} \tilde{\gamma}_0 \hat{k}_1 \hat{D}^{(1)}_{l_{12}-\delta_2 s_{12}} + \frac{m}{4(k_1\tilde{p}_2)} \hat{D}^{(1)}_{l_{12}-\delta_2 s_{12}} \hat{k}_1 \tilde{\gamma}_0. \quad (44)$$

In expressions (41)–(44), the functions $B^{(0)}_r$ and 4-vector $D^{(1)}_r$ can be written as

$$B^{(0)}_r = (\eta_1^2 + \eta_2^2) J_r(\alpha_{12}) + \eta_1\eta_2 [J_{r-1}(\alpha_{12}) + J_{r+1}(\alpha_{12})], \quad (45)$$

$$D^{(1)}_r = \eta_1 [e_1^* J_r(\alpha_{12}) + e_1 J_{r-1}(\alpha_{12})] + \eta_2 [e_2^* J_{r-(1+\delta_2)/2}(\alpha_{12}) + e_2 J_{r-(1-\delta_2)/2}(\alpha_{12})]. \quad (46)$$

Thus, we can see that, in the interference region, there occur processes of correlated emission (absorption) of photons of the two waves from the product electron–positron pair. As a result, the amplitude for the process, as given by Eqs. (38)–(46), has the same form as that in the field of a single wave.

We now investigate the kinematics of the photoproduction of an electron–positron pair on a nucleus in the interference region. Writing down explicitly relations (31) for the amplitudes represented by the diagrams in Figs. 1*a* and 1*b*, we find after some simple algebra that the kinematical features of the photoproduction of an electron–positron pair on a nucleus are identical for these two amplitudes. Specifically, the electron–positron pair is generated in the plane spanned by the incident-photon momentum $\mathbf{k}'$ and the wave vector $\mathbf{k}_1$, provided that the following relation holds:

$$\frac{\mathbf{k} \times \mathbf{p}_\pm}{(k\tilde{p}_\pm)} = \frac{\mathbf{k} \times \mathbf{k}'}{(kk')}. \quad (47)$$

The absolute value of this vector equation gives the sought relation between the polar angles and energies of the pair and the angle of the photon incidence (here, the corresponding azimuthal angles take equal values); that is,

$$a_\pm = \cot(\theta'/2), \quad (48)$$

where

$$a_\pm = (|\mathbf{p}_\pm|/\kappa_\pm)\sin\theta_\pm, \quad \theta' = \angle(\mathbf{n}, \mathbf{k}'). \quad (49)$$

We note that, in Eqs. (48) and (49), the quantities $\kappa_\pm$ and the angles $\theta_\pm$ are determined by expression (27). On the basis of Eq. (48), we can easily obtain the relations

$$\nu_\pm = \frac{|\mathbf{p}_\pm|}{E_\pm} = \left[\cos\theta_\pm + \sin\theta_\pm \tan\frac{\theta'}{2}\right]^{-1}, \quad \kappa_\pm = \frac{E_\pm}{b_\pm}, \quad (50)$$

where

$$b_\pm = 1 + \cot\theta_\pm \cot(\theta'/2). \quad (51)$$

By virtue of this, the energy-conservation law [zeroth component of the first relation in Eq. (35) or Eq. (37)] for arbitrary wave intensities is significantly simplified, assuming the form

$$\omega' = E_- + E_+ + \frac{1}{2}(\eta_1^2 + \eta_2^2) m^2 \left(\frac{b_+}{E_+} + \frac{b_-}{E_-}\right) + l_{12}\Omega_{12} \quad (52)$$

or

$$\omega' = E_- + E_+ + \frac{1}{2}(\eta_1^2 + \eta_2^2) m^2 \left(\frac{b_+}{E_+} + \frac{b_-}{E_-}\right) + l_{12}\Omega_{12} - \frac{1}{2}(1+\delta_2)\omega_1 - \frac{1}{2}(1-\delta_2)\omega_2. \quad (53)$$

After some simple transformations, the first relation in (50) can be represented in the form of a quadratic equation for the pair emission angles,

$$(1+\nu_\pm)\tan^2\frac{\theta_\pm}{2} - 2\left(\nu_\pm \tan\frac{\theta'}{2}\right)\tan\frac{\theta_\pm}{2} + (1-\nu_\pm) = 0. \quad (54)$$

It follows from (54) that the pair emission angles are determined by the velocities $\nu_\pm$ of the translational

motion of the pair constituents and by the angle of photon incidence; that is,

$$\tan\frac{\theta_\pm}{2} = \frac{\nu_\pm}{(1+\nu_\pm)\nu_{\min}}\left[\frac{m}{E_{\min}} \pm \sqrt{1-\left(\frac{\nu_{\min}}{\nu_\pm}\right)^2}\right], \quad (55)$$

where

$$\nu_{\min} \equiv \cos(\theta'/2), \quad E_{\min} \equiv m/\sin(\theta'/2) \quad (56)$$

is the minimum velocity and the minimum electron (positron) energy. It can be seen from (55) that, in contrast to what we have in the noninterference region, the velocities of electron and positron translational motion in the interference region are bounded from below by a quantity that is dependent on the angle of photon incidence [see Eq. (56)]. It should be emphasized that Eqs. (55) and (56) are valid for arbitrary intensities of the two waves.

Let us find out how the process of pair photoproduction on a nucleus proceeds in the interference region near the threshold—that is, in the case where the incident-photon energy is such that the electron and positron are produced with energies close to $E_{\min}$ ($\nu_\pm \longrightarrow \nu_{\min}$):

$$\frac{\nu_\pm - \nu_{\min}}{\nu_\pm} \ll 1. \quad (57)$$

If condition (57) is satisfied, it is easy to obtain, on the basis of relation (55), the angles at which the electron-positron pair is emitted. We have

$$\theta_\pm = \frac{1}{2}\theta' \pm \sqrt{2\left(\frac{\nu_\pm - \nu_{\min}}{\nu_\pm}\right)} \approx \frac{1}{2}\theta'; \quad (58)$$

that is, the electron–positron pair is emitted within a narrow cone along the bisector of angle between the wave vector $\mathbf{k}_1$ and incident-photon momentum $\mathbf{k}'$ [the $\pm$ sign in Eq. (58) in front of the square root refers both to the electron and to the positron]. It is peculiar to this process that, as the energy grows (far from the threshold), the direction of electron and positron emission recedes from the bisector of this angle (see Fig. 2). In the limit of ultrarelativistic energies ($E_\pm \gg m$), they are emitted either near the direction of the incident-photon momentum $\mathbf{k}'$ or near the direction of the wave vector $\mathbf{k}_1$ [see Eq. (55)]; that is, these angles are given by

$$\theta_\pm = \begin{cases} \theta' - (m^2/2E_\pm^2)\cot(\theta'/2) \\ (m^2/2E_\pm^2)\cot(\theta'/2) \ll 1. \end{cases} \quad (59)$$

We note that expression (59) is valid for not overly small angles $\theta' \gg (m/E_\pm)^2$. On the basis of Eqs. (52) and (53) [in the cases of emission (absorption) of photons that is correlated in such a way that their numbers in the two waves are equal or differ by unity], we can obtain the threshold frequency of the incident photon in the

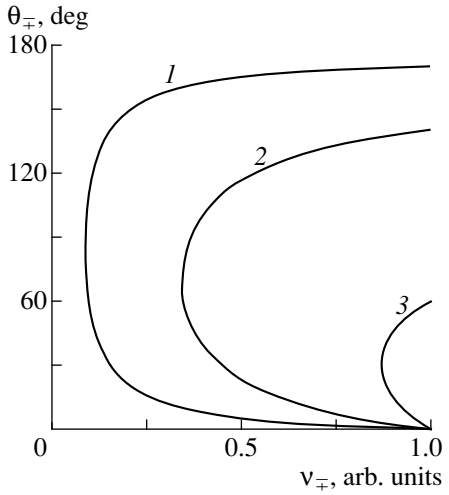

Fig. 2. Electron (positron) emission angle $\theta_\mp$ [see Eq. (55)] as a function of the electron (positron) velocity $\nu_\mp$ for various values of the angle of photon incidence: (*1*) $\theta' = 170°$ ($\nu_{\min} = 0.09$), (*2*) $\theta' = 140°$ ($\nu_{\min} = 0.34$), and (*3*) $\theta' = 60°$ ($\nu_{\min} = 0.87$).

partial process,

$$\omega'_{\min} = (2 + \eta_1^2 + \eta_2^2)E_{\min} + l_{12}\Omega_{12} \quad (60)$$

or

$$\omega'_{\min} = (2 + \eta_1^2 + \eta_2^2)E_{\min} + l_{12}\Omega_{12} - \frac{1}{2}(1+\delta_2)\omega_1 - \frac{1}{2}(1-\delta_2)\omega_2. \quad (61)$$

From Eqs. (56), (60), and (61), it can be seen that, by specifying the angles θ' and the incident-photon energy, we can smoothly change the minimal energy of the product electron and the product positron. Let us assume that the incident-photon momentum is nearly antiparallel to the wave vector $\mathbf{k}_1$,

$$\Delta\theta' = (\pi - \theta') \ll 1. \quad (62)$$

From Eq. (56), we then find that the minimum nonrelativistic velocity of the electron and the positron is given by

$$\nu_{\min} \approx \frac{1}{2}\Delta\theta' \ll 1 \quad (63)$$

and that, in the case specified by Eq. (52), for example, the threshold frequency for the incident photon takes the form

$$\omega'_{\min} = 2\left(m + \frac{1}{2}m\nu_{\min}^2 + \frac{1}{2}m\nu_1^2 + \frac{1}{2}m\nu_2^2\right) + l_{12}\Omega_{12}, \quad (64)$$

where $\nu_{1,2} = \eta_{1,2}$ is the rate of electron (positron) oscillations in the first and the second wave. We emphasize that the second term in the parenthetical expression on

the right-hand side of Eq. (64) has the meaning of the minimal kinetic energy of the electron (positron)—there is no such minimum in the noninterference region—while the third and the fourth term correspond to the energy of oscillations. It should also be noted that, since we use the Born approximation, the values of the angle $\Delta\theta'$ (62) cannot be overly small; that is,

$$\Delta\theta' \gg 2Z/137. \tag{65}$$

In the opposite limiting case where the incident-photon momentum is nearly parallel to the wave vector $\mathbf{k}_1$,

$$\theta' \ll 1, \tag{66}$$

it follows from Eq. (56) that the ultrarelativistic minimal energy of the electron and the positron is

$$E_{\min} = 2m/\theta' \gg m. \tag{67}$$

The angles (58) of electron and positron emission are then given by

$$\theta_\pm = \frac{1}{2}\theta' \pm \frac{m}{E_{\min}}\sqrt{1-\left(\frac{E_{\min}}{E_\pm}\right)^2} \ll 1. \tag{68}$$

If the angle between the incident-photon momentum $\mathbf{k}'$ and the wave vector $\mathbf{k}_1$ is close neither to zero nor to π [that is, when relations opposite to the inequalities in (62) and (66) are satisfied], we arrive at relativistic values for the minimal energies of the electron and the positron.

In the interference region, multiphoton processes are determined by the Bessel functions $J_r(\alpha_{12})$ [see Eqs. (38)–(46)], while the conditions under which such processes become operative are formulated in terms of the quantum parameters α_{12} (17). In addition to the photoproduction of an electron–positron pair on a nucleus, there therefore basically proceed, in this case, processes of the stimulated correlated emission (absorption) of $l_{12} \lesssim \alpha_{12}$ photons of the two waves from the product electron and positron. As a result, the energy fraction emitted by the electron (positron) or absorbed by it from both waves is about $l_{12}\Omega_{12}/\omega' \lesssim \zeta_{\text{int}}$, where ζ_{int} is the quantum interference parameter determining the integrated features of the process in the region specified by Eq. (31),

$$\zeta_{\text{int}} = \xi_1\xi_2, \tag{69}$$

$\xi_{1,2}$ being given by expression (21). We define the region of moderately strong fields for the interference region (31) by imposing the condition $\zeta_{\text{int}} \ll 1$ on the quantum interference parameter. For the product of the intensities of the two waves, this implies fulfillment of the inequality

$$\eta_1\eta_2 \ll (\omega'/m)^2. \tag{70}$$

We note that the condition in (70) is less stringent than the analogous condition (22) in the noninterference region. Taking into account (70), we can disregard, in expressions (8) for the squares of the 4-momenta, the energies of the photons of the two waves against the incident-photon energy. It follows that $\tilde{q}_\pm^2 \neq m_*^2$, whence we conclude that the region of moderately strong fields that is specified by the condition in (70) is not a resonance region. If $\eta_1 \sim \eta_2$ in this region, we can set $\tilde{p}_\pm = p_\pm$, in which case the 4-momenta given by Eqs. (7) and (8) assume the form (23). In deriving the cross section from the amplitude given by Eqs. (38)–(46), there will arise terms in $d\sigma_{l_{12}}^{(0)}$ that are proportional to $\eta_{1,2}^0$, $\eta_{1,2}^2$, and $\eta_1\eta_2$ and to higher powers of the wave intensities; concurrently, $d\sigma_{l_{12}}^{(1)}$ will develop terms proportional to $\eta_{1,2}^2$ and $\eta_1\eta_2$ and to higher powers of these parameters. By virtue of (70), we can therefore disregard the amplitude $H_{l_{12}}^{(1)}$ given by the second equation in (39); for the same reason, we can neglect $B_r^{(0)}$ (45) and $D_r^{(1)}$ (46) in the amplitude $H_{l_{12}}^{(0)}$ given by the first equation in (39) and perform summation there over s_{12}. As a result, we obtain $S_{l_{12}}^{(1)} = 0$ and $S_{l_{12}}^{(0)} = J_{l_{12}}(\alpha_{12})S_*$, where S_* in the amplitude for the photoproduction of an electron–positron pair on a nucleus in the absence of an external field. For the production of an electron–positron pair by an unpolarized photon on a nucleus in the field of two moderately intense waves satisfying the condition in (70), the result obtained by averaging, over the polarizations of the pair constituents, the partial differential cross section in the interference region (31) has the form

$$d\sigma_{l_{12}}^{(0)} = J_{l_{12}}^2(\alpha_{12})d\sigma_*, \tag{71}$$

where $d\sigma_*$ is the differential cross section for the process where a photon produces, on a nucleus, an electron and a positron of specified energies and directions of emission in the absence of an external field [12] and where the quantum interference parameter is given by

$$\alpha_{12} = -\eta_1\eta_2\frac{m^2}{\Omega_{12}}\left(\frac{b_+}{E_+} + \frac{b_-}{E_-}\right). \tag{72}$$

It should be emphasized that, in the partial cross section (71), the integral index l_{12} indicates that equal numbers of photons in the two waves are emitted or absorbed ($s = \pm l$); on the contrary, there is no similar correlation between the indices l and s in expressions (25) and (28) for the noninterference region. From Eq. (71), it can be seen that, in the region of moderately strong fields satisfying the condition in (70), the partial cross section for the photoproduction of an electron–positron pair on a nucleus factorizes into the probability of the correlated emission (absorption) of equal numbers of photons of the two waves and the cross section for the photoproduction of an electron–positron pair on a nucleus in the absence of an external field. It is important that, in the interference region, this correlation between the

numbers of photons in the two waves is irremovable; that is, the cross section (71) cannot be represented as the product of the probabilities of emission and absorption in each of the two waves separately, as this may occur in the noninterference region [see Eq. (28)]. It should also be noted that, in expression (71), the electron and positron emission angles in the parameters $b_\mp$ (51) are determined by relation (55). In the region of moderately strong fields that is specified by the condition in (70), the threshold frequency of the incident photon is given by

$$\omega'_* = (2 + \eta_1^2 + \eta_2^2)E_{\min}, \tag{73}$$

and we can set $E_\pm = E_{\min}$ in the cross section (71) near the threshold, in which case the quantum interference parameter α_{12} (72) becomes

$$\alpha_{12} = -2\eta_1\eta_2\frac{E_{\min}}{\Omega_{12}}. \tag{74}$$

If, in addition to the condition in (70), the wave intensities satisfy the inequalities

$$\eta_1\eta_2 \gtrsim \begin{cases} \omega_{1,2}/m & \text{for} \quad E_\pm \sim m \\ \omega_{1,2}E_\pm/m^2 & \text{for} \quad E_\pm \gg m, \end{cases} \tag{75}$$

we have $\alpha_{12} \gtrsim 1$; hence, $\gamma_{1,2} \sim \alpha_{12}/\xi_{2,1} \gg \alpha_{12}$ [see Eqs. (20) and (72)]. Taking this into account, one can easily show [13] that, for wave intensities satisfying the conditions in (70) and (75), the partial cross section (25) in the noninterference region is much smaller than the corresponding cross section (71) in the interference region:

$$R = \frac{d\sigma_{ls}}{d\sigma^{(0)}_{l_{12}}} = \frac{|I_{ls}|^2}{J^2_{l_{12}}(\alpha_{12})} \sim (\gamma_1\gamma_2)^{-1} \ll 1, \quad \text{for} \quad l, s \ll \gamma_{1,2}. \tag{76}$$

Let us estimate the field strengths and the cross-section ratios (76) for relativistic energies of the incident photon and of the product electron–positron pair ($\omega' \sim m$, $E_\mp \sim m$). In this case, we find that, in the region of optical frequencies ($\omega_{1,2} \sim 10^{15}$ s^{-1}), the quantum interference parameter α_{12} is about unity when the field strengths in the two waves have values of $F_{1,2} \sim 10^6$–10^7 V/cm [see Eqs. (72) and (10)], which are widely used in present-day physical experiments. For such field strengths and such energies of the pair, the Bunkin–Fedorov quantum parameters are $\gamma_{1,2} \sim 3 \times 10^3$. Taking this into account, we find from Eq. (76) that the cross-section ratio in question is $R \sim 10^{-7}$ for multiphoton processes where the numbers of photons satisfies the inequality $l, s \ll 3 \times 10^3$.

Thus, we conclude that, if the electron and positron emission angles and energies are recorded simultaneously in the plane spanned by the wave vector of the light wave and the momentum of the incident photon moving in the nuclear field, the process in which the photoproduction of an electron–positron pair on a nucleus is accompanied by the correlated multiphoton emission (absorption) of equal numbers of photons in the two waves can be much more probable than the analogous process in the noninterference region.

The partial cross section (71) can be summed over all emission and absorption processes. This will yield a result similar to that obtained in the noninterference region: for moderately strong fields satisfying the condition in (70), all essentially quantum contributions are canceled out completely upon the above summation [see Eq. 29)]:

$$d\sigma = \sum_{l_{12}=-\infty}^{\infty} d\sigma^{(0)}_{l_{12}} = d\sigma_*. \tag{77}$$

5. CONCLUSIONS

The results deduced from our analysis of the photoproduction of an electron–positron pair on a nucleus in the field of two light waves propagating in one direction can be summarized as follows:

(i) The photoproduction of an electron–positron pair on a nucleus in the field of two waves depends greatly on the kinematics of the incident photon and of the product electron–positron pair. Owing to this, we can single out two kinematical regions: the noninterference one [if relations (31) are not satisfied], where the conditions under which multiphoton processes come into play are governed by the Bunkin–Fedorov quantum parameters γ_j (16), and the interference one [if relations (31) are satisfied], where multiphoton processes are controlled by the quantum interference parameters α_{12} (17).

(ii) For moderately strong fields [$\xi_{1,2} \ll 1$; see Eq. (22)], the partial cross section in the noninterference region factorizes into the cross section for the photoproduction of an electron–positron pair on a nucleus in the absence of external fields and the probability of the emission (absorption) of a specific number of photons of the first and the second wave [see Eq. (25)]. It has been shown that, for wave intensities such that the quantum interference parameter α_{12} is much less than unity, processes leading to the photoproduction of an electron–positron pair on a nucleus and processes involving the absorption and emission of photons of the first and the second wave by the electron and the positron proceed independently [see Eq. (28)].

(iii) In the photoproduction of an electron–positron pair on a nucleus in the field of two light waves, an interference effect has been discovered that occurs if the electron–positron pair is produced in the plane spanned by the wave vector of the light wave and the incident-photon momentum. In this case, the Bunkin–Fedorov parameters are equal to zero, so that multiphoton processes are controlled by the quantum interfer-

ence parameter α_{12} (17). Because of this, there occurs correlated emission (absorption) of photons by the electron (positron) of the pair, the numbers of these photons in the two waves being equal or being different by unity. It has been shown that, for the electron and the positron energy, there is a lower bound E_{min} (56), which depends greatly on the angle between the incident-photon momentum $\mathbf{k}'$ and the wave vector $\mathbf{k}_1$. If the incident-photon momentum is nearly parallel or nearly antiparallel to the wave vector, the minimal electron (positron) energy is, respectively, ultrarelativistic [$E_{min} \gg m$; see Eq. (67)] or nonrelativistic [$\nu_{min} \ll 1$; see Eq. (63)]. Otherwise, we have $E_{min} \sim m$. Herein lies a significant difference between the photoproduction of an electron–positron pair on a nucleus in the interference region and the analogous process in the noninterference region. Near the threshold, the electron–positron pair is emitted into a narrow cone around the bisector of the angle between the incident-photon momentum and the wave vector of the light wave [see Eq. (58)]. As the energy is increased, however, the electron and positron momenta deflect ever more pronouncedly from the bisector of this angle; in the limit of ultrarelativistic energies, the emission direction is close to either the incident-photon momentum or the wave vector [see Eq. (59)].

(iv) For moderately strong fields [$\xi_{int} \ll 1$; see the condition in (70)], the partial cross section for the photoproduction of an electron–positron pair on a nucleus in the field of two light waves has been obtained in the interference region. This expression factorizes into the cross section for the photoproduction of an electron–positron pair on a nucleus in the absence of external fields and the probability of the correlated emission (absorption) of equal numbers of photons in the two waves [see Eq. (71)]. The latter probability cannot be represented as the product of the probability of the emission (absorption) of photons in individual waves separately, in contrast to what occurs in the noninterference region. It has been shown that the partial cross section for the processes where there is a correlated emission (absorption) of equal numbers of photons in the two waves and where the electron and the positron are emitted at given angles and with given energies can considerably exceed the cross section for the analogous process in any other geometric arrangement [see Eq. (76)].

REFERENCES

1. A. V. Borisov *et al.*, Izv. Vyssh. Uchebn. Zaved., Fiz., No. 2, 12 (1981).
2. A. E. Kazakov and S. P. Roshchupkin, Preprint No. 115, FIAN (Lebedev Institute of Physics, Academy of Sciences of USSR, Moscow, 1983).
3. S. P. Roshchupkin, Izv. Vyssh. Uchebn. Zaved., Fiz., No. 8, 12 (1983).
4. S. P. Roshchupkin, Laser Phys. **6**, 837 (1996).
5. S. P. Roshchupkin and O. B. Lysenko, Laser Phys. **9**, 494 (1999).
6. S. P. Roshchupkin and O. B. Lysenko, Zh. Éksp. Teor. Fiz. **116**, 1210 (1999) [JETP **89**, 647 (1999)].
7. S. P. Roshchupkin, Zh. Éksp. Teor. Fiz. **106**, 102 (1994) [JETP **79**, 54 (1994)].
8. S. P. Roshchupkin, Zh. Éksp. Teor. Fiz. **109**, 337 (1996) [JETP **82**, 177 (1996)].
9. F. V. Bunkin and M. V. Fedorov, Zh. Éksp. Teor. Fiz. **49**, 1215 (1965) [Sov. Phys. JETP **22**, 844 (1965)].
10. M. M. Denisov and M. V. Fedorov, Zh. Éksp. Teor. Fiz. **53**, 1340 (1967) [Sov. Phys. JETP **26**, 779 (1968)].
11. F. V. Bunkin, A. E. Kazakov, and M. V. Fedorov, Usp. Fiz. Nauk **107**, 559 (1972) [Sov. Phys. Usp. **15**, 416 (1972)].
12. V. B. Berestetskiĭ, E. M. Lifshitz, and L. P. Pitaevskiĭ, *Quantum Electrodynamics* (Nauka, Moscow, 1980; Pergamon, Oxford, 1982).
13. *Handbook of Mathematical Functions*, Ed. by M. Abramowitz and I. A. Stegun (Dover, New York, 1971; Nauka, Moscow, 1979).

Translated by A. Isaakyan

Physics of Atomic Nuclei, Vol. 64, No. 2, 2001, pp. 253–255. Translated from Yadernaya Fizika, Vol. 64, No. 2, 2001, pp. 299–302.

NUCLEI
Theory

Chaos in a Supercritical Atom

D. U. Matrasulov

Department of Thermal Physics, Uzbek Academy of Sciences, ul. Katartal 28, Tashkent, 700135 Republic of Uzbekistan

Received August 26, 1999; in final form, January 11, 2000

Abstract—Stochastization of a supercritical atom (with a nuclear charge number Z in excess of 137) under the effect of a periodic perturbation is investigated. The Hamiltonian for a relativistic electron in the Coulomb field of a $Z > 137$ charge is obtained. A simple analytic formula is derived for the critical external-field strength corresponding to the onset of stochastization. The diffusion coefficient is evaluated. © *2001 MAIK "Nauka/Interperiodica".*

In contemporary physics, much attention has recently been given to the realms of superheavy elements. In particular, rapidly growing interest in the synthesis and chemistry of actinide and transactinide nuclei continues stimulating intensive investigations into the properties of superheavy elements [1, 2]. That superheavy atoms are of relativistic nature—because of a large charge of the nucleus in such an atom, the motion of its electrons is described by relativistic equations—complicates problems to be solved in these investigations. In the present study, we analyze the classical dynamics of a relativistic electron in the field of a supercharged ($Z > 137$) nucleus under the effect of a periodic perturbation. An atom whose nucleus has a charge number in excess of 137 is referred to as a supercritical atom [3, 4]. The quantum-mechanical properties of supercritical atoms were explored in a number of studies (see, for example, [3–5]). For deep energy levels in the lower continuum, the semiclassical dynamics of such atoms was investigated in [4, 5]. Experimentally, such supercritical states are generated in slow collisions of heavy ions whose total charge number is greater than 137 [6–8]. So far, investigations into dynamical chaos have been performed predominantly for nonrelativistic systems. Only a few articles [9–13] have been devoted to studying chaotic behavior in relativistic systems. Stochastization of a subcritical ($Z <$ 137) relativistic hydrogen-like atom, where relativistic corrections to highly excited states are small, was investigated in [11, 12]. In contrast to a subcritical atom, a supercritical one is essentially a relativistic object [3–5]. It is well known [3, 6] that the approximation of pointlike charges is inapplicable in studying the motion of a relativistic electron in the field of a $Z > 137$ Coulomb center. For this reason, it is necessary to regularize the problem with allowance for a finite size of the nucleus. The regularization in question consists in redefining the Coulomb potential as

$$V(r) = \begin{cases} -\dfrac{Z\alpha}{r} & \text{for} \quad r > R \\ -\dfrac{Z\alpha}{R} f\left(\dfrac{r}{R}\right) & \text{for} \quad 0 < r < R, \end{cases}$$

where $f(r/R)$ is a cutoff function that takes into account a finite size of the nucleus and R is its radius (hereafter, we use the system of units where $\hbar = m = c = 1$). We will consider the case of $f(r/R) = 1$ (surface distribution of the nuclear charge). The relativistic momentum, which is given by

$$p = \sqrt{(\varepsilon - V)^2 - \frac{M^2}{r^2} - 1},$$

where ε is the energy of the electron being considered and M is its orbital angular momentum, can then be recast into the form

$$p = \begin{cases} \sqrt{\left(\varepsilon + \dfrac{Z\alpha}{r}\right)^2 - \dfrac{M^2}{r^2} - 1} & \text{for} \quad r > R \\ \sqrt{\left(\varepsilon + \dfrac{Z\alpha}{R}\right)^2 - \dfrac{M^2}{r^2} - 1} & \text{for} \quad 0 < r < R. \end{cases}$$

The turning points correspond to zero values of the momentum p. One of these points,

$$r_1 = M\left[\left(\varepsilon + \frac{Z\alpha}{R}\right)^2 - 1\right]^{-1},$$

lies within the nucleus, while the other,

$$r_2 = \frac{|\varepsilon Z| - \sqrt{\varepsilon^2 Z^2 \alpha^2 - (\varepsilon^2 - 1)(Z^2\alpha^2 - M^2)}}{\varepsilon^2 - 1},$$

is outside it.

Taking into account a finite size of the nucleus, we can therefore determine the action functional for $Z > M$ as

$$\pi n = I_1 + I_2, \tag{1}$$

where

$$I_1 = \int_{r_1}^{R} \sqrt{\left(\varepsilon + \frac{Z\alpha}{r}\right)^2 - \frac{M^2}{r^2} - 1}\, dr$$

$$= \frac{\pi}{\sqrt{-A}} - \sqrt{C}\ln\sqrt{B^2 - 4AC} - \sqrt{AR^2 + BR + C} + \frac{B}{2\sqrt{-A}}\arcsin\frac{\sqrt{2AR + B}}{\sqrt{B^2 - 4AC}} + \sqrt{C}\ln\left|\frac{2C\sqrt{AR^2 + BR + C}}{R}\right| + \frac{2C}{R} + B, \quad (2)$$

$$I_2 = \int_{R}^{r_2} \sqrt{\left(\varepsilon + \frac{Z\alpha}{R}\right)^2 - \frac{M^2}{r^2} - 1}\, dr$$

$$= a'\left[\sqrt{R^2 - a^2} - a\arccos\left|\frac{a}{R}\right|\right]. \quad (3)$$

Here, $A = \varepsilon^2 - 1$, $B = 2\varepsilon Z$, and $C = Z^2 - M^2$ in (2), and $a' = (\varepsilon + Z/R)^2 - 1$ and $a = M/a'$ in (3).

Substituting (2) and (3) into (1) and solving the resulting equation for ε in the approximation specified by the relationships $|\varepsilon| \ll 1$ and $M \sim Z\alpha$, we can derive the expression for the Hamiltonian of a relativistic electron in the field of a supercharged nucleus ($Z > 137$) in terms of the action–angle variables. The result is

$$H_0 = \varepsilon \approx -\frac{g}{Z}c(R, g)\exp\left\{-\frac{\pi n}{g}\right\}, \quad (4)$$

where $c(r, g) = \exp(g - R)$ and $g = \sqrt{Z^2\alpha^2 - M^2}$.

The fundamental frequency is given by

$$\omega_0 = \frac{dH_0}{dn} = \frac{\pi}{Z\alpha}c(R, g)\exp\left\{-\frac{\pi n}{g}\right\}. \quad (5)$$

For $Z > M$, the equation for the trajectory in the region $r > R$ has the form [14]

$$\frac{Z^2\alpha^2 - M^2}{r} = \sqrt{M^2\varepsilon^2 + (Z^2\alpha^2 - M^2)}\cosh\left(\phi\sqrt{\frac{Z^2\alpha^2}{M^2} - 1}\right) + \varepsilon Z\alpha. \quad (6)$$

At $Z \sim M$ ($\varepsilon \sim 0$), we have

$$\frac{Z^2\alpha^2 - M^2}{r} \approx \sqrt{M^2\varepsilon^2 + (Z^2\alpha^2 - M^2)} \times (1 - \phi^2)\sqrt{\frac{Z^2\alpha^2}{M^2} - 1} + \varepsilon Z\alpha$$

or

$$\frac{Z^2\alpha - M^2}{r} \approx \sqrt{Z^2\alpha - M^2}(M - \phi\sqrt{Z^2\alpha - M^2}) + \varepsilon Z\alpha.$$

For $r < R$, the equation for the trajectory has the form

$$1/r = a_0\cos\phi, \quad (7)$$

where

$$a_0 = M^{-1}\left[\left(\varepsilon + \frac{Z\alpha}{R}\right)^2 - 1\right],$$

ϕ being a polar angle.

Let us now consider the interaction of this supercritical atom with the linearly polarized monochromatic perturbation field

$$V = \epsilon\cos\omega t\sin\theta[x\sin\psi + y\cos\psi], \quad (8)$$

where θ and ψ are Euler angles. In order to analyze the supercritical atom for stochasticity, we assume the orbital angular momentum M to be fixed, thereby reducing the number of degrees of freedom to unity.

The total Hamiltonian can be represented as

$$H = -\frac{\sqrt{Z^2\alpha^2 - M^2}}{Z\alpha}\exp\left\{-\frac{\pi n}{\sqrt{Z^2\alpha^2 - M^2}}\right\} + \epsilon\cos\omega t\sin\theta\sum(x_k\sin\psi\cos k\lambda + y_k\cos\psi\sin k\lambda), \quad (9)$$

where λ is an Euler angle and x_k and y_k are the Fourier components of the electron dipole moment. The explicit expressions for them are [14]

$$x_k = \frac{i}{k\omega_0 T}\int_0^T e^{ik\omega_0 t}dx$$

$$= \frac{i}{k\omega_0 T}\int_0^T \exp[ik\omega_0(2|\varepsilon Z|\xi - \sin\xi)] \times \sin\xi\left\{\cos\frac{2g^{-1}}{a - \cos\xi} - \frac{1}{a - \cos\xi}\sin\frac{2g^{-1}}{a - \cos\xi}\right\}d\xi, \quad (10)$$

$$y_k = -\frac{i}{k\omega_0 T}\int_0^T e^{ik\omega_0 t}dy$$

$$= -\frac{iMb^{-5/2}}{k\omega_0 T}\int_0^{T_1}\frac{e^{ik\omega_0 t}\sin 2\xi d\xi}{\sqrt{M^2\cos^2\xi - b^2}} + \frac{i}{k\omega_0 T}\int_{T_1}^T \exp[ik\omega_0(2|\varepsilon Z|\xi - \sin\xi)] \times \sin\xi\left\{\sin\frac{2g^{-1}}{a - \cos\xi} - \frac{1}{a - \cos\xi}\cos\frac{2g^{-1}}{a - \cos\xi}\right\}d\xi, \quad (11)$$

where

$$a = \sqrt{Z^2 - M^2}\exp\{-\pi n/\sqrt{Z^2 - M^2}\},$$

$$T = 2\pi/\omega_0, \quad b = \left(\varepsilon + \frac{Z}{R}\right)^2 - 1, \quad T_1 = \frac{(R - r_0)}{2M}.$$

Evaluating the integrals in (10) and (11) by the stationary-phase method, we arrive at

$$x_k = 0, \quad y_k = \frac{R^2\exp\{-\pi n/g\}}{\pi k^2}. \tag{12}$$

In order to analyze the supercritical atom for stochasticity, it is necessary to find, as was done in [12, 13, 15], the resonance width

$$\Delta\nu_k = (8\omega_0' r_k \epsilon)^{1/2},$$

where $r_k = \sqrt{x_k^2 + y_k^2}$ and $\omega_0' = d\omega_0/dn$.

From Chirikov's stochasticity criterion [13, 14], which has the form

$$2.5\left[\frac{\Delta\nu_k + \Delta\nu_{k+1}}{\omega_0(k+1) - \omega_0(k)}\right]^2 > 1,$$

where $\omega_0(k+1) - \omega_0(k) = \omega/(k+1) - \omega/k$ is the spacing between the neighboring resonances, we find that the critical external-field strength corresponding to the onset of the stochastization of electron motion is

$$\epsilon_{cr} = \frac{\sqrt{Z^2\alpha^2 - M^2}\exp\{-\pi n/\sqrt{Z^2\alpha^2 - M^2}\}}{20Zk(k+1)^2(\sqrt{r_k} + \sqrt{r_{k+1}})^2}. \tag{13}$$

Taking into account (12), we reduce the critical field to the form

$$\epsilon_{cr} = \pi k\frac{gc(R, g)\exp\{-2\pi n/g\}}{20Z(2k^2 + 2k + 1)}. \tag{14}$$

In just the same way as in [13, 15], we calculate the diffusion coefficient as

$$D = \frac{\pi}{2}\frac{\epsilon^2 R^2}{c(R, g)(Z\alpha)^3}\exp\{-2\pi n/g\}. \tag{15}$$

In summary, stochastization of a supercritical hydrogen-like atom ($Z > 137$) interacting with a monochromatic field has been investigated. Analytic formulas for this case have been obtained, which reveal that the critical field strength for the onset of stochastization is much less for a supercritical atom than for a subcritical atom ($Z < 137$), which was investigated in [13]. This can be explained by the fact that the condensation of levels has an exponential character [see Eq. (4)]. The above results can be of use in studying processes accompanying slow collisions of heavy ions (with a total charge in excess of 137) that interact simultaneously with a monochromatic radiation field.

REFERENCES

1. V. Pershina and B. Fricke, Preprint No. 98-26, GSI (Darmstadt, 1998).
2. S. Holmann, Preprint No. 99-02, GSI (Darmstadt, 1999).
3. J. Pomeranchuk and J. Smorodinsky, J. Phys. (Moscow) **9**, 97 (1945).
4. V. D. Mur, V. S. Popov, and D. N. Voskresenskiĭ, Pis'ma Zh. Éksp. Teor. Fiz. **28**, 140 (1978) [JETP Lett. **28**, 129 (1978)].
5. V. D. Mur and V. S. Popov, Yad. Fiz. **28**, 837 (1978) [Sov. J. Nucl. Phys. **28**, 429 (1978)].
6. A. A. Grib, S. G. Mamaev, and V. M. Mostepanenko, *Vacuum Quantum Effects in Strong Fields* (Énergoatomizdat, Moscow, 1988).
7. V. S. Popov, Yad. Fiz. **17**, 621 (1973) [Sov. J. Nucl. Phys. **17**, 322 (1973)].
8. J. Rafelski, B. Müller, and W. Greiner, Phys. Rep. **34**, 249 (1978).
9. A. A. Chernikov, T. Tel, G. Vattay, and G. M. Zaslavsky, Phys. Rev. A **40**, 4072 (1989).
10. Kim Jung-Hoon and Lee Hai-Woong, Phys. Rev. E **53**, 4242 (1996).
11. S. P. Drake, C. P. Dettmann, and N. J. Cornish, Phys. Rev. E **53**, 1351 (1996).
12. D. U. Matrasulov, Zh. Tekh. Fiz. **69** (2), 127 (1999) [Tech. Phys. **44**, 249 (1999)].
13. D. U. Matrasulov, Phys. Rev. A **60**, 700 (1999).
14. L. D. Landau and E. M. Lifshitz, *The Classical Theory of Fields* (Nauka, Moscow, 1988; Pergamon, Oxford, 1975).
15. N. B. Delone, V. P. Kraĭnov, and D. L. Shepelyanskiĭ, Usp. Fiz. Nauk **140**, 355 (1983) [Sov. Phys. Usp. **26**, 551 (1983)].

Translated by S. Slabospitsky

Physics of Atomic Nuclei, Vol. 64, No. 2, 2001, pp. 256–260. Translated from Yadernaya Fizika, Vol. 64, No. 2, 2001, pp. 303–307.

ELEMENTARY PARTICLES AND FIELDS
Experiment

^{75}Se as a New Neutrino Source for Calibrating Low-Threshold Detectors of Solar Neutrinos

V. N. Kornoukhov

Institute of Theoretical and Experimental Physics, Bol'shaya Cheremushkinskaya ul. 25, Moscow, 117259 Russia

Received July 5, 2000

Abstract—A new artificial neutrino source on the basis of the ^{75}Se isotope for calibrating low-threshold solar-neutrino detectors like GNO, SAGE, and LENS is considered. It is shown that ^{75}Se possesses some advantages over sources based on ^{51}Cr: the energies of its basic neutrino lines are close to the endpoint of the neutrino spectrum associated with proton–proton interactions in the solar cycle, and the production cross section for the former and its half-life are much larger. A Russian L-2 heavy-water reactor can be used to generate the required activity of ^{75}Se in an optimal mode. © *2001 MAIK "Nauka/Interperiodica".*

1. INTRODUCTION

The problem of solar neutrinos is one of the pressing problems in contemporary physics and astrophysics. As a matter of fact, the problem consists in that, according to the results from four experiments that recorded solar neutrinos (chlorine–argon experiment [1], Kamiokande [2], GALLEX [3], and SAGE [4]), the fluxes of solar neutrinos are sizably less than that predicted by the standard solar model.

In order to solve this problem, it is necessary to continue Ga–Ge experiments with the aim of improving the accuracy of the results already obtained (SAGE [4] and GNO [5] experiments) and to launch new experiments to implement an on-line detection of low-energy neutrino fluxes from proton–proton interactions and electron capture in a ^{7}Be nucleus (for example, this could be achieved with the recently proposed LENS detector employing a target based on Yb [6]).

In order to interpret correctly the results of experiments that record solar neutrinos, it is necessary to calibrate preliminarily the detectors involved by using artificial neutrino sources whose parameters are known to within 5%. A number of *K*-capture sources were proposed as artificial neutrino sources for calibrating solar-neutrino detectors (^{51}Cr, ^{65}Zn, and ^{37}Ar [7–9]). It should be recalled that artificial neutrino sources based on the ^{51}Cr isotope successfully operated in GALLEX [10] and SAGE [11] experiments.

For the GNO and SAGE detectors, a calibration experiment is required for a high-precision determination of the efficiency of their operation, while, for the LENS detector, such an experiment is needed above all for measuring the cross section for neutrino capture by a ^{176}Yb nucleus. It should be noted here that the LENS detector makes use of the reaction in which low-energy solar neutrinos are captured by a target based on the ^{176}Yb isotope [6]. Upon neutrino capture in a ^{176}Yb nucleus, there arise excited isomeric states of the ^{176}Lu nucleus, which decay into a long-lived isomeric state with lifetime τ = 50 ns. In this case, the neutrino-capture reaction is characterized by the presence of two events (one from the electron produced as the result of neutrino capture and the other from the photon deexciting the long-lived isomeric state of ^{176}Lu) at the same place of the detector with a mean delay time of 50 ns.

In the present study, we discuss the possibility of using the ^{75}Se isotope for calibrating the low-threshold detectors SAGE, GNO, and LENS. This isotope has a number of important advantages over artificial neutrino sources based on ^{51}Cr: the half-life of the former is longer by a factor of 4.3, and the energy of its basic neutrino lines is close to the endpoint of the neutrino spectrum associated with proton-proton interactions of the solar cycle.

2. NEUTRINO RADIATION FROM AN ARTIFICIAL NEUTRINO SOURCE ON THE BASIS OF ^{75}Se

Upon electron capture, ^{75}Se transforms into ^{75}As, releasing a total energy of 863 keV (the relevant half-life is $T_{1/2}$ = 119.79 d) [12]. The most probable transitions are accompanied by the energy release of 462.9 keV (95.9%), 584.1 keV (1.7%), 598.9 keV (0.7%), and 863.6 keV (1%) [12]. The diagram of ^{75}Se decay is displayed in the figure, where we can also see the neutrino energy with allowance for the binding energy and the probabilities of electron capture from the *K* and *L* shells. We note that the energy of basic neutrino lines is close to the highest energies of neutrinos from proton–proton interactions, whereas the energy of weak lines is close to the energy of neutrinos from the solar cycle that are emitted in electron capture by a ^{7}Be nucleus.

1063-7788/01/6402-0256$21.00

The neutrino-interaction cross section in the inverse-beta-decay reaction was calculated according to the formula [13]

$$\sigma(E_\nu) = \sigma_0 F(E_e, Z)(E_\nu - Q + m_e) \times \sqrt{(E_\nu - Q + m_e)^2 - m_e^2} M^2, \quad (1)$$

where E_ν is the neutrino energy in MeV, $F(E_e, Z)$ is the Fermi function [14], m_e is the electron mass in MeV, Q is the difference of $A(Z+1)$ and $A(Z)$, $\sigma_0 = G_F^2/\pi = 1.63 \times 10^{-44}$ cm^2/MeV^2 (if the energy is measured in MeV), and the relevant matrix element squared is $M^2 = (g_A/g_V)^2 B(\mathrm{GT}) = (1.267)^2 B(\mathrm{GT})$; we have used here natural units where $\hbar = c = 1$. The values of the Fermi function $F(E_e, Z)$ were borrowed from [14]. The matrix elements for the transitions to the excited states of ^{176}Lu were estimated in terms of the Gamow–Teller strength function B(GT), whose values were determined in experiments studying (n, p) and (^{3}He, t) scattering [15]; for ^{71}Ge, they were taken from [16].

The results of the calculations are presented in Tables 1 and 2. The cross sections for the capture of neutrinos from the ^{75}Se source by the ^{71}Ga and ^{176}Yb nuclei are 2.88×10^{-45} and 0.344×10^{-43} cm^2, respectively. From the calculation, it follows that the contribution to the capture cross section for ^{71}Ga from the ^{75}Se source is determined by transitions to the ground state of ^{71}Ge, amounting to 97% of the total cross section. Thus, a comparison of the results obtained by calibrating a gallium detector with the aid of sources based on ^{51}Cr and ^{75}Se will make it possible to determine independently the cross sections for capture in the ground state of ^{71}Ge and in its excited states.

In calculating the number of events of the capture of neutrinos from a source based on ^{75}Se (and, for the sake of comparison, from the source based on ^{51}Cr) in the SAGE, GNO, and LENS detectors, it was assumed that the neutrino source, together with a passive shielding, is arranged at the detector center. For the LENS detector, which contains 10 t of ytterbium, the length of the path traveled by neutrinos in a detector material was taken to be 295 cm, while the concentration of ^{176}Yb atoms was set to 4.1×10^{19} atom/cm^3. The geometry of the calibration experiment with the GNO detector is analogous to the geometry of the GALLEX experiment [10]. The duration of the calibration experiment was assumed to be three months, while the activity of the source was set to 1 MCi.

Under these conditions, the number of events in the GNO detector for ^{51}Cr will be very close to that for ^{75}Se (242 and 237, respectively). In the LENS detector, the number of events will be 109 for ^{51}Cr and 92 for ^{75}Se (only events leading to the excitation of the 195-keV level of the ^{176}Lu nucleus were taken into account in the last case).

From these calculations, it follows that, in order to achieve a 5% precision (only statistical errors are taken into account here) in calibrating the LENS detector, the activity of the artificial neutrino source based on ^{75}Se (^{51}Cr) is required to be 4.4 MCi (4.3 MCi).[1)] In calibrating the GNO detector, the required activity is 1.7 MCi for ^{75}Se and 1.9 MCi for ^{51}Cr. A similar calculation for the SAGE detector reveals that an artificial neutrino source of activity as low as about 0.45 MCi is sufficient to perform relevant experiments, since the rate at which the ^{71}Ge isotope is produced is much higher in a metal target than in the GNO detector based on a solution of gallium chloride (owing to an order of magnitude higher concentration of Ga atoms).

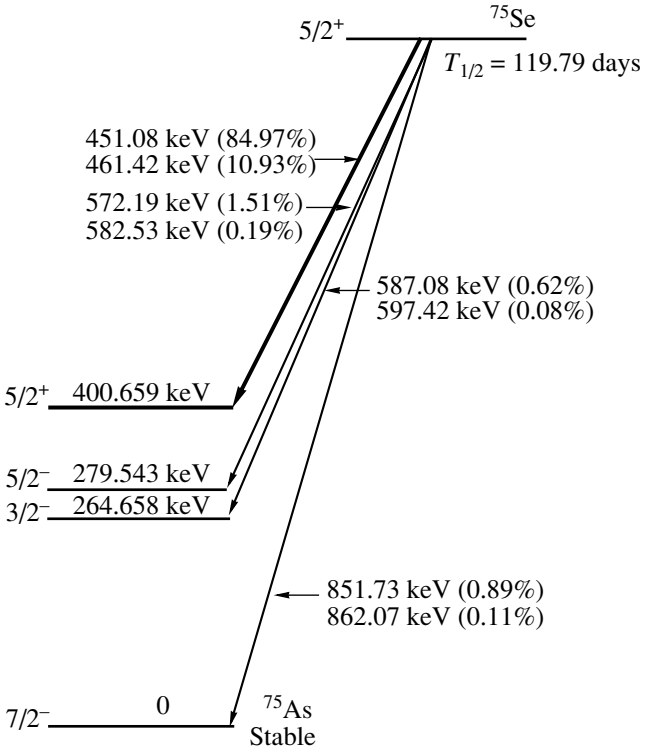

Diagram of ^{75}Se decay (shown in the diagram are neutrino lines whose energies are quoted with allowance for the electron binding energy in the K and L shells)

3. DEVELOPING AN ARTIFICIAL NEUTRINO SOURCE ON THE BASIS OF ^{75}Se

The ^{75}Se isotope is formed upon neutron capture by ^{74}Se. For thermal neutrons, the capture cross section is 51.8 b, while the effective resonance integral is 520 b (see Table 3). The material of the target must be enriched in ^{74}Se and depleted in ^{76}Se, since the latter has a large cross section for the capture of thermal neutrons (85 b) and will substantially reduce the effective neutron flux. It is worth noting that ^{75}Se is used in industry (production of defectoscopes) and medicine (radiopharmaceuticals for medical diagnosis) [18].

[1)]Here, allowances are made for the time (7 days) it takes for delivering the source to the underground laboratory.

Table 1. Effective cross section for neutrino capture by ^{71}Ga nuclei into the ground state and the excited states of the ^{71}Ge nucleus at E_x = 175 and 500 keV (with allowance for the contribution from each neutrino line in the spectrum of the source)

Source	σ_{eff}, 10^{-45} cm^2			Total cross section, 10^{-45} cm^2
	Ground state, B(GT) = 0.087	E_x = 175 keV, B(GT) = 0.005	E_x = 500 keV, B(GT) = 0.01	
^{51}Cr	5.286	0.206	0.135	5.627
^{75}Se	2.791	0.087	0.002	2.880

Note: Here and in Table 2, B(GT) is the Gamow–Teller strength function [15, 16].

The production of selenium enriched in the ^{74}Se isotope does not involve serious technical difficulties, because SeF_6, a gaseous selenium compound that is available at room temperature, makes it possible to use the ultracentrifuging technique, which is well developed in Russia [19]. Since this procedure is very expensive, the optimum enrichment of selenium in ^{74}Se must not be higher than 90 to 95% (at a ^{76}Se concentration of about 10 to 5%).

Selenium is known to have not less than five allotropic modifications; however, only gray hexagonal selenium, which is characterized by the melting temperature of 170°C and the boiling temperature of 685°C (its density is 4.807 g/cm^3), is stable. Selenium is very active chemically; therefore, it must be hermetically sealed during irradiation and subsequent utilization. If selenium is used for a target, it is important to know the temperature dependence of the pressure of its vapors (this pressure changes from 15 mm Hg at 450°C to 760 mm Hg at 685°C [20]), since, for reactor safety, it will be necessary to calculate the required hermetic sealing.

Table 2. Effective cross section for neutrino capture by ^{176}Yb nuclei into the excited states of the ^{176}Lu nucleus at E_x = 195 and 339 keV (with allowance for the contribution from each neutrino line in the spectrum of the source)

Source	σ_{eff}, 10^{-43} cm^2		Total cross section, 10^{-43} cm^2
	E_x = 195 keV, B(GT) = 0.21	E_x = 339 keV, B(GT) = 0.12	
^{51}Cr	0.554	0.228	0.782
^{75}Se	0.336	0.008	0.344

Table 3. Cross section for neutron capture by stable selenium isotopes [17]

Isotope (concentration, %)	σ, b (thermal neutrons)	I, b (resonance integral)
^{74}Se (0.9)	51.8	520
^{76}Se (9.1)	85	40.3
^{77}Se (7.6)	42	30.1
^{78}Se (23.6)	0.43	–
^{80}Se (49.9)	0.61	2.0
^{82}Se (8.9)	0.044	0.039

Questions associated with the production of ^{75}Se were comprehensively studied in [18], where it was shown that, if selenium enriched in ^{74}Se to 100% is exposed to a neutron flux of density 2×10^{14} cm^{-2} s^{-1}, the resulting specific activity ranges between 2.9×10^{13} and 4.4×10^{13} Bq/g (784 to 1189 Ci/g), depending on the characteristic target dimensions (from 1 to 5 mm) and the irradiation time (0.3 yr).

On the basis of the above, we can say that a target must be a pellet or a rod made from pressed selenium powder enriched in the ^{74}Se isotope and enclosed in a hermetic casing from ultrapure aluminum. The diameter of the target must be between 5 and 6 mm in order to avoid the effect of thermal and resonance blocking, whereas the mass of highly enriched selenium must lie in the range 0.8–1.3 kg in order to achieve an activity of 1 MCi.

In Russia, there are a few reactors appropriate for obtaining so high an activity of ^{74}Se. These are the high-energy fast-neutron reactor BN-600, which possesses special irradiation properties [21]; the research reactors SM-3 and MIR [22]; and the L-2 heavy-water reactor Mayak [23, 24]. If we take into consideration the reactor operating period (130 d), the neutron flux density (10^{14}–2×10^{14} cm^{-2} s^{-1}), effective target cooling, and the possibility of loading large amounts of the initial material (distributed over a large volume), preference should be given to the L-2 reactor. This reactor makes it possible to produce a ^{75}Se isotope of high specific activity: from 737 to 875 Ci/g at an enrichment of 90% in ^{74}Se (see Table 4). For generating an activity of 1 MCi, 1.5 kg (1.26 kg) of selenium is required for targets of dimensions $\varnothing 5 \times 6$ mm ($\varnothing 3 \times 3$ mm). The total activity of ^{75}Se that can be achieved with the aid of this reactor by irradiating targets highly enriched in the ^{74}Se isotope is not less than a few MCi at an irradiation duration of 130 d (this estimate was obtained on the basis of ^{60}Co amounts produced by the reactor over a year [23]).

It should be noted that the same enriched initial material can be used three or four times, with the activity of the artificial neutrino source after the third irradiation being about 75 to 80% of the activity obtained upon the first activation.

4. GAMMA RADIATION AND HEAT RELEASE FROM ARTIFICIAL NEUTRINO SOURCES

Gamma radiation from the artificial neutrino source being considered consists of two components: radiation accompanying the decay of the selenium isotope ^{75}Se proper into the excited states of ^{75}As and gamma radiation from isotopes obtained as the result of the activation of some elements appearing in selenium and in a casing material (aluminum) as admixtures. The activation of aluminum and selenium isotopes other than ^{74}Se does not lead to the formation of gamma impurities that are hazardous either from the viewpoint of the physics of the experiment being discussed or for the personnel running it, because all product isotopes are short-lived or stable. Radionuclides that originate from the irradiation of selenium isotopes with fast neutrons in the (n, p), (n, α), and $(n, 2n)$ reactions and which possess hard gamma radiation are not hazardous either, because they have a small production cross section (which is especially important for the long-lived isotope ^{74}As, its half-life being 17.78 d) or are short-lived like ^{76}As (1.1 d) and ^{73}Se (7.2 h). Moreover, the fraction of fast neutrons at the place where the initial material is arranged is small in the L-2 reactor (heavy water is a good moderator of neutrons).

Hence, the requirements on the purity of selenium and aluminum (the mass of the aluminum casing is commensurate with the selenium mass) with respect to hazardous impurities are high. It should also be noted that the technology for purifying selenium is well developed, so that it can be obtained in a form free from the admixtures of elements whose isotopes can be responsible for the production of dangerous radionuclides (in particular, the concentrations of Fe, Ga, Cd, As, and Ag can be reduced to values not exceeding 2×10^{-5}, 10^{-5}, 10^{-5}, 10^{-4}, and 10^{-5}%, respectively).

It follows that, if the purity of selenium and the casing material is sufficiently high, an adverse effect is expected primarily from the gamma radiation originating from ^{75}Se proper and including the lines of energies 821.6 keV (0.000137%), 617.8 keV (0.00444%), 572.2 keV (0.0356%), 400.66 keV (11.48%), 279.54 keV (25.20%), and 264.66 keV (59.3%) [12]. That ^{75}Se features high-energy gamma lines (those at 821.6, 617.8, and 572.2 keV) substantially toughens requirements on biological protection for artificial neutrino sources based on ^{75}Se in relation to that for artificial neutrino sources based on ^{51}Cr.

An important merit of the ^{75}Se isotope as a basic element of artificial neutrino sources is that, owing to its long half-life, there arises the possibility of storing it for a period of up to three weeks until the complete decay (or a considerable reduction of the activity) of potentially present short-lived radioisotopes possessing hard gamma radiation such as ^{72}Ga, ^{24}Na, ^{76}As, and ^{140}La. Concurrently, the activity of ^{75}Se decreases only by 12%.

Table 4. Production of ^{75}Se at the L-2 reactor (enrichment in ^{74}Se and ^{76}Se is 90 and 10%, respectively) [25]

Target dimensions (mm)	Specific activity, Ci/g	Selenium mass for generating 1 MCi, kg
ø3 × 3	875	1.26
ø5 × 6	737	1.5

The decay of ^{75}Se releases energy (in the form Auger electrons, characteristic x rays, and photons) in the amount of 2357 W per 1 MCi of its activity (for the sake of comparison, we indicate that the energy release from the decay of ^{51}Cr of the same activity is 217 W). Therefore, developing means for protection from radiation and for efficient heat removal is an engineering problem of paramount importance in constructing artificial neutron sources on the basis of the ^{75}Se isotope.

5. CONCLUSION

The isotope proposed in this study possesses a number of advantages over the isotope ^{51}Cr used previously: the half-life of the former is longer than the half-life of the latter by a factor of 4.3 (this makes it possible to relax the requirements on the time of calibration experiments), the energy of its basic neutrino lines is close to the endpoint of the neutrino spectrum associated with proton—proton interactions occurring on the Sun, the initial material is characterized by a high purity in hazardous admixtures, and the cross section for ^{75}Se formation is a few times as large as the cross section for ^{51}Cr formation. Moreover, artificial neutrino sources based on the ^{75}Se isotope are advantageous in that they provide the possibility of independently determining the cross section for capture to the ^{71}Ge ground state, whereby the interpretation of the results obtained by measuring the flux of solar neutrinos with a gallium detector will be refined substantially.

In order to generate the required activity of ^{75}Se in an optimal mode, a Russian heavy-water reactor of the L-2 type has been proposed, which makes it possible to produce this isotope with a specific activity of 875 Ci/g by using selenium targets highly enriched in the ^{74}Se isotope.

ACKNOWLEDGMENTS

I am grateful to J.-F. Cavaignac and M. Cribier for the proposal to investigate the possibility of creating an artificial neutrino source on the basis of the ^{75}Se isotope. I am indebted to G.T. Zatsepin and I.R. Barabanov for the support of this study. Thanks are also due to B.P. Kochurov and V.N. Konev for enlightening discussions on the problems associated with the production of ^{75}Se at reactors of the L-2 type.

REFERENCES

1. B. T. Cleveland, T. Daily, R. Davis, Jr., *et al.*, in *Proceedings of the Fourth Solar Neutrino Conference, Heidelberg, Germany, April 8–11, 1997*, Ed. by W. Hampel (Max-Planck-Institut für Kernphysik, Heidelberg, 1997), p. 85.
2. Y. Suzuki, in *Proceedings of the 17th International Conference on Neutrino Physics and Astrophysics, Helsinki, June 13–19, 1996*, Ed. by K. Enquist, K. Huitu, and J. Maalampi (World Sci., Singapore, 1997), p. 73.
3. GALLEX Collab. (P. Anselmann *et al.*), Phys. Lett. B **342**, 440 (1995).
4. SAGE Collab. (J. N. Abdurashitov *et al.*), Phys. Lett. B **328**, 234 (1994).
5. E. Bellotti *et al.*, Proposal for a Permanent Gallium Neutrino Observatory (GNO) at Laboratori Nazionali del Gran Sasso (Feb. 1996).
6. R. Raghavan, Phys. Rev. Lett. **78**, 3618 (1997).
7. V. A. Kuz'min, Candidate's Dissertation in Mathematics and Physics (Lebedev Inst. of Physics, USSR Acad. Sci., Moscow, 1967); R. S. Raghavan, in *Proceedings of the Informal Conference on Status and Future of Solar Neutrino Research, Upton, New York, 1978*, Ed. by G. Friedlander, Brookhaven National Laboratory Report No. 50879, Vol. 2, p. 270.
8. L. W. Álvarez, Lawrence Radiation Laboratory, Physics Notes, Memo No. 767 (1973) (unpublished).
9. W. C. Haxton, Phys. Rev. C **38**, 2474 (1988).
10. GALLEX Collab. (H. Hampel *et al.*), Phys. Lett. B **420**, 114 (1998).
11. E. P. Veretenkin *et al.*, in *Proceedings of the Fourth Solar Neutrino Conference, Heidelberg, Germany, April 8–11, 1997*, Ed. by W. Hampel (Max-Planck-Institut für Kernphysik, Heidelberg, 1997), p. 126.
12. Nucl. Data Sheets **86**, 785 (1999).
13. G. V. Domogatskiĭ, Candidate's Dissertation in Mathematics and Physics (Lebedev Inst. of Physics, USSR Acad. Sci., Moscow, 1970).
14. B. S. Dzhelepov, L. N. Zyryanova, and Yu. P. Suslov, *Beta Processes* (Nauka, Leningrad, 1972).
15. M. Fujiwara, Report to the LENS Collaboration (Grenoble, June 17–18, 1999); Ch. Goodman, Report to the LENS Collaboration (Grenoble, June 17–18, 1999).
16. H. Ejiri *et al.*, Phys. Lett. B **433**, 257 (1998).
17. Nuclear Data (NUDAT) Retrieval Program, Brookhaven National Laboratory, http://www.nndc.bnl.gov/
18. A. S. Gerasimov, T. S. Zaritskaya, and A. P. Rudik, *A Reference Book on the Generation of Nuclides at Nuclear Reactors* (Énergoatomizdat, Moscow, 1989).
19. A. Pokidyshev and M. Pokidysheva, Nucl. Instrum. Methods Phys. Res. A **438**, 7 (1999).
20. *Properties of Elements: A Reference Book*, Ed. by M. E. Drits (Metallurgiya, Moscow, 1997), Vol. 2.
21. D. N. Abdurashitov, V. N. Gavrin, A. V. Zvonarev, *et al.*, At. Énerg. **80**, 101 (1996).
22. S. N. Danshin, in *Proceedings of the Fourth Solar Neutrino Conference, Heidelberg, Germany, April 8–11, 1997*, Ed. by W. Hampel (Max-Planck-Institut für Kernphysik, Heidelberg, 1997), p. 414.
23. A. D. Dodonov, V. P. Petrunin, V. N. Tyazhkorob, *et al.*, in *Proceedings of the Conference on Improved Heavy-Water Reactors, Nov. 18–20, 1997* (Inst. Teor. Éksp. Fiz., Moscow, 1998), p. 87.
24. B. P. Kochurov, V. N. Konev, V. N. Kornoukhov, *et al.*, Preprint No. 37-98, ITÉF (Institute of Theoretical and Experimental Physics, Moscow, 1998).
25. V. N. Kornoukhov, Preprint No. 18-99, ITÉF (Institute of Theoretical and Experimental Physics, Moscow, 1999).

Translated by A. Isaakyan

Physics of Atomic Nuclei, Vol. 64, No. 2, 2001, pp. 261–265. Translated from Yadernaya Fizika, Vol. 64, No. 2, 2001, pp. 308–312.

ELEMENTARY PARTICLES AND FIELDS
Experiment

40-MCi Tritium Source of Antineutrinos

B. S. Neganov[1)], V. N. Trofimov[1)], A. A. Yukhimchuk[2)], and L. N. Bogdanova

Institute of Theoretical and Experimental Physics, Bol'shaya Cheremushkinskaya ul. 25, Moscow, 117218 Russia

Received February 21, 2000; in final form, July 7, 2000

Abstract—Some technical and technological aspects of development, design, and safe operation of an artificial tritium source with an antineutrino activity of 40 MCi for experiments to measure the neutrino magnetic momentum are considered. © *2001 MAIK "Nauka/Interperiodica".*

1. INTRODUCTION

Low-energy neutrino reactions are a sensitive and precise probe for testing the Standard Model of electroweak interactions—in particular, for studying the nonstandard electromagnetic properties of the neutrino. The problem of the (anti)neutrino magnetic moment (specifically, of its existence and magnitude), as well as the motivation of its laboratory searches, is well known [1–3].

Laboratory measurements of the neutrino magnetic moment μ_ν are based on extracting its contribution to the cross section for (anti)neutrino–electron scattering. At nonzero μ_ν, the differential cross section $d\sigma/dT$, where T is the kinetic energy of the scattered electron, receives contributions not only from standard weak (W) interactions but also from electromagnetic (EM) interactions. At low energy transfers ($T \ll E_\nu$), these contributions behave absolutely differently: $(d\sigma/dT)_W$ is virtually constant, whereas $(d\sigma/dT)_{\mathrm{EM}}$ increases in proportion to $1/T$ with decreasing energy. In order to improve the sensitivity to μ_ν, it is necessary to reduce the threshold for scattered-electron detection.

The experimental scheme comprises a source (generator) of (anti)neutrinos and a detector. Since neutrino interaction with matter is extremely weak, a high neutrino-flux density in the detector is a necessary requirement on the source, the most important albeit not the only one.

Four types of (anti)neutrino generators can be used in experimental neutrino physics. These are nuclear reactors and β-active isotopes for the electron antineutrino, accelerators predominantly for the muon neutrino and antineutrino, and the Sun for the electron neutrino. In recent years, ever greater attention has been given to artificial beta-active sources of activity 5–50 MCi [4–11] as an alternative to reactors. The use of ^{51}Cr sources for calibrating the solar-neutrino detectors in the GALLEX and SAGE experiments was the first experience of this kind. In relation to reactors, artificial sources of neutrinos would provide the following advantages: (i) more intense antineutrino fluxes; (ii) a considerable suppression of the correlated background, including that from inverse beta decay; (iii) small dimensions, which enable one to use low-background underground laboratories and flux modulation to subtract the uncorrelated background; (iv) rather wide possibilities of choosing the energy range; (v) knowledge of the (anti)neutrino spectrum to a high precision.

An additional important advantage of a tritium source of antineutrinos is that it is possible to dispense with a passive shielding between the source and the detector: because of a low endpoint energy of the decay spectrum (E_0 = 18.6 keV), bremsstrahlung does not escape from the source. Moreover, available technologies are capable of producing highly purified tritium.

In a proposal to measure the neutrino magnetic moment [4, 5], it was shown that the use of a 40-MCi tritium source of (anti)neutrinos (4 kg of tritium), together with detectors ensuring an electron-detection threshold in the range $E_{\mathrm{thr}} \simeq 1$–10 eV, would permit significantly reducing the laboratory limit on the (anti)neutrino magnetic moment achieved in reactor experiments [12].

A spherical source of activity 40 MCi generates an (anti)neutrino-flux density of $F = 6.4 \times 10^{14}$ cm^{-2} s^{-1} in a compact assembly of detectors (volume of a few liters) that is arranged within the source (Fig. 1) [5]. This value is more than one order of magnitude greater than the (anti)neutrino fluxes obtained in reactor experiments [12].

Silicon cryodetectors based on the effect of ionization conversion into heat, which are presently being developed [5], and strip avalanche germanium detectors employing internal signal amplification [13] can be used to detect electrons of energy between about 1 and 10 eV. The estimates from [5, 13] show that, within one to two years of low-background measurements, a laboratory limit on the neutrino magnetic moment can be obtained at a level of the most stringent astrophysical constraints $\mu_\nu \leq (1–3) \times 10^{-12}\ \mu_B$ [14].

[1)] Joint Institute for Nuclear Research, Dubna, Moscow oblast, 141980 Russia.
[2)] All-Russia Institute of Experimental Physics, Sarov, 607190 Russia.

Promising substances for storage of hydrogen isotopes

	P_{dec}, mm Hg at 25°C	Decomposition temperature, °C	H_2 content in hydrides		Density, g/cm^3	
			cm^3/g	cm^3/cm^3	metal	hydride
UH_3	10^{-6}–10^{-4}	420–430	~140	~1570	18.9	11.9
TiH_2	~10^{-9}	550–620	~468	~1700	4.5	3.8
TiT_2				~1700		3.3–4.1
Mg_2NiH_4	~10^{-2}	~240	~418	~1074	3.47	2.71
ZrCoH	~10^{-5}	340–350	~186	~1415	7.68	6.54
$LaNi_3Mn_2H_6$	~10^{-2}	270	~127			
$LaNi_{5-x}Al_xH_y$ x = 0–1, y = 6.7–4.1	~10^{-1}–10	180–250	80–100	550–690	9.66–7.41	8.25–6.54
PdH	30–50	~150	~105	~800	11.9	
H_2 liquid		–253		780		
T_2 liquid		–251		1000		

Note: The content of hydrogen is presented for the stoichiometric hydride. The actual content of hydrogen in a hydride is somewhat lower and depends on the metal state.

It very difficult, both in the scientific and in the technological aspect, and expensive to construct a tritium source of ultrahigh activity. Owing to the reduction of nuclear weapons, large amounts of tritium have recently become available for fundamental research. Such a unique situation is unlikely to occur again in the future, and it would be inexcusable to miss this opportunity.

In the present study, we consider some technical and technological aspects of the development and safe operation of a 40-MCi tritium source of (anti)neutrinos.

2. STATE OF TRITIUM IN THE SOURCE

In order to achieve a maximum (anti)neutrino-flux density in the detector volume, it is necessary to ensure a maximum volume density of tritium within the source body. At the same time, such a source must be absolutely safe under any conditions, including extreme ones. Obviously, it is most appropriate to store tritium chemically bound with hydride-forming metals. On one hand, such metals are characterized by the highest volume density of hydrogen; on the other hand, tritium has low equilibrium pressures in them at room temperatures. The table lists the properties of some substances that show promise as candidates for hydrogen storage [15–18].

It can be seen that Ti is the most promising material in this respect. It has the lowest equilibrium pressure at room temperature (about 10^{-9} mm Hg), the highest temperature of hydride decomposition, and the maximum volume concentration of hydrogen. The volume concentration of tritium in Ti is nearly 1.7-fold higher than in the liquid state. At the same time, a source based on titanium tritide can be safely used within a wide temperature range extending up to 500°C, whereas storage of liquid tritium requires a special powerful cryogenic apparatus capable of maintaining the tritium temperature at about 20 K despite its heat release.

A high purity of titanium in the radioactive admixtures of the uranium family is another important factor in favor of choosing Ti as a tritium carrier, because it is predominantly these admixtures that contribute to the background [19].

3. SOURCE SAFETY

Since the source being discussed is of an unprecedentedly high activity (40 MCi), it is necessary to ensure its absolute safety at all stages of the operating cycle.

Here, heat release in the source and its self-heating due to tritium radioactive decay present one of the main problems in designing such a source. If the temperature rises uncontrollably, there is the danger of the conversion of tritium into a gas phase and, as a consequence, of its leakage into the atmosphere owing to diffusion or the destruction of the source casing.

According to the results of calorimetric measurements, only 30% of the energy of tritium beta decay is converted into heat. The rest of the energy is carried away by (anti)neutrinos. In this case, the heat release is dH/dt = 0.324 W/g = 1.944 W/mol T_2 [17]. This corresponds to 1.3 kW per 4 kg of tritium. The temperature field over the source volume was calculated by using the ANSYS code for the design in Fig. 1. In this calculation, it was assumed that there is natural heat exchange at the source surface. The density of titanium tritide–deuteride $Ti(DT)_{1.9}$ was taken to be 3.5 g/cm^3 at a 96% concentration of tritium in the initial DT mixture [18]; the thermal conductivity and the heat capacity were set to λ = 0.154 W/(cm K) and C = 0.605 J/(g deg) [17, 20]. Figure 2 demonstrates the results of the calculations.

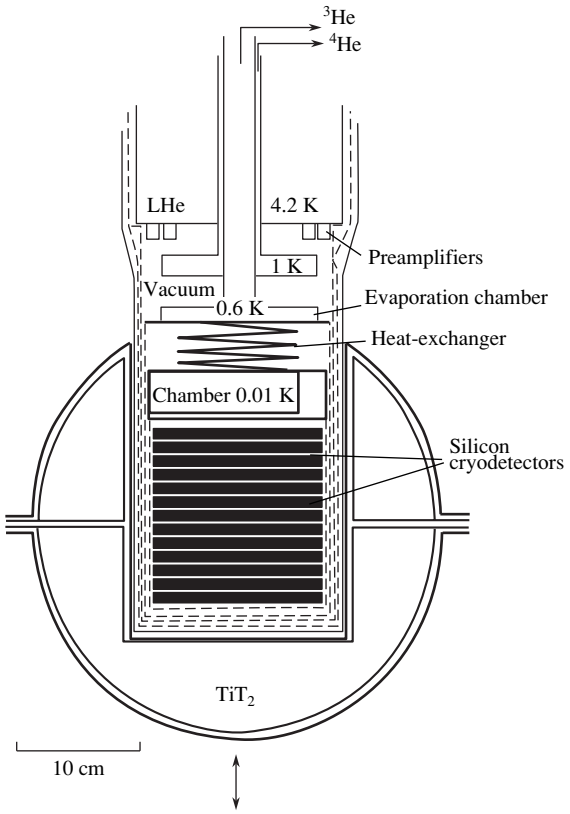

Fig. 1. Layout of the experiment: the assembly of semiconductor detectors of mass 3 to 4 kg that is placed within a tritium source (TiT_2). The active and passive shielding, electronics, and cryogenic devices are not shown.

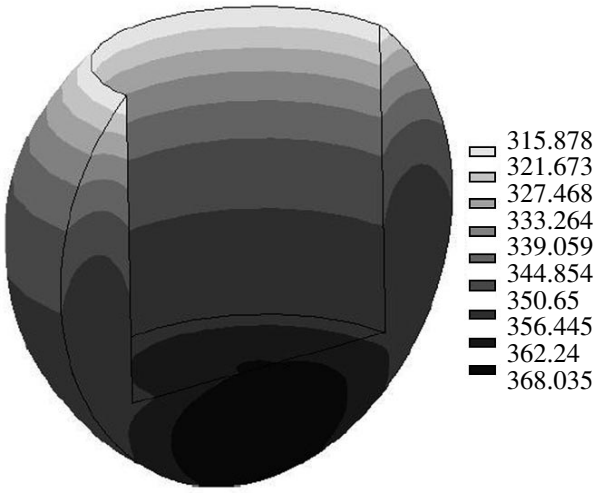

Fig. 2. Distribution of temperature within the source in the case of free convective heat exchange with the environment.

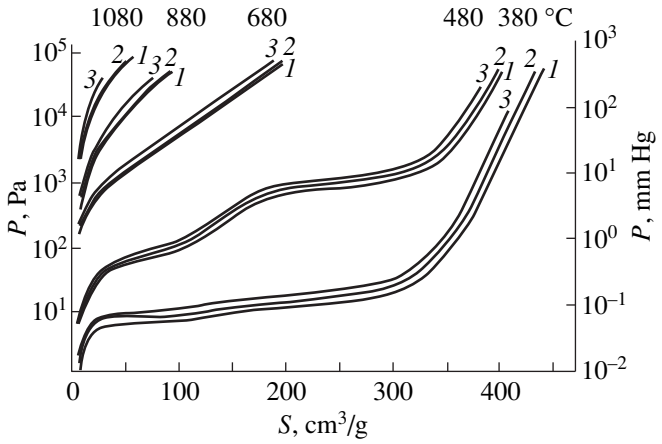

Fig. 3. Isotherms of the Ti–H (D, T) system [22]: the equilibrium pressure P (mm Hg, Pa) as a function of the degree S of saturation of the Ti–H (D, T) system at five temperature values indicated on the curves [S (in cm^3/g) is the volume of the gaseous hydrogen isotope at standard temperature and pressure (P = 1 bar, T = 293 K) per 1 g Ti]: (*1*) hydrogen, (*2*) deuterium, and (*3*) tritium.

It can be seen that the temperature at the hottest point of the source is 368°C. This prevents a safe operation of a source of the above design with a smooth external surface. If, however, the external surface of the source is finned with a finning coefficient of 15, then the temperature decreases by one order of magnitude [21], and the conditions of long and safe storage of tritium are automatically realized for this design. Nevertheless, it is necessary to provide the possibility of additional ventilation of the source under actual experimental conditions.

The transportation of the source presents more serious problems. In accordance with modern international regulations, rather stringent requirements are placed upon the casing used for transportation. The casing must ensure an enhanced shielding of the source and prevent the radioactive pollution of the environment in emergency situations, including those that arise when

(1) a shock impact simulating transport accidents is applied;

(2) the encased source falls from some height onto a pin;

(3) some objects fall onto the encased source;

(4) the casing is submerged in water;

(5) the encased source is hit by gun bullets and fragments of some conventional weapons;

(6) a heat pulse simulating a fire in a transport vehicle is applied.

It is obvious that, to meet these requirements, the source must be transported in a special shielding container. In this case, there will be no free convective heat exchange with the source surface, and the source will be heated at a rate of about 200 deg/h. As a consequence, titanium tritide will undergo decomposition accompanied by the release of gaseous tritium. Figure 3 shows the equilibrium pressures of the hydrogen isotopes over titanium hydride at various temperatures. It can be seen that, even at 380°C and a saturation degree of 410 cm^3/g, the tritium pressure can reach 100 mm Hg.

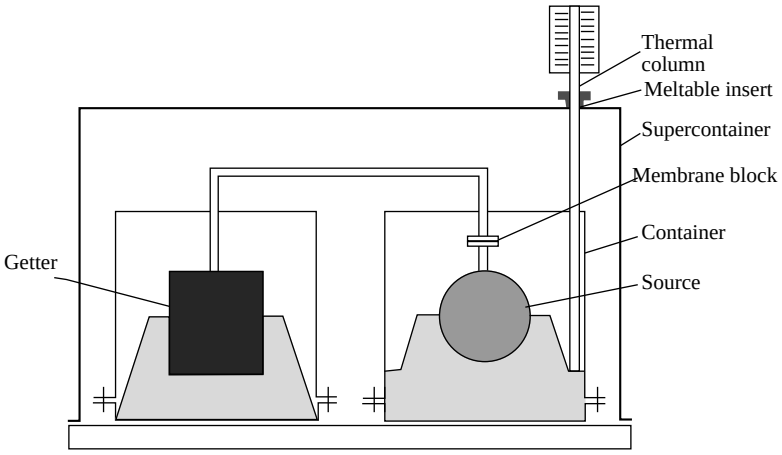

Fig. 4. Layout of the container for transportation.

As the temperature rises further, the equilibrium pressure of tritium also increases and can exceed atmospheric pressure. Therefore, the design of the casing must also ensure the removal of heat released in tritium decay during source operation and storage and prevent the heating of the source under conditions simulating a fire.

Figure 4 displays one of the possible designs that can be used to overcome the problem. The source is placed into a protective container equipped with a thermal column [23] to remove heat released in tritium beta decay. This container can ensure fulfillment of only the first five of the requirements mentioned above. In the case of fire, however, the thermal column can become a source of additional heat from the outside and cause a faster heating of the source than in the case where there is no natural heat exchange. In order to suppress this process, it is necessary to switch off the thermal column as soon as the temperature of the environment rises above a certain value. This can be achieved with the aid of a meltable insert actuated at a preset limiting temperature. Nevertheless, the temperature in the source will begin to increase, and the pressure created by tritium released in the gas phase (see Fig. 3) can eventually destroy the source casing.

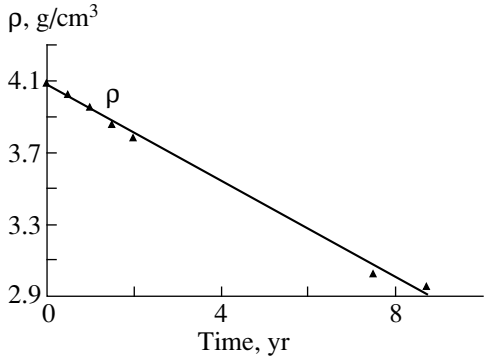

Fig. 5. Density of titanium tritide–deuteride as a function of storage time.

In order to prevent such a situation, gaseous tritium is removed to a getter through a membrane block as soon as a preset limiting pressure is attained. Titanium can be used as a working material of the getter, since it has a low equilibrium pressure even at high temperatures (Fig. 3), provided that its degree of saturation is low. The getter must be arranged in a container similar to the container of the source and connected to the latter by a system of rigid gas pipes. The best solution is to place the containers and the gas pipes within a supercontainer (Fig. 4).

The next point to be taken into account in designing the source is associated with its swelling owing to ^{3}He accumulation in the solid phase of tritide. Figure 5 shows an experimental curve that illustrates a decrease in the density of titanium tritide–deuteride versus the storage time. In order to increase the neutrino flux, it is tempting to have titanium tritide pressed to a maximum density of 4.09 g/cm^3. However, this density will decrease with time, and the source casing will experience high loads that can result in violation of its integrity and even to its destruction. To prevent this, provision should be made in the source design for arranging appropriate compensators.

4. CONCLUSION

It is possible that, for some problems discussed here, alternative technical solutions will be found in constructing the source. In particular, an actual source can have a different shape, although the geometric arrangement proposed in [5] is optimal for ensuring a maximum particle flux in the detector. Nevertheless, the final choice of design can be made only with allowance for the structural features of the detection system, the background conditions of a specific laboratory, and the technological requirements for the production and operation of the source in an experimental setup. How-

ever, the main conclusion of this study on the possibility of constructing and safely running a 40-MCi tritium source of antineutrinos will remain valid.

ACKNOWLEDGMENTS

We are grateful to A.N. Golubkov and A.V. Sten'gach for stimulating discussions on the properties of the substances presented in the table, to N.S. Ganchuk for kindly placing at our disposal the results obtained from a calculation of the regime of source heating, and to A.F. Fadeeva and N.Yu. Tumanova for their assistance in the preparation of the manuscript.

This work was supported by the Department of Atomic Science and Technology of the Ministry for Atomic Energy of the Russian Federation (contract no. 66.04.19.19.99.802).

REFERENCES

1. G. G. Raffelt, Phys. Rep. **320**, 319 (1999).
2. M. B. Voloshin, M. I. Vysotskiĭ, and L. B. Okun', Zh. Éksp. Teor. Fiz. **91**, 754 (1986) [Sov. Phys. JETP **64**, 446 (1986)].
3. P. Vogel and J. Engel, Phys. Rev. D **39**, 3378 (1989).
4. B. Neganov, V. Trofimov, and V. Stepankin, J. Low Temp. Phys. **93**, 754 (1993).
5. V. N. Trofimov, B. S. Neganov, and A. A. Yukhimchuk, Yad. Fiz. **61**, 1373 (1998) [Phys. At. Nucl. **61**, 1271 (1998)].
6. A. V. Davydov and Yu. N. Isaev, Yad. Fiz. **59**, 486 (1996) [Phys. At. Nucl. **59**, 459 (1996)].
7. A. V. Golubchikov, O. A. Zaĭmidoroga, O. Yu. Smirnov, and A. P. Sotnikov, Yad. Fiz. **59**, 1989 (1996) [Phys. At. Nucl. **59**, 1916 (1996)].
8. V. N. Kornoukhov, Yad. Fiz. **60**, 639 (1997) [Phys. At. Nucl. **60**, 558 (1997)].
9. B. R. Bergelson, A. V. Davydov, Yu. N. Isaev, and V. N. Kornoukhov, Yad. Fiz. **61**, 1347 (1998) [Phys. At. Nucl. **61**, 1245 (1998)].
10. L. A. Mikaélyan, I. I. Sinev, and S. A. Fayans, Pis'ma Zh. Éksp. Teor. Fiz. **67**, 435 (1998) [JETP Lett. **67**, 453 (1998)].
11. L. Barabanov, P. Belli, R. Bernabei, *et al.*, Nucl. Phys. B **546**, 19 (1999).
12. F. Reines, H. S. Gurr, and H. W. Sobel, Phys. Rev. Lett. **37**, 315 (1976); G. S. Vidyakin, V. N. Vyrodov, I. I. Gurevich, *et al.*, Pis'ma Zh. Éksp. Teor. Fiz. **55**, 212 (1992) [JETP Lett. **55**, 206 (1992)]; A. I. Derbin, L. A. Popeko, *et al.*, Pis'ma Zh. Éksp. Teor. Fiz. **57**, 755 (1993) [JETP Lett. **57**, 768 (1993)].
13. A. S. Starostin and A. G. Beda, in *Proceedings of International Conference on Nonaccelerator Physics, NANP-99, Dubna, 1999*; Yad. Fiz. **63**, 1370 (2000) [Phys. At. Nucl. **63**, 1297 (2000)]; hep-ex/0002063.
14. G. Raffelt, Phys. Rev. Lett. **64**, 2856 (1990).
15. *Hydrogen: Properties, Production, Storage, Transportation, and Application. A Reference Book*, Ed. by D. Yu. Gamburg and N. F. Dubovkin (Khimiya, Moscow, 1989).
16. M. M. Antonova, *Properties of Metal Hydrides: A Reference Book* (Naukova Dumka, Kiev, 1975).
17. P. C. Souers, *Hydrogen Properties for Fusion Energy* (Univ. of California Press, 1986).
18. A. I. Vedeneev, A. A. Golubkov, L. V. Artemov, *et al.*, Preprint No. 68-98, RFYaTs–VNIIÉF (All-Russia Research Institute of Experimental Physics, Russian Federal Nuclear Center, Sarov, 1998).
19. G. Hausser, Annu. Rev. Nucl. Part. Sci. **45**, 543 (1995).
20. *Physical Quantities: A Handbook*, Ed. by I. S. Grigor'eva and E. Z. Meilikhova (Énergoizdat, Moscow, 1991).
21. M. A. Mikheev, *Foundations of Heat Transfer* (Moscow, 1947).
22. V. V. Sof'ina, Z. M. Azarkh, P. I. Gavrilov, *et al.*, Preprint No. 29-93, RFYaTs-VNIIÉF (All-Russia Research Institute of Experimental Physics, Russian Federal Nuclear Center, Arzamas-16, 1993).
23. V. A. Kuznetsov, *Nuclear Reactors of Space Power Facilities* (Atomizdat, Moscow, 1977); S. S. Kutateladze, in *Heat Transfer and Hydrodynamic Resistance* (Énergoatomizdat, Moscow, 1990).

Translated by E. Kozlovskiĭ

Physics of Atomic Nuclei, Vol. 64, No. 2, 2001, pp. 266–274. Translated from Yadernaya Fizika, Vol. 64, No. 2, 2001, pp. 313–322.

ELEMENTARY PARTICLES AND FIELDS
Experiment

Fluxes of Cosmic-Ray Muons and Atmospheric Neutrinos at High Energies

L. V. Volkova* and G. T. Zatsepin

Institute for Nuclear Research, Russian Academy of Sciences, pr. Shestidesyatiletiya Oktyabrya 7a, Moscow, 117312 Russia

Received December 22, 1999

Abstract—The problem of charm generation in the interactions of nucleons with nuclei of air atoms at energies inaccessible at present-day accelerators is discussed. Both experimental data on cosmic-ray muons and the predictions of QCD-based theoretical models are used in analyzing the behavior of the differential cross sections for charmed-particle production at high energies. The calculated fluxes of muons and neutrinos arriving at sea level both along the vertical and along the horizontal direction are presented, together with their approximations for the interval 2×10^2–10^{10} GeV. © *2001 MAIK "Nauka/Interperiodica".*

1. INTRODUCTION

The problem of the possible generation of muons in the atmosphere directly in the interactions between the nucleons of primary cosmic radiation and nuclei of air atoms or as the result of decays of very short-lived particles (those whose half-lives are much shorter than the half-lives of the pions and kaons) produced in such interactions was posed in cosmic-ray physics many years ago (see, for example, [1, 2]). In order to explore this channel of muon generation in the atmosphere, it was proposed to measure angular distributions of muons at sea level [2], and many theoretical and experimental studies have been devoted since then to the subject. When the discovery of particles of lifetimes about 10^{-11}–10^{-12} s in photoemulsion experiments conducted in cosmic rays [3] had been confirmed in accelerator experiments, interest in the problem was rekindled (see, for example, [4–14]). Different theoretical models were used in different studies to predict the behavior of the differential cross sections for charmed-particle production at high energies inaccessible to experimentalists at modern accelerators. As a result, different predictions for the fluxes of muons and neutrinos from charmed-particle decays in the atmosphere differed by a few orders of magnitude. However, the creation of new-generation giant neutrino telescopes that is foreseen in the near future can provide the possibility of launching experiments with cosmic neutrinos, thereby transforming neutrino astrophysics into an experimental science from a purely theoretical one. In view of this, knowledge of the fluxes of cosmic-ray muons and atmospheric neutrinos appears to be of paramount importance.

Indeed, the background to experiments with cosmic neutrinos is dominated by atmospheric neutrinos. It is the fluxes of atmospheric neutrinos that determine the areas that the arrays to be used must have for successfully studying diffuse fluxes of cosmic neutrinos, as well as the necessary operation time of such arrays and the minimum energy from which the investigation in question becomes possible. At the same time, constraints imposed on angular resolutions of arrays aimed at searches for pointlike neutrino sources in the Universe are chosen with allowance for these fluxes. Since there is a close genetic relation between cosmic-ray muons and atmospheric neutrinos (in the atmosphere, either of these two particle species originates from the decays of pions, kaons, and charmed particles), an experimental investigation of muons to a high precision may provide knowledge of atmospheric-neutrino fluxes to the corresponding precision.

On the basis of data on cosmic-ray muons and predictions of modern QCD-based models for the behavior of differential cross sections for charmed-particle generation, we calculate here the differential spectra of muons and neutrinos that were produced in the atmosphere and which arrive at sea level along the vertical or the horizontal direction. The accuracy of these calculations is discussed.

2. SPECTRUM OF PRIMARY NUCLEONS

The differential energy spectrum of primary nucleons, $P_N(E_N)$, that is based on direct measurements of the fluxes of primary particles with energies not higher than 1000 GeV/nucleon [15] can be represented in the form

$$P_N(E_N)dE_N = \frac{CE_N^{-(\gamma+1)}}{(1+1.8/E_N)^3 dE_N} \qquad (2.1)$$

$$[\text{nucleon}/(\text{cm}^2\ \text{s sr GeV})],$$

where E_N is the nucleon energy measured in GeV, $C = 2.6$, and $\gamma = 1.7$.

* e-mail: volkova@inr.npd.ac.ru

The analysis performed in [16, 17] reveals that, up to nucleon energies of about 3×10^5 GeV, this form of the primary-nucleon spectrum describes fairly well the entire body of experimental data on cosmic-ray muons arriving at sea level along the vertical or the horizontal direction. We assume that the spectrum of primary nucleons can be described by this form up to 3×10^6 GeV and further for $E_N \geq 3 \times 10^6$ GeV, but with $C = 228$ and $\gamma = 2$.

3. GENERATION OF CHARMED PARTICLES

3.1. Data on Charm Generation from Accelerator Experiments

The probability $dW^{\eta}_{NA}(E_N, E_\eta)/dE_\eta$ that a charmed particle η (D and $\bar{D}$ mesons or Λ_c baryon) whose energy takes values in the interval between E_η and $(E_\eta + dE_\eta)$ is produced in the interaction of a nucleon N of energy E_N with the nucleus A of an air atom can be written as

$$\frac{dW^{\eta}_{NA}(E_N, E_\eta)}{dE_\eta} = \frac{\sigma^{D\bar{D},\,\Lambda_c\bar{D}}_{NA}(E_N)}{\sigma^{NA}_{\text{in}}(E_N)} \frac{df_\eta(E_N, E_\eta)}{dE_\eta}, \quad (3.1)$$

where $\sigma^{NA}_{\text{in}}(E_N)$ is the cross section for the inelastic interaction of a nucleon with the nucleus of an air atom, $\sigma^{D\bar{D},\,\Lambda_c\bar{D}}_{NA}(E_N)$ stands for the cross sections describing the production of $D\bar{D}$ and $\Lambda_c\bar{D}$ pairs in such interactions, and $df_\eta(E_N, E_\eta)/dE_\eta$ represents the inclusive spectra of η particles.

Figure 1 displays the cross sections for charm production in proton–nucleon (pN) interactions according to accelerator experiments (points), perturbative QCD calculations in the next-to-leading order (NLO) [18–21] (solid curve), and calculations based on the model of quark–gluon strings (QGS model also known QGSM) [22–25] (asterisks). The accelerator experimental data presented here were borrowed from [26].

For energies $E_p \geq 2 \times 10^3$ GeV, the QGSM results [27] that were obtained for the cross sections describing the production of charmed-particle pairs in proton–proton interactions and which are normalized to accelerator data can be approximated as

$$\sigma^{D\bar{D}}_{pp}(E_p) = 0.48(\log E_p - 3.075) \text{ for } D\bar{D}\text{-pairs}, \quad (3.2)$$

$$\sigma^{\Lambda_c\bar{D}}_{pp}(E_p) = 0.07(\log E_p - 0.84) \text{ for } \Lambda_c\bar{D}\text{-pairs}. \quad (3.3)$$

These formulas are valid for the generation of charmed particles in proton–proton interactions. For interactions between a nucleon and the nucleus of an air atom with an atomic number A^{air}, the cross section for the production of charmed-particle pairs has the form

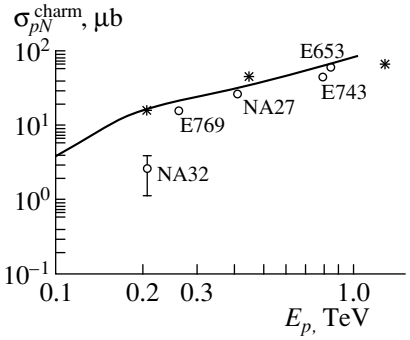

Fig. 1. Cross sections for charm generation in proton–nucleon interactions: (open circles) data from accelerator experiments as quoted in [26], (curve) results of the NLO calculation within perturbative QCD, and (asterisks) results of the QGSM calculations.

$$\sigma^{\eta\bar{\eta}}_{NA^{\text{air}}}(E_N) = \sigma^{\eta\bar{\eta}}_{pp}(E_N)(A^{\text{air}})^{\chi_\eta}, \quad (3.4)$$

where χ_η is a function of the projectile-nucleon-energy fraction $u = E_\eta/E_N$ carried away by a charmed particle. This function varies from 1 for $u \longrightarrow 0$ to about 0.5 for $u \longrightarrow 1$ [27]. We set it to about unity for the generation of $D\bar{D}$ mesons and to about two-thirds for baryon generation. These values of χ_η are compatible with data obtained in accelerator experiments that studied the cross sections for charmed-particle production as a function of the target atomic number.

Accelerator experiments show that the spectra of product D mesons reflect the leading-particle effect,

$$\frac{df^D(E_N, E_D)}{dE_D} \sim \left(1 - \frac{E_D}{E_N}\right)^{\delta}, \quad \delta = 5, \quad (3.5)$$

and that the spectra of Λ_c baryons are of a central character

$$\frac{df^{\Lambda_c}(E_N, E_{\Lambda_c})}{dE_{\Lambda_c}} \sim \left(1 - \frac{E_{\Lambda_c}}{E_N}\right)^{0.4}. \quad (3.6)$$

3.2. Theoretical Concepts of Charm Generation at High Energies

The charm-generation process is usually treated within various theoretical models based on QCD. The spectra of charm generation then prove to be very sensitive to the structure functions for the quark and gluon distributions with respect to the Bjorken variables x. For example, two calculations of the flux of cosmic-ray muons from charmed-particle decays within the same version of perturbative QCD [12] but with different gluon structure functions yielded results differing by a factor of about 20 to 40 for energies 100–1000 TeV.

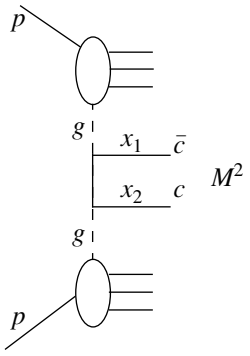

Fig. 2. Generation of a charmed quark–antiquark pair through gluon–gluon interactions in the NLO of perturbative QCD (M^2 is the square of the mass of the generated particle pair).

At energies of interest to our present consideration, it is necessary to know the structure functions for very small values of the variables ($x < 10^{-4}$). Schematically, the process of charmed-quark ($c\bar{c}$) generation in proton–proton (pp) interaction through gluon–gluon (gg) interaction (it is precisely the process that is basically responsible for charm generation at energies as high as those that are of interest to us in the present study) is illustrated in Fig. 2 (there, x_1 and x_2 are the Bjorken variables for gluons).

Because of the origin of primary cosmic radiation, the main contribution to the calculated fluxes of charmed particles that are generated in the atmosphere comes from $x = x_1 - x_2 \sim 0.1$–0.2. Since $x_1 x_2 = M^2/s$, where M^2 is the square of the mass of the product particle pair and s is the square of the total energy in the rest frame of the interacting protons, we have $x_2 \sim 10^{-4}$–10^{-5} for an incident proton of energy about 50 to 500 TeV in the laboratory frame.

In the NLO of perturbative QCD, the cross section for charm generation in proton–proton interactions is given by [19–22]

$$\sigma(pp \longrightarrow c\bar{c}) \sim \int dx_1 dx_2 \sigma_{gg}(M^2) f_g(x_1) f_g(x_2), \quad (3.7)$$

where f_g stands for the gluon structure functions, which are known from accelerator experiments to within 30% at all x values discussed above.

By studying the behavior of the spectra of product particles with increasing projectile-proton energy, we find that $xd\sigma/dx$ can change absolute value, but that it cannot change shape. An analysis of experimental data on cosmic-ray muons [17] reveals that, in the case of pion generation in the interactions between nucleons and nuclei of air atoms, scaling is violated only slightly in the fragmentation region over a broad energy range from a few GeV to a few hundred TeV. According to NLO calculations within perturbative QCD, such a violation for charmed-particle generation must be still weaker.

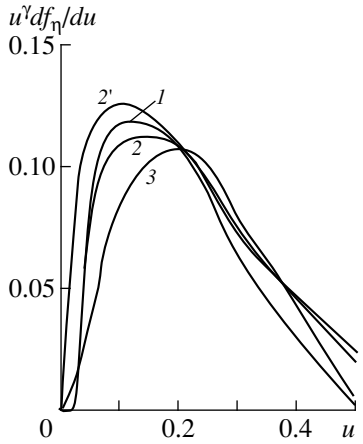

Fig. 3. Quantities $u^\gamma df_\eta/du$ versus the projectile-nucleon-energy fraction $u = E_\eta/E_N$ carried away by a charmed particle η: (curve *1*) results of the calculations performed under the assumption that the spectrum of product D mesons is of a scaling character and is proportional to $(1 - E_D/E_N)^5$; (curves *2* and *2'*) results of the QGSM calculations at $s^{1/2}$ = 123.2 GeV and 16 TeV, respectively; and (curve *3*) results of the NLO calculations within perturbative QCD at $s^{1/2}$ = 27.4 GeV.

Figure 3 shows the quantities $\left(\frac{E_\eta}{E_N}\right)^\gamma \frac{d f_\eta(E_\eta, E_N)}{d(E_\eta/E_N)}$ as functions of the projectile-nucleon-energy fraction E_η/E_N carried away by a charmed particle η. These quantities integrated over the spectra of primary nucleons determine the fluxes of muons and neutrinos generated by charmed-particle decays in the atmosphere. From Fig. 3, we can see that, although the energy of interacting nucleons changes in a very broad region, the quantities in question show very small variations in going over from one model to another.

3.3. Charm Generation according to Data on Cosmic-Ray Muons

As was indicated above, muon generation through decays of very short-lived particles is a long-standing problem in cosmic-ray physics.

The underground experiments that measured the fluxes of cosmic-ray muons in the Colar Gold Field mine in India yielded the value of $R = (1 \pm 0.4) \times 10^{-3}$ for the ratio of the number of muons (generated promptly in the interactions of nucleons with nuclei of air atoms or in decays of particles whose lifetimes are much shorter than those of pions or kaons) of energy in excess of 10 TeV to the number product pions with corresponding energy [28]. According to data from the Baksan neutrino observatory, this ratio is about 1.5×10^{-3} [29].

Calculations assuming that scaling is not violated in the fragmentation region of the interactions between

Table 1. Explicit expressions used in the present calculations for the quantities $w_{\max}$, $w_{\min}$, and $f(w)$ characterizing the kinematics of three-body charmed-particle decays being considered

Decay process	$w_{\min}$	$w_{\max}$	$f(w)$
$\Lambda_c \longrightarrow \Lambda_0 + \mu + \nu$	$\left(\frac{m_\mu}{m_{\Lambda_c}}\right)^2$	$1-\left(\frac{m_{\Lambda_0}}{m_{\Lambda_c}}\right)^2$	$\left[(1-w)(m^2_{\Lambda_c, D}\cdot 0.96 - m^2_{\Lambda_0, K}) \times\left(1+\ln\frac{(1-w)(m_{\Lambda_c, D}\cdot 0.96)}{m^2_{\Lambda_0, K}}\right)\right] / R_{\Lambda_c, D}$
$D \longrightarrow K + \mu + \nu$	$\left(\frac{m_\mu}{m_D}\right)^2$	$1-\left(\frac{m_K}{m_D}\right)^2$	

Note: $R_{\Lambda_c} = 0.633$ and $R_D = 1.03$.

nucleons and nuclei of air atoms and employing the cross sections for charmed-particle generation that were obtained within the QGSM at high energies [27] and which were normalized to the cross sections measured in accelerator experiments can explain experimental data quoted in [10] for cosmic-ray muons. From the analysis performed in [10], it follows that, at about 70 TeV, the contribution from charmed particles to the flux of cosmic-ray muons arriving at sea level along the vertical direction is equal to the contribution from pions and kaons. These calculations describe well experimental results obtained at Moscow State University with an x-ray emulsion calorimeter that measured angular distributions of muon fluxes up to energies of a few tens of TeV [30].

The spectra of particles in cosmic rays descend fast with increasing energy; therefore, only an upper limit on charmed-particle contribution to muon generation can be extracted from experimental data on cosmic-ray muons because of low statistical significance of these data.

4. FLUXES OF COSMIC-RAY MUONS AND ATMOSPHERIC NEUTRINOS

4.1. Charm-Induced Fluxes of Muons and Neutrinos

The inputs that we employ in calculating the fluxes of cosmic-ray muons and atmospheric neutrinos generated in the interaction of primary cosmic radiation with nuclei of air atoms as the result of charmed-particle decay (such muons and neutrinos are usually referred to as prompt ones, whereas those that originate from pion and kaon decays are called ordinary muons and neutrinos) are the following: (i) the cross sections that were calculated for charmed-particle production in proton–proton interactions on the basis of QGSM and which were normalized to the latest data from accelerator experiments [see Eqs. (3.2) and (3.3)]; (ii) the dependences of these cross sections on the air atomic number [see Eq. (3.4)]; and (iii) the spectra of D mesons and Λ_c baryons consistent with accelerator data [see Eqs. (3.5) and (3.6); according to the assumptions presented in Subsections 3.2 and 3.3, these spectra undergo no changes in the fragmentation region of particle generation over the entire region of energies considered here].

The number of muons or neutrinos (muon or electron ones) generated per event of nuclear interaction of a nucleon in the atmosphere that arrive at sea level at an angle θ with respect to the vertical direction and which are produced in the decays of charmed particles can be represented in the form (here, we disregard the energy losses of muons in air)

$$\alpha^{\text{charm}}_{\mu,\nu}(E_{\mu,\nu},\theta) = \sum_i W^\eta_{\text{sl}} \int_{w_{\min}}^{w_{\max}} \int_0^1 b\varphi^\eta(u)(1-u)^\delta \times \sigma^{D\bar{D},\Lambda_c\bar{D}}_{NA}(E_{\mu,\nu}/(uw))/\sigma^{NA}_{\text{in}}(E_{\mu,\nu}/(uw)) \times w^\gamma f(w)/(1+E_{\mu,\nu}/(wE^{\text{cr}}_\eta(\theta)))\,du\,dw, \quad (4.1)$$

where summation is performed over all types of charmed particles and where $b = 1.08$ and $\delta = 5$ for the D mesons and $b = 1.4$ and $\delta = 0.4$ for Λ_c baryons. The notation used in expression (3.1) is the following: W^η_{sl} is the probability of charmed-particle decay into a muon and a neutrino; $w = E_{\mu,\nu}/E_\eta$; $w_{\max}$, $w_{\min}$, and $f(w)$ are associated with the kinematics of the three-body decay of a charmed particle into a muon and a neutrino; $u = E_\eta/E_N$; $\varphi^\eta(u) = u^{\gamma-1}$ for D mesons, and $\varphi^\eta(u) = u^\gamma$ for Λ_c baryons; and $E^{\text{cr}}_\eta(\theta) = m_\eta/(c\tau_{0\eta}\zeta(\theta))$ is the critical energy of the charmed particle η (the energy value at which the probability for the particle to decay over a unit range with respect to nuclear interaction is equal to the probability for this particle to undergo interaction), where m_η is the rest mass of the particle η, $\tau_{0\eta}$ is its lifetime in its rest frame, c is the speed of light, θ is the angle of particle arrival with respect to the vertical direction, and $\zeta(\theta) = \rho(h,\theta)/h$ [here, $\rho(h,\theta)$ is the air density in the atmosphere at a depth h].

Tables 1 and 2 present the values of the quantities $w_{\max}$, $w_{\min}$, and $f(w)$, which are associated with the kinematics of the three-body decay of a charmed particle into a muon and a neutrino; the critical energies of the relevant charmed particles; and the probabilities

Table 2. Critical energies of charmed particles η and probabilities W_{sl}^{η} of semileptonic decays into muons and neutrinos

Particle η	$E_{\eta}^{cr}(0°)$, GeV	$E_{\eta}^{cr}(90°)$, GeV	W_{sl}^{η} [31]
$D^{\pm}$ mesons	4.01×10^7	3.93×10^8	0.07
D_0, $\bar{D}_0$ mesons	1.02×10^8	9.99×10^8	0.032
Λ_0 baryon	2.59×10^8	2.54×10^9	<0.02

W_{sl}^{η} of their semileptonic decays (the rest masses and the critical energies are expressed in GeV; the values of the probabilities of semileptonic decays, the rest masses, and the lifetimes were borrowed from [31]).

4.2. Comparison with the Results Presented in Other Studies

The fluxes of prompt cosmic-ray muons arriving at sea level along the vertical direction were calculated in a number of other studies. Their results are displayed in Fig. 4.

Curves *1* and *1'* were computed in [12] on the basis of perturbative QCD for, respectively, the soft and the hard version of the gluon structure functions (within the measurement errors, either version is compatible with the entire body of experimental data). Here, we can clearly see the dependence of the calculations being discussed on the gluon structure functions: at energies in the range 10–1000 TeV, the muon fluxes as calculated for the two versions of the structure functions differ by a factor of 10 to 50.

The results of the calculations performed in [10] (curve *2'*) differ from the results of the present study (curve *2*), since some parameters (W_{sl}^{η} and δ for *D* mesons) were set to different values in [10] and here and since different normalizations of the primary-nucleon spectra were used (γ = 1.65 and 1.7 in [10] and in the present study, respectively).

The muon fluxes computed in [13] (curve *3*) differ strongly from our present results (by a factor of about 45 at a muon energy of 10^5 GeV, for example). If we take into account the distinctions between the normalizations of the primary-nucleon spectra in these two studies, the difference being discussed reduces to a factor about 30. The remaining distinction can be attributed to the difference in the spectra adopted for charmed particles generated in nucleon interactions in the atmosphere. Indeed, the number of charmed particles, I_{η}, generated per event of nuclear interactions of nucleons in the atmosphere can be represented as

$$I_{\eta} \sim \int_0^1 u^{\gamma} \frac{\sigma_{NA}^{D\bar{D},\,\Lambda_c\bar{D}}(E_{\eta}/u)}{\sigma_{in}^{NA}(E_{\eta}/u)} \frac{df_{\eta}(u)}{du} du. \qquad (4.2)$$

The cross sections for charmed-particle generation in the interactions of 10^6-GeV nucleons (and it is precisely the nucleons of these energies that are responsible for the generation of muons being discussed) are nearly coincident in these two studies.

Figure 5 shows the I_{η} values calculated here and in [13] for the different charmed particles. For I_{η} to take the same value as in [13] for *D* mesons at 10^5 GeV, pro-

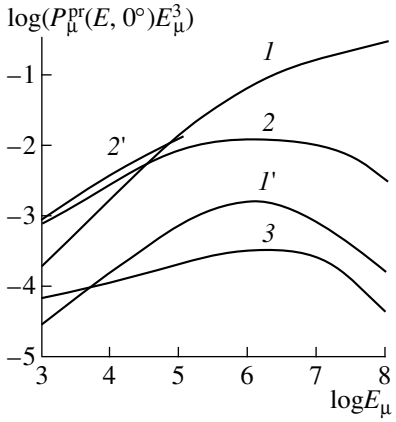

Fig. 4. Differential spectra $P_{\mu}^{pr}(E_{\mu}, 0°)$ of cosmic-ray muons originating from charmed-particle decays in the atmosphere and arriving at sea level along the vertical direction according to the results obtained in (curves *1*, *1'*) [12], (curve *2*) the present study, (curve *2'*) [10], and (curve *3*) [13] {$P_{\mu}^{pr}(E_{\mu}, 0°)$ is expressed in units of [muon/(cm^2 s sr GeV)], while E_{μ} is measured in GeV}.

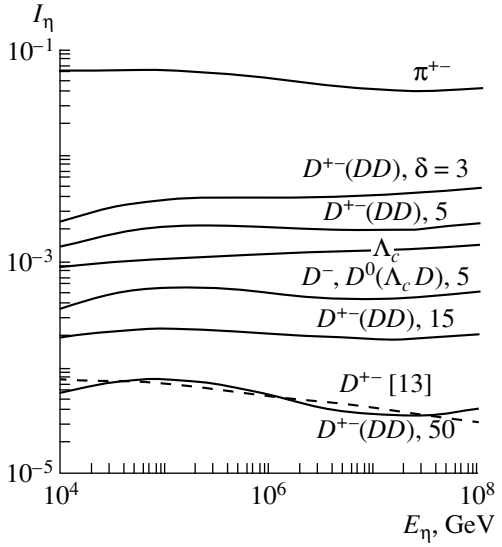

Fig. 5. Numbers I_{η} of various charmed particles η generated per event of nuclear interactions of nucleons in the atmosphere according to the calculations performed in (solid curves) the present study and (dashed curve) [13].

Table 3. Fitted values of A and γ in the approximations of the differential energy spectra (in units of [particle cm^{-2} s^{-1} sr^{-1} GeV^{-1}]) of prompt muons and neutrinos arriving at sea level along the vertical and the horizontal direction

θ, deg \ $E_{\mu,\nu}$, GeV	10^3–10^4	10^4–3×10^5	3×10^5–3×10^6	3×10^6–10^9
		A		
0	1.2×10^{-5}	4.6×10^{-5}	4.15×10^{-2}	1.15×10^{-2}
90	1.2×10^{-5}	4.6×10^{-5}	4.1×10^{-3}	1.65×10^{-2}
		γ		
0	1.4	1.55	2.09	2
90	1.4	1.55	1.91	2

vided that the D-meson spectrum is proportional to $(1-u)^\delta$, it was necessary to set $\delta = 50$.

4.3. Approximation of Fluxes of Prompt Muons and Neutrinos

In various calculations and estimations for the fluxes of prompt muons and neutrinos, it is useful to have approximations of the differential spectra $P^{\rm pr}_{\mu,\nu}(E_{\mu,\nu}, \theta)$ of these particles (the number of muons or neutrinos arriving at sea level at an angle θ with respect to the vertical direction with energies in the interval between $E_{\mu,\nu}$ and $E_{\mu,\nu} + dE_{\mu,\nu}$). For possible approximations, we have

$$P^{\rm pr}_{\mu,\nu}(E_{\mu,\nu}, 0^\circ)dE_{\mu,\nu} = \frac{AE_{\mu,\nu}^{-(\gamma+1)}}{1+3\times10^{-8}E_{\mu,\nu}}dE_{\mu,\nu}, \quad (4.3)$$

$$P^{\rm pr}_{\mu,\nu}(E_{\mu,\nu}, 90^\circ)dE_{\mu,\nu} = \frac{AE_{\mu,\nu}^{-(\gamma+1)}}{1+2.9\times10^{-6}E_{\mu,\nu}^{0.685}}dE_{\mu,\nu}. \quad (4.4)$$

The expressions in the denominators of the approximations of the spectra are determined by the fact that the exponent of the primary-nucleon spectrum changes from $\gamma = 1.7$ to $\gamma = 2$ at an energy value around 3×10^6 GeV and the fact that, at very high energies, nuclear interactions with nuclei of air atoms must be taken into account even for charmed particles. The values of the parameters A and γ are quoted in Table 3.

The above approximations are valid for the muon spectra calculated without allowing for the energy lost in the atmosphere. However, the error that this introduces in muon fluxes is very small at the energies that are of interest to us in the present case. Indeed, the fluxes of muons from charmed particles become commensurate with the flux of muons from pion and kaon decays only at about 70 TeV for the vertical and at 700 TeV for the horizontal direction. At such energy values, the energy loss is as small as, respectively, 0.3 and 10% of the particle energy.

4.4. Fluxes of Cosmic-Ray Muons at Sea Level

Figure 6 displays the differential fluxes of cosmic-ray muons at sea level for particles arriving along the vertical and the horizontal direction. The curves carrying the "pr" label represent the prompt-muon fluxes calculated in this study with allowance for the energy losses of muons in the atmosphere. The fluxes of muons from pion and kaon decays ($\pi + K$) were borrowed from [16], but these fluxes were rescaled by taking into account the change in the normalization of the primary-nucleon spectrum (γ is equal to 1.65 in [16] and to 1.7 in the present study). The figure also shows the muon fluxes estimated here for the prompt generation of $\mu^\pm$ pairs ($\mu\mu$ curve). Kudryavtsev and Ryazhskaya [32] considered the generation of muon pairs in the atmosphere by photons. They state that, from energies somewhat higher than a few PeV, this process begins to make a greater contribution to the production of cosmic-ray muons than pion and kaon decays.

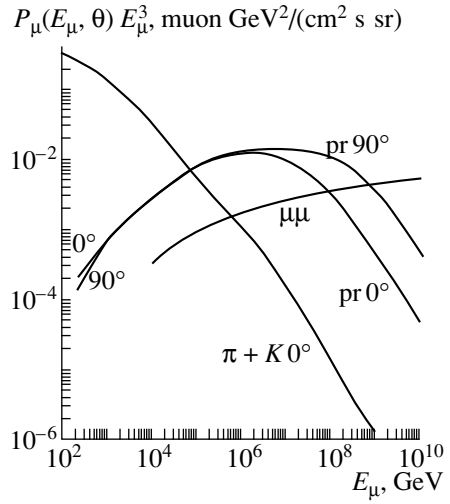

Fig. 6. Differential spectra $P_\mu(E_\mu, \theta)$ of cosmic-ray muons generated in the atmosphere that arrive at sea level along the vertical ($\theta = 0°$) or horizontal ($\theta = 90°$) direction: ($\pi + K$ curve) muons from pion and kaon decays, (pr curves) muons from charmed-particle decays, and ($\mu\mu$ curve) our estimate of the prompt generation of muon pairs.

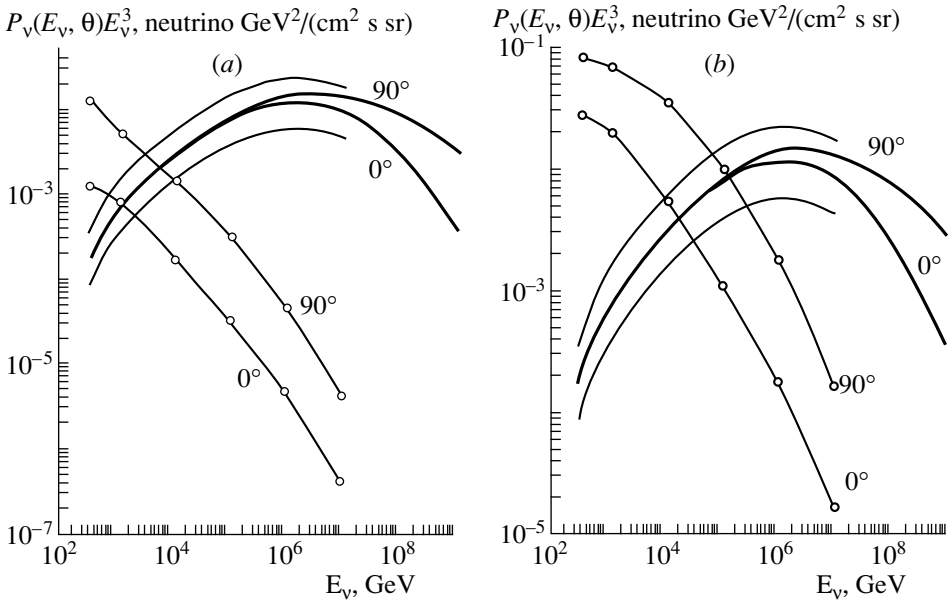

Fig. 7. Differential spectra $P_\nu(E_\nu, \theta)$ of atmospheric (*a*) electron (ν_e) and (*b*) muon (ν_μ) neutrinos generated in the atmosphere that arrive at sea level along the vertical ($\theta = 0°$) or horizontal ($\theta = 90°$) direction: (curves with circles) neutrinos from pion and kaon decays, (thick solid curves) neutrinos from charmed-particle decays, and (upper and lower thin solid curves) neutrino fluxes originating from charmed-particle decays and arriving at sea level along the vertical direction according to the calculations performed under the assumption that the charm-production cross section is, respectively, twice and one-half as large as that given by Eqs. (3.2) and (3.3).

4.5. Atmospheric-Neutrino Fluxes at Sea Level

The differential spectra of atmospheric neutrinos arriving at sea level along the vertical and the horizontal direction are shown in Fig. 7*a* (electron neutrinos and antineutrinos) and Fig. 7*b* (muon neutrinos and antineutrinos). The spectra of neutrinos from pion and kaon decays (curves with circles) were borrowed from [33] and rescaled to a different normalization of the primary-nucleon spectrum ($\gamma = 1.65$ and 1.7 in [33] and in the present study, respectively). Thick solid curves represent the prompt-neutrino spectra calculated here. Thin solid curves delimit the interval of uncertainties in the neutrino fluxes due to the second-order uncertainties in the cross sections for charmed-particle production around the values quoted in Eqs. (3.2) and (3.3).

On the basis of the data displayed in these figures, one can easily estimate the energy from which the charmed-particle contribution to neutrino fluxes exceeds the contribution from pion and kaon decays. For muon (electron) neutrinos arriving at sea level along the vertical direction, this occurs at an energy of about 10 TeV (1 TeV). The difference between the two cases is associated with the differences between the fluxes of muon and electron neutrinos from pion and kaon decays, the former being much greater at the energies being considered (the fluxes of muon neutrinos receive significant contributions from $\pi_{\mu 2}$ and $K_{\mu 2}$ decays, while the fluxes of electron neutrinos are generated predominantly in K_{e3} decays).

The differential spectra of atmospheric neutrino fluxes from pion and kaon decays, $P_\nu^{\mathrm{conv}}(E_\nu, \theta)$, can be approximated as

$$P_\nu^{\mathrm{conv}}(E_\nu, \theta)dE_\nu = AE_\nu^{-(\gamma+1)}dE_\nu. \qquad (4.5)$$

For electron and muon neutrinos arriving at sea level in the vertical and the horizontal direction, the values of A and γ are listed in Table 4.

4.6. Accuracy of the Calculation of Neutrino Fluxes

The uncertainties in the calculation of neutrino fluxes generated in the atmosphere in pion and kaon decays stem predominantly from inaccuracies in our knowledge of primary-nucleon fluxes and of the relationship between the numbers of pions and kaons from nucleon–nucleus interaction.

Direct measurements of the fluxes of nucleons with energies up to about 1000 GeV are accurate to within 20% [15]. At higher energies, the accuracy of direct measurements is poorer; however, an analysis of data on cosmic-ray muons [34] gives sufficient grounds to believe that the accuracy of our knowledge of the primary-nucleon spectrum remains on the same order of magnitude up to nucleon energies of a few hundred TeV. Accordingly, the accuracy of the values presented here for the neutrino fluxes from pion and kaon decays—recall that this accuracy is related to the accuracy achieved in estimating the fluxes of primary nucleons—is not poorer than 20% at neutrino energies up to

Table 4. Fitted values of A and γ in the approximations of the differential energy spectra (in units of [particle cm^{-2} s^{-1} sr^{-1} GeV^{-1}]) of electron and muon neutrinos originating from pion and kaon decays and arriving at sea level along the vertical and the horizontal direction

θ, deg \ E_ν, GeV	10^3–10^4	10^4–10^5	10^5–10^6	$\geq 10^6$
		ν_e; A		
0	0.1	0.1	0.58	7
90	0.32	0.32	5.8	70
		ν_e; γ		
0	2.7	2.7	2.85	3.03
90	2.6	2.6	2.85	3.03
		ν_μ; A		
0	2.05	2.05	11.5	278
90	0.6	6	110	2780
		ν_μ; γ		
0	2.65	2.65	2.8	3.03
90	2.3	2.55	2.8	3.03

a few tens of TeV. A similar argument applies to neutrinos generated in the decays of charmed particles.

In the present calculations, data on pion and kaon production that were obtained in accelerator experiments at a projectile-proton energy of about 20 GeV were used to establish the relationship between the numbers of product pions and kaons, and it was assumed that this relationship undergoes no changes in the fragmentation region at still higher energies. This assumption is confirmed by the analysis of data on cosmic-ray muons [16].

The accuracy in calculating the neutrino fluxes from charmed-particle decays is determined primarily by the accuracy of our knowledge of the charm-production cross section, provided that we assume that, in the fragmentation region, the differential spectra of product charmed particles remain virtually unchanged with increasing energy (this assumption is justified by the arguments presented in Subsections 4.2 and 4.3). The accuracy currently achieved for the charm-production cross section can be assessed on the basis of the data in Fig. 1.

5. CONCLUSION

The present analysis has revealed that, by using data on charm generation from accelerator experiments and the predictions that the QGSM and the NLO calculations within perturbative QCD yield for charm production at energies inaccessible at modern accelerators, it is possible to describe data on cosmic-ray muons from experiments at the Colar Gold Fields mine, Baksan Neutrino Observatory, and Moscow State University (data obtained with an x-ray emulsion calorimeter) up to muon energies of a few hundred TeV (the corresponding effective energies of primary nucleons that are responsible for such muons are about a few thousand TeV). The possible contribution of the prompt production of muon pairs to the fluxes of cosmic-ray muons at high energies is much less than the contribution from charmed-particle decays (at muon energies in the range 3×10^3–10^5 GeV, the former contribution is about 10% of the latter). Photonuclear interactions induced by photons produced in neutral-pion decays generate muons in amounts of about 3 to 10% of the number of muons that originate from charmed-particle decays; the decays of rho and omega mesons yield about 1.5% of this number. The contribution of B mesons and Λ_b baryons is small at the energies being considered, but it can grow with increasing energy.

According to the results obtained in the present study, the contribution of charmed-particle decays to atmospheric-neutrino fluxes becomes commensurate with the contribution from pion and kaon decays at about 10 TeV for muon neutrinos; at still higher energies, the entire flux of these neutrinos is determined by charmed-particle decays (for neutrinos arriving at sea level along the vertical direction). For electron neutrinos, this occurs at a neutrino energy of about 1 TeV. For the horizontal direction, the corresponding energies are one order of magnitude higher.

To summarize the above, we note that, in discussing problems associated with possible experiments devoted to studying cosmic neutrinos, it is of paramount importance to take into account the generation of atmospheric neutrinos, because this process appears to be the main source of background to the experiments being discussed.

For the muon and neutrino spectra calculated in the present study, we have constructed approximations accurate to within 5%.

REFERENCES

1. P. H. Barret *et al.*, Rev. Mod. Phys. **24**, 133 (1952).
2. I. S. Alekseev and G. T. Zatsepin, in *Proceedings of the International Conference on Cosmic-Ray Physics, Moscow, 1960*, Vol. 2, p. 326.
3. K. Niu, E. Mikumoto, and Y. Maeda, Prog. Theor. Phys. **46**, 1644 (1971).
4. H. Inazawa and K. Kobayakawa, Prog. Theor. Phys. **69**, 1195 (1983).
5. L. V. Volkova and G. T. Zatsepin, Yad. Fiz. **37**, 353 (1983) [Sov. J. Nucl. Phys. **37**, 212 (1983)].
6. C. Castagnoli *et al.*, Nuovo Cimento A **82**, 78 (1984).
7. L. V. Volkova and G. T. Zatsepin, Izv. Akad. Nauk SSSR, Ser. Fiz. **49**, 1386 (1985).
8. H. Inazawa, K. Kobayakawa, and T. Kitamura, J. Phys. G **12**, 59 (1986).
9. K. Mitsui, Y. Minorikawa, and H. Komori, Nuovo Cimento C **9**, 995 (1986).
10. L. V. Volkova, W. Fulgione, P. Galeotti, and O. Saavedra, Nuovo Cimento C **10**, 465 (1987).
11. É. V. Bugaev, V. A. Naumov, S. I. Sinegovskiĭ, and E. S. Zaslavskaya, Izv. Akad. Nauk SSSR, Ser. Fiz. **53**, 1351 (1989).
12. E. Zas, F. Halzen, and R. A. Vázquez, Astropart. Phys. **1**, 297 (1993).
13. M. Thunman, G. Indelman, and P. Gondolo, Astropart. Phys. **5**, 309 (1996).
14. V. A. Naumov, T. S. Sinegovskaya, and S. I. Sinegovsky, Nuovo Cimento A **111**, 129 (1998).
15. W. R. Webber and S. A. Lezniak, Astrophys. Space Sci. **30**, 361 (1974).
16. L. V. Volkova, G. T. Zatsepin, and L. A. Kuz'michev, Yad. Fiz. **29**, 1252 (1979) [Sov. J. Nucl. Phys. **29**, 645 (1979)].
17. A. V. Apanasenko, L. V. Volkova, and G. T. Zatsepin, in *Proceedings of XXIV International Cosmic Ray Conference, Roma, 1995*, Vol. 2, p. 660.
18. G. Altarelli, M. Diemoz, G. Martinelli, and P. Nason, Nucl. Phys. B **308**, 724 (1988).
19. P. Nason, S. Dawson, and R. K. Ellis, Nucl. Phys. B **327**, 49 (1989).
20. W. Beenakker, H. Kuijf, W. L. van Neerven, and J. Smith, Phys. Rev. D **40**, 54 (1989).
21. W. Beenakker, W. L. van Neerven, R. Meng, *et al.*, Nucl. Phys. B **351**, 507 (1991).
22. A. B. Kaidalov and K. A. Ter-Martirosyan, Yad. Fiz. **39**, 1545 (1984) [Sov. J. Nucl. Phys. **39**, 979 (1984)].
23. A. B. Kaidalov and O. I. Piskunova, Yad. Fiz. **43**, 1545 (1986) [Sov. J. Nucl. Phys. **43**, 994 (1986)].
24. A. B. Kaidalov, Yad. Fiz. **45**, 1452 (1987) [Sov. J. Nucl. Phys. **45**, 902 (1987)].
25. A. de Rujula, E. Fernández, and J. J. Gómez-Cadenas, Nucl. Phys. B **405**, 80 (1993).
26. Yu. M. Shabelski, Talk given at HERA Monte Carlo Workshop, DESY, Hamburg, Apr. 27–30, 1998.
27. A. B. Kaĭdalov and O. I. Piskunova, Preprint No. 157, ITÉF (Inst. of Theoretical and Experimental Physics, Moscow, 1985).
28. H. Adarkar, S. R. Dugad, M. S. Krishnaswami, *et al.*, in *Proceedings of XXI International Cosmic Ray Conference, Adelaide, 1990*, Vol. 9, p. 319.
29. Yu. M. Andreev, A. E. Chudakov, V. I. Gurentsov, and I. M. Kogai, in *Proceedings of XXI International Cosmic Ray Conference, Adelaide, 1990*, Vol. 9, p. 301.
30. G. T. Zatsepin *et al.*, Izv. Akad. Nauk, Ser. Fiz. **58** (12), 119 (1994).
31. Particle Data Group, Eur. Phys. J. C **3**, 1 (1998).
32. V. A. Kudryavtsev and O. G. Ryazhskaya, in *Proceedings of XXV International Cosmic Ray Conference, Durban, 1997*, Vol. 6, p. 429.
33. L. V. Volkova, Yad. Fiz. **31**, 1510 (1980) [Sov. J. Nucl. Phys. **31**, 784 (1980)].
34. Y. Muraki *et al.*, Phys. Rev. D **28**, 40 (1983).

Translated by A. Isaakyan

Physics of Atomic Nuclei, Vol. 64, No. 2, 2001, pp. 275–293. From Yadernaya Fizika, Vol. 64, No. 2, 2001, pp. 323–341.

ELEMENTARY PARTICLES AND FIELDS
Theory

Analytic Results for $e^+e^- \longrightarrow t\bar{t}$ and $\gamma\gamma \longrightarrow t\bar{t}$ Observables near the Threshold up to the Next-to-Next-to-Leading Order of NRQCD*

A. A. Penin[1] and A. A. Pivovarov[2]

Received December 22, 1999; in final form, April 4, 2000

Abstract—We present an analytic description of top–antitop pair production near the threshold in e^+e^- annihilation and $\gamma\gamma$ collisions. A set of basic observables being considered includes total cross sections, forward–backward asymmetry, and top-quark polarization. Threshold effects relevant to the basic observables are described by three universal functions related to *S*-wave production, *P*-wave production, and *S*–*P* interference. These functions are computed analytically up to the next-to-next-to-leading order of NRQCD. The total $e^+e^- \longrightarrow t\bar{t}$ cross section near the threshold is obtained in the next-to-next-to-leading order in a closed form including the contribution originating from the axial coupling of top quarks that is mediated by the *Z* boson. The effects of the running of the strong coupling constant and the finite top-quark width are taken into account analytically for the *P*-wave production and *S*–*P* wave interference. © *2001 MAIK "Nauka/Interperiodica"*.

1. INTRODUCTION

Being heavy, the top quark undergoes fast weak decays. A relatively large width Γ_t of the top quark is mainly saturated by the decay channel $t \longrightarrow Wb$ and keeps the effective energy of the top–antitop system in the complex plane far enough from the cut along the positive semiaxis. Thus, it serves as a sufficient infrared cutoff for long-distance effects avoiding the problem of strong coupling. This allows one to bypass possible nonperturbative regions and is a key observation for the theoretical study of the top–antitop pair production near the two-particle threshold [1]. Because the relevant scale $\sqrt{\Gamma_t m_t}$, where m_t is the top-quark mass, is much larger than $\Lambda_{\rm QCD}$, the QCD perturbation-theory expansion is applicable to the theoretical description of physical phenomena near the top-quark threshold if singular Coulomb effects are properly taken into account [1–3]. Owing to this feature, processes involving top quarks appear to be a unique laboratory for perturbative investigation of threshold effects. Experimental study of the top–antitop pair threshold production is planned at the Next Linear Collider in both high energy e^+e^- annihilation and $\gamma\gamma$ collisions [4]. High-quality experimental data that can be obtained in such experiments, along with their very accurate theoretical description, make the processes of top–antitop pair threshold production a promising field for investigating quark–gluon interactions.

This investigation concerns both general features of interaction and precise quantitative properties as a determination of numerical values of the strong-coupling constant α_s and the top-quark mass and width. Although the main features are rather similar in both e^+e^- and $\gamma\gamma$ processes of top-quark pair threshold production, strong-interaction and relativistic corrections are different for them. Therefore, a joint analysis of these two processes extends possibilities of studying fine details of top-quark threshold dynamics. In addition to the total cross sections, which are mainly saturated by the *S*-wave final state of the top quark–antiquark pair, there is a set of observables sensitive to the *P*-wave component. For example, the *S* and *P* partial waves of the final-state top quark–antiquark pair produced in $\gamma\gamma$ collisions can be separated by choosing the same or opposite helicities of colliding photons [2]. This provides an opportunity of directly measuring the *P*-wave amplitude, which is strongly suppressed in the threshold region in relation to the *S*-wave amplitude. On the other hand, the forward–backward asymmetry of the quark–antiquark pair production in e^+e^- annihilation [5, 6] and top–quark polarization [6, 7] are determined by *S*–*P* interference in both processes. This provides two additional independent probes of the top-quark interactions.

The finite-order perturbation theory of QCD breaks down in the threshold region of particle production due to the presence of singular $(\alpha_s/\beta)^n$ Coulomb terms. Here, β is the heavy-quark velocity. However, resummation of these Coulomb contributions, which are most

* This article was submitted by authors in English.

[1] Institut für Theoretische Teilchenphysik, Universität Karlsruhe, D-76128 Karlsruhe, Germany; on leave of absence from the Institute for Nuclear Research, Russian Academy of Sciences, pr. Shestidesyatiletiya Oktyabrya 7a, Moscow, 117312 Russia.

[2] Institut für Physik, Johannes-Gutenberg-Universität, D-55099 Mainz, Germany; on leave of absence from the Institute for Nuclear Research, Russian Academy of Sciences, pr. Shestidesyatiletiya Oktyabrya 7a, Moscow, 117312 Russia.

important quantitatively in the threshold region, is possible and can be systematically performed within nonrelativistic QCD (NRQCD) [8] (for the recent development of the NRQCD effective theory approach see [9–16]). Note that the characteristic scale $\alpha_s m_t$ of the Coulomb effects for the top-quark production is comparable numerically with the cutoff scale $\sqrt{\Gamma_t m_t}$ for infrared effects, and the Coulomb effects are not suppressed by the top-quark width. To determine higher order corrections in the QCD coupling constant and relativistic corrections in the case where Coulomb effects have to be taken into account beyond the finite-order perturbation theory, the perturbative expansion for the complete correlation function should be performed near the Coulomb approximation rather than the free Green's functions, which is the standard pattern of perturbation theory for the infrared-safe high-energy processes.

Recently, theoretical description of the heavy quark–antiquark threshold dynamics in NRQCD was substantially developed. The evaluation of next-to-leading order (NLO) and next-to-next-to-leading order (NNLO) corrections to the heavy-quark threshold production in e^+e^- annihilation was performed both in the analytic approach [17–25] and numerically [26–30], while the NLO corrections to the heavy-quark threshold production in $\gamma\gamma$ collisions were computed analytically [31]. The analysis of NNLO corrections in the last case is still absent. However, this analysis is necessary for careful quantitative study of the process since the NNLO contribution is found to be relatively large in the case of the top-quark production in the e^+e^- annihilation [26, 27] and one can expect that some large corrections emerge also in the case of the top-quark threshold production in $\gamma\gamma$ collisions. Moreover, a semianalytic analysis of the high-order corrections to the cross section for top-quark threshold production in e^+e^- annihilation has been performed so far [26–30], while the essential part of corrections has been taken into account numerically [3]. Therefore, the complete analytic description of the process is also desirable.[3)] Furthermore, the forward–backward asymmetry and top-quark polarization [6], as well as the axial contribution to the $e^+e^- \longrightarrow t\bar{t}$ process [28], were analyzed in NLO only numerically. In this case, the numerical study is more involved because of the need for constructing the *P*-wave Green's function, which leads to more singular differential equations in comparison with the *S* wave. The case of *P*-wave production in the $\gamma\gamma$ collision [2, 31] clearly demonstrates that the numerical analysis [28] with the explicit cutoff of the hard-momentum contribution is insufficient for an accurate account of the finite top-quark width for these quantities because the relativistic effects are not properly taken into account.

[3)]When this work was at its final stage, letter [22] appeared where the photon-mediated top-quark production in e^+e^- annihilation was analyzed analytically.

In the present paper, we give a simultaneous analysis of several observables relevant to the $e^+e^- \longrightarrow t\bar{t}$ annihilation and $\gamma\gamma \longrightarrow t\bar{t}$ collisions near the top-quark production threshold in high orders of NRQCD. The total cross sections are computed in NNLO of NRQCD, which includes α_s^2, $\alpha_s\beta$, and β^2 corrections in the coupling constant α_s and in the heavy-quark velocity β to the nonrelativistic Coulomb approximation. Explicit analytic expressions for the soft part of the corrections are obtained. The threshold cross section for the $t\bar{t}$ production in e^+e^- annihilation is obtained in closed form including the contribution due to the top quark axial coupling. The hard part of the correction to the $\gamma\gamma \longrightarrow t\bar{t}$ threshold cross section is found with logarithmic accuracy. The forward–backward asymmetry of the top quark–antiquark pair production in e^+e^- annihilation and top-quark polarization in both e^+e^- annihilation and $\gamma\gamma$ collisions are computed up to NLO.

The paper is organized as follows. In Section 2, the nonrelativistic approximation for the basic observables of the top quark–antiquark pair production near the threshold is formulated. In Section 3, the threshold effects are described by three universal functions that are related to the *S*- and the *P*-wave production and *S*–*P*-wave interference and are computed analytically in NRQCD. In Section 4, we present a numerical analysis and the discussion of the results. Section 5 is devoted to our conclusions. Some explicit analytic formulas are given in the Appendices.

2. THE NONRELATIVISTIC APPROXIMATION NEAR THE PRODUCTION THRESHOLD

In this section, we describe the set of observables which will be analyzed: the total cross sections, the forward–backward asymmetry, and the polarization of the top quark. We formulate the nonrelativistic approximation for these observables that is the stage of the complete NRQCD analysis. In Subsection 2.5 we dwell upon the peculiarities of the introduction of a finite width of the top quark.

2.1. Effective Theory Description of the Heavy-Quark Threshold Dynamics

Near the threshold, the heavy quarks are nonrelativistic so that one may treat both the strong-coupling constant and heavy-quark velocity as small parameters. The threshold expansion of the QCD loop integrals was developed in [14]. However, to take properly into account the singular threshold effects, one has to go beyond the finite-order QCD perturbation theory. For this purpose, the expansion in β should be performed directly in the QCD Lagrangian within the effective field theory framework. The first step to construct the effective theory is to identify all the scales appearing in the problem. The threshold dynamics is characterized

by the following four scales [14]: (i) the hard scale (energy and momentum scale like m_q); (ii) the soft scale (energy and momentum scale like βm_q); (iii) the potential scale (energy scales like $\beta^2 m_q$, while momentum scales like βm_q); and (iv) the ultrasoft scale (energy and momentum scale like $\beta^2 m_q$). The ultrasoft scale is the only one relevant for gluons. By integrating out the momenta of the order of the hard scale of QCD, one arrives at the effective theory of NRQCD [8]. Because the NRQCD Lagrangian does not explicitly include the heavy-quark velocity, the power counting rules are necessary to construct the regular expansion in this parameter. The list of the power counting rules for dimensionally regularized NRQCD and their relation to the threshold expansion [14] can be found in [16]. Integrating out the soft modes and the potential gluons of NRQCD, one obtains the effective theory of potential NRQCD [13], which contains potential quarks and ultrasoft gluons as active particles and is relevant for an analysis of the threshold effects. In potential NRQCD, the quark dynamics is governed by the effective nonrelativistic Schrödinger equation and by their interaction with ultrasoft gluons. To obtain a regular perturbative expansion in β, this interaction should be expanded in multipoles. Note that some spurious infrared and ultraviolet divergences appear in the process of scale separation at intermediate steps of calculation but they cancel each other in the final results for physical observables. The dimensional regularization has been recognized as a powerful tool to deal with these divergences [9–35].

If the ultrasoft effects are neglected, propagation of the quark–antiquark pair in the color singlet state is described in the potential NRQCD by the Green's function $G(\mathbf{x}, \mathbf{y}, E)$ of the Schrödinger equation

$$(\mathcal{H} - E)G(\mathbf{x}, \mathbf{y}, E) = \delta(\mathbf{x} - \mathbf{y}), \qquad (1)$$

where $\mathcal{H}$ is the effective nonrelativistic Hamiltonian. Near the threshold, the singular $(\alpha_s/\beta)^n$ Coulomb terms should be summed in all orders of α_s. Thus, in the threshold region, one has to develop the expansion in β and α_s around some nonperturbative solution which properly incorporates the threshold effects, for example, around the nonrelativistic Coulomb solution. In this case, the leading-order approximation for the nonrelativistic Green's function is obtained with the Coulomb Hamiltonian

$$\mathcal{H}_C = -\frac{\Delta_{\mathbf{x}}}{m_t} + V_C(x),$$

where $\Delta_{\mathbf{x}} = \partial_{\mathbf{x}}^2$ is the kinetic-energy operator, $V_C(x) = -C_F\alpha_s/x$ is the Coulomb potential, and $x = |\mathbf{x}|$. The harder scale contributions are represented by the higher-dimensional operators in $\mathcal{H}$ and by the Wilson coefficients of the operators entering into the nonrelativistic Hamiltonian leading to the expansion in β and α_s. On the other hand, the radiation/absorption of the ultrasoft gluons by the interacting quark–antiquark pair, the effect of retardation, does not contribute to NLO and NNLO (the leading ultrasoft effects in heavy quarkonium have been recently computed in [25]). Thus, the nonrelativistic Green's function of (1) is the basic object in the NRQCD analysis of the threshold effects up to NNLO. In Subsections 2.2–2.4, we relate the observables of the $e^+e^- \longrightarrow t\bar{t}$ annihilation and the $\gamma\gamma \longrightarrow t\bar{t}$ collisions in the threshold region to this Green's function.

2.2. Cross Sections

We study the normalized cross sections for the top quark–antiquark pair production in e^+e^- annihilation

$$R^e(s) = \frac{\sigma(e^+e^- \longrightarrow t\bar{t})}{\sigma(e^+e^- \longrightarrow \mu^+\mu^-)}$$

and in $\gamma\gamma$ collisions

$$R^\gamma(s) = \frac{\sigma(\gamma\gamma \longrightarrow t\bar{t})}{\sigma(e^+e^- \longrightarrow \mu^+\mu^-)},$$

where the leptonic cross section

$$\sigma(e^+e^- \longrightarrow \mu^+\mu^-) = \frac{4\pi\alpha_{\mathrm{QED}}^2}{3s}$$

is the standard normalization factor. Here, α_{QED} is the fine-structure constant and s is the total energy of the colliding electrons in their center-of-mass frame. For unpolarized initial states, the following decomposition of the total cross sections is useful:

$$R^e(s) = \frac{D_V}{q_t^2}R^v(s) + D_A R^a(s), \qquad (2)$$

$$R^\gamma(s) = \frac{R^{++}(s) + R^{+-}(s)}{2}, \qquad (3)$$

where R^v (R^a) corresponds to the top-quark vector (axial) coupling in e^+e^- annihilation, R^{++} (R^{+-}) corresponds to the colliding photons of the same (opposite) helicity in the $\gamma\gamma$ collisions, $D_{V,A}$ are the standard combinations of the electroweak coupling constants (see below), and q_t is the top-quark electric charge. The cross section for the polarized electron/positron initial states is discussed, for example, in [36].

Near the threshold, the cross sections are determined by the imaginary part of the correlation functions of the nonrelativistic vector/axial quark currents, which can be related to the nonrelativistic Green's function and its derivatives at the origin. In NNLO, the (potential) NRQCD provides the following representation of the cross sections:

$$R^v(s) = \frac{6\pi q_t^2 N_c}{m_t^2}\left(C^v(\alpha_s) + B^v\frac{k^2}{m_t^2}\right)\mathrm{Im}\,G(0, 0, k), \quad (4)$$

$$R^a(s) = \frac{4\pi N_c}{m_t^4} C^a(\alpha_s)\partial_{\mathbf{xy}}^2 \operatorname{Im} G(\mathbf{x}, \mathbf{y}, k), \quad (5)$$

$$R^{++}(s) = \frac{24\pi q_t^4 N_c}{m_t^2}\left(C^{++}(\alpha_s) + B^{++}\frac{k^2}{m_t^2}\right)\operatorname{Im} G(0, 0, k), \quad (6)$$

$$R^{+-}(s) = \frac{32\pi q_t^4 N_c}{m_t^4} C^{+-}(\alpha_s)\partial_{\mathbf{xy}}^2 \operatorname{Im} G(\mathbf{x}, \mathbf{y}, k), \quad (7)$$

where $k^2 = -m_t E$, $E = \sqrt{s} - 2m_t$ is the quark-pair energy measured from the threshold $2m_t$. The symbol $\partial_{\mathbf{xy}}^2$ is used for the operator

$$\partial_{\mathbf{xy}}^2 f(\mathbf{x}, \mathbf{y}) \equiv \sum_{i=1}^{3} \partial_{x_i}(\partial_{y_i} f(\mathbf{x}, \mathbf{y})|_{y=0})\big|_{x=0}$$

that extracts the partial P wave of the Green's function. The standard electroweak factors read

$$D_V = q_e^2 q_t^2 + 2q_e q_t v_e v_t d + (v_e^2 + a_e^2) v_t^2 d^2,$$

$$D_A = (v_e^2 + a_e^2) a_t^2 d^2,$$

$$q_e = -1, \quad v_e = -1 + 4\sin^2\theta_W, \quad a_e = -1,$$

$$q_t = 2/3, \quad v_t = 1 - 8\sin^2\theta_W, \quad a_t = 1,$$

$$d = \frac{1}{16\sin^2\theta_W \cos^2\theta_W}\frac{s}{s - M_Z^2}.$$

The coefficients $C^i(\alpha_s)$ and B^i are the NRQCD parameters which are responsible for matching the effective and full theory cross sections in the limit of weak coupling in NNLO. The coefficients

$$C^i(\alpha_s) = 1 + c_1^i C_F\frac{\alpha_s}{\pi} + c_2^i C_F\left(\frac{\alpha_s}{\pi}\right)^2 + \ldots$$

account for the hard QCD corrections and are determined by the corresponding amplitudes with on-shell heavy quarks at rest. The numerical values of these hard coefficients in the leading-order approximation have long been known [37–40] and are given by

$$c_1^v = -4, \quad c_1^a = -2,$$

$$c_1^{++} = \frac{\pi^2}{4} - 5, \quad c_1^{+-} = -4.$$

The coefficient C^v has recently been computed in NNLO in different schemes [22, 26, 27]. Starting from NNLO, the hard coefficients acquire anomalous dimensions and the calculation of the NNLO correction requires an accurate separation of hard and soft contributions. At the same time, these coefficients are independent of the normalization point of the strong-coupling constant in a fixed order of perturbative expansion, and one can use different normalization points of α_s entering into the coefficients C^i (the hard scale μ_h) and the nonrelativistic Green's function (the soft scale μ_s) (see Subsection 3.1).

The coefficients B^i in Eqs. (4) and (6) describe the pure relativistic cross-section corrections which appear when the cross section is evaluated in terms of the correlation function of nonrelativistic quark currents. Because the corresponding correction first appears in the $O(\beta^2)$ order, the coefficients B^i can be taken in the leading order in α_s. The coefficient B^v is related to the nonrelativistic expansion of the vector current and is equal to $B^v = 4/3$ [8]. The calculation of the coefficient B^{++} necessary for the consistent description of the $\gamma\gamma$ cross section in NRQCD in NNLO is more involved because the amplitude of the $\gamma\gamma \longrightarrow t\bar{t}$ transition is determined by the nonrelativistic expansion of the T product of two vector currents [31, 41]. However, this coefficient can be found by direct comparison with the relativistic expression for the cross section expanded in the velocity of the heavy quark (see Subsection 3.1).

For the noninteracting quarks (the Born approximation), we obtain the following results for the cross sections ($\beta = \sqrt{1 - 4m_t^2/s}$):

$$R^v(\beta) = \frac{3}{2} q_t^2 N_c \theta(\beta^2)(\beta + O(\beta^3)),$$

$$R^a(\beta) = N_c \theta(\beta^2)(\beta^3 + O(\beta^5)),$$

$$R^{++}(\beta) = 6q_t^4 N_c \theta(\beta^2)(\beta + O(\beta^3)),$$

$$R^{+-}(\beta) = 8q_t^4 N_c \theta(\beta^2)(\beta^3 + O(\beta^5)).$$

Note that the cross sections R^v and R^{++} are saturated by the S-wave contribution and are proportional to the Green's function at the origin, while R^a and R^{+-} cross sections are saturated by the P-wave contribution and are proportional to the derivative of the Green's function at the origin. As a consequence, they are suppressed by the factor β^2 in comparison to R^v and R^{++}. In the present paper, we study the corrections to the total cross sections R^e and R^γ up to the NNLO of NRQCD. Thus, R^a is a NNLO contribution to the total cross section R^e, and only the leading contribution to R^a is important. On the contrary, the R^{+-} part can be separated from R^γ by fixing the opposite helicities of the colliding photons. This makes possible the direct study of the P-wave production; therefore, the evaluation of the corrections to R^{+-} cross section is of practical interest.

Concluding this Subsection, we should also mention that the electroweak corrections to the cross sections are known with one-loop accuracy. They have

been obtained in [42] for e^+e^- annihilation and in [43] for $\gamma\gamma$ collisions.

2.3. Forward–Backward Asymmetry

The next important parameter related to the threshold production is the asymmetry of the differential cross sections. This parameter gives more detailed information on the process and allows one to obtain independent experimental data for further test of the theory. The forward–backward asymmetry of the top-quark production is defined as the difference of the cross sections averaged over the forward and backward hemispheres with respect to the electron-beam direction divided by the total cross section. Nonvanishing asymmetry appears in e^+e^- annihilation due to the axial coupling of the top quark to the Z boson. The expression of this parameter for energies near the threshold is given by [5]:

$$A_{\mathrm{FB}} = \frac{E_{VA}}{D_V}\left(1 + \frac{c_1^a - c_1^v}{2}\frac{C_F\alpha_s}{\pi}\right)\Phi(k), \qquad (8)$$

where

$$E_{VA} = q_e q_t a_e a_t d + 2v_e a_e v_t a_t d^2$$

is the electroweak factor. The expression for the asymmetry in (8) is given in NLO, and the explicit correction of order of α_s is taken in the linear approximation that results in the manifest difference between axial and vector hard coefficients in this order.

The dynamical quantity is the function

$$\Phi(k) = \frac{1}{m_t}\frac{\mathrm{Re}\int\tilde{G}^*(p,k)\tilde{F}(p,k)p^3dp}{\int\tilde{G}^*(p,k)\tilde{G}(p,k)p^2dp} \qquad (9)$$

that describes the overlap of the partial S and P waves. Here, $\mathbf{p}\tilde{F}(p, k)$ and $\tilde{G}(p, k)$ are the Fourier transforms of $i\partial_y G(\mathbf{x}, \mathbf{y}, k)|_{y=0}$ and $G(x, 0, k)$, respectively. In the Born approximation, the expression for the function $\Phi(\beta)$ can be found in the simple explicit form $\Phi(\beta) = \mathrm{Re}\beta$. It vanishes for real values of energy below the threshold.

2.4. Top-Quark Polarization

The longitudinal top-quark polarization in the process $e^+e^- \longrightarrow t\bar{t}$ averaged over the production angle reads [6, 44]

$$\langle P_L\rangle = -\frac{4}{3}\frac{D_{VA}}{D_V}\left(1 + \frac{c_1^a - c_1^v}{2}\frac{C_F\alpha_s}{\pi}\right)\Phi(k),$$

where

$$D_{VA} = q_e q_t v_e a_t d + (v_e^2 + a_e^2)v_t a_t d^2$$

and $\Phi(k)$ is given by (9). This function also enters into the expression for the averaged longitudinal top-quark polarization in the $\gamma\gamma \longrightarrow t\bar{t}$ process involving colliding photons with the same helicity [7]

$$\langle P_L\rangle = \pm 2\left(1 + \frac{c_1^{+-} - c_1^{++}}{2}\frac{C_F\alpha_s}{\pi}\right)\Phi(k),$$

where signs $\pm$ correspond to the positive/negative-helicity photons.

The extension of the above expressions to the general electron/positron polarization and photon helicity and to other components of the polarization vector can be found elsewhere [6, 7].

2.5. Effects of the Finite Top-Quark Width

As mentioned above, the sufficiently large t-quark decay width suppresses the nonperturbative effects of strong interactions at large ($\sim 1/\Lambda_{\mathrm{QCD}}$) distances and makes the perturbation theory applicable to the description of the t-quark threshold dynamics. The near-threshold dynamics is nonrelativistic and is rather insensitive to the hard-momentum details of t-quark decays. Therefore, as the leading-order approximation, the instability of the top quark can be parametrized with the constant mass operator. The finite top-quark width can then be taken into account by direct replacement $m_t \longrightarrow m_t - i\Gamma_t/2$ in the relevant argument $s - 4m_t^2$ describing the functional dependence of physical quantities near the threshold. Such a replacement is equivalent to the energy shift $E \longrightarrow E + i\Gamma_t$ [1]. This approximation accounts for the leading imaginary electroweak contribution to the leading-order NRQCD Lagrangian. Since the essential features of the physical situation are reflected in this approximation, we neglect the electroweak effects in higher orders in the strong coupling constant and heavy-quark velocity.

However, in the case of P-wave production and S–P-wave interference, the above prescription is insufficient for the proper description of the entire effect of the nonzero top-quark width [2] and more thorough analysis is necessary (see Subsections 3.2, 3.3).

In the context of the finite top-quark lifetime, we should also mention that the nonfactorable corrections due to the top-quark interaction with the decay products are suppressed in the total cross sections [45] but should be taken into account as NLO contributions to the angular distribution and top-quark polarization [46].

3. NONRELATIVISTIC GREEN'S FUNCTION BEYOND THE LEADING ORDER

The basic quantity in the analysis of the threshold effects is the nonrelativistic Green's function of

Schrödinger equation (1). The Green's function has the standard partial-wave decomposition

$$G(\mathbf{x}, \mathbf{y}, k) = \sum_{l=0}^{\infty}(2l+1)(xy)^l P_l(\mathbf{x}\cdot\mathbf{y}/xy)G_l(x, y, k), \quad (10)$$

where $P_l(z)$ is the Legendre polynomial. Note that the partial waves of the Green's function $G^{\mathrm{C}}(\mathbf{x}, \mathbf{y}, k)$ of the Coulomb interaction Schrödinger equation are known in the explicit form

$$G_l^{\mathrm{C}}(x, y, k) = \frac{m_t k}{2\pi}(2k)^{2l}e^{-k(x+y)} \times \sum_{m=0}^{\infty}\frac{L_m^{2l+1}(2kx)L_m^{2l+1}(2ky)m!}{(m+l+1-\nu)(m+2l+1)!}, \quad (11)$$

where $\nu = \lambda/k$, $\lambda = \alpha_s C_F m_t/2$ with α_s taken at the soft scale μ_s, and $L_m^{\alpha}(z)$ is the Laguerre polynomial, which is chosen in the form

$$L_m^{\alpha}(z) = \frac{e^z z^{-\alpha}}{m!}\left(\frac{d}{dz}\right)^m (e^{-z}z^{m+\alpha}).$$

However, we need to know the nonrelativistic Green's function for the NNLO Hamiltonian of the form

$$\mathcal{H} = \mathcal{H}_{\mathrm{C}} + \Delta\mathcal{H},$$

where the correction to the Coulomb Hamiltonian has the form

$$\Delta\mathcal{H} = -\frac{\Delta_{\mathbf{x}}^2}{4m_t^3} + \Delta_1 V(x) + \Delta_2 V(x) + \Delta_{\mathrm{NA}}V(x) + \Delta_{\mathrm{BF}}V(\mathbf{x}, \partial_{\mathbf{x}}, \mathbf{S}). \quad (12)$$

Here, the first term is the standard correction to the kinetic energy operator, $\Delta_{\mathrm{NA}}V(x) = -C_A C_F \alpha_s^2/(2m_t x^2)$ is the so-called non-Abelian potential of quark–antiquark interaction [47], and $\Delta_{\mathrm{BF}}V(\mathbf{x}, \partial_{\mathbf{x}}, \mathbf{S})$ is the standard long-known Breit–Fermi potential (only the overall color factor C_F is new). The Breit–Fermi potential includes the quark-spin operator $\mathbf{S}$ [48]. In NNLO, the cross section R^v is saturated with the final-state configuration of $t\bar{t}$ pair with $l = 0$, $S = 1$, while the cross section R^{++} is saturated with the $l = 0$, $S = 0$ configuration. In the $l = 0$ states, the Breit–Fermi potential takes the form

$$\Delta_{\mathrm{BF}}V(x) = \frac{C_F\alpha_s}{x}\frac{\Delta_{\mathbf{x}}}{m_t^2} + A^i\frac{C_F\alpha_s\pi}{m_t^2}\delta(\mathbf{x}),$$

where $A^v = 11/3$ corresponds to the spin-one final state of the $e^+e^- \longrightarrow t\bar{t}$ production and $A^{++} = 1$ corresponds to the zero-spin final state of the $\gamma\gamma \longrightarrow t\bar{t}$ production.

The terms $\Delta_i V$ ($i = 1, 2$) represent the first- and the second-order perturbative QCD corrections to the Coulomb potential [49, 50]:

$$\Delta_1 V(x) = \frac{\alpha_s}{4\pi}V_{\mathrm{C}}(x)(C_0^1 + C_1^1\ln(x\mu_s)),$$

$$\Delta_2 V(x) = \left(\frac{\alpha_s}{4\pi}\right)^2 V_{\mathrm{C}}(x)(C_0^2 + C_1^2\ln(x\mu_s) + C_2^2\ln^2(x\mu_s)),$$

where

$$C_0^1 = a_1 + 2\beta_0\gamma_{\mathrm{E}}, \quad C_1^1 = 2\beta_0,$$

$$C_0^2 = \left(\frac{\pi^2}{3} + 4\gamma_{\mathrm{E}}^2\right)\beta_0^2 + 2(\beta_1 + 2\beta_0 a_1)\gamma_{\mathrm{E}} + a_2,$$

$$C_1^2 = 2(\beta_1 + 2\beta_0 a_1) + 8\beta_0^2\gamma_{\mathrm{E}}, \quad C_2^2 = 4\beta_0^2,$$

$$a_1 = \frac{31}{9}C_A - \frac{20}{9}T_F n_f,$$

$$a_2 = \left(\frac{4343}{162} + 4\pi^2 - \frac{\pi^4}{4} + \frac{22}{3}\zeta(3)\right)C_A^2 - \left(\frac{1798}{81} + \frac{56}{3}\zeta(3)\right)C_A T_F n_f - \left(\frac{55}{3} - 16\zeta(3)\right)C_F T_F n_f + \left(\frac{20}{9}T_F n_f\right)^2,$$

$$\beta_1 = \frac{34}{3}C_A^2 - \frac{20}{3}C_A T_F n_f - 4C_F T_F n_f.$$

Here, α_s is defined in $\overline{MS}$ renormalization scheme. The invariants of the color-symmetry $SU(3)$ group have the following numerical values for QCD: $C_A = 3$, $C_F = 4/3$, $T_F = 1/2$, $n_f = 5$ is the number of light quark flavors, $\beta_0 = 11C_A/3 - 4T_F n_f/3$ is the first β-function coefficient, $\gamma_{\mathrm{E}} = 0.577216\ldots$ is the Euler constant, and $\zeta(z)$ is the Riemann ζ function. Solution to (1) with Hamiltonian (12) can be found within the standard nonrelativistic perturbation theory around the Coulomb Green's function as the leading-order approximation:

$$G(\mathbf{x}, \mathbf{y}, k) = G_{\mathrm{C}}(\mathbf{x}, \mathbf{y}, k) + \Delta G(\mathbf{x}, \mathbf{y}, k),$$
$$\Delta G(\mathbf{x}, \mathbf{y}, k) = -\int G_{\mathrm{C}}(\mathbf{x}, \mathbf{z}, k)\Delta\mathcal{H}G_{\mathrm{C}}(\mathbf{z}, \mathbf{y}, k)d\mathbf{z} + \ldots. \quad (13)$$

In the previous section, the threshold effects in the basic observables were reduced to three universal functions: the Green's function at the origin, which is saturated by the S-wave contribution; the derivative of the Green's function at the origin which is saturated by the P-wave contribution; and the function $\Phi(k)$, which describes the S–P-wave interference. These functions are analyzed in detail in Subsections 3.1–3.3.

3.1. S-Wave Production

Only the $l = 0$ component of Green's function (10) contributes to its value at the origin:

$$G(0, 0, k) = G_0(0, 0, k).$$

The explicit expression for the Coulomb part of the Green's function has the form

$$G_0^{\mathrm{C}}(x, 0, k)|_{x\to 0} = \frac{m_t}{4\pi}\left(\frac{1}{x} - 2\lambda\ln(2x\mu_f)\right.$$
$$\left. - 2\lambda\left(\frac{k}{2\lambda} + \ln\left(\frac{k}{\mu_f}\right) + 2\gamma_{\mathrm{E}} - 1 + \Psi_1(1-\nu)\right)\right), \quad (14)$$

where $\Psi_n(z) = d^n\ln\Gamma(z)/dz^n$ and $\Gamma(z)$ is the Euler Γ function. The energy-independent finite part of this expression is chosen for convenience. Equation (14) can most easily be obtained from the general expression for the Coulomb partial waves:

$$G_l^{\mathrm{C}}(x, 0, k) = \frac{m_t k}{2\pi}(2k)^{2l}e^{-kx}\Gamma(l+1-\nu)$$
$$\times U(l+1-\nu, 2l+2, 2kx), \quad (15)$$

where $U(a, b, z)$ is the confluent hypergeometric function. In the short-distance limit $x \longrightarrow 0$, the Coulomb Green's function $G^{\mathrm{C}}(\mathbf{x}, 0, k) = G_0^{\mathrm{C}}(x, 0, k)$ has $1/x$ and $\ln(x)$ divergent terms. These terms, however, are energy independent and do not contribute to the cross section. Hence, these terms can be subtracted with no effect on any physical results. The quantity μ_f in Eq. (14) is an auxiliary parameter, the factorization scale, which drops out of the physical observables.

The NLO correction $\Delta_1 G$ to (14) due to the first iteration of $\Delta_1 V$ term of the QCD potential has been found in [18], where the simple and efficient technique for computation of higher order terms was formulated. The NLO correction is evaluated in the form

$$\Delta_1 G_0(0, 0, k) = \frac{\alpha_s\beta_0}{2\pi}\frac{\lambda m_t}{2\pi}$$
$$\times\left(\sum_{m=0}^{\infty} F(m)^2(m+1)(L_1(k) + \Psi_1(m+2))\right.$$
$$- 2\sum_{m=1}^{\infty}\sum_{n=0}^{m-1} F(m)F(n)\frac{n+1}{m-n} + 2\sum_{m=0}^{\infty} F(m)(L_1(k)$$
$$\left. - 2\gamma_{\mathrm{E}} - \Psi_1(m+1)) - \gamma_{\mathrm{E}}L_1(k) + \frac{1}{2}L_1(k)^2\right),$$

where

$$L_1(k) = \ln\left(\frac{\mu_s e^{C_0^1/C_1^1}}{2k}\right)$$

and

$$F(m) = \frac{\nu}{(m+1)(m+1-\nu)}.$$

The NNLO correction $\Delta_2^{(2)}G$ due to the $\Delta_2 V$ part of the potential and the correction $\Delta_2^{(1)}G$ due to the second iteration of the $\Delta_1 V$ part of the correction to the Coulomb static potential have been obtained in [18, 19]. While the technique is rather straightforward, the results of the calculations are cumbersome and explicit formulas are relegated to Appendix A.

The method of calculation of the correction to the Green's function at the origin due to logarithmic terms in the potential is described in detail in [21]. It is based on the representation of the Coulomb Green's function as an expansion in Laguerre polynomials (11). This representation is very close to the standard physical expansion in the eigenfunctions that makes the technique transparent and easily interpretable in physical terms. It is equally suitable for any partial-wave contribution as shown in [31], where results for P-wave production were found. The results for the S-wave part of the corrections were reproduced within a different technical framework based on an integral representation of the Coulomb Green's function in [20].

The corrections to the Coulomb Green's function at the origin due to Δ^2, V_{NA}, and V_{BF} terms have been presented in [26, 27] and formally have the form

$$\Delta_{\Delta^2,\,\mathrm{NA},\,\mathrm{BF}}G = \frac{m_t}{4\pi}\frac{k^2}{m_t^2}\left(\frac{5}{8}k + 4\lambda\left(\ln\left(\frac{k}{\mu_f}\right)\right.\right.$$
$$\left.\left. + \gamma_{\mathrm{E}} + \Psi_1(1-\nu)\right) - \frac{11}{8}C_F\alpha_s\nu\Psi_2(1-\nu)\right) \quad (16)$$
$$+ \pi\frac{C_F\alpha_s}{m_t^2}\left(5 - A^i + 2\frac{C_A}{C_F}\right)G_{\mathrm{C}}(0, 0, k)^2.$$

In the course of evaluation of this correction to the nonrelativistic Green's function, one encounters the ultraviolet divergence in the imaginary part of the Green's function contained in the last term of (16). This divergence is related to the singular behavior of the Coulomb Green's function at the origin. The particular form of this divergence depends on the regularization procedure. The divergence appears in the process of scale separation and is a consequence of the fact that the nonrelativistic approximation is not adequate for the description of the short distance effects. The hard coefficient $C^{v,++}$ computed within the same regularization procedure as the Green's function must have an infrared singular term which exactly cancels the one appearing in the Green's function. The hard coefficient can be evaluated by matching the effective and full-theory cross sections in the weak-coupling limit [17, 26] or by explicit separation of the hard and soft contribu-

tions using, for example, the scale factorization in the dimensional regularization [22, 34, 35]. Let us consider the cancellation of the divergences and determination of the hard coefficient in the matching scheme. The natural regularization for the analysis of the hard part of the corrections is the dimensional one [32, 33]. In $4 - 2\varepsilon$ dimensions the infrared divergence of the hard contribution in NNLO has the form of the first-order pole in ε. The Coulomb Green's function at the origin in Eq. (16) can be regularized in the same way to ensure the finiteness of the cross section by the explicit cancellation of divergent parts which are represented in a comparable form. The dimensionally regularized Coulomb Green's function at the origin takes the form (see Appendix B)

$$G_{\rm C}^{\rm dr}(0,0,k) = -\frac{m_t}{4\pi}\left(k + 2\lambda\left(-\frac{1}{2\varepsilon} + \ln\left(\frac{k}{\mu_f}\right) + \gamma_{\rm E} + \Psi_1(1-\nu)\right)\right) + O(\varepsilon). \quad (17)$$

Note that, in contrast to (14), expression (17) has no divergence in the Born approximation. The Green's function in this approximation is a nonrelativistic free propagator and is proportional to k. The first-order pole in ε appears only in the first order in α_s. The $O(\alpha^2)$ singular $1/\varepsilon$ term in the imaginary part of Eq. (16) is proportional to $\mathrm{Im}(G_{\rm C}(0,\,0,\,k))$ and, therefore, can be absorbed by the redefinition of the hard coefficient $C^{v,\,++}$. For the Green's function, this redefinition results in the substitution $G_{\rm C}^{\rm dr}(0,0,k) \longrightarrow G_{\rm C}^{s}(0,0,k)$ in (16), where the "subtracted" Green's function reads

$$G_{\rm C}^{s}(0,0,k) = G_{\rm C}^{\rm dr}(0,0,k) - \frac{m_t\lambda}{4\pi}\frac{1}{\varepsilon}. \quad (18)$$

Within the redefined hard coefficient, the $O(\alpha^2)$ "ultraviolet" $1/\varepsilon$ term stemming from the corrections to the Green's function (16) exactly cancels the $O(\alpha^2)$ "infrared" $1/\varepsilon$ term of the hard part of the corrections. This can be explicitly checked for the C^v coefficient since its singularity is determined by the one of the hard renormalization coefficients of the nonrelativistic vector current [32, 33]. Then, the finite coefficient $C^{v,\,++}$ can be found directly by matching the effective theory expression for the cross sections and the result of perturbative QCD calculation of the spectral density in the formal limit $\alpha_s \ll \beta \ll 1$ up to the order α_s^2 for $\mu_h = \mu_s$. Equations (4) and (6) in the matching limit take the form

$$R^v = \frac{3}{2}N_c q_t^2\beta\Big[(1 + (1-B^v)\beta^2) + C_F\frac{\alpha_s}{\pi}\left(\frac{\pi^2}{2}\frac{1}{\beta} + c_1^v + \frac{\pi^2}{3}\beta\right) + C_F\left(\frac{\alpha_s}{\pi}\right)^2\left(C_F\frac{\pi^4}{12}\frac{1}{\beta^2} + \pi^2\left(C_F\frac{c_1^v}{2} + \frac{1}{8}\left(-C_1^1\ln\left(\frac{2\beta m_t}{\mu_s}\right) + C_0^1 - 2\beta_0\gamma_{\rm E}\right)\right)\frac{1}{\beta} + C_F\frac{5\pi^4}{36} + c_2^v - C_F\pi^2\left(\frac{5-A^v}{2} + \frac{C_A}{C_F}\right)\ln\left(\frac{\beta m_t}{\mu_f}\right)\right)\Big], \quad (19)$$

$$R^{++} = 6N_c q_t^4\beta\Big[(1 + (1-B^{++})\beta^2) + C_F\frac{\alpha_s}{\pi}\left(\frac{\pi^2}{2}\frac{1}{\beta} + c_1^{++} + \frac{\pi^2}{3}\beta\right) + C_F\left(\frac{\alpha_s}{\pi}\right)^2\left(C_F\frac{\pi^4}{12}\frac{1}{\beta^2} + \pi^2\left(C_F\frac{c_1^{++}}{2} + \frac{1}{8}\left(-C_1^1\ln\left(\frac{2\beta m_t}{\mu_s}\right) + C_0^1 - 2\beta_0\gamma_{\rm E}\right)\right)\frac{1}{\beta} + C_F\frac{5\pi^4}{36} + c_2^{++} - C_F\pi^2\left(\frac{5-A^{++}}{2} + \frac{C_A}{C_F}\right)\ln\left(\frac{\beta m_t}{\mu_f}\right)\right)\Big], \quad (20)$$

where the terms of the relative order $O(\beta^2)$ are retained. Comparing (19) with the NNLO QCD result for the cross section R^v expanded in the velocity of the heavy quark near the threshold [32, 51], we find

$$c_2^v = \tilde{c}_2^v - c_1^v\frac{\beta_0}{2}\ln\left(\frac{m_t}{\mu_h}\right) + \pi^2\left(\frac{2}{3}C_F + C_A\right)\ln\left(\frac{m_t}{\mu_f}\right), \quad (21)$$

where the coefficient $\tilde{c}_2^v$ has been obtained in [26, 27]

$$\tilde{c}_2^v = \left(\frac{39}{4} - \zeta(3) + \frac{4\pi^2}{3}\ln 2 - \frac{35\pi^2}{18}\right)C_F - \left(\frac{151}{36} + \frac{13}{2}\zeta(3) + \frac{8\pi^2}{3}\ln 2 - \frac{179\pi^2}{72}\right)C_A + \left(\frac{44}{9} - \frac{4\pi^2}{9} + \frac{11}{9}n_f\right)T_F.$$

The first logarithm in (21) is determined by the renormalization group running of the strong coupling constant in the hard momentum regime and is proportional to the first coefficient of the β function. Thus, both the hard coefficient and the Green's function do not depend on the normalization point of α_s in the fixed order of perturbation theory so one can use different scales for α_s in these quantities. The second logarithm corresponds to the anomalous dimension of the hard coefficient and precisely cancels the factorization-scale dependence of the Green's function due to Eq. (16). This cancellation makes the total result independent of the factorization scale. Note that the use of different hard and soft normalization scales leads to the incomplete cancellation of the factorization scale dependence, which, however, is an $O(\alpha_s^3)$ effect.

As was mentioned above, one can bypass the direct matching by the consistent use of the dimensional regularization, where the factorization and matching are automatic [14, 34, 35]. In this approach, the hard coefficient is completely determined by the hard renormalization coefficient of the nonrelativistic vector current [22]. However, to compute the corrections to the Green's function in this case, one has to define accurately the Breit–Fermi Hamiltonian in $3 - 2\varepsilon$ dimensions [22, 35] (in our analysis, we use the three-dimensional Breit–Fermi Hamiltonian, and the direct matching is necessary, though the ultraviolet and infrared divergent terms cancel each other explicitly).

The NNLO analysis of the R^{++} cross section is still absent, and the constant in the hard coefficient is unknown. The logarithmic part of the NNLO contribution to $C^{++}(\alpha_s)$ reads

$$c_2^{++} = \tilde{c}_2^{++} - c_1^{++}\frac{\beta_0}{2}\ln\left(\frac{m_t}{\mu_h}\right) + \pi^2(3C_F + C_A)\ln\left(\frac{m_t}{\mu_f}\right), \quad (22)$$

where $\tilde{c}_2^{++}$ is a constant to be determined. The relativistic correction to this cross section, however, can be extracted from the calculations presented earlier in the literature. Comparing the known result [52]

$$R^{++}(\beta) = 6q_t^4 N_c \beta\left(1 + \frac{2}{3}\beta^2 + O(\beta^4)\right) \quad (23)$$

with our expression (20), we find $B^{++} = 1/3$. The Green's function at the origin can be written in the form that includes only single poles in the energy variable. This form seems to be natural for the Green's function of the nonrelativistic Schrödinger equation:

$$G(0, 0, E) = \sum_{m=0}^{\infty}\frac{|\psi_{0m}(0)|^2}{E_{0m} - E} + \frac{1}{\pi}\int_0^{\infty}\frac{|\psi_{0E'}(0)|^2}{E' - E}dE', \quad (24)$$

where $\psi_{0m,E'}(0)$ is the wave function at the origin, the sum goes over the bound states, and the integral goes over the states of the continuous spectrum. In this way the corrections to the Green's function stemming from the discrete spectrum reduce to corrections to Coulomb bound-state energies

$$E_{0m} = E_{0m}^{\mathrm{C}}(1 + \Delta_1 E_{0m} + \Delta_2 E_{0m})$$

and to the values of Coulomb bound-state wave functions at the origin:

$$|\psi_{0m}(0)|^2 = |\psi_{0m}^{\mathrm{C}}(0)|^2(1 + \Delta_1\psi_{0m}^2 + \Delta_2\psi_{0m}^2),$$

where

$$E_{0m}^{\mathrm{C}} = -\frac{\lambda^2}{(m+1)^2}, \quad |\psi_{0m}^{\mathrm{C}}(0)|^2 = \frac{\lambda^3}{\pi(m+1)^3},$$

$$\Delta_2 E_{0m} = \Delta_{\Delta^2,\,\mathrm{NA,\,BF}}E_{0m} + \Delta_2^{(2)}E_{0m} + \Delta_2^{(1)}E_{0m},$$

$$\Delta_2\psi_{0m}^2 = \Delta_{k^2}\psi_{0m}^2 + \Delta_{\Delta^2,\,\mathrm{NA,\,BF}}\psi_{0m}^2 + \Delta_2^{(2)}\psi_{0m}^2 + \Delta_2^{(1)}\psi_{0m}^2,$$

and $\Delta_{k^2}\psi_{0m}^2$ is the correction due to relativistic corrections parametrized by the coefficients B^i which we include into the definition of the wave function.

In NLO, an explicit analytic expression for the corrections to the bound-state parameters has the form [20, 21, 53]

$$\Delta_1 E_{0m} = \frac{\alpha_s\beta_0}{\pi}(\bar{L}_1(m) + \Psi_1(m+2)),$$

$$\Delta_1\psi_{0m}^2 = \frac{\alpha_s\beta_0}{2\pi}\Big(3\bar{L}_1(m) + \Psi_1(m+2)$$

$$-2(m+1)\Psi_2(m+1) - 1 - 2\gamma_{\mathrm{E}} + \frac{2}{m+1}\Big),$$

where $\bar{L}_1(m) = L_1(\lambda/(m+1))$. The expressions for the NNLO corrections to the energy levels [20, 21, 53] and wave functions at the origin [20, 21] are rather cumbersome and are given in Appendices C and D.

The continuum contributions in (24) can be directly found by subtracting the discrete part of these equations expanded around the Coulomb approximation up to NNLO,

$$\sum_{m=0}^{\infty}\frac{|\psi_{0m}^{\mathrm{C}}(0)|^2}{E_{0m}^{\mathrm{C}} - E}\Big(1 + \Delta_1\psi_{0m}^2 + \Delta_2\psi_{0m}^2$$

$$+\frac{(1 + \Delta_1\psi_{0m}^2)\Delta_1 E_{0m} + \Delta_2 E_{0m}}{1 - E/E_{0m}^{\mathrm{C}}} + \frac{\Delta_1 E_{0m}^2}{(1 - E/E_{0m}^{\mathrm{C}})^2}\Big),$$

from the result obtained within the nonrelativistic perturbation theory for the Green's function at the origin (13) multiplied by $(1 - B^i E/m_t)$. This procedure removes the double and triple poles from (13) and leaves only the single poles in expression (24) for the Green's function.

An important consequence of the relatively large top-quark width is that most of the Coulomb resonances are smoothed out. The numerical analysis shows that only the ground-state resonance in the cross sections is distinguishable. Its separation from others is not completely covered by the infrared cutoff provided by the top-quark width. Indeed, using the pure Coulomb formulas for estimation within an order of magnitude, we find the value

$$|E_{00}^{\mathrm{C}} - E_{01}^{\mathrm{C}}| = \frac{3\lambda^2}{4m_t} \approx 0.6\ \mathrm{GeV}$$

to be compared with the top-quark width $\Gamma_t = 1.43$ GeV. The second spacing between radial excitations for the

$l = 0$ partial wave and the first spacing for the $l = 1$ partial wave are, however, much smaller,

$$\left|E_{01}^{\mathrm{C}} - E_{02}^{\mathrm{C}}\right| = \left|E_{10}^{\mathrm{C}} - E_{11}^{\mathrm{C}}\right| = \frac{5}{36}\frac{\lambda^2}{m_t} \approx 0.11\ \mathrm{GeV},$$

and are completely smeared out with the top-quark width.

In the limit of vanishing top-quark width, the NNLO approximation for the energy of the resonance in e^+e^- annihilation reads

$$\begin{aligned} E_{00}^{v} = -\frac{\lambda^2}{m_t}\Bigg(1 + \frac{\alpha_s}{4\pi}2C_1^1(L_1(\lambda) + 1 - \gamma_{\mathrm{E}}) \\ + \left(\frac{\alpha_s}{4\pi}\right)^2\Bigg(2C_1^2(L_2(\lambda) + 1 - \gamma_{\mathrm{E}}) \\ + (C_1^1)^2\Bigg((L_1(\lambda) - \gamma_{\mathrm{E}})^2 + 1 - \frac{\pi^2}{3} - \Psi_3(1)\Bigg) \\ + 2C_2^2\Bigg((L(\lambda) + 1 - \gamma_{\mathrm{E}})^2 - 1 + \frac{\pi^2}{6}\Bigg)\Bigg) \\ + C_F^2\alpha_s^2\Bigg(\frac{C_A}{C_F} + \frac{1}{48}\Bigg)\Bigg), \end{aligned} \tag{25}$$

where

$$L(\lambda) = \ln\left(\frac{\mu_s}{2\lambda}\right), \quad L_2(\lambda) = \ln\left(\frac{\mu_s e^{C_0^2/C_1^2}}{2\lambda}\right).$$

This value is related to the energy of the resonance of the top-quark production in the $\gamma\gamma$ collision by hyperfine splitting,

$$E_{00}^{v} - E_{00}^{++} = \frac{4}{3}\frac{\lambda^2}{m_t}C_F^2\alpha_s^2.$$

The convergence of the perturbation-theory series (25) is not fast. For some typical values of the soft normalization scale, the series for the resonance energy reads

$$\begin{aligned} E_{00}^{v} &= E_{00}^{\mathrm{LO}}(1 + 0.36 + 0.30), \quad \mu_s = 25\ \mathrm{GeV}, \\ E_{00}^{v} &= E_{00}^{\mathrm{LO}}(1 + 0.58 + 0.38), \quad \mu_s = 50\ \mathrm{GeV}, \\ E_{00}^{v} &= E_{00}^{\mathrm{LO}}(1 + 0.68 + 0.45), \quad \mu_s = 75\ \mathrm{GeV}, \\ E_{00}^{v} &= E_{00}^{\mathrm{LO}}(1 + 0.74 + 0.50), \quad \mu_s = 100\ \mathrm{GeV}. \end{aligned} \tag{26}$$

The poor convergence of the series for the resonance energy can be assigned to high infrared sensitivity of the pole mass (see, for example, [54]). The convergence can be manifestly improved by removing the pole mass from the theoretical expressions in favor of some less infrared-sensitive mass parameter, for example, the short-distance [20], potential-subtracted [22], or 1*S* mass [24]. Note that all the mass definitions are perturbatively equivalent in a finite order of the expansion. The infrared-safe mass parameters, however, are "closer" to the physical observables since the corresponding perturbative series, in contrast to the pole mass, are supposed to be convergent.

Due to the finite top-quark width, the location of the peak (maximum) of the cross section is not given only by the position of the ground-state resonance but is also affected by the contribution of the higher (smeared out) resonances and the continuum contribution. Due to this effect, the absolute value of the NNLO peak energy (25) measured from the threshold is less than the absolute value of the energy of the ground-state resonance $E_{00}^{v,++}$ by about 200 MeV, i.e., ~7%. This shift is essentially smaller than the one related to the perturbative QCD corrections to Coulomb values but is considerably larger than the leading nonperturbative contribution due to the gluon condensate [55], which is suppressed parametrically as $(\Lambda_{\mathrm{QCD}}/\lambda)^4 < 1\%$.

3.2. P-Wave Production

The derivative of the Green's function at the origin is saturated with its $l = 1$ component and is explicitly given by the relation

$$\partial_{\mathbf{xy}}^2 G(\mathbf{x}, \mathbf{y}, k) = 9G_1(0, 0, k).$$

For the Coulomb Green's function given in (15), we obtain the closed formula for the $l = 1$ partial-wave Green's function at the small space separation of a particle:

$$\begin{aligned} G_1^{\mathrm{C}}(x, 0, k)|_{x\to 0} = \frac{m_t}{36\pi}\Bigg(\frac{3}{x^3} + \frac{3\lambda}{x^2} + \frac{6\lambda^2 - 3k^2}{2x} \\ + 2\lambda(k^2 - \lambda^2)\ln(2x\tilde{\mu}_f) + \lambda\Bigg(2(k^2 - \lambda^2)\Bigg(\frac{k}{2\lambda} \\ + \ln\left(\frac{k}{\tilde{\mu}_f}\right) + 2\gamma_{\mathrm{E}} - \frac{11}{6} + \Psi_1(1 - \nu)\Bigg) + \frac{k^2}{2}\Bigg)\Bigg), \end{aligned} \tag{27}$$

where $\tilde{\mu}_f$ is the analog of the parameter μ_f for the $l = 0$ partial wave. In the short-distance limit $x \longrightarrow 0$, the derivative of the Coulomb Green's function (or the $l = 1$ partial wave) has $1/x^n$ ($n = 1, 2, 3$) and $\ln(x)$ singularities. In contrast to the case of the *S*-wave production, the value at the origin for the partial *P*-wave Green's function contains divergent terms that depend explicitly on the energy (or wave vector) *k*. However, these terms do not contribute to the cross section for the vanishing top-quark width $\Gamma_t = 0$ because they have no discontinuity across the physical cut in the complex energy plane in the approximation of zero top-quark width. The case of the nonzero top-quark width requires a more detailed analysis given below.

The correction to the $l = 1$ partial wave at the origin due to the first iteration of $\Delta_1 V$ term of the QCD potential has been found in [31]:

$$\Delta_1 G_1(0,0,k) = \frac{\alpha_s\beta_0}{2\pi}\frac{\lambda m_t k^2}{18\pi}\Bigg(\sum_{m=0}^{\infty}\tilde{F}(m)^2(m+1)$$
$$\times(m+2)(m+3)(L_1(k)+\Psi_1(m+4))$$
$$-2\sum_{m=1}^{\infty}\sum_{n=0}^{m-1}\tilde{F}(m)\tilde{F}(n)\frac{(n+1)(n+2)(n+3)}{m-n}$$
$$+2\sum_{m=0}^{\infty}\tilde{F}(m)\Bigg(2\tilde{J}_0(m)+(m+1)(m+2)L_1(k)$$
$$+(1+\nu)(\tilde{J}_1(m)+(m+1)L_1(k))$$
$$+\frac{\nu(\nu+1)}{2}(\tilde{J}_2(m)+2L_1(k))\Bigg)+\tilde{I}(k)\Bigg),$$

where

$$\tilde{F}(m) = \frac{\nu(\nu^2-1)}{(m+2-\nu)(m+1)(m+2)(m+3)},$$
$$\tilde{J}_0(m) = -2\Psi_1(m+1)-4\gamma_E+3,$$
$$\tilde{J}_1(m) = (m+1)(-\Psi_1(m+2)-2\gamma_E+2),$$
$$\tilde{J}_2(m) = \frac{(m+1)(m+2)}{2}\Bigg(-\Psi_1(m+3)-2\gamma_E+\frac{3}{2}\Bigg),$$
$$\tilde{I}(k) = -\frac{(\gamma_E-1)^2}{2}-\frac{\pi^2}{12}-(4-3\gamma_E)\nu$$
$$+\frac{1-9\gamma_E+6\gamma_E^2+\pi^2}{4}\nu^2+\frac{1-3\gamma_E}{2}\nu^3+\frac{1-\gamma_E}{4}\nu^4$$
$$+\Bigg(\gamma_E-1-3\nu+\frac{9-12\gamma_E}{4}\nu^2+\frac{3}{2}\nu^3+\frac{1}{4}\nu^4\Bigg)L_1(k)$$
$$+\Bigg(-\frac{1}{2}+\frac{3}{2}\nu^2\Bigg)L_1(k)^2.$$

For the derivative of the Green's function at the origin (or for the $l = 1$ partial wave), the analog of Eq. (24) reads

$$\partial^2_{\mathbf{xy}}G(\mathbf{x},\mathbf{y},E)$$
$$=\sum_{m=0}^{\infty}\frac{|\psi'_{1m}(0)|^2}{E_{1m}-E-i0}+\frac{1}{\pi}\int_0^{\infty}\frac{|\psi'_{1E'}(0)|^2}{E'-E-i0}dE',$$

where

$$|\psi'_{1m,E'}(0)|^2 = \partial_{\mathbf{x}}\psi^*_{m,E'}(\mathbf{x})\partial_{\mathbf{y}}\psi_{m,E'}(\mathbf{y})|_{x,y=0}.$$

Here, E_{1m} is the $l = 1$ bound-state energy. In the NLO approximation, these quantities read [31]

$$E_{1m} = -\frac{\lambda^2}{m_t(m+2)^2}$$
$$\times\Bigg(1+\frac{\alpha_s}{4\pi}2C_1^1(\bar{L}_1(m+1)+\Psi_1(m+4))\Bigg)$$

and

$$|\psi'_{1m}(0)|^2 = \frac{\lambda^5}{\pi}\frac{(m+1)(m+3)}{(m+2)^5}$$
$$\times\Bigg(1+\frac{\alpha_s}{4\pi}C_1^1\Bigg(5\bar{L}_1(m+1)+5\Psi_1(m+4)$$
$$-\frac{\pi^2}{3}(m+2)-1+2\sum_{n=0}^{m-1}\frac{(n+1)(n+2)(n+3)}{(m+1)(m+3)(m-n)^2}\Bigg)\Bigg).$$

The continuum contribution is obtained in the same way as it was done in the previous section for the *S*-wave production.

In the case of *P*-wave production, the simple shift $E \longrightarrow E + i\Gamma$ in the nonrelativistic approximation is not sufficient to describe properly the total effect of the nonzero top-quark width [2]. Indeed, Eq. (27) in the limit $x \longrightarrow 0$ with the nonvanishing width has the divergent imaginary part with the leading power singularity $\sim\Gamma_t/x$ related to the free Green's function singularity and the logarithmic singularity $\sim\Gamma_t\alpha_s\ln(x)$ produced by the Coulomb gluon exchange. The presence of these singularities clearly indicates that the coefficient of the constant term linear in Γ_t gets a contribution from the large momentum region and cannot be obtained within the pure nonrelativistic approximation. As the hard coefficients, it should be computed in relativistic theory. This contribution is not suppressed parametrically in comparison to the pure nonrelativistic contribution in the threshold region. At $E = 0$, for example, the ratio of the relativistic (proportional to Γ_t) and nonrelativistic (Coulomb) contributions is of order $\Gamma_t/\alpha_s^2 m_t \sim 1$. Since we are interested in the NLO corrections, the $O(\Gamma_t\alpha_s)$ term also has to be taken into account. By construction, the nonrelativistic effective theory has to reproduce the perturbation-theory predictions in the formal matching limit $\alpha_s, \beta \ll \Gamma_t/m_t \ll 1$, where both effective theory and perturbation theory descriptions are valid. Thus, one has to compute $O(\Gamma_t)$ and $O(\Gamma_t\alpha_s)$ terms in the relativistic perturbation theory and then to fix the parameters of the effective nonrelativistic theory so that it reproduces the perturbative results in the matching limit. In the relativistic perturbation theory, the relevant contributions can be obtained by inserting the complex momentum-dependent mass operator to the top-quark propagator at $\beta = 0$

(only the leading terms in Γ_t/m_t should be retained). In the leading order in α_s, this procedure has been done in [2]. The result reads

$$G_1^{\mathrm{C}}(0,0,k)|_{\Gamma_t} = \frac{m_t^3}{36\pi} g_1 \Gamma_t,$$

where g_1 is a coefficient coming from the relativistic treatment with the numerical value $g_1 \approx 0.185$. For the $O(\Gamma_t\alpha_s)$ term, the necessary calculation has been performed in [31]. It has been shown that the proper relativistic analysis leads to fixing the auxiliary parameter of Eq. (27) $\tilde{\mu}_f = g_2 m_t$, where g_2 is the coefficient coming from the relativistic treatment. Its numerical value is $g_2 \approx 0.13$.

Here, we should note also the problem of the previous numerical analysis of the *P*-wave contribution [28]. Solving Schrödinger equation (1) numerically for the finite top-quark width, one has to introduce an explicit ultraviolet cutoff for the nonrelativistic expressions divergent in the large-momentum region. To get rid of the cutoff dependence, one has to compute the hard contribution within the relativistic approximation using the similar prescription for the infrared cutoff. This, however, has not been done; as a consequence, the $O(\Gamma_t)$ and $O(\Gamma_t\alpha_s)$ contributions to the cross section were not determined within the numerical framework of [28].[4)] On the other hand, the total $O(\Gamma_t)$ contribution to the cross section is numerically small in comparison with that of the completely regular nonrelativistic terms of (27), which saturate the total result for energies not far below the threshold.

3.3. S–P Interference

In the zero-width approximation, function (9) can be decomposed as

$$\Phi(E) = \Phi_{\mathrm{pol}}(E) + \Phi_{\mathrm{con}}(E),$$

where Φ_{con} and Φ_{pol} are the continuum and bound-state poles contributions, respectively. It is known [7, 44] that the continuum contribution is not affected by the Coulomb effects, and above the threshold one has the Born approximation result

$$\Phi_{\mathrm{con}}^{\mathrm{C}}(E) = \mathrm{Re}\sqrt{\frac{E}{m_t}}$$

even for the Coulomb Green's function in Eq. (9). Below the threshold, in the Coulomb approximation, one obtains

$$\Phi_{\mathrm{pol}}^{\mathrm{C}}(E) = \left(\sum_{m=0}^{\infty} \frac{\phi_m^{\mathrm{C}}}{(E_{1m}^{\mathrm{C}} - E)^2}\right)\left(\sum_{m=0}^{\infty} \frac{|\psi_m(0)|^2}{(E_{0m}^{\mathrm{C}} - E)^2}\right)^{-1}, \quad (28)$$

where the quantities

$$\phi_m^{\mathrm{C}} = \frac{\lambda^4}{m_t\pi}\frac{(m+1)(m+3)}{(m+2)^5}$$

measure the overlap of the *S*- and *P*-wave functions. Note that in the zero-width limit, the function $\Phi_{\mathrm{pol}}^{\mathrm{C}}$ does not vanish due to the Coulomb degeneration of the energy levels with different l: $E_{0m+1}^{\mathrm{C}} = E_{1m}^{\mathrm{C}}$. It was indicated in [44] that the continuum contribution has no soft corrections. Thus, in NLO, we have the simple result for a finite top-quark width:

$$\Phi_{\mathrm{con}}(E) = \mathrm{Re}\sqrt{\frac{E + i\Gamma_t}{m_t}}.$$

The corrections to the pole contribution are less trivial. They can be computed using the powerful technique developed in [18, 21, 31]. The result reads

$$\Phi_{\mathrm{pol}}(E) = \mathrm{Re}\left(\sum_{m=0}^{\infty} \frac{\phi_m}{(E_{0(m+1)} - E + i\Gamma_t)(E_{1m} - E - i\Gamma_t)}\right) \times \left(\sum_{m=0}^{\infty} \frac{|\psi_m(0)|^2}{(E_{0m} - E)^2 + \Gamma_t^2}\right)^{-1}, \quad (29)$$

where

$$\phi_m = \phi_m^{\mathrm{C}}\left(1 + \frac{\alpha_s\beta_0}{\pi}\left(4L(m+1) + 4\Psi(m+4) + \frac{m}{m+3} - 2 - \frac{\pi}{6}(m+2) + \sum_{n=0}^{m-1}\frac{(n+1)(n+2)(n+3)}{(m+1)(m+3)(m-n)^2}\right)\right).$$

In (29), we retain the finite top-quark width to get a nonvanishing result since the Coulomb degeneration is removed by the logarithmic corrections to the potential. Strictly speaking, our approach is valid only if the level splitting $E_{0m+1} - E_{1m}$ is much smaller than the top-quark width (which is realized for the actual values of these quantities). At $E_{0m+1} - E_{1m} > \Gamma_t$, the nonrelativistic analysis is not applicable for the *S–P* interference below the threshold because the double poles of Eq. (28) disappear and the nonrelativistic contribution is not enhanced in comparison to the relativistic one in this case.

Note that, for the finite top-quark width, the interference of the free $l = 0$ and $l = 1$ partial waves results in the logarithmically divergent $O(\Gamma_t)$ term in the numerator of Eq. (9) (this term does not explicitly include the factor Γ_t, but it is suppressed in comparison to the leading term, which is proportional to $1/\Gamma_t$ as the leading

[4)] Recently, the $O(\Gamma_t)$ contribution has been estimated within the numerical approach [30] by using the physical (relativistic) phase space for the unstable top quark to regularize the divergence of the nonrelativistic approximation.

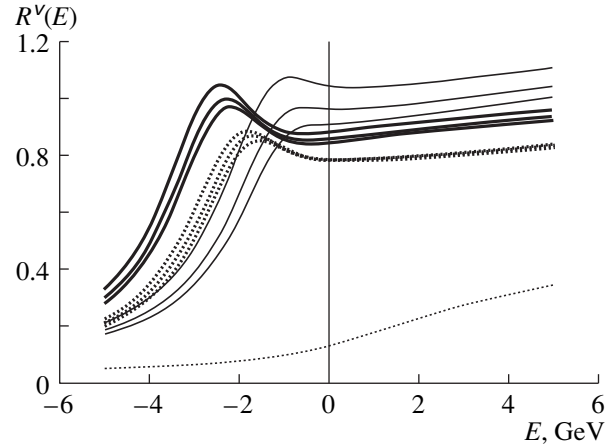

Fig. 1. Normalized cross section $R^V(E)$ in the leading order (thin solid curves), in NLO (thick dotted curves), and in NNLO (thick solid curves) for m_t = 175 GeV, Γ_t = 1.43 GeV, $\alpha_s(M_Z)$ = 0.118, and μ_s = 50, 75, and 100 GeV. The thin dotted curve corresponds to the result in the Born approximation.

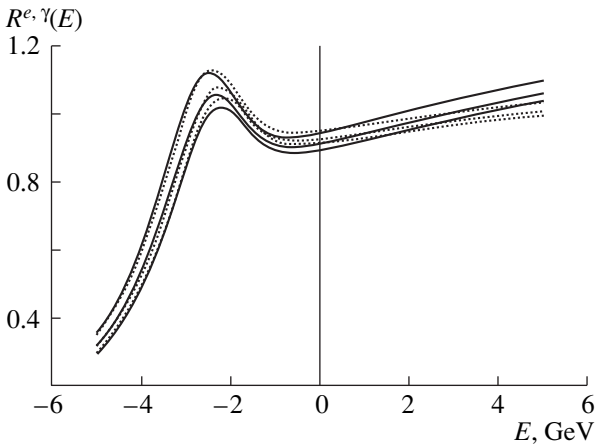

Fig. 2. Normalized cross sections $R^e(E)$ (dotted curves) and $R^\gamma(E)$ (solid curves) in NNLO for $\tilde{c}_2^{++} = 0$, m_t = 175 GeV, Γ_t = 1.43 GeV, $\alpha_s(M_Z)$ = 0.118, $\sin^2\theta_W$ = 0.232, M_Z = 91.2 GeV, and μ_s = 50, 75, and 100 GeV.

term in the denominator of Eq. (9) for the free quark Green's function). This divergent term is of the same origin as the divergence in the *P*-wave amplitude discussed in Subsection 3.2. This term can be accurately calculated only within the relativistic approximation. In contrast to the *P*-wave production, this term is parametrically suppressed above the threshold in comparison to the nonrelativistic continuum contribution by at least the factor $\sqrt{\Gamma_t/m_t}$ at $E \sim 0$ and can be safely omitted. However, it becomes important below the resonance region when the nonrelativistic contribution becomes small. Moreover, the denominator on the right-hand side of Eq. (9) decreases rapidly below the ground state pole. Therefore, a small uncertainty in the numerator would lead to a large uncertainty in the function $\Phi(k)$, and a reliable estimation of its numerical value is not possible in this region within the nonrelativistic approximation. Strictly speaking, the accurate determination of the function Φ below the ground-state pole requires the calculation of the relativistic $O(\Gamma_t)$ contribution to the *S*-wave cross section [the denominator of (9)], which is not usually considered since it does not lead to the divergence in the nonrelativistic expression.

4. DISCUSSION

The results of the numerical analysis for the physical observables based on the obtained analytic expressions are plotted in Figs. 1–4.

The constant $\tilde{c}_2^{++}$ appearing in the hard coefficient $C^{++}(\alpha_s)$ in the $O(\alpha_s^2)$ order remains unknown. The calculation of this parameter is necessary for the formal completion of the NNLO analysis. To find its numerical value, one has to compute the $O(\alpha_s^2)$ perturbative QCD correction to the $\gamma\gamma$ cross section near the threshold in the formal limit $\alpha_s \ll \beta \ll 1$ and to compare it with the $O(\alpha_s^2)$ term in (20). In the case of e^+e^- annihilation, however, the analogous contribution parametrized by $\tilde{c}_2^V$ is relatively small (about 10% of the total NNLO correction) and the correction to the physical observables in NNLO is saturated with the soft part of the total contribution determined by the corrections to the parameters of the nonrelativistic Green's function. Thus, one can reasonably hope that a similar situation can also take place for $\gamma\gamma$ collisions. However, the

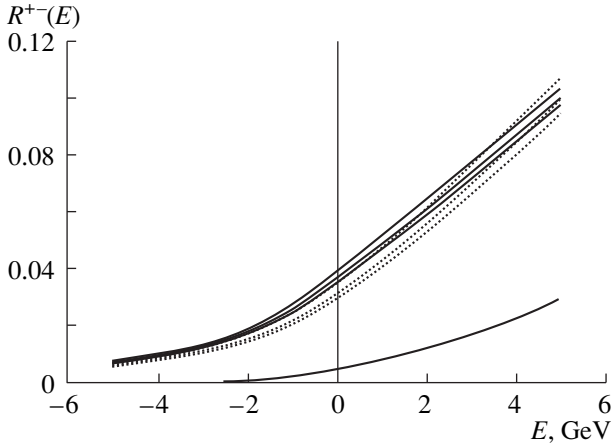

Fig. 3. Normalized cross section $R^{+-}(E)$ in the leading order (dotted curves) and in NLO (thick solid curves) for m_t =175 GeV, Γ_t =1.43 GeV, $\alpha_s(M_Z)$ = 0.118, and μ_s = 50, 75, and 100 GeV. The thin solid curve corresponds to the result in the Born approximation.

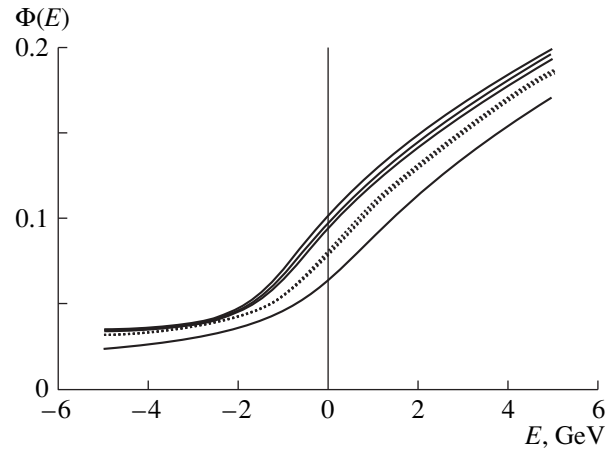

Fig. 4. As in Fig. 3, but for the function $\Phi(E)$.

importance of this parameter for physical observables is not crucial; it affects only the overall normalization of the cross sections. For example, it does not shift the position of the resonance, which is an important characteristic of the production, and does not enter the ratio $R^{++}(E)/R^{++}(0)$. For the numerical analysis of the cross section R^γ, we set $\tilde{c}_2^{++} = 0$.

In our approach, we deal with the soft corrections by summing them into the energy denominators of the discrete part of the Green's function. In other words, we treat the soft corrections as effective corrections to the parameters of the Green's function written in a fixed functional form. The same approach has been advocated in [22, 27, 29, 30, 56], where all the corrections to the Green's function have been found (numerically or analytically) in the form (24). In [26], however, part of the NNLO corrections have not been resummed to the energy denominators of the discrete part of the Green's function. On the other hand, the Schrödinger equation (1) has been solved numerically in [27, 29, 30, 56]; i.e., the NLO and the NNLO correction to the Coulomb Hamiltonian have been taken into account effectively in all orders of nonrelativistic series (13) for the Green's function, while we work strictly in NNLO. Our formulas reproduce the numerical result for R^v of the most recent numerical analysis [29, 30, 56] with 1–3% accuracy that can be assigned to the contribution of the higher iterations of the NLO and NNLO corrections to the potential in Eq. (13) beyond NNLO.

For the total cross sections, which are dominated by the *S*-wave contribution, we find the typical value of the NNLO corrections to be of the order of ~20% in the overall normalization of the cross sections and ~40% in the resonance energies expressed in terms of the top-quark pole mass, i.e., of the order of the NLO ones (see Fig. 1). Though the inclusion of the NLO corrections results in a considerable stabilization of the theoretical results for the cross sections against changing the normalization point, the NNLO corrections do not lead to better stability as compared to NLO. In the overall normalization of the cross sections, the NLO and NNLO corrections cancel each other to a large extent, while the NLO and NNLO corrections to the resonance energies are of the same sign and shift the resonance farther from the threshold. They also make the peak more distinguishable, which is the main difference between the leading Coulomb and NNLO approximations.

The leading-order approximations for R^e and R^γ cross sections are the same up to the normalization factor $2q_t^2$. Up to the overall factor, the difference between the cross sections is determined by NNLO QCD and relativistic corrections (see Fig. 2). Above the threshold, this difference is determined by the difference between B^{++} and B^v coefficients and between *P*-wave contributions to Eqs. (2) and (3), i.e., by the pure relativistic corrections. Below the threshold in the resonance region, this difference is determined also by A^i coefficients and is quite sensitive to the value of α_s.

Though the use of an infrared safe mass parameter instead of the pole mass improves the convergence of the series for the resonance energies, it does not affect the huge NNLO corrections to the cross section normalization. Moreover, it is not clear if there exist physically motivated mass and strong-coupling parameters providing fast uniform convergence of the perturbative expansion for the cross sections in the threshold region. The absence of such a parametrization would mean the unavoidable significance of the high-order terms of the threshold expansion. Some high-order effects have been already considered in the literature. The leading logarithmic corrections of the form $\alpha_s^{n+1}\ln^n\beta$ have been computed [22]. These corrections originate from the corrections to the Green's function due to the high iterations of the Δ^2 kinetic term and the non-Abelian and the Breit–Fermi potential of (12) and can be taken into account by the renormalization group evolution of the hard coefficient $C^{v,++}$ from $\mu_f = m_t$ down to $\mu_f = \beta m_t$ [22]. The corresponding corrections to the R^v cross section are ±5%. In [29], the running of the strong coupling constant has been taken into account by introducing the energy dependent soft normalization point of α_s entering the Coulomb potential in the numerical solution of the Schrödinger equation. The resummation of the renormalization group logarithms has an essential (up to 10%) effect in the resonance region and reduces the normalization-scale dependence of the result. Furthermore, the effect of retardation which introduces a new type of contributions absent in NLO and NNLO has been analyzed for the low-lying resonances [25]. The characteristic scale of the leading ultrasoft contribution was found to be about –5% for the square of the ground state wave function at the origin and +100 MeV for the ground-state pole position.

The result for the axial coupling contribution to the $e^+e^- \longrightarrow t\bar{t}$ cross section is in good agreement with the

numerical analysis presented in [28]. Up to the trivial normalization, this contribution coincides with the cross section R^{+-} (Fig. 3). Numerically, it does not exceed 2% of the total cross section and is less than the uncertainty resulting from the normalization scale dependence.

The cross section R^{+-} and the function $\Phi(k)$ have no contribution from the ground-state resonance; therefore, they are rather smooth because the top-quark width smears the higher resonance contributions very efficiently (Figs. 3, 4). These quantities are rather insensitive to variation in the normalization scale. A typical NLO correction to R^{+-} is about 10%, while the one to $\Phi(k)$ is about 15% [the corrections to the forward–backward asymmetry and top-quark polarization also include the hard normalization factors which have not been included to $\Phi(k)$ and the nonfactorable corrections discussed in Subsection 2.4]. Our result for the function $\Phi(k)$ (Fig. 4) is in good agreement with the results of numerical analysis [5, 6] for the energies above the ground-state resonance. There is some discrepancy between the results below the resonance. However, a reliable estimate for the function Φ is not possible in this region with the pure nonrelativistic treatment of the top-quark width, as was explained in Subsection 3.3.

The final remark of this section concerns the optimal choice of the normalization and factorization scales. The hard scale appears in the hard coefficients as $\ln(m_t/\mu_h)$; i.e., the typical hard scale of the problem is the top-quark mass. Though in a fixed order of the perturbative expansion the hard coefficients do not depend on μ_h, one can set $\mu_h \sim m_t$ to minimize the potentially large logarithmic contributions of the higher order terms. In practice, the NNLO results are almost independent of μ_h when $\mu_h \sim m_t$. On the other hand, the requirement of convergence of the perturbative expansion around the Coulomb Green's function restricts the allowed range for the choice of a soft normalization point that can be used for reliable estimates. The soft physical scale of the problem is determined by the natural infrared cutoff related to the top-quark width $\sqrt{m_t\Gamma_t}$ that measures the distance to the nearest singularity in the complex energy plane and/or by the characteristic scale of the Coulomb problem λ, i.e., $\mu_s \sim 15$ GeV. Both scales are rather close to each other for the case of the top quark, which makes possible a uniform description of both perturbative QCD and Coulomb resonance effects. Indeed, for $\mu_s \sim 15$ GeV, the soft NLO correction, for example, to energy level (25), reaches its minimal magnitude. However, at this scale, the NNLO correction exceeds the NLO one and the series for the energy levels seems to diverge. Moreover, for such a low soft normalization point, the NNLO corrections to the wave function at the origin that cannot be eliminated by the quark mass redefinition become uncontrollable. This is not surprising since the normalization scale is defined in a rather artificial $\overline{MS}$ scheme that has little to do with peculiarities of $t\bar{t}$ physics and there is no reason for a literal coincidence of parameter μ_s with any physical scale of the process. The relative weight of the NNLO correction to the Green's function, as well as the dependence of the cross sections on μ_s, is stabilized at $\mu_s \gtrsim 40$ GeV, which can be considered as an optimal choice of the soft normalization point. The price one pays for using different soft and hard normalization scales is the incomplete cancellation of the factorization scale dependence, but this effect is suppressed by an additional power of α_s. Another source of the dependence on the factorization scale is factorized form (4), (6) of the cross sections, where some higher order μ_f-dependent terms are retained. The numerical analysis, however, shows that the results are rather insensitive to the factorization scale chosen in the region $\mu_f \sim m_t$.

5. CONCLUSION

The basic observables of the top-quark pair production in e^+e^- annihilation and $\gamma\gamma$ collisions have been considered in the threshold region. The threshold effects are described by three universal functions related to the *S*- and the *P*-wave production and *S–P* interference which have been computed analytically within (potential) NRQCD. An explicit analytic expression for the soft part of the NNLO corrections to the total cross section has been obtained. The threshold $e^+e^- \longrightarrow t\bar{t}$ cross section has been obtained in NNLO in closed form including the contribution due to the top-quark axial coupling. The forward–backward asymmetry of the quark–antiquark pair production in e^+e^- annihilation and top-quark polarization in both processes have been computed analytically up to NLO. The running of the strong-coupling constant and the finite top-quark width effects in the *P*-wave production and *S–P*-wave interference have been taken into account properly within the analytic approach.

In combination, these uncorrelated observables form an efficient tool for investigating quark interactions. As independent sources, they can also be used for determination of the theoretical uncertainty in the numerical values of the strong-coupling constant α_s, the top-quark mass, and the top-quark width extracted from the experimental data on top–antitop production.

The high-order corrections turn out to be relatively large for all observables and important for the accurate description of the top-quark physics near the production threshold.

ACKNOWLEDGMENTS

This work is supported in part by Volkswagen Foundation under contract no. I/73611 and Russian Foundation for Basic Research (project no. 97-02-17065). The

work of A.A. Penin is supported in part by the Russian Academy of Sciences, grant No. 37. The present stay of A.A. Pivovarov in Mainz, where the paper has been completed, was made possible due to an Alexander von Humboldt fellowship.

APPENDIX A

The correction $\Delta_2^{(2)}G$ due to the $\Delta_2 V$ part of the potential has the form [18]

$$\Delta_2^{(2)}G = \left(\frac{\alpha_s}{4\pi}\right)^2\frac{C_F\alpha_s m_t^2}{4\pi}\Bigg(\sum_{m=0}^{\infty}F(m)^2((m+1)(C_0^2 + L(k)C_1^2 + L(k)^2C_2^2) + (m+1)\Psi_1(m+2) \times (C_1^2 + 2L(k)C_2^2) + K(m)C_2^2) + 2\sum_{m=1}^{\infty}\sum_{n=0}^{m-1}F(m)F(n)\Bigg(-\frac{n+1}{m-n}(C_1^2 + 2L(k)C_2^2) + K(m,n)C_2^2\Bigg) + 2\sum_{m=0}^{\infty}F(m)(C_0^2 + L(k)C_1^2 + (L(k)^2 + J(m))C_2^2 - (2\gamma_E + \Psi_1(m+1))(C_1^2 + 2L(k)C_2^2)) + L(k)C_0^2 + \left(-\gamma_E L(k) + \frac{1}{2}L(k)^2\right)C_1^2 + I(k)C_2^2\Bigg),$$

where

$$L(k) = \ln\left(\frac{\mu_s}{2k}\right),$$

$$K(m) = (m+1)\left(\Psi_1(m+2)^2 - \Psi_2(m+2) + \frac{\pi^2}{3} - \frac{2}{(m+1)^2}\right) - 2(\Psi_1(m+1) + \gamma_E),$$

$$K(m,n) = 2\frac{n+1}{m-n}\left(\Psi_1(m-n) - \frac{1}{n+1} + 2\gamma_E\right) + 2\frac{m+1}{m-n}(\Psi_1(m-n+1) - \Psi_1(m+1)),$$

$$J(m) = 2(\Psi_1(m+1) + \gamma_E)^2 + \Psi_2(m+1) - \Psi_1(m+1)^2 + 2\gamma_E^2,$$

$$I(k) = \left(\gamma_E + \frac{\pi^2}{6}\right)L(k) - \gamma_E L(k)^2 + \frac{1}{3}L(k)^3.$$

The correction $\Delta_2^{(1)}G$ due to the second iteration of $\Delta_1 V$ term has the form [19]

$$\Delta_2^{(1)}G = \left(\frac{\alpha_s}{4\pi}\right)^2\frac{(C_F\alpha_s)^2 m_t^3}{2k}\Bigg(\sum_{m=0}^{\infty}H(m)^3(m+1) \times (C_0^1 + (\Psi(m+2) + L(k))C_1^1)^2 - 2\sum_{m=1}^{\infty}\sum_{n=0}^{m-1}\frac{n+1}{m-n}C_1^1\Bigg(H(m)^2H(n)\Bigg(C_0^1 + \left(\Psi(m+2) + L(k) - \frac{1}{2}\frac{1}{m-n}\right)C_1^1\Bigg) + H(m)H(n)^2\Bigg(C_0^1 + \Bigg(\Psi(n+2) + L(k) - \frac{1}{2}\frac{n+1}{(m-n)(m+1)}\Bigg)C_1^1\Bigg)\Bigg) + 2(C_1^1)^2\Bigg(\sum_{m=2}^{\infty}\sum_{l=1}^{m-1}\sum_{n=0}^{l-1}H(m)H(n)H(l)\frac{n+1}{(l-n)(m-n)} + \sum_{m=2}^{\infty}\sum_{n=1}^{m-1}\sum_{l=0}^{n-1}H(m)H(n)H(l)\frac{l+1}{(n-l)(m-n)} + \sum_{n=2}^{\infty}\sum_{m=1}^{n-1}\sum_{l=0}^{m-1}H(m)H(n)H(l)\frac{(l+1)(m+1)}{(n+1)(n-l)(n-m)}\Bigg)\Bigg),$$

where

$$H(m) = \frac{1}{m+1-\nu}.$$

APPENDIX B

We define the dimensionally regularized value of the Coulomb Green's function at the origin directly through the relation

$$G_C^{\mathrm{dr}}(0,0,k) = \int d^d p\,\tilde{G}(p,k)$$

with $d = 3 - 2\varepsilon$. Representing the momentum space Green's function as

$$\tilde{G}(p,k) = \frac{m_t}{8\pi^3}\int_0^{\infty}\left(\frac{1+t}{t}\right)^{\nu}dt\frac{4k^2(1+2t)}{(p^2 + k^2(1+2t)^2)^2},$$

one obtains

$$G_C^{\mathrm{dr}}(0,0,k) = \frac{m_t k}{2\pi}\left(\frac{\mu_f}{k}\right)^{2\varepsilon}\int_0^{\infty}\left(\frac{1+t}{t}\right)^{\nu}\frac{dt}{(1+2t)^{2\varepsilon}}.$$

Here, we omit inessential factors related to the precise definition of integration measure in d dimensions that lead to the multiplication of the Green's function with an additional quantity $1 + O(\varepsilon)$ and can be taken into account by the redefinition of μ_f scale. The integral on the right-hand side of this equation reads

$$\int_0^\infty \left(\frac{1+t}{t}\right)^\nu \frac{dt}{(1+2t)^{2\varepsilon}}$$

$$= 2^{-2\varepsilon} B(-1+2\varepsilon, 1-\nu)\, {}_2F_1\left(2\varepsilon, -1+2\varepsilon; 2\varepsilon-\nu; \frac{1}{2}\right),$$

where $B(z, w)$ is the Euler B function and ${}_2F_1(a, b; c; z)$ is the hypergeometric function. Upon expanding the above expression in ε around $\varepsilon = 0$, one arrives at the final result for the dimensionally regularized Coulomb Green's function. The factorization scale μ_f in (17) is chosen in such a way that it is true as written. Note that the Green's function regularized in this way does not automatically match the hard coefficient computed in the $\overline{MS}$ scheme of the orthodox dimensional regularization [32, 33].

APPENDIX C

The NNLO corrections to the square of the Coulomb ${}^3S_1$ and ${}^1S_0$ heavy-quark bound-state wave function at the origin have the form [21]

$$\Delta_{k^2}\psi^2_{0m} = B^i \frac{C_F^2\alpha_s^2}{4(m+1)^2},$$

$$\Delta_{\Delta^2,\,\mathrm{NA},\,\mathrm{BF}}\psi^2_{0m} = -C_F^2\alpha_s^2\left(\frac{15}{8}\frac{1}{(m+1)^2}\right.$$

$$+\left(\frac{5-A^i}{2}+\frac{C_A}{C_F}\right)\left(-\ln\left(\frac{\mu_f(m+1)}{\lambda}\right)\right.$$

$$\left.\left.+\gamma_\mathrm{E}+\Psi_1(m+1)-\frac{1}{(m+1)}\right)\right),$$

$$\Delta_2^{(2)}\psi^2_{0m} = \left(\frac{\alpha_s}{4\pi}\right)^2\left(3(C_0^2+\bar{L}(m)C_1^2+\bar{L}(m)^2C_2^2)\right.$$

$$+\left(-1-2\gamma_\mathrm{E}+\frac{2}{m+1}+\Psi_1(m+2)\right.$$

$$\left.-2(m+1)\Psi_2(m+1)\right)(C_1^2+2\bar{L}(m)C_2^2)$$

$$+\left(\frac{K(m)}{m+1}+2K(m)-2\Psi_1(m+2)\right.$$

$$+2\sum_{n=0}^{m-1}\frac{m+1}{(n-m)(n+1)}K(m,n)$$

$$\left.+2\sum_{n=m+1}^{\infty}\frac{m+1}{(n-m)(n+1)}K(n,m)\right)C_2^2\Big),$$

$$\Delta_2^{(1)}\psi^2_{0m} = \left(\frac{\alpha_s}{4\pi}\right)^2\left(3\left(C_0^1+(\bar{L}(m)+\Psi_1(m+2))C_1^1\right)^2\right.$$

$$+2C_1^1\left(\sum_{n=0}^{m-1}\frac{(n+1)(m+1)}{(n-m)^3}\left(C_0^1\right.\right.$$

$$\left.+\left(\bar{L}(m)+\Psi_1(n+2)+\frac{1}{2}\frac{n+1}{(n-m)(m+1)}\right)C_1^1\right)$$

$$-\sum_{n=m+1}^{\infty}\frac{(m+1)^2}{(n-m)^3}\left(C_0^1+\left(\bar{L}(m)+\Psi_1(n+2)\right.\right.$$

$$\left.\left.\left.-\frac{1}{2}\frac{1}{n-m}\right)C_1^1\right)\right)+2C_1^1(C_0^1+(\bar{L}(m)+\Psi_1(m+2))C_1^1)$$

$$\times\left(-\frac{5}{2}+\sum_{n=0}^{m-1}\frac{n+1}{(n-m)^2}U(m,n)\right.$$

$$\left.-\sum_{n=m+1}^{\infty}\frac{m+1}{(n-m)^2}U(m,n)\right)+2(C_1^1)^2\left(\frac{1}{2}\right.$$

$$-\sum_{n=0}^{m-1}\frac{n+1}{(n-m)^2}+\sum_{n=m+1}^{\infty}\frac{m+1}{(n-m)^2}$$

$$+\frac{1}{2}\sum_{n=0}^{m-1}\frac{n+1}{(n-m)^3}U(m,n)$$

$$+\frac{1}{2}\sum_{n=m+1}^{\infty}\frac{(m+1)^2}{(n-m)^3(n+1)}U(m,n)$$

$$+\sum_{n=1}^{m-1}\sum_{l=0}^{n-1}\left(\frac{(l+1)(n+1)}{(n-m)^2(l-m)^2}-\frac{(l+1)(m+1)}{(n-m)^2(l-m)(n-l)}\right.$$

$$\left.-\frac{(l+1)(m+1)}{(l-m)^2(n-m)(n-l)}\right)$$

$$+\sum_{n=m+1}^{\infty}\sum_{l=0}^{m-1}\left(-\frac{(l+1)(m+1)}{(n-m)^2(l-m)^2}\right.$$

$$\left.+\frac{(l+1)(m+1)^2}{(n-m)^2(l-m)(n-l)(n+1)}\right.$$

$$-\frac{(l+1)(m+1)}{(l-m)^2(n-m)(n-l)}\Bigg)$$

$$+\sum_{n=2}^{\infty}\sum_{l=m+1}^{n-1}\Bigg(\frac{(m+1)^2}{(n-m)^2(l-m)^2}$$

$$+\frac{(l+1)(m+1)^2}{(n-m)^2(l-m)(n-l)(n+1)}$$

$$+\frac{(m+1)^2}{(l-m)^2(n-m)(n-l)}\Bigg)\Bigg)\Bigg),$$

where $\bar{L}(m) = L(\lambda/(m+1))$ and

$$U(m,n) = 3 + \frac{n+1}{m+n+2} - 2\frac{(n+1)^2}{(n-m)(n+m+2)}.$$

APPENDIX D

The NNLO corrections to the Coulomb $^3S_1$ and $^1S_0$ heavy-quark bound-state energy levels have the form [20, 21, 53]

$$\Delta_{\Delta^2,\,\mathrm{NA},\,\mathrm{BF}}E_{0m}$$

$$= \frac{C_F^2\alpha_s^2}{(m+1)}\left(\frac{C_A}{C_F} + \frac{5-A^i}{2} - \frac{11}{16}\frac{1}{(m+1)}\right),$$

$$\Delta_2^{(2)}E_{0m} = 2\left(\frac{\alpha_s}{4\pi}\right)^2\Bigg(C_0^2 + \bar{L}(m)C_1^2 + \bar{L}(m)^2C_2^2$$

$$+\Psi_1(m+2)(C_1^2 + 2\bar{L}(m)C_2^2) + \frac{K(m)}{(m+1)}C_2^2\Bigg),$$

$$\Delta_2^{(1)}E_{0m}$$

$$= \left(\frac{\alpha_s}{4\pi}\right)^2\Bigg((C_0^1 + (\bar{L}(m) - 2 + \Psi_1(m+2))C_1^1)$$

$$\times(C_0^1 + (\bar{L}(m) + \Psi_1(m+2))C_1^1)$$

$$+\Bigg(\frac{2}{(m+1)}(\gamma_\mathrm{E} + \Psi_1(m+2)) - 2\Psi_2(m+1)$$

$$-(m+1)\Psi_3(m+1)\Bigg)(C_1^1)^2\Bigg).$$

REFERENCES

1. V. S. Fadin and V. A. Khoze, Pis'ma Zh. Éksp. Teor. Fiz. **46**, 417 (1987) [JETP Lett. **46**, 525 (1987)]; Yad. Fiz. **48**, 487 (1988) [Sov. J. Nucl. Phys. **48**, 309 (1988)].
2. V. S. Fadin and V. A. Khoze, Yad. Fiz. **53**, 1118 (1991) [Sov. J. Nucl. Phys. **53**, 692 (1991)]; I. I. Bigi, V. S. Fadin, and V. A. Khoze, Nucl. Phys. B **377**, 461 (1992); I. I. Bigi, F. Gabbiani, and V. A. Khoze, Nucl. Phys. B **406**, 3 (1993); J. H. Kühn, E. Mirkes, and J. Steegborn, Z. Phys. C **57**, 615 (1993).
3. W. Kwong, Phys. Rev. D **43**, 1488 (1991); M. J. Strassler and M. E. Peskin, Phys. Rev. D **43**, 1500 (1991); M. Jezabek, J. H. Kühh, and T. Teubner, Z. Phys. C **56**, 653 (1992); Y. Sumino *et al.*, Phys. Rev. D **47**, 56 (1993).
4. E. Accomando *et al.*, Phys. Rep. **299**, 1 (1998).
5. H. Murayama and Y. Sumino, Phys. Rev. D **47**, 82 (1993).
6. R. Harlander *et al.*, Phys. Lett. B **346**, 137 (1995).
7. V. S. Fadin, V. A. Khoze, and M. I. Kotsky, Z. Phys. C **64**, 45 (1994).
8. W. E. Caswell and G. E. Lepage, Phys. Lett. B **167**, 437 (1986); G. E. Lepage *et al.*, Phys. Rev. D **46**, 4052 (1992); G. T. Bodwin, E. Braaten, and G. E. Lepage, Phys. Rev. D **51**, 1125 (1995).
9. A. V. Manohar, Phys. Rev. D **56**, 230 (1997).
10. M. Luke and A. V. Manohar, Phys. Rev. D **55**, 4129 (1997).
11. B. Grinstein and I. Z. Rothstein, Phys. Rev. D **57**, 78 (1998).
12. M. Luke and M. J. Savage, Phys. Rev. D **57**, 413 (1998).
13. A. Pineda and J. Soto, Nucl. Phys. B (Proc. Suppl.) **64**, 428 (1998).
14. M. Beneke and V. A. Smirnov, Nucl. Phys. B **522**, 321 (1998).
15. P. Labelle, Phys. Rev. D **58**, 093013 (1998).
16. H. W. Griesshammer, Preprint No. UW-98-22 (1998).
17. A. H. Hoang, Phys. Rev. D **56**, 5851 (1997).
18. J. H. Kühn, A. A. Penin, and A. A. Pivovarov, Nucl. Phys. B **534**, 356 (1998).
19. A. A. Penin and A. A. Pivovarov, Phys. Lett. B **435**, 413 (1998).
20. K. Melnikov and A. Yelkhovsky, Phys. Rev. D **59**, 114009 (1999).
21. A. A. Penin and A. A. Pivovarov, Nucl. Phys. B **549**, 217 (1999).
22. M. Beneke, A. Singer, and V. A. Smirnov, Phys. Lett. B **454**, 137 (1999).
23. M. Beneke and A. Singer, Preprint No. CERN-TH/99-163 (1999).
24. A. H. Hoang, Preprint No. CERN-TH/99-152 (1999).
25. B. A. Kniehl and A. A. Penin, Preprint No. DESY/99-099 (1999).
26. A. H. Hoang and T. Teubner, Phys. Rev. D **58**, 114023 (1998).
27. K. Melnikov and A. Yelkhovsky, Nucl. Phys. B **528**, 59 (1998).
28. J. H. Kühn and T. Teubner, Eur. Phys. J. C **9**, 221 (1999).
29. T. Nagano, A. Ota, and Y. Sumino, Preprint No. TU-562 (1999).
30. A. H. Hoang and T. Teubner, Preprint No. CERN-TH/99-59 (1999).
31. A. A. Penin and A. A. Pivovarov, Nucl. Phys. B **550**, 375 (1999).
32. A. Czarnecky and K. Melnikov, Phys. Rev. Lett. **80**, 2531 (1998).

33. M. Beneke, A. Signer, and V. A. Smirnov, Phys. Rev. Lett. **80**, 2535 (1998).
34. A. Pineda and J. Soto, Phys. Lett. B **420**, 391 (1998); Phys. Rev. D **59**, 016005 (1999).
35. A. Czarnecky, K. Melnikov, and A. Yelkhovsky, Preprint No. BNL-HET-98/44 (1999).
36. J. H. Kühn, Preprint No. TTP-96-18 (Karlsruhe Univ., 1996); hep-ph/9707321.
37. R. Karplus and A. Klein, Phys. Rev. **87**, 848 (1952); G. Källen and A. Sarby, K. Dan. Vidensk. Selsk. Mat. Fys. Medd. **29** (17), 1 (1955); R. Barbieri *et al.*, Phys. Lett. B **57**, 535 (1975).
38. L. J. Reinders, H. R. Rubinstein, and S. Yazaki, Nucl. Phys. B **181**, 109 (1981); J. Jérzak, E. Laemann, and P. M. Zerwas, Phys. Rev. D **25**, 1218 (1982).
39. I. Harris and L. M. Brown, Phys. Rev. **105**, 1656 (1957); R. Barbieri *et al.*, Nucl. Phys. B **154**, 535 (1979).
40. R. Barbieri *et al.*, Nucl. Phys. B **192**, 61 (1981); J. H. Kühn and P. M. Zerwas, Phys. Rep. **167**, 321 (1988).
41. A. A. Pivovarov, Phys. Rev. D **47**, 5183 (1993).
42. B. Grzadkowski *et al.*, Nucl. Phys. B **281**, 18 (1987); R. J. Guth and J. H. Kühn, Nucl. Phys. B **368**, 38 (1992); W. Beenakker *et al.*, Nucl. Phys. B **365**, 24 (1991).
43. A. Denner, S. Dittmaier, and M. Strobel, Phys. Rev. D **53**, 44 (1996).
44. B. M. Chibisov and M. V. Voloshin, Mod. Phys. Lett. A **13**, 973 (1998).
45. V. S. Fadin, V. A. Khoze, and A. D. Martin, Phys. Rev. D **49**, 2247 (1994); K. Melnikov and O. Yakovlev, Phys. Lett. B **324**, 217 (1994).
46. K. Fujii, T. Matsui, and Y. Sumino, Phys. Rev. D **50**, 4341 (1994); R. Harlander *et al.*, Z. Phys. C **73**, 477 (1997); M. Peter and Y. Sumino, Phys. Rev. D **57**, 6912 (1998).
47. S. N. Gupta and S. F. Radford, Phys. Rev. D **24**, 2309 (1981); Erratum: **25**, 3430 (1982); S. N. Gupta, S. F. Radford, and W. W. Repko, Phys. Rev. D **26**, 3305 (1982).
48. L. D. Landau and E. M. Lifshitz, *Relativistic Quantum Theory* (Nauka, Moscow, 1968; Pergamon, Oxford, 1974), Part 1.
49. W. Fisher, Nucl. Phys. B **129**, 157 (1977); A. Billoire, Phys. Lett. B **92**, 343 (1980).
50. M. Peter, Phys. Rev. Lett. **78**, 602 (1997); Nucl. Phys. B **501**, 471 (1997); Y. Schröder, Phys. Lett. B **447**, 321 (1999).
51. A. H. Hoang, Phys. Rev. D **56**, 7276 (1997).
52. K. A. Ispiryan *et al.*, Yad. Fiz. **11**, 1278 (1970) [Sov. J. Nucl. Phys. **11**, 712 (1970)].
53. A. Pineda and F. J. Yndurain, Phys. Rev. D **58**, 094022 (1998).
54. M. Beneke and V. M. Braun, Nucl. Phys. B **426**, 301 (1994); I. I. Bigi *et al.*, Phys. Rev. D **50**, 2234 (1994).
55. M. B. Voloshin, Nucl. Phys. B **154**, 365 (1979); H. Leutwyler, Phys. Lett. B **98**, 447 (1981).
56. O. Yakovlev, Phys. Lett. B **457**, 170 (1999).

Physics of Atomic Nuclei, Vol. 64, No. 2, 2001, pp. 294–304. Translated from Yadernaya Fizika, Vol. 64, No. 2, 2001, pp. 342–351.

ELEMENTARY PARTICLES AND FIELDS
Theory

Axion Self-Energy in a Magnetic Field

L. A. Vassilevskaya, N. V. Mikheev, and A. Ya. Parkhomenko

Yaroslavl State University, Sovetskaya ul. 14, Yaroslavl, 150000 Russia

Received January 14, 2000; in final form, March 29, 2000

Abstract—The axion self-energy in an external magnetic field is investigated. It is shown that, in addition to the standard contribution due to axion interaction with virtual fermions, there exists the contribution induced by photon exchange. For the two contributions, expressions that take exactly into account an external field are obtained, and the limit of an ultrastrong magnetic field is explored for them. The question of whether two-dimensional QED, which effectively arises in the limit of a strong magnetic field, is applicable to calculating the virtual-fermion-induced contribution to the axion self-energy is analyzed. © *2001 MAIK "Nauka/Interperiodica".*

1. INTRODUCTION

The interaction of quantum particles with active matter (for example, plasma or an external magnetic field) in higher orders of perturbation theory can significantly affect the properties of particles. In particular, effects associated with such interactions can change the particle mass (or induce an effective mass) and generate anomalous magnetic and electric moments. If such changes in the properties of particles are sizable, they affect the kinematics of quantum processes.

The problem of the axion-mass value [1, 2] and of the axion lifetime is of paramount importance for cosmology, since the axion is considered as one of the main candidates for dark-matter particles in the Universe. In quantum theory, the axion, which is introduced as a massless particle, acquires mass owing to mixing with the π^0 meson [3],

$$m_a = \frac{m_\pi f_\pi}{f_a}\left(\frac{z}{(1+z)(1+z+w)}\right)^{1/2} \simeq 0.60\ \text{eV}\left(\frac{10^7\ \text{GeV}}{f_a}\right), \quad (1.1)$$

where $m_\pi \simeq 135$ MeV and $f_\pi \simeq 93$ MeV are the neutral-pion mass and decay constant, respectively, and where we have used the quark-mass ratios $z = m_u/m_d = 0.568 \pm 0.042$ and $w = m_u/m_s = 0.0290 \pm 0.0043$ [4]. It can be seen that the axion mass is determined by the energy scale of the breakdown of $U_{\text{PQ}}(1)$ symmetry (Peccei–Quinn symmetry) of the theory f_a; according to the current estimates, it is rather small, $m_a \lesssim 10^{-3}$ eV, since astrophysical data yield a large value for this scale, $f_a \gtrsim 10^8$ GeV [5].

Having traversed a region where there is an external electromagnetic field, an axion acquires an electromagnetic correction to the mass. The field shift of the axion mass squared is determined by the real part of the $a \longrightarrow a$ transition amplitude ΔM induced by an external electromagnetic field,

$$\delta m_a^2 = -\text{Re}\Delta M. \quad (1.2)$$

The imaginary part of the amplitude ΔM determines the axion-decay probability W_a,

$$\text{Im}\,\Delta M = E_a W_a, \quad (1.3)$$

where E_a is the axion energy. For an analysis of the properties of an axion that propagates in an external classical field, it is of great interest to calculate this amplitude.

2. GENERAL EXPRESSION FOR THE TRANSITION AMPLITUDE

In the existing axion models, the interaction of the axion with a fermion f of mass m_f is described by the Lagrangian

$$\mathcal{L}_{af}^{(\text{D})}(x) = \frac{g_{af}}{2m_f}[\bar{f}(x)\gamma^\mu\gamma_5 f(x)]\partial_\mu a(x), \quad (2.1)$$

where $g_{af} = C_f m_f/f_a$ is the dimensionless Yukawa coupling constant; C_f is a dimensionless factor that is dependent on the specific model of the invisible axion; $\gamma_5 = -i\gamma^0\gamma^1\gamma^2\gamma^3$, γ^μ being the set of the Dirac γ matrices [6]; $\partial_\mu a(x) = \partial a(x)/\partial x^\mu$; and $f(x)$ and $a(x)$ are the quantized fermion and axion fields.[1)]

In the lowest nonvanishing order of perturbation theory in g_{af}, the axion-to-axion ($a \longrightarrow a$) transition amplitude is described by the fermion loop diagram (see Fig. 1). We note that, in order to derive a correct result in calculating amplitudes involving not less than two axion fields that interact with fermions (for example, the amplitude corresponding to the axion self-energy diagram in Fig. 1), it is necessary, as was indi-

[1)]Here, we use the system of units where $\hbar = c = 1$ and the pseudo-Euclidean metric of signature $(+---)$.

cated for the first time in [7], to use the Lagrangian involving the derivative, such as that in Eq. (2.1), rather than the pseudoscalar Yukawa coupling, $\mathscr{L}_{af}^{(P)} = -ig_{af}(\bar{f}\gamma_5 f)a$.

The S-matrix element associated with the contribution of virtual charged fermions (see the diagram in Fig. 1) is given by

$$S_{if} = \frac{i^2}{2!}\sum_f \langle a(q')|\int d^4x d^4y T\{\mathscr{L}_{af}^{(D)}(x)\mathscr{L}_{af}^{(D)}(y)\}|a(q)\rangle$$

$$= \sum_f \frac{i^2 g_{af}^2}{4m_f^2}\int \frac{d^4x d^4y e^{-i(qx)+i(q'y)}}{\sqrt{2E_aV\times 2E_a'V}} \tag{2.2}$$

$$\times \mathrm{tr}\{G_F(y,x)(q\gamma)\gamma_5 G_F(x,y)(q'\gamma)\gamma_5\},$$

where $|a(q)\rangle$ and $|a(q')\rangle$ are the vectors of the initial and the final state of the axions with 4-momenta $q^\mu = (E_a, \mathbf{q})$ and $q'^\mu = (E_a', \mathbf{q}')$, respectively; $(q\gamma) = q_\mu\gamma^\mu$; V is the normalization volume; and $G_F(x,y)$ is the charged-fermion propagator.

In an arbitrary constant uniform electromagnetic field, the propagator for a fermion with charge e_f possesses neither gauge nor translation invariance. The noninvariant component can be factored out in the form of a phase, so that the propagator can be represented as [8]

$$G_F(x,y) = e^{i\Omega(x,y)}S_F(x-y), \tag{2.3}$$

where

$$\Omega(x,y) = -e_f\int_y^x d\xi^\mu\left[A_\mu(\xi) + \frac{1}{2}F_{\mu\nu}(\xi-y)^\nu\right]. \tag{2.4}$$

We note that the expression for the phase in (2.4) does not depend on the path of integration between the points x and y of four-dimensional spacetime [8].

In a constant uniform electromagnetic field, the noninvariant phases of two fermion propagators cancel out in two-point loop diagrams (including the axion self-energy diagram), making no contribution to the amplitude. Proceeding from the definition of phase in (2.4), we do indeed obtain

$$\Omega(x,y) + \Omega(y,x) = -\frac{e_f}{2}F_{\mu\nu}(x-y)^\nu\int_y^x d\xi^\mu$$

$$= -\frac{e_f}{2}F_{\mu\nu}(x-y)^\mu(x-y)^\nu = 0,$$

because the constant field tensor $F_{\mu\nu}$ can be factored outside the integral sign together with 4-vector $(x-y)^\nu$, so that the resulting vector integral reduces to the 4-vector $(x-y)^\mu$. In view of this, the S-matrix element

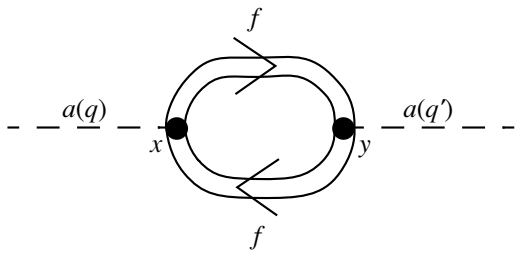

Fig. 1. Diagram representing the axion-to-axion ($a \longrightarrow a$) transition in the lowest order of perturbation theory in an external electromagnetic field.

proves to be translation- and gauge-invariant and takes the form

$$S_{if} = \sum_f \frac{i^2 g_{af}^2}{4m_f^2}\,\frac{(2\pi)^4\delta^{(4)}(q-q')}{2E_aV} \tag{2.5}$$

$$\times\int d^4X e^{-i(qX)}\mathrm{tr}\{S_F(-X)(q\gamma)\gamma_5 S_F(X)(q\gamma)\gamma_5\},$$

where $X = x - y$. In the S-matrix element, we have isolated a four-dimensional delta function expressing the law of energy–momentum conservation. This is due to the fact that the initial and the final state are formed by electrically neutral particles. Therefore, we can use, in this case, the standard definition of the invariant amplitude [6],

$$S_{if} = \frac{i(2\pi)^4\delta^{(4)}(q-q')}{2E_aV}M_{a\to a}, \tag{2.6}$$

whereby we arrive at the following result:

$$M_{a\to a} = \sum_f \frac{ig_{af}^2}{4m_f^2}\int d^4X e^{-i(qX)} \tag{2.7}$$

$$\times \mathrm{tr}\{S_F(-X)(q\gamma)\gamma_5 S_F(X)(q\gamma)\gamma_5\}.$$

The invariant part $S(X)$ of the fermion propagator (2.3) can be expanded in a complete set of 4×4 matrices [6]. Upon substituting such expressions into the transition amplitude, evaluation of the traces of the γ matrix becomes rather cumbersome. However, the calculations can be simplified considerably by representing $S_F(X)$ as the sum of two terms involving the product of an even and an odd number of Dirac matrices:

$$S_F(X) = S_+(X) + S_-(X), \quad \gamma_5 S_\pm\gamma_5 = \pm S_\pm. \tag{2.8}$$

On the basis of the commutation properties of the γ matrices, it can be deduced that $S_+(X)$ ($S_-(X)$) is proportional to the even (odd) number of Dirac matrices. The expression for the amplitude can then be reduced to the form

$$M_{a\to a} = M_+ + M_-,$$

$$M_\pm = \mp\sum_f \frac{ig_{af}^2}{4m_f^2}\int d^4X e^{-i(qX)} \tag{2.9}$$

$$\times \mathrm{tr}\{S_\pm(-X)(q\gamma)S_\pm(X)(q\gamma)\}.$$

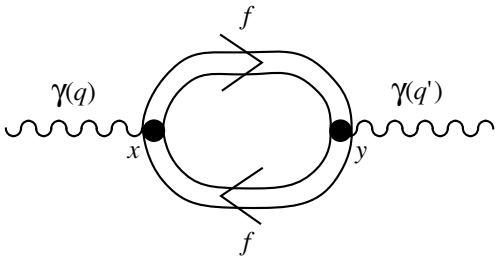

Fig. 2. Diagram describing the photon-to-photon ($\gamma \longrightarrow \gamma$) transition in the lowest order of perturbation theory in an external electromagnetic field.

We note that the contributions M_+ and M_- are equal; this can be demonstrated by using the gauge invariance of the photon self-energy. Indeed, this self-energy is determined by the photon-to-photon ($\gamma \longrightarrow \gamma$) transition amplitude,

$$iM_{\gamma\to\gamma} = \Pi_{\mu\nu}\varepsilon^{\mu}\varepsilon^{\nu *}, \tag{2.10}$$

where ε^{μ} is the photon polarization vector. The Feynman diagram for the process $\gamma \longrightarrow \gamma$ in the one-loop approximation is presented in Fig. 2. By taking into account the results of the above analysis for the axion, we can recast the photon self-energy into the form

$$\Pi_{\mu\nu} = -\sum_f 4\pi\alpha Q_f^2 \int d^4X e^{-i(qX)} \times \mathrm{tr}\{S(-X)\gamma_\mu S(X)\gamma_\nu\}, \tag{2.11}$$

where q_μ is the photon 4-momentum, Q_f is the relative fermion charge in the loop, and $\alpha \simeq 1/137$ is the fine-structure constant. Substituting the propagators in the form (2.8) into Eq. (2.11) and using the gauge-invariance condition $(q\Pi q) = 0$, we obtain the integral relation

$$\int d^4X e^{-i(qX)} \mathrm{tr}\{S_+(-X)(q\gamma)S_+(X)(q\gamma) + S_-(-X)(q\gamma)S_-(X)(q\gamma)\} = 0, \tag{2.12}$$

whence it follows that M_+ is equal to M_-.

By using this relation, we can reduce the $a \longrightarrow a$ transition amplitude to the form

$$M_{a\to a} = -\sum_f \frac{ig_{af}^2}{2m_f^2}\int d^4X e^{-i(qX)} \times \mathrm{tr}\{S_+(-X)(q\gamma)S_+(X)(q\gamma)\} = \sum_f \frac{ig_{af}^2}{2m_f^2}\int d^4X e^{-i(qX)}\mathrm{tr}\{S_-(-X)(q\gamma)S_-(X)(q\gamma)\}. \tag{2.13}$$

For a subsequent evaluation of the transition amplitude, it is necessary to know the explicit form of the invariant part $S_F(X)$ of the fermion propagator (2.3). We will analyze the axion self-energy in an external magnetic field by using an exact expression for the propagator in the field of this configuration.

3. EXTERNAL MAGNETIC FIELD

Within the proper-time formalism [9], the translation- and gauge-invariant part $S_F(X)$ of the fermion propagator (2.3) in a constant uniform magnetic field **B** can be represented as [8]

$$S_F(X) = -\frac{i\beta}{2(4\pi)^2}\int_0^\infty \frac{ds}{s^2}\left\{(X\tilde{\Lambda}\gamma)\cot(\beta s) - i(X\tilde{\varphi}\gamma)\gamma_5 - \frac{\beta s}{\sin^2(\beta s)}(X\Lambda\gamma) + m_f s[2\cot(\beta s) + (\gamma\varphi\gamma)]\right\} \times \exp\left(-i\left[m_f^2 s + \frac{1}{4s}(X\tilde{\Lambda}X) - \frac{\beta\cot(\beta s)}{4}(X\Lambda X)\right]\right), \tag{3.1}$$

where $\varphi_{\alpha\beta} = F_{\alpha\beta}/B$ and $\tilde{\varphi}_{\alpha\beta} = (1/2)\varepsilon_{\alpha\beta\mu\nu}\varphi^{\mu\nu}$ are, respectively, the dimensionless tensor of the external-magnetic-field strength and its dual; $\Lambda_{\alpha\beta} = (\varphi\varphi)_{\alpha\beta}$ and $\tilde{\Lambda}_{\alpha\beta} = (\tilde{\varphi}\tilde{\varphi})_{\alpha\beta} = g_{\alpha\beta} + \Lambda_{\alpha\beta}$; and $\beta = e_f|B| = e_f\sqrt{-(FF)/2}$. In the propagator $S_F(X)$, the part even in the product of the Dirac matrices has the form

$$S_+(X) = -\frac{i\beta m_f}{2(4\pi)^2}\int_0^\infty \frac{ds}{s}[2\cot(\beta s) + (\gamma\varphi\gamma)] \times \exp\left(-i\left[m_f^2 s + \frac{1}{4s}(X\tilde{\Lambda}X) - \frac{\beta\cot(\beta s)}{4}(X\Lambda X)\right]\right). \tag{3.2}$$

We note that, in $S_+(X)$, the dependence on the 4-coordinate X is entirely absorbed in the phase factor.

By substituting the expression for $S_+(X)$ into the transition amplitude (2.13), we obtain

$$M_{a\to a} = \sum_f \frac{ig_{af}^2\beta^2}{8(4\pi)^4}\int_0^\infty \frac{ds_1 ds_2}{s_1 s_2}\exp\{-im_f^2(s_1+s_2)\} \times \mathrm{tr}\{[2\cot(\beta s_1) + (\gamma\varphi\gamma)](q\gamma) \times [2\cot(\beta s_2) + (\gamma\varphi\gamma)](q\gamma)\} \times \int d^4X \exp\left\{-i(qX) - \frac{i}{4}\left[\frac{s_1+s_2}{s_1 s_2}(X\tilde{\Lambda}X) - \frac{\beta\sin(\beta(s_1+s_2))}{\sin(\beta s_1)\sin(\beta s_2)}(X\Lambda X)\right]\right\}. \tag{3.3}$$

Here, the integral with respect to the 4-coordinate X is a generalized Gaussian integral,

$$\int d^nX \exp\left\{-i(qX) - \frac{i}{4}(XAX)\right\} = \frac{(-4\pi i)^{n/2}}{(\det A)^{1/2}}\exp\{i(qA^{-1}q)\}, \tag{3.4}$$

where A is a symmetric $n \times n$ matrix, $\det A$ is its determinant, and A^{-1} is the matrix inverse to A.

For the sake of completeness, explicit expressions for the matrices A and A^{-1} and for $\det A$ are presented immediately below for the case corresponding to the transition amplitude (3.3):

$$A_{\mu\nu} = \frac{s_1+s_2}{s_1 s_2}\tilde{\Lambda}_{\mu\nu} - \frac{\beta\sin(\beta(s_1+s_2))}{\sin(\beta s_1)\sin(\beta s_2)}\Lambda_{\mu\nu},$$

$$(A^{-1})_{\mu\nu} = \frac{s_1 s_2}{s_1+s_2}\tilde{\Lambda}_{\mu\nu} - \frac{\sin(\beta s_1)\sin(\beta s_2)}{\beta\sin(\beta(s_1+s_2))}\Lambda_{\mu\nu}, \quad (3.5)$$

$$\det A = \left(\frac{i^3\beta(s_1+s_2)\sin(\beta(s_1+s_1))}{s_1 s_2\sin(\beta s_1)\sin(\beta s_2)}\right)^2.$$

A direct calculation of the trace in the transition amplitude (3.3) presents no serious difficulties. By taking into account expressions (3.4) and (3.5), we can recast the transition amplitude into the form

$$M_{a\to a}(q^2, q_\perp^2, \beta) = \sum_f \frac{g_{af}^2\beta}{8\pi^2}\int_0^\infty \frac{dt}{\sin(\beta t)} \times \int_0^1 du[q_\parallel^2\cos(\beta t) - q_\perp^2\cos(\beta t u)] \times \exp\left\{-i\left[m_f^2 t - \frac{q_\parallel^2}{4}t(1-u^2) + q_\perp^2\frac{\cos(\beta t u)-\cos(\beta t)}{2\beta\sin(\beta t)}\right]\right\}, \quad (3.6)$$

where $q_\perp^2 = (q\Lambda q)$ and $q_\parallel^2 = (q\tilde{\Lambda}q) = q^2 + q_\perp^2$. In deriving the last formula, we went over to the new integration variables $t = s_1 + s_2$ and $u = (s_1 - s_2)/t$.

The analysis of the transition amplitude (3.6) shows that the integral with respect to t diverges at the lower limit. This is a manifestation of the ultraviolet divergence that appears in the field-free part of the amplitude and which can be removed by renormalizing the axion mass and the axion wave function. The external-field-induced part of the amplitude in (3.6) is free from divergences. We restrict our consideration to calculating the field-induced component of the amplitude ΔM,

$$\Delta M(q^2, q_\perp^2, \beta) = M_{a\to a}(q^2, q_\perp^2, \beta) - M_{a\to a}(q^2, 0, 0), \quad (3.7)$$

which can be represented in the form

$$\Delta M(q^2, q_\perp^2, \beta) = \sum_f \frac{g_{af}^2}{8\pi^2}\int_0^1 du[q_\parallel^2 J(u,1) - q_\perp^2 J(u,u)]. \quad (3.8)$$

Here, we have introduced the integral

$$J(u, v) = \int_0^\infty \frac{dt}{t}\left\{\frac{\beta t\cos(\beta t v)}{\sin(\beta t)}e^{-i\Phi} - e^{-i\Phi_0}\right\},$$

$$\Phi = \left[m_f^2 - \frac{q_\parallel^2}{4}(1-u^2)\right]t + \frac{q_\perp^2}{2\beta}\frac{\cos(\beta t u)-\cos(\beta t)}{\sin(\beta t)}, \quad (3.9)$$

where

$$\Phi_0 = \left[m_f^2 - \frac{q^2}{4}(1-u^2)\right]t.$$

The integral $J(u, v)$ features no ultraviolet divergence because the integrand vanishes at the lower limit of integration.

We note that the expression in (3.8) represents the $a \longrightarrow a$ transition amplitude induced by an external field of arbitrary intensity. If, for the axion on the mass shell, its small mass is disregarded ($q^2 = q_\parallel^2 - q_\perp^2 = m_a^2 \simeq 0$), expression (3.8) for the amplitude reduces to that quoted in [10].

By using the definition in (1.2), we can represent the virtual-fermion-induced correction to the axion mass squared, $(\delta m_a^2)_{\mathrm{FL}}$, in the form

$$(\delta m_a^2)_{\mathrm{FL}} = -\sum_f \frac{g_{af}^2}{8\pi^2}\int_0^1 du\,\mathrm{Re}[q_\parallel^2 J(u,1) - q_\perp^2 J(u,u)]. \quad (3.10)$$

3.1. Crossed-Field Limit

The $a \longrightarrow a$ transition amplitude in a magnetic field is determined by three invariant parameters, q^2, $q_\perp^2$, and β. In the case where the purely field parameter β is small—that is, $\beta \ll q_\perp^2$—the crossed-field limit is realized ($E = B$, $\mathbf{E} \perp \mathbf{B}$). This situation arises when an ultrarelativistic particle moves in a relatively weak constant uniform magnetic field, in which case the characteristics of processes involving this particle (amplitudes, probabilities, and so on) are dependent only on the product $\beta^2 q_\perp^2$, which is proportional to the invariant field variable $\chi_f^2 = \beta^2 q_\perp^2/m_f^6$ referred to as a dynamical parameter.

The $a \longrightarrow a$ transition amplitude in a crossed field can be derived from expression in (3.8) by making the substitutions $q_\parallel^2 = q^2 + q_\perp^2$ and $q_\perp^2 = m_f^6\chi_f^2/\beta^2$ and by going over to the limit $\beta \longrightarrow 0$. The result is

$$\Delta M = \frac{g_{af}^2}{16\pi^2}\left\{2q^2\int_0^1 du\left(\frac{\ln 3}{3} + \ln\eta + \frac{2C}{3} + \frac{i\pi}{3}\right.\right.$$

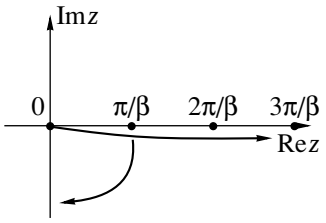

Fig. 3. Complex plane of the variable and contour of integration in the integral in Eq. (3.9)

$$-\int_0^{\eta} dz\, f(z)\Bigg) - m_f^2\chi_f^2\int_0^1 du(1-u^2)\eta^2\frac{df(\eta)}{d\eta}\Bigg\}, \quad (3.11)$$

where

$$\eta = \left[\frac{4}{\chi_f(1-u^2)}\right]^{2/3}\left[1-\frac{q^2(1-u^2)}{4m_f^2}\right],$$

$C \simeq 0.5772$ is the Euler constant [11], and $f(\eta)$ is the Hardy–Stokes function

$$f(\eta) = i\int_0^{\infty} dz \exp\left\{-i\left(\eta z + \frac{z^3}{3}\right)\right\}.$$

The above expression for the amplitude coincides with the result obtained in [12, 13]. The axion self-energy in a crossed field was also studied in [14]; however, the expression presented there is more cumbersome and involves an additional factor of 1/2.

3.2. Strong-Magnetic-Field Limit

The axion transition amplitude (3.8) is of special interest because it was calculated for an arbitrary strength of the magnetic field. In [15–17], this amplitude was calculated in the strong-field limit by using the formalism developed in [18], but the results were different in those studies. For the amplitude in (3.8), it is straightforward to find the strong-field limit when the purely field parameter β is the largest energy scale of the problem; that is, $\beta \gg q^2, q_\perp^2, m_f^2$.

In calculating the strong-field limit, we note that the integral in (3.9) is generally taken in the complex plane of the variable of integration along the positive semiaxis. The integrand has a set of poles on the real axis, and it is necessary to circumvent these poles from below, as is demonstrated in Fig. 3. Rotating this contour in the clockwise direction in such a way that it becomes coincident with the imaginary semiaxis—this corresponds to the substitution $t \longrightarrow -i\tau$—we reduce the integral in Eq. (3.9) to the form

$$J(u, v) = \int_0^{\infty}\frac{d\tau}{\tau}\left\{\frac{\beta\tau\cosh(\beta\tau v)}{\sinh(\beta\tau)}e^{-\Phi} - e^{-\Phi_0}\right\},$$

$$\Phi = \left[m_f^2 - \frac{q_\parallel^2}{4}(1-u^2)\right]\tau + \frac{q_\perp^2}{2\beta}\frac{\cosh(\beta\tau)-\cosh(\beta\tau u)}{\sinh(\beta\tau)}, \quad (3.12)$$

$$\Phi_0 = \left[m_f^2 - \frac{q^2}{4}(1-u^2)\right]\tau.$$

Going over to the limit $\beta \longrightarrow \infty$ and retaining terms to the first order in β^{-1} inclusive, we then obtain

$$J(u, v) \simeq \frac{4\beta e^{-q_\perp^2/2\beta}\delta_{v,1}}{4m_f^2 - q_\parallel^2(1-u^2)}, \quad (3.13)$$

where $\delta_{v,1}$ is a Kronecker delta symbol. By substituting this asymptotic expression into the axion transition amplitude (3.8) and taking the integral with respect to u, we reduce the $a \longrightarrow a$ transition amplitude recast by a strong magnetic field into the form

$$\Delta M \simeq \sum_f \frac{g_{af}^2\beta}{2\pi^2}e^{-q_\perp^2/2\beta}F(z), \quad (3.14)$$

where $z = 4m_f^2/q_\parallel^2$. Here, we have introduced the function $F(z)$ as

$$F(z) = \begin{cases} \dfrac{1}{2\sqrt{1-z}}\left[\ln\left|\dfrac{\sqrt{1-z}-1}{\sqrt{1-z}+1}\right| - i\pi\Theta(z)\Theta(1-z)\right], \\ z < 1 \\ \dfrac{1}{\sqrt{z-1}}\arctan\dfrac{1}{\sqrt{z-1}}, \quad z \geq 1, \end{cases} \quad (3.15)$$

where $\Theta(z)$ is a Heaviside step function. The existence of the imaginary part of the amplitude ΔM in the kinematical region $0 < z < 1$ indicates that, in a magnetic field, axion decay into the fermion pair ($a \longrightarrow \bar{f}f$) becomes possible for $q_\parallel^2 > 4m_f^2$ [10].

Taking into account the definition in (1.2), we find that, in the limit of a strong magnetic field, the virtual-fermion-induced correction to the axion mass squared $(\delta m_a^2)_{\mathrm{FL}}$ has the form

$$(\delta m_a^2)_{\mathrm{FL}} \simeq -\sum_f \frac{g_{af}^2\beta}{2\pi^2}e^{-q_\perp^2/2\beta}\mathrm{Re}F(z). \quad (3.16)$$

We note that the axion self-energy in the limit of a strong magnetic field was investigated in [15–17] by using an approximate expression for the charged-fermion propagator. The results obtained in [15, 16] differ from those in (3.14)–(3.16) and are incorrect in our opinion. The result from [17] formally coincides with expression (3.16), but, in fact, it is merely a correct guess, since there is no physical substantiation of the method used there to evaluate the axion self-energy. It would be of interest to analyze in detail the reason

behind the discrepancy between the relevant results for the $a \longrightarrow a$ transition amplitude.

Since the translation- and gauge-invariant part $S_F(X)$ of the fermion propagator (2.3) in a constant uniform electromagnetic field depends only on the difference $X_\mu = (x-y)_\mu$, we can represent it in the form of the Fourier integral

$$S_F(X) = \int \frac{d^4p}{(2\pi)^4} e^{-i(pX)} S_F(p). \tag{3.17}$$

Substituting (3.17) into the general expression (2.7), we obtain the $a \longrightarrow a$ transition amplitude in the momentum representation:

$$M_{a\to a} = \sum_f \frac{ig_{af}^2}{4m_f^2} \int \frac{d^4p}{(2\pi)^4} \times \mathrm{tr}\{S_F(p)(q\gamma)\gamma_5 S_F(p-q)(q\gamma)\gamma_5\}. \tag{3.18}$$

In the limit of a strong magnetic field, the Fourier transform of the fermion propagator $S_F(p)$ is simplified considerably, effectively becoming two-dimensional. In momentum space, the leading external-field-induced contribution to the propagator is given by [15]

$$S_F(p) \simeq 2\Pi_- \frac{(p\gamma)_\parallel + m_f}{p_\parallel^2 - m_f^2} e^{-p_\perp^2/\beta}, \tag{3.19}$$

where $p_\perp^2 = (p\Lambda p)$ and $p_\parallel^2 = (p\tilde{\Lambda}p) = p^2 + p_\perp^2$ are, respectively, the transverse and the longitudinal component of p^2; $(p\gamma)_\parallel = (p\tilde{\Lambda}\gamma)$; and $\Pi_- = [2 + i(\gamma\varphi\gamma)]/4$.

Substituting the approximate expression (3.19) for the propagator $S_F(p)$ into (3.18) and evaluating the integral with respect to momenta in the two-dimensional Euclidean space orthogonal to the magnetic-field-strength vector, we obtain the external-field-induced component of the amplitude in the form

$$\Delta M \simeq \sum_f \frac{ig_{af}^2\beta}{4\pi m_f^2} e^{-q_\perp^2/2\beta} \times \int \frac{d^2p_\parallel}{(2\pi)^2} \frac{2(pq)_\parallel^2 - p_\parallel^2 q_\parallel^2 - q_\parallel^2 (pq)_\parallel - m_f^2 q_\parallel^2}{(p_\parallel^2 - m_f^2)(p_\parallel^2 - 2(pq)_\parallel + q_\parallel^2 - m_f^2)}, \tag{3.20}$$

where $p_{\parallel\mu} = (\tilde{\Lambda}p)_\mu$ and $(pq)_\parallel = (p\tilde{\Lambda}q)$. The Feynman parametrization [6] was used in [15] to calculate ΔM; in [16], this amplitude was derived by the Fock–Schwinger proper-time method [19]. By way of example, we perform an analysis of the amplitude in (3.20) on the basis of the Feynman parametrization.[2)] We have

$$\Delta M \simeq \sum_f \frac{ig_{af}^2\beta}{4\pi m_f^2} e^{-q_\perp^2/2\beta} \times \int_0^1 dx\{2(qTq) - q_\parallel^2(T\tilde{\Lambda}) - q_\parallel^2(qV) - m_f^2 q_\parallel^2 S\}, \tag{3.21}$$

where $(qTq) = T_{\mu\nu} q_\parallel^\mu q_\parallel^\nu$, $(T\tilde{\Lambda}) = T_{\mu\nu}\tilde{\Lambda}^{\mu\nu}$, and $(qV) = V_\mu q_\parallel^\mu$. By S, V_μ, and $T_{\mu\nu}$, we mean here a scalar, a vector, and a tensor integral, respectively. The scalar and the tensor integral are finite, and it is easy to calculate them. The results are

$$S = \int \frac{d^2p_\parallel}{(2\pi)^2} \frac{1}{[p_\parallel^2 - 2x(pq)_\parallel + xq_\parallel^2 - m_f^2]^2} = \frac{i}{4\pi[m_f^2 - q_\parallel^2 x(1-x)]}, \tag{3.22}$$

$$V_\mu = \int \frac{d^2p_\parallel}{(2\pi)^2} \frac{p_{\parallel\mu}}{[p_\parallel^2 - 2x(pq)_\parallel + xq_\parallel^2 - m_f^2]^2} = \frac{ixq_{\parallel\mu}}{4\pi[m_f^2 - q_\parallel^2 x(1-x)]}. \tag{3.23}$$

The tensor integral

$$T_{\mu\nu} = \int \frac{d^2p_\parallel}{(2\pi)^2} \frac{p_{\parallel\mu}p_{\parallel\nu}}{[p_\parallel^2 - 2x(pq)_\parallel + xq_\parallel^2 - m_f^2]^2} \tag{3.24}$$

diverges, and it must be properly regularized. In this context, it is of interest to explore the stability of the amplitude in (3.21) to various regularization methods.

Momentum-cutoff method. A direct calculation of the tensor integral (3.24) by the momentum-cutoff method [20] yields

$$T_{\mu\nu} = \frac{i}{4\pi}\left\{\frac{x^2 q_{\parallel\mu}q_{\parallel\nu}}{m_f^2 - q_\parallel^2 x(1-x)} + \frac{\tilde{\Lambda}_{\mu\nu}}{2}\left[1 + \ln\frac{m_f^2 - q_\parallel^2 x(1-x)}{\Delta}\right]\right\}, \tag{3.25}$$

where Δ is a cutoff parameter for the square of the momentum with respect to which integration is performed, $p_\parallel^2 (\Delta \gg q_\parallel^2, m_f^2)$. This logarithmically divergent tensor integral appears in amplitude (3.21) as the difference of contractions, which is finite:

$$2(qTq) - q_\parallel^2(T\tilde{\Lambda}) = \frac{ix^2(q_\parallel^2)^2}{4\pi[m_f^2 - q_\parallel^2 x(1-x)]}. \tag{3.26}$$

[2)] The proper-time method yields the same final results.

Hence, the external-magnetic-field-induced amplitude (3.21) can be reduced to the form

$$\Delta M^{(\mathrm{cut})} \simeq \sum_f \frac{g_{af}^2\beta}{2\pi^2} e^{-q_\perp^2/2\beta}\left[F(z)-\frac{1}{2z}\right], \qquad (3.27)$$

where the function $F(z)$ is given by (3.15). This result, which does not coincide with the limiting amplitude (3.14), is presented as the axion self-energy in [15], but it is incorrect, in our opinion. The reason is that the regularization method used is not impeccable. It is noteworthy that, in the difference $2(qTq) - q_\parallel^2(T\tilde{\Lambda})$ of the contractions, which appears in the tensor integral, there is an indefinite form of the "infinity minus infinity" type. That this indefinite form is evaluated incorrectly by the momentum-cutoff method can be demonstrated by considering the example of the photon self-energy, for which there arises a gauge-noninvariant expression. Let us demonstrate this explicitly. In perfect analogy with the axion transition amplitude (3.21), it can be found that, in the strong-magnetic-field limit, the contraction $(q\Pi q)$ in the photon self-energy (2.11) (by virtue of the gauge invariance of QED in external fields, this contraction must vanish) can be represented as

$$(q\Pi q) \simeq \sum_f -4\alpha\beta Q_f^2 e^{-q_\perp^2/2\beta} \times \int_0^1 dx\{2(qTq) - q_\parallel^2(T\tilde{\Lambda}) - q_\parallel^2(qV) + q_\parallel^2 m_f^2 S\}. \qquad (3.28)$$

The substitution of the scalar, vector, and tensor integrals [Eqs. (3.22), (3.23), and (3.25), respectively] into the contraction $(q\Pi q)$ yields

$$(q\Pi q) \simeq \sum_f -i\frac{\alpha}{\pi}\beta Q_f^2 q_\parallel^2 e^{-q_\perp^2/2\beta} \neq 0, \qquad (3.29)$$

which demonstrates that the photon self-energy as calculated by the method used in [15] does not possess the property of gauge invariance.

To overcome this difficulty, Borisov and Sizin [16] renormalize the $a \longrightarrow a$ transition amplitude by means of the double-subtraction procedure

$$\Delta M_R(q_\parallel^2) = \Delta M(q_\parallel^2) - \Delta M(m_a^2) - (q_\parallel^2 - m_a^2)\frac{d\Delta M(q_\parallel^2)}{dq_\parallel^2}\bigg|_{q_\parallel^2 = m_a^2}. \qquad (3.30)$$

It should be noted, however, that, in a strong magnetic field, this procedure does not have the physical meaning of a renormalization of anything (the procedure of axion-mass and axion-wave-function renormalization is applied only to the divergent vacuum component of the axion transition amplitude—the finite external-electromagnetic-field-induced component of the amplitude needs no renormalization); moreover, it also leads to an incorrect result:[3)]

$$\Delta M_R \simeq \sum_f \frac{g_{af}^2\beta}{2\pi^2} e^{-q_\perp^2/2\beta}\left[F(z)-\frac{1}{z}\right]. \qquad (3.31)$$

Dimensional-regularization method. Since the axion transition amplitude (3.18) contains an even number of the matrices γ_5 under the trace sign, this trace can be reduced to a form admitting a generalization to the case of n-dimensional space. This circumstance makes it possible to use the dimensional-regularization method [21, 22] to remove divergences in amplitude (3.21) in the momenta. The tensor integral (3.24) calculated by this method can be represented as

$$T_{\mu\nu} = \frac{i}{(4\pi)^{1-\varepsilon}} \frac{\Gamma(1+\varepsilon)}{[m_f^2 - q_\parallel^2 x(1-x)]^\varepsilon} \times \left[\frac{x^2 q_{\parallel\mu} q_{\parallel\nu}}{m_f^2 - q_\parallel^2 x(1-x)} - \frac{\tilde{\Lambda}_{\mu\nu}}{2\varepsilon}\right], \qquad (3.32)$$

where $\varepsilon = 1 - n/2$, so that the difference of the contractions of $T_{\mu\nu}$ in amplitude (3.21) proves to be independent of ε and has the form

$$2(qTq) - q_\parallel^2(T\tilde{\Lambda}) = \frac{iq_\parallel^2}{4\pi}\left[\frac{x^2 q_\parallel^2}{m_f^2 - q_\parallel^2 x(1-x)} - 1\right]. \qquad (3.33)$$

It is useful to note that, in effective two-dimensional QED, $\tilde{\Lambda}_{\mu\nu}$ plays the role of a metric tensor, so that its contraction in n-dimensional space is given by $\tilde{\Lambda}_{\mu\nu}\tilde{\Lambda}^{\mu\nu} = n = 2(1-\varepsilon)$. By substituting the difference of contractions in the form (3.33) and the scalar and vector integrals (3.22) and (3.23) into the amplitude (3.21), we obtain the expression

$$\Delta M^{(\mathrm{dim})} \simeq \sum_f \frac{g_{af}^2\beta}{2\pi^2} e^{-q_\perp^2/2\beta} F(z), \qquad (3.34)$$

which exactly coincides with the amplitude in (3.14). Thus, the above analysis has shown that the result calculated by using the approximate expression (3.19) for the propagator depends on the method of regularization and that only the method of dimensional regularization makes it possible to obtain the correct expression for the axion transition amplitude within effective two-dimensional QED [18]. The use of this method for the photon self-energy also leads to a correct gauge-invariant result. It is interesting to note that an attempt at using, for the above purposes, the Pauli–Villars regularization method [23], which proved to be appropriate for calculating the photon self-energy, leads to an incorrect

[3)] For the sake of simplicity, we have considered the case of zero axion mass.

result for the external-field-induced component of the axion transition amplitude.

The reason behind the discrepancy between the results obtained by using the different regularization methods lies in the nature of the approximate propagator (3.19), which takes into account only the contribution of the charged fermion occupying the first Landau level. The use of this propagator in calculating two-points loop diagrams is illegitimate in general when the square of the virtual fermion momentum becomes commensurate with or larger than the strength of the external magnetic field. In this region of integration with respect to momentum in the loop, it is necessary to take into account the contribution from higher Landau levels, which removes the ultraviolet divergence in the field-induced component of the amplitude. We note that the application of dispersion relations to derive the axion transition amplitude [17] does not remove the uncertainty associated with employing the approximate propagator (3.19) since this method requires a physically motivated subtraction procedure.

4. VIRTUAL-PHOTON CONTRIBUTION TO THE AXION SELF-ENERGY

In addition to the above fermion-loop-induced contribution to the axion self-energy, there exists a contribution generated by a virtual photon. The diagram corresponding to the invariant amplitude for the $a \longrightarrow a$ transition mediated by a photon is illustrated in Fig. 4. The existence of this extra channel is due to the special features of axion–photon interaction. Let us dwell on this point at some length. In an external electromagnetic field, there exists the effective axion–photon Lagrangian

$$\mathcal{L}_{a\gamma}(x) = g_{a\gamma}\tilde{F}^{\mu\nu}[\partial_\nu A_\mu(x)]a(x). \tag{4.1}$$

Here, $g_{a\gamma} = \alpha\xi/2\pi f_a$ is the axion–photon coupling constant, where $\xi = E/N - 1.92 \pm 0.08$ is a parameter on the order of unity that is determined by a specific axion model [5], E and N being quantities that characterize the electromagnetic and the color anomaly, respectively, and $A_\mu(x)$ is the 4-potential of the photon field. The effective Lagrangian (4.1) arises at the loop level owing to the triangle diagram and can be considered to be local under the assumption that the square of the axion (photon) 4-momentum is small in relation to the square of the charged-fermion mass in the loop. Since an analysis of the axion self-energy will be performed near the axion mass shell, the above requirement is satisfied to a high precision.

It should be noted that, in the presence of an external field, the photon propagator is modified by the interaction with the virtual fermions, whereby the dispersion properties of the photon modes change. For a further analysis, it is convenient to use the representation of the photon propagator in the form [24]

Fig. 4. Diagram describing the axion-to-axion ($a \longrightarrow a$) transition induced by a virtual photon in an external electromagnetic field.

$$G_{\mu\nu} = \sum_{\lambda=1}^{3} \frac{b_\mu^{(\lambda)} b_\nu^{(\lambda)}}{(b^{(\lambda)})^2} \frac{-i}{q^2 - \sum_f \mathcal{P}_f^{(\lambda)}}, \tag{4.2}$$

where we have used the basis $b_\mu^{(\lambda)}$ [$b_\mu^{(\lambda)} b_\mu^{(\lambda')} = (b^{(\lambda)})^2 \delta_{\lambda\lambda'}$] constructed from the photon 4-momentum q_μ and the strength tensor $F_{\mu\nu}$ for an external electromagnetic field:

$$\begin{aligned} b_\mu^{(1)} &= (qF)_\mu, \quad b_\mu^{(2)} = (q\tilde{F})_\mu, \\ b_\mu^{(3)} &= q^2(qFF)_\mu - (qFFq)q_\mu, \quad b_\mu^{(4)} = q_\mu. \end{aligned} \tag{4.3}$$

The basis in (4.3) is complete; it is the most convenient for analyzing photon processes in an external field, since the 4-vectors $b_\mu^{(\lambda)}$ ($\lambda = 1, 2, 3$) constitute a set of eigenvectors of the photon self-energy $\Pi_{\mu\nu}$ that correspond to the eigenvalues $\mathcal{P}_f^{(\lambda)}$.

The invariant amplitude for the $a \longrightarrow a$ transition through a virtual photon is described by the diagram in Fig. 4. The relevant expression can be represented as

$$M^{(\gamma)} = -ig_{a\gamma}^2 (q\tilde{F}G(q)\tilde{F}q). \tag{4.4}$$

From this expression, we can see that a photon of the second polarization mode with $\varepsilon_\mu^{(2)} = b_\mu^{(2)}/\sqrt{-(b^{(2)})^2}$ and, hence, the $\lambda = 2$ part of the photon propagator (4.2) contribute to the amplitude. Upon the substitution of the photon propagator (4.2), the correction to the axion mass squared takes the form

$$(\delta m_a^2)_\gamma = -\mathrm{Re}M^{(\gamma)} = \frac{g_{a\gamma}^2 \beta^2 q_\parallel^2}{\alpha} \mathrm{Re} \frac{1}{q^2 - \sum_f \mathcal{P}_f^{(2)}}. \tag{4.5}$$

In the one-loop approximation, the external-field-induced contribution to the eigenvalue $\mathcal{P}_f^{(2)}$ of the second photon polarization mode has the form [24]

$$\mathcal{P}_f^{(2)} = -\frac{Q_f^2 \alpha}{2\pi} \int_0^1 du \int_0^\infty \frac{dt}{t} \left\{ \frac{\beta t}{\sin(\beta t)} \left[q_\parallel^2 (1-u^2)\cos(\beta t) \right. \right.$$

$$-q_\perp^2\left(\cos(\beta u t)-\frac{u\sin(\beta u t)\cos(\beta t)}{\sin(\beta t)}\right)\Big]e^{-i\Phi} \qquad (4.6)$$

$$-q^2(1-u^2)e^{-i\Phi_0}\Big\},$$

where the phases $\Phi(t, u)$ and $\Phi_0(t, u)$ are defined in (3.9). In the strong-magnetic-field limit ($\beta \gg q_\parallel^2, q_\perp^2, m_f^2$), the expression for the eigenvalue $\mathcal{P}_f^{(2)}$ is significantly simplified to become

$$\mathcal{P}_f^{(2)} \simeq -\frac{2Q_f^2\alpha\beta}{\pi}\left[\frac{4m_f^2}{q_\parallel^2}F\left(\frac{4m_f^2}{q_\parallel^2}\right)-1\right], \qquad (4.7)$$

where $F(z)$ is the function defined in (3.15). It should be noted that, in the kinematical region below the threshold for the production of a fermion–antifermion pair ($q_\parallel^2 < 4m_f^2$), the eigenvalue $\mathcal{P}_f^{(2)}$ is real and negative, so that the amplitude for the transition $a \longrightarrow a$ through a virtual photon [see Eq. (4.4)] is real-valued in this kinematical region and has no poles. Attention should also be given to the fact that, in the kinematical region $q_\parallel^2 < 4m_e^2$, the correction $(\delta m_a^2)_\gamma$ is positive in contrast to the negative correction (3.10), which is induced by virtual fermions.

5. ELECTROMAGNETIC CORRECTION TO THE AXION MASS

The existence of the external-electromagnetic-field-induced correction to the axion self-energy can lead to a change in the dispersion relation for the axion, so that a detailed analysis of this correction is generally needed. In the present study, we will not perform a comprehensive analysis of the dispersion relations for the axion, restricting our consideration to the case of zero momentum ($\mathbf{q} = 0$). The corresponding values of the invariant variables are

$$q_\parallel^2 = m_a^2, \quad q_\perp^2 = 0. \qquad (5.1)$$

At this momentum value, the contribution to the axion self-energy determines an electromagnetic correction to the axion mass m_a.

If the invariant variables are given by (5.1), the virtual-fermion-induced correction to the axion mass squared (3.10) has the form

$$(\delta m_a^2)_{\mathrm{FL}} = -\sum_f \frac{g_{af}^2 m_a^2}{8\pi^2}\int_0^1 du\int_0^\infty \frac{dt}{t}\left(\frac{\beta t}{\tan(\beta t)}-1\right) \times \cos\left[t\left(m_f^2-\frac{m_a^2}{4}(1-u^2)\right)\right]. \qquad (5.2)$$

In the limit of a strong-magnetic field ($\beta \gg m_f^2$) and a small axion mass ($m_a \ll m_f$), the double integral in (5.2) can easily be calculated; as a result, the fermion-induced correction to the axion mass squared can be recast into the form

$$(\delta m_a^2)_{\mathrm{FL}} \simeq -\frac{m_a^2\beta}{8\pi^2 f_a^2}\sum_f C_f^2, \qquad (5.3)$$

where f_a is the energy scale of the breakdown of Peccei–Quinn symmetry and C_f is a parameter that characterizes axion–fermion interaction and which is on the order of unity, its specific value being determined by the choice of axion model [5].

In order to deduce the virtual-photon-induced correction (4.5) under the condition in (5.1), we note that, at zero momentum transfer, the eigenvalue of the second-mode photon is given by

$$\mathcal{P}_f^{(2)} = -m_a^2 G_f(\beta), \qquad (5.4)$$

where

$$G_f(\beta) = \frac{Q_f^2\alpha}{2\pi}\int_0^1 du(1-u^2)\int_0^\infty \frac{dt}{t}\left(\frac{\beta t}{\tan(\beta t)}-1\right) \times \exp\left\{-it\left(m_f^2-\frac{m_a^2}{4}(1-u^2)\right)\right\}. \qquad (5.5)$$

For the photon-induced correction to the square of the axion mass, this yields

$$(\delta m_a^2)_\gamma = \frac{g_{a\gamma}^2\beta^2}{\alpha}\mathrm{Re}\frac{1}{1+\sum_f G_f(\beta)}. \qquad (5.6)$$

In contrast to the fermion-induced correction (5.2), which is proportional to the axion mass squared m_a^2 and which vanishes for the originally massless axion, the photon-induced correction is virtually independent of m_a^2 and remains nonzero even in the massless-axion limit. In the case of a strong magnetic field ($\beta \gg m_f^2$), the function in (5.5) assumes the simple form

$$G_f(\beta) \simeq \frac{Q_f^2\alpha\beta}{3\pi m_f^2}, \qquad (5.7)$$

and the virtual-photon-induced correction (5.6) becomes

$$(\delta m_a^2)_\gamma = \frac{g_{a\gamma}^2\beta^2}{\alpha}\left(1+\frac{\alpha\beta}{3\pi}\sum_f\frac{Q_f^2}{m_f^2}\right)^{-1}. \qquad (5.8)$$

In order to perform a further numerical analysis of corrections to the axion mass squared, we note first of all that the leading contribution to all fermion-induced

corrections comes from the electron since this particle is a fermion that shows the highest sensitivity to the effect of an external electromagnetic field. In numerically estimating the correction in (5.3), which is induced by fermion loops, we therefore take into account only the electron contribution. The result is then given by

$$(\delta m_a^2)_{\rm FL} \simeq -3.3\times 10^{-29}\ {\rm eV}^2 \times C_e^2 \frac{B}{B_0}\left(\frac{10^8\ {\rm GeV}}{f_a}\right)^2\left(\frac{m_a}{10^{-2}\ {\rm eV}}\right)^2. \quad (5.9)$$

It can be seen that this correction is suppressed in direct proportion to the square of the axion mass and in inverse proportion to the square of the energy scale of violation of Peccei–Quinn symmetry.

In analyzing the virtual-photon-induced correction (5.8), we note that, at magnetic-field strengths of about $B \sim B_0$, radiative corrections to the photon propagator are small (a virtual photon is nearly unaffected by an external field), whence it follows that the photon-induced correction to the square of the axion mass becomes

$$(\delta m_a^2)_\gamma \simeq 1.26\times 10^{-15}\ {\rm eV}^2 \times \xi^2\left(\frac{B}{B_0}\right)^2\left(\frac{10^8\ {\rm GeV}}{f_a}\right)^2, \quad (5.10)$$

where ξ is a parameter on the order of unity [see the explanation of the notation after Eq. (4.1)], which is determined by a specific model of the axion [5]. As long as the external-field effect on a virtual photon can be disregarded ($B \ll 3\pi B_0/\alpha \simeq 1.3\times 10^3 B_0$), this correction is proportional to the square of the magnetic-field strength. When the magnetic-field strength achieves a value of 10^{17} G or higher, the external-magnetic-field effect on a virtual photon becomes sizable; according to (5.8), the quadratic dependence then gives way to a linear dependence. According to the scalar virial theorem [25] as applied to magnetized astrophysical objects, magnetic fields of strength about 10^{17} G are the maximum possible for such objects.

Still stronger magnetic fields, those of order 10^{23}–10^{24} G, could exist in the early Universe [26]. It should be emphasized that, under such conditions, the axion is a massless particle. To explain this, it should be recalled that, at the above values of the magnetic field, matter exists in the form of a quark–gluon and electron–positron plasma. Since π^0 mesons have not yet been produced, the standard mechanism of axion-mass generation cannot be operative. Therefore, there is no way to produce the axion mass in the absence of alternative mechanisms. According to (5.3), the contribution of fermion loops is proportional to the bare axion mass and vanishes in this case, whereas the photon-induced contribution (5.8) is nonzero for the originally massless axion. In this case, there arises an external-field-induced axion mass:

$$\delta m_a \simeq 0.058\ {\rm eV} \times \xi\left(\frac{10^8\ {\rm GeV}}{f_a}\right)\left(\frac{B}{10^{23}\ {\rm G}}\right)^{1/2}. \quad (5.11)$$

With decreasing external field, the axion mass decreases in proportion to the square root of the strength of this field. The above estimate indicates that, in the early Universe, the axion could have a mass at a level of the current upper limit, $m_a \lesssim 10^{-3}$ eV [5], in the presence of a magnetic field of strength $B \sim 10^{23}$ G.

6. CONCLUSION

We have studied the contribution that a constant external electromagnetic field induces in the axion self-energy. This contribution coincides with the real part of the $a \longrightarrow a$ transition amplitude in absolute value, but it has an opposite sign.

The external magnetic field has been taken into account exactly in the virtual-fermion-induced contribution. The limit of a strong magnetic field has been obtained, and the results are compared with the well-known expressions for this contribution that were found by using the technique of two-dimensional QED, which effectively arises in this limit. It has been shown that, in calculating the fermion contribution to the axion self-energy, indeterminate forms arise, which can be correctly evaluated only by means of dimensional regularization.

Since the axion features an effective interaction with photons in an external magnetic field, it is necessary to take additionally into account the virtual-photon-induced contribution to the axion self-energy. For this photon-induced contribution, we have obtained an expression that includes the external magnetic field exactly and which allows for virtual-photon interaction with the external magnetic field; on this basis, we have deduced the strong-field limit.

A numerical analysis of the resulting fermion- and photon-induced contributions has been performed at zero momentum transfer. In this case, the above contributions yield a magnetic correction to the axion mass. It has been shown that, in strong magnetic fields of $B \sim 10^{17}$ G, which can exist in magnetized astrophysical objects, the corrections to the axion mass are negligibly small. It has been indicated that the photon-induced correction to the axion mass does not vanish at zero bare mass of the axion, thereby determining its mass. Under the conditions of the early Universe ($B \sim 10^{23}$ G), this magnetic mass is commensurate with the current upper limit on the axion mass, $m_a \lesssim 10^{-3}$ eV, and decreases with field in inverse proportion to the square root of its strength.

ACKNOWLEDGMENTS

This work was supported by the Russian Foundation for Basic Research (project no. 98-02-16694).

REFERENCES

1. R. D. Peccei and H. R. Quinn, Phys. Rev. Lett. **38**, 1440 (1977); Phys. Rev. D **16**, 1791 (1977).

2. S. Weinberg, Phys. Rev. Lett. **40**, 223 (1978); F. Wilczek, Phys. Rev. Lett. **40**, 279 (1978).
3. W. A. Bardeen and S. H. H. Tye, Phys. Lett. B **74**, 580 (1978); J. Kandaswamy, P. Salomonson, and J. Schechter, Phys. Rev. D **17**, 3051 (1978); M. Srednicki, Nucl. Phys. B **260**, 689 (1985); H. Georgi, D. B. Kaplan, and L. Randall, Phys. Lett. B **169**, 73 (1986); W. A. Bardeen, R. D. Peccei, and T. Yanagida, Nucl. Phys. B **279**, 401 (1987).
4. J. Gasser and H. Leutwyler, Phys. Rep. **87**, 77 (1982).
5. G. G. Raffelt, *Stars as Laboratories for Fundamental Physics* (Univ. of Chicago Press, Chicago, 1996).
6. V. B. Berestetskiĭ, E. M. Lifshitz, and L. P. Pitaevskiĭ, *Quantum Electrodynamics* (Nauka, Moscow, 1989; Pergamon, Oxford, 1982).
7. G. Raffelt and D. Seckel, Phys. Rev. Lett. **60**, 1793 (1988).
8. C. Itzykson and J.-B. Zuber, *Introduction to Quantum Field Theory* (McGraw-Hill, New York, 1980; Mir, Moscow, 1984), Vol. 1.
9. J. Schwinger, Phys. Rev. **82**, 664 (1951).
10. N. V. Mikheev and L. A. Vassilevskaya, Phys. Lett. B **410**, 203 (1997).
11. A. P. Prudnikov, Yu. A. Brychkov, and O. I. Marichev, *Integrals and Series* (Nauka, Moscow, 1981; Gordon and Breach, New York, 1986).
12. N. V. Mikheev, A. Ya. Parkhomenko, and L. A. Vassilevskaya, Phys. Rev. D **60**, 035001 (1999).
13. L. A. Vassilevskaya, N. V. Mikheev, and A. Ya. Parkhomenko, Yad. Fiz. **62**, 1812 (1999) [Phys. At. Nucl. **62**, 1687 (1999)].
14. V. V. Skobelev, Zh. Éksp. Teor. Fiz. **113**, 1558 (1998) [JETP **86**, 850 (1998)].
15. V. V. Skobelev, Yad. Fiz. **61**, 2236 (1998) [Phys. At. Nucl. **61**, 2123 (1998)].
16. A. V. Borisov and P. E. Sizin, Zh. Éksp. Teor. Fiz. **115**, 3 (1999) [JETP **88**, 1 (1999)].
17. A. V. Borisov and P. E. Sizin, hep-ph/9904356.
18. Yu. Loskutov and V. Skobelev, Phys. Lett. A **56**, 151 (1975).
19. V. A. Fock, *Works on Quantum Field Theory* (Leningrad. Gos. Univ., Leningrad, 1957).
20. A. I. Akhiezer and V. B. Berestetskii, *Quantum Electrodynamics* (Nauka, Moscow, 1981; Wiley, New York, 1965).
21. G. 't Hooft and M. Veltman, Nucl. Phys. B **44**, 189 (1972).
22. L. Ryder, *Quantum Field Theory* (Cambridge Univ. Press, Cambridge, 1985; Mir, Moscow, 1987).
23. W. Pauli and F. Villars, Rev. Mod. Phys. **21**, 434 (1949).
24. A. E. Shabad, Ann. Phys. (N.Y.) **90**, 166 (1975); A. E. Shabad and V. V. Usov, Astrophys. Space Sci. **102**, 327 (1984).
25. D. Lai and S. L. Shapiro, Astrophys. J. **383**, 745 (1991).
26. A. Brandenburg, K. Enqvist, and P. Olsen, Phys. Rev. D **54**, 1291 (1996); J. Ahonen, K. Enqvist, and G. Raffelt, Phys. Lett. B **366**, 224 (1996); M. Joyce and M. Shaposhnikov, Phys. Rev. Lett. **79**, 1193 (1997).

Translated by A. Isaakyan

Physics of Atomic Nuclei, Vol. 64, No. 2, 2001, pp. 305–317. Translated from Yadernaya Fizika, Vol. 64, No. 2, 2001, pp. 352–366.

ELEMENTARY PARTICLES AND FIELDS
Theory

Higgs Bosons and Neutrinos in the Left–Right Model

O. M. Boyarkin*
Belarussian State Pedagogical University, ul. Sovetskaya 18, Minsk, 220050 Belarus
Received March 3, 2000; in final form, June 15, 2000

Abstract—The left–right asymmetric model featuring the bidoublet and two triplets of Higgs fields is investigated. It was established that, from an analysis of the reaction $l^-\gamma \longrightarrow W^-\nu_l$, it is possible to deduce not only information about the properties of the singly charged Higgs bosons $\tilde{\delta}^{(-)}$ and $h^{(-)}$ but also an answer to the question of whether the neutrino is a Majorana or a Dirac particle. The processes $f_i\bar{f}_j \longrightarrow \Delta_1^{(--)}\tilde{\delta}^{(+)}$ and $e^-\mu^- \longrightarrow \Delta_{1,2}^{(--)}\gamma$ leading to the production of doubly charged Higgs bosons are investigated. It is shown that information about the properties of singly charged Higgs bosons can also be obtained by studying the ultrahigh-energy cosmic neutrinos from the reaction $e^-\nu_e \longrightarrow \mu^-\nu_\mu$. © *2001 MAIK "Nauka/Interperiodica".*

1. INTRODUCTION

One of the most important problems in contemporary physics is to answer the question of whether non-Abelian gauge theories featuring a spontaneous breakdown of symmetry are true theories that describe actual interactions in nature. Higgs bosons—and among these, a special role is played by charged bosons—appear to be a necessary element. The reasons for this are the following: (i) Their detection would be an indisputable argument in favor of going beyond the Standard Model (SM). (ii) Singly charged Higgs bosons, along with charged gauge bosons, determine the potential of neutrino interaction with matter—since the effect of these bosons on the potential is significant [1], the conclusions derived for the neutrino masses and mixing angles on the basis of the Mikheev–Smirnov–Wolfenstein effect [2] must be revised should the existence of these bosons be confirmed. (iii) The detection of a doubly charged Higgs boson would be an indirect corroboration of the Majorana character of the neutrinos.

The objective of this study is to analyze processes involving charged physical Higgs bosons within the model based on the $SU(2)_L \times SU(2)_R \times U(1)_{B-L}$ gauge group. The main argument in favor of choosing this model is that its Higgs sector includes elements common to popular extensions of the SM such as the minimal supersymmetric standard model, the SM modification involving two doublets of the Higgs fields [3], and the model based on the $SU(3)_L \times U(1)_N$ gauge group [4].

The ensuing exposition is organized as follows. In Section 2, we derive the Lagrangians describing the interaction of charged Higgs bosons both with gauge bosons and with matter fields for the most general form of the scalar potential proposed in [5]. Equations relating the parameters of the Higgs sector to the neutrino-oscillation parameters are also presented there. In Section 3, we study collider experiments with Higgs bosons both in real and in virtual states and problems associated with the detection of Higgs bosons in interactions of the ultrahigh-energy neutrinos with matter. In Section 4, we discuss our results.

2. LEFT–RIGHT ASYMMETRIC MODEL: $SU(2)_L \times SU(2)_R \times U(1)_{B-L}$ ($g_L \neq g_R$)

We will study the nonsupersymmetric left–right model involving the bidoublet

$$\Phi\left(\frac{1}{2}, \frac{1}{2}, 0\right) = \begin{pmatrix} \Phi_1^0 & \Phi_2^+ \\ \Phi_1^- & \Phi_2^0 \end{pmatrix}$$

and two triplets

$$\Delta_L(1, 0, 2) = \begin{pmatrix} \delta_L^{++} \\ \delta_L^+ \\ \delta_L^0 \end{pmatrix}, \quad \Delta_R(0, 1, 2) = \begin{pmatrix} \delta_R^{++} \\ \delta_R^+ \\ \delta_R^0 \end{pmatrix}.$$

We will make use of the most general form of the Higgs potential V as proposed in [5]. In Appendix A, we present the explicit expression for V [(A.1)] and necessary information about the structure of the sector of charged physical Higgs bosons.

The interaction of leptons and the physical Higgs bosons is determined by the Yukawa Lagrangian, which we choose in the form

$$\mathcal{L}_Y = -\sum_{a,b}\{h_{ab}\bar{\Psi}_{aL}\Phi\Psi_{bR} + h'_{ab}\bar{\Psi}_{aL}\tilde{\Phi}\Psi_{bR} + if_{ab}[\Psi_{aL}^T C\tau_2(\boldsymbol{\tau}\cdot\boldsymbol{\Delta}_L)\Psi_{bL} + (L \longrightarrow R)] + \text{h.c.}\}, \quad (1)$$

* e-mail:boyarkin@bspu.unibel.by

where Ψ_{aL} (Ψ_{aR}) denotes the left-handed (right-handed) lepton doublet; $\tau_{1,2,3}$ are the Pauli matrices; C is the charge-conjugation matrix; $\tilde{\Phi} = \tau_2\Phi^*\tau_2$; $a, b = e, \mu, \tau$; and h_{ab}, h'_{ab}, and f_{ab} are, respectively, the bidoublet and the triplet Yukawa constants of lepton coupling to the Higgs bosons. After spontaneous symmetry breaking, which is realized according to the chain

$$SU(2)_L \times SU(2)_R \times U(1)_{B-L} \longrightarrow SU(2)_L \times U(1)_Y \longrightarrow U(1)_Q,$$

we obtain 14 physical Higgs bosons. Of these, eight are charged (four singly charged $h^{(\pm)}$ and $\tilde{\delta}^{(\pm)}$ bosons and four doubly charged $\Delta_{1,2}^{(\pm\pm)}$ bosons) and six are neutral bosons (four scalars $S_{1,2,3,4}$ and two pseudoscalar $P_{1,2}$). By going over from the gauge basis to the basis of pure mass states and using Eq. (1), we can find the Lagrangians for the interactions of physical Higgs bosons with leptons and gauge bosons. For the sector of charged Higgs bosons, the explicit expressions for these Lagrangians are given by {there, α_i, ρ_i, and β_i are constants appearing in the Higgs potential [see Eq. (A.1) in Appendix A]}

$$\begin{aligned}\mathscr{L}_{l\nu}^{sc} = \sum_{a,b}\Bigg\{ & d_2\Bigg[\frac{h'_{ab}k_2 - h_{ab}k_1}{k_+}\bar{\nu}_{aL}l_{bR} \\ & - \frac{h_{ab}k_2 - h'_{ab}k_1}{k_+}\bar{N}_{aR}l_{bL}\Bigg]h^{(+)} \\ & + \sqrt{2}\,f_{ab}\Bigg[\left(\frac{d_3\beta k_0^2}{(\alpha+\rho_1-\rho_3/2)v_R^2}h^{(+)} - d_3\tilde{\delta}^{(+)}\right)\dot{l}^c_{aL}\nu_{bL} \\ & + \left(\frac{d_1k_0}{v_R}h^{(+)} + \frac{d_1\beta k_0}{(\alpha+\rho_1-\rho_3/2)v_R}\tilde{\delta}^{(+)}\right)\dot{l}^c_{aR}N_{bR}\Bigg] + \text{h.c.}\Bigg\},\end{aligned} \tag{2}$$

where

$$\langle\delta^0_{L,R}\rangle = \frac{v_{L,R}}{\sqrt{2}}, \quad \langle\Phi_1^0\rangle = k_1, \quad \langle\Phi_2^0\rangle = k_2,$$

$$v_L \ll \max(k_1, k_2) \ll v_R, \quad k_\pm = \sqrt{k_1^2 \pm k_2^2},$$

$$k_0 = \frac{k_-^2}{\sqrt{2}k_+}, \quad \beta = \frac{k_+^2(\beta_1k_1 + 2\beta_3k_2)}{2k_-^2k_0},$$

$$d_1 = \left[1 + \left(1 + \frac{\beta^2}{(\alpha+\rho_1-\rho_3/2)^2}\right)\frac{k_0^2}{v_R^2}\right]^{-1/2},$$

$$d_2 = \left(1 + \frac{k_0^2}{v_R^2}\right)^{-1/2},$$

$$d_3 = \left[1 + \frac{\beta^2k_0^2}{(\alpha+\rho_1-\rho_3/2)^2v_R^2}\right]^{-1/2}, \quad \alpha = \frac{\alpha_3k_+^2}{2k_-^2},$$

ν_a (N_a) describes the light (heavy) neutrino of generation a (both neutrinos can be either left-handed or right-handed), l_a describes the charged lepton, and the superscript c denotes charge-conjugation operation;

$$\begin{aligned}\mathscr{L}_{WZ}^{sc} = \Bigg\{ & -\frac{g_Lg_Rc_Wc_\varphi bk_-^2}{\sqrt{2}k_+}h^{(+)} \\ & - \frac{g_Lg_Rg's_W(g'^{-1}s_Wc_\varphi + g_R^{-1}s_\varphi)}{c_W}\Bigg[ak_0h^{(+)} \\ & + \frac{a\beta k_0}{(\alpha+\rho_1-\rho_3/2)}\tilde{\delta}^{(+)}\Bigg]\Bigg\}W_{R\mu}Z_{1\mu}\end{aligned} \tag{3}$$

$$- \frac{eg_Ls_\varphi v_L(g'g_R^{-1} + g_Rg'^{-1})}{c_W}\Bigg(\frac{d\beta k_0^2}{(\alpha+\rho_1-\rho_3/2)v_R^2}h^{(+)} - d\tilde{\delta}^{(+)}\Bigg)W_{L\mu}Z_{1\mu} + \text{h.c.},$$

where $c_W = \cos\theta_W$, $s_W = \sin\theta_W$, $c_\varphi = \cos\varphi$, $s_\varphi = \sin\varphi$, $c_\xi = \cos\xi$, $s_\xi = \sin\xi$, $W_{R\mu} = -s_\xi W_{1\mu} + c_\xi W_{2\mu}$, $W_{L\mu} = c_\xi W_{1\mu} + s_\xi W_{2\mu}$, φ (ξ) is the angle of mixing of the neutral (charged) gauge bosons, and θ_W is the Weinberg angle;

$$\begin{aligned}\mathscr{L}_{W\gamma}^{sc} = \Bigg\{ & \left[\frac{eg_Rk_0\beta d_1}{2d_2^2(\alpha+\rho_1-\rho_3/2)} - \frac{eg_Lv_La^2}{2d_3d_2^2}\right]\tilde{\delta}^{(+)} \\ & + \frac{eg_Rk_0d_1}{2}h^{(+)}\Bigg\}W_{R\mu}A_\mu,\end{aligned} \tag{4}$$

$$\begin{aligned}\mathscr{L}_l^{dc} = & -\sum_{a,b} f_{ab}(\dot{l}^c_{aL}l_{bL}c_{\theta_d} - \dot{l}^c_{aR}l_{bR}s_{\theta_d})\Delta_1^{(++)} \\ & + (1 \longrightarrow 2, \theta_d \longrightarrow \theta_d - \pi/2),\end{aligned} \tag{5}$$

$$\begin{aligned}\mathscr{L}_Z^{dc} = & [(\alpha_Lc_{\theta_d}^2 + \alpha_Rs_{\theta_d}^2)\Delta_1^{(--)}\partial_\mu\Delta_1^{(++)} \\ & + (\alpha_L^2c_{\theta_d}^2 + \alpha_R^2s_{\theta_d}^2)\Delta_1^{(--)}\Delta_1^{(++)}Z_\mu \\ & + (1 \longrightarrow 2, \theta_d \longrightarrow \theta_d + \pi/2) \\ & - s_{\theta_d}c_{\theta_d}(\alpha_L - \alpha_R)\Delta_1^{(--)}\partial_\mu\Delta_2^{(++)} \\ & - s_{\theta_d}c_{\theta_d}(\alpha_L^2 - \alpha_R^2)\Delta_1^{(--)}\Delta_2^{(++)}Z_\mu + \text{h.c.}]Z_\mu,\end{aligned} \tag{6}$$

$$\mathscr{L}_{\delta W}^{dc} = \frac{ig_La^2}{db^2}[\tilde{\delta}^{(-)}\partial_\mu(c_{\theta_d}\Delta_1^{(++)} - s_{\theta_d}\Delta_2^{(++)})$$

$$-\partial_\mu\tilde{\delta}^{(-)}(c_{\theta_d}\Delta_1^{(++)} - s_{\theta_d}\Delta_2^{(++)})]W_{L\mu}$$
$$+\frac{ig_R a\beta k_0}{b^2(\alpha+\rho_1-\rho_3/2)v_R}[\partial_\mu\tilde{\delta}^{(-)}(s_{\theta_d}\Delta_1^{(++)} + c_{\theta_d}\Delta_2^{(++)}) \quad (7)$$
$$-\tilde{\delta}^{(-)}\partial_\mu(s_{\theta_d}\Delta_1^{(++)} + c_{\theta_d}\Delta_2^{(++)})]W_{R\mu},$$

$$\mathcal{L}_{hW}^{dc} = \frac{ig_R a k_0}{v_R}[\partial_\mu h^{(-)}(s_{\theta_d}\Delta_1^{(++)} + c_{\theta_d}\Delta_2^{(++)}) \quad (8)$$
$$-h^{(-)}\partial_\mu(s_{\theta_d}\Delta_1^{(++)} + c_{\theta_d}\Delta_2^{(++)})]W_{R\mu},$$

where $c_{\theta_d} = \cos\theta_d$, $s_{\theta_d} = \sin\theta_d$,

$$\tan 2\theta_d = \frac{2k_-^2[\beta_3(k_1^2+k_2^2)+\beta_1 k_1 k_2]}{k_1^2(2\rho_1-\rho_3-4\rho_2)v_R^2},$$

$$g' = \frac{1}{\sqrt{c_W^2 e^{-2} - g_R^{-2}}},$$

$$\alpha_L = e[2\cot 2\theta_W c_\varphi - g' s_\varphi c_W^{-1} g_R^{-1}],$$

$$\alpha_R = e[-2c_W^{-1}s_W c_\varphi + s_\varphi c_W^{-1} g'^{-1} g_R^{-1}(g_R^2 - g'^2)].$$

It turns out that, in the left–right model—as in any gauge theory where the neutrino acquires mass owing to the spontaneous breakdown of symmetry—the Yukawa coupling constants are related to the neutrino-oscillation parameters. By way of example, we indicate that, for the case of two lepton generations, we have the relations [6]

$$m_D^e = c_{\varphi_e}s_{\varphi_e}(-m_1 c_{\theta_\nu}^2 - m_3 s_{\theta_\nu}^2 + m_2 c_{\theta_N}^2 + m_4 s_{\theta_N}^2), \quad (9)$$

$$M_D = c_{\varphi_e}s_{\varphi_X}c_{\theta_\nu}s_{\theta_\nu}(m_1 - m_3) + s_{\varphi_e}c_{\varphi_X}c_{\theta_N}s_{\theta_N}(m_4 - m_2), \quad (10)$$

$$f_{eX}v_R = s_{\varphi_e}s_{\varphi_X}c_{\theta_\nu}s_{\theta_\nu}(m_3 - m_1) + c_{\varphi_e}c_{\varphi_X}c_{\theta_N}s_{\theta_N}(m_4 - m_2), \quad (11)$$

$$f_{ee}v_R = (s_{\varphi_e}c_{\theta_\nu})^2 m_1 + (c_{\varphi_e}c_{\theta_N})^2 m_2 + (s_{\varphi_e}s_{\theta_\nu})^2 m_3 + (c_{\varphi_e}s_{\theta_N})^2 m_4, \quad (12)$$

$$f_{XX}v_R = f_{ee}v_R(\varphi_e \longrightarrow \varphi_X, \theta_\nu \longrightarrow \theta_\nu + \pi/2), \quad (13)$$

$$f_{ll'}v_L = f_{ll'}v_R(\varphi_l \longrightarrow \varphi_l + \pi/2, \varphi_{l'} \longrightarrow \varphi_{l'} + \pi/2), \quad (14)$$

$$m_D^X = m_D^e(\varphi_e \longrightarrow \varphi_X, \theta_\nu \longrightarrow \theta_\nu + \pi/2), \quad M_D' = M_D(\varphi_e \longleftrightarrow \varphi_X), \quad (15)$$

where $X = \mu, \tau$; $M_D = h_{eX}k_1 + h'_{eX}k_2$; $M'_D = h_{Xe}k_1 + h'_{Xe}k_2$; $l, l' = e, \mu$, and τ; $m_D^l = h_{ll}k_1 + h'_{ll}k_2$; φ_l is the mixing angle within the generation l; θ_ν (θ_N) is the angle of mixing between the ν (N) neutrinos from the e and X generations; m_1 (m_2) is the mass of the light (heavy) electron neutrino; m_3 (m_4) is the mass of the light (heavy) neutrino belonging to the X generation; and $c_{\varphi_e} = \cos\varphi_e$, $s_{\varphi_e} = \sin\varphi_e$, etc. The off-diagonal Yukawa coupling constants lead, on one hand, to nonzero mixing angles both within and between the neutrino generations and, on the other hand, to the existence of the flavor-violating currents at the tree level. As can be seen from the above formulas, the left–right model is advantageous in that we always can obtain nonvanishing θ_ν values even at zero off-diagonal Yukawa coupling constants. For example, the constants h_{eX}, h'_{eX}, and f_{eX} can vanish in the case of degeneracy of the neutrino masses ($m_1 = m_3$, $m_2 = m_4$) as well.

3. COLLIDER AND COSMIC-RAY EXPERIMENTS

In this section, we investigate processes involving neutrinos and charged Higgs bosons. We begin by discussing reactions at accelerators. It is known that the planned 500-GeV electron–positron collider (Next Linear Collider) and muon colliders (First Muon Collider and Next Muon Collider) can also operate in the $\gamma\gamma$ and $l^\pm\gamma$ ($l = e, \mu$) modes. This is possible owing to the processes of classical photon bremsstrahlung from a l^-l^+ beam and to the Compton scattering of laser photons on l^- and l^+. The process

$$l^-\gamma \longrightarrow W^-\nu_l \quad (16)$$

is among the most interesting ones for observations in the $l^\pm\gamma$ mode.

This is because the differential cross section for reaction (16) in the c.m. frame vanishes at a 180° angle between the W and γ momenta in the case where the W-boson anomalous magnetic moment μ_γ is given by [7]

$$\mu_\gamma = e/m_W. \quad (17)$$

It is precisely this value of the anomalous magnetic moment that is predicted by the SM and by its extensions. There is, however, a class of so-called composite models, where it is assumed that all particles or at least some of them that, within the SM, were considered to be elementary and pointlike are in fact composite and extended objects. The fundamental constituents, referred to as preons, interact via the exchange of quanta of the hypercolor gauge field. This interaction is asymptotically free and renormalized; possesses the property of infrared confinement; and, below the characteristic energy scale Λ, becomes strong and binds all preons into hypercolor-singlet states, in the same way as the conventional strong interaction does for composite hadrons at Λ_{QCD}. At energies $\sqrt{s}$ in excess of Λ, manifestations of the compositeness of particles are readily observable. At these energies, multiparticle production processes dominate over ordinary binary scat-

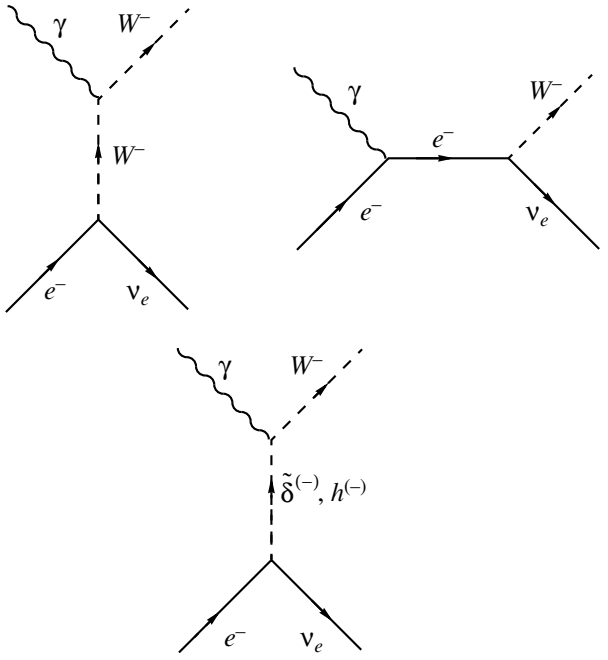

Fig. 1. Feynman diagrams for the process $l^-\gamma \longrightarrow W^-\nu_l$.

tering processes. One of the manifestations of the composite structure of the W bosons at energies $\sqrt{s}$ less than Λ would be a deviation of the anomalous magnetic moment from the value given by (17). Thus, investigation of reaction (16) would be a good test for non-Abelian gauge theories featuring a spontaneous breakdown of symmetry.

Let us investigate reaction (16) from a different point of view—namely, we will address the question of whether this reaction can furnish information about the structure of the Higgs sector of the SM extension under study. In the case being considered, the process in (16) is characterized by two more diagrams that are associated with the exchanges of singly charged Higgs bosons in the t channels (see Fig. 1). The differential cross section for unpolarized primary particles now has the form

$$\frac{d\sigma}{dt} = \left(\frac{d\sigma}{dt}\right)_{\rm SM} + \frac{3e^2t}{16\pi s^2}\left[\frac{(f_{ll}\tau)^2}{(t-m_{\tilde\delta}^2)^2+\Gamma_{\tilde\delta}^2 m_{\tilde\delta}^2} + \frac{\kappa_{ll}^2}{(t-m_h^2)^2+\Gamma_h^2 m_h^2}\right], \quad (18)$$

where

$$\tau = \frac{g_L v_L c_\xi a^2}{2\sqrt{2}b^2} - \frac{g_R k_0 s_\xi \beta a d}{2\sqrt{2}b^2 c_{\rm Y}},$$

$$\kappa_{ll} = \frac{g_R k_0 s_\xi a b \alpha_{ll}}{2}, \quad \alpha_{ab} = \frac{h'_{ab}k_2 - h_{ab}k_1}{k_+},$$

$$c_{\rm Y} = \alpha + \rho_1 - \rho_3/2,$$

while the differential cross section $(d\sigma/dt)_{\rm SM}$ for process (16) in the SM is given by [7]

$$\left(\frac{d\sigma}{dt}\right)_{\rm SM} = \frac{e^4 u}{32\pi s_{\rm W}^2 s^3 (t-m_W^2)^2}(u^2+s^2-2m_W^2 t). \quad (19)$$

By taking into account the definition of m_l and m_D^l, we obtain

$$\alpha_{ll} = \frac{2k_1k_2m_l - k_+^2 m_D^l}{k_-^2 k_+}. \quad (20)$$

If the Yukawa Lagrangian in the form (A.4) is used in the quark sector, the $\tilde\delta^{(\pm)}$ and $h^{(\pm)}$ bosons do not interacted with quarks. For $m_{\tilde\delta}$ and m_h, there are no constraints in this case that follow from measurement of the inclusive cross section for the reaction $b \longrightarrow s\gamma$. We can then state that the masses of these bosons must be larger than 44.1 GeV, since it is this result that follows from an analysis of LEP experiments (at a 95% C.L.) [8].

As follows from [18], the partial differential cross section $(d\sigma/d(\cos\theta))_h$ associated with $h^{(-)}$ exchange increases either upon going over to large mixing angles within the neutrino generation or upon changing the original electron beam by the muon one. But even at $u = 0$, it appears to be very small. For example, $(d\sigma/d(\cos\theta))_h$ amounts to a few tenths of fb at $\varphi_{e,\mu} \sim 10^{-2}$ and $m_h = 100$ GeV.

Nearly the same situation prevails for $(d\sigma/d(\cos\theta))_{\tilde\delta}$ at $c_{\rm Y} \sim 1$ and $(v_L)_{\max} \sim 2$ GeV. It is also necessary to take into account the possibility that the combination $c_{\rm Y}$ of the scalar-potential parameters is small ($c_{\rm Y} \ll 1$). This is compatible with the inequality

$$\rho_1 - \rho_3/2 < 0,$$

which follows from the condition of vacuum stability [5]. At $u = 0$ and $c_{\rm Y} = 10^{-2}$, the differential cross section for process (16) as a function of $\sqrt{s}$ is displayed in Fig. 2 for various values of $m_{\tilde\delta}$.

There is one more factor that leads to a nonvanishing cross section at $u = 0$. It is associated with taking into account the total decay width of the W boson. It is necessary to estimate this factor, at least by order of magnitude. From [9], we know that a mere substitution of the Breit–Wigner expression

$$\frac{-i(\delta_{\mu\nu} - q_\mu q_\nu/m_W^2)}{q^2 - m_W^2 + i\Gamma_W m_W}$$

for the *W*-boson propagator

$$\frac{-i(\delta_{\mu\nu} - q_\mu q_\nu/m_W^2)}{q^2 - m_W^2}$$

leads to a breakdown of gauge invariance; as a result, the unitary limit is violated for the reaction cross section. The degree of this violation is not large (it is proportional to Γ_W/m_W), but, in our case, where we are dealing with the vanishing of the cross section, it is mandatory to take into account the factor of *W*-boson instability. In order to preserve gauge invariance and, consequently, to ensure fulfillment of the Ward identity, the modification of the propagator must be accompanied by a modification of the vertex function. Following [10], we represent the *W*-boson propagator and vertex function as

$$\left[\delta_{\mu\nu} - \frac{q_\mu q_\nu}{m_W^2}(1 + i\gamma_W)\right]\frac{1}{q^2 - m_W^2 + q^2\gamma_W},$$

$$V_{\mu\nu\alpha} = V^0_{\mu\nu\alpha}(1 + i\gamma_W),$$

where $\gamma_W = \Gamma_W/m_W$ and $V^0_{\mu\nu\alpha}$ is the *W*-boson vertex function in the tree approximation. The differential cross section for process (16) can now be obtained from (18) by means of the substitution

$$\left(\frac{d\sigma}{dt}\right)_{\rm SM} \longrightarrow \frac{e^4}{64\pi s_W^2 s^3[(t - m_W^2)^2 + t^2\gamma_W^2]} \times \{2u(u^2 + s^2 - 2m_W^2 t) + \gamma_W^2[u(5s^2 + 4st + 2t^2) + m_W^2 t(s + 4t)]\}. \quad (21)$$

The calculations show that, at $u = 0$ and $\sqrt{s} = 123$ GeV, the term on the right-hand side of (21) attains a maximum value of 0.82 fb. Thus, we conclude that, if the differential cross section for reaction (16) at $u = 0$ amounts to a few fb, there are the following possibilities: (i) The *W*-boson anomalous magnetic moment differs from the value predicted by the SM. (ii) There exist charged physical Higgs bosons whose emergence is due to the presence of the scalar triplet in the theory, whence it follows that the neutrino is a Majorana particle. In order to distinguish between cases (i) and (ii), it is necessary to measure the differential cross section at zero scattering angle. Agreement with the relevant SM result would imply that version (ii) is valid. Otherwise, version (i) is realized.

If expression (A.2) is used for the Yukawa Lagrangian, the $h^{(\pm)}$ boson interacts with quarks. For the process

$$\bar{u}d \longrightarrow W^-\gamma, \quad (22)$$

we then have an extra (with respect to the SM case) diagram involving $h^{(-)}$ exchange in the *s* channel. There now arises the question of whether we can hope that,

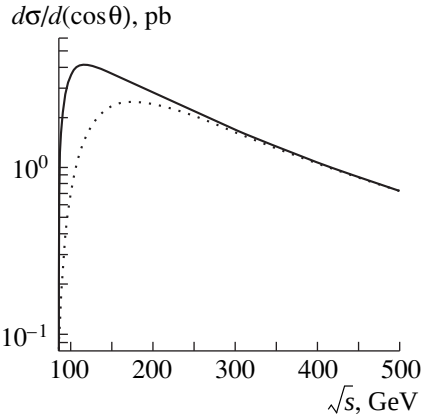

Fig. 2. Differential cross section for the process $e^-\gamma \longrightarrow W^-\nu_e$ as a function of $\sqrt{s}$ at $\xi = 10^{-2}$, $g_R = 1.4g_L$, $\nu_L = 1.7 \times 10^{-2}$ GeV, $k_1 = 10$ GeV, and $c_Y = 10^{-2}$: (solid curve) $m_{\tilde{\delta}} = 42$ GeV and (dotted curve) $m_{\tilde{\delta}} = 120$ GeV.

owing to the resonance-enhancement mechanism, the partial cross section $(d\sigma/d(\cos\theta))_h$ at $u = 0$ will appear to be within reach of experimental possibilities. The calculations yield

$$\left(\frac{d\sigma}{d(\cos\theta)}\right)_h = \left(\frac{eg_R s_\xi}{32\sqrt{\pi}}\right)^2 \frac{3(s - m_W^2)}{s[(s - m_h^2)^2 + \Gamma_h^2 m_h^2]} \times [(m_u \sin 2\beta - m_d)^2 + (m_d \sin 2\beta - m_u)^2], \quad (23)$$

where

$$\sin 2\beta = 2k_1 k_2/k_+^2.$$

If the parameters are set to the values

$$\xi = 10^{-2}, \quad m_u = 2 \text{ MeV}, \quad m_d = 15 \text{ MeV}, \quad m_h = 120 \text{ GeV}, \quad k_1 = 10 \text{ GeV}$$

and if $u = 0$, the cross section for process (22) involving the $h^{(-)}$ resonance is 1.6 fb. With increasing k_1 and m_h, $(d\sigma/d(\cos\theta))_h$ decreases. If quarks are combined into hadrons, the angular distribution for reaction (22) at $\cos(\theta = 180°)$ has a deep minimum rather than a zero. Thus, attempts at detecting $h^{(\pm)}$ Higgs bosons by using the reaction

$$ab \longrightarrow W^-\gamma X,$$

where $a, b = p, \bar{p}$, seem hopeless.

Further, we addressed the process

$$f_i\bar{f}_j \longrightarrow \Delta_1^{(--)}\tilde{\delta}^{(+)}, \quad (24)$$

where f_i is a pointlike fermion of flavor *i*. Figure 3 presents the Feynman diagrams for the case of leptons. The first (second) diagram corresponds to the neutrino of right-hand (left-hand) circular polarization. For quarks, only the first diagram contributes. If we neglect

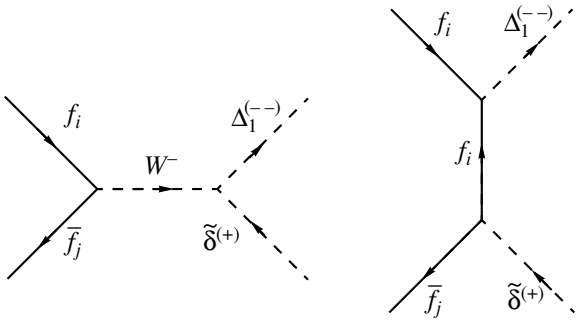

Fig. 3. Feynman diagrams for the process $f_i\bar{f}_j \longrightarrow \Delta_1^{(--)}\tilde{\delta}^{(+)}$.

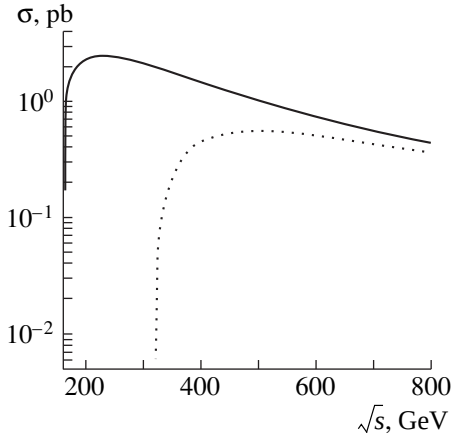

Fig. 4. Total cross section for the process $u\bar{d} \longrightarrow \Delta_1^{(--)}\tilde{\delta}^{(+)}$ as a function of $\sqrt{s}$ at $\theta_d = 0$: (solid curve) $m_{\Delta_1} = 120$ GeV and $m_{\tilde{\delta}^{(+)}} = 42$ GeV and (dotted curve) $m_{\Delta_1} = 200$ GeV and $m_{\tilde{\delta}^{(+)}} = 120$ GeV.

the fermion masses, the total cross section corresponding to this diagram has the form

$$\sigma_{u\bar{d}\to\Delta_1^{(--)}\tilde{\delta}^{(+)}} = \frac{g_L^4 c_\xi^2 \beta_{\Delta_1\tilde{\delta}}}{64\pi s[(s-m_W^2)^2+\Gamma_W^2 m_W^2]} \tag{25}$$
$$\times\{2[(m_{\Delta_1}^2-m_{\tilde{\delta}}^2)^2-\beta^2 s/6]+s(s-2m_{\Delta_1}^2-2m_{\tilde{\delta}}^2)\},$$

where

$$\beta_{\Delta_1\tilde{\delta}} = \sqrt{\left(1-\frac{m_{\Delta_1}^2+m_{\tilde{\delta}}^2}{s}\right)^2-\left(\frac{2m_{\Delta_1}m_{\tilde{\delta}}}{s}\right)^2}.$$

The cross section (25) as a function of energy in the c.m. frame is presented in Fig. 4 for various values of m_{Δ_1} and $m_{\tilde{\delta}}$. Under the assumption that

$$m_{\Delta_1} < 2m_{W_R}, \quad m_{\tilde{\delta}} < m_{W_R} + m_{Z_2},$$

nearly all 100% of product Higgs bosons decay through the channels

$$\Delta_1^{(--)} \longrightarrow \tau^-\tau^-, \quad \tilde{\delta}^{(+)} \longrightarrow \tau^+\bar{\nu}_\tau.$$

The background to the process in (24) is dominated by the contribution from the reaction

$$u\bar{d} \longrightarrow W^-Z. \tag{26}$$

If only the τ-lepton decay channels are used to detect the final states of reactions (24) and (26), the cross section for reaction (26) must be multiplied by $\mathrm{Br}(W^- \longrightarrow \tau^-\bar{\nu}_\tau)\,\mathrm{Br}(Z \longrightarrow \tau^-\tau^+) = 3.66\times10^{-3}$; the corresponding factor for reaction (24) is about unity. Since the cross section for reaction (26) is only a few times as large as the cross section $\sigma_{u\bar{d}\to\Delta_1^{(--)}\tilde{\delta}^{(+)}}$, it is obvious that, with the aid of the τ-lepton identification of the Higgs bosons produced in the reactions

$$ab \longrightarrow \Delta_1^{(--)}\tilde{\delta}^{(+)}X \quad (a, b = p, \bar{p}),$$

we can reliably separate the signal from the background.

Let us now consider lepton-flavor-violating reactions. The intensity of these reactions is controlled by off-diagonal Yukawa coupling constants. Many studies were devoted to setting upper limits on these constants (see [11] and references therein). The most stringent constraints follow from searches for the decay process

$$\mu^- \longrightarrow e^-e^+e^-. \tag{27}$$

Within the left–right model, this process in the second-order of perturbation theory is associated with diagrams featuring virtual $\Delta_{1,2}^{(--)}$, S_1, and S_2 Higgs bosons. For the decay width, the calculations yield

$$\Gamma_{\mu^-\to e^-e^+e^-} = \frac{\tau m_\mu^5}{96(2\pi)^3}, \tag{28}$$

where

$$\tau = (f_{ee}f_{e\mu})^2\left(\frac{1}{m_{\Delta_1}^4}+\frac{1}{m_{\Delta_2}^4}\right)$$
$$+\frac{\alpha_{e\mu}^2}{4k_+^2}\left(\frac{m_e c_{\theta_0}s_{\theta_0}-\alpha_{ee}k_+s_{\theta_0}^2}{m_{S_1}^2}-\frac{m_e s_{\theta_0}c_{\theta_0}+\alpha_{ee}k_+c_{\theta_0}^2}{m_{S_2}^2}\right)^2$$
$$+\frac{4m_e f_{ee}f_{e\mu}\alpha_{e\mu}}{m_\mu k_+}\left(\frac{1}{m_{\Delta_1}^2}+\frac{1}{m_{\Delta_2}^2}\right)$$
$$\times\left(\frac{m_e c_{\theta_0}s_{\theta_0}-\alpha_{ee}k_+s_{\theta_0}^2}{m_{S_1}^2}-\frac{m_e s_{\theta_0}c_{\theta_0}+\alpha_{ee}k_+c_{\theta_0}^2}{m_{S_2}^2}\right),$$

and where we have set $\theta_d = 0$ for the sake of simplicity. If the upper limit of 10^{-12} from [12] is used for the ratio $\Gamma_{\mu^- \to e^- e^+ e^-}/\Gamma_{\mu \to \text{all}}$, we arrive at the constraint

$$\sqrt{\tau} < 2.32 \times 10^{-11}\ \text{GeV}^{-2} \tag{29}$$

for determining the Yukawa coupling constants.

The smallness of the off-diagonal Yukawa coupling constants leads to the conclusion that the most optimal way to measure them at high energies is to study lepton-flavor-violating reactions, which are either governed by the mechanism of *s*-channel resonance enhancement or described by the Feynman diagrams that contain only one vertex featuring Yukawa coupling constants. Such reactions are exemplified by the process

$$e^-\mu^- \longrightarrow \Delta_i^{(--)}\gamma \quad (i = 1, 2), \tag{30}$$

which can be investigated at muon colliders either in the electron-beam or in the fixed-electron-target mode. In the second order of perturbation theory, the relevant Feynman diagrams are displayed in Fig. 5. Assuming that primary particles are polarized, disregarding the lepton masses, and setting $i = 1$, we represent the total cross section as

$$\sigma_{e^-\mu^- \to \Delta_1^{(--)}\gamma} = \frac{2e^2 f_{e\mu}^2 (c_{\theta_d}^2 P_+ + s_{\theta_d}^2 P_-)(s^2 - m_{\Delta_1}^4)}{\pi s[(s - m_{\Delta_1}^2)^2 + \Gamma_{\Delta_1}^2 m_{\Delta_1}^2]}, \tag{31}$$

where $P_\pm = (1 \pm \lambda_e)(1 \pm \lambda_\mu)$, λ_l being the polarization of the primary lepton.

The quantity $\sigma_{e^-\mu^- \to \Delta_1^{(--)}\gamma}$ is maximal near the threshold $(\sqrt{s})_{\text{thr}}$. There are, however, two factors that restrict our possibilities in studying the near-threshold behavior of reaction (30):

(i) Owing to a finite lifetime of the $\Delta_1^{(--)}$ boson, the threshold $(\sqrt{s})_{\text{thr}}$ is smeared over the energy region of width about $\Delta E_1 = \Gamma_{\Delta_1 \to \text{all}}$.

(ii) The inclusion of radiative corrections to the process being considered and the contributions from diagrams involving soft-photon bremsstrahlung results not only in the cancellation of infrared divergences but also in the dependence of the cross section on the quantity ΔE_γ, which corresponds to the energy value below which real photons cannot be recorded in experiments. The quantity ΔE_γ is determined by the energy resolution of the detector used in a given experiment.

The decay width of the Δ_1 boson is much less than ΔE_γ. At $f_{\tau\tau} = 0.9$ and $m_{\Delta_1} = 400$ GeV, it is as small as 0.25 MeV, whereas, for example, the photonic energy threshold of the electromagnetic calorimeter used in the OPAL detector is 1 GeV. Figure 6 illustrates the behavior of $\sigma_{e^-\mu^- \to \Delta_1^{(--)}\gamma}$ in the energy range from $(\sqrt{s})_{\text{thr}}$ +

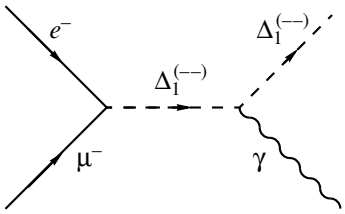

Fig. 5. Feynman diagrams for the process $e^-\mu^- \longrightarrow \Delta_1^{(--)}\gamma$.

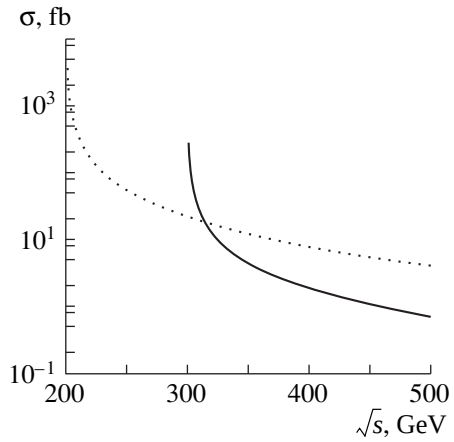

Fig. 6. Total cross section for the process $e^-\mu^- \longrightarrow \Delta_1^{(--)}\gamma$ as a function of $\sqrt{s}$ at $\lambda_e = 0.8$, $\lambda_\mu = 0.9$, and $\Delta E_\gamma = 1$ GeV: (solid curve) $m_{\Delta_1} = 200$ GeV and $f_{e\mu} = 3 \times 10^{-3}$ and (dotted curve) $m_{\Delta_1} = 300$ GeV and $f_{e\mu} = 10^{-4}$.

ΔE_γ to 500 GeV. Since there is virtually no background to reaction (30), then it follows from the data in Fig. 6 that studying this reaction is one of the most precise means for assessing the quantity $f_{e\mu} m_{\Delta_1}^{-2}$.

Let us now proceed to discuss reactions involving cosmic neutrinos of ultrahigh energies. Active galaxy cores represent one of the sources of such neutrinos. Since a typical luminosity of active galaxy cores is between 10^{44} and 10^{47} erg/s, we can assume that the evolution of active galaxy cores is determined by gravity—that is, by the accretion of matter to a supermassive ($M \geq 10^6 M_\odot$) black hole. In the vicinity of an active galaxy core, protons accelerated to ultrahigh energies interact either with matter or with radiation, generating pions, whose decay products include photons and neutrinos. The maximum energy of neutrinos from active galaxy cores is on the order of 10^{10} GeV. The products of the decay of pions generated in inelastic collisions of protons with photons that constitute the cosmic microwave radiation background appear to be another source of ultrahigh-energy neutrinos. The energy of the neutrinos generated by this source may be as high as

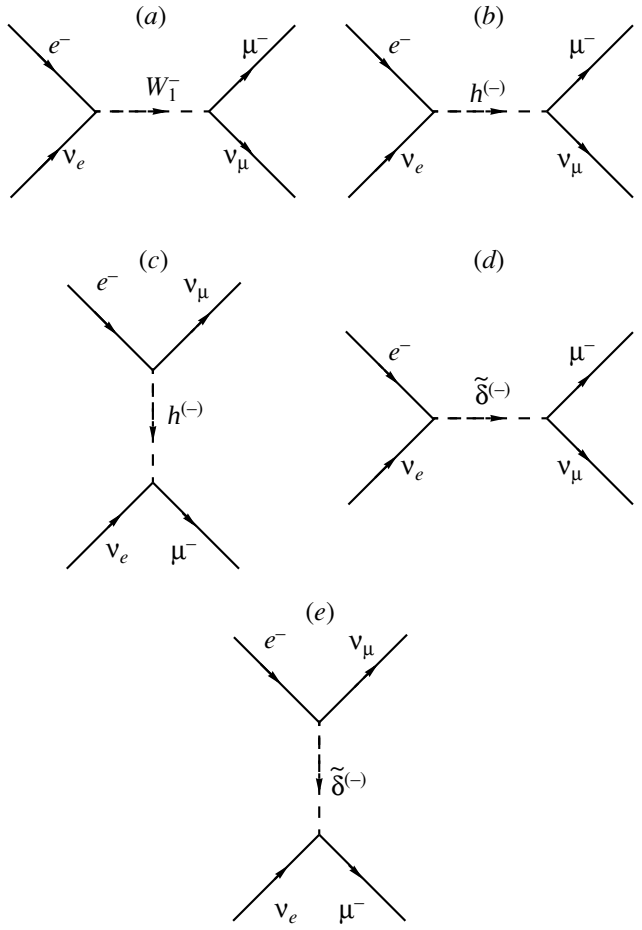

Fig. 7. Feynman diagrams for the process $e^-\nu_e \longrightarrow \mu^-\nu_\mu$.

10^{12} GeV. There are a large number of studies devoted to estimating the diffuse fluxes of neutrinos originating from active galaxy cores and from the cosmic microwave radiation background (see [13] and references therein). Obviously, cosmic neutrinos of ultrahigh energies can be used to determine the properties of singly charged Higgs bosons. In this respect, the highest hopes are pinned on reactions involving virtual Higgs bosons in the *s* channel such as

$$e^-\nu_e \longrightarrow W^-Z, \tag{32}$$

$$e^-\nu_e \longrightarrow W^-\gamma, \tag{33}$$

$$e^-\nu_e \longrightarrow \mu^-\nu_\mu. \tag{34}$$

The processes in (32)–(34) can be studied at the BAIKAL NT-200, NESTOR, and AMANDA neutrino telescopes.

By way of example, we consider in detail the process in (34). The Feynman diagrams for this reaction are shown in Fig. 7. For the sake of convenience, we study separately the cases of electrons having right- and left-hand circular polarization. The total cross section is written as

$$\begin{aligned}\sigma_L &= \frac{1}{32\pi s^2}\Bigg((1-\lambda_\nu)\Bigg(\frac{g_L^4 c_\xi^4 s^3}{3[(s-m_W^2)^2+\Gamma_W^2 m_W^2]}\\ &+\frac{2g_L^2 c_\xi^2 f_{e\mu}^2 (s-m_W^2)}{[(s-m_W^2)^2+\Gamma_W^2 m_W^2]}\Bigg(\frac{s^2}{2}-m_{\tilde\delta}^2 s\\ &+\frac{m_{\tilde\delta}^2\Gamma_{\tilde\delta^{(-)}}^2 - m_{\tilde\delta}^4}{2}N_{\tilde\delta}+2m_{\tilde\delta}^3\Gamma_{\tilde\delta^{(-)}}Q_{\tilde\delta}\Bigg)+(f_{e\mu})^2\Bigg(4(f_{e\mu})^2\\ &-\frac{2g_L^2 c_\xi^2\Gamma_W\Gamma_{\tilde\delta^{(-)}}m_W m_{\tilde\delta}}{(s-m_W^2)^2+\Gamma_W^2 m_W^2}\Bigg)\Bigg(s+m_{\tilde\delta}^2 N_{\tilde\delta}+\frac{m_{\tilde\delta}^3 - m_{\tilde\delta}\Gamma_{\tilde\delta^{(-)}}^2}{\Gamma_{\tilde\delta^{(-)}}}Q_{\tilde\delta}\Bigg)\Bigg)\\ &+(1+\lambda_\nu)\frac{4f_{ee}^2 f_{\mu\mu}^2 s^3}{(s-m_{\tilde\delta}^2)^2+\Gamma_{\tilde\delta^{(-)}}^2 m_{\tilde\delta}^2}\Bigg)\end{aligned} \tag{35}$$

for electrons having left-hand circular polarization and as

$$\begin{aligned}\sigma_R &= \frac{1}{128\pi s^2}\Bigg((1-\lambda_\nu)\frac{(\alpha_{ee}\alpha_{\mu\mu})^2 s^3}{(s-m_h^2)^2+\Gamma_{h^{(-)}}^2 m_h^2}\\ &+(1+\lambda_\nu)\alpha_{e\mu}^4\Bigg(s+m_h^2 N_h+\frac{m_h^3 - m_h\Gamma_{h^{(-)}}^2}{\Gamma_{h^{(-)}}}Q_h\Bigg)\Bigg)\end{aligned} \tag{36}$$

for electrons having right-hand circular polarization.

Here, λ_ν denotes the neutrino helicity, and

$$N_k = \ln\left|\frac{m_k^4+\Gamma^2 m_k^2}{(s+m_k^2)^2+\Gamma_k^2 m_k^2}\right|,$$

$$Q_k = \arctan\left(\frac{s+m_k^2}{\Gamma_k m_k}\right)-\arctan\left(\frac{m_k}{\Gamma_k}\right),$$

with $k = \tilde\delta^{(-)}, h^{(-)}$.

For electron having left-hand circular polarization and neutrinos having right-hand circular polarization, the deviations from the SM predictions are very small because they depend primarily on $f_{e\mu}$. For example, these deviations are about 0.1% at $f_{e\mu} = 3\times10^{-2}$. We also recall that the height of the *W*-boson-resonance peak in this channel (Glashow resonance) is 10^4 pb.

It was shown in [14] that, even if the seesaw relation

$$m_{\nu_l} m_{N_l} = m_l^2$$

holds, it is necessary to distinguish between two possibilities within the left–right model: (i) The angles φ_l of mixing within the neutrino generation are small (10^{-5}–10^{-6})—this may correspond either to the case of $\nu_L = 0$

or to the case of $v_L \neq 0$. (ii) At nonvanishing v_L, the values of the angle φ_l can be on the order of 10^{-2}.

For the masses of the left-handed neutrinos and for the angle θ_ν of mixing between the neutrino generations, we will use their experimental upper limits ($\theta_\nu \leq 0.03$) and set

$$\theta_\nu = \theta_N, \quad m_{N_e} = 1 \text{ TeV}, \quad m_{N_\mu} = 1.5 \text{ TeV}.$$

In order to suppress $e^- \rightleftharpoons \mu^-$ oscillations, it is necessary to assume that the bidoublet off-diagonal constants $h_{e\mu}$ and $h'_{e\mu}$ satisfy the relation

$$k_2 h_{e\mu} + k_1 h'_{e\mu} = 0.$$

By taking into account the definitions of m_W and M_D, we then obtain

$$\alpha_{e\mu} = \Omega k_+/k_2, \tag{37}$$

where

$$\Omega = \frac{\sqrt{(1+\rho_t\Delta\rho_0 - 4k_1^2/v_R^2)[2g_L^{-2}m_W^2 - k_1^2(1+\rho_t\Delta\rho_0)]}M_D}{2g_L^{-2}m_W^2 - 2k_1^2(1+\rho_t\Delta\rho_0) + 4k_1^4/v_R^2},$$

$\rho_t = 3G_F m_t^2/\sqrt{2}\,\pi^2$ (m_t is the t-quark mass), and k_1 takes values in the interval from 0 to $2g_L^{-2}m_W^2/(1+\rho_t\Delta\rho_0)$. In Eq. (37), we have replaced v_L by its upper boundary [14],

$$v_L < \rho_t\Delta\rho_0 g_L^{-1}\sqrt{4m_W^2 - 2c_W^2 m_Z^2}, \tag{38}$$

which follows from an analysis of the CDF and D0 experiments that measured the parameter ρ_0,

$$\rho_0 = 1 + \Delta\rho_0 = \frac{m_W^2}{c_W^2 m_Z^2(1+\rho_t)}.$$

In the case of $M_D \neq 0$, the quantity $\alpha_{e\mu}$ is extremely small even at large values of φ_e and φ_μ. For example, we have $\alpha_{e\mu} = 1.8 \times 10^{-5}$ at $\varphi_e = 2.5 \times 10^{-2}$, $\varphi_\mu = 3 \times 10^{-2}$, and $k_1 = 70$ GeV. Because α_{ll} is determined by Eq. (20), the above estimate is valid for α_{ee} as well. At the same time, $\alpha_{\mu\mu}$ can be as large as values about 10^{-2} even at small angles φ_μ.

The left–right model admits large values for the bidoublet off-diagonal and diagonal constants either in the case of degeneracy of the bidoublet vacuum expectations, $M_D = 0$, or in the case of quasidegeneracy $M_D \approx 0$. In the former case, these constants become arbitrary because the only condition imposed on them is that their sum must vanish. In this case, we have

$$\alpha_{ab} = 2h'_{ab}.$$

Even at anomalously great values of $\alpha_{e\mu}$ (for example, 2×10^{-2}), the cross sections for the right-hand circular polarization of electrons and the left-hand circular polarization of neutrinos can amount only to values of about 3×10^{-3} fb. Hence, the cases of the initial $e_L^-\nu_{eL}$ and $e_R^-\nu_{eR}$ are of prime interest to us.

Figure 8 shows the total cross section σ_{LL} for the left-hand circular polarization of initial leptons. We cannot rule out the possibility that the height of the $\tilde{\delta}^{(-)}$-resonance peak, $(\sigma_{LL})_{\tilde{\delta}}$—it is determined by the values of $m_{\tilde{\delta}}$, f_{ee}, and $f_{\mu\mu}$—exceeds the height of the Glashow peak, σ_W. By way of example, we indicate that, at $m_{\tilde{\delta}} = 65$ GeV, $f_{ee} = 5.5 \times 10^{-2}$, and $f_{\mu\mu} = 7.5 \times 10^{-1}$, the ratio of the heights of these peaks is

$$(\sigma_{LL})_{\tilde{\delta}}/\sigma_W \sim 10.$$

In analyzing the cross section for the process in (34) with initial $e_R^-\nu_{eR}$, it is necessary to specify the choice of the Yukawa Lagrangian in the quark sector. If we make use of expression (A.4), the total decay width of the $h^{(-)}$ boson takes the form

$$\Gamma_{h^{(-)}} = \sum_l \Gamma_{h^{(-)} \to l\nu_{lR}} + \Gamma_{h^{(-)} \to W_1 Z_1}, \tag{39}$$

where the partial decay widths are defined in Appendix B (we assume here that $m_h < m_{W_2}, m_{Z_2}, m_{N_l}$). If the

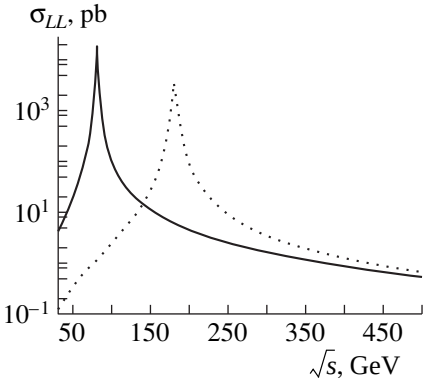

Fig. 8. Cross section σ_{LL} as a function of $\sqrt{s}$ at $\lambda_\nu = 1$, $f_{\tau\tau} = 0.9$, $f_{\mu\mu} = 0.75$, $f_{ee} = 8.5 \times 10^{-2}$, and $k_1 = 100$ GeV: (solid curve) $m_{\tilde{\delta}} = 100$ GeV and (dotted curve) $m_{\tilde{\delta}} = 180$ GeV.

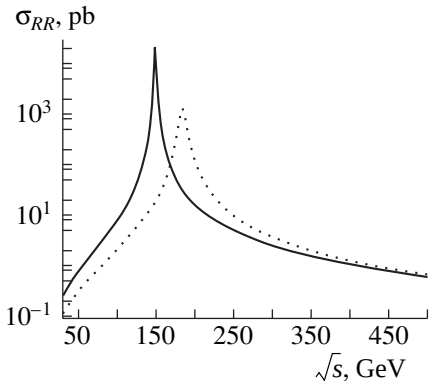

Fig. 9. Cross section σ_{RR} as a function of $\sqrt{s}$: (solid curve) m_h = 150 GeV and (dotted curve) m_h = 185 GeV. For both curves, we choose $\varphi_e = 8 \times 10^{-3}$, $\varphi_\mu = \varphi_\tau = 10^{-2}$, and k_1 = 115 GeV.

angles of mixing within a neutrino generation are small ($\varphi_e \sim 10^{-6}$, $\varphi_\mu \sim 10^{-5}$), $\Gamma_{h^{(-)} \to e^- \nu_{eR}}$ and $\Gamma_{h^{(-)} \to \mu^- \nu_{\mu R}}$ are about a few eV and a few keV, respectively. For $m_h < m_W + m_Z$, the problem of evaluating $\alpha_{\tau\tau}$ becomes more important, because this quantity determines the width with respect to the decay channel $h^{(-)} \longrightarrow \tau^- \nu_{\tau R}$. It should be recalled that, at present, there is no experimental information about the Yukawa coupling constants associated with the tau lepton. In order to obtain a rough estimate of $\Gamma_{h^{(-)} \to \tau^- \bar{\nu}_{\tau L}}$, we choose

$$m_{N_\tau} = 2 \text{ TeV}, \; m_{\nu_\tau} = 24 \text{ MeV}$$

and assume that there exists mixing between τ and μ neutrinos that is characterized by the angles of $\theta_\nu = \theta_N = 0.03$. A transition to the Yukawa Lagrangian (A.2) means the opening of the quark-decay channels, in which case expression (39) must be supplemented with the terms $\Gamma_{h^{(-)} \to \bar{c}s}$ and $\Gamma_{h^{(-)} \to \bar{t}b}$ given by

$$\Gamma_{h^{(-)} \to \bar{c}s} = \frac{3}{16\pi k_+^2 m_h \cos^2 2\beta}\left[1 - \frac{(m_c + m_s)^2}{m_h^2}\right]$$

$$\times [(m_c^2 + m_s^2)(1 + \sin^2 2\beta) - 4 m_c m_s \sin 2\beta]$$

$$\times w(m_h^2, m_c^2, m_s^2),$$

$$\Gamma_{h^{(-)} \to \bar{t}b} = \Gamma_{h^{(-)} \to \bar{c}s}(m_c \longrightarrow m_t, m_s \longrightarrow m_b),$$

$$\tan\beta = k_1/k_2.$$

At small values of the angle φ_l, the cross section σ_{RR} is extremely small. Even in this case, however, the height of the $h^{(-)}$-resonance peak can be as large as a few hundred fb. For example, we have $(\sigma_{RR})_h$ = 376 fb at $\varphi_e = 2 \times 10^{-6}$, $\varphi_\mu = 6 \times 10^{-4}$, and m_h = 45 GeV.

For the Lagrangian $\mathcal{L}_Y$ in the form (A.2), Fig. 9 shows the cross section σ_{RR} as a function of $\sqrt{s}$ for large values of φ_l.

It can be seen from Fig. 9 that, at specific parameter values, the cross section obtained here exceeds the corresponding SM cross section by a few orders of magnitude and that the height of the $h^{(-)}$-resonance peak is a few times as great as the height of the Glashow peak. We emphasize that, within the left–right model, there are no grounds to rule out the situation where the Glashow resonance overlaps the $\tilde{\delta}^{(-)}$ or the $h^{(-)}$ resonance.

4. CONCLUSION

We have shown that the absence of zeros in the differential cross section for the reaction

$$l^- \gamma \longrightarrow W^- \nu_l$$

at a scattering angle of 180° may suggest not only a composite structure of the W boson but also the existence of the $\tilde{\delta}^{(-)}$ Higgs boson appearing in the theories featuring the triplet of scalar fields. A detection of a signal from the $\tilde{\delta}^{(-)}$ boson in turn would confirm the Majorana character of the neutrino.

Investigation of the production of charged Higgs bosons in the reactions

$$f_i \bar{f}_j \longrightarrow \Delta_1^{(--)} \tilde{\delta}^{(+)}, \quad e^- \mu^- \longrightarrow \Delta_{1,2}^{(--)} \gamma$$

and observation of their decay products will furnish information about the Yukawa coupling constants $f_{\tau\tau}$, $f_{e\mu}$, $h_{\tau\tau}$, and $h'_{\tau\tau}$. Let us recall reactions that show the greatest promise for setting constraints on the remaining Yukawa coupling constants. The constants $f_{\mu\mu}$ and f_{ee} can be measured either by using the $\Delta_i^{(--)}$ resonance in the reactions [15]

$$\mu^- \mu^- \longrightarrow W^- W^-, \quad e^- e^- \longrightarrow W^- W^-$$

or by studying $\Delta_i^{(--)}$-boson production in the processes [16]

$$\mu^- \mu^- \longrightarrow \Delta_i^{(--)} \gamma, \quad e^- e^- \longrightarrow \Delta_i^{(--)} \gamma.$$

Information about h_{ee}, h'_{ee}, $h_{\mu\mu}$, $h'_{\mu\mu}$, $h_{e\mu}$, and $h'_{e\mu}$ can be deduced from the features of the reactions [17]

$$e^- \mu^+ \longrightarrow e^- \mu^+, \quad e^- \mu^+ \longrightarrow e^+ \mu^-.$$

At the same time, we can also derive constraints on the neutrino masses and mixing angles by solving Eqs. (9)–(15) with the known values of the Yukawa coupling constants and known vacuum expectation values. Thus,

the results obtained here confirm the previous conclusions [14, 18]; that is, in the extensions of the SM, all parameters of neutrino oscillations are determined simultaneously in studying the Higgs sector.

APPENDIX A

The Higgs field potential proposed in [5] has the form

$$\begin{aligned}
V &= -\mu_1^2[\mathrm{tr}(\Phi^\dagger\Phi)] - \mu_2^2[\mathrm{tr}(\tilde{\Phi}\Phi^\dagger) + \mathrm{tr}(\tilde{\Phi}^\dagger\Phi)] \\
&- \mu_3^2[\mathrm{tr}(\Delta_L\Delta_L^\dagger) + \mathrm{tr}(\Delta_R\Delta_R^\dagger)] + \lambda_1\{[\mathrm{tr}(\Phi\Phi^\dagger)]^2\} \\
&+ \lambda_2\{[\mathrm{tr}(\tilde{\Phi}\Phi^\dagger)]^2 + [\mathrm{tr}(\tilde{\Phi}^\dagger\Phi)]^2\} \\
&+ \lambda_3[\mathrm{tr}(\tilde{\Phi}\Phi^\dagger)\mathrm{tr}(\tilde{\Phi}^\dagger\Phi)] + \lambda_4\{\mathrm{tr}(\Phi\Phi^\dagger)[\mathrm{tr}(\tilde{\Phi}\Phi^\dagger) \\
&+ \mathrm{tr}(\tilde{\Phi}^\dagger\Phi)]\} + \rho_1\{[\mathrm{tr}(\Delta_L\Delta_L^\dagger)]^2 + [\mathrm{tr}(\Delta_R\Delta_R^\dagger)]^2\} \\
&+ \rho_2[\mathrm{tr}(\Delta_L\Delta_L)\mathrm{tr}(\Delta_L^\dagger\Delta_L^\dagger) + \mathrm{tr}(\Delta_R\Delta_R)\mathrm{tr}(\Delta_R^\dagger\Delta_R^\dagger)] \\
&+ \rho_3[\mathrm{tr}(\Delta_L\Delta_L^\dagger)\mathrm{tr}(\Delta_R\Delta_R^\dagger)] + \rho_4[\mathrm{tr}(\Delta_L\Delta_L)\mathrm{tr}(\Delta_R^\dagger\Delta_R^\dagger) \\
&+ \mathrm{tr}(\Delta_L^\dagger\Delta_L^\dagger)\mathrm{tr}(\Delta_R\Delta_R)] \\
&+ \alpha_1\{\mathrm{tr}(\Phi\Phi^\dagger)[\mathrm{tr}(\Delta_L\Delta_L^\dagger) \\
&+ \mathrm{tr}(\Delta_R\Delta_R^\dagger)]\} + \alpha_2[\mathrm{tr}(\Phi\tilde{\Phi}^\dagger)\mathrm{tr}(\Delta_R\Delta_R^\dagger) \\
&+ \mathrm{tr}(\Phi^\dagger\tilde{\Phi})\mathrm{tr}(\Delta_L\Delta_L^\dagger)] + \alpha_2^*[\mathrm{tr}(\Phi^\dagger\tilde{\Phi})\mathrm{tr}(\Delta_R\Delta_R^\dagger) \\
&+ \mathrm{tr}(\tilde{\Phi}^\dagger\Phi)\mathrm{tr}(\Delta_L\Delta_L^\dagger)] + \alpha_3[\mathrm{tr}(\Phi\Phi^\dagger\Delta_L\Delta_L^\dagger) \\
&+ \mathrm{tr}(\Phi^\dagger\Phi\Delta_R\Delta_R^\dagger)] + \beta_1[\mathrm{tr}(\Phi\Delta_R\Phi^\dagger\Delta_L^\dagger) \\
&+ \mathrm{tr}(\Phi^\dagger\Delta_L\Phi\Delta_R^\dagger)] + \beta_2[\mathrm{tr}(\tilde{\Phi}\Delta_R\Phi^\dagger\Delta_L^\dagger) \\
&+ \mathrm{tr}(\tilde{\Phi}^\dagger\Delta_L\Phi\Delta_R^\dagger)] + \beta_3[\mathrm{tr}(\Phi\Delta_R\tilde{\Phi}^\dagger\Delta_L^\dagger) \\
&+ \mathrm{tr}(\Phi^\dagger\Delta_L\tilde{\Phi}\Delta_R^\dagger)].
\end{aligned} \tag{A.1}$$

By means of (A.1), we can derive formulas for going over from the gauge basis to the basis of pure mass states. For the physical charged Higgs bosons, we have

$$h^{(\pm)} = d_2\Phi_+^{(\pm)} + \frac{d_1k_0}{v_R}\delta_R^\pm + \frac{d_3\beta k_0^2}{(\alpha+\rho_1-\rho_3/2)v_R^2}\delta_L^\pm,$$

$$\tilde{\delta}^{(\pm)} = \frac{d_1\beta k_0}{(\alpha+\rho_1-\rho_3/2)v_R}\delta_R^\pm - d_3\delta_L^\pm,$$

$$\Delta_1^{(\pm\pm)} = c_{\theta_d}\delta_L^{(\pm\pm)} + s_{\theta_d}\delta_R^{(\pm\pm)},$$

$$\Delta_2^{(\pm\pm)} = -s_{\theta_d}\delta_L^{(\pm\pm)} + c_{\theta_d}\delta_R^{(\pm\pm)},$$

where

$$\Phi_+^{(\pm)} = \frac{k_1\Phi_1^{(\pm)} + k_2\Phi_2^{(\pm)}}{k_+},$$

$$\Phi_-^{(\pm)} = \frac{k_1\Phi_2^{(\pm)} - k_2\Phi_1^{(\pm)}}{k_+}.$$

The squares of the masses of these bosons are given by

$$m_{\Delta_1}^2 = \frac{\alpha_3k_-^2 + 4\rho_2v_R^2}{2} + \frac{\{k_-^2[\beta_3(k_1^2+k_2^2)+\beta_1k_1k_2]\}^2}{2k_1^4(4\rho_2+\rho_3-2\rho_1)v_R^2},$$

$$m_{\Delta_2}^2 = \frac{\alpha_3k_-^2 - (2\rho_1-\rho_3)v_R^2}{2} - \frac{\{k_-^2[\beta_3(k_1^2+k_2^2)+\beta_1k_1k_2]\}^2}{2k_1^4(4\rho_2+\rho_3-2\rho_1)v_R^2},$$

$$m_h^2 = \alpha(v_R^2+k_0^2) + \frac{\beta^2k_0^2}{\alpha+\rho_1-\rho_3/2},$$

$$m_{\tilde{\delta}}^2 = (\rho_3/2-\rho_1)v_R^2 - \frac{\beta^2k_0^2}{\alpha+\rho_1-\rho_3/2}.$$

In the case of degeneracy of the bidoublet vacuum expectations ($k_1 = k_2 = k_g$), the requirement ensuring the compatibility of the existence of the minima,

$$\frac{\partial V}{\partial\Phi_1^0} = 0, \quad \frac{\partial V}{\partial\Phi_2^0} = 0,$$

leads to the condition

$$\alpha_3(v_L^2+v_R^2)/2 + (\beta_3-\beta_2)v_Lv_R = 0.$$

This condition in turn results in redefining the $h^{(\pm)}$-boson mass. The calculations yield

$$m_h^2 \approx \beta_1v_Lv_R + \left(\frac{\rho_3}{2}-\rho_1\right)\frac{v_L^2v_R^2}{k^2}.$$

In order to estimate v_L, it is necessary to use the inequality in (38). Setting $(\rho_3/2-\rho_1) \approx \beta_1 \approx 1$ and $v_R \approx 10^3$ GeV and using an upper limit on v_L, we obtain $m_h \leq 140$ GeV. Thus, even in the case of degeneracy of the bidoublet vacuum expectations, the $h^{(\pm)}$ boson can become as heavy as the singly charged Higgs boson of the minimal supersymmetric extension of the Standard Model, where the relevant masses satisfy the conditions

$$m_{H^{(\pm)}} > m_W.$$

If, in the case of degeneracy of the bidoublet vacuum expectations, the conventional expression for the

Yukawa Lagrangian,

$$\mathcal{L}_Y = -\sum_{a,b}(h_{ab}^{(q)}\bar{Q}_{aL}\Phi Q_{bR} + h_{ab}^{(q)'}\bar{Q}_{aL}\tilde{\Phi}Q_{bR} + \text{h.c.}), \quad (A.2)$$

where Q_{aL} (Q_{aR}) describes the left-handed (right-handed) quark doublet, is used in the quark sector, the diagonal mass matrices for the up and down quarks in the symmetric left–right models satisfy the relation

$$\mathcal{M}_u = \mathcal{M}_d. \quad (A.3)$$

For the condition in (A.3) to be violated, we can introduce the extra Higgs triplets $\Delta_L'(1, 0, 2/3)$ and $\Delta_R'(0, 1, 2/3)$ and supplement the Lagrangian (A.2) with the terms [19]

$$-\sum_{a,b}[f_{ab}^{(q)}Q_{aL}^T C\tau_2(\boldsymbol{\tau}\cdot\boldsymbol{\Delta}_L')Q_{bL} + (L \longrightarrow R) + \text{h.c.}].$$

There is another way associated with introducing the extra bidoublet $\Phi_u(1/2, 1/2, 0)$ that interacts with up and down quarks, but which contributes only to the mass of the up quark [20]. In either approach, however, there occurs an undesirable increase in the number of physical Higgs bosons. In the asymmetric version of the left–right model, it is not necessary to complicate the Higgs sector in order to arrive at the condition $\mathcal{M}_u \neq \mathcal{M}_d$. Instead of (A.2), we can use, by way of example, the Lagrangian

$$\mathcal{L}_Y = -\sum_{a,b}(h_{ab}^{(q)}\bar{Q}_{aL}\tau_-\Phi\tau_+Q_{bR} + h_{ab}^{(q)'}\bar{Q}_{aL}\tau_-\Phi^*\tau_+Q_{bR}), \quad (A.4)$$

where $\tau_\pm = \tau_1 \pm i\tau_2$, which is similar in form to the corresponding SM Lagrangian. In turn, the use of Lagrangian (A.4) reduces only the flavor-diagonal couplings of the up and down quarks to the neutral Higgs bosons.

APPENDIX B

The decay width of the charged Higgs bosons are given by

$$\Gamma_{\tilde{\delta}^{(-)}} = \sum_l(\Gamma_{\tilde{\delta}^{(-)}\to l^-\nu_{lR}} + \Gamma_{\tilde{\delta}^{(-)}\to l^- N_{lL}}) + \Gamma_{\tilde{\delta}^{(-)}\to W_1Z_1},$$

$$\Gamma_{h^{(-)}} = \sum_l(\Gamma_{h^{(-)}\to l^-\nu_{lL}} + \Gamma_{h^{(-)}\to l^- N_{lR}}) + \Gamma_{h^{(-)}\to W_1Z_1},$$

where

$$\Gamma_{\tilde{\delta}^{(-)}\to l^-\nu_{lR}} = \frac{4f_{ll}^2d^2}{16\pi m_{\tilde{\delta}}^3}\left(\frac{m_{\tilde{\delta}}^2 - m_l^2 - m_{\nu_l}^2}{2} - m_l m_{\nu_l}\right) \times w(m_{\tilde{\delta}}^2, m_l^2, m_{\nu_l}^2),$$

$$\Gamma_{\tilde{\delta}^{(-)}\to l^- N_{lL}} = \frac{4f_{ll}^2a^2\beta^2k_0^2}{16\pi m_{\tilde{\delta}}^3(\alpha - \rho_1 - \rho_3/2)^2v_R^2} \times\left(\frac{m_{\tilde{\delta}}^2 - m_l^2 - m_{N_l}^2}{2} - m_l m_{N_l}\right)w(m_{\tilde{\delta}}^2, m_l^2, m_{N_l}^2),$$

$$\Gamma_{\tilde{\delta}^{(-)}\to W_1Z_1} = \frac{(g_Rg_Ls_W^2c_\varphi s_\xi a\beta k_0)^2}{16\pi c_W^2 m_{\tilde{\delta}}^3(\alpha + \rho_1 - \rho_3/2)^2} \times\left[\frac{(m_{\tilde{\delta}}^2 - m_{W_1}^2 - m_{Z_1}^2)^2}{4m_{W_1}^2m_{Z_1}^2} + 2\right]w(m_{\tilde{\delta}}^2, m_{W_1}^2, m_{Z_1}^2),$$

$$\Gamma_{h^{(-)}\to l^-\nu_{lL}} = \Gamma_{\tilde{\delta}^{(-)}\to l^-\nu_{lR}}\left[\sqrt{2}f_{ll}d \longrightarrow \frac{b(h_{ll}'k_2 - h_{ll}k_1)}{k_+}, m_{\tilde{\delta}} \longrightarrow m_h\right],$$

$$\Gamma_{h^{(-)}\to l^- N_{lR}} = \Gamma_{\tilde{\delta}^{(-)}\to l^- N_{lL}}\left[\frac{ak_0}{v_R} \longrightarrow \frac{b(h_{ll}k_2 - h_{ll}'k_1)}{k_+}, m_{\tilde{\delta}} \longrightarrow m_h\right],$$

$$\Gamma_{h^{(-)}\to W_1Z_1} = \Gamma_{\tilde{\delta}^{(-)}\to W_1Z_1}\left[\frac{g_Rg_Ls_W^2c_\varphi s_\xi a\beta k_0}{c_W(\alpha + \rho_1 - \rho_3/2)} \longrightarrow \frac{g_Rg_Lc_\varphi s_\xi bk_-^2}{\sqrt{2}k_+c_W}, m_{\tilde{\delta}} \longrightarrow m_h\right],$$

$$\Gamma_{\Delta_{1,2}} \simeq \frac{f_{\tau\tau}^2m_\tau^2}{8\pi m_{\Delta_{1,2}}}\sqrt{1 - \frac{4m_\tau^2}{m_{\Delta_{1,2}}^2}},$$

$$w(a, b, c) = [a^2 + b^2 + c^2 - 2(ab + ac + bc)]^{1/2}.$$

REFERENCES

1. O. M. Boyarkin and A. N. Sen'ko, Izv. Vyssh. Uchebn. Zaved., Fiz., No. 1, 32 (2000).
2. L. Wolfenstein, Phys. Rev. D **17**, 2369 (1978); S. P. Mikheev and A. Yu. Smirnov, Yad. Fiz. **42**, 1441 (1985) [Sov. J. Nucl. Phys. **42**, 913 (1985)].
3. G. Kane and H. Haber, Phys. Rep. **117**, 75 (1985).
4. M. Singer, J. W. F. Valle, and J. Schechter, Phys. Rev. D **22**, 738 (1980); R. Foot, H. N. Long, and A. Tran Tuan, Phys. Rev. D **50**, R34 (1994).
5. N. G. Deshpande *et al.*, Phys. Rev. D **44**, 837 (1991).
6. G. G. Boyarkina and O. M. Boyarkin, Yad. Fiz. **60**, 683 (1997) [Phys. At. Nucl. **60**, 601 (1997)].
7. O. Karnig and K. Mikaelian, Phys. Rev. D **30**, 1115 (1984).
8. G. Alexsander *et al.*, Phys. Lett. B **370**, 174 (1996).

9. G. López Castro *et al.*, Mod. Phys. Lett. A **6**, 3679 (1991); M. Nowakowski and A. Pilaftsis, Z. Phys. C **60**, 121 (1993).
10. U. Baur and D. Zeppenfeld, Preprint No. MAD/PH/878, UB-HET-95-02 (Madison, 1995).
11. R. N. Mohapatra, Phys. Rev. D **46**, 2990 (1992).
12. Particle Data Group, Eur. Phys. J. C **3**, 1 (1998).
13. F. Stecker *et al.*, in *Proceedings of Workshop on High Energy Neutrino Astrophysics, Honolulu, 1992*, Ed. by V. Stenger *et al.* (World Sci., Singapore, 1993), p. 1.
14. G. G. Boyarkina and O. M. Boyarkin, Yad. Fiz. **61**, 757 (1998) [Phys. At. Nucl. **61**, 683 (1998)].
15. T. G. Rizzo, Phys. Lett. B **116**, 23 (1982); O. M. Boyarkin and D. Rein, Phys. Rev. D **53**, 361 (1996).
16. R. A. Alanakyan, Phys. Lett. B **402**, 130 (1997).
17. G. G. Boyarkina and O. M. Boyarkin, Eur. Phys. J. C **13**, 99 (2000).
18. G. G. Boyarkina and O. M. Boyarkin, in *Proceedings of Eighth Lomonosov Conference on Elementary Particle Physics, Moscow, 1997*, Ed. by A. Studenikin (Interregional Centre for Advanced Studies, Moscow, 1998), p. 321; Izv. Vyssh. Uchebn. Zaved., Fiz., No. 11, 83 (1998).
19. R. N. Mohapatra, Fortschr. Phys. **31**, 185 (1983).
20. R. M. Francis *et al.*, Phys. Rev. D **43**, 2369 (1991).

Translated by A. Isaakyan

Physics of Atomic Nuclei, Vol. 64, No. 2, 2001, pp. 318–325. Translated from Yadernaya Fizika, Vol. 64, No. 2, 2001, pp. 367–375.

ELEMENTARY PARTICLES AND FIELDS
Theory

Parameters *S*, *T*, and *U* of Radiative Corrections and Masses of Scalar Leptoquarks in the Minimal Model Featuring Four-Color Symmetry

A. D. Smirnov*

Yaroslavl State University, ul. Sovetskaya 14, Yaroslavl, 150000 Russia

Received December 21, 1999; in final form, March 23, 2000

Abstract—The contributions to the parameters *S*, *T*, and *U* of radiative corrections are discussed within the minimal model featuring four-color symmetry of the Pati–Salam type. A numerical analysis of these contributions is given for the Higgs mechanism of mass generation for scalar leptoquarks and the simplest version of scalar-leptoquark mixing. It is shown that up-to-date experimental data on *S*, *T*, and *U* are compatible with the existence of relatively light scalar leptoquarks (of masses about 1 TeV or below), still lighter scalar leptoquarks (of masses below 1 TeV) improving the agreement of theoretical results with experimental data on *S*, *T*, and *U*.

1. INTRODUCTION

At present, the Standard Model (SM) of electroweak and strong interactions, which is based on the $SU_c(3) \times SU_L(2) \times U(1)$ group, is considered as a reliable theoretical basis for describing the interactions of quarks, leptons, and gauge fields at energies of present-day colliders. At the same time, it is of interest to investigate those versions of new physics beyond the SM (supersymmetry, left–right symmetry, etc.) that could manifest themselves with increasing energy of colliding particles.

Possible versions of new physics include that which is based on four-color symmetry between quarks and leptons of the Pati–Salam type [1]. The prediction of new gauge particles, vector leptoquarks, mediating a pointlike interaction between quarks and leptons and having masses about the mass scale M_c of the breakdown of four-color symmetry, is an obvious consequence of this symmetry. Depending of the choice of model, a lower limit on M_c can change from $M_c \sim 10^{12}$ GeV [2] or $M_c \sim 10^5$–10^6 GeV [3] in the Grand Unification models featuring four-color symmetry as an intermediate stage of symmetry breaking to $M_c \sim$ 1000 TeV [4], $M_c \sim 100$ TeV, or even lower value in models where four-color symmetry is primary [4–9].

It is worth noting that four-color symmetry of quarks and leptons can manifest itself not only through vector leptoquarks but also through scalar leptoquarks, whose existence is quite natural in schemes involving four-color symmetry [10–12]. This brings about the question of deducing constraints on the scalar-leptoquark masses from available experimental data. A lower limit of 250 GeV [13] results from nonobservation of these objects in direct-production experiments. At such mass values, the scalar leptoquarks can manifest themselves of present-day accelerators only through radiative corrections. It is of interest to estimate constraints on the scalar-leptoquark masses on the basis of existing data on radiative corrections.

It is well known that, in processes involving light external fermions ($m_f \ll m_Z$), electroweak radiative corrections from new physics are dominated by radiative corrections induced by vacuum polarization (so-called indirect radiative corrections). For the case where the masses of new particles, m_{new}, are much larger than the *Z*-boson mass ($m_{\text{new}} \gg m_Z$), these corrections can be taken into account in terms of three parameters—for example, the Peskin–Takeuchi parameters *S*, *T*, and *U* [14]. For these parameters of new physics, experimental data yield the constraints

$$\begin{aligned} S_{\text{new}}^{\text{exp}} &= -0.16 \pm 0.14(-0.10), \\ T_{\text{new}}^{\text{exp}} &= -0.21 \pm 0.16(+0.10), \\ U_{\text{new}}^{\text{exp}} &= 0.25 \pm 0.24(+0.01), \end{aligned} \qquad (1)$$

where the central values correspond to $m_H = m_Z$, while their variations for $m_H = 300$ GeV are given parenthetically [13]. Note that, by definition, these parameters vanish in the SM:

$$S_{\text{new}}^{\text{SM}} = 0, \quad T_{\text{new}}^{\text{SM}} = 0, \quad U_{\text{new}}^{\text{SM}} = 0. \qquad (2)$$

An analysis reveals that scalar leptoquarks possessing a nontrivial $SU_L(2)$ structure contribute to the parameters *S*, *T*, and *U*, whence it follows that constraints on their masses can be extracted from available data on these parameters. In this connection, it would be of interest to

* e-mail: smirnov@univ.uniyar.ac.ru

find the contributions to the parameters *S*, *T*, and *U* from scalar leptoquarks within a relatively simple gauge model that predicts the existence of such particles.

Here, this program is accomplished within the minimal model featuring four-color symmetry. For the $SU_L(2)$-doublet structure, constraints on the scalar-leptoquark masses are further discussed on the basis of data from (1) on the parameters *S*, *T*, and *U*.

2. SCALAR SECTOR OF THE MODEL

Here use is made of the minimal model featuring four-color quark-lepton symmetry [5, 6]. The model is based on the $SU_V(4) \times SU_L(2) \times U_R(1)$ group, and it is the most economical SM extension featuring four-color quark–lepton symmetry in the number of newly introduced gauge fields. Its fermion sector contains only known quarks and leptons forming $SU_V(4)$ quartets in each generation. With respect to the $SU_L(2) \times U_R(1)$ group, the left-handed fermions are zero-hypercharge doublets, while the right-handed fermions are singlets characterized by the hypercharge $Y_R = \pm 1$ for the upper and lower fermions, respectively.

In addition to the photon, gluons, and the $W^\pm$ and *Z* bosons, the gauge sector contains new particles, color triplets of vector leptoquarks $V^\pm_{\alpha\mu}$ ($\alpha = 1, 2, 3$) with charges of $\pm 2/3$ and an extra neutral *Z*' boson.

In general, the scalar sector of the model contains four multiplets,

$$(4, 1, 1): \Phi^{(1)} = \begin{pmatrix} S^{(1)}_\alpha \\ \dfrac{\eta_1 + \chi^{(1)} + i\omega^{(1)}}{\sqrt{2}} \end{pmatrix},$$

$$(1, 2, 1): \Phi^{(2)}_a = \delta_{a2}\frac{\eta_2}{\sqrt{2}} + \phi^{(2)}_a,$$

$$(15, 2, 1): \Phi^{(3)}_a = \begin{pmatrix} (F_a)_{\alpha\beta} & S^{(+)}_{a\alpha} \\ S^{(-)}_{a\beta} & 0 \end{pmatrix} + \Phi^{(3)}_{15,a} t_{15},$$

$$(15, 1, 0): \Phi^{(4)} = \begin{pmatrix} F^{(4)}_{\alpha\beta} & \dfrac{1}{\sqrt{2}} S^{(4)}_\alpha \\ \dfrac{1}{\sqrt{2}} S^{*(4)}_\beta & 0 \end{pmatrix} + (\eta_4 + \chi^{(4)}) t_{15},$$

which transform according to, respectively, the (4, 1, 1), (1, 2, 1), (15, 2, 1), and (15, 1, 0) representations of the $SU_V(4) \times SU_L(2) \times U_R(1)$ group. Here, $\Phi^{(3)}_{15,a} = \delta_{a2}\eta_3 + \phi^{(3)}_{15,a}$; η_1, η_2, η_3, and η_4 are vacuum expectation values; t_{15} is the 15th generator of $SU_V(4)$ group; $a = 1, 2$ is the $SU_L(2)$ index; and $\alpha, \beta = 1, 2, 3$ are the $SU_c(3)$ color indices.

The $SU_L(2)$-doublet multiplets $\Phi^{(2)}$ and $\Phi^{(3)}$ have Yukawa-type couplings to fermions, whereby the latter acquire masses via spontaneous breakdown of symmetry. Concurrently, the splitting of the quark and lepton masses is achieved in each generation owing to the $\Phi^{(3)}$ multiplet.

The $\Phi^{(3)}$ multiplet contains two scalar-leptoquark doublets $S^{(\pm)}_{a\alpha}$ with SM hypercharge $Y^{\mathrm{SM}}_{S^{(\pm)}} = 1 \pm 4/3$; eight scalar-gluon doublets F_{ja}, $j = 1, 2, \ldots, 8$ with $Y^{\mathrm{SM}}_F = 1$; and the doublet $\Phi^{(3)}_{15,a}$, which, being mixed with the doublet $\Phi^{(2)}_a$ via the superposition

$$\Phi^{(\mathrm{SM})}_a = \Phi^{(2)}_a \cos\beta + \Phi^{(3)}_{15,a} \sin\beta,$$

$$\Phi'_a = -\Phi^{(2)}_a \sin\beta + \Phi^{(3)}_{15,a} \cos\beta,$$

forms the SM doublet

$$\Phi^{(\mathrm{SM})} = \begin{pmatrix} \Phi^{(\mathrm{SM})}_1 \\ \dfrac{\eta + \chi^{(\mathrm{SM})} + i\omega}{\sqrt{2}} \end{pmatrix}$$

with the SM vacuum expectation value $\eta = \sqrt{\eta_2^2 + \eta_3^2} = (\sqrt{2}G_\mathrm{F})^{-1/2} \approx 250$ GeV and one extra scalar doublet

$$\Phi' = \begin{pmatrix} \Phi'_1 \\ \dfrac{\chi' + i\omega'}{\sqrt{2}} \end{pmatrix}.$$

Here, the angle β is determined by the ratio of the vacuum expectation values as $\tan\beta = \eta_3/\eta_2$.

Let us consider the original Lagrangian of the scalar fields

$$L^{\mathrm{scalar}} = (D_\mu \Phi^{(1)}_A)^* D_\mu \Phi^{(1)}_A + (D_\mu \Phi^{(2)}_a)^* D_\mu \Phi^{(2)}_a + \mathrm{tr}((D_\mu \Phi^{(3)}_a)^+ D_\mu \Phi^{(3)}_a) + \mathrm{tr}((D_\mu \Phi^{(4)})^+ D_\mu \Phi^{(4)}). \quad (3)$$

An analysis of this Lagrangian shows that, in addition to the SM Goldstone modes $\Phi^{(\mathrm{SM})}_1$ and ω, the model under consideration also involves the Goldstone modes $\omega^{(1)}$ and

$$S_0 = \left[-\frac{\eta_1}{2} S^{(1)} + \sqrt{\frac{2}{3}} \left(\eta_3 \frac{S^{(+)}_2 + S^{*(-)}_2}{\sqrt{2}} + \eta_4 S^{(4)} \right) \right] \Big/ \sqrt{\frac{\eta_1^2}{4} + \frac{2}{3}(\eta_3^2 + \eta_4^2)}, \quad (4)$$

which are associated with the breakdown of four-color symmetry. Since the mode S_0 is formed by the fields $S_{2\alpha}^{(+)}$, $\overset{*}{S}_{2\alpha}^{(-)}$, $S_\alpha^{(1)}$, and $S_\alpha^{(4)}$ with an electric charge of 2/3, the mixing of these fields is mandatory, and they can be represented as superpositions of the Goldstone mode S_0 and the physical leptoquarks S_1, S_2, and S_3 that have an electric charge of 2/3 and which are orthogonal to this mode. In general, these superpositions are given by

$$\begin{aligned} S_2^{(+)} &= \sum_k C_k^{(+)} S_k, \quad \overset{*}{S}_2^{(-)} = \sum_k C_k^{(-)} S_k, \\ S^{(1)} &= \sum_k C_k^{(1)} S_k, \quad S^{(4)} = \sum_k C_k^{(4)} S_k, \end{aligned} \tag{5}$$

where $C_k^{(\pm)}$, $C_k^{(1)}$, and $C_k^{(4)}$ ($k = 0, 1, 2, 3$) are the elements of the 4×4 unitary mixing matrix.

In the unitary gauge, the Goldstone modes are eliminated,

$$\Phi_1^{(\mathrm{SM})} = 0, \quad \omega = 0, \quad \omega^{(1)} = 0, \quad S_0 = 0;$$

for the physical fields, we then have two triplets of up scalar leptoquarks, $S_{1\alpha}^{(+)}$ and $S_{1\alpha}^{(-)}$, with electric charges of 5/3 and 1/3, respectively; three scalar leptoquarks $S_{k\alpha}$, $k = 1, 2, 3$, with an electric charge of 2/3; eight doublets of scalar gluons, F_{ja} with $Y_F^{\mathrm{SM}} = 1$; the extra $SU_c(3)$-color-singlet doublet Φ' with $Y_{\Phi'}^{\mathrm{SM}} = 1$; the SM Higgs boson $\chi^{(\mathrm{SM})}$; and the scalar fields $\chi^{(1)}$, $\chi^{(4)}$, and $F_j^{(4)}$, $j = 1, 2, \ldots, 8$. An analysis reveals, however, that these scalars, the vector leptoquarks $V^{\pm}$, and the new Z' boson do not contribute to the parameters S, T, and U.

3. SCALAR-SECTOR CONTRIBUTIONS TO THE PARAMETERS S, T, AND U

In general case, the electroweak radiative corrections induced by new physics through vacuum polarization can be described in terms of the corresponding self-energy functions $\Pi_{AA}(k^2)$, $\Pi_{AZ}(k^2)$, $\Pi_{ZZ}(k^2)$, and $\Pi_{WW}(k^2)$ for the photon, the Z boson, and the W boson, respectively. In the case where the masses m_{new} of new particles are much greater than m_Z ($m_{\mathrm{new}} \gg m_Z$), we can approximate these functions by fast convergent power series in k^2 and retain the first two terms in these expansions [14]. We then have six expansion coefficients [because of $U_{\mathrm{em}}(1)$ gauge invariance, $\Pi_{AA}(0) = \Pi_{AZ}(0) = 0$]. Three linear combinations of these coefficients, together with ultraviolet divergences, are absorbed upon renormalizing three input SM parameters (for instance, e^2, $\sin^2\theta_W$, and m_Z), while the remaining three independent combinations can be used as three parameters describing indirect radiative corrections in the approximation being considered. Various sets of such three parameters are presented in the literature; here, we use the Peskin–Takeuchi parameters S, T, and U [14].

The input equations for the Peskin–Takeuchi parameters S, T, and U [14] can be expressed in terms of the coefficients in the expansions of the self-energy functions for the photon, the Z boson, and the W boson as

$$\begin{aligned} \alpha S &= 4 s_W c_W [s_W c_W (\Pi'_{ZZ}(0) - \Pi'_{AA}(0)) \\ &\quad - (c_W^2 - s_W^2)\Pi'_{ZA}(0)], \\ \alpha T &= \frac{1}{c_W^2 m_Z^2}[\Pi_{WW}(0) - c_W^2 \Pi_{ZZ}(0)], \\ \alpha U &= 4 s_W^2 [\Pi'_{WW}(0) - c_W^2 \Pi'_{ZZ}(0) \\ &\quad - c_W^2 \Pi'_{AA}(0) - 2 c_W s_W \Pi'_{ZA}(0)], \end{aligned}$$

where $\Pi_{XY}^{\mu\nu}(k^2) = g^{\mu\nu}\Pi_{XY}(k^2) + (k^\mu k^\nu$ terms) are the self-energy functions for the fields X and Y with $\Pi_{XY}(k^2) = \Pi_{XY}(0) + k^2 \Pi'_{XY}(0) + \ldots$; here, X and Y stand for the fields A_μ, Z_μ, and $W_\mu^{\pm}$, which interact with fermions in a standard way (in what follows, we disregard small Z–Z' mixing). To indirect radiative corrections, the discarded $k^\mu k^\nu$ terms make contributions of order $(m_f/m_Z)^2$, which are very small in the case of light external fermions. It should be emphasized that the formalism of the parameters S, T, and U is appropriate for describing indirect electroweak radiative corrections only if the masses m_{new} of new particles are much greater than the Z-boson mass ($m_{\mathrm{new}} \gg m_Z$). The resulting relative error in the radiative corrections is of order $(m_Z/m_{\mathrm{new}})^2$.

The scalar-gluon doublets F_j, $j = 1, 2, \ldots, 8$, and doublet Φ' interact with the fields A_μ, Z_μ, and $W_\mu^{\pm}$ in a standard way. Their contributions to the parameters S, T, and U can be expressed in terms of the contributions from one scalar doublet Φ with a hypercharge Y_Φ^{SM} [6], which are depicted by the diagrams in Fig. 1, and can be represented as

$$S^{(\Phi)} = -k_\Phi \frac{Y_\Phi^{\mathrm{SM}}}{12\pi} \ln\frac{m_1^2}{m_2^2}, \tag{6}$$

$$T^{(\Phi)} = k_\Phi \frac{1}{16\pi c_W^2 s_W^2 m_Z^2} f_1(m_1, m_2), \tag{7}$$

$$U^{(\Phi)} = k_\Phi \frac{1}{12\pi} f_2(m_1, m_2), \tag{8}$$

where

$$f_1(m_1, m_2) = m_1^2 + m_2^2 - \frac{2 m_1^2 m_2^2}{m_1^2 - m_2^2} \ln\frac{m_1^2}{m_2^2}, \tag{9}$$

$$f_2(m_1, m_2) = -\frac{5m_1^4 + 5m_2^4 - 22m_1^2m_2^2}{3(m_1^2 - m_2^2)^2} + \frac{m_1^6 - 3m_1^4m_2^2 - 3m_1^2m_2^4 + m_2^6}{(m_1^2 - m_2^2)^3}\ln\frac{m_1^2}{m_2^2}, \quad (10)$$

where m_1 and m_2 are the masses of, respectively, the upper and the lower component of the doublet Φ. Here, $Y^{\mathrm{SM}}_{\Phi'} = Y^{\mathrm{SM}}_{F_j} = 1$; we also have $k_{\Phi'} = 1$ and $m_a = m_{\Phi'_a}$ for the multiplet Φ' and $k_\Phi = 8$ and $m_a = m_{F_{ja}}$ for the multiplet F_j.

The scalar-leptoquarks contributions to the parameters *S*, *T*, and *U* have a more complicated form. In addition to the standard interactions of photons, *Z* bosons, and $W^\pm$ bosons with the scalar-leptoquark doublets $S_a^{(\pm)}$ and the gauge interactions

$$L_{X_i^0 S^{(k)} S^{(k)}} = i g_{X_i^0 S^{(k)} S^{(k)}} X^0_{i\mu}(\partial_\mu \overset{*}{S}{}^{(k)}_\alpha S^{(k)}_\alpha - \mathrm{h.c.}), \quad k = 1, 4,$$

$$\sum_{i,j} L_{X_i^0 X_j^0 S^{(k)} S^{(k)}} = \sum_{i,j} g_{X_i^0 S^{(k)} S^{(k)}} g_{X_j^0 S^{(k)} S^{(k)}} X^0_{i\mu} X^0_{j\mu} (\overset{*}{S}{}^{(k)}_\alpha S^{(k)}_\alpha)$$

characterized by gauge coupling constants

$$g_{X_i^0 S^{(1)} S^{(1)}} = g_{X_i^0 S^{(4)} S^{(4)}} = -(2/3)|e|\{1, -t_\mathrm{W}\}, \quad i = 1, 2, \quad (11)$$

where $X^0_{i\mu} = \{A_\mu, Z^0_\mu\}$, with Z^0_μ standing for the *Z* boson interacting with fermions in a conventional way (without allowance for *Z*–*Z*' mixing), we also have the interactions of the fields A_μ, Z_μ, and $W^\pm_\mu$ with the vector and scalar leptoquarks having a charge of 2/3:

$$L_{X_i^0 S_n^{(2/3)} V} = g_{X_i^0 S_n^{(2/3)} V} X^0_{i\mu}[(\overset{*}{S}{}^{(2/3)}_{n\alpha} V_{\alpha\mu}) + \mathrm{h.c.}],$$

$$L_{W S_1^{(+)} V} = g_{W S_1^{(+)} V}[\overset{*}{W}{}^{(+)}_\mu (S^{(+)}_{1\alpha} \overset{*}{V}_{\alpha\mu}) + \mathrm{h.c.}],$$

$$L_{W S_1^{(-)} V} = g_{W S_1^{(-)} V}[\overset{*}{W}{}^{(+)}_\mu (S^{(-)}_{1\alpha} \overset{*}{V}_{\alpha\mu}) + \mathrm{h.c.}].$$

The coupling constants for these interactions are proportional to vacuum expectation values; that is,

$$g_{X_i^0 S^{(2/3)}_{1,2} V} = -\frac{2}{3\sqrt{3}}|e| g_4 \eta_3 \left\{1, \frac{1}{s_\mathrm{W} c_\mathrm{W}}\left(\mp\frac{3}{2} - s_\mathrm{W}^2\right)\right\}, \quad (12)$$

$$g_{X_i^0 S^{(1)} V} = \frac{1}{3}|e| g_4 \eta_1 \{1, -t_\mathrm{W}\}, \quad (13)$$

$$g_{X_i^0 S^{(4)} V} = -\frac{2}{3}\sqrt{2/3}|e| g_4 \eta_4 \{1, -t_\mathrm{W}\}, \quad (14)$$

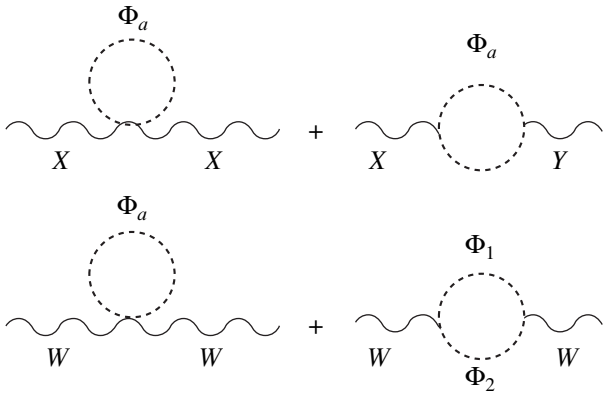

Fig. 1. Diagrams representing the contributions to the parameters *S*, *T*, and *U* from the scalar gluons F_j and an extra doublet Φ' ($\Phi_a = \Phi'_a$, F_{ja}, where $a = 1, 2$, $j = 1, 2, \ldots, 8$, and *X* and *Y* stand for a photon or a *Z* boson).

$$g_{W S_1^{(\pm)} V} = \mp\sqrt{2/3} g_2 g_4 \eta_3, \quad (15)$$

where $S^{(2/3)}_{n\alpha} = \{S^{(+)}_{2\alpha}, \overset{*}{S}{}^{(-)}_{2\alpha}, S^{(1)}_\alpha, S^{(4)}_\alpha\}$, $n = 1, 2, 3, 4$, are scalar leptoquark fields with a charge of 2/3. These fields are expressed in terms of the fields $S_{k\alpha}$ ($k = 1, 2, 3$) of physical leptoquarks with a charge of 2/3 by means of Eq. (5). This leads to interactions of the fields $X^0_{i\mu}$ with physical leptoquarks. The emerging coupling constants $g_{X_i^0 S_1^{(\pm)} S_1^{(\pm)}}$, $g_{W S_1^{(\pm)} S_k}$, $g_{X_i^0 S_k S_l}$, $g_{X_i^0 S_k V}$, and $g_{W S_1^{(\pm)} V}$ are determined by the standard interactions of photons, *Z* bosons, and $W^\pm$ bosons with the scalar-leptoquark doublets $S_a^{(\pm)}$ and by Eqs. (11)–(15) and (5). As a result, the coupling constant $g_{Z^0 S_k V}$ (as well as $g_{W S_1^{(\pm)} V}$) proves to be proportional to the vacuum expectation value η_3, while $g_{A S_k V}$ vanishes ($g_{A S_k V} = 0$) in the unitary gauge.

Figure 2 shows the self-energy diagrams describing the contributions to the parameters *S*, *T*, and *U* from the leptoquarks. Omitting the details of the calculations, we present the calculated contributions $S^{(\mathrm{LQ})}$, $T^{(\mathrm{LQ})}$, and $U^{(\mathrm{LQ})}$ from the leptoquarks to the parameters *S*, *T*, and *U*. They are given by

$$S^{(\mathrm{LQ})} = \frac{n_c}{12\pi}\left\{-\sum_{+,-}\sum_k \left|C_k^{(\pm)}\right|^2 Y^{\mathrm{SM}}_\pm \ln\frac{m_\pm^2}{m_k^2} + \frac{1}{2}\sum_k\sum_l B_{kl} f_2(m_k, m_l) + \xi^2\left[\sum_k |C_{1k}|^2 \times\left(-12\frac{m_V^2 f_1(m_k, m_V)}{(m_k^2 - m_V^2)^2} + f_2(m_V, m_k)\right)\right.\right. \quad (16)$$

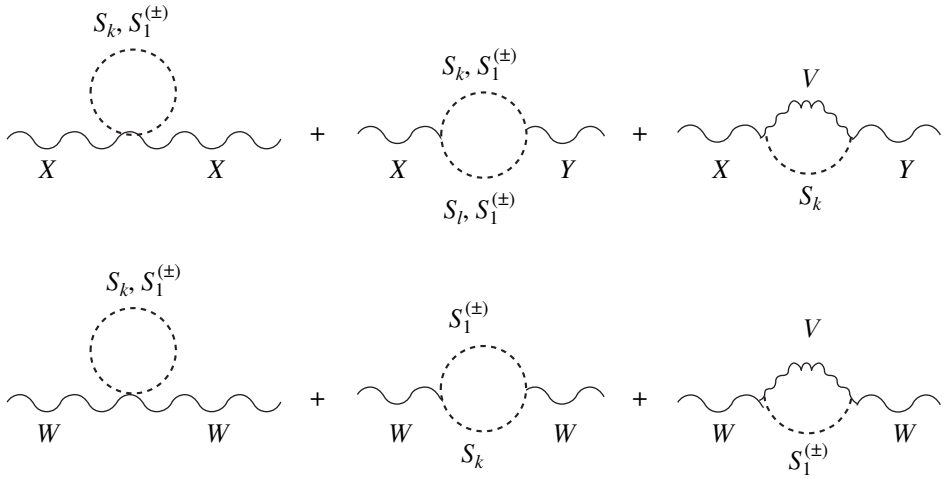

Fig. 2. Diagrams representing the contributions to the parameters S, T, and U from the scalar leptoquarks $S_1^{(\pm)}$ and S_k, $k, l = 1, 2, 3$ (V is a vector leptoquark, and X and Y stand for a photon or a Z boson).

$$+\frac{1}{2}\sum_{+,-}\ln\frac{m_V^2}{m_\pm^2}-\frac{2}{3}\ln\frac{m_+^2}{m_-^2}\Bigg]\Bigg\},$$

$$T^{(\mathrm{LQ})} = \frac{n_c}{16\pi s_\mathrm{W}^2 c_\mathrm{W}^2 m_Z^2}\Bigg\{\sum_{+,-}\sum_k\left|C_k^{(\pm)}\right|^2 f_1(m_\pm, m_k)$$

$$-\frac{1}{2}\sum_k\sum_l B_{kl} f_1(m_k, m_l)+\xi^2\sum_{+,-}\sum_k|C_{2k}|^2 \qquad (17)$$

$$\times\left[\frac{1}{2}(f_1(m_\pm, m_V)-f_1(m_k, m_V))+4m_V^2 f_3(m_\pm, m_k; m_V)\right]\Bigg\},$$

$$U^{(\mathrm{LQ})} = \frac{n_c}{12\pi}\Bigg\{\sum_{+,-}\sum_k\left|C_k^{(\pm)}\right|^2 f_2(m_\pm, m_k)$$

$$-\frac{1}{2}\sum_k\sum_l B_{kl} f_2(m_k, m_l)+\xi^2\sum_{+,-}\sum_k|C_{2k}|^2$$

$$\times\left[\frac{1}{2}(f_2(m_\pm, m_V)-f_2(m_k, m_V))\right.$$

$$\left.-6m_V^2\left(\frac{f_1(m_\pm, m_V)}{(m_\pm^2-m_V^2)^2}-\frac{f_1(m_k, m_V)}{(m_k^2-m_V^2)^2}\right)\right]\Bigg\}, \qquad (18)$$

where $f_1(m_1, m_2)$ and $f_2(m_1, m_2)$ are defined by Eqs. (9) and (10) and where

$$f_3(m_1, m_2; m_V) = \frac{m_1^2 m_2^2\ln(m_1^2/m_2^2)+m_V^2(-m_1^2\ln(m_1^2/m_V^2)+m_2^2\ln(m_2^2/m_V^2))}{(m_1^2-m_V^2)(m_2^2-m_V^2)}.$$

In Eqs. (16)–(18), we have also used the notation

$$B_{kl} = \left|\overset{*}{C}{}_k^{(+)}C_l^{(+)}-\overset{*}{C}{}_k^{(-)}C_l^{(-)}\right|^2,$$

$$C_k^{(\pm)} = \frac{1}{\sqrt{2}}(\sqrt{1-\xi^2}C_{1k}\pm C_{2k}),\quad k, l = 1, 2, 3,$$

$$\xi^2 = \frac{2}{3}\eta_3^2/\left(\eta_1^2/4+\frac{2}{3}(\eta_3^2+\eta_4^2)\right) = \frac{2}{3}g_4^2\eta_3^2/m_V^2;$$

$Y_\pm^{\mathrm{SM}} = 1 \pm 4/3$; $n_c = 3$; $m_k = m_{S_k}$, $m_\pm = m_{S_1^{(\pm)}}$, and m_V is the vector-leptoquark mass; g_4 is the $SU_V(4)$ coupling constant; and C_{1k} and C_{2k} are two orthonormalized complex vectors. In general, the vectors C_{1k} and C_{2k} can be parametrized in terms of three mixing angles and three phases; for example,

$$C_{1k} = \{c_{13}c_{12}, c_{13}s_{12}e^{i\delta_{12}}, s_{13}e^{i\delta_{13}}\},$$

$$C_{2k} = \{-c_{23}s_{12}e^{-i\delta_{12}}-s_{23}s_{13}c_{12}e^{i(-\delta_{13}+\delta_{23})},$$

$$c_{23}c_{12}-s_{23}s_{13}s_{12}e^{i(-\delta_{13}+\delta_{12}+\delta_{23})}, s_{23}c_{13}e^{i\delta_{23}}\},$$

where $c_{ij} = \cos\theta_{ij}$ and $s_{ij} = \sin\theta_{ij}$, θ_{ij} and δ_{ij} being the mixing angles and phases. Expressions (16)–(18), which represent the contributions to the parameters S, T, and U from the scalar leptoquarks, differ substan-

tially from expressions (6)–(8), which correspond to the relevant contributions from ordinary scalar doublets.

First, the contributions in (17) and (18) from the scalar leptoquarks to the parameters *T* and *U* are not positive definite because of mixing as given by (5). The mixing of the components of two scalar doublets as a possible mechanism of obtaining negative *T* and *U* values is considered in [15]. In our case, the mixing between the components of the doublets of scalar leptoquarks with a charge 2/3 is due to the presence of the Goldstone mode S_0 in the scalar-leptoquark sector and is an intrinsic feature of the model being considered.

Second, there is a distinction in the case of degenerate scalar-leptoquark masses, $m_k = m_- = m_+ \equiv m_S$, where expressions (16)–(18) yield

$$S^{(\mathrm{LQ})} = \frac{n_c\xi^2}{12\pi}\left[-12m_V^2\frac{f_1(m_S, m_V)}{(m_S^2 - m_V^2)^2} + f_2(m_S, m_V) + \ln\frac{m_V^2}{m_S^2}\right], \quad (19)$$

$$T^{(\mathrm{LQ})} = 0, \quad U^{(\mathrm{LQ})} = 0,$$

whereas the contributions in (6)–(8) to the parameters *S*, *T*, and *U* from ordinary scalar doublets vanish in the case of degenerate masses. It should be noted, however, that, for a large vector-leptoquark mass, the parameter ξ^2 is small, in which case the nonzero contribution in (19) to the parameter *S* is also small. In the particular cases of $m_S \gg m_V$, $m_S = m_V$, and $m_S \ll m_V$, the contribution in (19) becomes $S^{(\mathrm{LQ})} = -5n_c\xi^2/36\pi$, $S^{(\mathrm{LQ})} = -n_c\xi^2/3\pi$, and $S^{(\mathrm{LQ})} = -(n_c\xi^2/12\pi)(41/3 + 2\ln(m_V^2/m_S^2))$, respectively.

Let us consider the case of the simplest mixing, where the fields $S_2^{(+)}$ and $\overset{*}{S}{}_2^{(-)}$ in (5) contain (in addition to the Goldstone mode S_0) only two physical leptoquarks S_1 and S_2—that is, $s_{13} = s_{23} = 0$. Neglecting the small parameter ξ^2, we can then represent the scalar-leptoquark doublets in the form

$$S^{(+)} = \begin{pmatrix} S_1^{(+)} \\ cS_1 + sS_2 \end{pmatrix}, \quad S^{(-)} = \begin{pmatrix} S_1^{(-)} \\ -s\overset{*}{S}_1 + c\overset{*}{S}_2 \end{pmatrix}, \quad (20)$$

where $c = \cos\theta$ and $s = \sin\theta$, θ being the mixing angle ($\theta = \pi/4 - \theta_{12}$, $\theta_{13} = \theta_{23} = 0$). In this case, expressions (16)–(18) are simplified significantly to become

$$S^{(\mathrm{LQ})} = \frac{n_c}{12\pi}\left\{-Y_+^{\mathrm{SM}}\left[c^2\ln\frac{m_+^2}{m_1^2} + s^2\ln\frac{m_+^2}{m_2^2}\right] - Y_-^{\mathrm{SM}}\left[s^2\ln\frac{m_-^2}{m_1^2} + c^2\ln\frac{m_-^2}{m_2^2}\right] + 4c^2s^2 f_2(m_1, m_2)\right\}, \quad (21)$$

$$T^{(\mathrm{LQ})} = \frac{n_c}{16\pi s_{\mathrm{W}}^2 c_{\mathrm{W}}^2 m_Z^2}\{c^2[f_1(m_+, m_1) + f_1(m_-, m_2)] + s^2[f_1(m_+, m_2) + f_1(m_-, m_1)] - 4c^2s^2 f_1(m_1, m_2)\}, \quad (22)$$

$$U^{(\mathrm{LQ})} = \frac{n_c}{12\pi}\{c^2[f_2(m_+, m_1) + f_2(m_-, m_2)] + s^2[f_2(m_+, m_2) + f_2(m_-, m_1)] - 4c^2s^2 f_2(m_1, m_2)\}, \quad (23)$$

where $m_+ = m_{S_1^{(+)}} = m_{5/3}$, $m_- = m_{S_1^{(-)}} = m_{1/3}$, and $m_{1,2} = m_{S_1, S_2} = m_{2/3, 2/3'}$. Hereafter, the indices of 5/3, 1/3, and 2/3 on the masses denote the electric charges of the corresponding scalar leptoquarks.

At θ = 0, expressions (21)–(23) represent the contributions from the scalar-leptoquark doublets at small ξ^2 without their mixing and coincide with expressions (6)–(8) at $Y_\Phi^{\mathrm{SM}} = Y_{S^{(\pm)}}^{\mathrm{SM}}$ and $k_\Phi = n_c$.

4. INTERACTION WITH THE STANDARD-MODEL HIGGS DOUBLET AND SCALAR-LEPTOQUARK MASSES

A first numerical analysis of the contributions in (16)–(18) versus available experimental data on the parameters *S*, *T*, and *U* revealed that some scalar leptoquarks may be rather light (possibly, their masses are not very far from the SM mass scale). Moreover, these leptoquarks can improve the agreement between the experimental data on the parameters *S*, *T*, and *U* with theoretical results if the scalar-leptoquark masses and mixing angle are treated as independent parameters [16]. Below, we present the results of a numerical analysis of the contributions in (16)–(18) for the case where the scalar-leptoquark masses and mixing angle are generated by the Higgs symmetry-breaking mechanism from the scalar potential of scalar-leptoquark interaction with the standard Higgs doublet. At present, this mechanism of generation of scalar leptoquark masses seems the most natural; moreover, it will be shown below that it enables us to reduce the region of admissible values of the adjustable parameters and to obtain new constraints on the scalar-leptoquark masses.

Generally, that part of the scalar potential for scalar leptoquarks which contributes to their masses can be written as

$$V(\Phi^{(\mathrm{SM})}, S) = \sum_{+,-}[m_\pm^{(0)2}(\overset{+}{S}{}^{(\pm)}S^{(\pm)}) + \beta_\pm(\overset{+}{\Phi}{}^{(\mathrm{SM})}\Phi^{(\mathrm{SM})})(\overset{+}{S}{}^{(\pm)}S^{(\pm)}) + \gamma_\pm(\overset{+}{\Phi}{}^{(\mathrm{SM})}S^{(\pm)})(\overset{+}{S}{}^{(\pm)}\Phi^{(\mathrm{SM})})] + [\delta(\overset{+}{\Phi}{}^{(\mathrm{SM})}S^{(+)})(\overset{+}{\Phi}{}^{(\mathrm{SM})}S^{(-)}) + \mathrm{h.c.}], \quad (24)$$

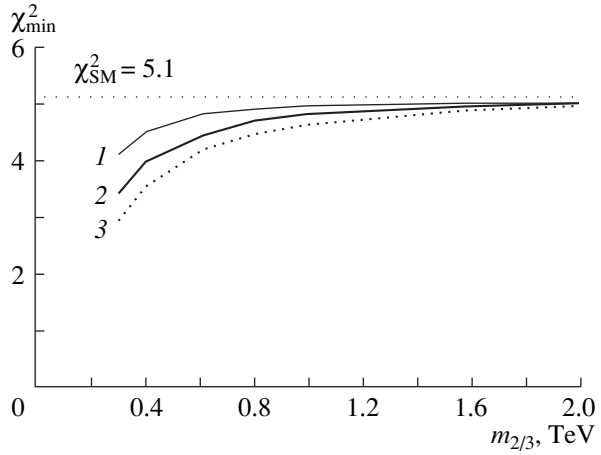

Fig. 3. $\chi^2_{\min}(m_{2/3}, \delta)$ as a function of the mass $m_{2/3}$ of the lightest scalar leptoquark at δ = (*1*) 0.5, (*2*) 1.0, and (*3*) 1.5 for m_H = 300 GeV.

where $m_{\pm}^{(0)2}$ is a parameter that has dimensions of mass squared, while $\beta_{\pm}$, $\gamma_{\pm}$, and δ are dimensionless coupling constants. Upon symmetry breaking, the potential (24) generates the scalar-leptoquark mass term

$$V(\Phi^{(SM)}, S) = \sum_{+,-} m_{\pm}^2 (\overset{*}{S}_1^{(\pm)} S_1^{(\pm)}) + (S_2^{(+)}, \overset{*}{S}_2^{(-)}) * M \begin{pmatrix} S_2^{(+)} \\ \overset{*}{S}_2^{(-)} \end{pmatrix} + \ldots, \quad (25)$$

where $m_{\pm}^2 = m_{\pm}^{(0)2} + \beta_{\pm}\eta^2/2$ are the masses of the up scalar leptoquarks and

$$M = \begin{pmatrix} M_{11} & M_{12} \\ M_{21} & M_{22} \end{pmatrix} = \begin{pmatrix} m_+^2 + \gamma_+\eta^2/2 & \overset{*}{\delta}\eta^2/2 \\ \delta\eta^2/2 & m_-^2 + \gamma_-\eta^2/2 \end{pmatrix} \quad (26)$$

is the mass matrix for the down scalar leptoquarks.

At real δ values, the mass matrix (26) leads to the following masses for the scalar leptoquarks with an electric charge of 2/3 and the following mixing angle θ:

$$m^2_{2/3,\,2/3'} = [M_{11} + M_{22} \mp \sqrt{(M_{11} - M_{22})^2 + 4M_{12}^2}]/2, \quad (27)$$

$$\tan 2\theta = -2M_{12}/(M_{11} - M_{22}). \quad (28)$$

Here, $m_{2/3}$ and $m_{2/3'}$ are the masses of, respectively, the lightest and the heaviest scalar leptoquark.

In what follows, we treat the masses $m_{2/3}$ and $m_{2/3'}$ and the dimensionless coupling constants γ_+, γ_-, and δ in the potential as adjustable parameters and calculate the masses m_+ and m_- and the mixing angle θ on the basis of Eqs. (26)–(28). The values obtained in this way for the masses $m_{2/3}$, $m_{2/3'}$, m_+, and m_- and for the mixing angle θ determine the scalar-leptoquark contributions (21)–(23) to the parameters *S*, *T*, and *U*. Note that, for perturbation theory to be valid, the coupling constants γ_+, γ_-, and δ in the potential (24) must not be overly large, which constrains the allowed region of the adjustable masses and mixing parameters in Eqs. (16)–(18) and (21)–(23).

5. NUMERICAL ANALYSIS AND DISCUSSION OF THE RESULTS

In order to clarify the effect of scalar-leptoquark doublets on the parameters *S*, *T*, and *U*, it is assumed here that the scalar-gluon doublets F_{ja} and the extra doublet Φ'_a are nearly degenerate in mass, so that their contributions to *S*, *T*, and *U* can be disregarded. A numerical analysis of the contributions (21)–(23) of scalar leptoquarks to the parameters *S*, *T*, and *U* was performed on the basis of data in (1) by minimizing the χ^2 functional defined as

$$\chi^2 = \frac{(S - S_{\text{new}}^{\text{exp}})^2}{(\Delta S)^2} + \frac{(T - T_{\text{new}}^{\text{exp}})^2}{(\Delta T)^2} + \frac{(U - U_{\text{new}}^{\text{exp}})^2}{(\Delta U)^2},$$

where *S*, *T*, and *U* are the scalar-leptoquark contributions (21)–(23), while ΔS, ΔT and ΔU are the experimental errors in (1). It should be noted that the values in (2) that correspond to the SM agree with the experimental data in (1) at a level of $\chi^2 = 5.1$ and $\chi^2 = 4.1$ at m_H = 300 GeV and $m_H = m_Z$, respectively.

Minimizing χ^2 at *S*, *T*, and *U* from (21)–(23) by varying $m_{2/3'}$ and the coupling constants γ_+ and γ_- at fixed $m_{2/3}$ and δ, we obtained $\chi^2_{\min}$ as a function of $m_{2/3}$, (the mass of the lightest scalar leptoquark) and δ, $\chi^2_{\min}(m_{2/3}, \delta)$. Its dependence on $m_{2/3}$ at δ = 0.5, 1.0, and 1.5 is displayed in Figs. 3 and 4 at m_H = 300 GeV and $m_H = m_Z$, respectively.

According to these graphs, the experimental data on *S*, *T*, and *U* admit the existence of a scalar leptoquark with a charge of 2/3 in a wide mass range from large mass values, in which case scalar-leptoquark contributions to *S*, *T*, and *U* are small, to a mass $m_{2/3}$ of 1 TeV or below (in this case, the remaining scalar leptoquarks have masses on the same order of magnitude if the coupling constants γ_+, γ_-, and δ are not very large). It is interesting to note that the lighter scalar leptoquarks (of mass below 1 TeV) even improve the agreement between the theoretical results and experimental data—they make negative contributions to *S* and *T*, rendering their values closer to the experimental data in (1), as contrasted against the SM zero values in (2).

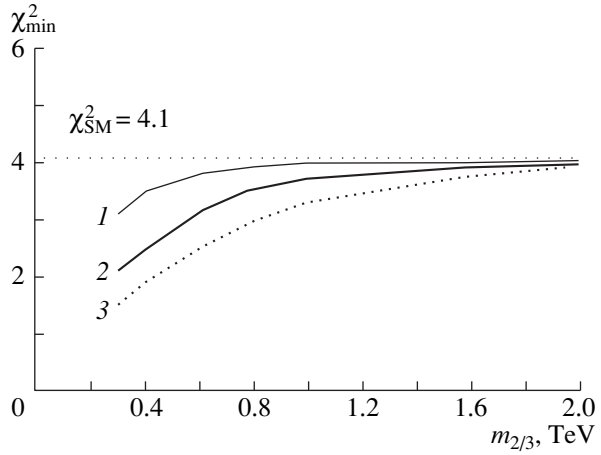

Fig. 4. As in Fig.3, but for $m_H = m_Z$.

By way of example, we indicate that at $\delta = 1$ and

$$m_{2/3} = 300 \text{ GeV}, \quad m_{1/3} = 350 \text{ GeV},$$
$$m_{5/3} = 380 \text{ GeV}, \quad m_{2/3'} = 390 \text{ GeV},$$

it follows from (21)–(23) that

$$S^{(LQ)} = -0.054, \quad T^{(LQ)} = -0.040,$$
$$U^{(LQ)} = -4 \times 10^{-4}.$$

At $m_H = 300$ GeV, these contributions agree with those in (1) at a level of $\chi^2 = 3.5$ (the corresponding SM value is $\chi^2 = 5.1$).

At the same value of $\delta = 1$, the contributions (21)–(23) of the scalar leptoquarks that have the masses

$$m_{2/3} = 300 \text{ GeV}, \quad m_{1/3} = 360 \text{ GeV},$$
$$m_{5/3} = 360 \text{ GeV}, \quad m_{2/3'} = 390 \text{ GeV}$$

are

$$S^{(LQ)} = -0.028, \quad T^{(LQ)} = -0.156,$$
$$U^{(LQ)} = -0.001;$$

these values agree with the data in (1) at $m_H = m_Z$, the relevant χ^2 value being 2.1 to be compared with the SM value of $\chi^2 = 4.1$.

The existence of relatively light scalar leptoquarks (of masses about 1 TeV or below) may be compatible with other experimental data—in particular, with the most stringent constraints on leptoquark masses from nonobservation of rare decays like $K_L^0 \longrightarrow \mu e$ since, in the model being considered, the constants of scalar-leptoquark coupling to quarks and leptons are proportional to the ratio of the quark masses to the SM vacuum expectation value [12] and are therefore small.

6. CONCLUSION

In summary, the contributions to the parameters *S*, *T*, and *U* from the scalar-leptoquark doublets, scalar gluons and an extra scalar doublet have been calculated within the minimal model featuring four-color symmetry.

It has been shown that, in contrast to the contributions from ordinary scalar (or fermion) doublets, the contributions to the parameters *T* and *U* from the scalar-leptoquark doublets are not positive definite in the model because of the mixing of the scalar leptoquark fields having an electric charge of 2/3.

On the basis of available experimental data on the parameters *S*, *T*, and *U*, a numerical analysis of the contributions to *S*, *T*, and *U* from scalar-leptoquark doublets has been performed for the Higgs leptoquark-mass-generation mechanism and the simplest version of leptoquark mixing.

It has also been shown that experimental data on the parameters *S*, *T*, and *U* admit the existence of scalar leptoquarks of masses ranging between large values and about 1 TeV or below and that lighter scalar leptoquarks (of mass below 1 TeV) even slightly improve the agreement between the theoretical results and experimental data in relation to the SM case.

ACKNOWLEDGMENTS

I am grateful to A.V. Povarov for assistance in the preparation of numerical calculations.

This work was supported by the program Universities of Russia: Basic Research (grant no. 1157).

REFERENCES

1. J. C. Pati and A. Salam, Phys. Rev. D **10**, 275 (1974).
2. E. M. Freire, Phys. Rev. D **43**, 209 (1991).
3. G. Senjanovič and A. Sokorac, Z. Phys. C **20**, 255 (1983).
4. R. R. Volkas, Phys. Rev. D **53**, 2681 (1996).
5. A. D. Smirnov, Phys. Lett. B **346**, 297 (1995).
6. A. D. Smirnov, Yad. Fiz. **58**, 2252 (1995) [Phys. At. Nucl. **58**, 2137 (1995)].
7. R. Foot, Phys. Lett. B **420**, 333 (1998).
8. R. Foot and G. Filewood, Phys. Rev. D **60**, 115002 (1999).
9. A. Blumhofer and B. Lampe, Eur. Phys. J. C **7**, 141 (1999).
10. W. Buchmüller, R. Rückl, and D. Wyler, Phys. Lett. B **191**, 442 (1987).
11. J. L. Hewett and T. G. Rizzo, Phys. Rev. D **56**, 5709 (1997).
12. A. V. Povarov and A. D. Smirnov, Yad. Fiz. **64**, 78 (2001) [Phys. At. Nucl. **64**, 74 (2001)].
13. Particle Data Group (C. Caso *et al.*), Eur. Phys. J. C **3**, 1 (1998).
14. M. E. Peskin and T. Takeuchi, Phys. Rev. D **46**, 381 (1992).
15. L. Lavoura and L. F. Li, Phys. Rev. D **48**, 234 (1993).
16. A. D. Smirnov, Phys. Lett. B **431**, 119 (1998).

Translated by S. Slabospitsky

Physics of Atomic Nuclei, Vol. 64, No. 2, 2001, pp. 326–331. Translated from Yadernaya Fizika, Vol. 64, No. 2, 2001, pp. 376–381.

ELEMENTARY PARTICLES AND FIELDS
Theory

Phenomenological Separable Potential of K^+N Interaction for $J \leq 15/2$

A. Ya. Berdnikov, Ya. A. Berdnikov, G. N. Dudchenkov, V. F. Kosmach, and A. P. Shishlo*

St. Petersburg State Technical University, Politekhnicheskaya ul. 29, St. Petersburg, 195251 Russia

Received December 22, 1999; in final form, May 22, 2000

Abstract—A nonlocal separable potential of K^+N interaction in the isospin-0 and isospin-1 S, P, D, …, J scattering channels is constructed. This potential describes satisfactorily the results of the SP92 phase-shift analysis (R. Arndt) at incident-kaon energies in the interval from 0 to 2.4 GeV. The off-shell amplitudes for kaon–nucleon scattering are calculated. They are shown to differ significantly from the commonly used off-shell amplitudes. © *2001 MAIK "Nauka/Interperiodica".*

1. INTRODUCTION

Both on-shell and off-shell amplitudes for scattering on nucleons are required for describing nuclear reactions initiated by strongly interacting probes. The simplest methods for calculating such amplitudes are based on the use of separable potentials. In this study, we propose a phenomenological separable potential of K^+N interaction. This potential, which allows for inelastic effects, reproduces the data of the SP92 phase-shift analysis [1] in the kaon-energy region extending up to 2.4 GeV.

For the isospin-0 and isospin-1 scattering channels, a potential was constructed in [2] that describes K^+N scattering for kaon energies up to 550 MeV in the S, P, and D partial waves. The parameters of this potential were determined from the best fit to the data from the phase-shift analysis reported in [3]. The new potential presented here reproduces the data of the more recent SP92 phase-shift analysis [1] of kaon–nucleon scattering in the S, P, D, F, G, H, I, and J partial waves of the isospin-1 channel and in the S, P, D, F, and G partial waves of the isospin-0 channel.

2. PHENOMENOLOGICAL SEPARABLE POTENTIAL OF K^+N INTERACTION

The on-shell and off-shell amplitudes for the elastic scattering of positive kaons by nucleons, $\hat{t}_\alpha(k, k', E)$, are calculated here as solutions to the Kadyshevsky equation

$$\hat{t}_\alpha(k, k', E) = V_\alpha(k, k') + \frac{1}{4}\int \frac{p^2 dp V_\alpha(k, p)\hat{t}_\alpha(p, k', E)}{E_K(p)E_N(p)(E - E(p) + i\varepsilon)}, \quad (1)$$

where $\varepsilon \longrightarrow 0$; k and k' are the relative momenta of the kaon and the nucleon before and after the scattering event, respectively; α stands for the set of spin–isospin indices; $\hat{t}_\alpha$ is the pseudoelastic amplitude; and E is the total energy of the K^+N system,

$$E(p) = E_K(p) + E_N(p), \quad E_x(p) = \sqrt{m_x^2 + p^2}, \quad x = K, N.$$

Here, m_K and m_N are, respectively, the kaon and the nucleon mass.

The on-shell pseudoelastic amplitude $\hat{t}_\alpha$ can be expressed in terms of the pseudoelastic phase shift $\hat{\delta}_\alpha$ as

$$\hat{t}_\alpha(k, k, E(k)) = -\frac{2E(k)}{i\pi k}(\exp(2i\hat{\delta}_\alpha) - 1).$$

The conventional scattering amplitude t_α is expressed in terms of the pseudoelastic amplitude $\hat{t}_\alpha$ as

$$t_\alpha(k, k', E) = \sqrt{\hat{\eta}_\alpha(k)\hat{\eta}_\alpha(k')}\hat{t}_\alpha(k, k', E),$$

where $\hat{\eta}_\alpha$ is the pseudoelastic inelasticity parameter.

The pseudoelastic parameters $\hat{\delta}_\alpha$ and $\hat{\eta}_\alpha$ are related to the conventional phase shift δ_α and the inelasticity parameter η_α, which are determined from a phase-shift analysis, by the equation

$$a = \frac{\eta_\alpha \exp(2i\delta_\alpha) - 1}{2i} = \hat{\eta}_\alpha \frac{\exp(2i\hat{\delta}_\alpha) - 1}{2i}. \quad (2)$$

The interaction potential in Eq. (1) is taken in the separable form (the index α is suppressed)

$$V(k, k') = \sum_{i=1}^{r} \lambda_i g_i(k) g_i(k'), \quad (3)$$

where r is the rank of the potential, λ_i are the parameters of the potential, and $g_i(k)$ are its form factors.

* e-mail: shishlo@twonet.stu.neva.ru

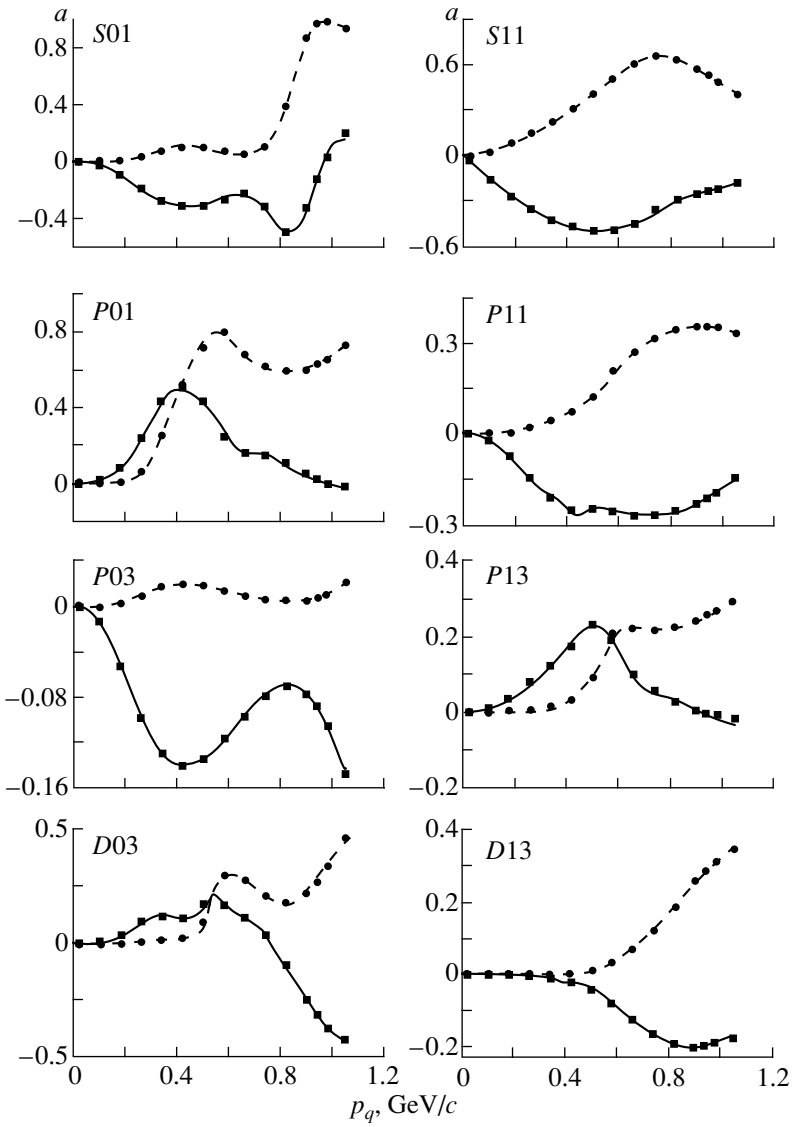

Fig. 1. Amplitudes a for K^+N scattering that are determined by expression (2) for the $S01$, $S11$, P, $D03$, and $D13$ partial waves (the channel index $L\{T, 2J\}$, where L is the spectroscopic notation for the orbital angular momentum, T is the isospin of the K^+N system, and J is its total angular momentum, is indicated in the figure) versus p_q (relative momentum of the kaon and the nucleon). Points represent the results of the SP92 phase-shift analysis [1]: (■) real parts of the amplitudes and (●) imaginary parts of the amplitudes. The solid and the dashed curves show, respectively, the real and the imaginary parts of the amplitudes calculated with the potential (3).

We determined the potential parameters through a two-step procedure. By solving the inverse scattering problem [4], we first calculated the form factors for the K^+N-scattering channels where the phase shift is of constant sign. Here, the rank of the potential was assumed to be equal to unity. After that, we parametrized the form factors $g_i(k)$ as

$$g_i(k) = \sqrt{\frac{E_K(k)E_N(k)}{m_K m_N}}k^l\left(\frac{1}{(k^2+\beta_{i1}^2)^{l+i}} + \frac{\gamma_i k^2}{(k^2+\beta_{i2}^2)^{l+i+1}} + \sum_{j=1}^{2} a_{ij}\exp\left\{-\left(\frac{k-b_{ij}}{c_{ij}}\right)^2\right\}\right), \quad (4)$$

where i is the rank number; l is the orbital angular momentum of the scattering channel; and β_{i1}, β_{i2}, γ_i, a_{ij}, b_{ij}, and c_{ij} are the potential parameters. At the second step, the potential parameters were varied in order to obtain the best fit to data from a phase-shift analysis.

We failed to achieve a satisfactory description of these data in the $D05$, $D15$, $I113$, and $J115$ channels. This was either because of the alternating sign of the relevant phase shift or because of its complicated energy dependence. For these channels, the procedure for determining the parameters started from the second step. We set the rank of the potential to the lowest possible value of two and discarded the last two Gaussian

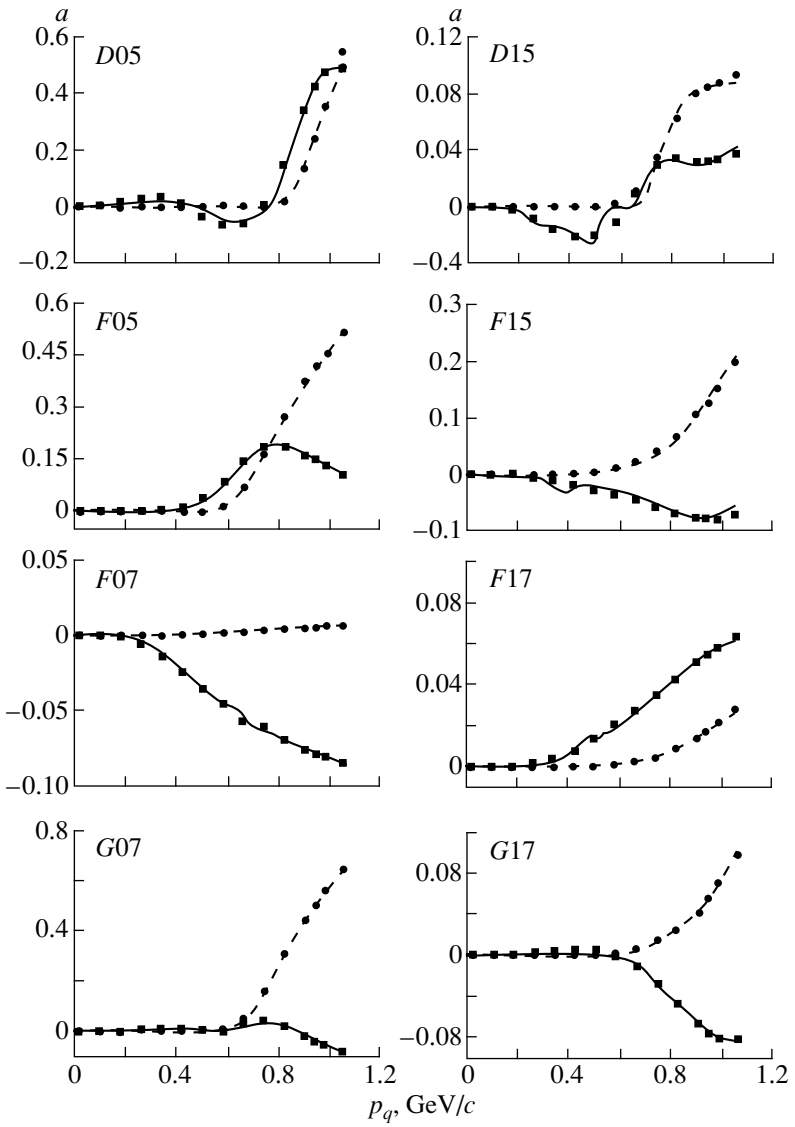

Fig. 2. As in Fig. 1, but for the partial-wave amplitudes $D05$, $D15$, F, $G07$, and $G17$.

terms in expression (4) for the form factors; the parameters a_{ij} in (4) were set to zero.

Tables 1 and 2 display the potential and the form-factors parameters for potentials of rank one and two, respectively.

Figures 1–3 demonstrate the quality of our fits to the data from the phase shift analysis reported in [1].

3. OFF-SHELL BEHAVIOR OF THE K^+N SCATTERING AMPLITUDES

At the moment, much attention is being given to the problem of possible modifications to the nucleon dimensions and properties in nuclear matter. Such information can be obtained, in particular, by studying the energy dependence of the ratios of the elastic cross sections for various types of target nuclei. The results obtained from an analysis of elastic K^+ scattering by light and extremely light nuclei suggest a possible modification to kaon–nucleon amplitudes in light nuclei [5, 6]. Among factors that affect the interpretation of these results, we would like to mention a correct description of the off-shell behavior of kaon–nucleon scattering amplitudes.

In describing the off-shell behavior of K^+N scattering amplitudes, use was made in [5, 6] of the approximation of the rank-one separable potential

$$t(k, k', k_0) = \frac{g(k)g(k')}{g^2(k_0)}t(k_0, k_0, k_0), \qquad (5)$$

where $g(p) = \exp(-p^2/\Lambda^2)$ and $\Lambda = 1.0$ GeV/c.

There, the form and the parameters of the form factors in (5) were assumed to be independent of the scat-

Table 1. Parameters of the rank-one K^+N potentials (the scattering channel index is $L\{T, 2J\}$, where L is the spectroscopic notation for the orbital angular momentum l, T is the isospin of K^+N system, and J is the total angular momentum of the system)

Channel $r = 1$	λ, GeV^{2l+2} a_1, GeV^{-2l-2}	γ b_1, GeV c^{-1}	β_1, GeV c^{-1} c_1, GeV c^{-1}	β_2, GeV c^{-1} a_2, GeV^{-2l-2}	b_2, GeV c^{-1}	c_2, GeV c^{-1}
$S01$	4.834×10^{-3}	24.717	0.2847	0.4009		
	–18.568	0.5394	0.4070	18.483	0.8825	0.1420
$P01$	–70.397	0.2479	1.7224	1.1814		
	2.200×10^{-2}	1.7259	0.3857	0.1809	-7.019×10^{-3}	0.4548
$P03$	1.4039	2.5351	0.6605	1.6746		
	–0.4797	0.7416	0.2893	–1.093	0.3372	0.2973
$D03$	-1.000×10^5	0.2393	6.8954	1.5765		
	3.537×10^{-2}	1.440×10^{-2}	0.2689	2.659×10^{-3}	0.5714	0.1532
$F05$	-1.000×10^3	1.5928	2.0019	1.2168		
	1.645×10^{-3}	1.7986	0.3996	2.766×10^{-2}	0.3782	0.3686
$F07$	1.5555	9.9950	0.7067	1.7889		
	0.6849	1.3427	0.1799	0.1884	0.9264	0.2676
$G07$	-5.000×10^5	–1.1046	1.6955	1.9788		
	2.811×10^{-3}	0.5112	0.2270	3.805×10^{-1}	0.2074	0.1099
$G09$	1.4824	23.000	0.7892	1.2995		
	19.999	5.608×10^{-3}	0.2498	2.201×10^{-2}	1.6172	0.5410
$S11$	1.6940	1.3866	0.5290	0.7539		
	–0.4603	0.9482	0.2162	0.6383	0.9461	0.4484
$P11$	11.402	2.9983	0.7857	2.9051		
	–0.4229	0.3579	0.1259	-4.631×10^{-2}	0.7433	0.1638
$P13$	–1.1561	0.1294	1.7583	1.3714		
	1.8513	4.367×10^{-4}	0.3530	0.2348	0.6529	0.1946
$D13$	7.000×10^3	1.1232	3.5188	0.7304		
	–0.3344	0.3813	0.4932	–0.1796	0.3249	6.806×10^{-2}
$F15$	2.500×10^2	1.9987	0.8344	1.9057		
	4.1760	5.334×10^{-3}	0.8157	–0.2282	0.1741	1.648×10^{-2}
$F17$	–850.0	1.0	1.3476	4.0		
	1.665×10^{-3}	1.0988	0.4448	1.829×10^{-2}	5.468×10^{-2}	0.3007
$G17$	7.0×10^4	1.1001	1.3887	2.1991		
	-6.737×10^{-4}	1.4508	4.0438	1.828×10^{-2}	0.5520	0.1572
$G19$	-6.0×10^2	4.0	1.3372	2.4989		
	4.603×10^{-3}	0.7749	0.3698	7.426×10^{-3}	0.6330	0.1523
$H19$	20.191	28.155	2.6200	0.8594		
	0.2437	0.9121	0.4145	–3.0451	0.4836	0.1272
$H111$	–15.003	18.983	1.2379	0.9408		
	–0.6877	0.5132	0.1862	–0.5960	0.5762	0.3658
$I111$	21.100	27.399	2.2300	1.1276		
	-1.158×10^{-4}	0.8931	0.4995	-6.456×10^{-2}	0.3051	0.5020
$J113$	1.1×10^5	33.381	11.0	1.0034		
	0.8369	7.155×10^{-2}	0.2064	–0.8369	0.4791	8.570×10^{-2}

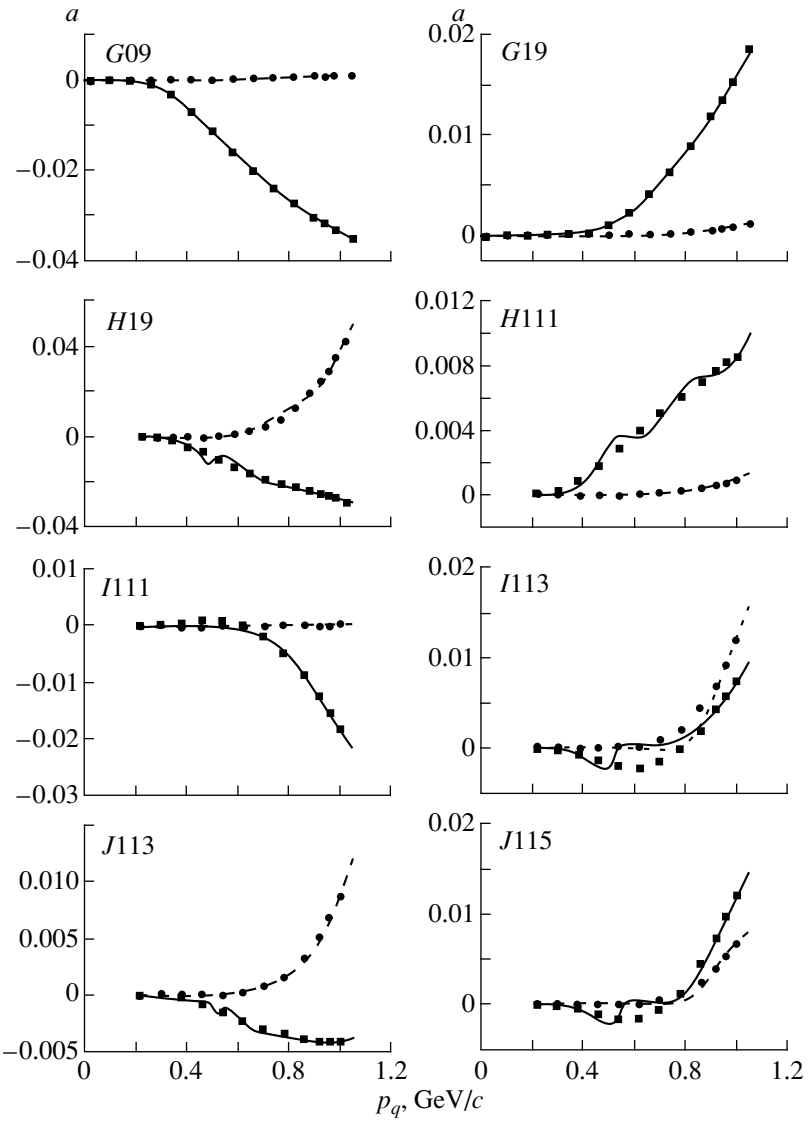

Fig. 3. As in Fig. 1, but for the partial-wave amplitudes *G*09, *G*19, *H*19, *H*111, *I*111, *I*113, *J*113, and *J*115.

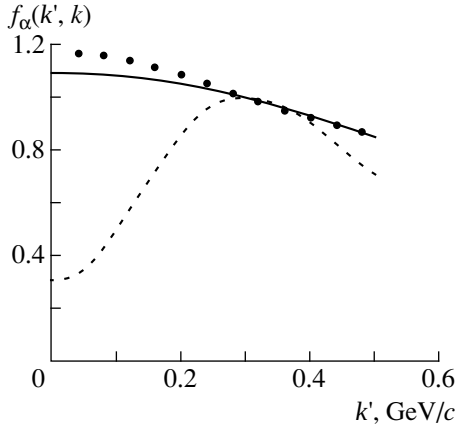

Fig. 4. Noyes–Kowalski function for K^+N elastic-scattering amplitudes (k = 300 MeV/c). Points represent the function given by expression (5). The solid and the dashed curve depict the functions calculated with the potential (3) in the *S*11 and the *S*01 scattering channel, respectively.

tering channel. For this parametrization of the off-shell behavior, the projectile–nucleon amplitudes change slowly with increasing distance from the mass shell; therefore, it is possible to neglect the off-shell contribution to kaon–nucleon interaction in a nucleus [5, 6].

In the present study, we analyze the off-shell behavior of the K^+N amplitudes $t_\alpha(k', k, k)$ found for the separable potential (3). We have calculated the half-off-shell Noyes–Kowalski functions

$$f_\alpha(k', k) = t_\alpha(k', k, k)/t_\alpha(k, k, k).$$

Recall that α stands for the set of spin–isospin indices of the channel.

The resulting functions f_α are strongly different for different scattering channels. Only in the *S*11 channel of K^+N scattering does the function f_α exhibits behavior similar to that prescribed by Eq. (5); for the remaining

Table 2. Parameters of the rank-two K^+N potentials (the notation is identical to that in Table 1)

Channel $r = 2$	λ_1, GeV^{2l+2} λ_2, GeV^{2l+4}	γ_1 γ_2	β_{11}, GeV c^{-1} β_{21}, GeV c^{-1}	β_{12}, GeV c^{-1} β_{22}, GeV c^{-1}
$D05$	−20.896	−4.5699	0.9506	1.0160
	11.992	0.1450	1.9281	0.5952
$D15$	−20.829	−3.6733	0.9199	0.8974
	11.997	1.0081×10^{-2}	1.4362	0.3704
$I113$	1.9912	10.335	0.7535	0.9181
	-3.0×10^5	6.3951	1.6472	1.2428
$J115$	3.002×10^2	−3.0788	0.8708	1.2756
	-1.0×10^5	4.8220	1.2382	1.0890

channels, the functions f_α are nonmonotonic and differ significantly from unity. By way of example, the function f_α determined by expression (5) is shown in Fig. 4, along with those that are calculated with the potential (3) for the $S11$ and the $S01$ channel.

4. CONCLUSION

The proposed separable potential of K^+N interaction describes satisfactorily the data from the modern phase-shift analysis SP92 [1].

This potential predicts different types of off-shell behavior for the partial amplitudes of kaon–nucleon scattering. A customary description of this behavior presumes the same form in all partial-wave channels [5, 6], but this is true only in the primary-energy region dominated by the contribution of the $S11$ partial wave.

REFERENCES

1. J. S. Hyslop, R. A. Arndt, L. D. Roper, *et al.*, Phys. Rev. D **46**, 961 (1992).
2. Ya. A. Berdnikov and A. P. Shishlo, Yad. Fiz. **49**, 528 (1989) [Sov. J. Nucl. Phys. **49**, 330 (1989)].
3. B. R. Martin *et al.*, Nucl. Phys. B **94**, 413 (1975).
4. C. Coronis and R. H. Landau, Phys. Rev. C **24**, 605 (1981).
5. M. F. Jiang and D. J. Ernst, Phys. Rev. C **51**, 857 (1995).
6. L. Kurth Kerr, B. C. Clark, S. Hama, *et al.*, nucl-th/9801003.

Translated by M. Kobrinsky

Physics of Atomic Nuclei, Vol. 64, No. 2, 2001, pp. 332–335. From Yadernaya Fizika, Vol. 64, No. 2, 2001, pp. 382–385.

ELEMENTARY PARTICLES AND FIELDS
Theory

Search for Quark Compositeness at the LHC: Transverse-Energy Distributions of Jets*

Z. U. Usubov

Joint Institute for Nuclear Research, Dubna, Moscow oblast, 141980 Russia

Received December 2, 1999; in final form, June 5, 2000

Abstract—Quark substructure effects that should manifest themselves at LHC energies are examined. The inclusive jet transverse-energy spectrum as would be observed by the ATLAS detector is predicted. The effect of the choice of parton distribution function and calorimeter nonlinearity on the compositeness effect is studied. The sensitivity of data to the quark-compositeness scale for low and high LHC luminosity is discussed. © *2001 MAIK "Nauka/Interperiodica".*

The test of QCD predictions provides a useful tool in probing the underlying dynamics and in seeking new physics such as quark compositeness and the existence of axigluons or other new particles. Measurement of the inclusive jet cross section and study of the dijet mass spectrum and angular distributions open a new window to this field. A relationship between jets and partons has been clearly demonstrated in high-statistics LEP, Tevatron, and HERA experiments. The existence of a quark substructure would appear as an excess of the high-P_t jets over the level predicted by QCD or as dijet angular distributions more isotropic than those expected from a pointlike-quark theory. Dijet angular distributions were studied in the CDF [1] and D0 [2] experiments at a center-of-mass energy of 1.8 TeV. The highest E_t reached so far at the Tevatron, about 500 GeV, corresponds to a distance scale of 10^{-17} cm. The experimental data were compared with QCD predictions, including compositeness. No evidence of quark substructure was found. Previous studies of dijet invariant-mass spectrum reported by UA1 [3] and UA2 [4] at $\sqrt{s}$ = 630 GeV and by CDF [5] also yielded data that were consistent with QCD predictions. The CDF [6] and D0 [7] results on high-mass Drell–Yan cross sections set a lower limit on the quark–electron compositeness scale about 5.5 TeV. From the ratio of charged-current to neutral-current cross sections measured in the CCFR fixed-target neutrino experiment [8] at Tevatron, a limit of about 8 TeV on Λ was achieved.

Searches for a quark substructure will be continued at future hadron colliders. We investigate here the effect of quark compositeness as would be seen by ATLAS [9] at the LHC. To simulate a scenario with a quark substructure, the event generator PYTHIA-5.7 [10] has been used. This has enabled one to use a simple phenomenological approach of contact interactions between quark constituents with a compositeness scale Λ [11], where the sign of the effective Lagrangian for a flavor diagonal definite-chirality current is positive (destructive interference) or negative (constructive interference). The data simulated within the Standard Model (SM) are compared with those obtained under the assumption of quark compositeness. The simulated event sample included the following hard-scattering subprocesses: qq, qg, gg, $g\gamma$, $q\gamma$, and $\gamma\gamma$. The γ^*/Z-, W-, and tt-production subprocesses are also allowed. To collect a sufficiently large number of events with high-P_t jets in a reasonable central processor unit time, a cut on the transverse momentum of the hard scattering subprocess was set to 1 and 1.2 TeV for low and high luminosity, respectively. Initial- and final-state QCD and QED radiation, fragmentation, and decay of partons and particles, as well as multiple interactions, were allowed. First-order running-α_s calculations were applied. The Λ_{QCD} value was chosen according to the parton-distribution-function parametrizations used in PYTHIA. For the Q^2 scale in the $2 \longrightarrow 2$ hard-scattering process, $Q^2 = (m_{t1}^2 + m_{t2}^2)/2$ was used. The detector performance was simulated by using the ATLFAST package [12], which provides a reliable estimate for the detector response to hadronic jets. Jets were reconstructed with ATLFAST using the standard procedure of summing the energy deposited in a cone of radius $\Delta R = \sqrt{\Delta\eta^2 + \Delta\phi^2} = 0.7$. All calorimeter cells with $E_t >$ 1.5 GeV were taken as possible initiators of clusters. The total E_t summed over all cells in a cone ΔR should be larger than 15 GeV. Jets were reconstructed down to $|\eta| \le 5.0$.

Figures 1 and 2 show the effect of compositeness on the inclusive jet energy spectrum for an integrated luminosity of 30 fb^{-1}. The case of constructive interference is shown; the destructive-interference case is similar. Only events with two jets of $E_t > 400$ GeV are included. The deviation from SM prediction under the assumption that all quarks are composite is shown.

* This article was submitted by the author in English.

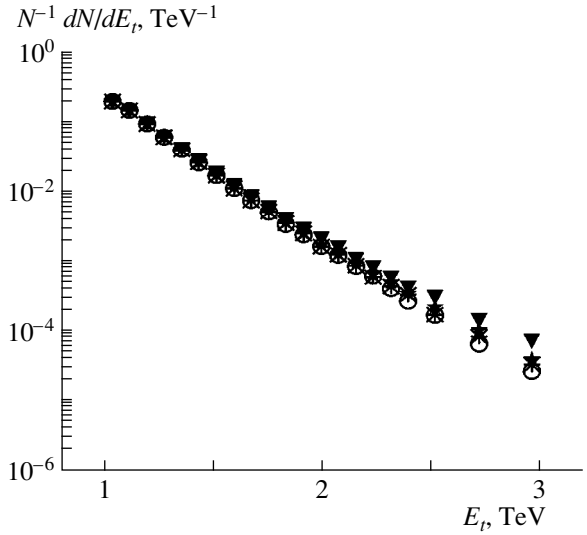

Fig. 1. E_t distribution for two leading jets according to the SM prediction (open circles) and with the effect of quark compositeness to the scales indicated: closed triangles, closed stars, and crosses correspond to $\Lambda^-_{\rm all}$ = 15, 20, and 25 TeV, respectively. The integrated luminosity was assumed to be 30 fb^{-1}.

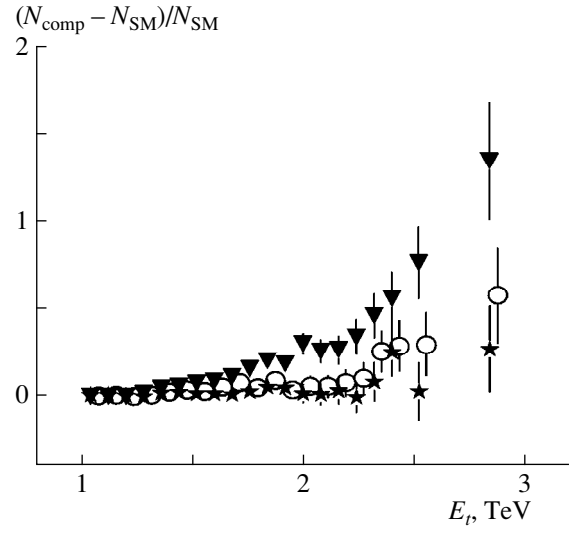

Fig. 2. Difference of the SM prediction and the effect of compositeness on the jet E_t distribution normalized to the SM rate. Closed triangles, open circles, and closed stars correspond to $\Lambda^-_{\rm all}$ = 15, 20, and 25 TeV, respectively. The errors correspond to an integrated luminosity of 30 fb^{-1}.

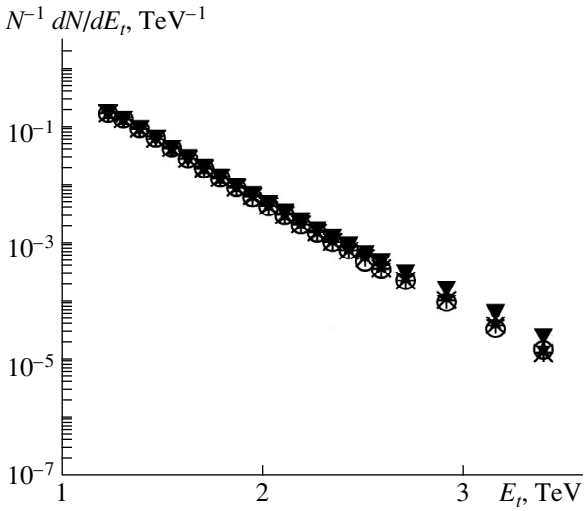

Fig. 3. As in Fig. 1, but for L = 300 fb^{-1}. Closed triangles, closed stars, and crosses correspond to $\Lambda^-_{\rm all}$ = 20, 30, and 40 TeV, respectively.

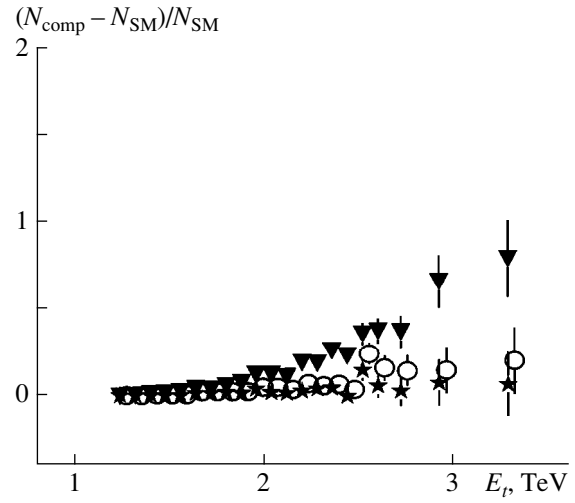

Fig. 4. As in Fig. 2, but for L = 300 fb^{-1}. Closed triangles, open circles, and closed stars correspond to $\Lambda^-_{\rm all}$ = 20, 30, and 40 TeV, respectively.

These figures demonstrate that the deviation is significant for the largest E_t values. Figures 3 and 4 show the effects on the jet E_t distribution for an integrated luminosity of 300 fb^{-1} and larger values of Λ.[1)]

The effects of compositeness could be masked by uncertainties in the parton distribution functions. Figure 5 shows a band corresponding to the results obtained with all the parton distribution functions in PYTHIA-5.7 (except for D01 and EHLQ1, which have large inconsistencies with present data). For this case, $\Lambda^-_{\rm all}$ = 15 TeV.

The nonlinear response of the hadron calorimeter can affect the observed difference between the SM and the compositeness scenario or may fake a compositeness signal. To study this effect, we considered a non-

[1)]Integrated luminosities of 30 (300) fb^{-1} should be collected after 3 (10) yr of data accumulation at the LHC.

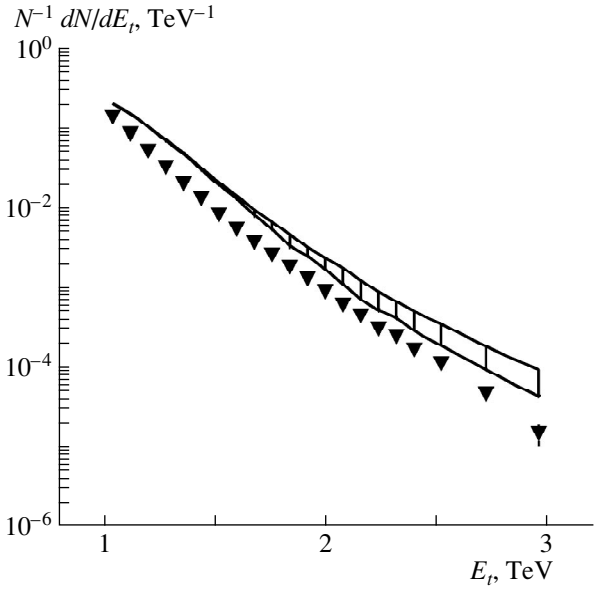

Fig. 5. Jet E_t spectrum indicating the uncertainty due to the present parton distribution functions. The integrated luminosity is assumed to be 30 fb^{-1}. The closed triangles correspond to the resulting predictions for calorimeter nonlinearity. $\Lambda^-_{\rm all}$ = 15 TeV for all cases.

linearity of the jet E_t scale according to the relation [13]

$$E_t(\text{meas}) = E_t \frac{1}{c(1 + (e/h - 1)b\ln E_t)}, \qquad (1)$$

where E_t(meas) and E_t are the measured and the true jet transverse energy, respectively; e/h = 1.36; and c is adjusted such that at 500 GeV the scale is unchanged. The parameter b controls the size of calorimeter nonlinearity. After introducing a correction, the residual uncertainty can be parametrized by this formula with b = 0.025 and corresponds to a 1.5% nonlinearity at 3 TeV. If no correction is made, b = 0.11 and there is a 5% nonlinearity at 3 TeV.

To illustrate the effect of nonlinearity, Fig. 6 shows the fractional deviation of the transverse energy spectrum measured by a nonlinear calorimeter from that measured by a linear one. The rates are normalized to be equal at 1.20 TeV. Two cases corresponding to b = 0.025 and b = 0.11 are shown. Comparison of this plot with Fig. 4 demonstrates that, at the worst, the effect of nonlinearity is similar in magnitude to that due to a composite scale of 20 TeV. If the 1.5% nonlinearity can be achieved, the effect is comparable to that of the 30-TeV composite scale. The points in Fig. 5 show distributions resulting with calorimeter nonlinearity inclusion.

In order to estimate the calorimeter nonlinearity part in the effect, we introduce the variable

$$R = \frac{R_n^{\rm nonlin} - R_n^{\rm lin}}{R_n^{\rm lin}}, \qquad (2)$$

where

$$R_n = \left.\frac{N(E_t > E_t^0)}{N(E_t < E_t^0)}\right|_{\rm comp} \Big/ \left.\frac{N(E_t > E_t^0)}{N(E_t < E_t^0)}\right|_{\rm SM}$$

and $N(E_t > E_t^0)$ ($N(E_t < E_t^0)$) is the number of events with $E_t > E_t^0$ ($E_t < E_t^0$). Figure 7, displaying R versus $\Lambda^-_{\rm all}$, demonstrates that the nonlinear calorimeter

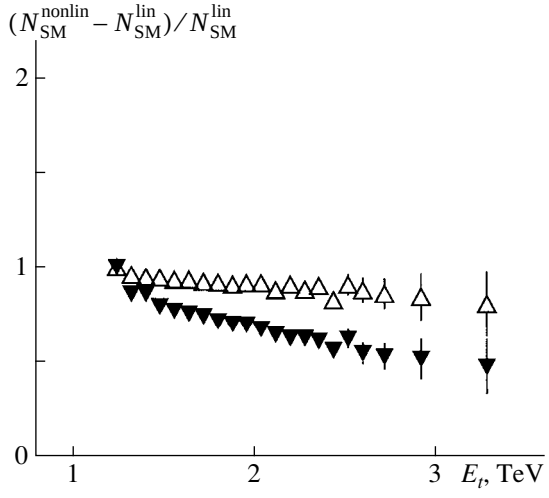

Fig. 6. Fractional difference between the E_t spectrum measured by a linear and nonlinear calorimeter. The closed and open triangles correspond to b = 0.11 and b = 0.025, respectively (see main body of the text). The rates were normalized at 1.20 TeV.

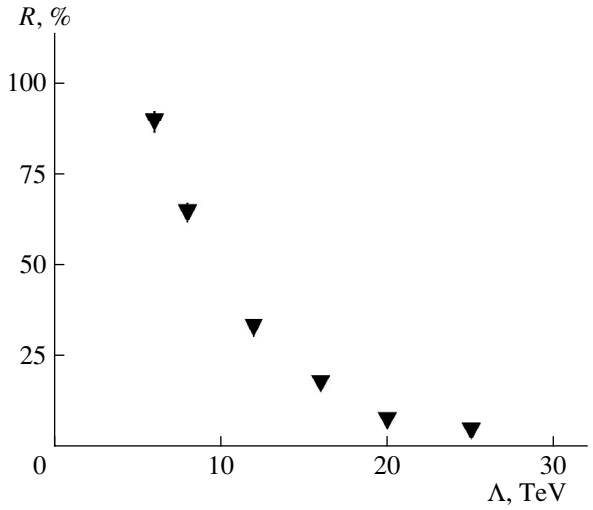

Fig. 7. Ratio R versus the compositeness scale $\Lambda^-_{\rm all}$ (see main body of the text). The integrated luminosity was assumed to be 30 fb^{-1}.

response almost doubles the effect at $\Lambda^{-}_{\text{all}} = 6$ TeV. We chose $b = 0.11$ and $E_t^0 = 1.5$ TeV.

In conclusion, the effects caused by quark compositeness have good chance to be observed by ATLAS at LHC. High transverse energy jet production at a center-of-mass energy of 14 TeV can give bounds to quark compositeness scale Λ above ~25(40) TeV for integrated LHC luminosity of 30 (300) fb^{-1}. We can note that Λ limit estimation using the inclusive E_t spectrum of jets is very sensitive to calorimeter nonlinearity effects and choice of parton distribution function.

ACKNOWLEDGMENTS

I would like to thank D. Froidevaux, I. Hinchliffe, and M. Bosman for help and valuable comments.

REFERENCES

1. F. Abe, H. Akimoto, A. Akopian, *et al.*, Phys. Rev. Lett. **77**, 5336 (1996); Erratum: **78**, 4307 (1997).
2. B. Abbott, M. Abolins, B. S. Acharya, *et al.*, Phys. Rev. Lett. **80**, 666 (1998).
3. C. Albajar, M. G. Albrow, O. C. Allkofer, *et al.*, Phys. Lett. B **209**, 127 (1988).
4. J. Alitti, R. Ansari, R. E. Ansorge, *et al.*, Z. Phys. C **49**, 17 (1991).
5. F. Abe, D. Amidei, G. Apollinari, *et al.*, Phys. Rev. D **41**, 1722 (1990); F. Abe, M. Albrow, H. Akimoto, *et al.*, Phys. Rev. Lett. **71**, 2542 (1993).
6. F. Abe, H. Akimoto, A. Akopian, *et al.*, Phys. Rev. Lett. **79**, 2198 (1997).
7. B. Abbott, M. Abolins, V. Abramov, *et al.*, Phys. Rev. Lett. **82**, 4769 (1999).
8. K. S. McFarland, C. G. Arroyo, B. J. King, *et al.*, Eur. Phys. J. C **1**, 509 (1998).
9. ATLAS Technical Proposal, Report No. CERN/LHCC/94-43 (CERN, 1994).
10. T. Sjostrand, Comput. Phys. Commun. **82**, 74 (1994); Preprint No. LU TP 95-20 (Lund University, 1995).
11. E. Eichten, K. Lane, and M. Peskin, Phys. Rev. Lett. **50**, 811 (1983); E. Eichten, I. Hinchliffe, K. Lane, and C. Quigg, Rev. Mod. Phys. **56**, 579 (1984).
12. E. Richter-Was, D. Froidevaux, and L. Poggioli, ATLAS Internal Note PHYS-No-079 (CERN, 1996).
13. M. Bosman, in *Proceedings of the VI International Conference on Calorimetry in High Energy Physics*, Frascati Physics Series (Frascati, 1996), Vol. VI, p. 299.

Physics of Atomic Nuclei, Vol. 64, No. 2, 2001, pp. 336–341. Translated from Yadernaya Fizika, Vol. 64, No. 2, 2001, pp. 386–391.

ELEMENTARY PARTICLES AND FIELDS
Theory

Nonstandard Magnetic Oscillations in the Nambu–Jona-Lasinio Model

M. A. Vdovichenko[1], K. G. Klimenko*, and D. Ebert[2], **

Institute for High Energy Physics, Protvino, Moscow oblast, 142284, Russia

Received November 2, 1999; in final form, February 2, 2000

Abstract—The Nambu–Jona-Lasinio model at nonzero values of an external magnetic field H and of the chemical potential is considered in the strong-coupling region $G > G_c$. The phase portrait of the model exhibits an infinitely large number of massless chiral-invariant phases and massive phases resulting from a spontaneous breakdown of chiral invariance. This phase structure is responsible for aperiodic oscillations of some thermodynamic parameters of the system, including the dynamical fermion mass, as functions of H^{-1}. *© 2001 MAIK "Nauka/Interperiodica".*

1. INTRODUCTION

It is well known that, for the majority of metals, the magnetization generated by an external magnetic field H oscillates at low temperatures as a function of the parameter $(eH)^{-1}$, where e is the absolute value of the electron charge. In modern condensed-matter physics, this phenomenon is referred to as the de Haas–Van Alphen effect. This effect was theoretically predicted and then observed experimentally more than 60 years ago [1–3]. Apart from the magnetization, some other thermodynamic characteristics of metals also oscillate in a magnetic field—periodically, as a rule, as functions of $(eH)^{-1}$ (standard magnetic oscillations) [2, 3].[3] Nevertheless, there are compounds like the degenerate magnetic semiconductor $HgCr_2Se_4$ where the magnetization and the electric resistance oscillate aperiodically as functions of $(eH)^{-1}$ [4]. Such oscillations, which cannot be explained within the simplest Fermi liquid models, will henceforth be referred to as nonstandard magnetic oscillations.[4]

The de Haas–Van Alphen effect is a very efficient tool for studying the Fermi surface and its topology and, consequently, the energy spectrum of conduction electrons [2]. This is the reason why magnetic oscillations are still being investigated; as to relevant theoretical studies, much attention has recently been given there to analysis of magnetic oscillations within relativistic quantum field theory (see, for example, [6, 7]). The problem in question is investigated within a broad program aimed at developing quantum theories with allowance for various external conditions (temperature, electromagnetic fields, etc.), which is expected to yield results covering applications in astrophysics and cosmology, heavy-ion physics, and the physics of neutron stars [8]. However, the relativistic de Haas–Van Alphen effect can also have applications in condensed-matter physics. The point is that modern facilities enable ever more precise measurements, whose results can be explained only by taking into account relativistic corrections. Further, the Fermi energy grows with increasing matter density. At high pressures and densities, the dynamics of an electron Fermi liquid therefore becomes essentially relativistic, so that the field-theoretical methods are required for simulating it.

In [6, 7], an effective Lagrangian L_{eff} for an external magnetic field at a nonzero value of the chemical potential μ was considered within QED. As a matter of fact, the one-loop effective Lagrangian L_{eff} for the problem being discussed is determined by the thermodynamic potential of a relativistic ideal gas of fermions at μ, $H \neq 0$. It turns out that, here, the thermodynamic potential itself and its derivatives with respect to H and μ—that is, respectively, the pressure, the magnetization, and the particle-number density of this relativistic system—exhibit standard oscillations as functions of the variable $(2eH)^{-1}$ with a frequency $(\mu^2 - M^2)$ (M is the electron mass), which is independent of the magnetic field at $\mu = \text{const}$.

Here, the effect of an external magnetic field H and of the chemical potential μ on the properties of the vacuum and on the allied phenomena of magnetic oscillations are considered within the simplest quantum the-

[1] Moscow State Institute of Radio Engineering, Electronics, and Automation (Technical University), pr. Vernadskogo 78, Moscow, 117454 Russia.

[2] Institut für Physik, Humbolt-Universität zu Berlin, Invalidenstrasse 110, D 10115, Berlin, Germany.

* e-mail: kklim@mx.ihep.su

** e-mail: debert@physik.hu-berlin.de

[3] At low temperatures, the ensemble of conduction electrons in metals forms a Fermi liquid. Even the simplest description of an electron Fermi liquid in terms of a degenerate ideal gas of nonrelativistic fermion quasiparticles leads to periodic oscillations in $(eH)^{-1}$ [3].

[4] In addition to nonstandard magnetic oscillations, the aforementioned semiconductor exhibits unusual temperature oscillations of the magnetization [5].

ory involving four-fermion interaction. Its Lagrangian, given by

$$L_\psi = \sum_{k=1}^{N} \bar\psi_k i\hat\partial\psi_k + \frac{G}{2N}\left[\left(\sum_{k=1}^{N}\bar\psi_k\psi_k\right)^2 + \left(\sum_{k=1}^{N}\bar\psi_k i\gamma_5\psi_k\right)^2\right], \quad (1)$$

is invariant under continuous chiral transformation $\psi_k \longrightarrow e^{i\theta\gamma_5}\psi_k$ ($k = 1, \ldots, N$). Theories like that specified by Eq. (1) are usually associated with the Nambu–Jona-Lasinio (NJL) model, which features the effect of a dynamical breakdown of chiral symmetry in the strong-coupling region [9]. In order to employ the nonperturbative method of $1/N$ expansion, we consider the N-fermion version of the original NJL model. Since the concept of a dynamical breakdown of chiral symmetry plays an important role in the modern theory of elementary particles, a large number of studies have been devoted so far to the analysis of this phenomenon with allowance for the effect of various external factors, including temperature and the chemical potential [10, 11], external (chromo)magnetic fields [12], and nontrivial spacetime topology and curvature [13], on the vacuum structure of models similar to that specified by Eq. (1). Moreover, the concerted effect of gravity and magnetic fields on the critical properties of various theories involving four-fermion interaction was considered in [14] and in some other studies. However, the properties of the ground state of the model whose Lagrangian is given by (1) have not yet been considered at nonzero values of the external magnetic field H and the chemical potential μ.

2. PHASE STRUCTURE OF THE MODEL AT $\mu, H \neq 0$

The phase structure of the model in question is controlled by the effective potential. In the leading order of the $1/N$ expansion, the effective potential at nonzero μ and H has the form

$$V_{H\mu}(\Sigma) = V_H(\Sigma) - \frac{eH}{4\pi^2}\sum_{k=0}^{\infty}\alpha_k\theta(\mu - s_k) \times\left\{\mu\sqrt{\mu^2 - s_k^2} - s_k^2\ln\left[\frac{\mu + \sqrt{\mu^2 - s_k^2}}{s_k}\right]\right\}, \quad (2)$$

where $s_k = \sqrt{\Sigma^2 + 2eHk}$ and

$$V_H(\Sigma) = V_0(\Sigma) - \frac{(eH)^2}{2\pi^2}\left\{\zeta'(-1, x) - \frac{1}{2}[x^2 - x]\ln x + \frac{x^2}{4}\right\} \quad (3)$$

is the effective potential at $\mu = 0$ and $H \neq 0$. In Eq. (3), we have used the following notation: $x = \Sigma^2/(2eH)$, $\zeta(\nu, x)$ is a generalized Riemann zeta function [15], $\zeta'(-1, x) = d\zeta(\nu, x)/d\nu|_{\nu=-1}$,

$$V_0(\Sigma) = \frac{\Sigma^2}{2G} - \frac{1}{16\pi^2}\left\{\Lambda^4\ln\left(1 + \frac{\Sigma^2}{\Lambda^2}\right) + \Lambda^2\Sigma^2 - \Sigma^4\ln\left(1 + \frac{\Lambda^2}{\Sigma^2}\right)\right\} \quad (4)$$

is the effective potential at zero μ and H, and Λ is the ultraviolet-cutoff parameter (this cutoff is necessary since the original model is nonrenormalizable). We also note that an auxiliary scalar field Σ, which enters into the equations of motion as a quantity proportional to $\bar\psi\psi$, appears in the argument of all functions in (2)–(4); since this field is, in particular, the argument of the effective potential, it is independent of spacetime coordinates. For any of the potentials in Eqs. (2)–(4), the point of the global minimum is the vacuum expectation value of the field Σ and coincides with the dynamical mass of fermion fields. The procedure of introducing the auxiliary field Σ in the NJL model is described in detail elsewhere [11].

At $\mu, H = 0$ and $G < G_c = 4\pi^2/\Lambda^2$, the stationarity condition for the potential (4) has no solutions other than the trivial one, $\Sigma = 0$—that is, there is no breakdown of chiral invariance in this case: the fermions remain massless. If $G > G_c$, the function $V_0(\Sigma)$ has a nontrivial global minimum (we denote by M the corresponding point). This implies a spontaneous breakdown of chiral symmetry and the appearance of a nonzero fermion mass, M. Obviously, M depends on G and Λ [11].

In the case of zero μ and $H \neq 0$, the chiral symmetry of the model appears to be spontaneously broken at any value of the coupling constant G [12], since $V_H(\Sigma)$ has a nonzero point of global minimum, $\Sigma_0(H)$.

In order to find out how the vacuum of the model behaves when both μ and H take nonzero values, it is necessary to analyze the function in (2) for the absolute minimum. For this purpose, we seek all solutions to the stationarity equation

$$\frac{\partial}{\partial\Sigma}V_{H\mu}(\Sigma) = \frac{\partial}{\partial\Sigma}V_H(\Sigma) + \frac{2eH\Sigma}{4\pi^2}\sum_{k=0}^{\infty}\alpha_k\theta(\mu - s_k)\ln\left[\frac{\mu + \sqrt{\mu^2 - s_k^2}}{s_k}\right] = 0 \quad (5)$$

and choose that which minimizes the potential (2); we then consider the properties of this global minimum versus μ and H. For the reasons of space, we omit here the details of this analysis, performed numerically, and present only basic results.

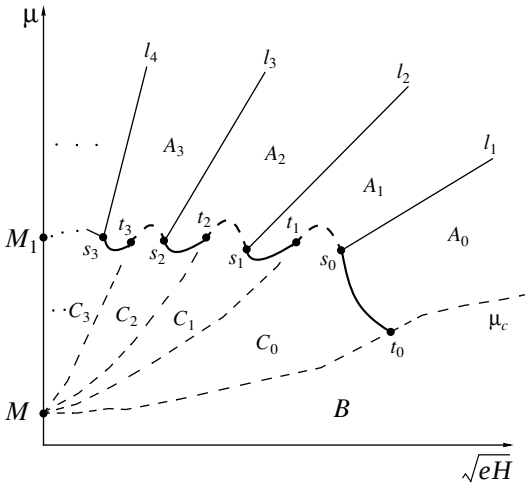

Phase portrait of Nambu–Jona-Lasinio model for $G_c < G < (1.225\ldots)G_c$ (here, M is the fermion mass at $\mu = H = 0$ and $M_1 = \sqrt{\Lambda^2/2 - 2\pi^2/G}$; a detailed description of the figure is given in the main body of the text).

In the figure, the phase portrait of the model in the $(\mu, \sqrt{eH})$ plane is shown for coupling-constant values in the interval $G_c < G < (1.225\ldots)G_c$. Here, we can see an infinite set of massless symmetric phases $A_0, A_1, \ldots$ and an infinite set of massive phases $C_0, C_1, \ldots$ characterized by a spontaneous breakdown of chiral symmetry. In addition, there arises one more massive phase B, where the fermion mass is equal to $\Sigma_0(H)$, as in the case of zero μ and nonzero H. The solid and dashed curves in the figure correspond to critical curves of, respectively, second- and first-order phase transitions. Thus, the boundary separating the massless and the massive phases (chiral boundary) contains an infinite number of tricritical points t_k, s_k ($k = 0, 1, 2, \ldots$). (The point on the phase plane is referred to as a tricritical point if, in any arbitrary small vicinity of this point, there occur both first- and second- order phase transitions.) The table presents the magnetic-field values corresponding to the tricritical points t_0 and s_0 versus the ratio G/G_c. We also note that a part of the chiral boundary—namely, the curve $t_0\mu_c$—is described by the equation $V_{H\mu}(0) = V_{H\mu}(\Sigma_0(H))$.

Obviously, the region above the chiral boundary (see figure) corresponds to the chiral-invariant ground state of the NJL model. This implies that, here, the global minimum of the potential (2) is achieved at the point $\Sigma = 0$. We will show that, in fact, this region splits into an infinite set of various massless phases $A_0, A_1, \ldots$.

External-magnetic-field values corresponding to the tricritical points t_0 and s_0 of the phase portrait (see figure) for various values of G/G_c

G/G_c	1.01	1.1	1.15	1.2
eH_{t_0}/Λ^2	0.0129…	0.08119…	0.10769…	0.12987…
eH_{s_0}/Λ^2	0.00614…	0.05639…	0.08088…	0.10338…

The thermodynamic-equilibrium state (ground state) of any quantum field theory is described by the thermodynamic potential whose space density $\Omega(\mu, H)$ is equal to the value of the effective potential at the point of global minimum. Below, $\Omega(\mu, H)$ is always associated with the thermodynamic potential. The thermodynamic potential is equal to the sign-reversed pressure in the system; in the case being considered, it assumes the form

$$\Omega(\mu, H) \equiv V_{H\mu}(0) = V_H(0) - \frac{eH}{4\pi^2}\sum_{k=0}^{\infty}\alpha_k\theta(\mu - \epsilon_k) \times \{\mu\sqrt{\mu^2 - \epsilon_k^2} - \epsilon_k^2\ln[(\sqrt{\mu^2 - \epsilon_k^2} + \mu)/\epsilon_k]\}, \quad (6)$$

where $\epsilon_k = \sqrt{2eHk}$. We then make use of the following well-known phase-transition criterion: at the points of first-order (second-order) phase transition, all partial derivatives of the thermodynamic potential with respect to any argument from the first (second) one undergo a discontinuity. Applying this criterion, we analyze the phase structure of the model above the chiral boundary. We are going to show that the curves $l_k = \{(\mu, H) : \mu = \sqrt{2eHk}\}$ ($k = 1, 2, \ldots$) represent critical curves of second-order phase transitions. For this purpose, we indicate that, below the curve l_1, only the term that corresponds to $k = 0$ makes a nonzero contribution to the sum on the right-hand side of Eq. (6). In the region below the curve l_2, the nonvanishing terms in the sum correspond to $k = 0$, 1, and so on. Taking this into account, we arrive at

$$\left.\frac{\partial\Omega}{\partial\mu}\right|_{(\mu, H)\to l_{k+}} - \left.\frac{\partial\Omega}{\partial\mu}\right|_{(\mu, H)\to l_{k-}} = 0, \quad (7)$$

$$\left.\frac{\partial^2\Omega}{(\partial\mu)^2}\right|_{(\mu, H)\to l_{k+}} - \left.\frac{\partial^2\Omega}{(\partial\mu)^2}\right|_{(\mu, H)\to l_{k-}} = -\left.\frac{eH\mu}{2\pi^2\sqrt{\mu^2 - \epsilon_k^2}}\right|_{\mu\to\epsilon_{k+}} \longrightarrow -\infty. \quad (8)$$

The equality in (7) means that the first derivative $\partial\Omega/\partial\mu$ is continuous on all curves l_k. However, it follows from (8) that each curve l_k corresponds to the second-order phase transition in the system since, there, the second derivative of the thermodynamic potential with respect to μ undergoes an infinite jump. Similarly, we can show that, on each of the curves l_k, the second derivatives $\partial^2\Omega/(\partial H)^2$ and $\partial^2\Omega/\partial\mu\partial H$ are discontinuous as well (they undergo infinite jumps).

The existence of an infinite set of massive phases C_k is caused by the specific structure of the stationarity Eq. (5). Our numerical calculations and the relevant

graphs show that, for $(\mu, H) \in C_k$, Eq. (5) usually has a few solutions, one of them, $\Sigma_k(\mu, H)$, corresponding to the global minimum of $V_{H\mu}(\Sigma)$. Upon intersection of the curve Mt_{k+1}, the global minimum jumps to another solution, $\Sigma_{k+1}(\mu, H)$, to the stationarity equation. This means that the system undergoes a first-order phase transition to the new phase C_{k+1}, and so on. In each of the phases C_k, the fermion mass equal to $\Sigma_k(\mu, H)$, depends on μ. On the contrary, the fermion mass $\Sigma_0(H)$ in the phase B is independent of μ. Another special feature of the phase B is that, in the ground state, the particle-number density $n \equiv -\partial\Omega/\partial\mu$ is identically equal to zero; however, it does not vanish in any of the phases C_k.

From statistical physics (see, for example, [3]), it is known that more than three curves of first-order phase transitions cannot intersect at the same point. This means that more than three phases cannot coexist in nature. In the figure, however, an infinite number of curves corresponding to first-order phase transitions intersect at the point M. As matter of fact, this contradiction is only apparent since M represents the point of a second-order phase transition [11]: it does not belong to any of the curves of first-order phase transitions and is not a point where the phases coexist.

3. STANDARD MAGNETIC OSCILLATIONS

We now consider the case of $\mu > M_1$ and $\mu = \text{const}$. In the (μ, H) plane, this case corresponds to the straight line that intersects the curves $l_1, \ldots, l_k, \ldots$ at the points $H_1, \ldots, H_k, \ldots$, respectively. Let us consider the particle-number density $n(H)$ and the magnetization $m(H) = -\partial\Omega/\partial H$ as functions of the magnetic field at $\mu = \text{const}$. From the aforementioned properties of the thermodynamic potential (6), it follows that, at $H \geq 0$, $n(H)$ and $m(H)$ are continuous functions having characteristic kinks at an infinite number of points $H_1, \ldots$. Functions that exhibit this type of behavior are usually referred to as oscillating functions. Thus, the presence of an infinite cascade of phases results in magnetic oscillations of the thermodynamic parameters in the NJL model. Below, we will demonstrate that these oscillations are of a standard character—that is, they are periodic in $(eH)^{-1}$.

To do this, we will follow the procedure adopted in condensed-matter physics [2, 3], representing the thermodynamic potential (6) as the sum of two terms, $\Omega(\mu, H) = \Omega_{\text{mon}} + \Omega_{\text{osc}}$. The first of these absorbs the monotonic part of the thermodynamic potential, while the second involves all oscillations. In order to obtain the explicit expression for Ω_{osc}, we use in (6) the Poisson summation formula [2, 3]

$$\sum_{n=0}^{\infty} \alpha_n \Phi(n) = 2\sum_{k=0}^{\infty} \alpha_k \int_0^{\infty} \Phi(x)\cos(2\pi k x)\,dx, \qquad (9)$$

where $\alpha_n = 2 - \delta_{n0}$. After some simple algebra (similar calculations within QCD were performed in [7]), we arrive at

$$\Omega_{\text{osc}} = \frac{\mu}{4\pi^{3/2}} \sum_{k=1}^{\infty} \left(\frac{eH}{\pi k}\right)^{3/2} \times [Q(\pi k\nu)\cos(\pi k\nu + \pi/4) + P(\pi k\nu)\cos(\pi k\nu - \pi/4)], \qquad (10)$$

where $\nu = \mu^2/(eH)$ and where the functions $P(x)$ and $Q(x)$ are related to the Fresnel integrals $C(x)$ and $S(x)$ by the equations [15]

$$C = \frac{1}{2} + \sqrt{\frac{x}{2\pi}}[P\sin x + Q\cos x],$$

$$S = \frac{1}{2} - \sqrt{\frac{x}{2\pi}}[P\cos x - Q\sin x].$$

For $x \longrightarrow \infty$, their asymptotic expansions are [15]

$$P(x) = x^{-1} - \frac{3}{4}x^{-3} + \ldots, \quad Q(x) = -\frac{1}{2}x^{-2} + \frac{15}{8}x^{-4} + \ldots.$$

From Eq. (10), it can be seen that, with increasing $(2eH)^{-1}$, the thermodynamic potential and all its derivatives (consequently, the pressure, the particle-number density, and the magnetization of the system under consideration) oscillate with the frequency μ^2. In just the same way as in QED [7], we have here standard (periodic) oscillations, since the frequency does not depend on the magnetic field.

4. NONSTANDARD MAGNETIC OSCILLATIONS

We now consider the case of $M < \mu < M_1$ and $\mu = \text{const}$. In the $(\mu, \sqrt{eH})$ plane, this case corresponds to the straight line traversing an infinite set of massive phases C_k. Here, the position $\Sigma(\mu, H)$ of the global minimum of the potential (2) depends on the parameters μ and H. It is obvious that, in each region C_k, $\Sigma(\mu, H)$ coincides with the relevant solution $\Sigma_k(\mu, H)$ to the stationarity equation. Upon intersecting the curves Mt_k (see figure), this quantity changes drastically. Below the chiral boundary, the thermodynamic potential of the system assumes the form $\Omega(\mu, H) \equiv V_{H\mu}(\Sigma(\mu, H))$. Using (9) on the right-hand side of (2), we find that the oscillating part of the thermodynamic potential can be represented as

$$\Omega_{\text{osc}} = \frac{\mu}{4\pi^{3/2}} \sum_{k=1}^{\infty} \left(\frac{eH}{\pi k}\right)^{3/2} [Q(\pi k\nu)\cos(2\pi k\omega + \pi/4) + P(\pi k\nu)\cos(2\pi k\omega - \pi/4)], \qquad (11)$$

where $\nu = \mu^2/(eH)$ and $\omega = (\mu^2 - \Sigma^2(\mu, H))/(2eH)$. From (11), it can be seen that the thermodynamic potential and all the parameters of the system that are associated with it oscillate as functions of the variable $(2eH)^{-1}$, the frequency $\mu^2 - \Sigma^2(\mu, H)$ of oscillations being dependent on H. Thus, we have, in this case, nonstandard (aperiodic) oscillations.

Finally, we would like to highlight yet another special feature of the model being considered. Here—in distinction to what occurs in QED—it is not only thermodynamic parameters of the system but also its dynamical parameters that oscillate. We mean above all the dynamical fermion mass $\Sigma(\mu, H)$ and all quantities associated with it. In order to demonstrate this, we use expression (9) in the stationarity Eq. (5). In the limiting case $H \longrightarrow 0$, we can then represent the oscillating part of the dynamical fermion mass as

$$\Sigma_{\rm osc}(\mu, H) \sim \frac{(eH)^{3/2}}{\mu\tilde{M}} \sum_{k=1}^{\infty} \frac{\sin(2\pi k\tilde{\omega} - \pi/4)}{k^{3/2}}, \qquad (12)$$

where $\tilde{\omega} = (\mu^2 - \tilde{M}^2)/(2eH)$ and $\tilde{M} \equiv M(\mu)$ is the fermion mass at $H = 0$ and nonzero μ.

5. CONCLUSION

We have shown that, in the relativistic strongly coupled ($G > G_c$) fermion system governed by Lagrangian (1) and placed in an external magnetic field, there can occur oscillations of thermodynamic parameters in $(eH)^{-1}$, either periodic or aperiodic (depending on the chemical-potential value). Moreover, the dynamical fermion mass and all physical quantities associated with it also oscillate.

Let us now estimate the interval of external-magnetic-field values at which nonstandard magnetic oscillations can be observed. For this purpose, we make use of the data in the table, which presents the results of numerical calculations for two tricritical points s_0 and t_0 of the model phase portrait (see figure). It is obvious that, if $H \in (0, H_{s_0})$, the thermodynamic parameters of the system as functions of the magnetic field can exhibit oscillatory behavior. At $\Lambda = 700$ MeV and $G/G_c \sim 1.1$, we easily estimate H_{s_0} at 10^{18} G.[5)]

This interval is so wide that it covers even magnetic-field values typical of neutron stars: it is well known [16] that the magnetic field is $H \sim 10^{12}$ G near their surface and reaches values of 10^{18} G near their center. If the interaction of particles constituting a neutron star is described on the basis of models of the NJL type, the magnetic-field dependence of quantities characterizing the star (magnetization, particle-number density, etc.) may have an oscillatory character in advancing from the surface to the center.

Despite the relativistic method of this study, we believe that our results are qualitatively correct for nonrelativistic strongly correlated electron systems as well; hence, it can prove to be applicable in solid-state physics.

[5)]In the system of units where the speed of light and the reduced Planck constant are equal to unity, we made use of the relation $m_e^2/e \sim 4.4 \times 10^{13}$ G, e and m_e being the electron charge and mass, respectively, from which we can easily find the relation between quantities having dimensions of MeV^2 and G.

ACKNOWLEDGMENTS

This study was supported by the Russian Foundation for Basic Research (project no. 98-02-16690) and by Deutsche Forschungs Gemeinschaft (DFG-project no. 436 RUS 113/477).

REFERENCES

1. L. D. Landau, *Collection of Works* (Nauka, Moscow, 1969), Vol. 1; W. J. de Haas and P. M. van Alphen, Proc. Amsterdam Acad. **33**, 1106 (1936)
2. I. M. Lifshits, M. Ya. Azbel', and M. I. Kaganov, *Electron Theory of Metals* (Nauka, Moscow, 1971; Consultants Bureau, New York, 1973); D. Shoenberg, *Magnetic Oscillations in Metals* (Cambridge Univ. Press, Cambridge, 1984; Mir, Moscow, 1986); I. M. Lifshits, *Selected Works* (Nauka, Moscow, 1994).
3. L. D. Landau and E. M. Lifshitz, *Statistical Physics* (Nauka, Moscow, 1976; Pergamon, Oxford, 1980), Part 1; Yu. B. Rumer and M. Sh. Ryvkin, *Thermodynamics, Statistical Physics and Kinetics* (Nauka, Moscow, 1977; Mir, Moscow, 1980).
4. A. D. Balaev, V. A. Gavrichkov, S. G. Ovchinnikov, *et al.*, Zh. Éksp. Teor. Fiz. **113**, 1877 (1998) [JETP **86**, 1026 (1998)].
5. S. G. Ovchinnikov, V. K. Chernov, A. D. Balaev, *et al.*, Pis'ma Zh. Éksp. Teor. Fiz. **62**, 620 (1995) [JETP Lett. **62**, 642 (1995)]; V. V. Val'kov and D. M. Dzebisashvili, Zh. Éksp. Teor. Fiz. **111**, 654 (1997) [JETP **84**, 360 (1997)].
6. P. Elmfors, D. Persson, and B.-S. Skagerstam, Phys. Rev. Lett. **71**, 480 (1993); Astropart. Phys. **2**, 299 (1994); D. Persson and V. Zeitlin, Phys. Rev. D **51**, 2026 (1995); J. O. Andersen and T. Haugset, Phys. Rev. D **51**, 3073 (1995); V. Ch. Zhukovskiĭ, T. L. Shoniya, and P. A. Éminov, Zh. Éksp. Teor. Fiz. **107**, 299 (1995) [JETP **80**, 158 (1995)]; V. Ch. Zhukovskiĭ, A. S. Vshivtsev, and P. A. Eminov, Yad. Fiz. **58**, 1274 (1995) [Phys. At. Nucl. **58**, 1195 (1995)]; V. R. Khalilov, Yad. Fiz. **61**, 1631 (1998) [Phys. At. Nucl. **61**, 1520 (1998)].
7. A. S. Vshivtsev and K. G. Klimenko, Zh. Éksp. Teor. Fiz. **109**, 954 (1996) [JETP **82**, 514 (1996)].
8. D. Bailin and A. Love, Phys. Rep. **107**, 325 (1984); I. A. Shushpanov and A. V. Smilga, Phys. Lett. B **402**, 351 (1996); S. Chakrabarty, Phys. Rev. D **54**, 1306 (1996); I. N. Mishustin, L. M. Satarov, H. Stocker, and W. Greiner, Phys. Rev. C **59**, 3343 (1999); **62**, 034901 (2000); hep-ph/0010223; D. Ebert and K. G. Klimenko, nucl-th/9911073.
9. Y. Nambu and G. Jona-Lasinio, Phys. Rev. **122**, 345 (1961); V. G. Vaks and A. I. Larkin, Zh. Éksp. Teor. Fiz. **40**, 282, 1392 (1961) [Sov. Phys. JETP **13**, 192 (1961)]; B. A. Arbuzov, A. N. Tavkhelidze, and R. N. Faustov, Dokl. Akad. Nauk SSSR **139**, 345 (1961) [Sov. Phys. Dokl. **6**, 598 (1961)].
10. S. Kawati and H. Miyata, Phys. Rev. D **23**, 3010 (1981); V. Bernard, U.-G. Meissner, and I. Zahed, Phys. Rev. D **36**, 819 (1987); Chr. V. Christov and K. Goeke, Acta

Phys. Pol. B **22**, 187 (1991); D. Ebert, Yu. L. Kalinovsky, L. Munchow, and M. K. Volkov, Int. J. Mod. Phys. A **8**, 1295 (1993).

11. A. S. Vshivtsev, V. Ch. Zhukovskiĭ, and K. G. Klimenko, Zh. Éksp. Teor. Fiz. **111**, 1921 (1997) [JETP **84**, 1047 (1997)]; A. S. Vshivtsev and K. G. Klimenko, Pis'ma Zh. Éksp. Teor. Fiz. **64**, 313 (1996) [JETP Lett. **64**, 338 (1996)].
12. S. P. Klevansky and R. H. Lemmer, Phys. Rev. D **39**, 3478 (1989); D. Ebert and M. K. Volkov, Phys. Lett. B **272**, 86 (1991); V. P. Gusynin, V. A. Miransky, and I. A. Shovkovy, Phys. Lett. B **349**, 477 (1996); I. A. Shovkovy and V. M. Turkowski, Phys. Lett. B **367**, 213 (1995); D. Ebert and V. Ch. Zhukovsky, Mod. Phys. Lett. A **12**, 2567 (1997); A. Yu. Babansky, E. V. Gorbar, and G. V. Shchepanyuk, Phys. Lett. B **419**, 272 (1998); K. G. Klimenko, Teor. Mat. Fiz. **89**, 211 (1991); Z. Phys. C **54**, 323 (1992).
13. T. Inagaki, T. Muta, and S. D. Odintsov, Mod. Phys. Lett. A **8**, 2117 (1993); E. Elizalde and S. Leseduarte, Phys. Rev. D **49**, 5551 (1994); H. Forkel, Phys. Lett. B **280**, 5 (1992); D. K. Kim and I. G. Koh, Phys. Rev. D **51**, 4573 (1995); A. S. Vshivtsev, M. A. Vdovichenko, and K. G. Klimenko, Zh. Éksp. Teor. Fiz. **114**, 418 (1998) [JETP **87**, 229 (1998)]; E. J. Ferrer, V. P. Gusynin, and V. de la Incera, Phys. Lett. B **455**, 217 (1999); A. S. Vshivtsev, A. K. Klimenko, and K. G. Klimenko, Yad. Fiz. **61**, 543 (1998) [Phys. At. Nucl. **61**, 479 (1998)].
14. T. Inagaki, T. Muta, and S. D. Odintsov, Prog. Theor. Phys. Suppl. **127**, 93 (1997).
15. *Higher Transcendental Functions (Bateman Manuscript Project)*, Ed. by A. Erdelyi (McGraw-Hill, New York, 1953; Nauka, Moscow, 1974), Vols. 1, 2.
16. S. L. Shapiro and S. A. Teukolsky, *Black Holes, White Dwarfs, and Neutron Stars: The Physics of Compact Objects* (Wiley, New York, 1983; Mir, Moscow, 1985).

Translated by O. Chernavskaya

Physics of Atomic Nuclei, Vol. 64, No. 2, 2001, pp. 342–345. From Yadernaya Fizika, Vol. 64, No. 2, 2001, pp. 392–395.

ELEMENTARY PARTICLES AND FIELDS
Theory

Cross Sections for *B*-Meson Hadroproduction and Up-to-Date Models*

O. I. Piskounova**

Lebedev Institute of Physics, Russian Academy of Sciences, Leninskiĭ pr. 53, Moscow, 117924 Russia

Received December 20, 1999; in final form April 27, 2000

Abstract—The cross sections for *B*-meson production as obtained on the basis of the PYTHIA code and the Quark–Gluon String Model (QGSM) are compared at energies of the proton colliders SPS, Tevatron, and LHC. Model predictions are based on the idea of exchanges of a supercritical Pomeron with phenomenological intercept $\Delta_{\mathbf{P}}(0) = 0.3$ for heavy-quark production. The transverse-momentum spectra of *B* mesons are also compared. It is shown that the cross sections calculated with PYTHIA using CTEQ structure functions are at odds with the asymptotic estimate of the cross sections for $B\bar{B}$ production within the QGSM. Asymmetries between the spectra of B^0 and $\bar{B}^0$ mesons also contradict the PYTHIA result. The reasons for the difference are discussed. *© 2001 MAIK "Nauka/Interperiodica".*

"…το της Πυθιας γραμμα φραζει τανυν."
Πλατων, Νομοι[1)]

1. INTRODUCTION

We cannot say that the complete knowledge on beauty-quark pair production has been obtained now, since the data that we have on $b\bar{b}$-production cross sections are not yet sufficient. In order to monitor the model ideas on the phenomenon, it seems useful to revise once in a while the collected data. The results of a few recent experiments [1–3] carried out at two energies of colliding protons, 630 GeV and 1.8 TeV, are presented in the literature.

In this article, two of the models are compared: on one hand, the phenomenological Quark–Gluon String Model (QGSM) [4], based on the idea of hadronic-amplitude duality and on the theory of a supercritical Pomeron, and, on the other hand, the widespread Monte Carlo code PYTHIA [5], which includes the results of QCD perturbative diagram calculations.

That the production cross sections grows with energy is a fact that was widely discussed in recent studies [6, 7]. The theory of a supercritical Pomeron postulates that cross sections grow in proportion to $s^{\Delta_{\mathbf{P}}(0)}$, where $\Delta_{\mathbf{P}}(0) = \alpha_{\mathbf{P}}(0) - 1$, $\alpha_{\mathbf{P}}(0)$ being the intercept of the Regge trajectory of the Pomeron.

The energy behavior of the production cross section in perturbative QCD is determined by the choice of gluon structure functions of interacting hadrons. The majority of these functions that are accepted now for Monte Carlo simulations of high-energy collisions are constructed to approximate the recent data from HERA that were measured up to $x = 10^{-4}$. It should be noted that all known gluon structure functions that satisfied these recent data can be taken for simulating $b\bar{b}$ production at LHC, because the value 10^{-4} is in the very region of x attributed to *B*-meson production at 14 TeV due to the estimate: $\bar{x} = 2m_B/(14\ \text{TeV}) \sim 10^{-4}$. One of those appropriate gluon distributions is the CTEQ structure function, which is involved in the PYTHIA code as a default distribution.

2. PARAMETERS DETERMINING THE CROSS SECTIONS FOR *B*-MESON PRODUCTION IN THE QGSM

The value of the major parameter of the QGSM determining the energy dependence of the cross section, $\Delta_{\mathbf{P}}(0)_{\text{eff}}$, must differ from the intercept value for one-Pomeron exchange, because the diagrams with multi-Pomeron exchanges should be taken into account in the calculations. This parameter depends on the mean value of transverse-momentum transfer in the process. Therefore, the energy dependences of the cross sections for the production of particles of different masses must be governed by different $\Delta_{\mathbf{P}}(0)_{\text{eff}}$ values.

The Q^2 dependence of $\Delta_{\mathbf{P}}(0)_{\text{eff}}$ can be illustrated well with the data obtained in the H1 experiment at HERA [8]. Pomeron exchange plays an important role in elec-

* This article was submitted by the author in English.

** e-mail: piskoun@sci.lebedev.ru

1) "as the Pythian oracle declares today," Plato, The Laws (translated by R. G. Bury, 1926).

tron–proton collisions too. The multihadron production occurs in this process owing to Pomeron exchange between the photon and a proton of the beam. The $\Delta(Q^2)$ data are shown in Fig. 1, where each point was extracted from the measured function $F_2(x, Q^2)$ by using the approximation featuring the simple dependence $F_2 \sim x^{-\Delta(Q^2)}$.

It should be noted that, in contrast to the case of proton–proton interactions, the theoretical curve in Fig. 1 was calculated [8] under the assumption of one-Pomeron exchange, which does not include cuts. The QGSM scheme for heavy-meson production must be similar to the one-Pomeron-exchange pattern because of energy conservation. For Δ_{eff}, we can therefore take the value of 0.3, which corresponds to the H1 data approximation at $Q^2 = (2m_B)^2$. It is worth emphasizing here that this value differs from $\Delta_{\text{eff}} = 0.12$, which was chosen for light-quark-meson production in early studies [7].

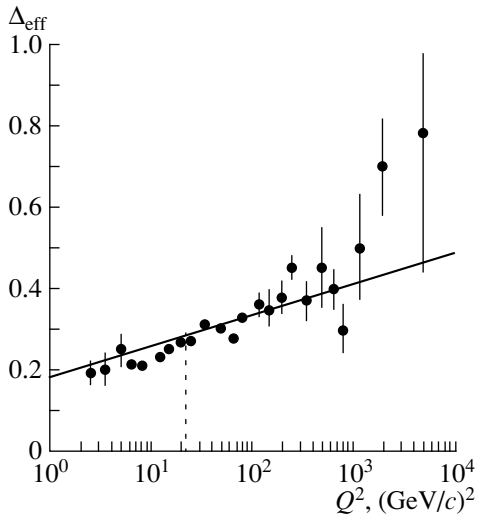

Fig. 1. $\Delta(Q^2)$ obtained in H1 [8] and one-Pomeron exchange approximation (solid line).

Another Regge trajectory parameter important for a model description of the inclusive cross sections for *B*-meson-pair production is $\alpha_\Upsilon(0)$, the intercept of $b\bar{b}$ trajectory. It provides an increasing cross section at energies slightly exceeding the threshold for *B*-pair production. There are various opinions on the value of this parameter. From the QGSM point of view, it may vary in the range between –16 and 0 [7]. Other authors prefer $\alpha_\Upsilon(0) = -9$ [9].

The value $\alpha_\Upsilon(0) = -16$ will be taken here to estimate the upper limit of growing cross section when it increases rapidly after the threshold. The parameter discussed above exists in the functions of fragmentation of quark–gluon strings into each sort of *B* mesons. Those functions are written in QGSM according to the rules fulfilled by the Regge asymptotic behavior [10].

For example, the function for *d*-quark string fragmentation into B^+ contains the following factors:

$$\mathcal{D}_d^{B^+}(z) = \frac{a_0^B}{z}(1-z)^{-\alpha_\Upsilon(0)+\lambda}(1+a_1^B z^2). \qquad (1)$$

Here, a_0^B is the density parameter for the fragmentation of a quark–gluon string into *B* mesons, and a_1^B is the parameter of string fragmentation asymmetry introduced in [7] to provide a transition between probabilities of the *B* production at $z \longrightarrow 0$ and $z \longrightarrow 1$. The value of a_1^B can be on the order of 10 and actually does not produce an impact on the value of the *B*-production cross section at energies higher than 1.8 TeV. The fragmentation function of the string beginning from *u* quark does not contain the parameter a_1^B. It is the fragmentation of nonleading type:

$$\mathcal{D}_u^{B^+}(z) = \frac{a_0^B}{z}(1-z)^{-\alpha_\Upsilon(0)+\lambda+1}. \qquad (2)$$

The calculations of $p_\perp$ spectra of the produced hadrons are also possible in the framework of QGSM, as was done in [11] for π mesons. The spectra can be described up to momenta on the order of a few GeV/*c* in this substantially nonperturbative model. The distributions were of exponential character at low $p_\perp$ in this approach. Therefore, the transverse-momentum distributions for heavy-flavor particles were not elaborated in this model.

3. PYTHIA MACHINERY

The version PYTHIA 5.7 was taken to calculate the spectra of *B* mesons at three energies of colliding protons: 630 GeV, 1.8 TeV, and 14 TeV. The CTEQ gluon structure functions [12] are used in this version to describe the increasing cross sections. On the one hand, the process of production of such heavy quarks as *b* is good enough for being described by the perturbative QCD diagram with gluon–gluon fusion. On the other hand, more and more low-*x* gluons are involved in this process at rising energy, and the cross section becomes dependent on the accuracy of the gluon structure function measured at low *x*.

As was mentioned in the Introduction, due to HERA experiments we have precise data on F_2 up to $x \sim 10^{-4}$, which is enough for the calculation of $b\bar{b}$ production at LHC energies. This way, CTEQ structure functions have to provide the correct description of increasing cross sections of $b\bar{b}$ pair production.

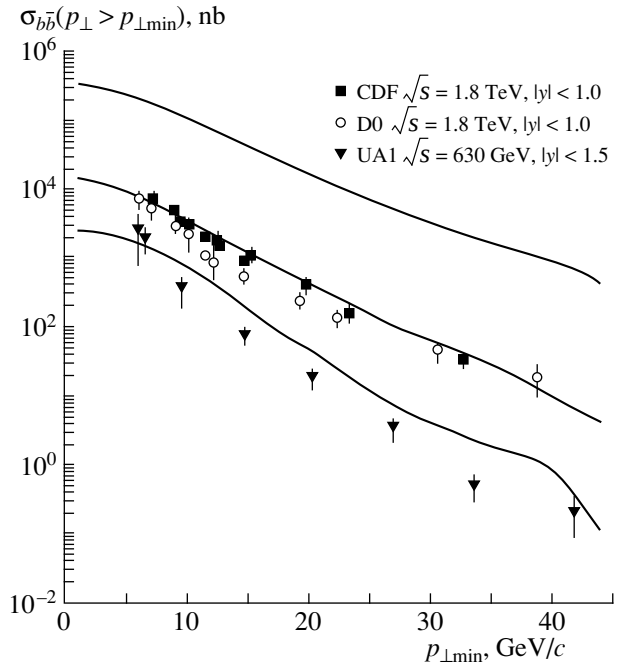

Fig. 2. Transverse-momentum distributions of B mesons fitted with PYTHIA.

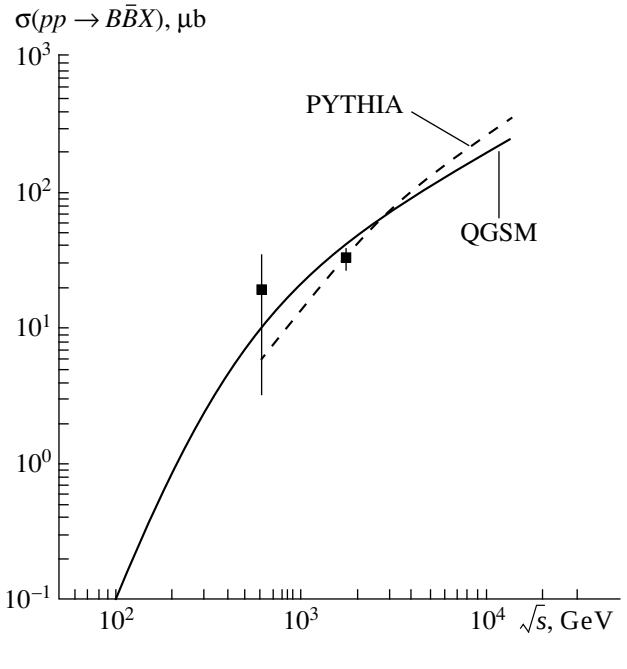

Fig. 3. Cross section for B meson as a function of energy.

However, b quarks can be obtained not only in gluon fusion process. Two additional ways exist to produce a $b\bar{b}$ pair. They are gluon splitting $gg \longrightarrow gg$, where gluons give a $b\bar{b}$ pair in the next-to-leading order of corrections, and heavy-flavor excitation $Q_i g \longrightarrow Q_i g$. In PYTHIA, these subprocesses are taken into account with massless matrix elements. It is a problem how to sum the resulting distributions from such different deposits.

It makes the $p_\perp$ spectra at 1.8 TeV comparable with the data obtained in CDF experiment (see Fig. 2). At the same time, the description of UA1 data is not good enough. It looks like the $p_\perp$ spectra were increased with additional fractions only by a factor and there is no difference between the patterns of spectra for different subprocesses. It leads to a rather flat form of transverse-momentum distributions at low $p_\perp$ in PYTHIA and, as a result, to a small total cross section of B production at various energies.

4. COMPARISON OF CROSS-SECTION ENERGY DEPENDENCES

The resulting energy dependences of the production cross section are shown in Fig. 3 for the PYTHIA program and for the QGS model as well.

As was mentioned, above the QGSM curve fitted to the data point of the CDF cross section was taken as rapidly increasing as is possible in this model. But the CDF value of cross section has been obtained due to PYTHIA (see Fig. 2). Thus the comparison of both models (see Fig. 3) is rather conventional because the result depends on the form of $p_\perp$ spectra at low transverse momenta accepted in PYTHIA.

5. PYTHIA AND QGSM PREDICTIONS FOR THE ASYMMETRY BETWEEN $B^0/\bar{B}^0$ SPECTRA

It would be interesting to consider the leading effect in the spectra of B mesons at various energies. The valuable asymmetry between B^0- and $\bar{B}^0$-meson spectra at LHC energy will be important for CP-violation measurements. The asymmetry dependence on rapidity, y, can be defined as

$$A(y) = \frac{dN^{B^0}/dy - dN^{\bar{B}^0}/dy}{dN^{B^0}/dy + dN^{\bar{B}^0}/dy}. \qquad (3)$$

The recent prediction of the rapidity dependence of such leading/nonleading asymmetry [13] provided by PYTHIA simulations gives zero value of $A(y)$ in a wide range of y in the central region (see Fig. 4). The $A(y)$ dependence in the fragmentation region $x_F \longrightarrow 1$ contradicts all similar asymmetry measurements for D meson spectra [14–17] The intersection of inclusive spectra of different type of B mesons gives the asymmetry passing through zero at some y_0, while the measured spectra of leading particles are always higher than nonleading-particle spectra, so the asymmetry is positive. Contrary to PYTHIA predictions, the asymmetry calculated in the framework of QGSM is a rising

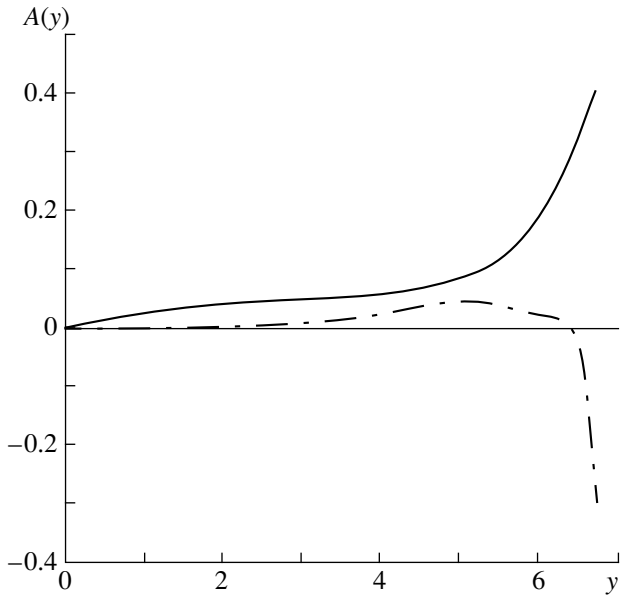

Fig. 4. $B^0/\bar{B}^0$ asymmetries at the LHC energy as given by (dash-dotted curve) PYTHIA [13] and by (solid curve) the QGS model; the value $\Delta_{\text{eff}} = 0.3$ corresponds to the production of the mass of the *B* meson.

function up to $x \longrightarrow 1$. This behavior is usually peculiar for the string approach because of a so-called "beam-drag" effect. The spectrum of particles of leading type seems as if it is dragged by beam valence quarks into the region $x_F \longrightarrow 1$. The valuable asymmetry in the central region given in QGSM prediction [18] is not small enough for it not to be taken into account in *CP*-violation measurements. It looks important to consider both these predictions in detail and to discuss the probability of nonzero asymmetry in the production spectra at LHC energy.

6. CONCLUSION

We have compared two approaches for the understanding of the heavy flavored particle production: one of them is mostly perturbative, and the other one is totally nonperturbative. This comparison shows that some different suggestion has to be made for low transverse-momenta distributions of *B* mesons to put into agreement both model predictions at LHC energy. The contradicting dependences for $B^0/\bar{B}^0$ asymmetry in the *B*-meson-production spectra might be important for *CP*-violation measurements.

ACKNOWLEDGMENTS

I would like to express my gratitude to A.B. Kaidalov, A. Kharchilava, and S. Baranov for numerous discussions. This work was supported by Deutsche Forschungs Gemeinschaft [grant no. 436 RUS 113/332/O(R)].

REFERENCES

1. UA1 Collab. (C. Albajar *et al.*), Phys. Lett. B **256**, 121 (1991).
2. CDF Collab. (F. Abe *et al.*), Phys. Rev. Lett. **75**, 1451 (1995); Phys. Rev. D **53**, 1051 (1996).
3. D0 Collab. (S. Abachi *et al.*), Phys. Lett. B **370**, 239 (1996).
4. A. Kaidalov, Phys. Lett. B **116**, 459 (1982); A. Kaidalov and K. A. Ter-Martirosyan, Phys. Lett. B **117**, 247 (1982).
5. T. Sjostrand, Comput. Phys. Commun. **82**, 74 (1994).
6. M. Mangano, P. Nason, and G. Ridolfi, Nucl. Phys. B **373**, 295 (1992).
7. O. I. Piskounova, Yad. Fiz. **56** (8), 176 (1993) [Phys. At. Nucl. **56**, 1094 (1993)].
8. A. Capella, A. Kaidalov, C. Merino, and J. Tran Thanh Van, Phys. Lett. B **337**, 358 (1994).
9. A. V. Berezhnoy, V. V. Kiselev, and A. K. Likhoded, Yad. Fiz. **60**, 359 (1997) [Phys. At. Nucl. **60**, 289 (1997)].
10. A. Kaidalov, Yad. Fiz. **45**, 1452 (1987) [Sov. J. Nucl. Phys. **45**, 902 (1987)].
11. O. I. Piskounova, A. I. Veselov, K. A. Ter-Martirosyan, *et al.*, Phys. Lett. B **158**, 175 (1985).
12. CTEQ Collab. (J. Botts *et al.*), Phys. Lett. B **304**, 239 (1996).
13. E. Norrbin, in *Proceedings of International Europhysics Conference on High Energy Physics, Tampere, 1999*, Ed. by K. Huitu, K. Kurki-Suonio, and J. Maalampi (Institute of Physics, Bristol, 2000); hep-ph/9909437; Phys. Lett. B **442**, 407 (1998).
14. E791 Collab. (E. M. Aitala *et al.*), Phys. Lett. B **411**, 230 (1997).
15. WA89 Collab. (M. I. Adamovich *et al.*), Eur. Phys. J. C **8**, 593 (1999).
16. SELEX Collab. (J. Russ *et al.*), in *Proceedings of International Conference on High Energy Physics, Vancouver, 1998*; M. Iori *et al.*, hep-ex/9910039.
17. M. Adamovich *et al.*, Nucl. Phys. B **495**, 3 (1997).
18. O. I. Piskounova, Nucl. Phys. B (Proc. Suppl.) **50**, 179 (1996); Yad. Fiz. **60**, 513 (1997) [Phys. At. Nucl. **60**, 439 (1997)]; hep-ph/9904208.

Physics of Atomic Nuclei, Vol. 64, No. 2, 2001, pp. 346–353. Translated from Yadernaya Fizika, Vol. 64, No. 2, 2001, pp.396–404.

ELEMENTARY PARTICLES AND FIELDS
Theory

Theoretical Analysis of the Formation of η Mesic Nuclei in $\gamma + A \longrightarrow N + {}_{\eta}A'$ Reactions

V. A. Tryasuchev
Tomsk Polytechnic University, Tomsk, 634004 Russia
Received October 25, 1999; in final form, April 14, 2000

Abstract—A model that describes the formation of η mesic nuclei in the $\gamma + A \longrightarrow N + {}_{\eta}A'$ reactions is formulated on the basis of the quasifree meson photoproduction on nuclei and the concept of a meson–nucleus optical potential. The amplitude of this reaction involving more than four nucleons is obtained in the general form within the nuclear shell model featuring intermediate coupling. The dependences of the cross sections for these reactions on the excitation levels of η mesic nuclei, on the discrete excitation levels of the nucleonic cores of these nuclei, on the type of emitted nucleon, and on the final-state interaction are analyzed for the incident-photon energies from the reaction threshold to 1 GeV. *© 2001 MAIK "Nauka/Interperiodica".*

1. INTRODUCTION

Liu and Haider [1, 2] stated that η mesic nuclei that involve many nucleons can exist and proposed an experiment that could discover them. However, the estimated probabilities of the formation of η mesic nuclei by pion beams were likely far from actual values, and this experiment failed [3], which gave rise to doubt about the very existence of η mesic nuclei. Information about a signal from η mesic nuclei in reactions with light ions was surprising. Since these experiments were beyond the mainstream of searches for η mesic nuclei [4], they were ambiguously interpreted. In my opinion, the question of whether η mesic nuclei exist will remain open until these nuclei are observed in those reactions and with those properties that were predicted theoretically.

It is well known that η mesic nuclei can be formed in various nuclear reactions accompanied by the production of η mesons and by subsequent interactions between these mesons and nuclei. In particular, η mesic nuclei can be formed in a photonuclear reaction like

$$\gamma + A \longrightarrow \eta + A' + \ldots \longrightarrow {}_{\eta}A' + \ldots,$$

where A' is some nuclear fragment whose velocity with respect to the product η meson is small. Reactions resulting in the formation of only two nuclear fragments are the simplest for a theoretical and, as I believe, for an experimental analysis. This can be, in particular, a reaction where a nucleon N appears to be one of such fragments:

$$\gamma + A \longrightarrow N + \eta + A' \longrightarrow N + {}_{\eta}A'. \qquad (1)$$

Figure 1 schematically represents the mechanism of this reaction. The first studies aimed at estimating the probability of the formation of η mesic nuclei in reactions of the type in (1) [5–7] brought about some questions associated with an insufficient validation of the model used to describe the reactions in question. At present, when η mesic nuclei are transforming from hypothetical objects into actual nuclei with properties becoming ever more precisely specified, the model of the formation of η mesic nuclei in reaction (1) requires a more rigorous and detailed validation, and this is one of the objectives in the present study. The formation of the extremely light η mesic nuclei ${}_{\eta}\mathrm{T}$ and ${}^{3}_{\eta}\mathrm{He}$ in reaction (1) on ${}^{4}\mathrm{He}$ target nuclei was considered in [7], where it was shown that the relevant cross sections do not exceed 1 μb. For a larger target mass number, we can expect a larger cross section for the formation of corresponding η mesic nuclei in reactions (1), so that an experimental investigation of η mesic nuclei would become possible. However, calculations for target nuclei consisting of more than four nucleons involve difficulties associated with the shell structure, the presence of several levels in heavy ($A > 6$) η mesic nuclei, and the possibility of the excitation of discrete levels in the nucleonic cores of systems formed by an η meson and a nucleus. These and other allied problems—in particular, the expected near-threshold behavior of the cross sections for reactions (1)—are discussed in this study by considering the example of the reactions $\gamma + {}^{12}\mathrm{C} \longrightarrow N + {}^{11}_{\eta}A$ and $\gamma + {}^{16}\mathrm{O} \longrightarrow N + {}^{15}_{\eta}A$.

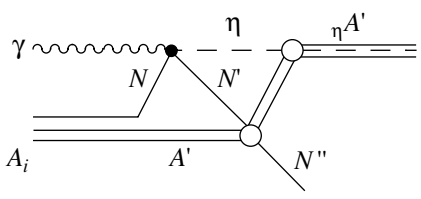

Fig. 1. Diagram describing a possible mechanism of the photoproduction of η mesic nuclei in $\gamma + A \longrightarrow N + {}_{\eta}A'$ reactions.

1063-7788/01/6402-0346$21.00 © 2001 MAIK "Nauka/Interperiodica"

2. DESCRIPTION OF THE FORMALISM

The total Hamiltonian for reaction (1) can be represented in the form

$$H = H_0 + V + U,$$

where H_0 is the Hamiltonian describing the free motion of all particles involved in the reaction and V and U are the interactions responsible for, respectively, η-meson photoproduction and η-meson scattering on a nucleus. The amplitude for reactions (1) can then be written as [8]

$$\langle \varphi_f|(V+U)|\Psi_i^{(+)}\rangle = \langle \chi_f^{(-)}|V|\Psi_i^{(+)}\rangle + \langle \chi_f^{(-)}|U|\varphi_i\rangle$$
$$= \langle \chi_f^{(-)}|T|\varphi_i\rangle,$$

where φ, χ, and ψ are eigenstates of the Hamiltonians H_0, $H_0 + U$, and H, respectively, while T is the transition operator for the photoproduction process in the absence of meson–nucleus interaction. The second equality in the last formula is valid by virtue of the relation

$$\langle \chi_f^{(-)}|U|\varphi_i\rangle = 0,$$

which is valid owing to the fact that the state φ_i does not involve the meson.

It is now convenient to rewrite the generic Eq. (1) for the reaction type in question as

$$\gamma(k, \boldsymbol{\varepsilon}_\lambda) + A_i(Q_i) \longrightarrow N(p) + {}_\eta A_f(Q_f), \qquad (1a)$$

where $k = \{k_0, \mathbf{k}\}$, $q = \{q_0, \mathbf{q}\}$, $p = \{p_0, \mathbf{p}\}$, $Q_i = \{Q_{0i}, \mathbf{Q}_i\}$, and $Q_f = \{Q_{0f}, \mathbf{Q}_f\}$ are the 4-momenta of the photon, meson, nucleon, initial nucleus, and final η mesic nucleus, respectively, while $\boldsymbol{\varepsilon}_\lambda$ is the photon polarization vector. The amplitude for reactions of the type in (1),

$$\langle f|\hat{T}_{\eta A}|i\rangle,$$

is calculated below. It is related to the differential cross section for such reactions by the equation

$$\frac{d\sigma}{d\Omega_N} = \frac{K_2}{2}\sum_{\lambda, J_f, M_f} |\langle f|\hat{T}_{\eta A}|i\rangle|^2, \qquad (2)$$

where K_2 is a kinematical factor; in the laboratory frame, it is given by

$$K_2 = (2\pi)^{-2}\frac{\mathbf{p}^2 p_0 Q_{0f}}{|\mathbf{p}|(k_0 + M) - k_0 p_0 \cos\theta_N}, \qquad (3)$$

where M is the target-nucleus mass and θ_N is the nucleon emission angle.

In order to calculate the reaction cross sections in the impulse approximation, it is necessary to know the amplitudes of η-meson photoproduction on protons and neutrons. These amplitudes have been calculated in the purely resonance model of the $\gamma N \longrightarrow N\eta$ processes by taking into account the contributions from the $P_{11}(1440)$, $D_{13}(1520)$, and $S_{11}(1535)$ resonances. The masses, total widths, and γ widths of these resonances were varied within the limits recommended in [9] in order to reproduce the most precise data on the near-threshold cross section for the process $\gamma p \longrightarrow \eta p$ [10]. Fixing the contribution from these resonances to the $\gamma n \longrightarrow \eta n$ amplitude by using data from [9], we obtain, in agreement with experimental data from [11], the ratio

$$\frac{\sigma(\gamma n \longrightarrow \eta n)}{\sigma(\gamma p \longrightarrow \eta p)} = 0.73 \qquad (4)$$

at the photon energy corresponding to the excitation of the $S_{11}(1535)$ resonance.

3. AMPLITUDES FOR $\gamma + A \longrightarrow N + {}_\eta A'$ REACTIONS ON p-SHELL NUCLEI

Using the second-quantization technique and taking into account the antisymmetry of the wave functions of the initial (A_i) and final (A_f, N) nucleon systems, we can recast the relevant amplitude into the form

$$\langle f|\hat{T}_{\eta A}|i\rangle$$
$$= \sqrt{A}\langle \psi_f|\sum_{n=1}^{A}\Psi_p^{(-)*}(x_A)\chi_q^{(-)*}(\mathbf{r}_n)e^{i\mathbf{k}\cdot\mathbf{r}_n}\hat{\mathbf{t}}_n\cdot\boldsymbol{\varepsilon}_\lambda|\psi_i\rangle, \qquad (5)$$

where $|\psi_i\rangle$ and $|\psi_f\rangle$ are the wave functions of the nucleus A_i consisting of A nucleons and the nucleus A_f consisting of $(A-1)$ nucleons, respectively; $\Psi_p^{(-)}(x_A) = \Phi_p^{(-)}(\mathbf{r}_A)\chi_\alpha(s_A)\chi_\beta(t_A)$ is the wave function of the nucleon emitted with the momentum $\mathbf{p}$ [x_A is the set of the variables $\{\mathbf{r}_A, s_A, t_A\}$, while $\Phi_p^{(-)}(\mathbf{r})$ is the spatial component of the wave function of the neutron interacting with the nucleus A_f]; and $\hat{t}_n^\lambda = \hat{\mathbf{t}}_n\cdot\boldsymbol{\varepsilon}_\lambda$ is the operator of η-meson photoproduction on an intranuclear nucleon. In the impulse approximation, this operator coincides with the operator of photoproduction on a free nucleon, its spin–isospin structure being given by

$$\hat{t}_n^\lambda = [\hat{K}^S + \hat{K}^V\tau_3 + \hat{\mathbf{L}}^S\cdot\boldsymbol{\sigma} + \hat{\mathbf{L}}^V\cdot\boldsymbol{\sigma}\tau_3]_n^\lambda, \qquad (6)$$

where $\boldsymbol{\sigma}$ and $\boldsymbol{\tau} = \{\tau_1, \tau_2, \tau_3\}$ are, respectively, the nucleon spin and isospin operators, while the superscripts S and V label, respectively, the isoscalar and the isovector component of the amplitude. For nucleons whose kinetic energies T_N are in excess of 50 MeV, their interaction with a nucleus can be rather accurately estimated on the basis of simple models—for example, by using the intranuclear-nucleon wave function

$$\Phi_p^{(-)}(\mathbf{r}) = \exp\left[\frac{1}{\beta}(iV_R + V_I)d(\mathbf{r})\right]\exp(i\mathbf{p}\cdot\mathbf{r}), \qquad (7)$$

which is a solution to the Schrödinger equation with uniform optical potential $V(\mathbf{r}) = V_R + iV_I$, where β is the velocity and $d(\mathbf{r})$ is the length of the proton path in the nucleus; following [12], this trajectory is treated here as

Energy eigenvalues for η mesic nuclei

	$^{11}_{\eta}\mathrm{B}(^{11}_{\eta}\mathrm{C})$	$^{15}_{\eta}\mathrm{N}(^{15}_{\eta}\mathrm{O})$
1*s*	–(27.5 + *i*16.75) MeV	–(30.2 + *i*16.85) MeV
1*p*	–(10.28 + *i*7.88) MeV	–(13.13 + *i*11.86) MeV

a classical one—that is, it is assumed to be parallel to the momentum **p**. Since the wave function (7) is applicable exclusively to calculations with a uniform nuclear density in a nucleus of radius *R*, the function $\Phi_p^{(-)}(\mathbf{r})$ appearing in (5) factorizes, according to the mean value theorem, as

$$\Phi_p^{(-)}(\mathbf{r}) = D\exp(i\mathbf{p}\cdot\mathbf{r}). \tag{8}$$

The quantity *D* is factored out of the matrix element in the form

$$D^*(V_R, V_I) = \int d^3x \frac{3}{4\pi R^3}\exp\left[\frac{1}{\beta}(-iV_R + V_I)d(\mathbf{x})\right]$$

$$= (2z^3)^{-1}[6(1+z)e^{-z} + (3z^2 - 3y^2 - 6y - 6)e^{-y} + y(3z^2 - y^2)], \tag{8a}$$

where

$$z = 2R\frac{iV_R - V_I}{\beta}, \quad y = RA^{-1/3}\frac{iV_R - V_I}{\beta}.$$

In calculating this integral, it was considered that a nucleon emitted from the outer nuclear layer of thickness $RA^{-1/3}$ must not undergo interaction. A quasistationary η–nucleus state is formed over a finite time, whereas knock-on nucleons are fast at any incident energies (with the exception of those that are close to the reaction threshold, which is considered below). Therefore, final-state interaction between the nucleons can be treated as that in ordinary nuclei consisting of $(A - 1)$ nucleons (see Fig. 1).

The wave function of the η meson in a nucleus can be represented in the form

$$\chi_q^{(-)}(\mathbf{r}) = \sum_{l=0}^{\infty}\frac{u_{nl}(r)}{r}P_l(\cos\theta), \tag{9}$$

where $P_l(\cos\theta)$ is a Legendre polynomial and the function $u_{nl}(r)$ is a solution to the radial Schrödinger equation

$$r^2\ddot{u}_{nl}(r) + [2\mu r^2(E_{nl} + U(r)) - l(l+1)]u_{nl}(r) = 0. \tag{10}$$

Here, μ is the reduced mass, and the depth of the spin-independent square-well potential $U(r)$ is determined from a fit to the η*N* free-scattering length [13]

$$a_0 = (0.717 + i0.263)\ \mathrm{fm}. \tag{11}$$

Equation (10) has an elementary solution at $l = 0$ and analytic solutions in the form of Riccati functions for $l > 0$. As usual, the conditions of energy quantization are obtained by matching the logarithmic derivatives of the wave functions $u_{nl}(r)$ at the boundary of the region where the potential is operative. The resulting energy eigenvalues of η mesic nuclei are presented in the table in the form

$$E = -(\varepsilon + i/2\cdot\Gamma),$$

where ε and Γ are, respectively, the binding energy of the quasistationary η–nucleus state and the width of the corresponding level.

The same wave functions were used for the members of the isotopic doublets $^{11}_{\eta}A$ and $^{15}_{\eta}A$ of η mesic nuclei.

By isolating the last term in the sum entering into amplitude (5), we obtain

$$\langle f|\hat{T}_{\eta A}|i\rangle = \sqrt{A}\langle\psi_f|\Psi_p^{(-)*}(x_A)\chi_q^{(-)*}(\mathbf{r}_A)e^{i\mathbf{k}\cdot\mathbf{r}_A}\mathbf{t}_A\cdot\boldsymbol{\varepsilon}_\lambda|\psi_i\rangle + \Delta, \tag{12}$$

where

$$\Delta = \sqrt{A}\langle\psi_f|\sum_{m=1}^{A-1}\Psi_p^{(-)*}(x_A)\chi_q^{(-)*}(\mathbf{r}_m)e^{i\mathbf{k}\cdot\mathbf{r}_m}\mathbf{t}_m\cdot\boldsymbol{\varepsilon}_\lambda|\psi_i\rangle. \tag{12a}$$

The first term in amplitude (12) corresponds to the quasifree photoproduction of mesons on nuclei, in which case the nucleon emitted from the nucleus carries away the entire momentum transfer associated with meson photoproduction. The residual nucleus A_f then appears to be a spectator [14] having the same momentum before and after the reaction event,

$$\mathbf{Q}_f = -\mathbf{p}_i, \tag{13}$$

where the nucleon momentum $\mathbf{p}_i$ in the nucleus before the meson-production event is taken to be equal to the value used in calculating the amplitudes for η-meson photoproduction on an intranuclear nucleon. As long as $|\mathbf{Q}_f| < 250$ MeV/*c*, the absolute value of the amplitude component under consideration is much greater than $|\Delta|$ (12a). With increasing $|\mathbf{Q}_f|$, the amplitude component responsible for quasifree photoproduction decreases sharply, so that the remaining component Δ of the amplitude becomes substantial. This component of the amplitude has yet to be clearly understood, but it is known that the component Δ in amplitude (12) can be neglected in calculating the cross sections if the $|\mathbf{Q}_f|$ value falls within the most probable interval of the momentum distribution of intranuclear nucleons—this relationship can be seen from Eq. (13). In what follows, we will consider reactions (1) in a kinematical region where $50 < |\mathbf{Q}_f| < 250$ MeV/*c* and therefore set $\Delta = 0$ in amplitude (12).

In calculating the amplitudes and cross sections for reactions (1), the contribution from the η-meson photoproduction on the *s*-shell nucleons of the ^{12}C and ^{16}O nuclei is neglected here, whereby the intricate problem of the contribution from the alpha-particle cores of the target nuclei to the cross sections for these reactions is removed from the present analysis. Within this approximation, it is sufficient to treat nuclei on the basis of the shell model featuring intermediate coupling [15, 16]. In this model, where the central potential is represented by a harmonic oscillator, the wave function of the ^{12}C nucleus is taken in the simple form whose spatial component possesses the highest possible symmetry in the *p*-shell nucleons:

$$\psi_i(J_i, M_i) = |(1s)^4; (1p)^8[44]L_i = 0, S_i = 0, T_i = 0\rangle. \quad (14)$$

Here J_i is the spin of the nucleus, and M_i is its projection; L_i, S_i, and T_i are, respectively, the total orbital angular momentum, spin, and isospin of the *p*-shell nucleons; and $[44] = [f_i]$ is the Young diagram [17] for these nucleons. The wave function of the ^{16}O nucleus with the closed *p* shell is written in the similar form

$$\psi_i(J_i, M_i) = |(1s)^4; (1p)^{12}[444]L_i = 0, S_i = 0, T_i = 0\rangle. \quad (15)$$

Within the approximations being used, the amplitude of reactions (1) for *p*-shell target nuclei whose spin and isospin are both equal to zero can be represented in the form (*LS* representation)

$$\begin{aligned}\langle f|\hat{T}_{\eta A}|i\rangle &= \sqrt{A-4}\\ &\times \sum_{\substack{L,S,T,[f],L_f,S_f,T_f,l\\ L^z,S^z,T^z,L_f^z,S_f^z,m,\tau,\nu}} a_{LST}^{[f]}\delta_{S_f,S}\delta_{L_f,L}\delta_{T_f,T}\delta_{[f_f],[f]}\\ &\times\langle L_f L_f^z, 1m|00\rangle\left\langle S_f S_f^z, \frac{1}{2}\xi\middle|00\right\rangle\\ &\times\left\langle T_f T_f^z, \frac{1}{2}\tau\middle|00\right\rangle\langle L_f L_f^z, l\nu|JM\rangle\\ &\times\langle JM, S_f S_f^z|J_f M_f\rangle H_{\xi\tau}^{\alpha\beta}(\lambda)G_l(\mathbf{Q}_f),\end{aligned} \quad (16)$$

where $\langle ..., ...|...\rangle$ are ordinary Clebsch–Gordan coefficients and $a_{LST}^{[f]}$ are single-particle fractional-parentage coefficients for *p*-shell nuclei. For ^{16}O, the relevant coefficient can take only one value (unity), while, for the ^{12}C nucleus with the *LS* configuration (14), the only nonzero fractional-parentage coefficient is

$$a_{1\,1/2\,1/2}^{[43]} = 1.$$

In Eq. (16),

$$H_{\xi\tau}^{\alpha\beta}(\lambda) = \sum_{s,t}\chi_\beta^+(t)\chi_\alpha^+(s)t_A^\lambda(s,t)\chi_\xi(s)\chi_\tau(t) \quad (17)$$

is the spin- and isospin-dependent amplitude for η-meson photoproduction on a nucleon, and we have also used the notation

$$\begin{aligned}G_l(\mathbf{Q}_f) &= \int d^3r\Phi_p^{(-)*}(\mathbf{r})e^{i\mathbf{k}\cdot\mathbf{r}}u_{nl}(\mathbf{r})/r\\ &= 4\pi N_l N_\eta(l)\sum_{\kappa=0}^{\infty}\sum_{n=-\kappa}^{\kappa}(i)^\kappa Y_n^\kappa(\hat{\mathbf{Q}}_f)\int\limits_{\Omega_r}[Y_n^\kappa(\hat{\mathbf{r}})]^*\\ &\times Y_m^1(\hat{\mathbf{r}})Y_\nu^1(\hat{\mathbf{r}})d\Omega_r D^*\int\limits_0^\infty j_\kappa(Q_f r)re^{-r^2/2r_0^2}\frac{u_{nl}(r)}{r}r^2dr,\end{aligned} \quad (18)$$

where $\mathbf{Q}_f = \mathbf{k} - \mathbf{p}$; $N_\eta(l)$ is the normalization factor for the *l*th partial wave of the η meson in the nucleus; and

$$N_1 = \left[\frac{8}{3r_0^5\sqrt{\pi}}\right]^{1/2}$$

is the normalization factor for the wave function of the *p*-shell nucleon of the nucleus, r_0 being the oscillator parameter taken to be 1.67 and 1.80 fm for the ^{12}C and ^{16}O nuclei, respectively.

4. CROSS SECTIONS FOR THE FORMATION OF η MESIC NUCLEI IN THE 1*s* STATE

Setting $l = 0$ in Eq. (16), we obtain the amplitude for the photoproduction of η mesic nuclei in the 1*s* state in the form

$$\begin{aligned}\langle f|\hat{T}_{\eta A}^{1s}|i\rangle &= \sqrt{\frac{A-4}{6}}\sum_{m,\xi}(-1)^{\xi-J_f+m}\left\langle T_f T_f^z, \frac{1}{2}\tau\middle|00\right\rangle\\ &\times\left\langle 1m, \frac{1}{2}\xi\middle|J_f - M_f\right\rangle H_{\xi\tau}^{\alpha\beta}(\lambda)G_0(Q_f),\end{aligned} \quad (19)$$

where

$$G_0(Q_f) = i\sqrt{4\pi}N_1 N_\eta(0)D^*Y_m^1(\hat{\mathbf{Q}}_f)I_{11}(Q_f); \quad (20)$$

$$I_{11}(Q_f) = \int\limits_0^\infty j_1(Q_f r)r^2u_{10}(r)e^{-r^2/2r_0^2}dr. \quad (21)$$

The differential cross sections for the reactions

$$\gamma + {}^{12}\mathrm{C} \longrightarrow p + {}^{11}_{\eta}B_{\mathrm{g.s.}}(1s), \quad (22p)$$

$$\gamma + {}^{12}\mathrm{C} \longrightarrow n + {}^{11}_{\eta}\mathrm{C}_{\mathrm{g.s.}}(1s), \quad (22n)$$

$$\gamma + {}^{16}\mathrm{O} \longrightarrow p + {}^{15}_{\eta}N_{\mathrm{g.s.}}(1s), \quad (23p)$$

$$\gamma + {}^{16}\mathrm{O} \longrightarrow n + {}^{15}_{\eta}\mathrm{O}_{\mathrm{g.s.}}(1s), \quad (23n)$$

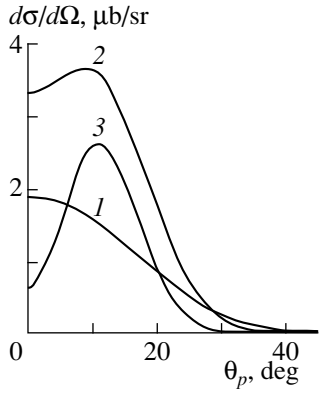

Fig. 2. Angular distribution of protons from the reaction $^{12}C(\gamma, p)^{11}_{\eta}B_{g.s.}(1s)$ in the laboratory frame for the incident-photon energies of k_0 = (*1*) 600, (*2*) 700, and (*3*) 800 MeV.

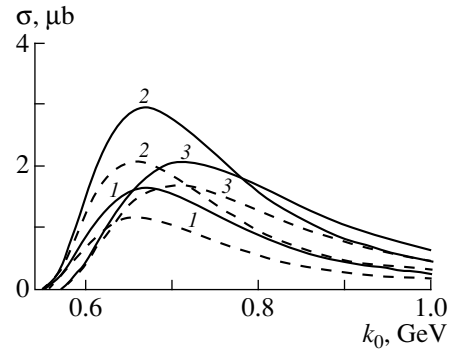

Fig. 3. Total cross sections for the reactions (solid curve *1*) $\gamma + {}^{12}C \longrightarrow p + {}^{11}_{\eta}B_{g.s.}(1s)$, (solid curve *2*) $\gamma + {}^{12}C \longrightarrow p + {}^{11}_{\eta}B^*(1s)$, (solid curve *3*) $\gamma + {}^{12}C \longrightarrow p + {}^{11}_{\eta}B^*(1p)$, (dashed curve *1*) $\gamma + {}^{12}C \longrightarrow n + {}^{11}_{\eta}C_{g.s.}(1s)$, (dashed curve *2*) $\gamma + {}^{12}C \longrightarrow n + {}^{11}_{\eta}C^*(1s)$, and (dashed curve *3*) $\gamma + {}^{12}C \longrightarrow n + {}^{11}_{\eta}C^*(1p)$ as functions of the incident-photon energy.

where the nucleon cores ^{11}A and ^{15}A of the product η mesic nuclei are in their ground states, can be represented in the form

$$\frac{d\sigma}{d\Omega_N} = K_2 \frac{Z\sqrt{\pi}|N_\eta(0)|^2}{r_0^5} \times \sum_\lambda (|K^N(\lambda)|^2 + |\mathbf{L}^N(\lambda)|^2)|I_{11}(Q_f)|^2|D|^2. \quad (24)$$

We have $K^p = K^S + K^V$ and $\mathbf{L}^p = \mathbf{L}^S + \mathbf{L}^V$ when the knock-on nucleons are protons ($N = p$) and $K^n = K^S - K^V$ and $\mathbf{L}^n = \mathbf{L}^S - \mathbf{L}^V$ when the knock-on nucleons are neutrons ($N = n$), $K^{S,V}$ and $\mathbf{L}^{S,V}$ in the operator form being given by (6). In addition to the convolutions of the Clebsch–Gordan coefficients, the factors Z involve the factor $8(A - 4)/3$; eventually, $Z = 128/9$ for reaction (22) and $Z = 32/3$ for reaction (23). Thus, the cross sections for reactions (22) and (23) differ only by a constant factor. For this reason, only the differential cross sections for $^{11}_{\eta}B_{g.s.}(1s)$ formation in reaction (22) is displayed in Fig. 2 (for various photon energies). The angular distribution of protons is concentrated predominantly in the forward hemisphere. With increasing energy of incident photons, the angular distribution of protons develops a maximum at $\theta_p \approx 12°$, whose position is stable to variations of the photon energy within the range under consideration (see Fig. 2). To a high precision, the ratio of the cross sections for reactions (1) resulting in the knockout of neutrons and protons is equal to the ratio in (4), a result that is due to the use of the impulse approximation. Curves *1* in Fig. 3 represent the total cross sections for reactions (22) as functions of the photon energy. Recall that the same wave functions were used for both members of each isotopic doublet of η mesic nuclei (see table). Curves *1* in Fig. 4 depict the total cross sections for reactions (23) as functions of the incident-photon energy. Although the number of nucleons in the ^{12}C nucleus is less than that in the ^{16}O nucleus, the total cross section for reaction (22*p*) is larger than that for reaction (23*p*) because the spin $J = 3/2$ of the $^{11}_{\eta}B_{g.s.}$ nucleus exceeds the spin $J = 1/2$ of the $^{15}_{\eta}N_{g.s.}$ nucleus (see curves *1* in Figs. 3, 4).

Because the η–nucleus interaction described by the potential $U(r)$ is independent of the nuclear spin, the set of the spin states of the product η mesic nuclei is complete. Therefore, it is convenient to calculate the squared absolute values of the amplitude by sampling the spins of various stationary excited states of their nucleon cores. As a result, we approximately obtain the differential cross sections for the reactions

$$\gamma + {}^{12}C \longrightarrow p + {}^{11}_{\eta}B^*(1s), \quad (25p)$$

$$\gamma + {}^{12}C \longrightarrow n + {}^{11}_{\eta}C^*(1s), \quad (25n)$$

$$\gamma + {}^{16}O \longrightarrow p + {}^{15}_{\eta}N^*(1s), \quad (26p)$$

$$\gamma + {}^{16}O \longrightarrow n + {}^{15}_{\eta}O^*(1s), \quad (26n)$$

where η mesic nuclei are formed with various spins. The cross sections for reactions (25) and (26) are determined by Eq. (24) with $Z = 192/9$ and 32, respectively. The ^{11}B nucleus has an excited discrete level at 5 MeV, whose quantum numbers coincide with those of the ground state. The contribution from this level to the cross sections for reactions (25) can be estimated by replacing the value of $Z = 192/9$ in expression (24) for the cross sections by

$$Z = (192 + 128\alpha)/9,$$

where α is the ratio of the spectroscopic factor for the stripping of one *p*-shell nucleon from the ^{12}C nucleus with the formation of the residual nucleus in the aforementioned excited state to the spectroscopic factor for the stripping accompanied by the formation of the residual nucleus in the ground state. For this ratio, the calculation in [16] on the basis of the nuclear model being considered yielded 0.30, and it is this value that was used in the present calculations. Figures 3 and 4 show the total cross sections calculated for reactions (25) and (26). These cross sections for nucleons with identical electric charges are approximately equal to each other owing to the inclusion of a low-lying ^{11}B level whose quantum numbers coincide with those of the ground state. In all probability, the cross-section values calculated for reactions (25) by approximate Eq. (24) must be treated as maximum possible values, because other estimations of the contribution from the discrete degrees of freedom of the nucleon core of the $^{11}_{\eta}$B nucleus yield the smaller value

$$Z \approx (183 + 128\alpha)/9$$

if use is made of the spectroscopic factors calculated in [16] for the dissociation reaction $^{12}\mathrm{C} \longrightarrow p + {}^{11}\mathrm{B}^*$. A calculation with data quoted in [18] for the strengths of the nuclear transitions $^{12}\mathrm{C} \longrightarrow p + {}^{11}\mathrm{B}^*$ leads to a still smaller value of *Z* in expression (24) for the cross section for reaction (25):

$$Z \approx (147 + 128\alpha)/9.$$

The cross sections for $^{11}_{\eta}$B* photoproduction that are calculated with above values of *Z* and with allowance for the possible excitations of the nucleon core are plotted in Fig. 5. As can be seen from this figure, the contribution from the discrete levels of the core to the cross section for reaction (25*p*) may be one-fourth as large as that presented in Fig. 3 (curves *2*). As might have been expected, the cross sections for the reactions that lead to neutron emission accompanying the formation of η mesic nuclei $^{11}_{\eta}$C and $^{15}_{\eta}$O are considerably smaller than those for the corresponding reactions that lead to proton emission (see Fig. 3, 4).

5. CROSS SECTIONS FOR THE FORMATION OF η-MESIC NUCLEI IN THE 1*p* STATE

Setting $l = 1$ in the general expression (16) for the amplitudes of the reactions being studied, we obtain the amplitudes for the formation of 1*p*-state η-mesic nuclei in reactions (1):

$$\langle f|\hat{T}^{1p}_{\eta A}|i\rangle = \sqrt{\frac{A-4}{6}} \sum_{m,\,\xi,\,\nu} (-1)^{\xi+m}$$

$$\times \langle 1-m, 1\nu\,|\,J\nu-m\rangle \langle J\nu-m, \frac{1}{2}-\xi\,|\,J_f M_f\rangle \qquad (27)$$

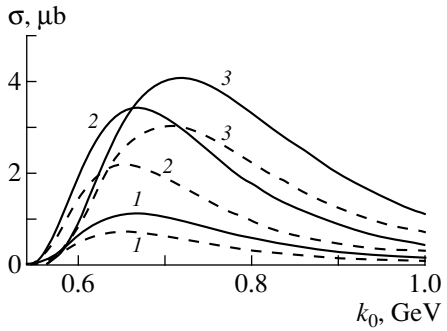

Fig. 4. As in Fig. 3 but for ^{16}O target nuclei.

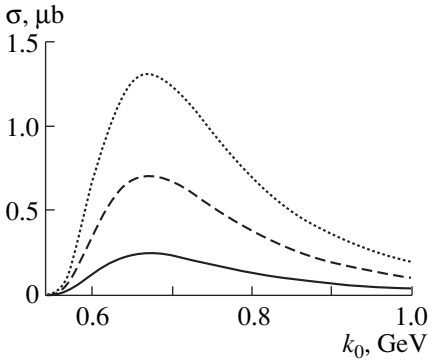

Fig. 5. Total cross sections for the formation of $^{11}_{\eta}$B* (1*s*) nuclei in the reaction $\gamma + {}^{12}\mathrm{C} \longrightarrow p + {}^{11}_{\eta}\mathrm{B}^*$ (1*s*) according to the present calculation with allowance for only those excited core states that are described in the main body of the text: (dotted curve) maximum possible result, (dashed curve) result obtained by using the computational data from [16], and (solid curve) result derived with allowance for data quoted in [18].

$$\times \langle T_f T^z_f, \frac{1}{2}\tau|00\rangle H^{\alpha\tau}_{\xi\tau}(\lambda) G_1(\mathbf{Q}_f).$$

By using the standard algebra of spherical harmonics, the tensor G_1 in the angular-momentum representation (18) can be recast into the form

$$G_1(\mathbf{Q}_f) = N_1 N_\eta(1) D^* \qquad (28)$$
$$\times \left[I_{10}(Q_f) - \sqrt{\frac{24\pi}{5}} Y^2_{m+\nu}(\hat{\mathbf{r}}) \langle 1m, 1\nu\,|\,2m+\nu\rangle I_{12}(Q_f) \right],$$

where

$$I_{1\kappa}(Q_f) = \int_0^\infty j_\kappa(Q_f r) e^{-r^2/2r_0^2} u_{11}(r) r^2 dr. \qquad (29)$$

In the approximation of completeness of the spins of product η mesic nuclei, the differential cross sections for the reactions

$$\gamma + {}^{12}\mathrm{C} \longrightarrow p + {}^{11}_{\eta}\mathrm{B}^*(1p), \qquad (30p)$$

$$\gamma + {}^{12}\mathrm{C} \longrightarrow n + {}^{11}_{\eta}\mathrm{C}^*(1p), \qquad (30n)$$

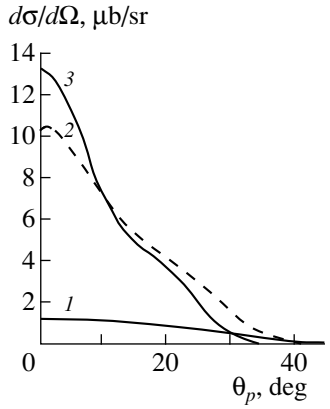

Fig. 6. Angular distribution of protons from the reaction $^{16}O(\gamma, p)\,^{15}_{\eta}N^*(1p)$ in the laboratory frame for the incident-photon energies of k_0 = (*1*) 600, (*2*) 700, and (*3*) 800 MeV.

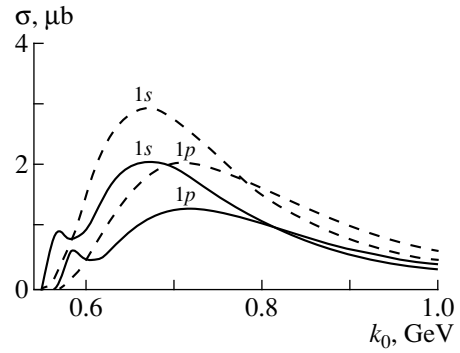

Fig. 7. Total cross sections for the reactions (curves 1*s*) $\gamma + {}^{12}C \longrightarrow p + {}^{11}_{\eta}B^*$ and (curves 1*p*) $\gamma + {}^{12}C \longrightarrow p + {}^{11}_{\eta}B^*$ as functions of the incident-photon energy according to the calculations (solid curves) with and (dashed curves) without allowance for final-state interaction.

$$\gamma + {}^{16}O \longrightarrow p + {}^{15}_{\eta}N^*(1p), \qquad (31p)$$

$$\gamma + {}^{16}O \longrightarrow n + {}^{15}_{\eta}O^*(1p) \qquad (31n)$$

can be represented as[1)]

$$\frac{d\sigma}{d\Omega_p} = ZK_2\frac{|N_\eta|^2}{r_0^5\sqrt{\pi}}|D|^2$$
$$\times\{7|I_{10}(Q_f)|^2 + [\sqrt{2}(9\cos^2\theta - 5) - 18\cos^2\theta + 2] \qquad (32)$$
$$\times \mathrm{Re}[I_{10}(Q_f)I_{12}^*(Q_f)]$$
$$+ [18 + 2\sqrt{2}(5 - \cos^2\theta)]|I_{12}(Q_f)|^2\},$$

where Z = 16/27 and 8/9 for reactions (30) and (31), respectively. Figure 6 shows the differential cross sections for reaction (31*p*) that were calculated by Eq. (32) at various photon energies. They exhibit a complicated structure at energies above 650 MeV. However, the general behavior characterized by predominantly forward emission remains similar to that in the formation of 1*s*-state η mesic nuclei (compare with Fig. 2). Curves *3* in Figs. 3 and 4 represent the total cross sections for the formation of 1*p*-state η mesic nuclei. The energy dependences of the total cross sections for these reactions and those considered above are markedly different: the maxima in the total cross sections are shifted toward higher photon energies to a greater extent than those in the cross sections for the corresponding reactions that lead to the formation of η mesic nuclei in 1*s* states (see Figs. 3 and 4). For knock-on nucleons of identical species, the absolute values of the cross sections for reactions (30) and (31) differ only slightly from those of the cross sections for reactions (25) and (26).

[1)]I apologize for making a mistake in calculating the cross sections for the formation of 1*p*-state η mesic nuclei in [19].

6. FINAL-STATE INTERACTION

The cross sections for reactions (1) are sizably affected by the final-state interaction (FSI) between the outgoing nucleon and a nucleus. This interaction is taken into account through the factor $|D|^2$ in front of the differential cross section derived with the emitted-nucleon wave function taken in the form of plane waves. If the total nuclear optical potential $V(\mathbf{r}) = V_R + iV_I$ borrowed from [14] is incorporated in the model under consideration, the differential and total cross sections for reactions (1) are reduced by a factor greater than 2. In this case, the inclusion of the real part of the potential in addition to the imaginary part enhances this suppression [19]. A considerable reduction of the cross section for reactions (1) owing to FSI is explained to a considerable extent by the fact that the model used here is oversimplified [see Eq. (7)]. In accordance with [20], the factor $|D|^2$ in front of the cross sections was therefore replaced by the expression

$$|E(V_I)|^2 = \int d^3x\frac{3}{4\pi R^3}\left|\Phi_p^{(-)}(\mathbf{x})\right|^2,$$

which is given by Eq. (8a) at

$$z = -4R\frac{V_I}{\beta}, \quad y = -2RA^{-1/3}\frac{V_I}{\beta},$$

whereby the diagonal terms in the expression from [20] for the cross section for the inclusive photoproduction of mesons on nuclei are justifiably identified with our expression for the quasifree photoproduction on a nucleus. Figures 7 and 8 show the cross sections calculated for the formation of η mesic nuclei in reactions (1) with allowance for the FSI as described above. It should be noted that Eq. (7) reflects adequately the interaction between nucleons and a nucleus only for nucleon energies above 50 MeV [12]—that is, somewhat higher than the reaction thresholds. When nucleons are formed

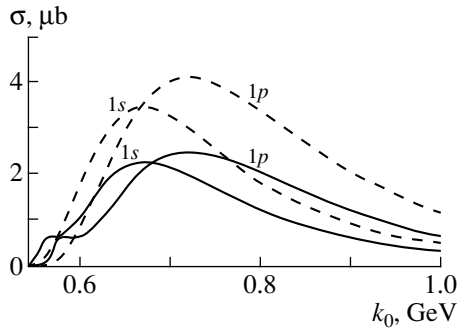

Fig. 8. As in Fig. 7 but for ^{16}O target nuclei.

with energies below 40 MeV, the effect of nucleon–nucleus interaction depends strongly on the state of a residual nucleus because the interaction predominantly proceeds through a giant dipole resonance and cannot be taken into account within a simple model. For reactions (1) near the threshold (T_p < 40 MeV), the FSI effect was taken from [18], where it was calculated for ^{12}C(γ, p)^{11}B* reactions. Note that this result, presented in Figs. 7 and 8, must be considered as a qualitative one—namely, a result that shows what can be expected from the FSI near the thresholds for reactions (1).

The near-threshold behavior of the cross sections for reactions (1) requires a dedicated investigation because the approximation Δ = 0 [see Eq. (12)] fails in this case, so that η mesic nuclei are formed through a different mechanism. In particular, reactions of the type in (1) may proceed, in this case, through the multiparticle mechanism

$$\gamma + A \longrightarrow {}_\eta A(1p) \longrightarrow {}_\eta A'(1s) + N \qquad (33)$$

because the transition

$${}_\eta A(1p) \longrightarrow {}_\eta A'(1s) + N \qquad (34)$$

is allowed owing to the difference in the binding energies of the 1s and 1p states of the η mesic nucleus (see table). It is interesting to note that the formation [(33)] and the decay [(34)] of η mesic nuclei can be responsible for nonobservation of the threshold anomalies in the cross sections for the production of η mesons on nuclei heavier than ^{4}He. The formation of 1s-state η mesic nuclei on ^{12}C and ^{16}O target nuclei in reaction (33) is forbidden because of their zero quantum numbers.

In conclusion, we note that more elaborate calculations of the cross sections for reactions (1) on the p-shell nuclei and a procedure for taking FSI into account are required to assess the contribution of the excited discrete states of the nucleon cores of η mesic nuclei to the cross sections for the reactions considered in the present study.

ACKNOWLEDGMENTS

I am grateful to Yu.F. Krechetov and A.Yu. Trifonov for their assistance in this study.

REFERENCES

1. L. C. Liu and Q. Haider, Phys. Lett. B **172**, 257 (1986); Erratum: **174**, 465 (1986).
2. L. C. Liu and Q. Haider, Phys. Rev. C **34**, 1845 (1986).
3. R. E. Crien, S. Bart, P. Pile, *et al.*, Phys. Rev. Lett. **60**, 2595 (1988).
4. P. Berthet *et al.*, Nucl. Phys. A **443**, 589 (1985).
5. A. I. Lebedev and V. A. Tryasuchev, J. Phys. G **17**, 1197 (1991).
6. A. I. Lebedev and V. A. Tryasuchev, Yad. Fiz. **58**, 642 (1995) [Phys. At. Nucl. **58**, 586 (1995)].
7. V. A. Tryasuchev, Yad. Fiz. **61**, 1600 (1998) [Phys. At. Nucl. **61**, 1489 (1998)].
8. M. L. Goldberger and K. M. Watson, *Collision Theory* (Wiley, New York, 1964; Mir, Moscow, 1967).
9. Partical Data Group (R. M. Barnett *et al.*), Phys. Rev. D **54**, 1 (1996).
10. B. Krusche, J. Ahrens, G. Anton, *et al.*, Phys. Rev. Lett. **74**, 3736 (1995).
11. B. Krusche, in *Proceedings of XXIII International Workshop on Gross Properties of Nuclei and Nuclear Excitation, 1995* (GSI, Darmstadt, 1995).
12. S. Fernbach, R. Serber, and T. B. Taylor, Phys. Rev. **75**, 1352 (1949).
13. M. Batinic, I. Dadic, I. Slaus, *et al.*, Preprint IRB-EF-02-96 (Rudjuer Boskovic Inst., Zagreb, 1996).
14. J. M. Laget, Nucl. Phys. A **194**, 81 (1972).
15. S. Cohen and D. Kurath, Nucl. Phys. **73**, 1 (1965).
16. A. N. Boyarkina, *Structure of p-Shell Nuclei* (Mosk. Gos. Univ., Moscow, 1973).
17. V. G. Neudatchin and Yu. F. Smirnov, *Nucleon Clusters in Light Nuclei* (Nauka, Moscow, 1969).
18. V. A. Zolenko and S. A. Soldatov, Yad. Fiz. **60**, 1971 (1997) [Phys. At. Nucl. **60**, 1803 (1997)].
19. V. A. Tryasuchev, Fiz. Élem. Chastits At. Yadra **30**, 1391 (1999) [Phys. Part. Nucl. **30**, 606 (1999)].
20. C. A. Engelbrecht, Phys. Rev. B **133**, 988 (1964).

Translated by R. Tyapaev

Physics of Atomic Nuclei, Vol. 64, No. 2, 2001, pp. 354–363. Translated from Yadernaya Fizika, Vol. 64, No. 2, 2001, pp. 405–414.

ELEMENTARY PARTICLES AND FIELDS
Theory

Reparametrization-Invariant Hamiltonian Formalism in the General Theory of Relativity

A. Borowiec and V. I. Smirichinski*
Joint Institute for Nuclear Research, Dubna, Moscow oblast, 141980 Russia
Received January 31, 2000

Abstract—A method is proposed that is appropriate for resolving the Hamiltonian constraint and which leads to a reparametrization-invariant reduced theory specified by a well-defined nonzero local Hamiltonian. This method is based on introducing a global (dependent only on time) conformal variable. The physical and geometric meaning of the variables in the reduced action functional is investigated. It is shown that, within the theory, the method of small perturbations is self-consistent. It is demonstrated that, in the theory of gravity, there are no wavelike excitations that make a negative contribution to the Hamiltonian. From an analysis of the reduced classical theory in the linear approximation, it follows that, at the first instants from the birth of the Universe, the extremely rigid equation of state appeared to be the effective equation of the state of gravity matter. *© 2001 MAIK "Nauka/Interperiodica".*

1. INTRODUCTION

At present, the commonly accepted Hamiltonian formulation of the general theory of relativity is based on the Arnovit–Deser–Misner (ADM) parametrization of the four-metric of the spacetime manifold [1]. Originally, this formulation was developed with the aim of quantizing the gravitational field. Intensive investigations have been performed in order to reveal the geometric and the dynamical meaning of the ADM parameters and the so-called physical sector of variables corresponding to graviton degrees of freedom [2–5]. Much attention has also been given to the initial-condition problem [2, 6–9] and to the problem of energy and surface terms [1, 10, 11].

Below, we list some as-yet-unsolved problems that hinder, in our opinion, a correct quantization of the gravitational field.

The first of these is the Hamiltonian problem. The point is that the general theory of relativity, which is a singular theory featuring primary and secondary first-class constraints, has a Hamiltonian that is proportional to constraints and which vanishes on the manifold specified by the equations of motion. This fact complicates an unambiguous definition of the generator of evolution for the state function in the quantum theory and the interpretation of the energy of the gravitational field. As to the direct quantization of constraints that yields, for example, the Wheeler–DeWitt equation, it leads to an unnormalized wave function for the state. In all probability, this will occur for all general covariant metric formulations of gravitation.

The second problem concerns the self-consistency of perturbation theory. It was noted by Kuchar [12] that, upon taking the divergence of the transverse constraint, the shift vector drops out from the constraint equation; as to the lapse function, it does not appear in the linearized constraint equation. Herein lies non-self-consistency complicating the formulation of perturbative quantum theory. Indeed, the metric representation of the state functional is based on the assumption that the components of the metric tensor g_{ik} can be taken to be independent variables. In classical theory, this assumption was formulated as the thin-sandwich theorem. According to this theorem, the initial values g_{ik}, together with the derivatives $g_{ik,0}$ (for appropriate boundary conditions), unambiguously determine the metric of spacetime. It is assumed that, if $g_{ik,0}$ and g_{ik} are specified on the initial hypersurface, it is possible, on the basis of four constraint equations, to find four unknown quantities—the lapse function and the shift vector—that determine completely the 4-metric of spacetime. In the linear approximation, this theorem is violated, so that we must fix, in some way, the lapse function and the shift vector. It follows that, in the linear approximation, available information is insufficient for determining, for example, the lapse function on the basis of fixed g_{ik} and $g_{ik,0}$ values. It is obvious that, if we have no well-defined perturbation theory at the classical level, we can hardly hope that the perturbative quantum theory of gravitation will be successful.

The next problem is that of reduction. By reduction, one implies the separation of the dynamical content of the theory on the constraint surface from redundant variables that are responsible for gauge arbitrariness. Undoubtedly, this problem is related to the aforementioned two. There are two methods for solving it. The first consists in imposing additional gauge conditions that eliminate redundant variables. The second is to resolve constraints. The first method is advantageous in

* e-mail: smirvi@thsun1.jinr.ru

1063-7788/01/6402-0354$21.00

that it is convenient and straightforward because the conditions in question are usually chosen in such a way as to simplify significantly the calculations. However, the method has some disadvantages—in particular, the applicability range of a specifically chosen gauge is rather narrow, and we cannot be positive about the compatibility of this gauge with actual dynamics. The method of resolving constraints, should we be able to implement it completely, would be an ideal tool for researchers, and this would mean that the true dynamics on the constraint manifold is found in the general case. However, it is difficult to realize this method technically because of the complicated structure of constraints.

It is possible that the true strategy for studying the reduction problem consists in combining the two methods.

In the present study, we try to solve all three problems indicated above.

1.1. Arnovit–Deser–Misner Parameters and Kinemetric Transformations

In order to construct the Hamiltonian formalism, it is necessary to separate space from time or to perform a so-called 3 + 1 partition of the spacetime into a set of spacelike hypersurfaces t = const. The Arnovit–Deser–Misner (ADM) parametrization

$$\begin{aligned} ds^2 &= g_{\alpha\beta}dx^\alpha dx^\beta \\ &= N^2dt^2 - h_{ij}(dx^i + N^i dt)(dx^j + N^j dt), \end{aligned} \tag{1}$$

which is unambiguously related to quantities that characterize the set of hypersurfaces t = const, is the most appropriate for this. Here, the lapse function N and the shift vector N^k are used to form the 4-vector $\nu^\alpha = (1/N, -N^k/N)$, which is a unit normal to the hypersurface. By additionally using the intrinsic metric h_{ij}, we can specify the second quadratic form as

$$b_{ij} = \frac{1}{2N}(\dot{h}_{ij} - \nabla_i N_j - \nabla_j N_i), \tag{2}$$

which determines the embedding of the three-dimensional hypersurface into the enveloping four-dimensional spacetime. Coordinate transformations that preserve a given partition into a set of hypersurfaces t = const are referred to as kinemetric transformations [13, 14]:

$$t' = t'(t),$$

$$x' = x'(t, x).$$

For the lapse function N and the shift vector N^k, the corresponding transformations are

$$N' = N\frac{dt}{dt'}, \tag{3}$$

$$N'^k = N^i \frac{\partial x'^k}{\partial x^i}\frac{\partial t}{\partial t'} - \frac{\partial x^i}{\partial t'}\frac{\partial x'^k}{\partial x^i}. \tag{4}$$

The first and the second quadratic form change in this case as rank-2 3-tensors. We can also find out how the ADM parameters change under nonkinemetric transformations [15], which correspond to a transition from one set of hypersurfaces to another. Nevertheless, we will use only kinemetric transformations because this corresponds to fixing a 3 + 1 partition. The conditions of this fixing will be specified below.

We note here that kinemetric transformations of coordinates include the reparametrization of time, $t' = t'(t)$. It is this reparametrization invariance of the action functional that plays a key role in defining the reduction procedure and in constructing a nonzero Hamiltonian.

1.2. Invariance under Time Reparametrization and Reduction

Let us consider the reparametrization-invariant system specified by

$$\begin{aligned} &W^E[p_i, q_i;\ p_0, q_0|t, N] \\ &= \int_{t_1}^{t_2} dt\left(-p_0\dot{q}_0 + \sum_i p_i\dot{q}_i - NH_E(q_0, p_0;\ q_i, p_i)\right), \end{aligned} \tag{5}$$

where

$$H_E(q_0, p_0;\ q_i, p_i) = [-p_0 + H(p_i, q_i)] \tag{6}$$

is the extended Hamiltonian.

The action functional (5) was constructed on the basis of the conventional action functional

$$W^R[p_i, q_i|q_0] = \int_{q_0(1)}^{q_0(2)} dq_0\left[\sum_i p_i\frac{dq_i}{dq_0} - H(p_i, q_i)\right] \tag{7}$$

of classical mechanics by introducing an additional pair of canonical variables, (p_0, q_0), and a Lagrange multiplier, N.

A reduction of the extended system specified by (5) to (7) means exactly solving the equations

$$\frac{\delta W}{\delta N} = 0 \longrightarrow -p_0 + H(p_i, q_i) = 0, \tag{8}$$

$$\frac{\delta W}{\delta q_0} = 0 \longrightarrow \dot{p}_0 = 0, \tag{9}$$

$$\frac{\delta W}{\delta p_0} = 0 \longrightarrow dq_0 = Ndt \equiv dT. \tag{10}$$

Equation (8) is a constraint, Eq. (9) is a conservation law, and Eq. (10) establishes a relation between the parameter of evolution for the reduced system specified by (7) and the Lagrange time,

$$dT = Ndt. \tag{11}$$

The Lagrange time is an invariant $[T(t') = T(t)]$.

In our case, the two times q_0 and T coincide. In relativistic mechanics specified by the action functional

$$W^E[p_i, q_i; p_0, q_0|t, N] = \int_{t_1}^{t_2} dt\left(-p_0\dot{q}_0 + \sum_i p_i\dot{q}_i - \frac{N}{2m}[-p_0^2 + p_i^2 + m^2]\right), \quad (12)$$

this is not so. In such a theory, the constraint equation

$$-p_0^2 + p_i^2 + m^2 = 0$$

is usually solved for the momentum appearing in the extended Hamiltonian with a negative sign; that is,

$$\frac{\delta W}{\delta N} = 0 \longrightarrow (p_0)_\pm = \pm\sqrt{p_i^2 + m^2}. \quad (13)$$

Thus, the variable conjugate to this momentum becomes the parameter of evolution for the corresponding reduced system:

$$W^R_{(\pm)}[p_i, q_i|q_0] = \int_{q_0(1)}^{q_0(2)} dq_0\left[\sum_i p_i\dot{q}_i \mp \sqrt{p_i^2 + m^2}\right]. \quad (14)$$

This corresponds to resolving the constraint equation.

A variation of the action functional (12) with respect to the additional momentum p_0 yields

$$\frac{\delta W}{\delta p_0} = -\frac{dq_0}{dt} + N\frac{p_0}{m} = 0$$
$$\longrightarrow T_{(q_0)_\pm} = \pm\int_0^{q_0} dq_0\frac{m}{\sqrt{p_i^2 + m^2}}. \quad (15)$$

On the manifolds specified by the equations of motion, formula (15) represents a Lorentz transformation of the proper time q_0 of a particle into the proper time $T = q_0\sqrt{1 - v^2}$ of an observer.

In contrast to what occurs in classical mechanics, the parameter of evolution here does not coincide with the Lagrange time, which is measured in the comoving reference frame.

We note that any reparametrization-invariant theory involves three times: (i) the coordinate time t [the corresponding Hamiltonian vanishes on the manifold specified by the constraint in (8)], which is unobservable; (ii) the invariant Lagrange time T constructed with the aid of the Lagrange multiplier (11) (in the case of relativistic mechanics, it coincides with the particle proper time);[1)] and (iii) the dynamical parameter of evolution for the corresponding reduced system {in our case [specified by Eq. (7)], this is q_0}.

The last two times are related by the equation of motion for the additional momentum. The idea of this classification of time in reparametrization-invariant theories was set forth by Gyngazov *et al.* [16], who also gave a prescription for a Hamiltonian reduction of such theories. Briefly, it amounts to the following.

In the process of Hamiltonian reduction, any extended system specified by

$$W^{ES}[p_i, q_i; p_0, q_0|t, N] = \int_{t_1}^{t_2} dt\left(-p_0\dot{q}_0 + \sum_i p_i\dot{q}_i - NH^{ES}(q_0, p_0; q_i, p_i)\right)$$

is split into two subsets of equations. The first is a set of reduced subsystems specified by

$$W^{RS}_{(1,2,\ldots)}[p_i, q_i|q_0] = \int_{q_0(1)}^{q_0(2)} dq_0\left[\sum_i p_i\frac{dq_i}{dq_0} - H^{RS}_{(1,2,\ldots)}\right]$$

and associated with various solutions to the Hamiltonian constraint equation

$$H^{ES} = 0 \longrightarrow P_{0(1,2,\ldots)} = H^{RS}_{(1,2,\ldots)}.$$

The second is determined by the equations for the additional momentum,

$$\frac{\delta W^{ES}}{\delta p_0} = 0 \longrightarrow \frac{dq_0}{dT} = -\frac{\partial H^{ES}}{\partial p_0} = \sqrt{\rho(q_0)}$$
$$\longrightarrow T(q_0) = \int_0^{q_0}\frac{dq_0}{\sqrt{\rho(q_0)}}, \quad (16)$$

and for the additional coordinate that reduces to the dynamical parameter of evolution. Equation (16) describes the evolution of the proper time with respect to the dynamical parameter of the reduced system.

It should be noted here that, for the Hamiltonian reduction, the following two statements are valid:

(i) The parameter of evolution for the reduced system is one of the original dynamical variables of the extended system.

(ii) The variational principle must be supplemented with a convention on the measurable time.

Thus, it is shown by exactly resolving the Hamiltonian constraint that one of the primary variables of the original extended system drops out from the phase space and becomes the parameter of evolution for the reduced system. The action functional for a reparametrization-invariant theory must be supplemented with a geometric convention according to which the measurable time interval is put into correspondence with the parameters and variables of the extended system. In addition, we have proper-time dynamics described by two equations, one for the additional momentum and one for the coordinate. In the special theory of relativity, proper-time dynamics is merely represented by the

[1)] By the term proper time, we will henceforth imply the Lagrange time.

relation between the proper time of an observer and the proper time of a particle (Lorentz transformation).

1.3. Formulation of the Problem

The main objectives of the present study are to construct consistently and to justify a Hamiltonian reduction for the general theory of relativity in a form as general as is possible, to perform a dynamical analysis of this system in the present context, and to formulate perturbation theory in the reduced theory and to investigate the linear approximation.

In accordance with all the aforesaid, this article is organized as follows. Section 2 is devoted to describing and justifying the method of Hamiltonian reduction implemented in the general theory of relativity by introducing a global variable and by resolving one Hamiltonian constraint. The meaning of the reduced action functional in relation to the original theory is discussed further. In Section 3, we formulate perturbation theory and analyze linearized theory.

1.4. Notation

In this article, we use the following notation. The signature of the metric of spacetime is (1, –1, –1, –1). The Greek indices $\alpha, \beta, \gamma, \ldots$ run through the values 0, 1, 2, 3 and denote world tensor indices. The Latin indices run through the values 1, 2, 3 and label space components of tensors. The symbol ∇_i denotes a covariant differentiation for the intrinsic metric h_{ij} of the spacelike hypersurface, while ∇_α denotes a covariant differentiation for the 4-metric of spacetime. The Riemann curvature tensor is defined as

$$R^i_{.klm}(h) = \frac{\partial\Gamma^i_{km}}{\partial x^l} - \frac{\partial\Gamma^i_{kl}}{\partial x^m} + \Gamma^i_{nl}\Gamma^n_{km} - \Gamma^i_{nm}\Gamma^n_{kl},$$

$$R_{km} = R^i_{.kim}, \quad \nabla_l\nabla_k A^i - \nabla_k\nabla_l A^i = -A^m R^i_{.mkl}.$$

2. HAMILTONIAN REDUCTION IN THE GENERAL THEORY OF RELATIVITY

2.1. Extended Action Functional

We proceed from the Einstein–Hilbert action functional, where an electromagnetic field is chosen for matter. We have

$$W(g|\mu) = \int d^4x\sqrt{-g}\left[-\frac{\mu^2}{6}R(g) - \frac{1}{4}F_{\mu\nu}F^{\mu\nu}\right], \quad (17)$$

$$\mu^2 = M_{\rm Pl}^2\frac{3}{8\pi}, \quad F_{\mu\nu} = \partial_\mu A_\nu - \partial_\nu A_\mu,$$

where $M_{\rm Pl}$ is the Planck mass. In order to perform a reparametrization-invariant Hamiltonian reduction, we must single out an additional variable and resolve the constraint with respect to the momentum conjugate to this variable. This variable must depend only on time; that is, it must be global. Naturally, there is no such variable in the original set of variables. Let us introduce it by parametrizing the metric as

$$g(t, x)_{\alpha\beta} = \left(\frac{\phi(t)}{\mu}\right)^2\bar{g}_{\alpha\beta}(t, x), \quad (18)$$

where $\phi(t)$ is a scalar conformal factor. Thus, we introduce the required additional global variable and formally fix a kinemetric group. Indeed, the function ϕ defined as that which is a scalar and which depends only on time preserves these properties only under kinemetric transformations. Under nonkinemetric transformations—for example, under the $t' = t'(t, x)$ tranformation—ϕ ceases to be a function that depends only on time. Thus, the action functional takes the form

$$W(\bar{g}|\phi) = \int d^4x\sqrt{-\bar{g}}\left[-\frac{\phi^2}{6}R(\bar{g}) + \phi\nabla^\alpha\nabla_\alpha\phi - \frac{1}{4}F_{\mu\nu}F^{\mu\nu}\right]. \quad (19)$$

For the metric $\bar{g}_{\alpha\beta}$, we choose the parametrization

$$\bar{g}_{\alpha\beta} = \begin{pmatrix} (\mathcal{N}N_0(t))^2 - N_kN^k & -N_k \\ -N_k & -h_{ij} \end{pmatrix}. \quad (20)$$

From the standard ADM parametrization, this parametrization differs only by a factorization of the lapse function into two factors, a local and a global one:

$$N(t, x) = \mathcal{N}(t, x)N_0(t). \quad (21)$$

Under kinemetric changes of variables, the global lapse function $N_0(t)$ transforms as

$$N_0' = N_0\frac{\partial t}{\partial t'};$$

at the same time, the local lapse function $\mathcal{N}(t, x)$ remains a kinemetric scalar. In terms of the ADM parametrization (20), the action functional can be represented as

$$W(\bar{g}|\phi) = \int dtd^3x\mathcal{N}N_0\sqrt{h}\left[\frac{\phi^2}{6}R(h) - \frac{4}{6}\overset{\odot}{\phi}\phi b + \frac{\phi^2}{6}(b_{ij}b^{ij} - b^2) - \overset{\odot}{\phi}^2 - \frac{1}{4}F_{ij}F^{ij}\right. \quad (22)$$

$$\left. + \frac{1}{2N_0^2\mathcal{N}^2}(F^i_{n.}F_{mi}N^nN^m + 2N^nF^i_{n.}F_{i0} + F^i_{0.}F_{0i})\right] + \Sigma,$$

where

$$\overset{\odot}{\phi} = \frac{1}{\mathcal{N}N_0}\frac{\partial\phi}{\partial t}, \quad (23)$$

$$b_{ij} = \frac{1}{2\mathcal{N}N_0}(\dot{h}_{ij} - \nabla_iN_j - \nabla_jN_i), \quad (24)$$

and

$$\Sigma = \int dt d^3x \Big[\partial_0 \Big(\sqrt{h}\dot{\phi} + \sqrt{h}\frac{1}{3}\phi^2 b \Big) - \frac{1}{3}\phi^2 \partial_i \sqrt{h}(\partial^i(\mathcal{N}N_0) + N^i b) \Big] \quad (25)$$

is a surface term.

To compensate for the introduction of two additional global variables, it is necessary to introduce two global conditions in order to preserve the original number of independent variables. One of these conditions can be chosen as

$$\int d^3x \sqrt{h} b = 0. \quad (26)$$

It diagonalizes the kinetic term in the action functional. The second global condition will be introduced below.

By going over to the first-order formalism, we obtain the action functional in the form

$$W^{(I)} = \int dt [P_0\dot{\phi} + \int d^3x (P^{ij}\dot{h}_{ij} + P^i\dot{A}_i) - H], \quad (27)$$

with the extended Hamiltonian being given by

$$H = N_0 \Big(-\frac{P_0^2}{4E} + \int d^3x \sqrt{h}\mathcal{N}\mathcal{H} \Big) + \int d^3x (2P^{ij}\nabla_i N_j + P^i F_{ni} N^n + P^i \partial_i A_0) - \Sigma, \quad (28)$$

where

$$\Sigma = \partial_0 \Big(-\frac{P_0}{2} \Big) - \frac{\phi^2}{3} \int d^3x \partial_i (\sqrt{h}(N_0 \partial^i \mathcal{N} + N^i b)), \quad (29)$$

$$\mathcal{H} = -\frac{\phi^2}{6} R(h) + \frac{6}{\phi^2 (\sqrt{h})^2} \Big(P^{ij}P_{ij} - \frac{1}{2}P^2 \Big) + \frac{1}{4}F_{ij}F^{ij} + \frac{1}{2}\frac{P_i P^i}{(\sqrt{h})^2}, \quad (30)$$

$$E = \int d^3x \frac{\sqrt{h}}{\mathcal{N}}. \quad (31)$$

Here, $\{P^{ij}, h_{ij}\}$, $\{P^i, A_i\}$ is the set of canonically conjugate variables, while $\{P_0(t), \phi(t)\}$ are additional global variables.

The set of constraints is given by

$$\frac{\delta W^{(I)}}{\delta N_0} = 0 \longleftrightarrow \frac{P_0^2}{4E} = \int d^3x \sqrt{h}\mathcal{N}\mathcal{H}, \quad (32)$$

$$\frac{\delta W^{(I)}}{\delta \mathcal{N}} = 0 \longleftrightarrow \frac{P_0^2}{4E^2\mathcal{N}^2} = \mathcal{H}, \quad (33)$$

$$\frac{\delta W^{(I)}}{\delta N^i} = 0 \longleftrightarrow -2\nabla_j P_i^j + P^j F_{ij} = 0, \quad (34)$$

$$\frac{\delta W^{(I)}}{\delta A_0} = 0 \longleftrightarrow \nabla_i P^i = 0. \quad (35)$$

We note that the constraint in (32) can be obtained from (33) by means of integration over space. The additional momentum satisfies the equation

$$\frac{\delta W^{(I)}}{\delta P_0} = 0 \longleftrightarrow \dot{\phi} = -N_0 \frac{P_0}{2E}. \quad (36)$$

2.2. Reduction

In accordance with the prescription of Hamiltonian reduction, we resolve constraint (32) for the additional momentum P_0; further, we use Eq. (33) to determine the local lapse function $\mathcal{N}$. As a result, we arrive at

$$P_0 = \pm 2 \int d^3x \sqrt{h}\sqrt{\mathcal{H}} \equiv H_{(R)}, \quad (37)$$

$$\mathcal{N} = \frac{|P_0|}{2E\sqrt{\mathcal{H}}}, \quad (38)$$

where $H_{(R)}$ is the generator of evolution with respect to ϕ.[2)] By taking into account solutions to the constraints in (37) and (38), we can recast the action functional into the form (the surface term is omitted here)

$$W^{(I)} = \int_{\phi_1}^{\phi_2} d\phi \int d^3x [P^{ij}\partial_\phi h_{ij} + P^i \partial_\phi A_i - 2\sqrt{h}\sqrt{\mathcal{H}} - (2P^{ij}\nabla_i N_j + P^i F_{ni} N^n + P^i \partial_i A_0)]. \quad (39)$$

On the manifold specified by the remaining transverse constraints (34) and (35), this action functional has a nonzero local Hamiltonian:

$$W^{(I)} = \int_{\phi_1}^{\phi_2} d\phi \int d^3x [P^{ij}\dot{h}_{ij} + P^i \dot{A}_i - H_{(R)}] \quad (40)$$

(an overdot denotes differentiation with respect to ϕ). The relevant reduced Hamiltonian is constructed from time-reparametrization invariants; it completely specifies the dynamics of the variables $\{P^{ij}, h_{ij}\}$ and $\{P^i, A_i\}$ entering into it. Since nondynamical variables (in particular, the local lapse function $\mathcal{N}$) are eliminated from this system, its dynamics is determined unambiguously.

In order to establish correspondence with the general theory of relativity, we need here the additional relations (36)–(38). We now recall that we have at our disposal an additional global condition that we must impose on the parameters of the extended action functional and which we choose in the form

$$E = \int d^3x \frac{\sqrt{h}}{\mathcal{N}} = V_0, \quad (41)$$

[2)]For the sake of definiteness, we will henceforth always take a negative sign in (37). Geometrically, this corresponds to the fact that the congruence of observers that is normal to the hypersurfaces t = const diverges with time.

where V_0 is a fixed constant, $\partial_\phi V_0 = 0$. Relations (38), (37), and (36) are written as

$$\mathcal{N} = \frac{|P_0|}{2V_0\sqrt{\mathcal{H}}}, \tag{42}$$

$$P_0 = -2\int d^3x\sqrt{h}\sqrt{\mathcal{H}}, \tag{43}$$

$$2V_0\frac{d\phi}{P_0} = -N_0 dt \equiv -d\eta. \tag{44}$$

Eliminating P_0 from (42) and (44) with the aid of (43), we can recast these equations into the form

$$\mathcal{N} = \frac{1}{\sqrt{\mathcal{H}}}\frac{d\phi}{d\eta}, \tag{45}$$

$$\frac{d\phi}{d\eta} = \frac{\int d^3x\sqrt{h}\sqrt{\mathcal{H}}}{V_0}, \tag{46}$$

where $d\eta$ is an interval invariant under time reparametrizations.

The dynamical system specified by the reduced action functional (40) and supplemented with relations (45) and (46) determines completely the metric of spacetime in the general theory of relativity in the coordinate frame where $g_{0i} = 0$.

Let us demonstrate theoretically how the above scheme works.

We specify the initial data $\{P^{ij}, h_{ij}\}|_{\phi=\phi_0}$ and $\{P^i, A_i\}|_{\phi=\phi_0}$, where P^{ij} and P_i satisfy the transverse constraints (34) and (35). By using the reduced Hamiltonian $H_{(R)}$, we then obtain $h_{ij}(\phi, x^i)$ and $A_i(\phi, x^i)$. From relation (46), we further find the dependence of ϕ on η; after that, we deduce the local lapse function $\mathcal{N}$ from (45). Thus, we completely determine the metric (18) of spacetime in the coordinate frame where all g_{0i} vanish.

We use the following classification of time: (i) the coordinate time t (the corresponding Hamiltonian vanishes on the manifold specified by the relevant constraint), which is unobservable; (ii) the invariant Lagrange time η constructed with the aid of the Lagrange multiplier N_0; and (iii) the dynamical parameter of evolution for the corresponding reduced system (it is equal to ϕ in our case).

In addition, the general theory of relativity specifies the measurable proper time of an observer at rest,

$$dT = \left(\frac{\phi(\eta)}{\mu}\right)\mathcal{N}(\phi, x^i)d\eta. \tag{47}$$

We would like to highlight the following special features of the reduced action functional:

(I) The Hamiltonian density $2\sqrt{\mathcal{H}}$ is a local function of field variables; moreover, it is a kinemetric scalar.

(II) The Hamiltonian density (and, hence, the reduced Hamiltonian itself) does not vanish on the manifold specified by the equations of motion; otherwise, this would contradict relation (45) (the lapse function cannot be equal to zero).

(III) The reduced Hamiltonian explicitly depends on time (on the evolution parameter ϕ).

The first two features are quite appealing from the point of view of interpreting the Hamiltonian density on the manifold specified by the equations of motion as measurable-energy density. The time dependence of the Hamiltonian complicates the construction of conservation laws—for example, the law of energy conservation. Nevertheless, we will further associate the concept of the physical energy of fields with the reduced Hamiltonian. In the next section, this question will be analyzed within linearized theory in more detail.

Here, we note that Eq. (45) directly relates the concept of the lapse function to the Hamiltonian density and, hence, to the density of the field energy.

Problems associated with the validation of the Hamiltonian reduction were investigated in [15, 17], where it was proven that no choice of coordinate frame can lead to the vanishing of the global momentum.

3. PERTURBATION THEORY

We begin to formulate perturbation theory by considering the reduced system specified by Eq. (40), for which we introduce the expansions

$$h_{ij} = h_{ik}^{(0)} + h_{ij}^{(1)} + h_{ij}^{(2)} + \ldots, \tag{48}$$

$$P^{ij} = P^{(1)ij} + P^{(2)ij} + \ldots, \tag{49}$$

where $h_{ij}^{(1)}$ and $P^{(1)ij}$ are perturbations of order λ, $\lambda \ll 1$, while $h_{ij}^{(2)}$ and $P^{(2)ij}$ are perturbations of order λ^2. The metric $h_{ik}^{(0)}$ is some background metric in whose vicinity the expansions are performed. Let us also assume that all perturbation fields admit a decomposition into the transverse and the longitudinal parts [2–5] with respect to the metric $h_{ik}^{(0)}$:

$$f_{ik} = f_{ik}^{TT} + f_{ik}^{T} + f_{ik}^{L}, \tag{50}$$

$$\nabla^i f_{ik}^{TT} = 0, \quad f_{ik}^{TT}h^{(0)ik} = 0, \quad f_{ik}h^{(0)ik} = f_{ik}^{T}h^{(0)ik}, \tag{51}$$

$$\nabla^i(f_{ik} - f_{ik}^{T}) = \nabla^i f_{ik}^{L}, \quad f_{ik}^{L}h^{(0)ik} = 0. \tag{52}$$

Hereafter, the covariant derivative is consistent with respect to the background metric as well. Since there are no nondynamical variables in the reduced action functional, consistent calculations within perturbation theory do not involve difficulties of fundamental character.[3)]

[3)] If difficulties of a technical character that are associated with complexity and nonlinearity are not considered to be fundamental.

3.1. Zero-Order Approximation

Let us assume that the metric of the zero-order approximation is the Friedmann–Robertson–Walker metric

$$\begin{aligned} ds^2_{(0)} &= h^{(0)}_{ij}dx^i dx^j \\ &= r_0^2(d\chi^2 + f^2(\chi)(d\theta^2 + \sin^2\theta d\phi^2)), \end{aligned} \tag{53}$$

where $f(\chi) = \{\sin\chi, \chi, \sinh\chi\}$ for the spaces of, respectively, positive, zero, and negative curvature and r_0 is a constant having dimensions of length.

In the zero-order approximation, $\mathcal{H}$ is given by

$$\mathcal{H} = \mathcal{H}^{(0)} + \ldots = -k\frac{\phi^2}{r_0^2} + \frac{1}{4}F_{ij}F^{ij} + \frac{1}{2}\frac{P_iP^i}{(\sqrt{h^{(0)}})^2} + \ldots, \tag{54}$$
$$k = 1, 0, -1.$$

Since the dynamics of matter fields is of no interest to us, we take the contribution of matter in the form of an effective constant C_0; that is,

$$\mathcal{H} = \mathcal{H}^{(0)} + \ldots = -k\frac{\phi^2}{r_0^2} + C_0 + \ldots, \tag{55}$$
$$k = 1, 0, -1.$$

Substituting (55) into the additional relations (46) and (45), we obtain

$$\begin{aligned} d\eta &\approx \frac{V_0 d\phi}{4\pi r_0^3 \int d\chi f^2(\chi)\sqrt{-k\frac{\phi^2}{r_0^2} + C_0}}, \\ \mathcal{N} &\approx \frac{4\pi r_0^3 \int d\chi f^2(\chi)}{V_0}. \end{aligned} \tag{56}$$

We now determine the constant V_0 in such a way that the local lapse function is $\mathcal{N} \approx 1$. For the cases of $k = 0, -1$—that is, for open spaces—the integral $\int_0^\infty d\chi f^2(\chi)$ and the constant $V_0(\chi)$ are divergent. We can then admit the existence of the limit

$$\mathcal{N} \approx \lim_{\chi\to\infty}\frac{4\pi r_0^3\int_0^\chi d\chi' f^2(\chi')}{V_0(\chi)} = 1, \tag{57}$$

in which case expression (46) takes the form

$$d\eta \approx \frac{d\phi}{\sqrt{-k\frac{\phi^2}{r_0^2} + C_0}}. \tag{58}$$

Thus, we have completely determined the metric in (18) in the zero-order approximation. With allowance for the above two relations, this metric determines the Friedmann–Robertson–Walker metric of the space filled with a photon gas whose energy density ε is proportional to C_0/ϕ^4. Relations (45) and (46) and the expression for $\mathcal{H}^{(0)}$ specify the law of evolution of the cosmological Friedmann metric in terms of the global motion of the system.

3.2. Linearized Approximation

We assume that interaction between matter and gravity is negligibly small. Moreover, only the effective constant C_0 is retained as the contribution of matter in this approximation, since we are going to investigate the dynamics associated exclusively with gravitational perturbations. We begin by considering the linearized constraint (34):

$$\nabla_i P^{(1)i}_j \approx 0. \tag{59}$$

Considering that $P^{(1)}_{ij}$ is expressed in terms of $\dot{h}^{(1)}_{ij}$ as

$$P^{(1)}_{ij} \approx \frac{1}{2}\sqrt{h^{(0)}}(\dot{h}^{(1)}_{ij} - h^{(0)}_{ij}\dot{h}^{(1)}), \quad \dot{h}^{(1)} = \dot{h}^{(1)}_{kl}h^{(0)kl}, \tag{60}$$

and that $h^{(0)}_{kl}$ is independent of time and using (59), we obtain

$$\nabla^i(h^{(1)}_{ij} - h^{(0)}_{ij}h^{(1)}) \approx 0. \tag{61}$$

The last expression is a corollary of the transverse constraint rather than a gauge condition. We now go over from the canonical set of variables $\{P^{(1)ij}, h^{(1)}_{ij}\}$ to a new set of variables $\{\tilde{P}^{ij}, \tilde{h}_{ij}\}, \left\{\frac{1}{3}P^{(1)}, h^{(1)}\right\}$ by means of the transformation

$$\begin{aligned} \tilde{P}^{ij} &= P^{(1)ij} - \frac{1}{3}h^{(0)ij}P^{(1)}, \\ \tilde{h}_{ij} &= h^{(1)}_{ij} - \frac{1}{3}h^{(0)}_{ij}h^{(1)}, \\ P^{(1)} &= h^{(0)}_{ij}P^{(1)ij}, \\ h^{(1)} &= h^{(0)}_{ij}h^{(1)ij}. \end{aligned} \tag{62}$$

This transformation is not canonical for $h^{(1)} \neq 0$, but it is nondegenerate, so that we can investigate the dynamics in question by using the new set of variables. The reduced action functional takes the form

$$W^{(I)} = \int d\phi\left[\int d^3x\left[\tilde{P}^{ij}\dot{\tilde{h}}_{ij} + \frac{1}{3}P^{(1)}\dot{h}_{(1)}\right] - H_{(R)}\right], \tag{63}$$

where

$$H_{(R)} = H^{(0)}_{(R)} + H^{(2)}_{(R)} + \ldots. \tag{64}$$

Apart from a time-dependent coefficient, the kinetic part $H^{(2)}_{(R)}$ can be written as

$$H^{(0)}_{(R)} \sim \int d^3x\frac{1}{\sqrt{h}}\left(\tilde{P}^{ij}\tilde{P}_{ij} - \frac{1}{6}P^{(1)2}\right). \tag{65}$$

The transverse expansion [2–5] for $\tilde{P}_{ij}$ has the form

$$\tilde{P}_{ij} = P_{ij}^{(TT)} + \nabla_i W_j + \nabla_j W_i + 2\left(\nabla_i\nabla_j W - \frac{1}{3}h_{ij}^{(0)}\Delta W\right), \quad (66)$$

where W_j is a transverse vector, $\nabla_i W^i = 0$, and $P_{ij}^{(TT)}$ is the traceless transverse part.

The constraint equation (59) can now be represented in the form

$$\nabla^i\left[\nabla_i W_j + \nabla_j W_i + 2\left(\nabla_i\nabla_j W - \frac{1}{3}h_{ij}^{(0)}\Delta W\right)\right] = \frac{1}{3}\nabla_j P^{(1)}. \quad (67)$$

Considering that the metric $h_{ij}^{(0)}$ is isotropic, $R(h^{(0)})_{ij} = 2kh_{ij}^{(0)}$, and that, if two vectors are equal to each other, their transverse and longitudinal parts are also equal, we have $W^i = 0$, and Eq. (67) reduces to

$$2\left(\Delta\nabla_j W - \frac{1}{3}\nabla_j\Delta W\right) = \frac{1}{3}\nabla_j P^{(1)}. \quad (68)$$

The last equation can be recast into the form

$$2\left(\nabla_j\Delta W + 2k\nabla_j W - \frac{1}{3}\nabla_j\Delta W\right) = \frac{1}{3}\nabla_j P^{(1)}, \quad (69)$$

whence we obtain

$$2\left(\frac{2}{3}\Delta W + 2kW\right) = \frac{1}{3}P^{(1)}. \quad (70)$$

We further consider the case of $k = 0$—that is, the case where the background metric is flat. We then have

$$4\Delta W = P^{(1)}. \quad (71)$$

In this case, the transverse expansion can be represented as

$$\tilde{P}_{ij} = P_{ij}^{(TT)} + 2\left(\nabla_i\nabla_j W - \frac{1}{3}h_{ij}^{(0)}\Delta W\right), \quad (72)$$

where W satisfies Eq. (71).

Taking into account the last expansion and calculating the right-hand side of (65), we arrive at

$$\int d^3x\frac{1}{\sqrt{h}}\left(\tilde{P}^{ij}\tilde{P}_{ij} - \frac{1}{6}P^{(1)2}\right) = \int d^3x\frac{1}{\sqrt{h}}\left[P_{ij}^{(TT)2} + 4\left(\nabla_i\nabla_j W - \frac{1}{3}h_{ij}^{(0)}\Delta W\right)\left(\nabla^i\nabla^j W - \frac{1}{3}h^{(0)ij}\Delta W\right) - \frac{1}{6}P^{(1)2}\right] = \int d^3x\frac{1}{\sqrt{h}}\left[P_{ij}^{(TT)2} + 4\left(\nabla_i\nabla_j W - \frac{1}{3}h_{ij}^{(0)}\Delta W\right) \times (\nabla^i\nabla^j W) - \frac{1}{6}P^{(1)2}\right] = \int d^3x\frac{1}{\sqrt{h}}\left[P_{ij}^{(TT)2} - \frac{2}{3}\nabla^i P^{(1)}\nabla_i W - \frac{1}{6}P^{(1)2}\right] = \int d^3x\frac{1}{\sqrt{h}}\left[P_{ij}^{(TT)2} + \frac{2}{3}P^{(1)}\Delta W - \frac{1}{6}P^{(1)2}\right] = \int d^3x\frac{1}{\sqrt{h}}[P_{ij}^{(TT)2}]. \quad (73)$$

We conclude that, in the second-order approximation, the quantity $P^{(1)}$ does not appear in the reduced Hamiltonian. This means that a variation of the reduced action functional with respect to $P^{(1)}$ leads to the equation

$$\dot{h}^{(1)} = 0. \quad (74)$$

Consequently, we can set $h^{(1)} = 0$ at the initial hypersurface, and this condition will be satisfied on all hypersurfaces at all subsequent instants of time. Thus, the pair of the variables $\{P^{(1)}, h^{(1)}\}$ drops out from the reduced Hamiltonian in the second-order approximation (linearized equations), and this follows from the transverse constraints and the Hamiltonian structure rather than from the gauge.

For the reduced Hamiltonian, we now present the full expression correct to the λ^2 terms inclusive. The quantity $\mathcal{H}$ then takes the form

$$\mathcal{H} \approx C_0\left(1 + \frac{1}{2}h_{ij}^{(TT)}h_{ij}^{(TT)}\right) + \left[\frac{6}{\phi^2}P_{ij}^{(TT)}P_{ij}^{(TT)} + \frac{\phi^2}{6}\frac{1}{4}\partial_k h_{ij}^{(TT)}\partial_k h_{ij}^{(TT)} + \frac{3}{2}\partial_l\partial_i(h_{ik}^{(TT)}h_{lk}^{(TT)})\right]. \quad (75)$$

Here, we have considered that a contribution that is proportional to λ^2 and which arises from the perturbation of the metric is added to the factor C_0 corresponding to the effective contribution of matter. It can be seen that, in $\mathcal{H}$, there is no contribution linear in λ. The reduced Hamiltonian assumes the form

$$H_{(R)} = 2\int d^3x\sqrt{h}\sqrt{\mathcal{H}} \approx \int d^3x\left[2\sqrt{C_0} + \frac{1}{\sqrt{C_0}}\left(\frac{6}{\phi^2}P_{ij}^{(TT)}P_{ij}^{(TT)} + \frac{\phi^2}{6}\frac{1}{4}\partial_k h_{ij}^{(TT)}\partial_k h_{ij}^{(TT)}\right)\right]. \quad (76)$$

Let us go over to a new set of variables $\{\pi^{ij}, \epsilon_{ij}\}$ by means of the transformations

$$\pi^{ij} = \frac{\sqrt{6}}{\phi}P^{(TT)ij}, \quad \epsilon_{ij} = \frac{\phi}{\sqrt{6}}h_{ij}^{(TT)}, \quad (77)$$

which are canonical in the limit of large ϕ. We then arrive at the reduced Hamiltonian in the form

$$H_{(R)} \approx \int d^3x [2\sqrt{C_0} + \frac{1}{\sqrt{C_0}}\left(\pi_{ij}\pi_{ij} + \frac{1}{4}\partial_k \epsilon_{ij}\partial_k \epsilon_{ij}\right) + \frac{\pi_{ij}\epsilon_{ij}}{\phi}]. \quad (78)$$

At ϕ values so large that the last term on the right-hand side of (78) can be disregarded, the reduced Hamiltonian $H_{(R)}$ exactly describes the wave equation, so that the concept of energy can be associated with this Hamiltonian.

A system specified by a Hamiltonian similar to that in (78) was analyzed in [18] within the holomorphic representation of the oscillatory approximation.

At small ϕ values, the Hamiltonian in (78) greatly depends on the evolution parameter. In this case, the reduced Hamiltonian can be represented in the form (we now investigate the more general case of $R^{(0)} = 6k/r_0^2$, $k = 1, 0, -1$)[4)]

$$H_{(R)} = \int d^3x \sqrt{h}\sqrt{\mathcal{H}} \approx \int d^3x \sqrt{h}\sqrt{-\frac{\phi^2}{r_0^2}k + \frac{6}{\phi^2}P_{ij}^{(TT)}P_{ij}^{(TT)}}. \quad (79)$$

The dynamical equation for $P_{ij}^{(TT)}$ has the form

$$\frac{d}{d\phi}P_{ij}^{(TT)} \approx 0; \quad (80)$$

that is, $P_{ij}^{(TT)}$ is independent of ϕ. The equation that relates the invariant time η to the evolution parameter ϕ (scale factor) has the form

$$d\eta \approx \frac{V_0 d\phi}{\int d^3x \sqrt{-\frac{\phi^2}{r_0^2}k + \frac{6}{\phi^2}P_{ij}^{(TT)}P_{ij}^{(TT)}}}. \quad (81)$$

Taking the integral in the denominator on the right-hand side of (81) to mean averaging over space and retaining only the space-averaged contribution to proper-time dynamics, we obtain

$$d\eta \sim \frac{d\phi}{\sqrt{-\frac{\phi^2}{r_0^2}k + \frac{C_1}{\phi^2}}}, \quad (82)$$

where C_1 is the averaged contribution from $6P_{ij}^{(TT)}P_{ij}^{(TT)}$. Equation (82) exactly replicates the dynamics of the scale factor of the cosmological Friedmann model for the extremely rigid equation of state for homogeneous matter.

[4)]We also set $C_0 = 0$.

Following the same line of reasoning, we can show that the averaged contribution of gravitational excitations to cosmological dynamics at large ϕ values corresponds to the Friedmann radiation-dominated Universe.

4. CONCLUSION

The reduction described above leads to a Hamiltonian theory invariant under time reparametrizations. The existence of a global partition of a 4-manifold into a family of spacelike hypersurfaces and the isolation of the dynamics of the global variable associated with this partition have made it possible to formulate, on the basis of the Einstein equations, a reduced theory featuring no nondynamical parameters. This version of solution to the reduction problem leads to a nonzero local Hamiltonian that serves as the generator of evolution of the reduced system with respect to the invariant parameter ϕ.

We note that the popular opinion that the gravitational energy is not localized in terms of the Hamiltonian formulation is based on the fact that the Hamiltonian conjugate to the noninvariant time t vanishes on the manifold specified by the equations of motion, so that a nonvanishing contribution can arise only from the surface terms in the action functional. If, however, the reduced Hamiltonian is associated with the concept of energy, we arrive at a well-defined local energy density for the gravitational field; moreover, this density is a kinemetric scalar. In this way, the Hamiltonian problem is solvable.

The proposed perturbation theory is free from drawbacks associated with ambiguities of nondynamical parameters like the lapse function, because they do not appear in the reduced Hamiltonian. The local lapse function, which is a nondynamical parameter, is determined in terms of the reduced Hamiltonian on the manifold specified by the equations of motion.

An analysis of linearized theory has revealed that there are no wave excitations of the gravitational field that make a negative contribution to the Hamiltonian. Since it is the Hamiltonian of linearized theory that determines the spectrum of particles in quantum theory, we can state that there are no particle-like gravitational excitations making a negative contribution to energy.

Yet another interesting statement can be made on the basis of a dynamical analysis of the reduced Hamiltonian of classical (nonquantum) theory in the limit of small ϕ: the effective equation of state for gravitational matter is the extremely rigid equation of state

$$\varepsilon = p.$$

ACKNOWLEDGMENTS

We are grateful to V.N. Pervushin, who formulated the problem considered here and made many enlighten-

ing comments, and to Yu.G. Paliĭ and V.V. Papoyan for stimulating discussions and advice.

This work was supported by the Bogolyubov–Infeld program.

REFERENCES

1. R. Arnovit, S. Deser, and C. W. Misner, Phys. Rev. **117**, 1595 (1960).
2. S. Deser, Ann. Inst. Henri Poincaré **VII**, 149 (1969).
3. M. Berger and D. Ebin, J. Diff. Geom. **3**, 379 (1969).
4. J. W. York, Ann. Inst. Henri Poincaré **XXI**, 319 (1974).
5. J. W. York, J. Math. Phys. **14**, 456 (1973).
6. A. Lichnerovicz, J. Math. Pure Appl. **23**, 37 (1944).
7. J. W. York, Phys. Rev. Lett. **26**, 1656 (1971).
8. J. W. York, Phys. Rev. Lett. **28**, 1082 (1972).
9. N. O. Murchanda and J. W. York, Phys. Rev. D **10**, 428 (1974).
10. T. Regge and C. Teitelboim, Ann. Phys. (N.Y.) **88**, 286 (1974).
11. V. N. Pervushin, V. V. Papoyan, G. A. Gogilidze, *et al.*, Phys. Lett. B **365**, 35 (1996).
12. K. Kuchar, J. Math. Phys. **11**, 3322 (1970).
13. A. L. Zel'manov, Dokl. Akad. Nauk SSSR **227**, 78 (1976) [Sov. Phys. Dokl. **21**, 147 (1976)].
14. Yu. S. Vladimirov, *Reference Frames in the Theory of Gravitation* (Énergoizdat, Moscow, 1982).
15. V. N. Pervushin and V. I. Smirichinski, Yad. Fiz. **61**, 142 (1998) [Phys. At. Nucl. **61**, 133 (1998)].
16. L. N. Gyngazov, M. Pawłowski, V. N. Pervushin, and V. I. Smirichinski, Gen. Relativ. Gravit. **30**, 1749 (1998).
17. V. N. Pervushin and V. I. Smirichinski, Yad. Fiz. **61**, 2294 (1998) [Phys. At. Nucl. **61**, 2180 (1998)].
18. V. N. Pervushin and V. I. Smirichinski, J. Phys. A **32**, 6191 (1999).

Translated by A. Isaakyan